

Université Fédérale



Toulouse Midi-Pyrénées

# THÈSE

Université  
de Toulouse

En vue de l'obtention du  
**DOCTORAT DE L'UNIVERSITÉ DE TOULOUSE**

Délivré par l'Institut National Polytechnique de Toulouse

---

Présentée et soutenue par

**Martin THOMAS**

Le 28 mai 2021

**Combustor-turbine interactions: Hot spot migration and thermal environment prediction for a better understanding and design of helicopter engines**

---

Ecole doctorale : **MEGEP - Mécanique, Energétique, Génie civil, Procédés**

Spécialité : **Dynamique des fluides**

Unité de recherche :

**CERFACS**

Thèse dirigée par

**Laurent GICQUEL et Florent DUCHAINE**

Jury

**M. Antonio ANDREINI**, Rapporteur

**Mme Marlene SANJOSE**, Rapporteur

**M. Stephane MOREAU**, Examineur

**M. Pascal BRUEL**, Examineur

**M. Nicolas GOURDAIN**, Examineur

**M. Laurent GICQUEL**, Directeur de thèse

**M. Florent Duchaine**, invité

**M. Charlie Koupper**, invité



---

## Abstract

This PhD thesis, funded by SAFRAN Helicopter Engines, focuses on Large Eddy Simulation (LES) of the FACTOR test rig to investigate combustor-turbine interactions in the context of next generation lean combustion engines. The FACTOR test rig is a full annular non-reactive lean combustion simulator with a single staged high-pressure turbine located at the DLR in Göttingen. Another test rig featuring three sectors or  $54^\circ$  of the full annular DLR test rig is available at the University of Florence. Both rigs provide a huge amount of validation data. In this thesis, certain aspects of LES in turbomachinery are investigated in detail and the manuscript is divided into two parts dealing respectively with the modeling of cooling systems and an analysis of the flow field in the combustion chamber and high-pressure vane passage. First, a heterogeneous and a homogeneous coolant injection model for multiperforated plates in combustion chambers are tested against experimental results. From this first study it is shown that the heterogeneous model allows for a more realistic coolant jet representation and should be retained for future simulations. In gas turbine engines the application of coolant systems is not only mandatory in the combustion chamber, but also in the first stages of the high-pressure turbine. The next section therefore investigates the previously presented heterogeneous injection model as a mean to model the effects of the NGV cooling system on the main flow and compares the simulation to a second one with a fully resolved coolant system. The second part deals with simulations that extend over combustion chamber and high-pressure vanes and specifically addresses the impact of the flow field in the combustor on the high-pressure vanes. The main objective here is to better understand wall temperature distribution on the turbine blade wall which is obtained by use of higher order statistics analysis to highlight thermally critical areas. Based on such coupled multiple component LES, a discussion is initiated to identify a path allowing to take into consideration the impact of the combustion chamber on isolated high-pressure vane simulations using different reconstructed unsteady inlet conditions.

**Keywords:** Large Eddy Simulation, Turbomachinery, Combustor-turbine interaction, FACTOR

---

## Résumé

Cette thèse, financée par SAFRAN Helicopter Engines, se concentre sur la simulation des grandes structures de la turbulence (LES) du banc d'essai FACTOR pour étudier les interactions chambre de combustion-turbine dans le contexte des moteurs à combustion de nouvelle génération. Le banc d'essai FACTOR est un simulateur annulaire complet de combustion pauvre non réactive composé d'une turbine haute pression à un étage situé au DLR à Göttingen. Un autre banc d'essai comportant trois secteurs ou  $54^\circ$  du DLR annulaire complet banc d'essai est également disponible à l'Université de Florence. Les deux appareils fournissent une grande quantité de données de validation. Dans cette thèse, certains aspects du LES dans les turbomachines sont étudiés en détail. Le manuscrit est divisé en deux parties traitant respectivement de la modélisation des systèmes de refroidissement et d'une analyse du champ d'écoulement dans la chambre de combustion et dans le passage des palettes haute pression. En premier lieu, un modèle d'injection de liquide de refroidissement hétérogène et homogène pour des plaques multi-perforées dans les chambres de combustion est comparé aux résultats expérimentaux. Cette première étude montre que le modèle hétérogène permet une représentation plus réaliste du jet de liquide de refroidissement et devrait être conservé pour de futures simulations. Dans les moteurs à turbine à gaz, l'application de systèmes de refroidissement est non seulement obligatoire dans la chambre de combustion, mais aussi dans les premiers étages de la turbine haute pression. Dans la section suivante, le modèle d'injection hétérogène présenté précédemment est étudié comme moyen de modéliser les effets du système de refroidissement NGV sur le flux principal. Cette simulation est alors comparée à une seconde avec un système de refroidissement entièrement résolu. La deuxième partie de cette thèse traite des simulations qui s'étendent sur la chambre de combustion et les palettes haute pression et s'intéresse spécifiquement à l'impact du champ d'écoulement dans la chambre de combustion sur les palettes haute pression. L'objectif principal est ici de mieux comprendre la répartition de la température de la paroi sur la paroi de l'aube de la turbine, qui est obtenue en utilisant une analyse statistique d'ordre supérieur pour mettre en évidence les zones thermiquement critiques. Sur la base de telles LES à composants multiples couplés, une discussion est amorcée pour identifier un chemin permettant de prendre en compte l'impact de la chambre de combustion sur des simulations de palettes haute pression isolées en utilisant différentes conditions d'entrée non stationnaires reconstruites.

**Mots clés:** simulation des grandes échelles, Turbomachine, interactions chambre-turbine, FACTOR

# Acknowledgements

First, I would like to thank Yoan Mery, who let me discover the world of LES and turbomachinery on the Silvercrest Engine almost a decade ago. This motivated me to specialize more in CFD and to work part time at the Combustion Institute of the German Aerospace Center in Stuttgart, where I learned a lot about tools and methods in CFD. In Montreal, I could apply my CFD knowledge in a collaboration with the experimentalist Etienne Robert and write my first scientific contribution. In Stanford I could deepen my knowledge on numerical methods together with Yu Lv and Mathias Ihme. Here I also met Thierry Poinso who pathed my way back to Europe and to CERFACS, where I worked on my PhD.

I wish to thank my supervisors Laurent and Florent for their help in the preparation of the defense, for their time and the numerous interactions we had during this work and Charlie additionally for his previous work I could base on. At this point, I also wish to acknowledge SAFRAN HE for funding this work and Lorenzo Pons for his interest in my work. I also thank the members of the jury for the detailed review of my work. Here I also wish to acknowledge Matthieu, my parrain de these and the ecole doctoral for their support in finalizing this work. In this context, I also want to give credits to the doctorials, a one week program to interact with other PhD students from various different fields. Here one could learn a lot about different topics and ways of working other PhD students were confronted with.

Specifically I wish to thank Alexander Krumme and Francois Cottier for the interesting technical discussions we had at the FACTOR meeting in Göttingen. In that respect I also wish to express my gratitude to the Antonio Adreini and his team who received me in Florence where I could get to know the experimental facilities and collaborate with Tommaso.

Mael my part time office mate was always very supportive during my time at CERFACS and SAFRAN HE. I also thank Fabien, Frederic, Soizic, Simon and Matthieu for the matches in the midday break. Without all the previous work from numerous other PhD students who directly or indirectly contributed to this work, I would never have gotten as far. I also acknowledge the work from the administrative staff and the computer support group, who always helped when there was an issue in their respective fields.

---

I also thank my new colleagues at Roche for the excellent working environment and support, which allowed me to discover an entirely new field of application for fluid dynamics.

In the end, I also thank my family for the unconditional support throughout this work. Special thanks also goes to my french family for the Corona home-office time and to Camille for les gateaux. Un grand merci also to Magali who always supported me and stayed by my side since we met in Stanford six years ago.

# Preamble

This PhD work, funded by SAFRAN, was performed within the framework of the FACTOR project ([www.factor-fp7.eu](http://www.factor-fp7.eu)) that has received funding from the European Union Seventh Framework Programme (FP7/ 2007-2018) under grant agreement number 265985.

This work was also granted access to the HPC resources of IDRIS ([www.idris.fr](http://www.idris.fr)) under the allocation 2018-A0032B10157 managed by GENCI (Grand Equipement National de Calcul Intensif).

---

# Contents

<b>Nomenclature</b>	<b>ix</b>
<b>List of Figures</b>	<b>xxii</b>
<b>List of Tables</b>	<b>xxiv</b>
<b>Chapter 1 General Introduction</b>	<b>1</b>
1.1 Aeronautical gas turbines . . . . .	2
1.2 The FACTOR project . . . . .	6
1.2.1 Test facilities . . . . .	6
1.2.2 CFD of the FACTOR test rig . . . . .	12
1.3 Objectives of this Thesis . . . . .	13
1.4 Organization of the Manuscript . . . . .	15
<b>Chapter 2 Simulation methods and diagnostics used in this work</b>	<b>19</b>
2.1 Computational Fluid Dynamics . . . . .	19
2.1.1 Governing equations . . . . .	22
2.1.2 The AVBP code . . . . .	27
2.2 Statistical tools and analysis of the LES predictions . . . . .	27
2.2.1 Higher order statistical moments . . . . .	28
2.2.2 Proper Orthogonal Decomposition . . . . .	30
2.2.3 Dynamic Mode Decomposition . . . . .	31
<b>Part I Cooling systems</b>	<b>33</b>
<b>Chapter 3 Effusion cooling systems</b>	<b>35</b>
3.1 Effusion Cooling models . . . . .	39
3.1.1 Homogeneous injection model . . . . .	40
3.1.2 Heterogeneous injection model . . . . .	40
3.2 Description of the test configuration . . . . .	43
3.3 Numerical Methodology . . . . .	44
3.4 Results and discussions . . . . .	46
3.4.1 Mean flow comparisons and validations . . . . .	47
3.4.2 RMS and turbulent quantities . . . . .	53
3.4.3 Unsteady feature in P40 . . . . .	55
3.5 Conclusion . . . . .	56

<b>Chapter 4</b>	<b>Assessment of a coolant injection model for cooled high-pressure vanes</b>	<b>59</b>
4.1	Introduction . . . . .	60
4.2	Coolant injection modeling . . . . .	61
4.3	Domain, mesh and LES modeling . . . . .	64
4.4	Results . . . . .	70
4.4.1	Mean flow operating conditions and flow organization . . . . .	70
4.4.2	Vane surface temperature predictions . . . . .	73
4.4.3	Investigation of the cooling film and mixing behavior . . . . .	75
4.5	Conclusion . . . . .	84
 <b>Part II Analysis of the combustor and high-pressure turbine flows</b>		<b>85</b>
<b>Chapter 5</b>	<b>Analysis of the chamber clocking position dependent heat load on the NGV surface</b>	<b>87</b>
5.1	Introduction . . . . .	87
5.2	Combustor-NGV Setup . . . . .	89
5.3	Results . . . . .	93
5.3.1	Flow field in the combustion chamber . . . . .	94
5.3.2	Flow field in the NGV passage . . . . .	108
5.4	Conclusion . . . . .	124
<b>Chapter 6</b>	<b>Towards accurate isolated stator LES</b>	<b>127</b>
6.1	Introduction . . . . .	127
6.2	Numerical Setup and Operating point . . . . .	129
6.3	Analysis of the flow field using POD . . . . .	131
6.3.1	Investigation of the flow field in the integrated domain . . . . .	131
6.3.2	Investigation of the flow field on P40 . . . . .	132
6.4	Towards predictive LES of isolated NGVs . . . . .	134
6.4.1	POD reconstructed flow field in P40 . . . . .	135
6.4.2	Impact of the inflow specification on the LES prediction of an isolated NGV . . . . .	138
6.4.3	Evolution of the flow field through the vane passage . . . . .	142
6.4.4	Impact on the high-pressure vanes . . . . .	148
6.5	Conclusions . . . . .	150
<b>Chapter 7</b>	<b>Combustor turbine interactions</b>	<b>153</b>
7.1	Introduction . . . . .	153
7.2	Experimental Setup . . . . .	154
7.3	Domain, Mesh and Numerical Setup . . . . .	155
7.4	Results . . . . .	157
7.4.1	Flow field in the combustor simulator . . . . .	157
7.4.2	Flow field in the high-pressure vane passage . . . . .	161
7.4.3	Flow field in the rotor . . . . .	165
7.5	Conclusions . . . . .	169

General conclusion and perspectives	169
Appendix A Impact of Sub grid Scale models on the flow field in the combustion chamber and nozzle	175
Appendix B Simulations of interest	187
Appendix C Publications	191
Bibliography	277

## CONTENTS

---



# Nomenclature

## Acronyms

<b>ACL</b>	<b>Axial Chord Length</b>
<b>CC</b>	<b>Combustion Chamber</b>
<b>CFD</b>	<b>Computational Fluid Dynamics</b>
<b>CERFACS</b>	<b>Centre Européen de Recherche et de Formation Avancée en Calcul Scientifique</b>
<b>CFL</b>	<b>Courant-Friedrichs-Lewis condition</b>
<b>DLR</b>	<b>Deutsches Luft- und Raumfahrtzentrum</b>
<b>DMD</b>	<b>Dynamic Mode Decomposition</b>
<b>DP</b>	<b>Design Point</b>
<b>FACTOR</b>	<b>Full Aerothermal Combuster Turbine interactiOns Research</b>
<b>HWA</b>	<b>Hot Wire Anemometry</b>
<b>IOP</b>	<b>Isothermal Operating Point</b>
<b>ITD</b>	<b>Inlet temperature distortions</b>
<b>LE</b>	<b>Leading Edge clocking case</b>
<b>LES</b>	<b>Large Eddy Simulation</b>
<b>LPP</b>	<b>Lean Partially Premixed</b>
<b>MISCOG</b>	<b>Multi Instance Solvers Coupled via Overlapping Grids</b>
<b>NASA</b>	<b>National Aeronautics and Space Administration</b>
<b>NGV</b>	<b>Nozzle Guide Vane</b>
<b>NO</b>	<b>Nitrogen Oxide</b>
<b>P40</b>	<b>Intersection between Combustion Chamber and high-pressure turbine</b>
<b>P41</b>	<b>Exit plane of the stator</b>
<b>P42</b>	<b>Exit plane of the rotor</b>
<b>PA</b>	<b>Passage clocking case</b>
<b>PDF</b>	<b>Probability density function</b>
<b>PIV</b>	<b>Particle Image Velocimetry</b>
<b>POD</b>	<b>Proper Orthogonal Decomposition</b>
<b>PVC</b>	<b>Processing Vortex Core</b>
<b>PS</b>	<b>Pressure Side</b>
<b>RANS</b>	<b>Reynolds Averaged Navier-Stokes</b>
<b>RMS</b>	<b>Root Mean Square</b>
<b>RPM</b>	<b>Rotation per Minute</b>
<b>RQL</b>	<b>Rich Quench Lean</b>
<b>SAS</b>	<b>Scale Adaptive Simulation</b>
<b>SGS</b>	<b>Sub-Grid Scale</b>
<b>SS</b>	<b>Suction Side</b>
<b>TET</b>	<b>Turbine Entry Temperature</b>
<b>TKE</b>	<b>Turbulent Kinetic Energy</b>

**Symbols**

$a_k(t)$	Coefficient
$A$	Set of reconstructed solutions
$A$	Area
$D$	Diameter
$E$	Enlargement
$M$	Blowing ratio
$i, j$	Counter
$K$	Kurtosis
$N$	Number of instantaneous solutions
$N_0$	Solution number of first zero crossing of $R_{uu}$
$R$	Autocorrelation coefficient
$S$	Skewness
$S$	Slope
$t$	Time
$t_{turb}$	Turbulent timescale
$T$	Temperature
$u$	Axial velocity
$V$	Velocity
$y^+$	Non-dimensional wall distance
$x$	Position vector
$\alpha$	Injection angle
$\Delta t$	Time step
$\Phi_k(x)$	Orthonormal basis function
$\rho$	Density
$\Sigma$	Diagonal matrix of eigenvalues
$\sigma$	Standard deviation
$\sigma$	Porosity
$\tau$	Time lag

**Subscripts**

$jet$	Jet
$k$	Mode number
$mod$	Model
$n$	Normal
$num$	Numerical
$r$	Radial
$t$	Tangential
$x$	Axial
$\infty$	Free stream

**Superscripts**

$-$	Averaged quantity
$'$	Fluctuating quantity

# List of Figures

1.1	Brayton cycle. . . . .	2
1.2	Schematic drawing of a gas turbine. . . . .	3
1.3	Specific core power as a function of temperature. . . . .	4
1.4	Effusion cooling systems for combustors. . . . .	5
1.5	Radial cut of NGV blade illustrating interior cooling and coolant ejection into freestream. . . . .	5
1.6	Numerical FACTOR domain. . . . .	6
1.7	Clocking positions for UNIFI and DLR test rigs. . . . .	7
1.8	Trisector test rig at the University of Florence without (left) and with (right) fitted high pressure vane cascade. . . . .	8
1.9	Positions of measurement planes are different with vanes (P40+, P41+). . . . .	9
1.10	Full annular FACTOR test rig at DLR Göttingen. . . . .	11
1.11	Measurement planes at the full annular FACTOR test rig at DLR Göttingen. . . . .	11
1.12	Overview of simulations presented in this work. . . . .	17
2.1	Historical development of numerical approaches. . . . .	20
2.2	Moore's Law - number of transistors on integrated circuit chips, doubling roughly every two years. . . . .	20
2.3	Numerical approaches for CFD. . . . .	21
2.4	Energy cascade. . . . .	22
3.1	Multiperforated combustion chamber liner with conventional rich-quench-lean combustor design with dilution holes. . . . .	36
3.2	Prognosis of resolvable cooling hole size. . . . .	38
3.3	Schematic drawing of an effusion cooling system. . . . .	39
3.4	Schematic drawing of the heterogeneous injection model. The injection angle of the real jets is indicated by $\alpha^{jet}$ and that for the heterogeneous injection model is marked by $\alpha^{het}$ . . . . .	41
3.5	Widening of cooling holes as a function of local grid resolution. . . . .	41
3.6	Injected axial momentum $\rho U$ [ $\frac{kg}{m^2s}$ ] prescribed at the boundary for five jets arranged in a staggered pattern. . . . .	41
3.7	Homogeneous (upper left) and heterogeneous (upper right) effusion cooling model and fully meshed cooling system (below) on a flat plate. . . . .	42
3.8	FACTOR combustion chamber. . . . .	43
3.9	Computational domain and local views of the grid. . . . .	45
3.10	FACTOR Meshes. . . . .	46

3.11	Cross sections through domain for homogeneous (upper) and heterogeneous (lower) injection model. . . . .	47
3.12	Mean velocity on the axial cross section (Upper: PIV, Middle: Homogeneous, Lower: Heterogeneous; Vertical red lines indicate the position of the extraction of vertical profiles shown in Fig. 3.13). (Isothermal Operating Point). . . . .	49
3.13	Vertical profiles of velocity components, Upper: after duct position, Lower: Downstream position (As indicated in Fig. 3.12). . . . .	50
3.14	Velocity plots and circumferentially averaged profiles on P40. a) Axial velocity [ $\frac{m}{s}$ ]. b) Radial velocity [ $\frac{m}{s}$ ]. c) Tangential velocity [ $\frac{m}{s}$ ]. View direction: Downstream. (Isothermal Operating Point). . . . .	51
3.15	Coolant air mass fraction on P40. View direction: Downstream. (Isothermal Operating Point). . . . .	52
3.16	Velocity on P40. a) Axial momentum [ $\frac{kg}{m^2s}$ ]. b) Radial velocity [ $\frac{m}{s}$ ]. c) Tangential velocity [ $\frac{m}{s}$ ]. View direction: Downstream. (Design Point). . . . .	52
3.17	Temperature [K] on P40 for design point. View direction: Downstream. . . . .	53
3.18	Plots of turbulent kinetic energy [ $\frac{m^2}{s^2}$ ] on cross sections through domain. (Isothermal Operating Point). . . . .	53
3.19	Turbulent kinetic energy [ $\frac{m^2}{s^2}$ ] on P40. View direction: Downstream. (Isothermal Operating Point). . . . .	54
3.20	Non-dimensionalized axial velocity RMS on P40. View direction: Downstream. (Isothermal Operating Point). . . . .	54
3.21	Turbulent timescale [s] on P40. View direction: Downstream. (Isothermal Operating Point). . . . .	55
3.22	Power spectral density of pressure for homogeneous and heterogeneous injection model from Dynamic Mode Decomposition of 2D solutions on P40. . . . .	56
3.23	Pressure amplitude for 315 Hz on P40 for homogeneous and heterogeneous injection modeling. . . . .	56
4.1	Geometric definitions of the holes. Example of the pressure side view of a cooled NGV (a). Normal blade view in the red square (b) and view of the A-A cut (c). $O$ is the center of the hole, $D$ the minimum diameter of the hole, $r$ the local radial coordinate defined on the hole surface $S_{hole}$ and $\alpha$ the inclination angle to the wall. . . . .	62
4.2	Domain used for the study: a) computational domain and b) NGV details. . . . .	65
4.3	2D temperature map including a hot spot and swirled flow imposed at the inlet boundary condition. Arrows evidence the swirled flow. . . . .	66
4.4	Cold mass flow distribution along the blade. Red circle $\circ$ represents the meshed holes LES and solid blue line $-$ the RANS simulation. . . . .	68
4.5	Time-averaged normal profiles of the mass flux $\rho U_i n_i$ at a coolant ejection hole located in the last cooling row at mid height of NGV1 for the meshed holes (a) and hole modeled (b) LES. . . . .	68

LIST OF FIGURES

---

4.6	Turbulent kinetic energy $TKE$ at a coolant ejection hole located in the last cooling row at mid height of NGV1 for the meshed holes (a) and hole modeled (b) LES. . . . .	69
4.7	Instantaneous isosurface of the coolant temperature to evidence the coolant injection near the surface blade of NGV1 in the meshed holes case (a) and hole modeled case (b). . . . .	69
4.8	Isentropic Mach number $Ma_{is}$ along NGV1 (a) and NGV2 (b) at mid height of the vanes. Red circles $\circ$ represent the meshed holes LES and the solid blue line $-$ represents the hole modeled LES. The axial extent of the cooling rows is indicated by lines. . . . .	71
4.9	Time-averaged total temperature field at mid-height. (a) Meshed holes and (b) hole modeled LES. . . . .	72
4.10	Radial total temperature profile at the axial plane P40 (a) and P41 (b). Red circle $\circ$ represents the meshed holes LES and solid blue line $-$ the hole modeled LES. . . . .	73
4.11	Time-averaged adiabatic wall temperature on NGV1 and NGV2 for both LES. . . . .	74
4.12	Radial profile of the surface temperature for NGV1 (a) and NGV2 (b). Red circle $\circ$ represents the meshed holes LES and solid blue line $-$ the hole modeled LES. . . . .	75
4.13	Cooling mass fraction near the leading edge of NGV1 at mid-height. Left: Resolved; Right: Modeled. . . . .	76
4.14	Profile of the coolant mass fraction for different axial positions at (a) $x/c = 0.25$ , (b) $x/c = 0.50$ , (c) $x/c = 0.75$ and (d) $x/c = 0.90$ at mid-height along NGV1. Red circles $\circ$ represent the meshed holes LES and the solid blue line $-$ the hole modeled LES. Pressure side (PS) is at the bottom and suction side (SS) at the top. $\delta$ is the film thickness. . . . .	77
4.15	Film thickness along (isocontour of $Y_{coolant} = 0.05$ ) the blades for NGV1 (a) and NGV2 (b) at mid-height. Red circles $\circ$ represent the meshed holes LES at the pressure side. Red triangles $\Delta$ represent the meshed holes LES at the suction side. The solid blue line $-$ represents the hole modeled LES at the pressure side. The dashed blue line $- - -$ represents the hole modeled LES at the suction side. Cooling row holes axial locations are indicated. . . . .	78
4.16	Control volume at mid-height to apply the mass balance in the coolant film. The control volume is delimited by the sections corresponding to the ejection exit of the coolant pipes $S_{cold}$ , the walls $S_{wall}$ , the thickness of the coolant $S_{\delta}$ and the film section $S_{film}$ . . . . .	78
4.17	Coolant film mass fraction $Y_{film}$ along NGV1(a) and NGV2(b) at mid-height. Red circles $\circ$ represent the meshed holes LES at the pressure side. Red triangles $\Delta$ represent the meshed holes LES at the suction side. The solid blue line $-$ represents the hole modeled LES at the pressure side. The dashed blue line $- - -$ represents the hole modeled LES at the suction side. . . . .	79

4.18	Mixing state at mid height along NGV1 (a) and NGV2 (b). Red circles $\circ$ represent the meshed holes LES at the pressure side. Red triangles $\Delta$ represent the meshed holes LES at the suction side. The solid blue line $-$ represents the hole modeled LES at the pressure side. The dashed blue line $- - -$ represents the hole modeled LES at the suction side. . . . .	81
4.19	$Y_{RMS}$ map at mid height on NGV1 and NGV2 at mid-height for both LES. Top (a) & (b), NGV1. Bottom (c) & (d), NGV2. Left (a) & (c), meshed holes. Right (b) & (d), hole modeled. The film thickness is represented by the white isoline. . . . .	82
4.20	Turbulent kinetic energy maps $TKE$ on NGV1 and NGV2 at mid-height for both LES. Top (a) & (b), NGV1. Bottom (c) & (d), NGV2. Left (a) & (c), meshed holes. Right (b) & (d), hole modeled. The film thickness is represented by the white isoline. . . . .	83
5.1	FACTOR geometry with leading edge and passage clocking positions.	91
5.2	Mesh on $H/h=0.5$ from end of duct to NGVs for LE clocking. . . .	92
5.3	Different views of the computational grid in the NGV domain. . . .	92
5.4	Frequency spectrum on P40 with marked peak at 500 Hz and 1000 Hz (PVC) calculated using a DMD on static pressure on instantaneous LES solutions. . . . .	93
5.5	Visualization of individual spatial POD modes calculated on pressure with isosurface for positive (red) and negative (blue) values. a) Visualization of mode 1 with 500 Hz peak. b) Visualization of mode 3 with 1000 Hz peak. . . . .	94
5.6	PVC visualized as instantaneous isosurface of pressure for the chamber only case for different time steps. The PVC is created by the swirler and breaks down shortly after leaving restraining duct. . . .	95
5.7	Central axial cross section cuts of an instantaneous flow field through the swirler from swirler to P40. (LE case, Design Point). . . . .	95
5.8	Central axial cross section cuts of the averaged axial velocity normalized by reference velocity (see Tab. 5.1) through the swirler from swirler to P40. $u_{nondim} = u/u_{ref}$ , $u_{ref,DP} = 51.3m/s$ , $u_{ref,IOP} = 37.5$ . Simulations: LE / PA clocking and combustion chamber (CC) only at design point; PIV experiment at isothermal operating point.	96
5.9	Central axial cross section cuts of the averaged tangential velocity $[\frac{m}{s}]$ field through the swirler from swirler to P40. (Design Point). . . .	97
5.10	Central axial cross section cuts of the non-dimensional pressure field through the swirler from swirler to P40. Pressure is non-dimensionalized by average pressure on P40 (CC: 147640 Pa, LE: 140325 Pa, PA: 141877 Pa). (Design Point). . . . .	97
5.11	Central axial cross section cuts of the temperature field through the swirler from swirler to P40. (Design Point). . . . .	98
5.12	Central axial cross section cuts of the $TKE [m^2/s^2]$ field through the swirler from swirler to P40. (Design Point). . . . .	98

LIST OF FIGURES

---

5.13	Flow quantities on line through center of the swirler (Red line on Fig. 5.3e). . . . .	100
5.14	Axial velocity [ $m/s$ ] in chamber after swirler (noted P* on Fig. 5.3e).	101
5.15	Radial velocity [ $m/s$ ] in chamber after swirler (noted P* on Fig. 5.3e).	101
5.16	Non-dimensional pressure $[-]$ in chamber after swirler (noted P* on Fig. 5.3e). Pressure is non-dimensionalized by average pressure on P40 (CC: 147640 Pa, LE: 140325 Pa, PA: 141877 Pa). . . . .	102
5.17	Temperature [ $K$ ] in chamber after swirler (noted P* on Fig. 5.3e). . . . .	102
5.18	$TKE$ [ $m^2/s^2$ ] in chamber after swirler (noted P* on Fig. 5.3e). . . . .	103
5.19	$T_{rms}$ [ $K$ ] in chamber after swirler (noted P* on Fig. 5.3e). . . . .	103
5.20	Radial and tangential velocity on P40. Black lines indicate middle axis of swirler and inclined grey lines indicate vane positions. View direction: Downstream. (Design Point). . . . .	104
5.21	Total quantities on P40 for LE and PA case. Total pressure non-dimensionalized by average value on P40 (LE: 141953 Pa; PA: 143523 Pa). Black lines indicate middle axis of swirler and inclined grey lines indicate vane positions. View direction: Downstream. . . . .	105
5.22	Azimuthal averaged profiles (minimum during investigation time, temporal average, maximum during investigation time) on P40 for PA and LE LES cases. . . . .	105
5.23	Non-dimensionalized flow field on P40. Comparison of design point simulation and isothermal operating point measurements. Values are non-dimensionalized by the time and space average value in the experimental investigation zone (see Tab. 5.2). View direction: Downstream. . . . .	107
5.24	Schematic drawing of important flow features in the chamber. Hot rotating flow from the swirler is represented by red arrows and the injected coolant is represented in blue. The effect of the velocity field on the coolant is represented by blue arrows. (View direction: Downstream). . . . .	108
5.25	Average temperature [ $K$ ] on $Hh=0.5$ . . . . .	108
5.26	Visualization of the hot spot by an isosurface of total temperature ( $T_{tot} = 470 K$ ). . . . .	109
5.27	Mean flow field on $h/H=0.5$ for LE and PA case. (Design point). . . . .	110
5.28	Mean $TKE$ [ $\frac{m^2}{s^2}$ ] field on $h/H=0.5$ for LE and PA case. (Design point). . . . .	111
5.29	Pressure profiles on blades for LE and PA case at design point for different heights. . . . .	112
5.30	Temperature profiles on blades for LE and PA case at design point for different heights. . . . .	112
5.31	Distinction of channel and vane for quantitative analysis of the flow. . . . .	113
5.32	Evolution of non-dimensional $TKE$ averaged on planes (see Fig. 5.31) over $x$ . . . . .	114
5.33	Evolution of non-dimensional temperature averaged on planes (see Fig. 5.31) over $x$ . . . . .	114

5.34	Evolution of non-dimensional $T_{rms}$ averaged on planes (see Fig. 5.31) over x. . . . .	115
5.35	FACTOR NGV section with investigation planes. . . . .	116
5.36	Evolution of static temperature on planes at successive axial positions through the NGV passage. Vane positions indicated on the right. View direction is downstream. . . . .	117
5.37	Temperature distribution over time in two different points on P40 (LE case). . . . .	118
5.38	Evolution of statistical moments (Standard deviation, skewness, kurtosis) for static temperature on planes at successive axial positions through the NGV passage. View direction is downstream. . . . .	119
5.39	Residual swirl core present in the study of Jacobi et al., visualized by an isosurface of total pressure. . . . .	120
5.40	Schematic drawing of secondary flow structures created with the presence of vanes in a swirled flow. . . . .	121
5.41	Visualization of the first pressure mode evidencing a PVC response on the NGV. . . . .	121
5.42	Secondary flow structures on NGV blade according to Wang et al. (swirler visible on the right-hand side). . . . .	122
5.43	Pressure fluctuations [Pa] on NGV surface at PVC frequency obtained by a DMD analysis of a set of coarse grid interpolated instantaneous solutions. Trace of vortex B well visible on both NGVs suction side. (LE case, design point). SS = Suction Side, PS = Pressure Side. . . . .	123
5.44	Temperature fluctuations relative to the local mean value on NGV surface at PVC frequency obtained by a DMD analysis of a set of coarse grid interpolated instantaneous solutions. Trace of vortex B well visible on both NGVs suction side. (LE case, design point). . . . .	123
5.45	Temperature and high order statistical moments on NGV surface for LE and PA case. SS = Suction Side, PS = Pressure Side. (Design point). . . . .	126
6.1	FACTOR domain and NGV setup. . . . .	129
6.2	FFT analysis of the ten most energetic temporal POD modes of pressure in the entire domain. . . . .	132
6.3	Visualization of spatial POD modes of pressure with isosurface for positive (red) and negative (blue) values. . . . .	132
6.4	Spatial POD and DMD analysis of temperature on P40. . . . .	133
6.5	Temporal POD and DMD analysis of temperature on P40. . . . .	133
6.6	Ratio of spatially averaged RMS value on P40 reconstructed by different number of modes and spatially averaged RMS value on P40 using all modes for variables imposed at the inlet ( $T$ , $\rho u$ , $\rho v$ , $\rho w$ ). . . . .	134
6.7	$TKE$ [ $m^2/s^2$ ] on P40 retrieved from simulations. a) Reference, b) All modes, c) Without first ten modes, d) First ten modes, e) Constant. . . . .	136

LIST OF FIGURES

---

6.8	$T_{rms}$ [ $K^2$ ] on P40 retrieved from simulation. a) Reference, b) All modes, c) Without first ten modes, d) First ten modes, e) Constant.	137
6.9	Temperature distribution on P40 over 40 ms (all nodes, 2000 instantaneous solutions). a) Reference, b) All modes, c) Without first ten modes, d) First ten modes, e) Constant. . . . .	137
6.10	Visualization of vortex structures in the NGV passage using an isosurface of Q-criterion ( $10^8$ ) on instantaneous solutions. a) Reference, b) All modes, c) Without first ten modes, d) First ten modes, e) Constant. (NGV2 in foreground, NGV1 behind). . . . .	138
6.11	Visualization of vortex structures in the NGV passage using an isosurface of Q-criterion ( $10^8$ ) on solutions averaged over 40 ms. a) Reference. b) All modes. c) Without first ten modes. d) First ten modes. e) Constant. (NGV1 in background, NGV2 foreground).	139
6.12	Instantaneous temperature [ $K$ ] plot on Hh=0.5 isosurface. NGV1: upper, NGV2: lower. a) Reference, b) All modes, c) Without first ten modes, d) First ten modes, e) Constant. . . . .	140
6.13	Average total temperature [ $K$ ] plot on Hh=0.5 isosurface. NGV1: upper, NGV2: lower. a) Reference, b) All modes, c) Without first ten modes, d) First ten modes, e) Constant. . . . .	141
6.14	Average $T_{rms}$ [ $K^2$ ] plot on Hh=0.5 isosurface. NGV1: upper, NGV2: lower. a) Reference, b) All modes, c) Without first ten modes, d) First ten modes, e) Constant. . . . .	142
6.15	Observation planes used for following discussions. . . . .	142
6.16	Average static temperature [ $K$ ] on P40 + 1 ACL. a) Reference, b) All modes, c) Without first ten modes, d) First ten modes, e) Constant. . . . .	143
6.17	Average static temperature [ $K$ ] on P41. a) Reference, b) All modes, c) Without first ten modes, d) First ten modes, e) Constant. . . . .	143
6.18	Temperature [ $K$ ] distribution on P41 over 40 ms. a) Reference, b) All modes, c) Without first ten modes, d) First ten modes, e) Constant. . . . .	144
6.19	$T_{rms}$ [ $K^2$ ] on P40 + 1 ACL. a) Reference, b) All modes, c) Without first ten modes, d) First ten modes, e) Constant. . . . .	145
6.20	$T_{rms}$ [ $K^2$ ] on P41. a) Reference, b) All modes, c) Without first ten modes, d) First ten modes, e) Constant. . . . .	145
6.21	$TKE$ and $T_{rms}$ over planes through the NGV passage (see Fig. 6.15 for locations). . . . .	146
6.22	Turbulent timescale calculated on the axial velocity component imposed on P40. Note that the values for Case a) correspond to those of Case b) and that due to constant inlet boundary conditions for Case e) no turbulent timescale can be calculated. . . . .	146
6.23	DMD analysis of pressure on P41. . . . .	147
6.24	Average temperature [ $K$ ] on NGV surface. NGV1: upper, NGV2: lower. a) Reference, b) All modes, c) Without first ten modes, d) First ten modes, e) Constant. . . . .	149

6.25	Temperature distribution NGVs over 40 ms. NGV1: upper, NGV2: lower. a) Reference, b) All modes, c) Without first ten modes, d) First ten modes, e) Constant. . . . .	149
6.26	$T_{rms}$ [K] on NGV surface. NGV1: upper, NGV2: lower. a) Reference, b) All modes, c) Without first ten modes, d) First ten modes, e) Constant. . . . .	149
7.1	Measurement planes at FACTOR test rig. . . . .	155
7.2	Numerical FACTOR domain. . . . .	156
7.3	Central axial cross section cuts of the instantaneous flow field through the swirler from swirler to P40. . . . .	158
7.4	Central axial cross section cuts of the averaged flow field through the swirler from swirler to P40. Upper row: Combustion Chamber & NGVs (Chapter 5); Bottom row: Combustion Chamber & Hp-turbine	158
7.5	Flow field on P40 (intersection between combustion chamber and stator) for simulation and experiment. View direction: downstream.	160
7.6	NGVs and Q-criterion of an instantaneous solution colored by static temperature. . . . .	161
7.7	Average flow field at channel mid height in the high-pressure vane passage. Hot spot impinges on NGV2. . . . .	162
7.8	Isentropic mach number on NGV surface at mid height of the channel.	162
7.9	Flow field on P41 (after stator) for simulations and experiment. View direction: downstream. . . . .	163
7.10	Flow field on P41 (after stator) for simulations and experiment. View direction: downstream. . . . .	164
7.11	Azimuthally averaged profiles on P41 (after stator) for simulations and experiment. . . . .	165
7.12	Vortex structures in rotor domain visualized by isosurface of Q-criterion and blade surface temperature [K] for one instantaneous solution. View on suction side of rotor 1. . . . .	166
7.13	Average flow field at channel mid height in the high-pressure vane passage. Hot spot impinges on NGV2. . . . .	166
7.14	Flow field on P42 (after rotor) for simulation and experiment. View direction: downstream. . . . .	168
A.1	Energy cascade. . . . .	176
A.2	Spatially averaged values of converged averaged flow fields on successive axial planes for different SGS models. . . . .	177
A.3	Comparison of SGS on mid-cut through domain. . . . .	177
A.4	Averaged axial (upper) and radial (lower) velocity profiles on lines through domain for simulations (DP) and PIV-experiment (IOP). Velocities are non-dimensionalized by the reference velocity (see Tab. 5.1). Distance from the exit of the duct is non-dimensionalized by the diameter of the swirler (63 mm). . . . .	178
A.5	Average flow field for Smagorinsky (upper), WALE (middle) and SIGMA (lower) on iso H/h=0.5 through domain. (Design Point). . . . .	179

## LIST OF FIGURES

---

A.6	Average flow field on iso $H/h=0.97$ for Smagorinsky (upper), WALE (middle) and SIGMA (lower) through domain. (Design Point). . . .	180
A.7	Averaged flow field on P40 for Smagorinsky, WALE and Sigma model and experimental data. . . . .	181
A.8	Averaged flow field on P40 for Smagorinsky, WALE and Sigma model and experimental data. . . . .	181
A.9	Averaged flow field on P41 for Smagorinsky, WALE and Sigma model and experimental data. . . . .	182
A.10	TKE [ $\frac{m^2}{s^2}$ ] on P41 for Smagorinsky, WALE and Sigma model and experimental data. . . . .	183
A.11	Q-criterion ( $1E+8$ ) of averaged solutions visualizes secondary flow structures on the NGV suction side. . . . .	183
A.12	Comparison of SGS models on the NGV surface. . . . .	184
A.13	Bladeprofiles at different heights. . . . .	185

# List of Tables

1.1	FACTOR operating conditions at the trisector test rig at the University of Florence without fitted high-pressure vanes. . . . .	9
1.2	Operating conditions of the full annular FACTOR test rig at DLR Göttingen. . . . .	10
1.3	Summary of operating points. . . . .	12
3.1	Geometrical and modeling parameters of the effusion cooling system (360°). . . . .	44
3.2	FACTOR operating conditions. . . . .	44
3.3	Mesh and associated computational cost (BEAUFIX Meteo France 360 processors). . . . .	46
3.2	Average values for turbulent quantities on P40. . . . .	54
4.1	Summary of the operating point of the blades. The Mach number and Reynolds number are computed at the trailing edge axial plane using the axial chord length (ACL). . . . .	64
4.2	Boundary conditions used in the meshed holes LES. . . . .	67
4.3	Summary of the LES computations and CPU cost for one convective time. Computations were performed with the High Performance Computing (HPC) resources of IDRIS on the Blue Gene machine TURING. . . . .	67
4.4	Main and coolant mass flow rates for both LES and total pressure $P_t$ and total temperature $T_t$ at the inlet of the domain (P40) and drop between the planes P40 and P41 (* values are imposed by the inlet boundary condition). . . . .	71
5.1	FACTOR operating conditions at the trisector test rig at the University of Florence without vanes. . . . .	90
5.2	Average values for turbulence quantities on P40 in experimental investigation zone used for non-dimensionalization. . . . .	106
5.3	Average values on first plane in vane passage used for non-dimensionalization. . . . .	113
6.1	Test cases with different inlet boundary conditions. . . . .	135
6.2	Static pressure [ $kPa$ ] on P40. . . . .	138
7.1	Inlet data for one sector of the FACTOR test rig at DLR Göttingen (Total mass flow in brackets). . . . .	156
7.2	Operating conditions for Experiment and Simulation. . . . .	156

## LIST OF TABLES

---

B.1	Summary of all LES performed on the FACTOR configuration in the work of C. Koupper. . . . .	188
B.2	Summary of the all LES performed on the FACTOR configuration.	189

# Chapter 1

## General Introduction

### Contents

---

1.1	Aeronautical gas turbines . . . . .	<b>2</b>
1.2	The FACTOR project . . . . .	<b>6</b>
1.2.1	Test facilities . . . . .	6
1.2.2	CFD of the FACTOR test rig . . . . .	12
1.3	Objectives of this Thesis . . . . .	<b>13</b>
1.4	Organization of the Manuscript . . . . .	<b>15</b>

---

Our modern society of today largely relies on airborne traffic for rapid exchange of people and goods. Indeed, over the last decades, air traffic has continued to grow at a rate of about 4.4 % per year, a rate especially driven by the explosion of air traffic in emerging countries [1]. Since the beginning of aviation, technological advancements led to tremendous changes in the design of aircraft, mainly focused on increasing reliability and efficiency. Today, environmental awareness [2], but also financial imperatives to reduce aircraft operating cost lead to the development of ever more efficient aircraft engines. As a result and to reduce  $\text{NO}_x$  emissions, next-generation aircraft engines will make use of new compact design low  $\text{NO}_x$  lean combustion technologies. Introducing such fundamental technological changes raises issues that have to be addressed in future development projects. Typically, shorter residence times due to the compact design and less mixing (due to the absence of dilution holes) will result in higher levels of swirl, turbulence and temperature non-uniformities at the exit of the combustion chamber if compared to current state-of-the-art rich quench lean combustors. Another consequence is that increased activity at the inlet of the turbine will adversely affect the flow field in the high-pressure turbine. The FACTOR project [3] is a common effort of European turbomachinery laboratories and manufacturers to gain insight in the flow field of next-generation low  $\text{NO}_x$  lean combustion geometries (details in Section 1.2). The goal of the project is to better understand and optimize the combustor-turbine interface through a better comprehension of interactions between the cooling system, secondary flows and mixing mechanisms. As a partner in the FACTOR project, CERFACS contributes by performing high fidelity Large

Eddy Simulations (LES) of combustor and complete single staged high-pressure turbine as a basis for deeper analysis and to complement experimental findings.

This chapter first introduces basic concepts of aeronautical gas turbines while addressing some of the fundamentals as a prelude to this work. In the following, the FACTOR project is presented and the content of each chapter composing this PhD work is introduced.

## 1.1 Aeronautical gas turbines

Due to their excellent power to weight ratio, gas turbines found a wide range of applications from small power generators of a few Watts to huge gas turbines of several Megawatts in the energy sector. For aircraft applications, the power to weight ratio is of major importance and solely explains why this type of engine remains the only possible choice to propel helicopters as well as high performance airplanes. Since gas turbines were first applied to aircraft in the 1940's, efficiency driven developments impacted many parts of the engine to yield today an overall efficiency close to 40 %. Design of such complex systems usually starts using the Brayton cycle [4] (see Fig. 1.1), where four distinct systems transformations are imposed to a fluid:

- 1 - 2 is an isentropic compression
- 2 - 3 is an isobaric heat addition
- 3 - 4 is an isentropic expansion
- 4 - 1 is an isobaric heat rejection

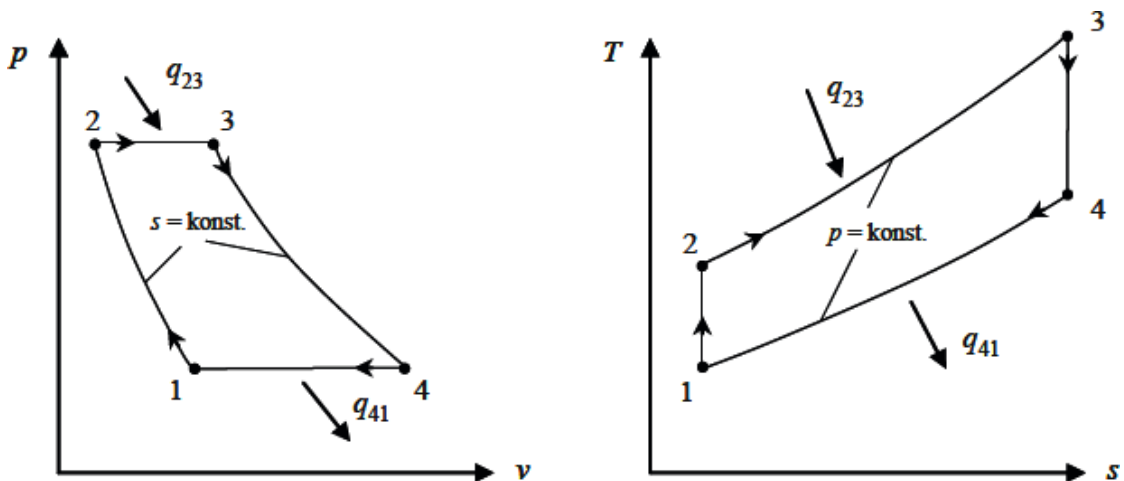
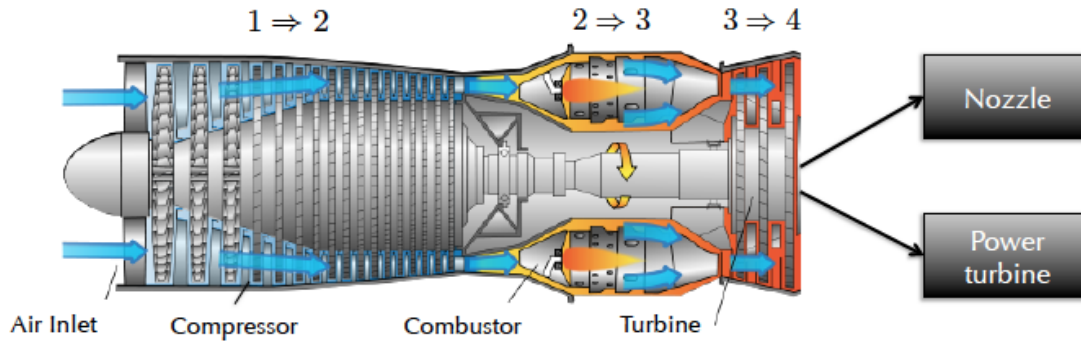


Figure 1.1: Brayton cycle [5].

In terms of physical components, the first process of the above-described cycle is associated to the compressor (see Fig. 1.2), where the air is compressed to achieve a higher power output per volume. In the combustion chamber, heat generated by



**Figure 1.2:** Schematic drawing of a gas turbine [6].

combustion is added to the fluid. The turbine then extracts mechanical work by expansion of hot gases, which are then ejected back to the atmosphere. Based on such a cycle, different engines can be obtained. In particular, turboshaft engines are optimized to generate a maximum of shaft power, whereas jet engines use the shaft power only to drive the compressor and are designed to generate a high velocity jet at the exit nozzle. As seen from this theoretical reference cycle, efficiency of the engine appears to be mainly determined by the Turbine Entry Temperature (TET, point 3 of Fig. 1.1), an observation which over decades of development lead to an ever increasing TET (see Fig. 1.3). Ultimately the TET has reached a point where it surpasses the heat resistance limits of monocrystal Ni-based superalloys used to manufacture the most thermally and mechanically stressed parts of the turbine resulting in the need for highly cooled components. In parallel to this increase in TET, it is important to note that the next big technological step in the development of aircraft engines will be the introduction of lean combustion technologies to reduce  $\text{NO}_x$  emission. Lean partially premixed combustion (LPP) seems indeed to be a promising path to significantly lower  $\text{NO}_x$ , as targeted in the European air traffic emission goals 2020. Such a change in combustor architecture is however coming with a significant price, that is less air at hand to dilute the hot products of reaction prior to their ingestion by the turbine. It is hence expected to yield stronger hot spots reaching very high temperatures, which is clearly detrimental to the turbine sustainability. To complexify the context, the generated hot spot will be accompanied by an increased swirling flow that will also penetrate the turbine and affect its aerodynamic performance as well as the mixing of the hot spot with the cold air injected by cooling systems. All of these issues are hence expected to have a strong impact on the efficiency of any new design if not well conceived.

Because of this specific above discussed content, the possibility to increase the TET (see Fig. 1.3) can only be partly granted thanks to improved heat resistant materials. To a larger extent performance gains could be achieved by developing more and more sophisticated cooling technologies applied in the combustion chamber (liners with effusion cooling system) as well as in high-pressure turbine blades allow for higher temperatures. In fact, this capacity is determined by the combustor exit temperatures and distributions on P40, the intersection plane between

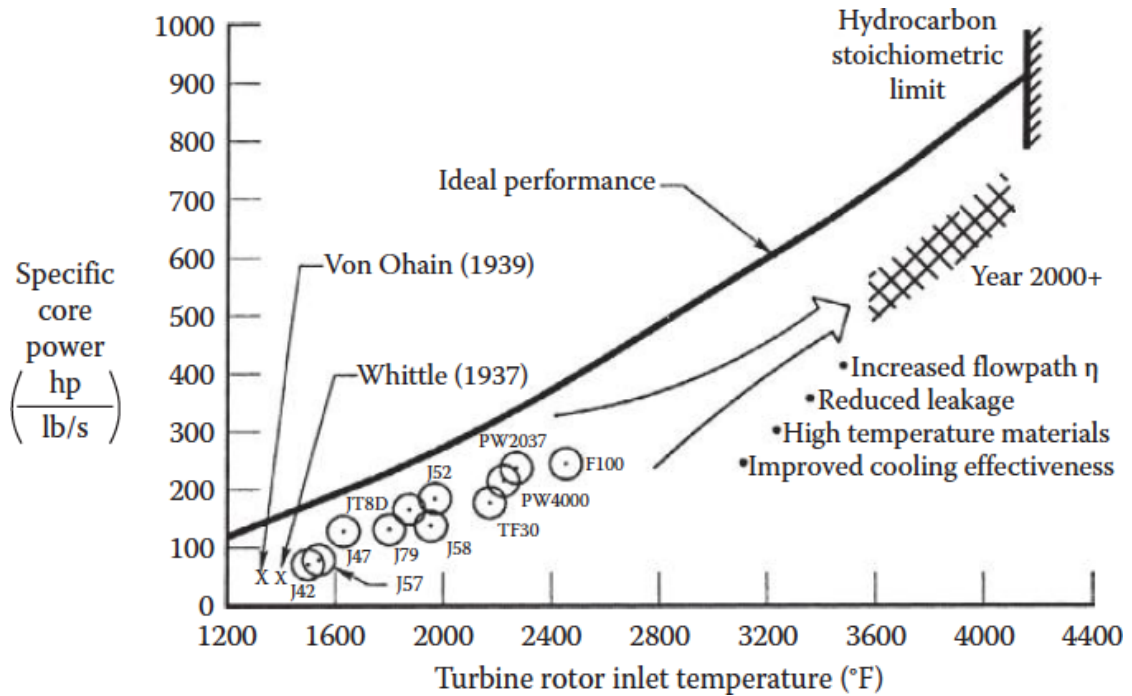


**Figure 1.3:** Specific core power as a function of temperature [7].

combustor and turbine. A better understanding of combustor-turbine interactions becomes hence a key point for engine manufacturers. Indeed, in view of harsher aerothermal conditions induced by next-generation compact design lean combustion technology, the design and development of adapted cooling systems is the only way to guarantee hot section component durability.

Since the 1950s, combustion temperatures in the engine are higher than thermal stress limits of materials used at that time. This led to the development of more and more sophisticated cooling systems. An additional challenge for aircraft engines is the huge range of operating conditions compared to stationary gas turbines. For example, recent designs rely on passive cooling systems in the form of thermal barrier coatings of heat resistant ceramic material that have been introduced to reduce the thermal stress components are exposed to. Another option are active cooling systems using the heat sink capacity of cold compressor bleed air to reduce material temperatures. This air can be furthermore reused to form a thermal barrier layer around components exposed to high thermal stress. Active cooling systems have to meet two different opposing design targets: First, thermal stress has to be reduced to levels that allow long term safe operation of the engine in different flight conditions. Second, the least amount of air possible should be used for cooling systems as this air is not available for combustion which reduces the overall efficiency of the engine and impacts emissions. Thirdly, active cooling systems in the turbine may lead to changes in the flow around the blades and induce thermal losses [8]. The liners of the combustion chamber and the nozzle guide vanes (NGV) at the exit of the combustor are the thermally most stressed parts of an engine and require sophisticated cooling systems. For combustion chamber liners, coolant is injected through thousands of submillimetric angled perforations

to form a closed coolant film on the inner side of the liner (see Fig. 1.4). In NGVs, sophisticated interior cooling systems reduce the temperature of the vanes (see Fig. 1.5). This recirculating air is then ejected into the flow to form a coolant film around the blade. In Part I of this manuscript both cooling systems are investigated and different modeling approaches are evaluated and validated against experimental data.

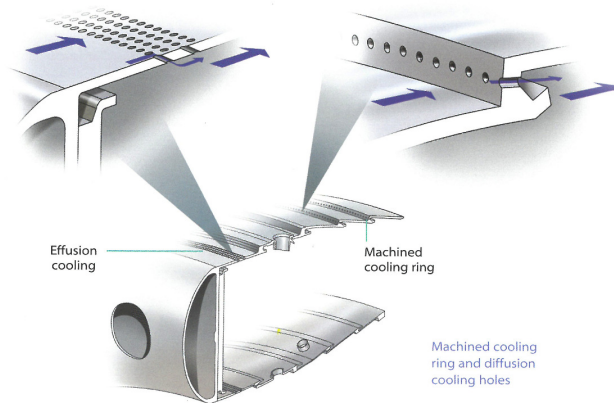


**Figure 1.4:** Effusion cooling systems for combustors [9].

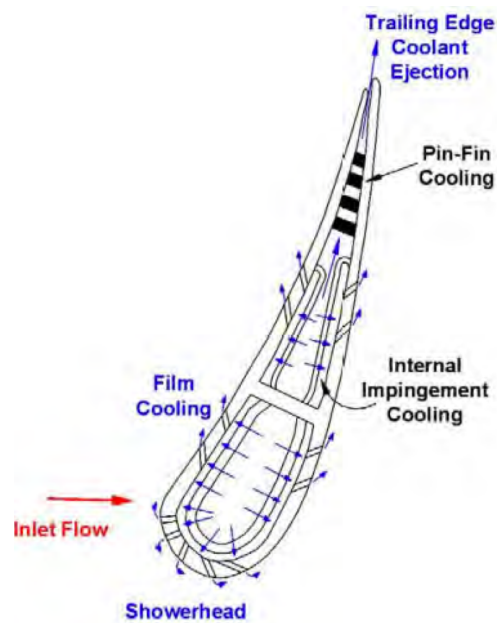


**Figure 1.5:** Radial cut of NGV blade illustrating interior cooling and coolant ejection into freestream [10].

## 1.2 The FACTOR project

New technological developments in aircraft engines are today essentially motivated by the need of reducing the environmental impact and operating cost of air traffic. In this context, the FACTOR (**F**ull **A**erothermal **C**ombustor-**T**urbine **I**nteracti**O**ns **R**esearch) project [3], launched in 2010, aims at investigating the interactions of combustion chamber and turbine for next-generation lean combustion chambers. Based on the conjoint use of CFD and three dedicated test rigs, the objective of the project is to reduce specific fuel consumption by an optimization of the combustor-high-pressure turbine interface design. This is sought through a better understanding of interactions between coolant and mean flow, secondary flows and hot streaks issued at the entry of the turbine stage. Particularities of the non-reactive FACTOR test rig design are the compactness and the absence of dilution holes, corresponding to the design of a lean combustion chamber (see Fig. 1.6). It is worth noting that the huge number of publications in the area of gas turbine component interactions in recent years and the wide range of applications of gas turbine engines underline the importance of the FACTOR research project.

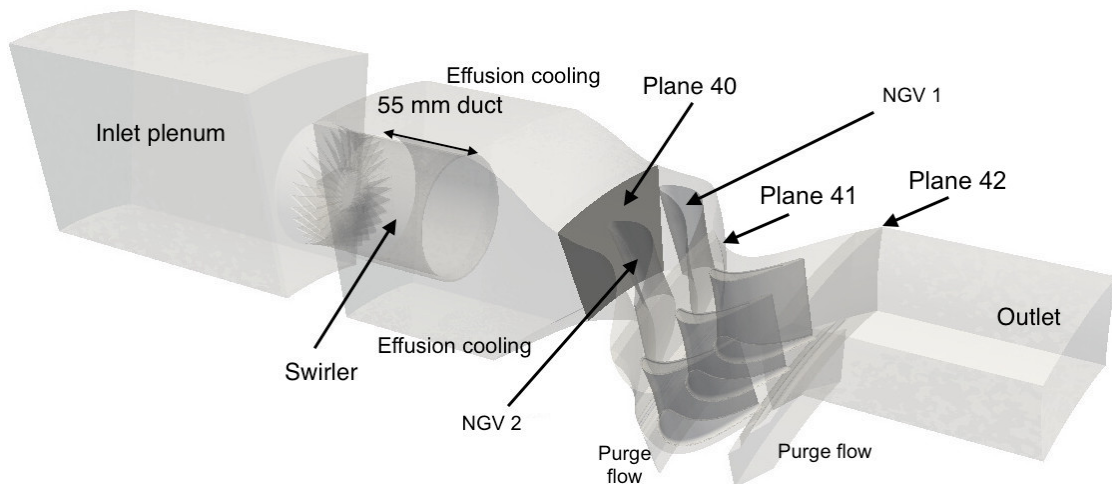


**Figure 1.6:** Numerical FACTOR domain [11].

### 1.2.1 Test facilities

The following specifically details the rigs of the project as well as associated CFD predictions. The tested operating conditions (see Tab. 1.1 and Tab. 1.2) have been defined in a way that turbine applications from different participating industrial partners can be represented, while staying at temperature levels that are not challenging for the materials. Part of the experimental tests from the FACTOR project are carried out at the NGTURB test bench at the DLR in Göttingen. In parallel, a trisector test rig featuring 54° of the Göttingen test rig combustion chamber and nozzle is also operated at the University of Florence. The justification for this second test bench is that first hand measurement data were needed for validation

purposes of the  $360^\circ$  bench as well as CFD computations. Finally, the blow-down turbine facility hosted by the university of Oxford is used to complement the flow analysis of the continuous DLR test rig.

As mentioned previously, the FACTOR project started in 2010 and is based on three complementary experimental test rigs. Experimental data from the tri-sector rig in Italy has been available before 2015 and contributed to the design process of the full annular test rig at DLR Göttingen. However, due to complexity, the full annular test rig at DLR Göttingen went into service after most numerical simulations had been conducted through the course of this project. Furthermore, in the experiment, the original design point was not completely matched. As a consequence, different computational domains as well as operating points are covered in this manuscript as presented hereafter. Note also the existence of different combustor - turbine clocking positions (see Fig. 1.7) studied at UNIFI and at the DLR, particularities that are also detailed here. For the DLR test rig there are two different clocking positions: Leading edge (LE), where the swirler is aligned with the NGV's leading edge, and passage (PA), where the swirler is aligned with the passage.

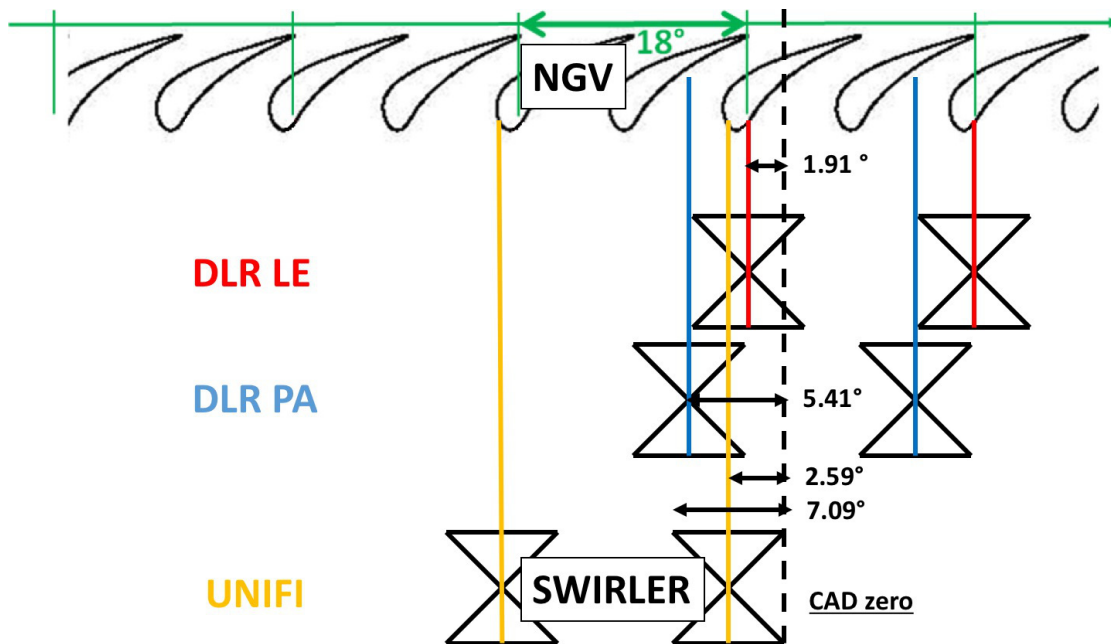


**Figure 1.7:** Clocking positions for UNIFI and DLR test rigs.

### Blow-down Oxford Turbine Research Facility

The Oxford Turbine Research Facility is a short duration test rig dedicated to the investigation of heat transfer and cooling systems [12]. The rig was designed in the 70s and 80s and is able to simulate realistic flow conditions for a high-pressure turbine stage. The Oxford rig was not subject to numerical investigations conducted at CERFACS and is therefore not detailed here.

### Trisector test rig at the University of Florence

The trisector test rig located at the university of Florence consists of three  $18^\circ$  sectors of the full annular geometry [13,14]. At this rig, experiments were conducted with and without fitted high-pressure nozzle as shown in Fig. 1.8. The first measurement plane, P40, is the exit plane of the combustor while the second plane, P41, is positioned right after the NGVs. Depending on the presence of vanes, one notes that measurement planes differ slightly due to accessibility constraints (see Fig. 1.9). Operating conditions of the UNIFI rig without fitted high-pressure nozzle used in this work are provided in Tab. 1.1 and are discussed hereafter.



**Figure 1.8:** Trisector test rig at the University of Florence without (left) and with (right) fitted high pressure vane cascade [14].

**a) Isothermal Operating point (IOP)** The isothermal operating point was defined in a way to respect most non-dimensional quantities (see Tab. 1.1) as derived by Koupper et al. (2014) [15]. Its objective is to allow for hot wire anemometry measurements on P40 to gather velocity data based on the temperature-dependent electrical resistance of a heated wire. In this case, the combination of two wires allows the reconstruction of different velocity components. Coupled to a high temporal resolution (50 kHz), the method allows to gather higher order statistical data which can then be used to validate high-fidelity simulations. To complement this diagnostic in P40, Particle Image Velocimetry (PIV) measurements in the cross section plane passing through the swirler axis are also made available. Finally, a 5-hole probe was used to gather pressure, temperature and velocity angle data on P40.

**b) Design Point (DP)** The design point (see Tab. 1.1) was defined to be representative for a large envelop of gas turbine engines while staying at temperature levels that are harmless for material and measurement devices. At the DP operating conditions, 5-hole probe data is available on P40.

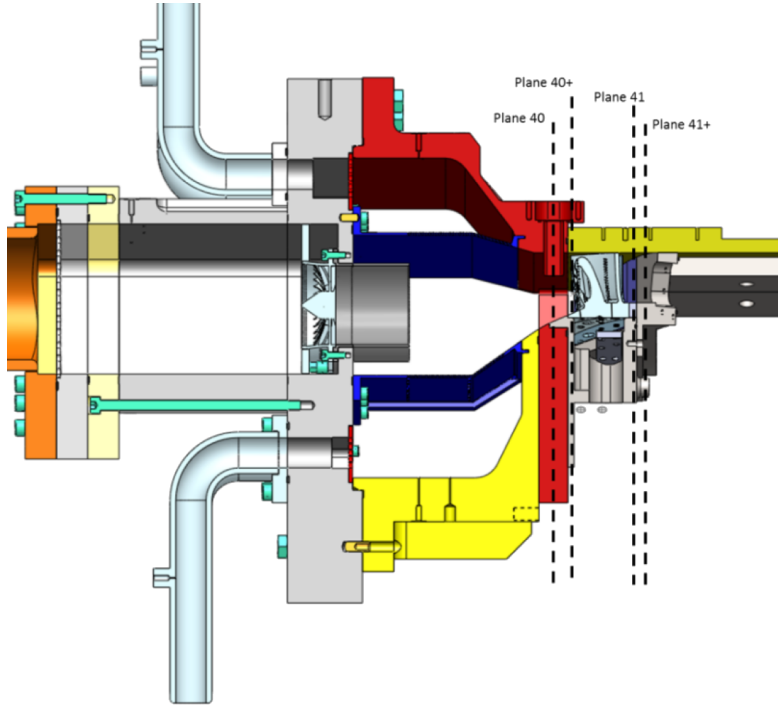


**Figure 1.9:** Positions of measurement planes are different with vanes (P40+, P41+).

**Table 1.1:** FACTOR operating conditions [16] at the trisector test rig at the University of Florence without fitted high-pressure vanes.

	IOP	DP
Static pressure on P40 [kPa]	115	147.65
Mach number on P40 [-]	0.113	0.108
Mass flow for 360° [kg/s]	4.8	4.8
Flow split swirler [-]	65%	65%
Flow split outer cavity [-]	21%	21%
Flow split inner cavity [-]	14%	14%
Swirler inlet temperature [K]	300	531
Coolant air temperature [K]	300	300
Reference Velocity [ $\text{m s}^{-1}$ ]	37.5	51.5
Swirler Reynolds number [-]	168 500	111 000
Swirler Mach number [-]	0.108	0.112

### Trisector test rig with high pressure vanes at the University of Florence

After data for DP & IOP had been acquired on the chamber only trisector bench, the test rig was equipped with five stator vanes resulting in an exit section with six flow passages. These vanes radially deviate the flow as seen in Fig. 1.8. In its final version, only the inner three NGVs are cooled, the outer two NGVs and the outer wall are uncooled. The middle swirler is aligned with the middle NGVs leading

edge. The clocking position is slightly different from that targeted at the full annular test rig (see Fig. 1.7). As a consequence, the operating points also slightly differ (see Tab. 1.3). Finally and due to geometrical constraints, the positions of P40 and P41 are shifted due to accessibility issues (see Fig. 1.9).

### Full annular test rig at DLR Göttingen

The full annular FACTOR test rig (see Fig. 1.10) at the DLR in Göttingen is built on the NG-turb test facility as a closed loop wind tunnel [17]. As previously said, the initially planned operating point was not entirely matched and pre-experiment CFD simulations use a different operating point (see Tab. 1.2) as well as clocking positions (see Fig. 1.7). Measurement data is available on several planes (see Fig. 1.11) as well as through pressure taps at different locations within the rig, notably on the NGV surface. Temperature measurements are available on the measurement planes as well as on the NGVs and rotor blades thanks to infrared thermography.

**Table 1.2:** Operating conditions of the full annular FACTOR test rig at DLR Göttingen.

Inlet pressure (static = total)	[kPa]	143
Outlet static pressure	[kPa]	53.7
Pressure ratio (total-to-static)		2.7
Swirler mass flow	[kg/s]	3.09
Combustor coolant feed total mass flow	[kg/s]	1.88
Combustor outer coolant mass flow	[kg/s]	0.95
High pressure side (upstream) blow-off	[kg/s]	0.26
Rotor front cavity coolant mass flow	[kg/s]	0.072
Rotor back cavity coolant mass flow	[kg/s]	0.072
NGV coolant feed mass flow	[kg/s]	0.6
Swirler air temperature	[K]	530
Coolant temperature (all nominal feeds)	[K]	300
Turbine rotor RPM	[rpm]	7700
Turbine rotor power	[kW]	507
Turbine rotor torque	[Nm]	570

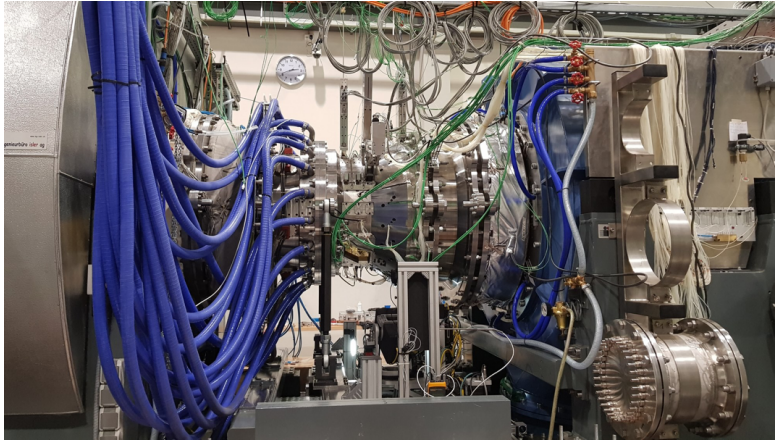


**Figure 1.10:** Full annular FACTOR test rig at DLR Göttingen.

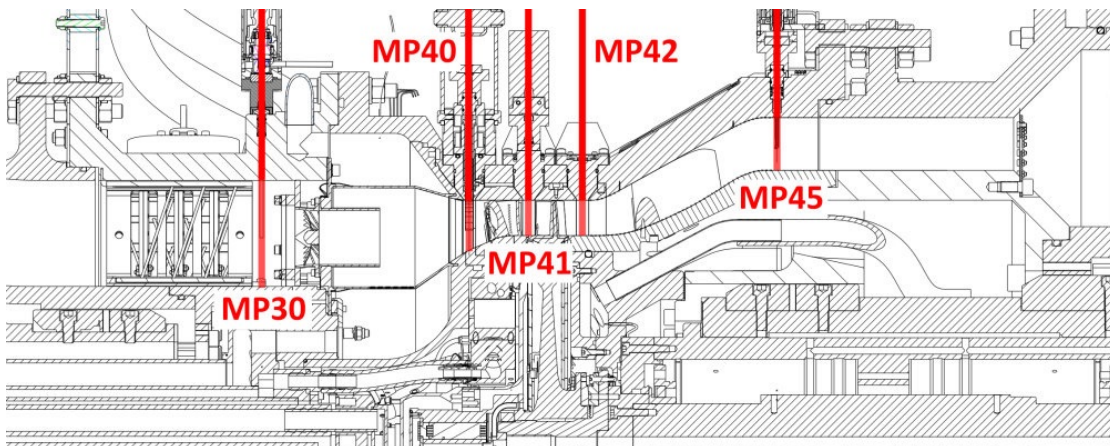


**Figure 1.11:** Measurement planes at the full annular FACTOR test rig at DLR Göttingen.

Having given details about the test rigs, all experimental operating points are summarized in Table 1.3. The isothermal operating point is denominated IOP and the design point is called DP. For both, there are slight differences depending on the rig: UNIFI/DLR and for the UNIFI rig: with or without the presence of vanes (NGV). Depending on the test rig, there are slight differences of clocking positions as illustrated in Figure 1.7.

**Table 1.3:** Summary of operating points.

Test rig	Domain	Operating point	Clocking position	Chapter
UNIFI				
	CC	IOP	-	3
	CC	DP	-	3
	CC + NGV	IOP <sub>NGV</sub>	UNIFI	-
	CC + NGV	DP <sub>NGV</sub>	UNIFI	4, 5, 6, Appendix A
DLR				
	Full annular rig	DP <sub>DLR</sub>	LE <sub>DLR</sub>	7
	Full annular rig	DP <sub>DLR</sub>	PA <sub>DLR</sub>	-

CC=Combustion Chamber

## 1.2.2 CFD of the FACTOR test rig

The FACTOR project's objective was to improve the understanding of combustor-turbine interactions and the transport of hot streaks in next-generation gas turbine engines based on a joint CFD and experimental approach. The previous discussion focused solely on experimental aspects. Within the FACTOR consortium, LES predictions were obtained by the CERFACS team and further simulations (RANS, URANS, SAS) were performed by other project partners. A brief overview of obtained results prior to this work is provided in the following.

At CERFACS high fidelity simulations are performed using the AVBP code. Details on individual simulations as well as more comprehensive information about the AVBP code is given in Chapter 2. Simulations performed by C. Koupper were conducted in accordance with the operating conditions of the UNIFI test rig without the high pressure nozzle. These simulations are continued in the present work and specific aspects are investigated in more detail. Further simulations are also performed considering the complete combustion chamber and attached single staged high-pressure turbine. Details on the present simulations relative to the existing experiments are presented in Tab. 1.3.

Several industrial partners of the FACTOR project also performed numerical simulations, mainly using RANS, URANS and SAS. Cottier et al. [18] performed URANS simulations of the FACTOR test rig with a domain extending over combustor module and attached high-pressure turbine or turbine only. They concluded that there is a strong impact of the combustor module on the mixing in the high-pressure turbine. Further numerical investigations performed at UNIFI targeted the investigation of the test rig and more specifically the impact of the cooling system [19] as well as the impact of the combustor outlet flow on the flow field in the high pressure nozzle [20]. Finally, researchers at the Van Karman institute performed RANS simulation on the FACTOR test rig which were then compared

to LES available at that time and performed by CERFACS [21]. The authors conclude that RANS may yield results similar to LES in terms of hot streak transport provided that inlet turbulence is correctly modeled and an adequate turbulence model is chosen.

### 1.3 Objectives of this Thesis

This PhD thesis was launched and funded by SAFRAN Helicopter Engines in partnership with CERFACS within the framework of the European project FACTOR.

This work expands on previous work by C. Koupper [16]. In his PhD, C. Koupper participated in the development of the FACTOR combustor module in close collaboration with UNIFI which provided experimental data for validation [15]. The outcome of the development was to retain a 55 mm duct design that allows to create a sustained recirculation zone in the chamber. From this, best practice guidelines for the numerical computation of the combustion chamber were developed [22] and complemented by the development of advanced diagnostics as well as validation procedures making use of the rich time resolved flow field data available from LES [23]. Finally, first integrated computations of the combustor fitted with vanes at its exit were performed to investigate potential clocking effects [24].

Based on these past experiences, the present work has complementary objectives naturally connected with this previous work. These are briefly summarized in the following:

- The investigation of coolant flows and interactions with the main flow field is one of the outcomes of the FACTOR project. In previous studies, the ability of the homogeneous coolant injection model [25], applied to the combustion chamber liners to account for the effusion cooling system, was found to be questionable. A novel heterogeneous model, initially proposed by [26], allows to represent discrete jets by prescribing discrete inlets on the liner surface, as reported in the thesis of R. Bizzari [27]. This new model is thus compared to the previously used homogeneous coolant injection model [25]. Validations are here obtained by comparing the homogeneous and heterogeneous model LES predictions with available data at the exit of the combustion chamber, i.e. P40.
- Alike in the combustion chamber, resolving the cooling system of the NGVs is very costly. To investigate possible cost-saving alternatives with regard to the fully integrated chamber + NGV simulation, the same heterogeneous coolant injection model is applied to the nozzle guide vanes to model its cooling system. The objective is here to evaluate the potential of such a model as well as the impact of the NGV cooling system on the main flow. Results of this collaborative work with M. Harnieh are presented in [28].

After investigations in the chamber and more specifically the cooling system in **Part I**, **Part II** of this work focuses on the investigation of the flow in chamber and attached high-pressure vanes.

- One objective in this context is to take advantage of the full time-resolved data set generated by LES by application of higher-order statistical tools developed by C. Koupper [29]. Typically, higher order statistics evidence potential thermally critical areas by marking the trace of the hot streak and their impact on the NGV wall temperature.
- A second objective results from the inherited industrial design approach and tries to identify methods for the improvement of isolated component simulations. On the basis of an integrated simulation of the combustion chamber and high pressure vanes, different approaches are tested to recover the flow field of the integrated simulation in isolated high pressure vane simulations. Indeed, using the steady mean field or the mean field with an added artificially created turbulence as inlet condition is not found to recover the flow field in an isolated domain [11]. Contrarily it is shown that recasting the full unsteady flow field obtained from the previous integrated simulation allows to recover the flow field in an isolated domain. The reason for the different results is specifically investigated and indicates that large scale disturbances and hot spot features are of primary importance. Hence, they should be considered for accurate predictions of isolated high-pressure vane CFD.
- Finally and with the availability of measurement data from the full annular FACTOR test rig at DLR Göttingen, LES of combustor and single staged high-pressure turbine are performed. In this simulation, techniques to model the cooling systems (liners and NGV) previously addressed in this work, are used. Results are presented in [30].

Note that specific elements of the work performed during this thesis were published in various articles. These are:

[a] Thomas, M., Dombard, J., Duchaine F., Gicquel, L., and Koupper, C. "Comparison of heterogeneous and homogeneous coolant injection models for Large Eddy Simulation of multiperforated liners present in a combustion chamber". In: *ASME Turbo Expo 2017: Turbine Technical Conference and Exposition*. GT2017-64622. 2017

[b] Thomas, M., Dombard, J., Duchaine F., Gicquel, L., and Koupper, C. "Advanced statistical analysis estimating the heat load issued by hot streaks and turbulence on a high-pressure vane in the context of adiabatic large eddy simulations". In: *ASME Turbo Expo 2019: Turbine Technical Conference and Exposition*. GT2017-64648. 2017

[c] Thomas, M., Dombard, J., Duchaine F., Gicquel, L., and Koupper, C. "Impact of realistic inlet condition on LES predictions of isolated high pressure vanes". In:

*12th International ERCOFTAC Symposium on Engineering Turbulence Modelling and Measurements*. ETMM2018 - 110. 2018

[d] Harnieh, M., Thomas, M., Bizzari, R., Duchaine F. and Gicquel, L. "Assessment of a coolant injection model on cooled high-pressure vanes in Large Eddy Simulation". In: *12th International ERCOFTAC Symposium on Engineering Turbulence Modelling and Measurements*. ETMM2018 - 111. 2018

[e] Martin, B, Thomas, M., Dombard, J., Duchaine F. and Gicquel, L. "Analysis of sand particle ingestion and erosion in a turbomachine using Large-Eddy Simulation". In: *ASME Turbo Expo 2019: Turbine Technical Conference and Exposition*. GT2019-91215. 2019

[f] Thomas, M., Dombard, J., Duchaine F., Gicquel, L., and Koupper, C. "Large-Eddy Simulation of combustor and complete single-stage high-pressure turbine of the FACTOR test rig". In: *ASME Turbo Expo 2019: Turbine Technical Conference and Exposition*. GT2019-91206. 2019

[g] Harnieh M., Thomas M., Bizzari R., Dombard J., Duchaine F., and Gicquel L. "Assessment of a coolant injection model on cooled high-pressure vanes with large-eddy simulation," In: *Flow, Turbulence and Combustion* 104, 643 - 672 (2020).

## 1.4 Organization of the Manuscript

After discussing the general scope of the manuscript, this section describes the content of parts and chapters. Chapter 1 & 2 give a general introduction about the topic and the numerical methods used in this work. To address the objectives and results discussed previously, the present PhD dissertation is constructed around two main parts and five chapters (see Fig. 1.12):

**Part I** contains a detailed discussion of cooling system modeling approaches applied to the combustion chamber liners and the NGVs.

- Chapter 3 discusses the impact of a homogeneous and a heterogeneous effusion cooling modeling approach on the flow field in the combustor module.
- Chapter 4 focuses on the application of the heterogeneous cooling modeling approach on the FACTOR NGVs. For this specific step, results are then compared to a simulation with a fully resolved cooling system.

**Part II** focuses on the simulation of a combustor and its high-pressure turbine. It includes an analysis of the flow field in such integrated domains. Additionally, different methods are investigated with the objective to extract relevant flow field information from one simulation, e.g. on the interface plane P40, and then feed them back into another simulation. Such methods are usually introduced to recover the flow field of an integrated combustor plus high-pressure vane simulation in an isolated stator or stage simulation. Therefore,

- Chapter 5 uses advanced statistical analysis of readily available LES data to trace the path of the hot streak and to mark clocking position dependent thermally critical areas in such simulations.
- Chapter 6 contains a novel approach to recover the flow field of integrated combustor + high-pressure vane simulations while performing isolated high-pressure vane simulations.
- Chapter 7 compares predictions of an integrated chamber & high-pressure turbine LES with the experimental data obtained from the full annular FACTOR test rig at DLR Göttingen.

Finally, the chapter **General Conclusions and Perspectives** summarizes the outcomes of this work and gives an outlook to future works that will follow.

Note that specific details are furthermore provided at the end of the manuscript in the Appendix section. These are:

- Appendix A: Sensitivity of simulations to the Sub-grid scale turbulence model used.
- Appendix B: Summary of LES on FACTOR.
- Appendix C: All publications written within the course of this work.

In Fig. 1.12, above mentioned chapters, their topic and the addressed test rig are presented to give a short visual insight into each chapter.

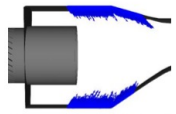
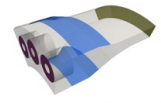
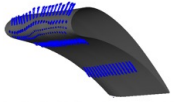
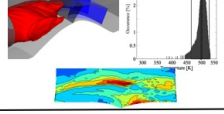
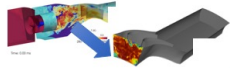
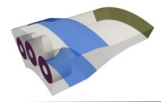
Chapter	Domain	Topic	Test rig	Operating point
3	Chamber only 	Effusion Cooling system 	UNIFI test rig 	Isothermal UNIFI Design point UNIFI
4	Vanes only 	NGV Cooling 	UNIFI test rig 	Design point UNIFI
5	Chamber + Vanes 	Advanced statistics 	UNIFI test rig 	Design point UNIFI
6	Vanes only 	Impact of inlet conditions 	UNIFI test rig 	Design point UNIFI
7	Chamber + HP-Turbine 	Fully integrated simulation 	DLR test rig 	Design point DLR

Figure 1.12: Overview of simulations presented in this work.



# Chapter 2

## Simulation methods and diagnostics used in this work

### Contents

---

2.1	Computational Fluid Dynamics . . . . .	<b>19</b>
2.1.1	Governing equations . . . . .	22
2.1.2	The AVBP code . . . . .	27
2.2	Statistical tools and analysis of the LES predictions . . . . .	<b>27</b>
2.2.1	Higher order statistical moments . . . . .	28
2.2.2	Proper Orthogonal Decomposition . . . . .	30
2.2.3	Dynamic Mode Decomposition . . . . .	31

---

### 2.1 Computational Fluid Dynamics

Over the last decades, computational fluid dynamics (CFD) has become a valuable and efficient tool to gain new insights in a range of different fluid mechanics problems [31–33]. CFD uses numerical methods to predict flow fields in diverse regimes and geometries. The history of CFD started with the application of numerical methods for weather forecast [34]. In the 1960s, first calculations were performed using linear potential equations, a strong simplification of the non-linear partial differential Navier-Stokes equations governing the motion of fluids (see Fig. 2.1). Increasing computational power (see Fig. 2.2), actually doubling every 2 years over the last decades [35], allowed to use more and more sophisticated approaches yielding more accurate predictions. Such resolution techniques helped to improve understanding and design of a large range of technical devices. The evolution in CFD has also allowed to diminish or even replace expensive fluidic experiments often needed in the design of complex devices. This finally resulted in reducing the time needed to design a new product.

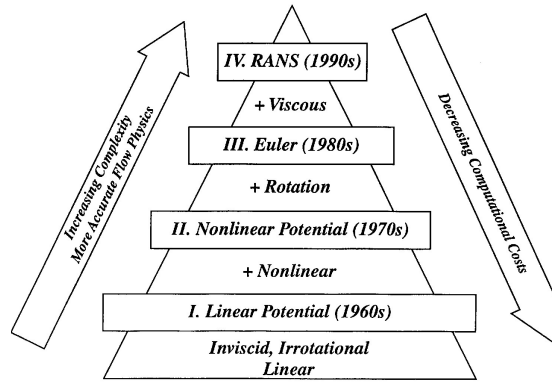


Figure 2.1: Historical development of numerical approaches [36].

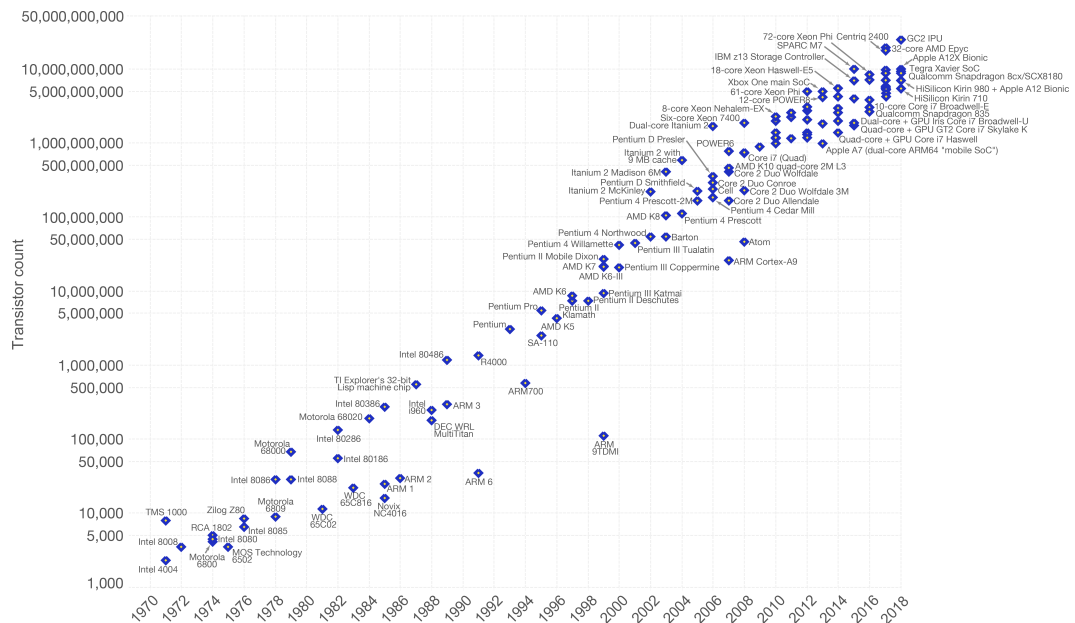


Figure 2.2: Moore’s Law - number of transistors on integrated circuit chips, doubling roughly every two years [37].

One of the major challenges for CFD is the non-linear nature of the model which results in the existence of different temporal and spatial scales in most flow fields rendering an accurate prediction of these flows a challenging task [38]. Today, most commonly applied approaches in industrial CFD are RANS and LES, whereas DNS remains in the academic context [32] (see Fig. 2.3). As detailed hereafter, different modeling levels are introduced in each framework.

**Reynolds Averaged Navier-Stokes (RANS):**

RANS simulations predict the time-averaged mean flow field of a given fluid mechanics problem [39]. To do so, Navier-stokes equations are Reynolds averaged, whereby one instantaneous quantity is decomposed in a fluctuating and a mean quantity. The product of fluctuating quantities arising from the nonlinear terms present in the Navies-Stokes equations yields unclosed terms, so-called Reynolds

stresses, that need to be modeled in order to close the mean field evolution equations. Note that for RANS, all unsteady flow contributions are modeled. Since its introduction, RANS had a long history of application as well as model developments that yield accurate flow predictions for given specific cases. In industry, RANS simulations are appreciated and routinely used because they are fast and low cost. Limits are however very often attained and complex industrial flow predictions are sometimes questionable.

### Large Eddy Simulation (LES):

In LES, filtered Navier-Stokes equations are solved [38, 40, 41]. Large geometry dependent flow structures are hence explicitly computed whereas small scale more homogeneous turbulence features, not resolved by the grid, are accounted for by so-called sub-grid scale models (detailed in Appendix A). These sub-grid scale models are needed to mimic the turbulent kinetic energy cascade (see Fig. 2.4) and drain energy from the resolved flow field which is finally dissipated into heat. In industrial geometries, near-wall behavior is usually accounted for by wall models, which significantly reduces computational cost compared to the academic and recommended wall resolved LES approach [42]. Today, LES finds more and more applications as it better captures the flow physics and allows new insights in unsteady flow phenomena [43]. The cost of LES is orders of magnitude higher than that of a steady-state RANS simulation which makes parallel computing on several hundreds of cores necessary to obtain results within reasonable time frames [44].

### Direct Numerical Simulation (DNS):

In DNS, all turbulent scales are resolved in time and space, which makes this approach very expensive and only applicable for academic cases. Currently, DNS is used to improve the understanding of basic fluid mechanics and to create databases for the development of new models [45] to be used either in RANS or LES.

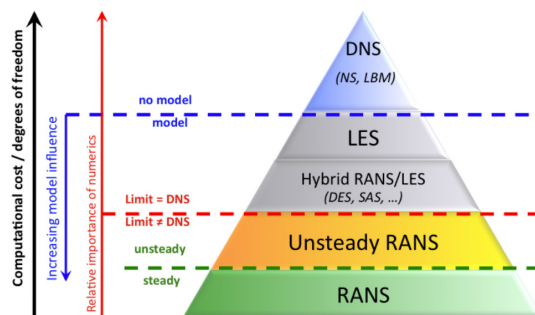


Figure 2.3: Numerical approaches for CFD [36].

As said earlier, decades of CFD simulations contributed to a clear improved understanding as well as an increased performance of all kinds of applications. In this work, being at the interface between an industrial context and advanced modeling methods in CFD, LES is used to investigate and eventually predict interaction phenomena of combustor and high-pressure turbine of the FACTOR test rig. Due

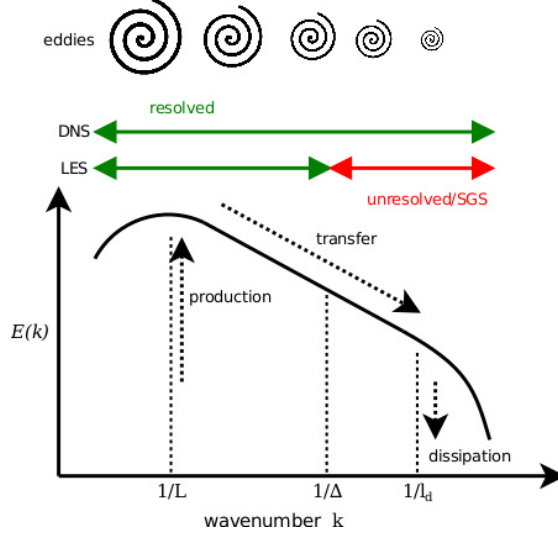


Figure 2.4: Energy cascade [36].

to the existence of different flow regimes in chamber (low Mach) and high-pressure turbine (high Mach), the usage of compressible Navier-Stokes equations becomes mandatory. These are described in the following section.

### 2.1.1 Governing equations

The compressible Navier-Stokes equations describe the conservation of mass (Eq. 2.1), momentum (Eq. 2.2) and total energy (Eq. 2.3) in fluid mechanics [46] and can be written as:

$$\frac{\partial \rho}{\partial t} + \frac{\partial}{\partial x_j}(\rho u_j) = 0, \quad (2.1)$$

$$\frac{\partial}{\partial t}(\rho u_i) + \frac{\partial}{\partial x_j}(\rho u_i u_j + P \delta_{ij} - \tau_{ij}) = 0, \quad (2.2)$$

$$\frac{\partial}{\partial t}(\rho E) + \frac{\partial}{\partial x_j}(\rho u_j E + u_i P \delta_{ij} + q_j - u_i \tau_{ij}) = 0, \quad (2.3)$$

where  $\rho$  is the fluid density,  $t$  is the time,  $x$  is the coordinate vector,  $u$  is the fluid velocity vector,  $P$  is the pressure,  $\tau_{ij}$  is the viscous stress tensor,  $E$  is the total energy and  $q$  the heat flux vector. The indices  $i, j$  denote the three dimensions of space. Pressure, density and temperature are linked by the state equation for perfect gases,

$$P = \rho r T, \quad (2.4)$$

where  $r = 287.0 \text{ J/kg}$  is the air gas constant. All fluids discussed in this work are Newtonian fluids which implies that the viscous stress tensor is linearly dependent on the velocity strain rate tensor:

$$s_{ij} = \frac{1}{2} \left( \frac{\partial u_i}{\partial x_j} + \frac{\partial u_j}{\partial x_i} \right). \quad (2.5)$$

Using the Stokes Hypothesis [47], the viscous stress tensor  $\tau_{ij}$  can thus be written as,

$$\tau_{ij} = 2\mu \left( s_{ij} - \frac{1}{3} s_{kk} \delta_{ij} \right), \quad (2.6)$$

Using the Sutherland law [48], the dynamic viscosity  $\mu$  can be calculated by:

$$\mu = \mu_{ref} \left( \frac{T}{T_{ref}} \right)^{2/3} \frac{T_{ref} + 110.4}{T + 110.4}, \quad (2.7)$$

with the reference values of  $\mu_{ref} = 1.71 \times 10^{-5} \text{ kg/m.s}$  and  $T_{ref} = 273.15 \text{ K}$  for air.

The heat flux vector  $q_i$  of Eq. 2.3 can be expressed by the Fourier law:

$$q_i = -\lambda \frac{\partial T}{\partial x_i}, \quad (2.8)$$

where the thermal conductivity  $\lambda$  is,

$$\lambda = \frac{\mu C_p}{Pr}. \quad (2.9)$$

Here,  $C_p$  is the specific heat capacity. The molecular Prandtl number  $Pr$  equals 0.75 for air and is supposed constant in time and space.  $C_p$  depends on temperature and composition, which is neglected here to improve readability.

## LES Governing Equations

In LES, filtered Navier-Stokes equations are solved on a grid resolving large scale geometry dependent flow structures, whereas small scale turbulence, geometry independent according to Kolmogorov's Hypothesis [49], is modeled using sub-grid scale models. Any quantity  $\Phi$  is thereby decomposed in a part  $\bar{\Phi}$  resolved by the computational grid and a part  $\Phi''$  unresolved by the computational grid or equivalently removed by spatial filtering,

$$\Phi = \bar{\Phi} + \Phi''. \quad (2.10)$$

Flow features not resolved by the computational grid are taken into account by so called sub-grid scale (SGS) models, to be discussed in the following section. To avoid additional SGS terms in the mass conservation equation, compressible Navier-Stokes equations are Favre-averaged [46]:

$$\tilde{\Phi} = \frac{\overline{\rho\Phi}}{\bar{\rho}}. \quad (2.11)$$

Using a spatial Favre filtering operation on a variable  $\Phi$  results in a separation of scales:

$$\widetilde{\phi(\vec{x}, t)} = \frac{1}{\bar{\rho}(\vec{x}, t)} \int_{-\infty}^{+\infty} \rho(\vec{x}', t) \phi(\vec{x}', t) G(\vec{x}' - \vec{x}) d\vec{x}', \quad (2.12)$$

where  $G$  is a filter function determining the size of the small scales. In most cases, the filter width is equal to the cubic root of the local cell volume. The Navier-Stokes equations (Eq. 2.1, Eq. 2.2 and Eq. 2.3) obtained after Favre filtering, can be written as:

$$\frac{\partial \bar{\rho}}{\partial t} + \frac{\partial}{\partial x_j} (\bar{\rho} \tilde{u}_j) = 0 \quad (2.13)$$

$$\frac{\partial}{\partial t} (\bar{\rho} \tilde{u}_i) + \frac{\partial}{\partial x_j} (\bar{\rho} \tilde{u}_j \tilde{u}_i + \bar{P} \delta_{ij} - \bar{\tau}_{ij} - \bar{\tau}_{ij}^{sgs}) = 0 \quad (2.14)$$

$$\frac{\partial}{\partial t} (\bar{\rho} \tilde{E}) + \frac{\partial}{\partial x_j} (\bar{\rho} \tilde{u}_j \tilde{E} + \bar{P} \tilde{u}_i \delta_{ij} + \bar{q}_j + \bar{q}_j^{sgs} - \tilde{u}_i (\bar{\tau}_{ij} + \bar{\tau}_{ij}^{sgs})) = 0 \quad (2.15)$$

The laminar filtered stress tensor and the filtered heat flux are then respectively approximated by:

$$\bar{\tau}_{ij} = \overline{2\mu \left( s_{ij} - \frac{1}{3} \delta_{ij} s_{kk} \right)} \simeq 2\bar{\mu} \left( \tilde{s}_{ij} - \frac{1}{3} \delta_{ij} \tilde{s}_{kk} \right), \quad (2.16)$$

$$\bar{q}_i = -\lambda \frac{\partial \bar{T}}{\partial x_i} \simeq -\bar{\lambda} \frac{\partial \tilde{T}}{\partial x_i}. \quad (2.17)$$

Compared to the original Navier-Stokes equations, two new unclosed terms describing the unresolved sub-grid scale contributions appear. The SGS heat flux vector  $\bar{q}_i^{sgs}$  is defined by:

$$\bar{q}_i^{sgs} = \bar{\rho} \left( \widetilde{u_i E} - \tilde{u}_i \tilde{E} \right), \quad (2.18)$$

and is modeled by the expression,

$$\bar{q}_i^{sgs} = -\lambda_{sgs} \frac{\partial \tilde{T}}{\partial x_i}, \quad (2.19)$$

introducing the SGS thermal conductivity  $\lambda_{sgs}$ :

$$\lambda_{sgs} = \frac{\nu_{sgs} \bar{\rho} \bar{C}_p}{Pr_{sgs}}, \quad (2.20)$$

where the SGS Prandtl number noted  $Pr_{sgs}$  is usually set to a constant value (about 0.6). Different approaches to obtain the sub-grid scale turbulent viscosity  $\nu_{sgs}$  are presented in the next section.

Equivalently to RANS, the SGS-Reynolds tensor,  $\bar{\tau}_{ij}^{sgs}$ , is unclosed and defined as,

$$\bar{\tau}_{ij}^{sgs} = -\bar{\rho} (\widetilde{u_i u_j} - \tilde{u}_i \tilde{u}_j). \quad (2.21)$$

Different approaches to model SGS contributions exist. Some of the models used in AVBP are reported in the following section and a comparison of the effect of these SGS modeling approaches on the flow field in the FACTOR test rig can be found in Appendix A.

### SGS-Models present in AVBP

SGS models try to estimate effects of small scale physical processes not adequately resolved on a given computational grid. For LES, many different kinds of SGS models have been developed and most of them rely on the Boussinesq's hypothesis [50], relating the sub-grid Reynolds stress tensor  $\tau_{ij}^{SGS}$  to the trace-less mean strain rate tensor,  $\overline{S_{ij}}$ :

$$\tau_{ij}^{SGS} = 2\mu_t \overline{S_{ij}} - \frac{1}{3} \delta_{ij} \tau_{ij}^{SGS}, \quad (2.22)$$

where  $\mu_t$  denotes the SGS eddy viscosity.  $\overline{S_{ij}}$  is defined by,

$$\overline{S_{ij}} = \frac{1}{2} \left( \frac{\partial U_i}{\partial x_j} + \frac{\partial U_j}{\partial x_i} \right). \quad (2.23)$$

The most commonly used SGS models are briefly presented in the following.

**Smagorinsky** The Smagorinsky model [51] is the most basic SGS model for LES applying an equilibrium assumption that assumes all energy received from large scale turbulence to be immediately and entirely dissipated. The main advantages are its robustness and ease of implementation in CFD codes. A direct consequence of its initial hypothesis is that in homogeneous isotropic turbulent flows, the correct amount of dissipation of turbulent kinetic energy is obtained. In general, the model is however too dissipative and not good for transitioning flows as found in high-pressure turbines [40]. For the Smagorinsky model, the turbulent viscosity  $\nu_{SGS}$  is related to the resolved strain rate tensor  $\tilde{S}_{ij}$  such that,

$$\nu_{SGS} = (C_s \Delta)^2 \sqrt{2\tilde{S}_{ij}\tilde{S}_{ij}}, \quad (2.24)$$

where  $\Delta$  is the filter width and  $C_s = 0.18$  the Smagorinsky coefficient.

**Wall adapting local eddy viscosity model (WALE)** The WALE model was developed by Nicoud et al. [52] in an attempt to improve near-wall predictions by recovering the turbulent viscosity scaling law close to solid boundaries. Indeed, in the vicinity of walls, the eddy viscosity naturally goes to zero. The model also produces zero eddy viscosity in pure shear flows and is thus able to reproduce the laminar to turbulent transition process through the growth of linear unstable modes. With this model, the turbulent viscosity closure reads,

$$\nu_{SGS} = (C_w \Delta)^2 \frac{(s_{ij}^d s_{ij}^d)^{3/2}}{(\tilde{S}_{ij} \tilde{S}_{ij})^{5/2} + (s_{ij}^d s_{ij}^d)^{5/4}}, \quad (2.25)$$

$$\text{with: } s_{ij}^d = \frac{1}{2} (\tilde{g}_{ij}^2 \tilde{g}_{ij}^2) - \frac{1}{3} \tilde{g}_{kk}^2 \delta_{ij}, \quad (2.26)$$

where  $C_w = 0.5$  is a model coefficient and  $\tilde{g}_{ij} = \frac{\partial \tilde{u}_i}{\partial x_j}$  the filtered velocity gradient.

**Sigma** The sigma model [53] yields similar predictions as the WALE model, with the important advantage that its contribution vanishes in laminar flows. In

this approach,  $\nu_{SGS}$  is related to singular values  $(\sigma_1, \sigma_2, \sigma_3)$  of the velocity gradient tensor:

$$\nu_{SGS} = (C_\sigma \Delta)^2 \frac{\sigma_3(\sigma_1 - \sigma_2)(\sigma_2 - \sigma_3)}{\sigma_1^2}, \quad (2.27)$$

where  $C_\sigma = 1.5$ .

After discussing different sub-grid scale turbulence models, the next section focuses on boundary conditions.

### Boundary conditions

In internal flow simulations, boundary conditions have a major impact on numerical predictions. In the context of LES, imposing boundary conditions in a hard way on conservative variables can lead to different types of numerical errors that can have a strong impact on simulation results. The reflection of waves is difficult to handle imposing boundary conditions in a hard way and usually leads to dispersion errors of the waves reflected by the wall [54]. To obtain a good LES prediction such effects have to be minimized. Characteristic boundary conditions have been specifically developed to reduce such problems.

Characteristic boundary conditions have been first introduced by Thompson [55] for Euler equations and then extended to viscous flows by Poinot and Lele [56]. This type of boundary condition distinguishes between outgoing waves that contain physical information (calculated inside the domain) and incoming waves entering the computational domain. The principle is to provide a solution from the balance between incoming and outgoing waves. Depending on the Mach number at the inlet/outlet, there are cases, where all waves travel out of the domain (supersonic outlet) or into the domain (supersonic inlet).

The accurate prediction of near-wall velocity gradients is a critical issue in internal flow simulations. There are two options to take the near-wall behavior into account: 1) Wall resolved LES and 2) Wall modeled LES. Fully wall-resolved simulations performed with a grid reaching  $y^+$  values close to 1 often remain out of reach for today's computational resources. Hence, the near-wall velocity gradient is often modeled [57]. The boundary layer is described by  $y^+$ , the non-dimensional wall distance and  $u^+$ , the non-dimensional wall velocity, defined as:

$$y^+ = \frac{y_{wall} u_\tau}{\nu_{wall}}, \quad u^+ = \frac{u_c}{u_\tau}, \quad (2.28)$$

where  $y_{wall}$  denotes the wall normal distance,  $\nu_{wall}$  the local kinematic viscosity of the fluid,  $u_c$  the mean velocity of all cell vertices not connected to the wall and  $u_\tau$  the friction velocity  $u_G = \sqrt{\frac{\tau_{wall}}{\rho}}$  where  $\tau_{wall} = \mu \frac{\partial u}{\partial y}|_{wall}$ . The logarithmic law of the wall (Eq. 2.30) was first described by von Karman (1930) [58]:

$$y^+ \leq 11.445 : u^+ = y^+, \quad (2.29)$$

$$y^+ > 11.445 : u^+ = \kappa^{-1} \log(Ey^+), \quad (2.30)$$

with  $\kappa = 0.42$  and  $E = 9.2$ . The most basic form of wall modeling for LES simply imposes such a law to evaluate the wall friction at the wall as a function of  $u$  instead of the SGS model. It is also to be noted that some blending may appear. For a fully developed flow, the law of the wall is described through a Van Driest-style damping function into the length scale [59]. These specific options are however not present in AVBP.

### 2.1.2 The AVBP code

Simulations presented in this work are performed using AVBP [60], a massively parallel CFD code developed at CERFACS. The code is based on an explicit cell-vertex formulation and solves the filtered compressible Navier-Stokes equations for conservative variables on hybrid unstructured meshes. AVBP is dedicated to LES and has been used and validated for a wide range of different applications [61–65]. In general, simulations are first converged using the second order accurate Lax-Wendroff scheme [66], then, a more accurate finite element two-step time-explicit Taylor Galerkin scheme (TTG4A or TTGC) is used for the discretization of convective terms. The TTGC scheme is third order accurate in time and space and the TTG4A scheme is fourth order accurate in time and third order in space [67]. These schemes ensure low diffusion and dispersion properties [68] and are therefore adequate for high fidelity simulations. Diffusive terms are discretized using a vertex centered formulation close to the Galerkin finite element method [69]. Time marching is done, respecting CFL (convection scheme) and Fourier [70] (diffusion scheme) numbers to guarantee linear stability. Note also that Colin-type artificial viscosity [71] is added to damp potential numerical oscillations naturally present with the used centered schemes. Finally, sub grid scale (SGS) turbulent contributions are computed using Smagorinsky [51], WALE [52] or Sigma [53] model (see previous section for details). In this document, all discussed grids have been designed according to a mesh refinement study performed by C. Koupper and to allow for a time step around  $4 \times 10^{-8}$  s. Specific details about all simulations presented herein are available in Appendix B.

## 2.2 Statistical tools and analysis of the LES predictions

After addressing numerical fundamentals, this section discusses the analysis tools used in this work to study the flow fields. First, higher order statistical moments (Skewness, Kurtosis) which allow to describe variable distributions are discussed. The following is dedicated to a presentation of different means to extract frequencies and dominant flow features.

### 2.2.1 Higher order statistical moments

To evaluate CFD simulations usually low order statistical moments (mean, variance) are used. Higher order statistical moments allow further insights in simulations and help to better understand different flow features and to evaluate their impact on the flow field. The main prerequisite for the application of higher order statistical methods is the availability of sufficiently long statistically stationary data. Over this duration, an adequately high number of 3D or interpolated 2D flow fields is stored at a constant time-interval. Here, operations to extract high order moments are first described by their continuous form and then approximated by their discrete representation. Note also that all quantities are one point statistics and refer to a unique location denominated by the vector position  $x$ . In this one point statistics context, describing the shape of probability density functions (PDF), of temperature for example, allows qualifying the evolution between turbine inlet temperature distortions (ITD) on P40 and temperature distributions on the adiabatic NGV surface.

The first statistical moment, the mean  $\overline{T(x)}$  of a quantity  $T(x, t)$ , defines the average of a quantity over a time interval or respectively a number  $N$  of equally spaced discrete realizations:

$$\overline{T(x)} = \frac{\int_{t_0}^{t_1} T(x, t) dt}{t_1 - t_0} \approx \frac{1}{N} \sum_{i=1}^N (T(x, t_i)) = \overline{T(x)}^d, \quad (2.31)$$

where  $t_0$  and  $t_1$  describe a time interval. Discrete quantities are marked by the superscript  $d$ . The standard deviation  $\sigma(x)$ , describes how far values are spread around the mean:

$$\begin{aligned} \sigma(x) &= \sqrt{\frac{1}{t_1 - t_0} \int_{t_0}^{t_1} (T(x, t) - \overline{T(x)})^2 dt}, \\ &\approx \sqrt{\frac{1}{N} \sum_{i=1}^N (T(x, t_i) - \overline{T(x)}^d)^2} = \sigma(x)^d. \end{aligned} \quad (2.32)$$

Skewness  $S(x)$ , the third statistical moment, is a measure for the asymmetry of a PDF, indicating whether the most probable value (mode value) is lower (positive skewness) or higher (negative skewness) than the mean:

$$\begin{aligned} S(x) &= \frac{1}{t_1 - t_0} \int_{t_0}^{t_1} \left( \frac{T(x, t) - \overline{T(x)}}{\sigma(x)} \right)^3 dt, \\ &\approx \frac{1}{N} \sum_{i=1}^N \left( \frac{T(x, t_i) - \overline{T(x)}^d}{\sigma(x)^d} \right)^3. \end{aligned} \quad (2.33)$$

Note the skewness of symmetric distributions (e.g. Gaussian) is 0, but the reverse is not true. For single peaked PDFs, the skewness can be interpreted as the distance

of the most probable value (mode value) to the mean. Kurtosis  $K(x)$ , the fourth statistical moment, indicates how 'peaked' the signal is around the mean value.  $K(x)$  is calculated by:

$$\begin{aligned} K(x) &= \frac{1}{t_1 - t_0} \int_{t_0}^{t_1} \left( \frac{T(x, t) - \overline{T(x)}}{\sigma(x)} \right)^4 dt, \\ &\approx \frac{1}{N} \sum_{i=1}^N \left( \frac{T(x, t_i) - \overline{T(x)^d}}{\sigma(x)^d} \right)^4. \end{aligned} \quad (2.34)$$

For a Gaussian PDF the Kurtosis value is  $K = 3$ . Distributions with a sharper peak have higher Kurtosis and those which are flatter show lower values. One point statistics allow to investigate distribution properties from a single variable. For a more detailed discussion of statistical tools used to describe turbulent flows, the reader is referred to Tennekes et al. (1972) [72].

To investigate turbulent timescales which have a major impact on the heat flux on the NGV surface, the application of two times statistical analysis becomes mandatory. Visualizations of turbulent timescales allow to reveal locally persistent features in the flow field, as well as vortical structures marked by short timescale values. In this work, autocorrelation is used to calculate turbulent timescales  $t_{turb}(x)$  from a set of instantaneous CFD predictions stored at constant time intervals over a statistically significant time period covering multiple flow-through times [23, 38]. To do so, one velocity component  $u(x, t_i)$  (in this work, due to availability of experimental data, the analysis is done on the axial velocity component) is first decomposed in a mean  $\overline{u(x)}$  and a fluctuating part  $u'(x, t_i)$ :

$$u'(x, t_i) = u(x, t_i) - \overline{u(x)}, \quad (2.35)$$

where the discrete mean value  $\overline{u(x)^d}$  is calculated by Eq. (2.31). The autocorrelation coefficient  $R_{ff}$  of a function  $f$  is then introduced,

$$R_{ff}(\tau) = \int_{-\infty}^{\infty} f(t)f(t + \tau)dt. \quad (2.36)$$

In discrete form the time lag  $\tau$  becomes,

$$\tau_j = \Delta t \times j \quad (2.37)$$

For a limited time interval and in discrete form, the autocorrelation coefficient  $R_{uu}(x, \tau_j)$  for different time lags  $\tau_j$  and normalized by  $u_{RMS}^2(x) = \frac{1}{N} \sum_{i=1}^N (u(x, t_i) - \overline{u(x)^d})^2$  can then be written as:

$$R_{uu}(x, \tau_j) = \frac{\frac{1}{N} \sum_{i=1}^N u'(x, t_i)u'(x, t_{i+j})}{u_{RMS}(x)^2}, \quad (2.38)$$

Provided that the available data set is stationary and long enough,  $R_{uu}(x, \tau_j)$  depends only on the time lag  $\tau_j$  and not on the choice of a specific solution  $i$ . The turbulent timescale  $t_{turb}$  for each point can then be obtained using,

$$\begin{aligned} t_{turb}(x) &= \int_0^\infty R_{uu}(x, \tau) d\tau, \\ &\approx \Delta t \sum_{j=1}^{N_0} R_{uu}(x, \tau_j), \end{aligned} \quad (2.39)$$

where  $N_0$  is the solution where the discrete autocorrelation coefficient  $R_{uu}(x, \tau_j)$  tends to 0 [73], meaning that the signal is not correlated anymore.

## 2.2.2 Proper Orthogonal Decomposition

After discussing statistical methods to evaluate data on single individual locations, this section addresses ways to analyze data on entire domains using spatial and temporal information. Proper Orthogonal Decomposition (POD) is a methodology to find an optimal lower dimensional description of a high dimensional data set [74]. POD determines the optimal set of modes to represent data based on the  $L_2$  norm (energy) [75]. The data is hence represented as a set of spatial modes that are independent of time and a set of temporal modes that are independent of space. Unlike Dynamic Mode Decomposition (see below), one temporal POD mode can contain several frequencies. To approximate a function  $z(x, t)$ , orthonormal basis functions  $\Phi_k(x)$  and temporal coefficients  $a_k(t)$  are used which guarantees an optimal representation with a limited set of functions, where  $x$  is the position,  $t$  is the time variable and index  $k$  stands for the mode number. As a consequence, any function  $z(x, t)$  can be approximated by:

$$z(x, t) = \sum_{k=0}^M a_k(t) \Phi_k(x). \quad (2.40)$$

The set of orthonormal basis functions has to respect,

$$\int_x \Phi_{k_1}(x) \Phi_{k_2}(x) dx = \begin{cases} 1, & \text{if } k_1 = k_2, \\ 0 & \text{otherwise,} \end{cases} \quad (2.41)$$

so that the temporal coefficients,  $a_k(t)$ , can be calculated as,

$$a_k(t) = \int_x z(x, t) \Phi_k(x) dx. \quad (2.42)$$

In its corresponding discrete form, the above problem is a singular value decomposition, which reads,

$$A = U \Sigma V^T, \quad (2.43)$$

where  $A$  is a matrix [nodes x instants] that contains the instantaneous solution data composed by the axial transverse and crossstream momentum as well as the

temperature hereafter noted  $(\bar{\rho}\tilde{u}, \bar{\rho}\tilde{v}, \bar{\rho}\tilde{w}, \tilde{T})$  for all nodes at all time steps of a given set of instantaneous solutions. The  $U$  matrix [nodes x modes] contains the spatial coefficients for all modes and all nodes, while  $\Sigma$  [modes x modes] is a diagonal matrix, containing the Eigenvalues of the POD and  $V^T$  [modes x instants] is a matrix containing the temporal coefficients.

Apart from analyzing the flow field, POD can also be used to recast a flow field at the inlet of a truncated domain using certain modes that represent specific flow features, as shown in Chapter 6.

### 2.2.3 Dynamic Mode Decomposition

Dynamic mode decomposition is a dimensionality reduction algorithm that allows to extract modes at a fixed oscillation frequency. Each mode is associated with an amplitude and a growth/decay rate. DMD was developed by Peter Schmid in 2008 [76] to extract dynamic features from flow data. Unlike POD, which seeks for the most energetic flow features independent of their temporal frequency, DMD allows to investigate data for features excited at the same frequency, independent of their amplitude. A DMD analysis is usually more sensitive to detect frequencies in a flow region than using individual local probes. Combining POD and DMD allows interesting insights in flow data as localized features, excited at a specific frequency, and their impact on the flow field can be easily distinguished.



# Part I

## Cooling systems

*The investigation of interaction between coolant systems and main flow is an important target of the FACTOR project. This part of the manuscript is dedicated to a detailed discussion of cooling systems applied in turbomachinery. As of today, resolving small scale cooling systems in full combustor simulations is possible but remains prohibitively expensive in the LES context, which makes the application of models mandatory. Combustion chamber liners are made of multiperforated plates that inject coolant air to keep hot combustion gases away from the walls and maintain the structural integrity of the chamber. Chapter 3 discusses two different existing modeling approaches for such cooling systems and compares the impact of such modeling on the FACTOR combustor simulator flow. Chapter 4 is dedicated to the use and validation of the heterogeneous injection model if applied for NGV cooling. Such a modeling approach allows indeed to take coolant injection in the turbine into account without costly resolving the entire coolant system.*



# Chapter 3

## Effusion cooling systems

### Contents

---

3.1	Effusion Cooling models . . . . .	<b>39</b>
3.1.1	Homogeneous injection model . . . . .	40
3.1.2	Heterogeneous injection model . . . . .	40
3.2	Description of the test configuration . . . . .	<b>43</b>
3.3	Numerical Methodology . . . . .	<b>44</b>
3.4	Results and discussions . . . . .	<b>46</b>
3.4.1	Mean flow comparisons and validations . . . . .	47
3.4.2	RMS and turbulent quantities . . . . .	53
3.4.3	Unsteady feature in P40 . . . . .	55
3.5	Conclusion . . . . .	<b>56</b>

---

Reduction of the specific fuel consumption of aircraft engines is usually obtained by optimizing the thermodynamic cycle, which can be achieved by increasing pressure ratios and higher combustion temperatures. Temperatures in the combustion chamber have thus increased to levels above the melting point of alloys used in gas turbine engines which makes the use of cooling systems mandatory [4]. However, due to efficiency driven increasing pressure ratios, the heat sink capacity of highly compressed air used to dissipate excess heat diminishes. This poses challenges for the design of small turbo engines with an inherently high surface to volume ratio. Another disadvantage of this trend is the associated higher temperatures of the reactants in the combustor. Such increasing severity of aerothermal operating conditions inside the combustion chamber are today controlled thanks to cooling technologies that guarantee component lifetimes which can reach many tens of thousands of operating hours [4]. Whilst wall cooling is essential to provide a satisfactory component durability of both, the turbine and the combustor, there is also a need to minimize the proportion of air used by the cooling system as air taken away from the combustion process leads to increasing  $\text{NO}_x$  emissions.

In the next decades, with the introduction of  $\text{NO}_x$  reducing lean combustion concepts, due to the absence of dilution holes, the liner cooling system will gain

in impact on the main flow in the chamber. Among a variety of different cooling technologies present within the combustion chamber, angled-multihole (effusion) cooling systems (see Fig. 3.1), also known as full coverage film cooling (FCFC), have proven to perform best reaching different opposing targets, like cooling efficiency, mechanical integrity, weight, durability and industrial fabrication. Indeed, effusion cooling systems provide a heat sink of coolant air on the outer side of the liner and, at the same time, create a thermal barrier layer by coalescence of injected micro-jets on the inner side of the liner, keeping hot combustion gases away from the walls.

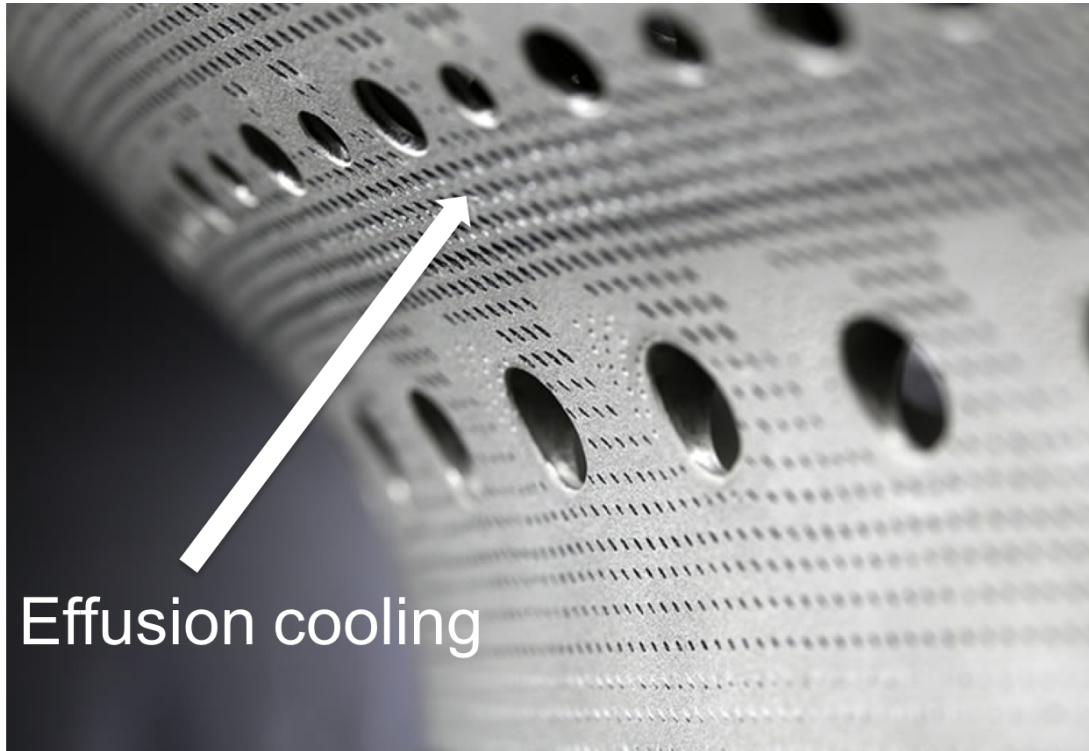


**Figure 3.1:** Multiperforated combustion chamber liner with conventional rich-quench-lean combustor design with dilution holes [77].

Research on liner cooling technologies started in the 1960s [78] when efficiency driven rising combustion temperatures first surpassed the melting point of heat resistant alloys known at the time. Due to manufacturing constraints, engine manufacturers first relied on slot cooling systems, creating a closed coolant film by injecting air through a slot along the wall. This however adds comparatively much weight to maintain structural integrity. The limitations of convective cooling systems for future higher combustion temperatures were first pointed out by Colladay (1970) [79] and the importance of exploiting the heat sink capacity of coolant air prior to its injection in the combustion chamber was discussed in [80]. Indeed, purely convective film cooling is insufficient as it only protects from convective heat flux and does not affect the radiative heat transfer resulting from luminous gases [81]. In the 80s, advances in manufacturing technology made the large-scale production of liner effusion cooling systems possible. These systems provide a

---

heat sink at the outer side of the liner and inject coolant air through a multitude of angled sub-millimetric perforations, creating a closed coolant film on the inner liner wall, which serves as a thermal barrier layer isolating the liners from the hot combustion gases. One of the main challenges in liner cooling system design is to maintain the integrity of the protective coolant film over a wide range of operating conditions in a highly turbulent flow field with local recirculation zones.

The main constraint for simulation of effusion cooling systems is the small scale of the perforations with respect to the global system. For explicit CFD codes, this entails prohibitively short time steps. Not to mention that fully resolving the cooling system with a sufficiently fine mesh requires a large portion of grid cells to be used only in this region. To circumvent this issue, a variety of different effusion cooling models can be found in literature. On a first level, all of these models reproduce the correct mass injection into the domain. Other models include the conservation of axial momentum. In coupled heat transfer (CHT) simulations, some models try to capture the correct heat loss due to convection inside the perforations [82]. More advanced models try to mimic the impact of discrete jets on the main flow [83, 84]. However, all discussed approaches are limited by the grid size which is often not fine enough to capture single jets. First numerical calculations of such systems can be found in Crawford et al. (1980) [85], where effusion cooling was modeled as discrete mass injections in a 2D boundary layer code. Hunter (1998) [86] investigated discrete mass injection in the boundary layer, at a short distance away from the wall and Heidmann and Hunter (2001) [87] found that a uniform injection on the entire surface better corresponds to experimental results than the previously investigated approach of discrete mass injections. Recently, Mazzei et al. (2016) [19] published a comparative study using Scale Adaptive Simulations (SAS) of a homogeneous injection approach and cell-wise injection, where the latter performs better in terms of heat transfer. Despite the vast advances in high-performance computing which today allow high fidelity LES of the entire combustion chamber, resolving the entire effusion cooling system will stay beyond reach for at least 10 more years [35, 84] (see Fig. 3.2). Performing simulations of the entire combustor geometry inevitably requires the application of effusion cooling models to take coolant flows into account.

In this work, two different injection modeling approaches are assessed on the FACTOR chamber. The first model, developed by Mendez and Nicoud (2008) [25] is a homogeneous injection model designed to capture the global impact on the flow field in industrial applications. The second model, presented by Bizzari et al. (2018) [88], allows to locally prescribe coolant jets on the liner surface. One motivation for investigating the impact of the cooling system on the main flow originates from the work of Koupper [16]. In these simulations, multiperforations relied on a homogeneous injection approach [25], from which coolant is injected at a flat angle to the surface, promoting the creation of a closed impenetrable coolant film on the liner. Therefore, the real 3D shape of the coolant flow may not be accurately reproduced which has been identified as impacting the flow predictions

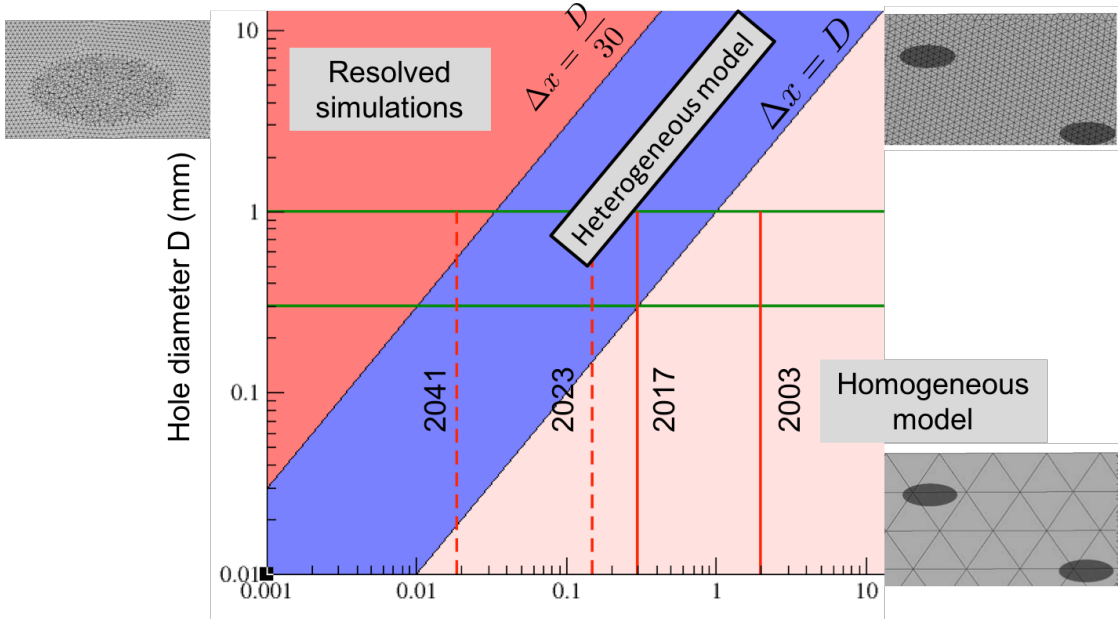


**Figure 3.2:** Prognosis of resolvable cooling hole size [27, 84].

on P40. The heterogeneous model [84] was developed to allow for a more realistic representation of the coolant system. In the heterogeneous modeling approach, coolant is injected through discrete wall areas composed of a predefined minimum number of grid cells. This causes the jets depending on the surface grid resolution to be represented with the original diameter for very fine grids or to be represented as a thickened jet, with a lower injection angle to conserve axial momentum, for a coarse grid. The heterogeneous model is thereby applicable on fine grids, where the jets are represented with the correct geometrical parameters and on coarse grids where it degenerates to the homogeneous injection model.

Detailed explanations and results for the present investigation are given in ASME GT2017-64622, reproduced hereafter. Simulations in this chapter are performed on the UNIFI test rig [14] for which the operating conditions are given in Table 1.1. Note that simulations are performed at isothermal operating conditions, where Hot Wire Anemometry (HWA) data on P40 and Particle Image Velocimetry (PIV) measurements partly covering a cross section through the swirler, are available. As complementary results, further investigations to increase the confidence in both modeling approaches are carried out at design point operating conditions, where temperature measurements on P40 allow the comparison of the coolant distribution, neglecting temperature changes due to aerodynamic effects. Finally, a DMD study of the flow field is also provided to distinguish traces of the swirler generated processing vortex core (PVC) on P40, which were found in experiments, but not in previous investigations by Koupper [16] using discrete probes.

The structure of this chapter is as follows. First, the two previously mentioned coolant injection models are presented. In the following, the general setup, the FACTOR combustion chamber simulation and operating conditions are described.

The next section discusses the prediction differences between both models. These are evidenced by comparing 2D plots and radial averaged profiles. A final conclusion summarizes the results and gives an outlook on future work.

### 3.1 Effusion Cooling models

This section briefly introduces the working principles of effusion cooling systems (see Fig. 3.3) and presents the two modeling approaches used in this work. The primary cooling technology of interest here is the so-called multiperforated plate or effusion liner. To reduce the temperature of combustion chamber walls, cool air is injected through a multitude of angled perforations to create a coolant film on the inner side of the liners. The performance of such an effusion cooling system hence mostly depends on its capability to create a closed coolant film under different operating conditions. Based on experimental findings and flow analysis, main influencing parameters dictating the effusion cooling efficiency are: the injection angle  $\alpha$ , the porosity  $\sigma$  and the hole shape [4].

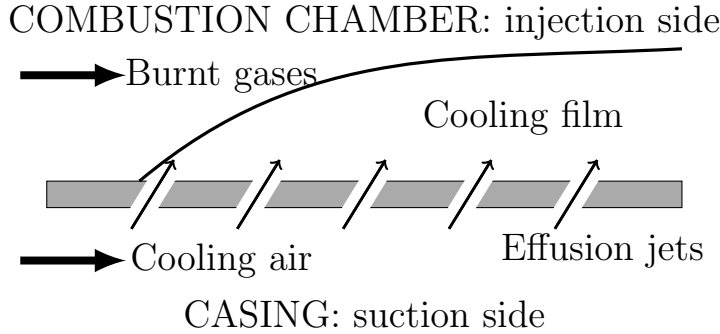


**Figure 3.3:** Schematic drawing of an effusion cooling system.

In this case, porosity  $\sigma$  is defined as the hole surface  $A_{holes}$  over the plate surface  $A_{plate}$ ,

$$\sigma = \frac{A_{holes}}{A_{plate}} = \frac{\sum_{holes} (\pi D^2 / (4 \cos(\alpha^{jet})))}{A_{plate}}, \quad (3.1)$$

while the injection angle  $\alpha^{jet}$  reads,

$$\alpha^{jet} = \tan^{-1} \left( \frac{U_n^{jet}}{U_t^{jet}} \right), \quad (3.2)$$

where  $U_n^{jet}$  is the wall-normal velocity component and  $U_t^{jet}$  is the wall tangential velocity component. Injection holes typically have a diameter  $D < 1 \text{ mm}$ , as well as shallow injection angles of the order of  $20^\circ$ . Increasing the number of holes while decreasing the hole diameter allows to use available coolant air more efficiently. Indeed, in that case, jets penetrate less into the main flow so coolant stays closer to the walls. However, small holes pose manufacturing problems and are more likely to be clogged [81]. In terms of modeling, two concepts are specifically addressed in this work. Note that for both approaches presented hereafter, the angle of the jet is considered to be equal to the angle of the injection hole.

### 3.1.1 Homogeneous injection model

The adiabatic homogeneous injection model [25] was developed to simulate the global impact of an effusion cooling system on the mean flow in complex industrial geometries. The model is local and does not rely on correlations or parameters linked to other parts of the domain. For the surface grid resolution, there are no requirements imposed by this model. The basic principle with the homogeneous injection model is to inject coolant air on the entire plate surface. To do so and to reproduce the film effect, the wall tangential velocity  $U_t$  is conserved, whereas the wall-normal velocity  $U_n$  is corrected to conserve the mass flow rate:

$$\rho U_t^{hom} = \rho U_t^{jet}. \quad (3.3)$$

$$\rho U_n^{hom} = \rho U_n^{jet} / \sigma, \quad (3.4)$$

Quantities related to the homogeneous injection model are marked by the superscript  $^{hom}$  and those related to the real jet by the superscript  $^{jet}$ . In that case, the injection angle for the homogeneous model,  $\alpha^{hom}$ , as compared to the original injection angle  $\alpha^{jet}$ , is defined as:

$$\tan(\alpha^{hom}) = \sigma \tan(\alpha^{jet}). \quad (3.5)$$

### 3.1.2 Heterogeneous injection model

The heterogeneous injection model (see Fig. 3.4) is designed to simulate the impact of an effusion cooling system at a reasonable level of CPU cost [84]. Contrarily to the homogeneous approach and to improve the prediction, the model intends to resolve jets by the grid. To do so, inlets are prescribed on discrete positions on the liner surface and the jet geometry is adapted depending on the local grid resolution. If the local grid resolution is insufficient to resolve the jet with the chosen number of grid cells, the jet is enlarged and the wall-normal velocity  $U_n$  is reduced to maintain the correct mass flow rate of each hole. Using such modeled perforations, the wall tangential velocity  $U_t$  is corrected to conserve the axial momentum of the cooling film just as previously done with the homogeneous model. Note finally that a velocity profile is prescribed on discrete surface areas. As indicated, in regions with insufficient mesh resolution, the model enlarges the surface injection areas for the effusion cooling holes up to the point where a homogeneous injection is recovered. On the contrary, if resolution is adequate to represent the jet geometry no modification is active.

For the heterogeneous injection model, the main influencing parameter is the enlargement, usually fixed at  $E = 3$  [84], which describes the minimum acceptable number of cells per hole. For a coarse grid where less than three cells are present within the true hole diameter, the jet diameter is enlarged (see Fig. 3.5a), whereas jets correctly represented are untouched (see Fig. 3.5b).

For the current study, a surface grid size of 0.25 mm in the liner region was chosen, so that jet diameters are enlarged by a factor of 1.5. Hence, the jet profile is represented by at least three characteristic cell lengths or the entire jet by around eight cells (see Fig. 3.6). Note also that, for shallow injection angles, the model

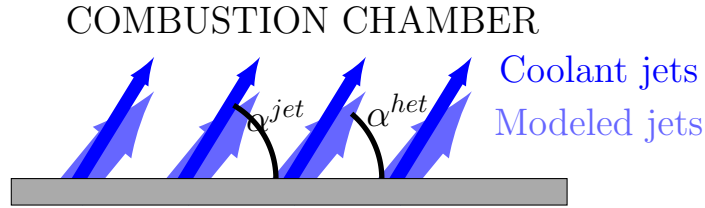


**Figure 3.4:** Schematic drawing of the heterogeneous injection model. The injection angle of the real jets is indicated by  $\alpha^{jet}$  and that for the heterogeneous injection model is marked by  $\alpha^{het}$ .

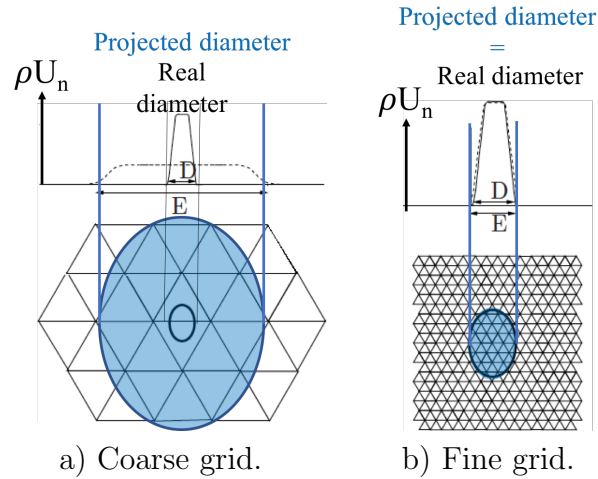


**Figure 3.5:** Widening of cooling holes as a function of local grid resolution (adapted from [84]).

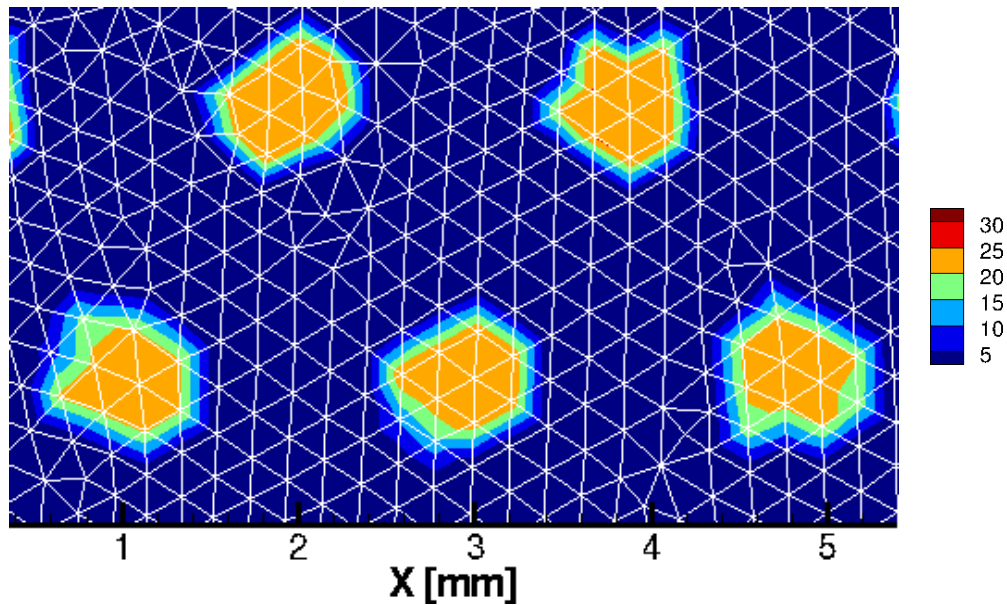


**Figure 3.6:** Injected axial momentum  $\rho U$  [ $\frac{kg}{m^2s}$ ] prescribed at the boundary for five jets arranged in a staggered pattern.

tries to take into account the elliptical hole shape. After geometric adaptation of the jet diameter to account for local grid resolution, the numerical porosity,  $\sigma_{num}$ , ranging from 1 for very fine meshes (fully resolved jets) to  $1/\sigma$  for very coarse meshes (homogeneous injection), is defined as the surface area of injection holes in the simulation  $A_{holes}^{num}$  over the real hole surface  $A_{holes}$ , i.e.:

$$\sigma_{num} = \frac{A_{holes}^{num}}{A_{holes}}. \quad (3.6)$$

Note that  $\sigma_{num}$  becomes a local parameter. To conserve the axial momentum of the cooling film using such adapted perforations, the procedure behind Equations 3.3 & 3.4 is applied with  $\sigma_{num}$ . As a result, the injection angle for the heterogeneous injection model  $\alpha^{het}$  becomes,

$$\sigma_{num} \tan(\alpha^{het}) = \tan(\alpha^{jet}). \quad (3.7)$$

For the heterogeneous injection model, variables prescribed at the locations of the coolant injection holes are calculated as follows:

$$\rho U_t^{het} = \rho U_t^{jet}. \quad (3.8)$$

$$\rho U_n^{het} = \rho U_n^{jet} / \sigma_{num}, \quad (3.9)$$

The impact of the two different modeling approaches on the flow field close to the liner wall is illustrated in Fig. 3.7. Clearly, the heterogeneous injection model allows for the coolant to penetrate further into the main flow, which increases mixing. On the contrary, the homogeneous model creates a closed coolant film in direct vicinity to the liner. The differences observed between both models potentially impact the flow field in the combustion chamber as investigated in the following.

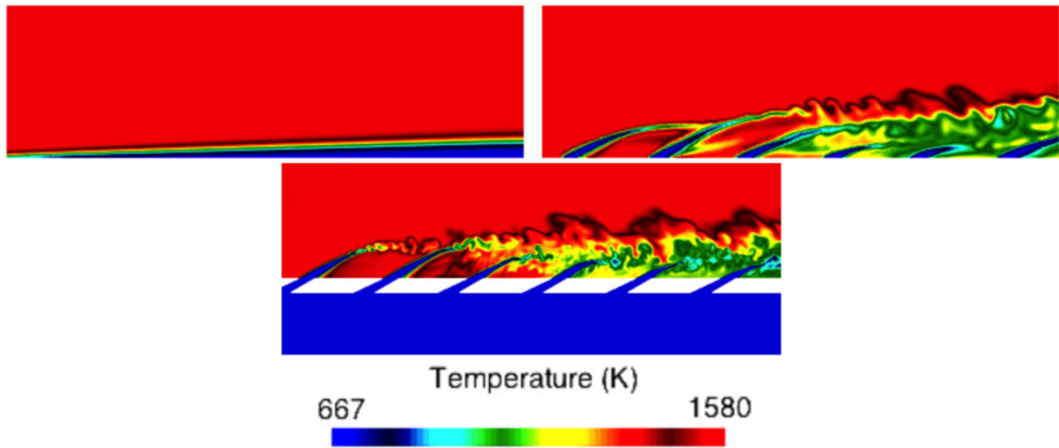


**Figure 3.7:** Homogeneous (left) and heterogeneous (right) effusion cooling model and fully meshed cooling system (below) on a flat plate [88].

## 3.2 Description of the test configuration

Having detailed two different effusion cooling models applied in this work, this section introduces the FACTOR combustor geometry, the operating conditions and the mesh used for the simulations. Note that the discussion here focuses only on an axial periodic domain that features  $1/20$  or  $18^\circ$  of the full annular non-reactive FACTOR test rig [15] (see Fig. 5.1). The domain is restricted to the combustor, where the main flow is constrained by a  $63\text{ mm}$  diameter duct of  $55\text{ mm}$  length to preserve the swirler generated vortex and avoid early interactions with coolant flow and neighboring swirlers. The swirler itself consists of 30 flat vanes with a length of  $20.5\text{ mm}$  around a central hub of diameter  $22\text{ mm}$ . Cavity flows feeding the effusion cooling system are not included and therefore not simulated. Hence, coolant air is directly injected through the liners. The effusion cooling system consists of four different panels (see Tab. 3.1): External 1 & 2 and Internal 1 & 2 (see Fig. 3.8). All effusion cooling holes have a diameter of  $D=0.5\text{ mm}$  and are arranged in a staggered pattern. Depending on the porosity of the real geometry, the modeling parameters differ for each surface (see Tab. 3.1).

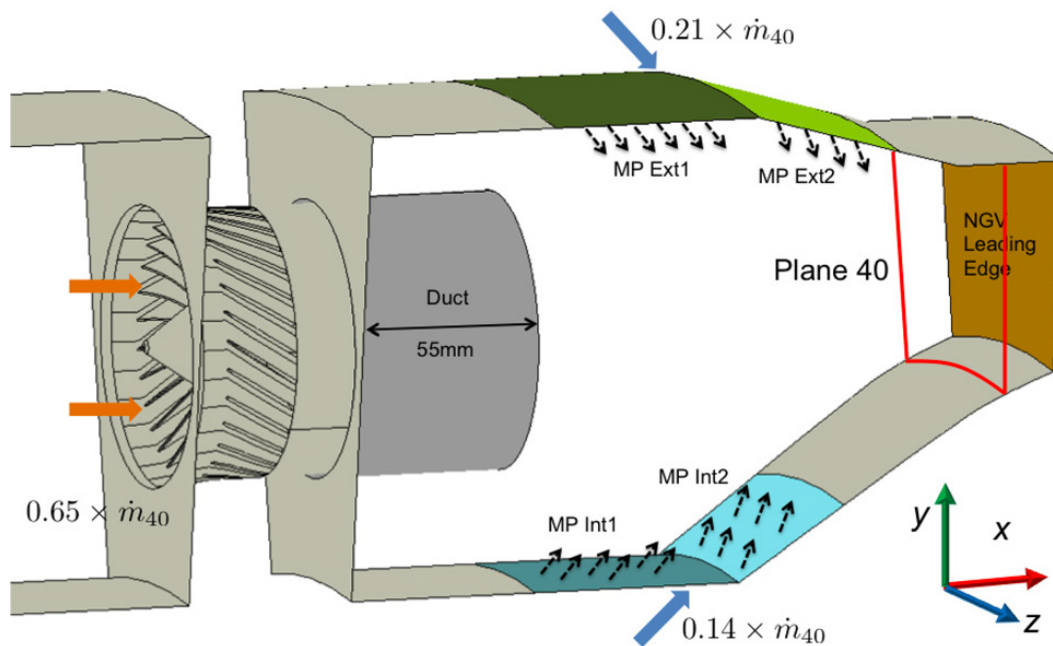


**Figure 3.8:** FACTOR combustion chamber [15].

Simulations are performed at isothermal operating conditions, where hot wire anemometry (HWA) as well as particle image velocimetry (PIV) measurement data are available [23, 89]. A second, non-isothermal, operating point, called design point (DP), is also simulated and allows for comparison of coolant distribution on P40 using temperature measurements. PIV measurements with an acquisition rate of  $12\text{ Hz}$  were performed over  $30\text{ s}$ . Only the mainstream was seeded with particles, which creates a blind zone close to the walls [16]. HWA was performed on 281 points on P40 (see Fig 3.8) at an acquisition frequency of  $20\text{ kHz}$  over a

**Table 3.1:** Geometrical and modeling parameters of the effusion cooling system ( $360^\circ$ ).

Panel	Number of rows	Holes/ Row	$\alpha$	$\sigma$	Mass flow [ $kg/s$ ]	Mass flow [%]	$\alpha_{hom}$	$\alpha_{het}$	$\sigma_{num}$
Ext 1	50	630	$60^\circ$	0.0773	0.624	13	$7.6^\circ$	$47.3^\circ$	1.60
Ext 2	24	850	$30^\circ$	0.115	0.384	8	$3.8^\circ$	$19.9^\circ$	1.60
Int 1	58	416	$60^\circ$	0.0957	0.48	10	$9.4^\circ$	$47.5^\circ$	1.59
Int 2	21	460	$30^\circ$	0.104	0.192	4	$3.5^\circ$	$19.3^\circ$	1.61

measurement period of 5 s. Isothermal operating (IOP) conditions for measurements and simulations (see Tab. 3.2) have been derived from Koupper (2015) [16] to meet most important dimensionless quantities of the hot design point (DP) of the FACTOR test rig. In total, four simulations are discussed in this section: Two simulations for each operating point with either of the two previously presented coolant injection models. Globally the operating points are well matched (i.e. IOP static pressure on P40: 114.85  $kPa$  (homogeneous); 114.9  $kPa$  (heterogeneous); 115  $kPa$  (target)) and differences are more marked in local temperature and velocity distributions as will be shown in the following. For the design point simulation using the homogeneous injection model the pressure on P40 is 147.64  $kPa$  and 147.62  $kPa$  for the prediction with the heterogeneous injection model.

**Table 3.2:** FACTOR operating conditions [16].

	IOP	DP
Static pressure on P40 [ $kPa$ ]	115	147.65
Mass flow [ $kg/s$ ]	4.8	4.8
Flow split swirler [-]	65%	65%
Flow split outer cavity [-]	21%	21 %
Flow split inner cavity [-]	14%	14 %
Swirler inlet temperature [ $K$ ]	300	531
Swirler Reynolds number [-]	168 500	111 000
Swirler Mach number [-]	0.108	0.112
Effusion cooling Reynolds number [-]	2340	2340

### 3.3 Numerical Methodology

Simulations presented in this work are performed using AVBP, a massively parallel CFD code developed at CERFACS. The code is based on an explicit cell-vertex formulation and solves the compressible Navier-Stokes equations for conservative variables on unstructured or hybrid grids. AVBP is dedicated to LES and has been

used and validated for a wide range of different applications [60–62]. The code has been extensively used for effusion jets [25,90] as well as jets in cross flow configurations [91] and finally also in LES with multiperforated plates [26,92]. In terms of method and for the FACTOR simulations, predictions are first converged using the Lax-Wendroff scheme [66], then the more accurate TTGC scheme [67] is chosen. The last scheme ensures low diffusion and dispersion properties [68] and is therefore adequate for high fidelity simulations. Note that in AVBP, time marching is done respecting CFL (convection scheme) and Fourier (diffusion scheme) conditions to guarantee stability. Finally, Colin-type artificial viscosity [71] is also activated to damp potential numerical oscillations naturally present with such schemes. Sub-Grid Scale (SGS) turbulent contributions are accounted for using the Smagorinsky model [51]. The SGS heat flux is related to the filtered temperature gradient with a SGS thermal conductivity computed with a SGS turbulent Prandtl number of 0.6.

When dealing with boundary conditions, effusion cooling systems are modeled using a homogeneous [25] and a heterogeneous [88] injection model. At the exit of the domain Navier-Stokes Characteristic Boundary Conditions (NSCBC) [56] are applied. To dissipate vortices close to the outlet, a sponge layer [93] adds additional dissipation close to the exit of the domain. At the inlet, a constant mass flow is imposed. Remaining walls are treated as adiabatic and are dealt with through a wall modeled LES approach [62]. To access turbulence quantities using autocorrelation [23,38], a constant time step of  $7 \times 10^{-8}$  s, corresponding to a CFL number [94] of 0.9 is used for the simulation. Finally, solutions are evaluated over a period of five flow through times (i.e. 50 ms in total) of the combustor module using the TTGC scheme.

For isothermal operating conditions a passive scalar allows tracking of the coolant flow whereas for design point operating conditions, coolant distribution corresponds due to the low Mach number very well to temperature maps.

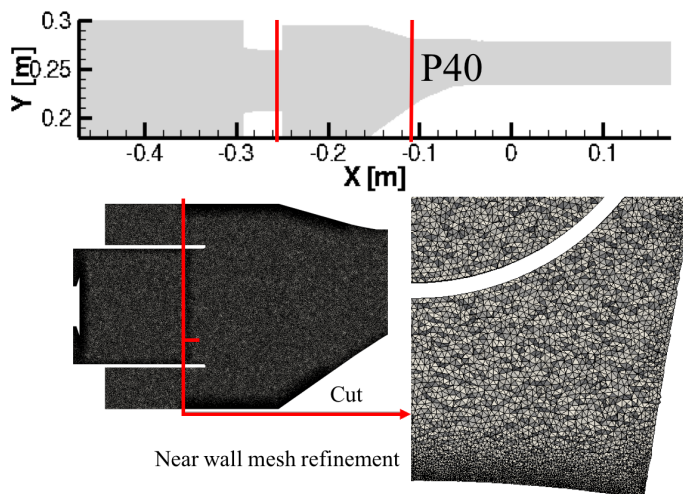


**Figure 3.9:** Computational domain and local views of the grid.

In terms of spatial representation, an unstructured tetrahedral grid containing about 50 million cells is used (see Fig. 3.9). Note that for this specific study,

the near wall region corresponding to the effusion cooling system is particularly refined. To avoid influence from the boundary on the flow region of interest, the domain covers a large entry plenum in front of the swirler and an exit sufficiently far away from P40 (see Fig. 3.9).

Note that in an industrial context, cost is an important and decisive factor for the application of a new model. To apply the heterogeneous injection model on the liners of the FACTOR geometry, the existing mesh (see Fig. 3.10a) was locally refined ( $\Delta X = 0.25 \text{ mm}$ ) in this area (see Fig. 3.10b) to guarantee a surface grid resolution of at least two cells per original hole diameter ( $D = 0.5 \text{ mm}$ ). Jets are thereby thickened by a factor of 1.5. At isogrid, the application of the heterogeneous injection model increases the computational cost by 0.3 %. However, compared to the original grid with a homogeneous injection model used by Koupper [16], the cost increases by 20 % (see Tab. 3.3). Such differences effectively result from the application of the new model which entails costly mesh refinements that are not necessary if using the homogeneous injection approach. The remaining question is the gain of such an approach as detailed in the next section.

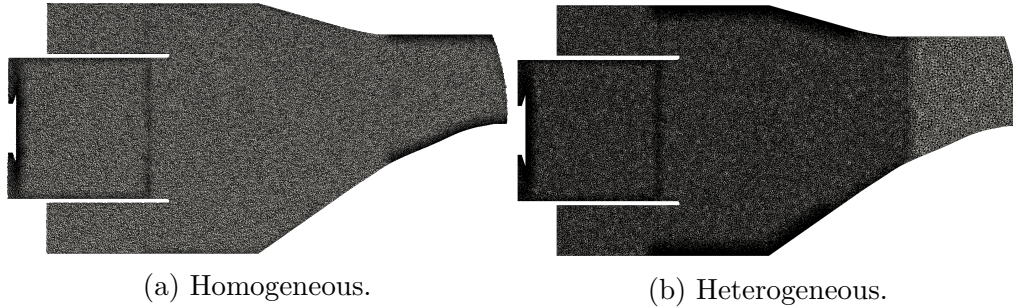


**Figure 3.10:** FACTOR Meshes.

**Table 3.3:** Mesh and associated computational cost (BEAUFIX Meteo France 360 processors).

Mesh	Cells	Vol min [ $m^3$ ]	dt [ $10^{-8} \text{ s}$ ]	CPU hours per 1 $ms$ of simulation
HOM	50 Mio	4.23E-14	7.5	1700
HET	55 Mio	2.89E-14	6.5	2000

### 3.4 Results and discussions

This section discusses the impact of the two different effusion cooling models on the mean flow fields as compared to experimental data. Globally, as detailed hereafter, both models lead to similar results, with differences in the near wall region as expected. These differences are due to coolant jets which, with the heterogeneous approach, penetrate further into the domain than in the homogeneous approach.

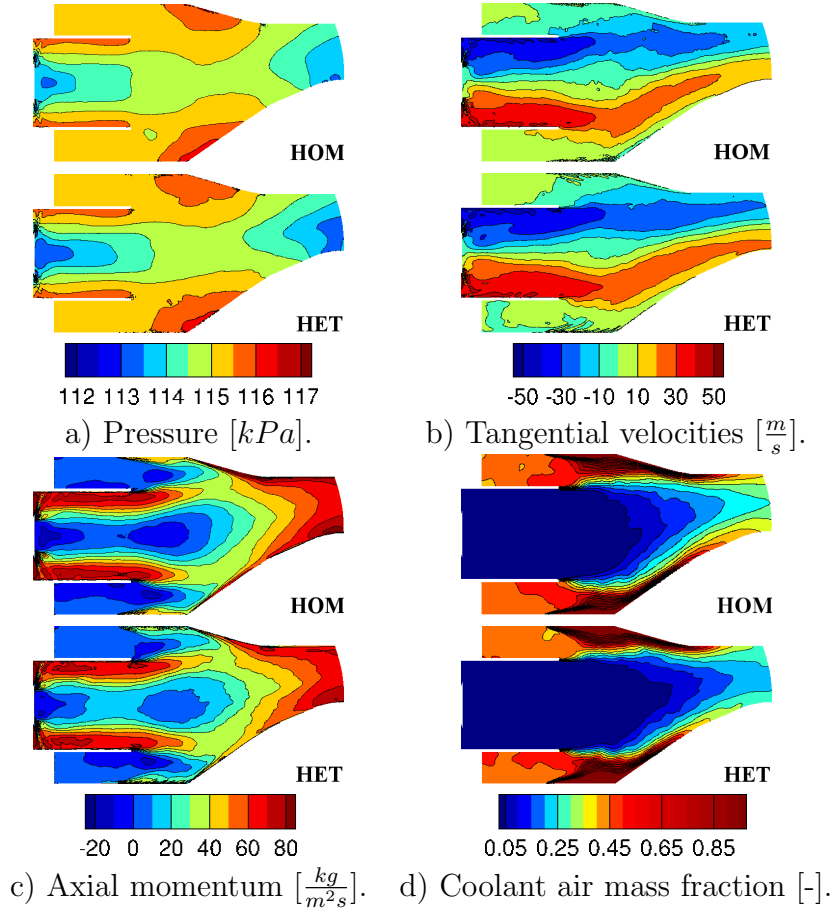


**Figure 3.11:** Cross sections through domain for homogeneous (upper) and heterogeneous (lower) injection model.

### 3.4.1 Mean flow comparisons and validations

In this section, the flow field is introduced and validated against experimental data. The isothermal operating point, with experimental data available on a cut plane through the swirler as well as on the exit plane, is addressed first. Then simulations at design point operating conditions, where experimental data is available on the exit plane only, are evaluated. The main quantities of both isothermal simulations are compared on a longitudinal plane going through the hub of the swirler, perpendicular to P40. This view allows a representation of the flow organization within the chamber. Both simulations show a similar pressure distribution (see Fig. 3.11a) with however slightly higher pressure values for the heterogeneous model. Note also that the depression observed within the duct is stronger for the heterogeneous injection model. The low pressure zone after the swirler is created by a recirculation zone induced by the strong rotation of the flow. After the duct, the swirler-generated vortex is no longer confined and breaks down, creating recirculation zones at the edges of the duct and in the center. The tangential velocities for both simulations are similar (see Fig. 3.11b). Both show a clear separation of fluid moving perpendicularly to the plane of observation in the middle of the domain as a result of the swirler induced rotation of the flow. In the simulation us-

ing the heterogeneous injection model, due to the steeper injection angle  $\alpha_{het}$  (see Eq. 3.5) the flow moves further away from the multiperforated walls as compared to the homogeneous injection model. The rotational movement in the heterogeneous model is stronger and better conserved when comparing the flow field close to the outlet of the domain. This stronger rotational movement in the simulation using the heterogeneous model also explains the stronger depression observed previously. Near the inner liner, where the inclination of the plate is stronger than for the exterior panel, this has a noticeable impact on the flow field (see Fig. 3.11c). Further, the central recirculation zone is stronger in the case using the homogeneous injection model. This will influence the axial velocity distribution in P40 (see Fig. 3.14) as discussed later. If focussing on Fig. 3.11d, the coolant distribution in the combustor clearly shows the effect of the heterogeneous model on the flow. Using the heterogeneous model, the coolant mixes more with the flow and reaches further into the domain than with the homogeneous modeling approach, where the coolant stays closer to the liner and moves at higher speeds. Due to this, one observes more mixing of coolant and main flow at the chamber outlet, if applying the heterogeneous model. Note that all these mentioned differences are in full agreement with reported analysis by Bizzari [27].

Obtained mean velocity fields of the two LES predictions can be further assessed and compared to available experimental data. To do so, the longitudinal plane going through the central hub of the swirler is again chosen (see Fig. 3.12). Velocity contours of the axial (Fig. 3.12a) and tangential velocity (Fig. 3.12b) show good agreement between both simulations and experiments. Indeed, both models capture the central re-circulation zone of the experiment (see Fig. 3.12a). Differences appear along the inner liner walls for which the axial velocity obtained with the homogeneous model is higher than in the heterogeneous approach. As mentioned previously, the visualization shows a stronger recirculation zone for the heterogeneous model, which manifests by a lower velocity in the center of the duct and a higher velocity close to the duct edges. The degree of accuracy in the measurements associated to the variations issued by the modeling approaches however can not allow any clear discrimination. Focusing on the near wall region, the radial velocity components issued by both simulations are again seen to be very similar (see Fig. 3.12b). Note that the PIV measurement cannot capture the upward movement of the coolant flow injected at the inner liner, since in the experiment only the main flow was seeded with particles. Hence, unlike the simulations, the PIV data shows velocities close to zero in the region near the liners. Figure 3.13, showing velocity profiles at two distinct positions marked on Fig. 3.12b), allows for a more quantitative comparison of previously discussed results. The first position shows the flow field right after the duct, the second one further downstream in the middle of the chamber. Differences between both modeling approaches are most evident close to the wall, but also in the middle of the cross section where the experimental results lie in-between those obtained from both LES predictions (see Fig. 3.13). Further away from the swirler, the velocities measured in the experiment are overall lower than those obtained from the simulations (see Fig. 3.13). At

this position, the axial velocity profile still features the same shape as right after the duct. The upper axial velocity peak at  $R=0.27\text{ m}$  is however slightly higher than that at  $R=0.22\text{ m}$  which is due to the geometrical shape of the chamber. One also notes that at this position axial velocities predicted in both simulations are higher than in the experiment.

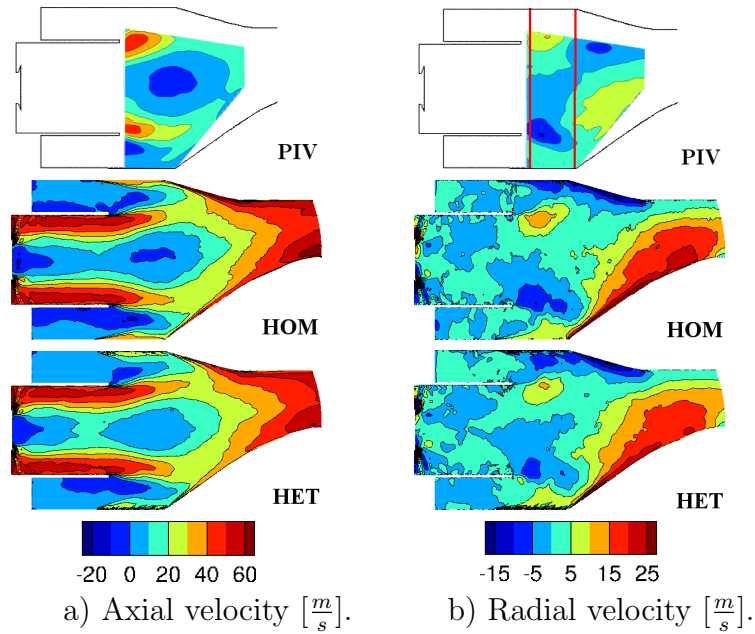


**Figure 3.12:** Mean velocity on the axial cross section (Upper: PIV, Middle: Homogeneous, Lower: Heterogeneous; Vertical red lines indicate the position of the extraction of vertical profiles shown in Fig. 3.13). (Isothermal Operating Point).

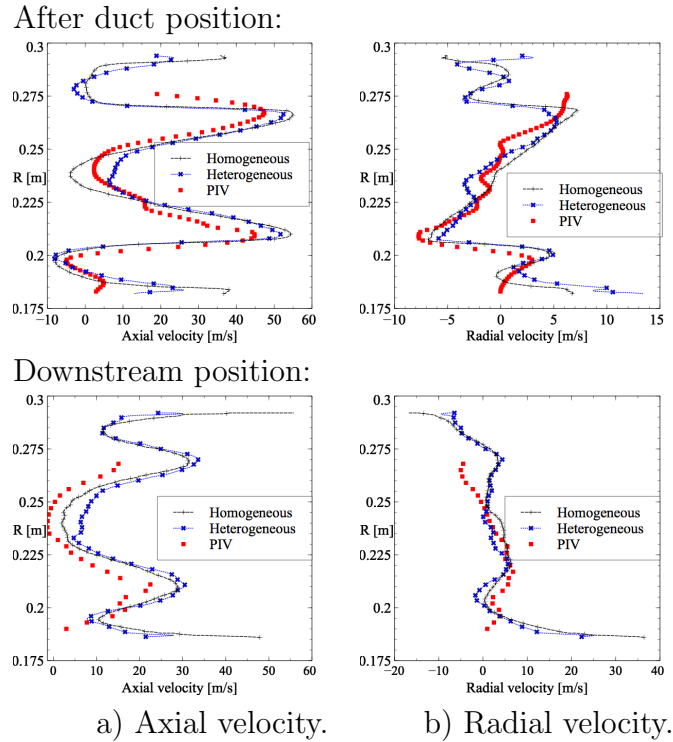


**Figure 3.13:** Vertical profiles of velocity components, Upper: after duct position, Lower: Downstream position (As indicated in Fig. 3.12).

Focusing now on the velocity field in P40, where hot wire anemometry data covering about 60 % of P40 is available for isothermal operating conditions, a direct comparison of the predictions with the data, Fig. 3.14, results in the following observations: First, both simulations compare well with experimental results. In the simulation using the homogeneous injection model, there is a higher axial velocity near walls, notably along the interior liners (see Fig. 3.14a). The higher velocities close to the liners if using the homogeneous injection approach are especially visible in the profile plot which allow for a more quantitative comparison. This goes with the observation that, when using the homogeneous injection model, a robust cooling film is created along the liners. This film can hardly be disturbed or penetrated, so there is less mixing with the surrounding flow. Injecting the coolant through discrete surfaces results in more mixing between coolant flow and main flow. On the interior liner, where the change of inclination is stronger as compared to the exterior combustion chamber walls, the injected coolant mixes more rapidly with the flow. It is noticeable that in the central zone covered by the measurement, the velocity in the experiment is higher than in the simulations, indicating that the velocity along the walls is probably too high in both simulations (see Fig. 3.14a). Regarding the radial velocity plots (see Fig. 3.14b), one observes that the heterogeneous model is in better agreement with the experimental data than the homogeneous injection model. For the tangential velocity components (see Fig. 3.14c), both models provide reasonable patterns that are in agreement with the data. The velocity profiles for radial and tangential velocity show the

typical shape for high levels of residual swirl found at the exit of the combustion chamber.

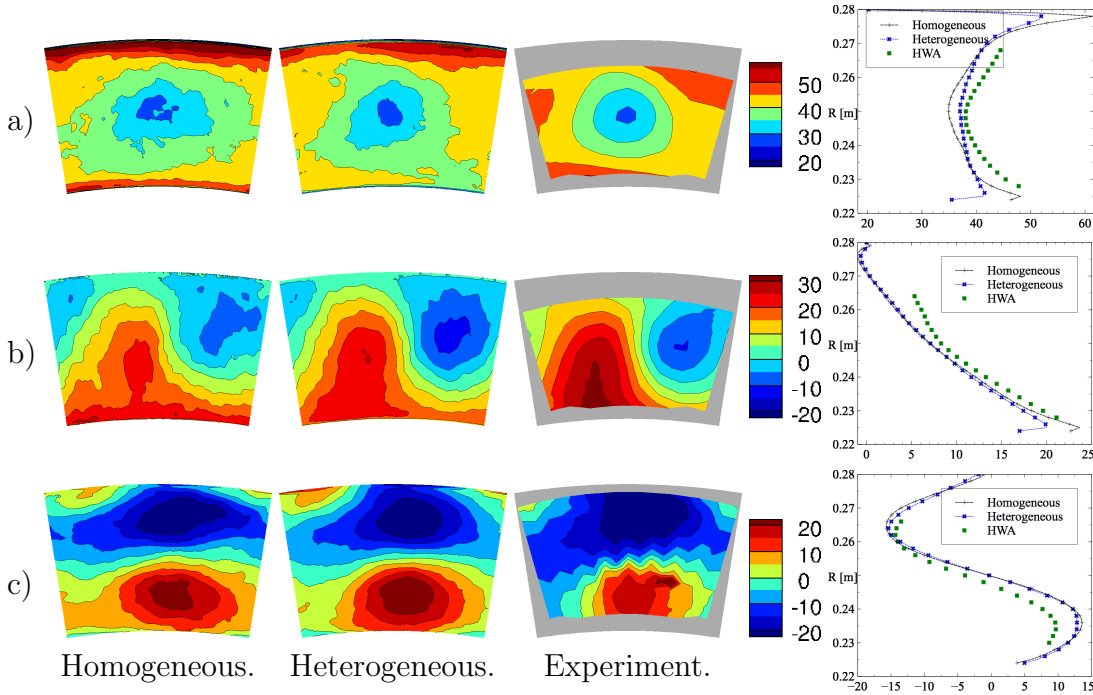


**Figure 3.14:** Velocity plots and circumferentially averaged profiles on P40. a) Axial velocity [ $\frac{m}{s}$ ]. b) Radial velocity [ $\frac{m}{s}$ ]. c) Tangential velocity [ $\frac{m}{s}$ ]. View direction: Downstream. (Isothermal Operating Point).

Looking at 2D maps of coolant mass fraction in the P40 plane, Fig. 3.15, one observes that using the heterogeneous injection model, coolant is arranged in a rounder shape which might indicate a better conserved processing vortex core. Along the walls, especially on the inner liner, the coolant distribution is more uniform using the homogeneous injection model, which again confirms that there is more mixing due to interaction with the swirl if applying the heterogeneous injection model. The high velocities on the interior walls, observed in Fig. 3.14, are mainly due to coolant injected through the interior liners. After comparing results for the isothermal operating point, the next section focuses on the design point, where coolant and main flow temperatures are different.

Evaluating in the following, velocity plots at design point operating conditions (see Fig. 3.16) where velocity measurements from a 5 hole pressure probe are available leads to similar observations. Again, both models show a good agreement with each other. In the liner region, due to the shallow injection angle, the axial momentum predicted by the homogeneous injection model is higher than in the simulation using the heterogeneous model (see Fig. 3.16a). Radial and tangential velocities show a good agreement between both models and capture the velocities measured in the experiment (see Fig. 3.16b,c). The radial velocity profiles show a closer match than previously discussed radial profiles for isothermal operating

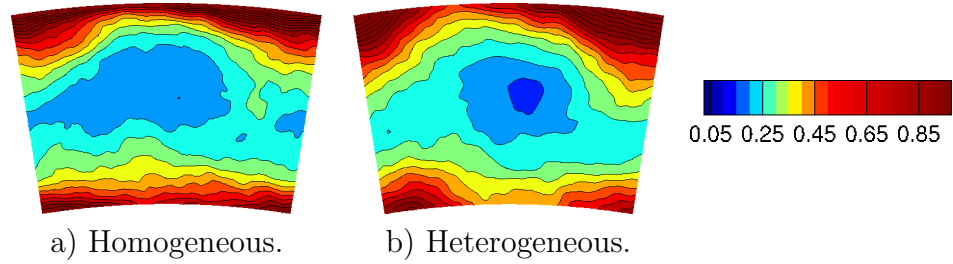


**Figure 3.15:** Coolant air mass fraction on P40. View direction: Downstream. (Isothermal Operating Point).

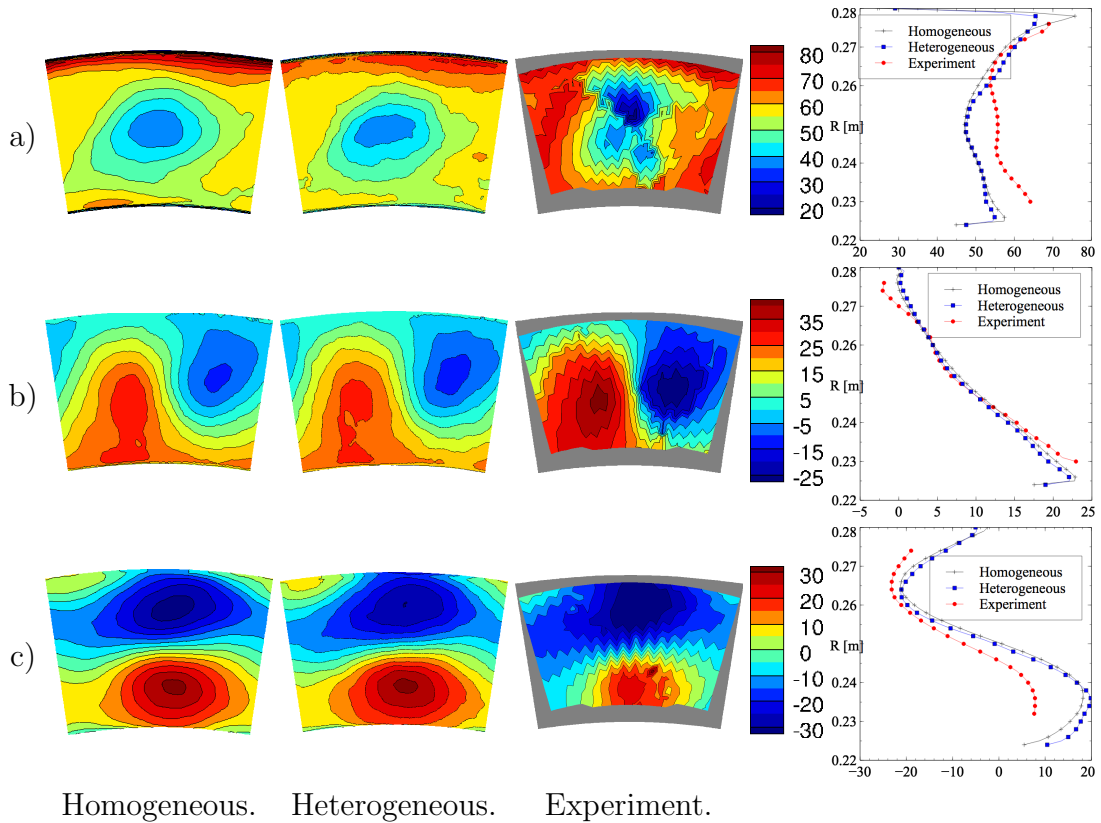
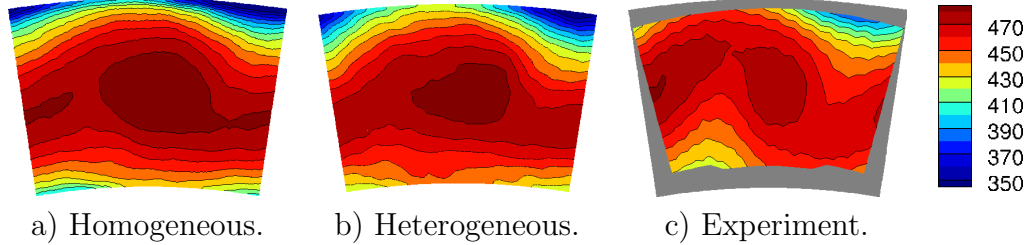


**Figure 3.16:** Velocity on P40. a) Axial momentum  $[\frac{kg}{m^2s}]$ . b) Radial velocity  $[\frac{m}{s}]$ . c) Tangential velocity  $[\frac{m}{s}]$ . View direction: Downstream. (Design Point).

conditions. As already observed for the isothermal operating point, tangential velocity profiles for the experiment in design point operating conditions show lower values than predicted by both models. Globally, the flow field comparing design and isothermal operating point is similar.

Studying the temperature field at the design point operating conditions allows to investigate the coolant distribution on P40 (see Fig. 3.17), neglecting temperature changes caused by aerodynamic effects. Due to the absence of dilution holes in the chamber design, the temperature distribution is highly non-uniform and a well marked hotspot can be observed in the middle of P40. In the simulation using the heterogeneous injection model (see Fig. 3.17b), coolant from the upper

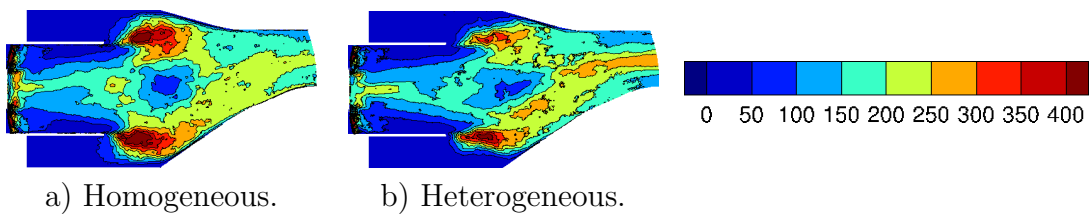
liner penetrates further into the domain compared to the simulation using the homogeneous injection model (see Fig. 3.17a) and thereby corresponds better to the experimental results. In the experiment, coolant is transported even further away from the liners than in both design point simulations, which is explained by higher radial velocities found in the experiment.



**Figure 3.17:** Temperature [K] on P40 for design point. View direction: Downstream.

### 3.4.2 RMS and turbulent quantities

Having discussed general aspects of the flow field in Section 3.4.1, one now focuses on turbulent features for isothermal operating conditions. Figure 3.18 shows the impact of the effusion cooling modeling on the turbulent kinetic energy of both simulations. Around the duct, due to shear layer interaction high levels of turbulence are created, when the flow leaves the confining duct and meets with the flow from neighboring swirlers. Using the heterogeneous model, turbulence created on the crosssection through the swirler seems to be pushed further inside the domain, away from the walls, which is linked to the steeper injection angle, if applying the heterogeneous model. Originating from the shear layers right after the duct, high levels of turbulence are seen to be transported through the entire chamber, up to P40, where a characteristic wavy pattern is created. The recirculation zone features low levels of turbulence in both models.

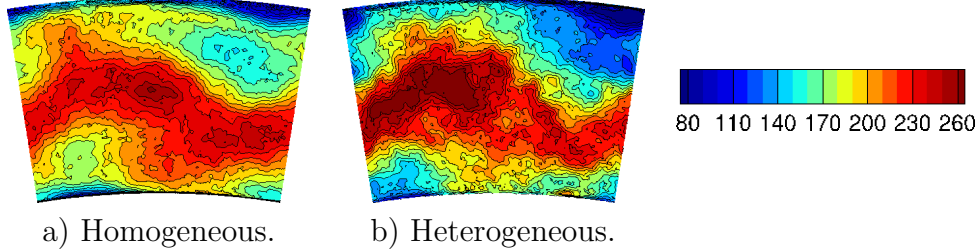


**Figure 3.18:** Plots of turbulent kinetic energy [ $\frac{\text{m}^2}{\text{s}^2}$ ] on cross sections through domain. (Isothermal Operating Point).

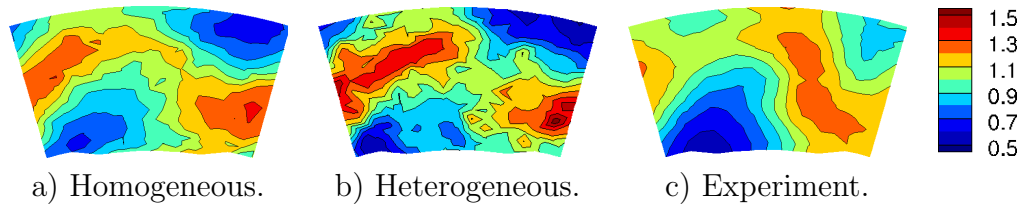
Despite these local differences in the combustor, both models obtain a similar pattern of turbulent kinetic energy (TKE) on P40 (see Fig. 3.19). The wave-like shape is caused by the PVC breaking down and interacting with neighboring PVCs shortly after leaving the duct. For the heterogeneous model, the average TKE on P40 is slightly higher than the value obtained using the homogeneous injection model (see Tab. 3.2). This might be due to the PVC being better preserved using

**Table 3.2:** Average values for turbulent quantities on P40.

	TKE [ $\frac{m^2}{s^2}$ ]	Turbulent timescale [ $10^{-4}s$ ]
Homogeneous	176	1.39
Heterogeneous	188	1.42
Experiment		1.59


**Figure 3.19:** Turbulent kinetic energy [ $\frac{m^2}{s^2}$ ] on P40. View direction: Downstream. (Isothermal Operating Point).

the heterogeneous model as detailed later. It is further noticed that on the upper right corner of P40, favored by coolant flow (previously shown on Fig. 3.15), shows lower values for TKE in the simulation using the heterogeneous injection model. Calculating the axial velocity RMS based on available HWA measurements allows a direct comparison with the corresponding evaluations using both predictions (see Fig. 3.20). On P40, experimental data and 2D maps obtained from both LES's show good agreement and the previously discussed wavy shape, caused by vortex breakdown, is again visible. The more pronounced S-shape observed in the experiment might originate from the fact that the experiment contains three-sectors, while the simulations are one sector periodic. While the rotational movement in the outer sectors in the experiment is slowed down due to wall interactions, the swirl in the middle is less reduced by the weaker movement of the neighboring swirlers. In the one-sector periodic simulation the rotational movement is reduced more due to the presence of neighboring equally strong swirled flows. The longer acquisition period of 5 s in the experiment as compared to 50 ms in the simulations explains the smoother shape of second order quantities in the experiment.


**Figure 3.20:** Non-dimensionalized axial velocity RMS on P40. View direction: Downstream. (Isothermal Operating Point).

Plots of turbulent timescale both capture the largely undiluted (see Fig. 3.15) hotspot as a region with large turbulent timescales (see Fig. 3.21). Position and magnitude are comparable between simulations and experiment, although in the

experiment access to longer acquisition time and fewer probe positions yield fields that are more uniform on P40.

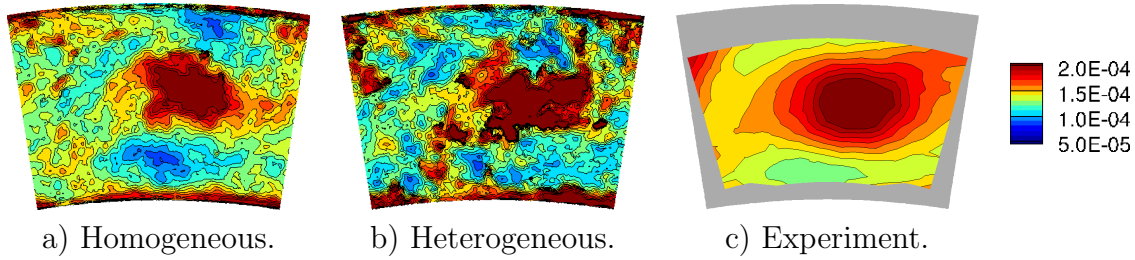


**Figure 3.21:** Turbulent timescale [s] on P40. View direction: Downstream. (Isothermal Operating Point).

### 3.4.3 Unsteady feature in P40

This section contains additional analysis of the LES predictions using dynamic mode decomposition (DMD, see Section 2.2.3) [76]. DMD analysis of instantaneous solutions allows to find traces of the PVC on P40 that were observed in the experiment, but not detected by Koupper [16] using a Fourier analysis on individual probes. DMD is a very recent post-processing method that similarly to a Fourier Transformation allows to extract frequencies and associated amplitudes in a signal. Compared to Fourier analysis, which is performed on single probes, DMD is more robust and allows to create 3D visualizations of amplitude as well as phase angle for an entire domain. Typically, a Dynamic Mode Decomposition (DMD) post-processing of a series of instantaneous solutions on P40 allows to reveal dominant frequencies and amplitudes on P40. For both injection models, peaks of the amplitude can be found at 315 Hz, the frequency of the PVC at isothermal operating conditions (see Fig. 3.22). The frequency spectrum obtained by Dynamic Mode Decomposition [76] of a set of instantaneous 2D solutions on P40 (see Fig. 3.22), shows similar values for both simulations. Both capture the PVC at a frequency of 315 Hz. However the PVC signal is stronger in the simulation using the heterogeneous injection model, possibly because of better conserved traces of the PVC. The decay of turbulent kinetic energy is indicated by Kolmogorov's  $-5/3$  law [49].

When visualizing the pressure amplitude at PVC frequency (315 Hz) one observes two peaks in the middle of P40 (see Fig. 3.23). If applying the heterogeneous injection model, the amplitude at PVC frequency is stronger, which may indicate a better preserved PVC in P40.

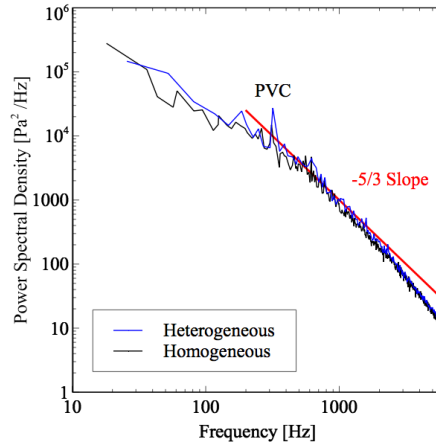


**Figure 3.22:** Power spectral density of pressure for homogeneous and heterogeneous injection model from Dynamic Mode Decomposition of 2D solutions on P40.

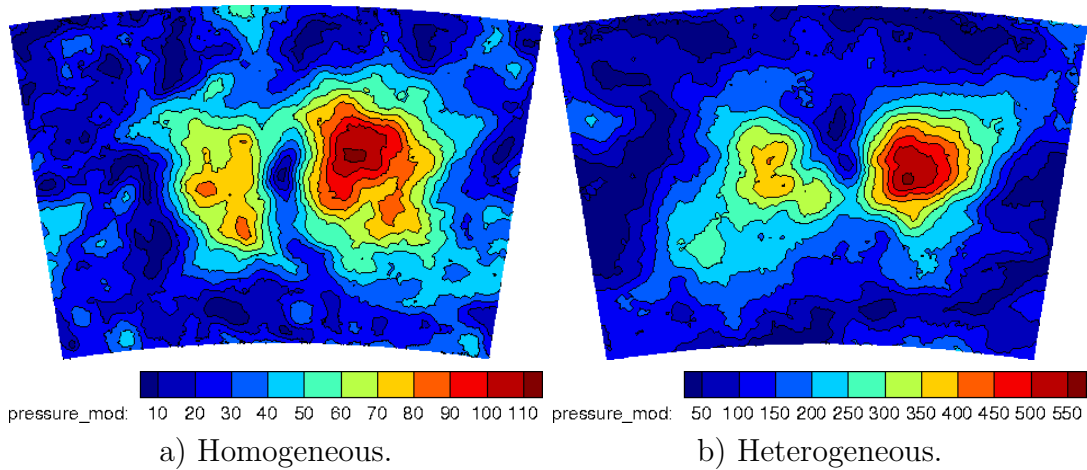


**Figure 3.23:** Pressure amplitude for 315 Hz on P40 for homogeneous and heterogeneous injection modeling.

### 3.5 Conclusion

In this study, two industrial scale applicable LES effusion cooling models were compared and evaluated against experimental data obtained from an engine representative lean combustion simulator test rig. The heterogeneous injection model can be applied to industrial gas turbine engines in the design process at a reasonable level of additional cost (+0.3 % using the same mesh, determined over a simulation time of 6 *ms*). Globally, the new model leads to similar results as the well-validated homogeneous injection model. In the near wall region, the application of the heterogeneous injection model leads to more realistic representation of the cooling film. More specifically, and as observed by C. Koupper, the vastly used homogeneous approach injects coolant at shallow angles to the surface and creates a closed impermeable coolant film that yields to a high momentum coolant flow close to the wall. In the heterogeneous modeling approach, the discrete injection as well as the steeper injection angles promote mixing with the main stream and

give a more realistic flow field prediction close to the liners. Applying the heterogeneous model leads to a stronger recirculation zone and the presence of the PVC is stronger at the exit of the combustor. In terms of model development, further work regarding jet velocity profiles and jet penetration depth is presented in the thesis of R. Bizzari [27]. Although the generic problem of one jet in a cross flow, upon which most simple modeling approaches are based on, is well investigated, the case of a jet array in the complex flow field of a lean combustion chamber is still a very new field of research. Multi-jet interactions are still not well understood and the insufficient accuracy of currently applied models requires the use of huge safety factors in cooling system design.

In the next chapter the heterogeneous coolant injection model, presented and thoroughly investigated in this chapter, is applied to model the coolant injection on high-pressure vanes.



# Chapter 4

## Assessment of a coolant injection model for cooled high-pressure vanes

### Contents

---

4.1	Introduction . . . . .	<b>60</b>
4.2	Coolant injection modeling . . . . .	<b>61</b>
4.3	Domain, mesh and LES modeling . . . . .	<b>64</b>
4.4	Results . . . . .	<b>70</b>
4.4.1	Mean flow operating conditions and flow organization .	70
4.4.2	Vane surface temperature predictions . . . . .	73
4.4.3	Investigation of the cooling film and mixing behavior .	75
4.5	Conclusion . . . . .	<b>84</b>

---

In gas turbine engines, the combustion chamber liners (discussed in Chapter 3) and parts of the high-pressure turbine require active cooling to keep the material temperatures below thermal stress limits. At the same time, the least amount of coolant should be used to conserve air for the combustion process in the chamber. To ensure long term safe operation of the engine, the NGV cooling system has to provide sufficient cooling over a wide range of operating conditions. NGVs are commonly cooled by use of interior cooling channels exploiting the heat sink capacity of the coolant air and by the creation of a coolant film on the NGV surface. The exterior coolant film created by injecting coolant air through multiple holes on the NGV surface keeps hot gases away from the blade. In the FACTOR combustor simulator, the main interest is to investigate component interactions and the impact of cooling systems on the main flow. Temperature levels are low ( $<530\text{ K}$ ) to allow for various measurements and to ensure a long component lifespan. The interior NGV cooling system is thereby simple and consists of two plena that feed 171 coolant ejection holes on each NGV. This chapter focuses on the aerodynamic behavior of the coolant in the main flow and compares a fully meshed cooling system simulation with another simulation where coolant is injected on

discrete surface patches. The goal is to validate the heterogeneous coolant injection model for the modeling of the exterior NGV cooling system, which allows to reduce cost if compared to a simulation with a fully meshed cooling system. The heterogeneous injection model is later on used to model the NGV cooling system in a fully integrated simulation of combustion chamber and high-pressure turbine (see Chapter 7). The present study is a collaborative work of M. Harnieh, M. Thomas and R. Bizzari. Results shown herein have been presented at the Engineering Turbulence Modelling and Measurements (ETMM) 2018 conference in the paper ETMM2018-111 [95] and published in the Journal of Flow, Turbulence and Combustion [28].

## 4.1 Introduction

To comply with new environmental regulations, the thermal efficiency of gas turbines has been improved by increasing the temperature at the exit of the combustion chamber. As a result, the thermal load on the Nozzle Guide Vanes (NGV) has significantly increased. Indeed, the combustion temperatures in current burners surpass the thermal stress limits of the blade material, which makes the use of sophisticated cooling systems inside and around vanes mandatory. One efficient solution is to bleed cold air from the compressor and re-inject it through coolant pipes placed around the most thermally stressed areas of the vanes. Around the vanes, the coolant forms a protective film, keeping hot gases away from the wall and thereby limiting the surface temperature. The turbulence generated in the flow affects the mixing between coolant and hot flow impacting the coolant film integrity and thereby its cooling efficiency. The numerical prediction of the cooling efficiency on cooled blades remains a challenge today. Reynolds Average Navier-Stokes (RANS) simulations have been used in the past decades to predict the thermal load on blades. Due to the size and the number of cooling holes, big efforts in terms of engineering hours for mesh generation and computational resources are needed to master such systems. To limit the associated cost, film cooling models have been implemented in RANS [96–98], the aim of these models being to inject the coolant flow on the wall without resolving the interior cooling system. However if implemented in the context of RANS, the predictions still suffer from a lack of accuracy to predict mixing [99–101] and obtained cooling efficiencies remain highly sensitive to RANS closure as well as to mesh resolution. To alleviate this issue, one solution is to perform Large-Eddy Simulations (LES) which resolve the most energetic turbulent structures on the mesh [102, 103]. However, resolving the entire NGV cooling system in LES requires a large number of cells to compute the flow in the cooling system, so modeling the impact of the cooling system presents itself as an attractive solution. The same situation has been encountered for the modeling of multiperforated plates of aeronautical combustion chamber liners, as already discussed in Chapter 3. To limit the associated computational cost, Mendez and Nicoud [104] have proposed a homogeneous model with the objective to inject the coolant homogeneously on the wall conserving the integrated mass flow rate and tangential momentum flux over the wall. In this homogenization process, the

dynamics of the jets is lost and the mixing with the hot flow is under-estimated. While addressing this specific weakness, Bizzari et al. (2018) [88] have proposed a LES model for multiperforated liners to take into account the position of perforations as well as the capacity of the local mesh resolution to properly represent the jets. In this approach, the cooling system is not meshed, but additional inlets for coolant flow are projected on the surface of the combustion chamber liners, or in this case, blades allowing to save significant CPU resources and human work to set up CAD and associated meshes. This new modeling approach provides better results compared to the homogeneous model, reproducing the dynamics of the jets if increasing the mesh resolution [27, 105]. The present work aims to evaluate this new modeling approach in the specific context of cooled NGV blades.

To assess the model, two simulations are carried out on the NGVs of the European project FACTOR (Full Aerothermal Combustor Turbine interactiOns Research) [3], experimentally studied at the DLR (Germany) [17] and at UNIFI (Italy) [106]. The DLR rig features a full annular non-reactive lean combustor demonstrator with one high-pressure turbine stage. At the exit of the combustor, the flow field features high levels of swirl, turbulence and temperature non-uniformities. The blades are cooled by a cold flow originating from internal plena and exiting through 171 holes on each vane. First, a fully meshed configuration is considered including the cooling system: i.e. the plena and the holes. Then, a second computation using the thickened hole model which does not consider the internal feeding plena is produced. Finally, comparisons of both predictions are detailed in an attempt to assess the capacity of the hole modeled approach for real applications.

The discussion around this specific objective is organized as follows. First, the modeling of the coolant injection is introduced in Section 4.2. Details on the numerical set up, computational domains and LES modeling are presented in Section 4.3. Finally, comparisons between the predictions with meshed and modeled cooling system are reported in Section 4.4 including a detailed analysis of the film cooling process taking place in both simulations. From this investigation, potential improvements of the model are proposed in the conclusion as a path for its use in the context of industrial and academic applications.

## 4.2 Coolant injection modeling

The coolant model, already described in Bizzari et al. [88], has initially been developed in the context of the combustion chamber as shown in Chapter 3. In the following, the coolant model is adapted and presented in more detail in the specific context of NGV cooling. To do so, the geometric parameters of the cooling holes are first presented. Next, the assumptions and mathematical details of the model are introduced. Finally, the validity of the model in this specific context is discussed.

The geometric parameters of the coolant injection holes to be modeled are shown on Fig. 4.1. Note that this specific configuration has the particularity of

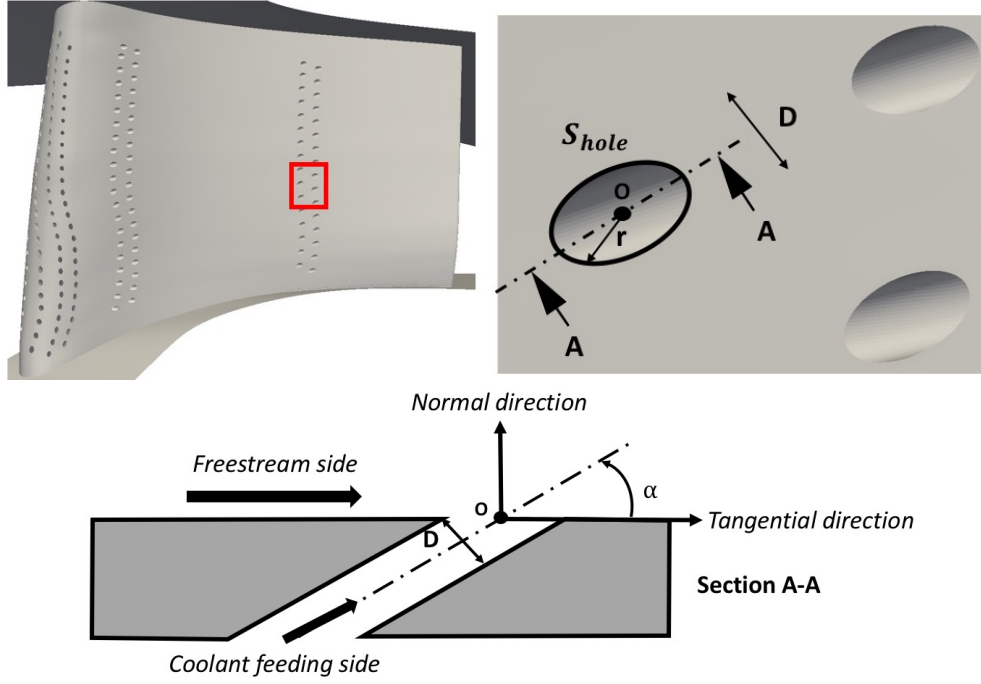


**Figure 4.1:** Geometric definitions of the holes. Example of the pressure side view of a cooled NGV (a). Normal blade view in the red square (b) and view of the A-A cut (c).  $O$  is the center of the hole,  $D$  the minimum diameter of the hole,  $r$  the local radial coordinate defined on the hole surface  $S_{hole}$  and  $\alpha$  the inclination angle to the wall.

using only cylindrical holes. The hole exit surfaces can be assumed to be elliptical and defined by the minimum diameter  $D$  of the hole surface  $S_{hole}$  and the inclination angle to the blade surface  $\alpha$ . A local radial coordinate  $r$  is defined on the hole surface and attached to the hole center  $O$ . The normal direction is then defined at the center of the hole while the tangential direction is chosen to be aligned with the projection of the jet velocity vector onto the blade wall.

The main idea of the model is to directly inject the coolant using an equivalent boundary on the wall surface without representing the coolant pipes inside the blades. In the following, each hole is independently considered and the contribution in terms of boundary fluxes of each hole is added. The injection of the coolant on the wall and for a given hole is represented by an axi-symmetric normalized distribution function  $f(r)$  centered on the hole center and defined on the total surface of the blade  $S_{tot}$  to geometrically identify the considered hole,

$$f(r) = 0.5 \left( 1 - \tanh \left( \frac{r - 0.5\Gamma D}{\beta \Delta x} \right) \right), \quad (4.1)$$

where  $\Delta x$  is the local mesh size,  $\Gamma$  is the thickening factor (if the hole is under-resolved, i.e.  $\frac{D}{\Delta x} < 3$ ) and  $\beta$  a numerical constant to limit the sharpness of the distribution function on the mesh to avoid numerical issues. Bizzari et al. [88] shows that  $\beta = 0.1$  is a correct value to represent the distribution function on usual meshes to avoid numerical stability problems. The normal and tangential velocity

profiles to be imposed by the model on the blade surface, respectively noted  $V_n^{model}$  and  $V_t^{model}$ , are assumed to be stationary and to follow the expressions,

$$V_n^{model} = A_n f(r), \quad (4.2)$$

$$V_t^{model} = A_t f(r), \quad (4.3)$$

where  $A_n$  and  $A_t$  are constant parameters of the model and the distribution function  $f(r)$  is used to impose the shape of the velocity profiles on the blade surface issued by the considered hole.

The model is built to conserve the mass and tangential momentum fluxes of the physical jet through the considered hole section  $S_{hole}$ . To do so, the model parameters  $A_n$  and  $A_t$  are determined following the conservation of the previous cited fluxes through the total surface of the blade  $S_{tot}$  containing only the considered hole between the physical and modeled jet,

$$\int_{S_{tot}} \rho V_n^{model} dS = \int_{S_{hole}} \rho V_n^{jet} dS, \quad (4.4)$$

$$\int_{S_{tot}} \rho V_n^{model} V_t^{model} dS = \int_{S_{hole}} \rho V_n^{jet} V_t^{jet} dS, \quad (4.5)$$

where  $V_n^{jet}$  and  $V_t^{jet}$  are the normal and tangential velocity profiles of the real jet, if known, and  $\rho$  is the density assumed uniform. Inserting the expressions of the modeled velocity profile in the conservation equations gives,

$$\int_{S_{tot}} \rho A_n f(r) dS = \int_{S_{hole}} \rho V_n^{jet} dS, \quad (4.6)$$

$$\int_{S_{tot}} \rho A_n A_t f^2(r) dS = \int_{S_{hole}} \rho V_n^{jet} V_t^{jet} dS, \quad (4.7)$$

resulting in expressions for  $A_n$  and  $A_t$ ,

$$A_n = \frac{\langle V_n^{jet} \rangle_{S_{hole}} S_{hole}}{\int_{S_{tot}} f(r) dS}, \quad (4.8)$$

$$A_t = \langle V_t^{jet} \rangle_{S_{hole}} \frac{\int_{S_{tot}} f(r) dS}{\int_{S_{tot}} f^2(r) dS}, \quad (4.9)$$

where  $\langle \bullet \rangle_S$  is the spatial average on section  $S$ . Note that the temperature profile is kept uniform on the hole. To apply the model in the context of turbine blades, one must know a priori the mass flow rate of each hole  $Q_{m,hole}$  to retrieve the surface averaged normal velocity and the jet angle to calculate the surface averaged tangential velocity. The jet angle is assumed to be equal to the geometric angle  $\alpha$  of the hole leading to the following expressions of the spatial averages of the velocity profiles,

$$\langle V_n^{jet} \rangle_{S_{hole}} = \frac{Q_{m,hole}}{\rho S_{hole}}, \quad (4.10)$$

$$\langle V_t^{jet} \rangle_{S_{hole}} = \frac{Q_{m,hole}}{\rho S_{hole} \tan(\alpha)}. \quad (4.11)$$

Such a modeling approach was originally proposed in the context of multi-perforated liners which operate in conditions that are different from the ones encountered for NGV flows, so deviations are expected between meshed holes and hole-modeled predictions. Indeed, the model assumes that the velocity profile is axi-symmetric, stationary and density as well as temperature are prescribed uniform on the hole section which differs from real cooling hole features present in turbines [107]. In terms of flow characteristic and response in the specific context of jets in cross flows, the operating condition of the jet issued by the cooling system is usually determined by use of the blowing and momentum ratios respectively noted  $M$  and  $J$ ,

$$M = \frac{\langle \rho V \rangle_{S_{hole}}}{\rho_{\infty} V_{\infty}}, \quad (4.12)$$

$$J = \frac{\langle \rho V^2 \rangle_{S_{hole}}}{\rho_{\infty} V_{\infty}^2}. \quad (4.13)$$

where  $\infty$  refers to the local free-stream condition. For combustion chamber liners typical values are  $5 < M < 20$  and  $30 < J < 90$  [26] while for blade cooling systems, typical values are around one for both  $M$  and  $J$  [108]. Inter-hole distances are also quite different, the overall number of holes and their proximity strongly impacting the resulting cooling film dynamics. Differences in flow responses as well as model sensitivities will thus arise depending on the context of use. One objective of the following discussion is to highlight such changes and their potential importance in the context of a hole modeled LES of NGVs.

### 4.3 Domain, mesh and LES modeling

In this section, the geometry, the numerical set up and LES modeling are introduced. Next, the resulting velocity profiles on the hole surfaces issued from the model are detailed and then compared to a meshed holes LES to highlight potential differences in terms of coolant injection.

The configuration addressed for the study focuses on the NGV section of the FACTOR test rig [3, 17, 106]. The operating point of the blades is given at P41, the exit plane of the stator, and summarized in Tab. 4.1.

Blade feature	Value
Axial chord length (ACL)	40 mm
Mach number	0.93
Reynolds number based on ACL	430 000

**Table 4.1:** Summary of the operating point of the blades. The Mach number and Reynolds number are computed at the trailing edge axial plane using the axial chord length (ACL).

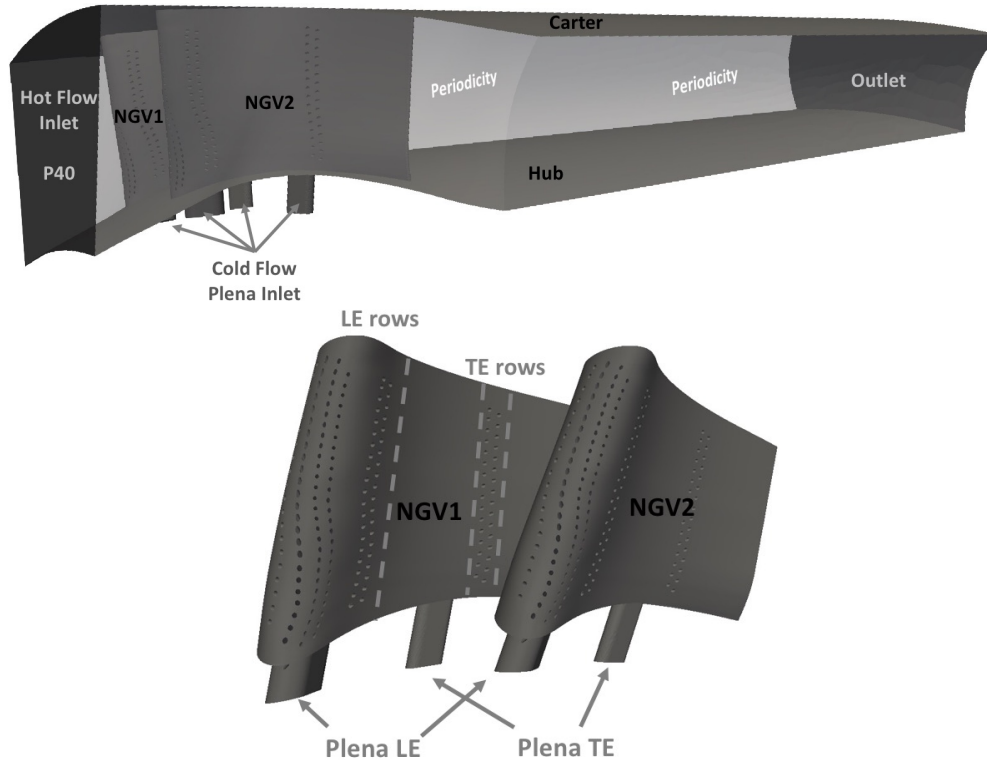


**Figure 4.2:** Domain used for the study: a) computational domain and b) NGV details.

For all computations discussed hereafter, the computational domain retained represents a  $18^\circ$  periodic sector ( $1/20^{th}$  of the full annular domain) of the high-pressure nozzle section of the FACTOR test rig containing two NGVs respectively denoted as NGV1 and NGV2 (see Fig. 4.2). The domain is axially limited by the turbine inlet plane (P40), which is well numerically and experimentally characterized, and located  $17\text{ mm}$  upstream the blades i.e.  $0.425$  Axial Chord Length (ACL). The outlet is located  $6$  ACLs downstream of the blades to avoid interactions between the flow region of interest with the outlet boundary (see Fig. 4.2a). In the real system, coolant around both NGVs is supplied by two plena for each NGV (see Fig. 4.2b). This coolant fluid is then used to generate a film on the NGV wall by exiting the blade internal system through perforations that are located for the first set near the blade leading edge (between  $x/c = 0$  and  $x/c = 0.3$ ) on the pressure and suction side. This specific set of holes are thereafter denoted as the leading edge (LE) rows (displayed in Fig. 4.2b). A second set of holes is located upstream of the trailing edge (between  $x/c = 0.6$  and  $x/c = 0.7$ ) on the pressure side and will be identified as the trailing edge (TE) rows.

All simulations rely on the resolution of the compressible LES equations [109, 110] for which subgrid-scale turbulent closure relies on the WALE model proposed by Nicoud and Ducros (1999) [111]. Note that for the discussed predictions, all walls are treated using an adiabatic logarithmic law of the wall to alleviate the overall cost imposed by a wall resolved LES and reproduce an industrial context

most likely encountered for such LES [33, 112, 113].

Inflow and outflow boundary conditions are specified using the Navier-Stokes Characteristic Boundary Condition (NSCBC) formalism [114, 115]. The inlet boundary condition is extracted from a time-averaged LES of an integrated computation of combustion chamber and NGVs, to be detailed in Chapter 5. In this section, the combustor operating point used to provide the inlet conditions on P40 corresponds to the design point at the UNIFI rig without blades as presented in Section 1.2.1 and discussed in Chapter 5. Note that the high-pressure vanes were installed at the UNIFI rig after these simulations were performed, so despite featuring vanes, the operating point in the combustor corresponds to the operating conditions at the UNIFI rig before vanes were added to the test rig. The time-averaged 2D maps of the mass flow distribution  $\rho U_i$  and static temperature  $T$  are extracted at the plane P40 and imposed at the inlet of the computational domain featuring a stationary field without turbulence injection and a hot spot of temperature aligned on NGV1 and a swirled flow as shown in Fig. 4.3. Note that due to the low Mach number at the exit of the combustion chamber, static and total values correspond quite well. The coolant mass flow rates  $Q_{m1}$  and  $Q_{m2}$  are imposed at the inlet of the plena at the temperature  $T_{cold} = 300\text{ K}$ , in agreement with the targeted operating point of the system, Tab. 4.2. The addition of a passive scalar allows tracking the coolant flow throughout the domain. Equivalently, at the outlet, the surface averaged static pressure is imposed to reach the operating point of the blades and the radial equilibrium is naturally obtained using a specific 3D NSCBC outlet boundary condition [22, 116].

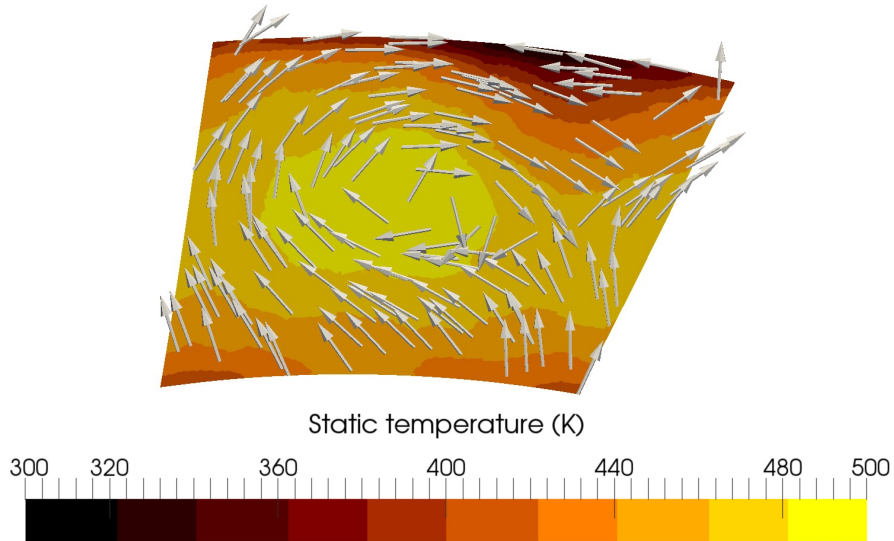


**Figure 4.3:** 2D temperature map including a hot spot and swirled flow imposed at the inlet boundary condition. Arrows evidence the swirled flow.

Finally, integration of the modeled equations is obtained by use of the finite element numerical explicit scheme TTG4A, 3<sup>rd</sup> order in space and 4<sup>th</sup> order in time [117].

Patch	Variable	Spatial mean value
Inlet	$Q_m$	$0.240 \text{ kg.s}^{-1}$
Inlet	$T_{inlet}$	$455 \text{ K}$
Plena LE	$Q_{m1}$	$0.012 \text{ kg.s}^{-1}$
Plena TE	$Q_{m2}$	$0.006 \text{ kg.s}^{-1}$
Plena LE & TE	$T_{cold}$	$300 \text{ K}$
Outlet	$P_{outlet}$	$87000 \text{ Pa}$
Wall		Adiabatic wall law

**Table 4.2:** Boundary conditions used in the meshed holes LES.

For the above discussed conditions, two LES are produced: a) a so-called meshed holes LES and b) a hole modeled LES. For the first one, the entire computational domain is considered: i.e. including the vane and the different internal cooling systems. The corresponding mesh is composed of 73 million of tetrahedra with 35 million elements needed to discretize the cooling system. Special refinement of the surface mesh at the cold flow injection location is done to discretize the diameter of holes with around 13 – 15 points. Note further that, to ensure that the locally strong gradients induced by the injection of the coolant are properly captured by the meshes, an adaptive mesh refinement process has been applied to refine the mixing regions between main flow and coolant jets [118, 119]. The second prediction, referred to as the hole modeled simulation uses a mesh that is derived from the meshed holes LES mesh without including plena and the pipes connecting the internal flow to the main flow. The resulting cell number is therefore 38 million cells and corresponds to the vane mesh of the meshed holes simulation. These changes in cell counts result in CPU costs presented in Tab. 4.3 for one flow through time defined as the time taken by a fluid particle generated at the inlet to reach the outlet following a streamline. It is worth to note that the projected holes are sufficiently resolved so that the thickening factor in Eq. 4.1 is  $\Gamma = 1$  meaning that the modeled coolant injection area is not enlarged in this context.

CASE	Number of cells	CPU cost (CPUH)
meshed holes LES	$73.10^6$	10 000
hole modeled LES	$38.10^6$	3000

**Table 4.3:** Summary of the LES computations and CPU cost for one convective time. Computations were performed with the High Performance Computing (HPC) resources of IDRIS on the Blue Gene machine TURING.

One requirement behind the hole modeled approach is the knowledge of mass flow distribution issued by each hole to be considered by the model. Equivalently, the meshed holes LES can only be considered as a reference if the corresponding mass flow distribution is known and controlled (a strong function of the coolant model is to reproduce the correct pressure loss distribution across all perforations). To

validate this specific point in the case of the meshed holes LES, the coolant mass flow rate distribution through the holes is gauged against available RANS predictions relying on a wall resolved RANS (see Fig. 4.4). Clearly, both predictions

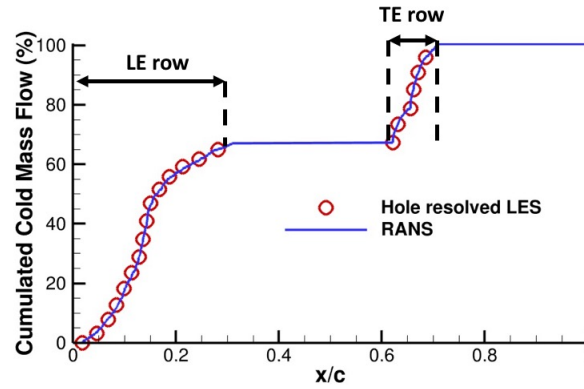


**Figure 4.4:** Cold mass flow distribution along the blade. Red circle  $\circ$  represents the meshed holes LES and solid blue line  $-$  the RANS simulation.

give equivalent coolant distributions confirming that the meshed holes LES can be used as the reference in this work. For the hole modeled LES, the distribution of the coolant mass flow rate is deduced from the meshed holes LES to limit sources of differences to the proposed modeling procedure.

In the meshed holes LES, the exiting jet profile is potentially unsteady and non axi-symmetric contrarily to the hole modeled approach. This non axi-symmetry and unsteady activity is confirmed by Figs. 4.5 & 4.6.

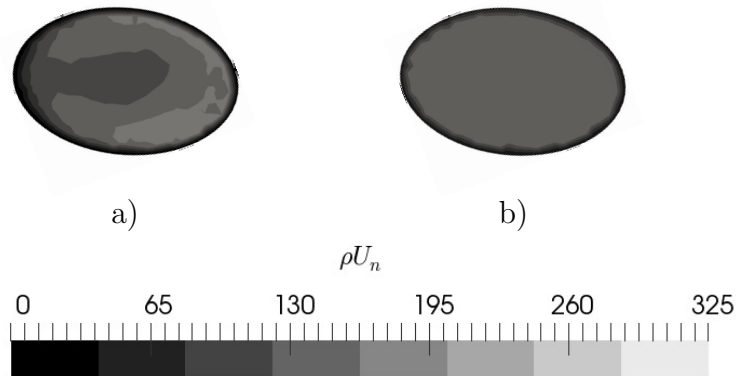


**Figure 4.5:** Time-averaged normal profiles of the mass flux  $\rho U_i n_i$  at a coolant ejection hole located in the last cooling row at mid height of NGV1 for the meshed holes (a) and hole modeled (b) LES.

In both cases, the 2D maps of the time-averaged normal profile of coolant mass flux are extracted for both predictions: *i.e.*  $\rho U_i n_i$  where  $n_i$  is the hole normal at the exit section of one specific hole of NGV1. Contrarily to the hole modeled LES (see Fig. 4.5b), the mass flux profile in the meshed holes LES is not axi-symmetric and shows a horse-shoe pattern (see Fig. 4.5a). The unsteady activity is evidenced

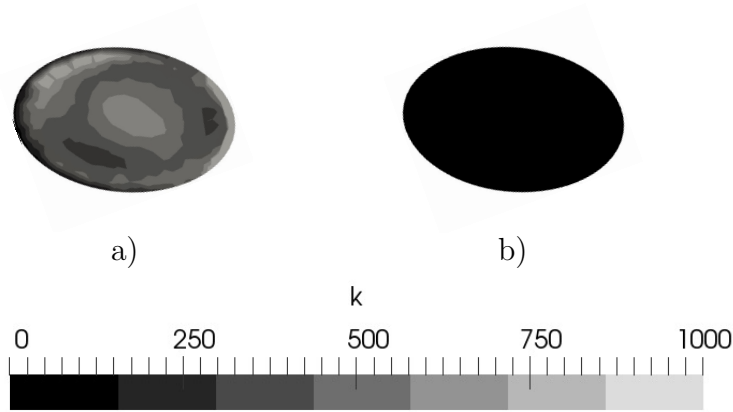


**Figure 4.6:** Turbulent kinetic energy  $TKE$  at a coolant ejection hole located in the last cooling row at mid height of NGV1 for the meshed holes (a) and hole modeled (b) LES.

through the profile of the turbulent kinetic energy  $TKE$  shown for both cases on Fig. 4.6. For the hole modeled prediction (see Fig. 4.6a), the turbulence intensity is around 5 % and located in the jet shear layer, a feature that is not taken into account by the hole modeled approach (see Fig. 4.6b). These different coolant flow topologies between a meshed holes and a hole modeled LES are expected.

Despite these coolant injection differences, the coolant jets issued from the model reproduce well the jet penetration and the thickness of the film as evidenced by a zoom on the near wall region of the coolant temperature isosurface (see Fig. 4.7). The jets issued from the hole modeled LES are more coherent compared to the meshed holes LES due to the lack of injected turbulence at the blade surface with the model. The remaining question is to what extent the coolant model

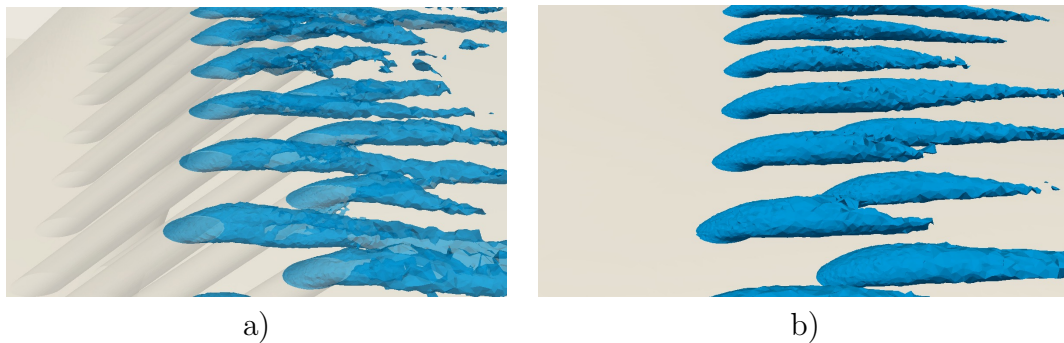


**Figure 4.7:** Instantaneous isosurface of the coolant temperature to evidence the coolant injection near the surface blade of NGV1 in the meshed holes case (a) and hole modeled case (b).

impacts the prediction and the development of the coolant film in comparison with the reference simulation. This specific question is the main subject of the remaining discussion, which focuses on the qualification of the modeling and the impact on the temperature of the NGV walls.

## 4.4 Results

In this section, detailed comparisons of both LES predictions are proposed to qualify the capacity of the hole modeled approach to reproduce accurately the coolant injection for complex NGV simulations. First, obtained operating conditions and flow organization issued by both LES are studied to ensure the comparability. Then, the effect of the model on the NGV surface temperature is investigated. Finally, the film evolution is more specifically addressed in both cases with emphasis on the ability of both simulations to reproduce the mixing process taking place between the hot and cold flows in the near wall film.

### 4.4.1 Mean flow operating conditions and flow organization

The wall temperature of a complex NGV geometry is the result of multiple factors that are tightly coupled. For uncooled NGVs and with adiabatic wall boundary conditions, the wall temperature is governed by the aerodynamics induced by the presence of the blade and the impact of the hot spot. When cooling systems are applied, the wall temperature is influenced by more complex phenomena and results from the mixing between the hot and cold stream as well as the associated aerodynamic response of the flow dictated by the operating point of the blade. In the case of film cooling, the discrete nature of the cold stream injection all around the blade boundary layer clearly hinders the analysis. As a consequence and prior to a deeper analysis of the hole modeled approach, a verification of the overall operating condition provided by the two simulations is mandatory.

This specific point is addressed in Tab. 4.4, where the mass flow traveling through the system, the total temperature  $T_t$  and pressure  $P_t$  at P40, corresponding to the inlet of the domain, are compared to ensure that both LES meet the same operating point. The drop of total variables between the plane 40 and plane P41 located 1.5 ACL downstream the inlet is evaluated to verify the impact of the blade on the aerodynamics for both LES. Note that  $P_t$  and  $T_t$  are here mass flow averaged on the considered planes. The pressure loss in the simulation with the modelled cooling system is slightly higher than for the other case, which can be explained by the modeled jets penetrating further into the flow and thereby generating higher losses. Using a mass-flow inlet in combination with a pressure outlet, this translates to higher inlet pressures for the simulation with the resolved cooling system.

Values confirm that both simulations meet the same operating point and that the coolant flow injection is equal in both cases. Here, the total pressure loss is not only determined by the losses generated by the presence of vanes in the flow, but also influenced by the addition of coolant (7.5% of mass flow on P40) inside the domain. When comparing both cases, the total pressure loss difference is found to be slightly more important for the meshed holes LES. The higher pressure loss in this case is due to higher losses in the near wall layer caused by increased interactions between the resolved coolant injection system and the main flow. This

CASE	meshed holes LES	hole modeled LES
Hot mass flow rate ( $kg.s^{-1}$ )	0.240*	
Cold mass flow rate ( $kg.s^{-1}$ )	0.018*	
$T_{t40}$ (K)	443*	
$P_{t40}$ (Pa)	149738	149619
$S_{w,40}$	0.19	0.19
$T_{t40} - T_{t41}$ (K)	0.1	0.4
$P_{t40} - P_{t41}$ (Pa)	4673	4483

**Table 4.4:** Main and coolant mass flow rates for both LES and total pressure  $P_t$  and total temperature  $T_t$  at the inlet of the domain (P40) and drop between the planes P40 and P41 (\* values are imposed by the inlet boundary condition).

difference is discussed later. For the overall comparison of both simulations, the pressure loss difference is however negligible.

The operating point of the blades is now studied by investigating the flow expansion through the vane passages for both LES. Figure 4.8 provides the isentropic Mach number profiles at mid height of both NGVs,

$$Ma_{is} = \sqrt{\frac{2}{\gamma - 1} \left[ \left( 1 + \frac{P_{stagn}}{\bar{P}} \right)^{\frac{\gamma-1}{\gamma}} - 1 \right]}, \quad (4.14)$$

where  $\bar{P}$  is the time-averaged pressure on the blade surface,  $P_{stagn}$  the pressure at the stagnation point and  $\gamma$  the local heat capacity ratio. Clearly, the expansion through NGV1 & NGV2 (see Figs. 4.8a&b) for both LES predictions is in good agreement. Differences remain local and appear for NGV2 (see Fig. 4.8b) on the

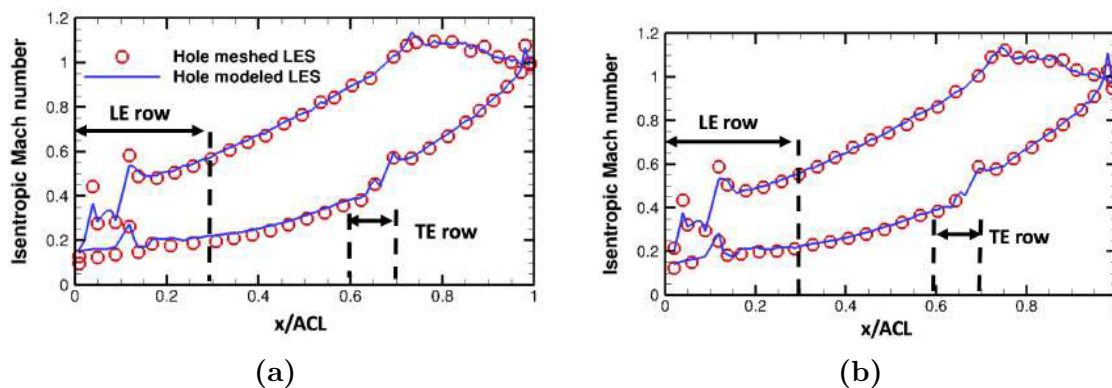


**Figure 4.8:** Isentropic Mach number  $Ma_{is}$  along NGV1 (a) and NGV2 (b) at mid height of the vanes. Red circles  $\circ$  represent the meshed holes LES and the solid blue line  $-$  represents the hole modeled LES. The axial extent of the cooling rows is indicated by lines.

pressure side and for NGV1 on the suction side (see Fig. 4.8a) for the axial positions  $0.7 < x/c < 0.9$ . For NGV2, this location corresponds to the TE injection

holes on the pressure side, indicating that the two approaches locally impact the aerodynamics of the flow in a different way.

Looking at the mean total temperature field at mid height on Fig. 4.9 confirms that NGV1 is impacted by the hot spot in both predictions. The cold flow issued from the NGV1 cooling system is thus expected to picture stronger gradients of total temperature than NGV2. Aside from this inflow difference between NGV1 and NGV2, total temperature maps appear very similar for both simulations except maybe in the region of the coolant flow injection near the blade surfaces. As already observed before, coolant jets are more marked in the hole-modeled LES compared to the meshed holes LES. As a result, the model is seen to impact total temperature distribution in the near-wall region. Later in this chapter, specific investigations of the mixing process in the coolant film will be presented to find the origins of these deviations.

To assess the hot spot transport between planes P40 and P41, the mass flow averaged mean total temperature field is further averaged in space for different radii in plane P40 and P41 yielding the radial profiles of Fig. 4.10. At plane P40,

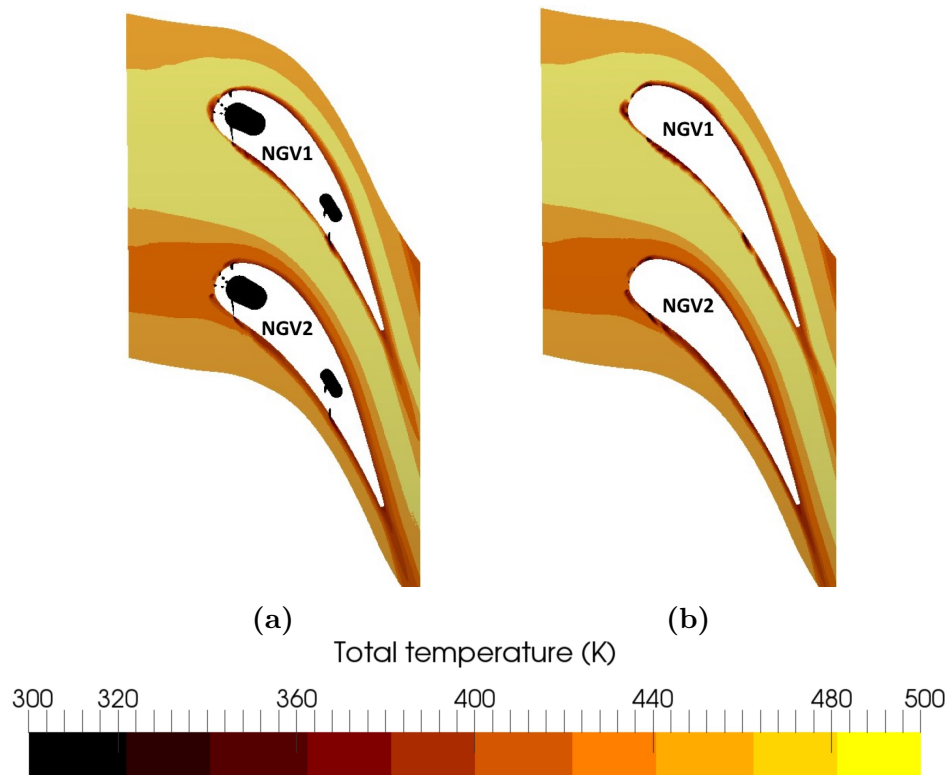


**Figure 4.9:** Time-averaged total temperature field at mid-height. (a) Meshed holes and (b) hole modeled LES.

no difference is noticed between both LES confirming that the inflow imposed is the same. In plane P41, the profiles appear also very similar and differences arise only near the carter (top section of the curves), between  $0.6 < h/H < 0.8$  show-

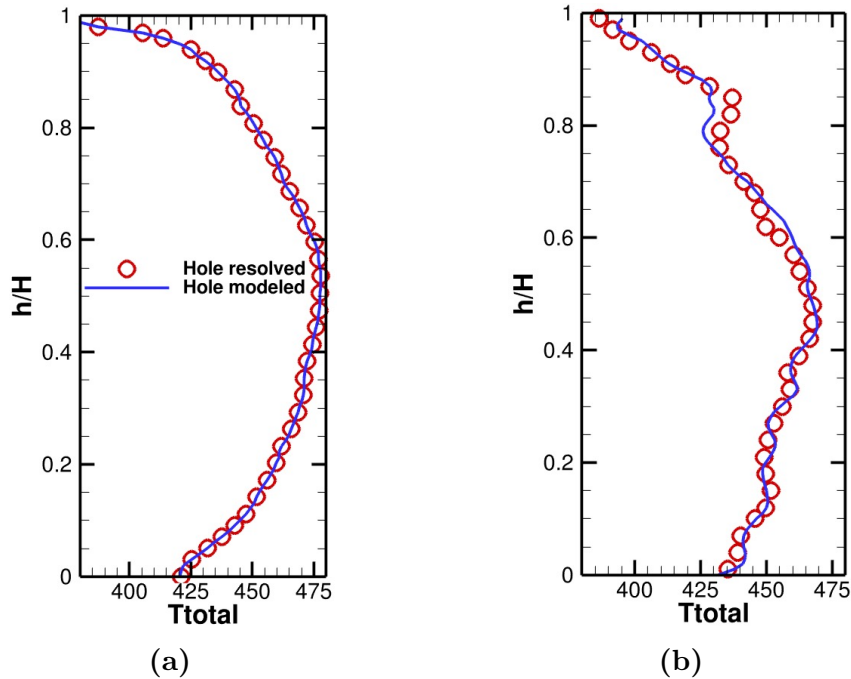


**Figure 4.10:** Radial total temperature profile at the axial plane P40 (a) and P41 (b). Red circle  $\circ$  represents the meshed holes LES and solid blue line  $-$  the hole modeled LES.

ing a weak impact of the model on the migration of the hot spot through the NGVs.

Overall, verifications of the mean operating point, flow expansion and flow topology confirm that both LES are equivalent with only minor differences attributed to the different coolant injection approaches. These findings clearly underline the limited impact of modeling, highlighting the suitability of the proposed approach for more efficient LES of such problems. Verification is however still needed. Since the objective is to predict surface temperatures and efficiency of designed film cooling strategies, blade temperature profiles are addressed in the following section.

#### 4.4.2 Vane surface temperature predictions

The impact of both models on the surface temperature distribution is displayed in Fig. 4.11. Agreement between both simulations for the surface temperature maps of both NGVs is confirmed. Indeed, both approaches capture all macroscopic features around the two blades. Patterns only locally deviate by small local temperature variations and limited spatial extents.

As anticipated, the surface temperature distribution on NGV1 (see Fig. 4.11a&c), seems to be strongly influenced by the swirled flow. For this blade, the swirled flow radially deviates the cold flow on the blade surface. This effect is stronger on the pressure side of NGV1 because of the impact of the hot spot and associated residual swirl at the same location. The effect is clearly weaker on NGV2,

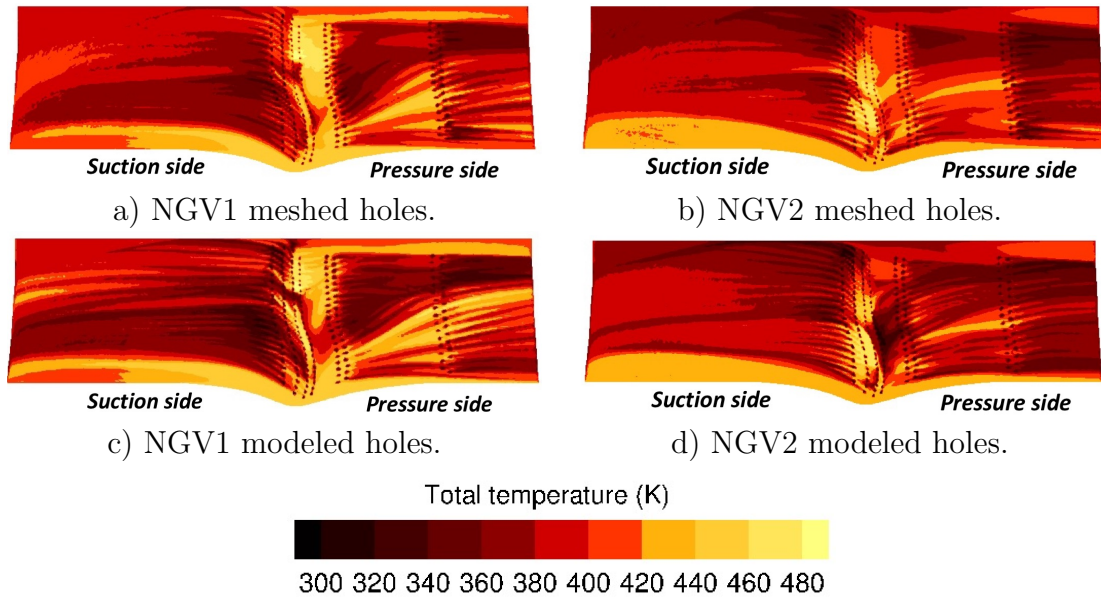


**Figure 4.11:** Time-averaged adiabatic wall temperature on NGV1 and NGV2 for both LES.

Fig. 4.11b&d). If focusing on the surface temperature obtained with the hole modeled LES, the patterns remain similar to the meshed holes LES predictions but peak values are more pronounced with the model. The deviation induced by the swirled flow seems not to be impacted by the model. Locally, the traces of the cold jets, visible by cold temperature zones at around  $T = 300 K$  on the blade surfaces appear more coherent for the hole modeled LES indicating that the mixing with the hot flow is less efficient. To quantify the impact of the model on the surface temperature distribution, the radial profiles of the surface temperature for both NGVs are plotted on Fig. 4.12 by averaging in space the total temperature for each radial position. These profiles confirm that for NGV1, both approaches are very close with a maximum deviation of  $10 K$  (2.5 %) and temperature peaks that are locally accentuated indicative of local cool or hot streams. The difference is more important for NGV2 with a maximum deviation of  $15 K$  (4 %) and observed over a larger radial extent. For both NGVs, the use of a hole modeled approach induces a surface temperature that is slightly colder at mid-height with no impact near the top and bottom walls, where the injected coolant does not reach. To conclude, a hole modeled approach does not fully recover the meshed holes prediction indicating that the near wall boundary layer flow is partially impacted. Since fundamental differences are present when using a hole modeled approach, such differences were expected compared to a fully meshed approach. In that respect, results also confirm that such an approach remains attractive while mixing between the coolant film and the external hot stream clearly differ. To find the origin of such a difference in the near wall film prediction, this region is specifically investigated in the next section.

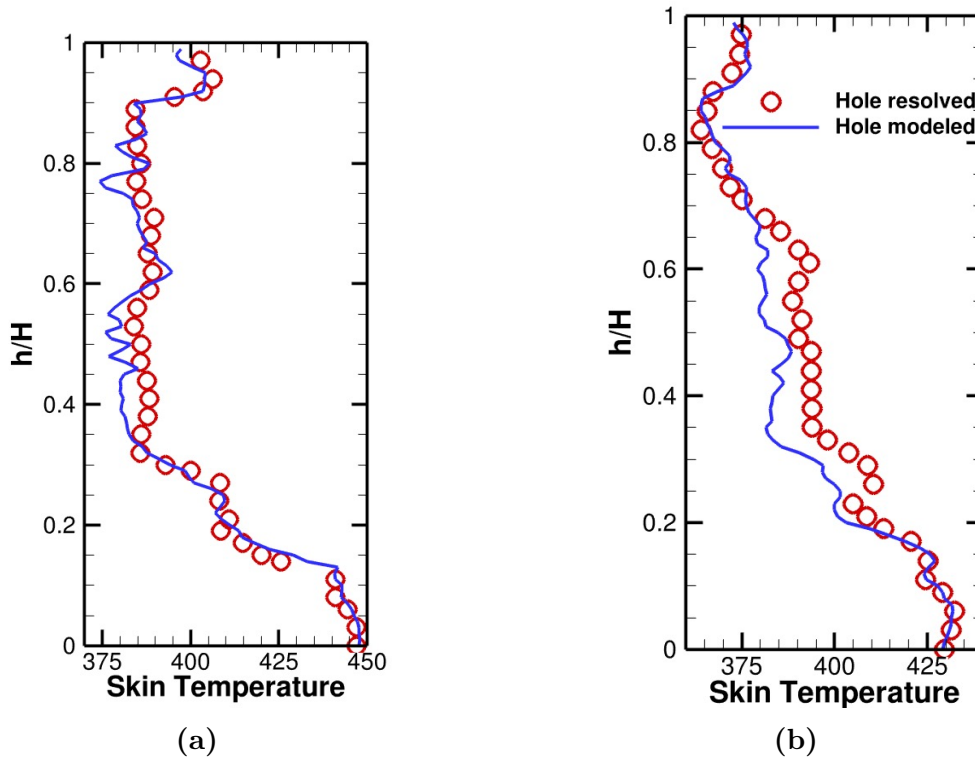


**Figure 4.12:** Radial profile of the surface temperature for NGV1 (a) and NGV2 (b). Red circle  $\circ$  represents the meshed holes LES and solid blue line  $-$  the hole modeled LES.

### 4.4.3 Investigation of the cooling film and mixing behavior

A key feature differentiating the predictions of the meshed holes LES and the modeled one is the coolant film development around the NGVs. To quantify and address this specific region of the flow, the coolant is traced in both simulations using the passive scalar hypothesis. Indeed, injecting such a scalar, noted  $Y_{coolant}$ , through the jet orifices, eases the analysis of the coolant films since it is not affected by compressible effects, viscous work or the non-uniformity of temperature fields imposed at the inlet. To track the coolant fluid,  $Y_{coolant}$  is imposed as 1 at the inlet of the cooling system and 0 at the inlet of the main flow. It is then transported by the flow through convection and diffusion, the retained diffusion coefficient  $D_{coolant}$  being that of air. From such an approach, one directly accesses the hot versus cold proportions of the fluid with  $Y_{hot} = 1 - Y_{coolant}$ . Such a passive scalar furthermore provides access to a clear vision of the film topology. In the following, the investigations will be focused only on the passive scalar at mid-height of the blades to exclude the effect of the residual swirl, end-walls and secondary flows. The instantaneous film topology near the leading edge of NGV1 is displayed at mid-height in Fig. 4.13 for both predictions. For the meshed holes as well as the hole modeled predictions, the coolant directly injected by the inlet plenum and through the coolant pipes clearly results in a coolant film along the blades. Indeed, after a local perturbation of the hot flow near the exit of each pipe, the coolant re-attaches on

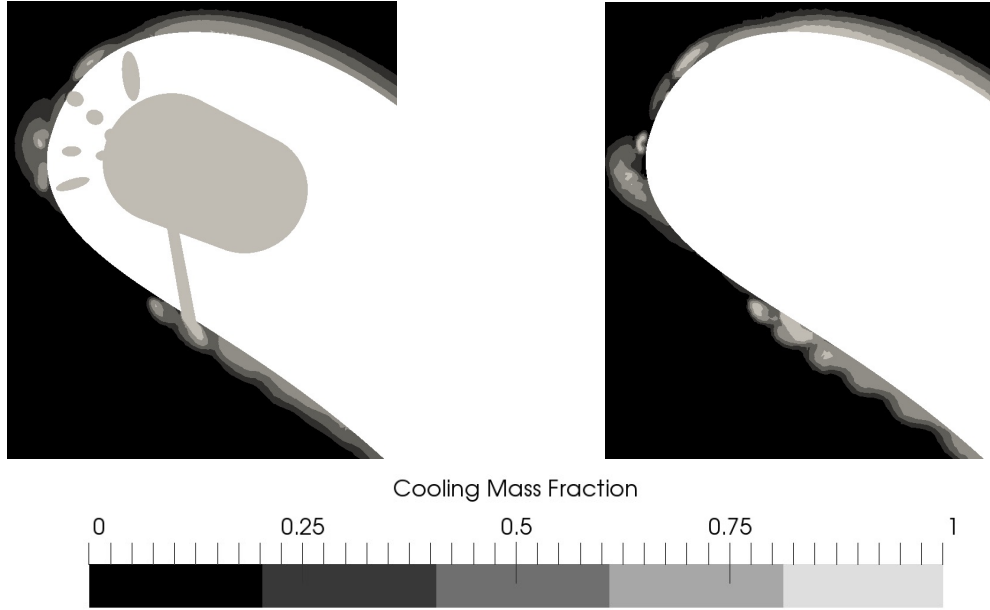


**Figure 4.13:** Cooling mass fraction near the leading edge of NGV1 at mid-height. Left: Resolved; Right: Modeled.

the wall in both simulations. The mean topology of the coolant distribution seems however more diffused in the meshed holes LES, indicating a difference of mixing between the two approaches. This impact seems also more important on the pressure side of the NGV. To illustrate the difference of coolant distribution, the profile of  $Y_{coolant}$  is plotted along the wall normal distance on both sides of NGV1 at different axial positions at mid-height of the blade on Fig. 4.14. Note that profiles are normalized by the local film thickness  $\delta$  defined as the normal distance from the wall up to the arbitrary position where  $Y_{coolant} = 0.05$ . If confronted to the mesh resolution near the blade walls, the film thickness is observed to be discretized by roughly 5 points, the wall point corresponding to a wall unit value  $y^+$  between 50 and 100 confirming that wall modeling is a crucial component. As a consequence, the resolved dynamics captured by the present LES in this region of the flow is under-resolved, stressing again the importance of modeling in such predictions. From Fig. 4.14a, at  $x/c = 0.25$ , on the suction side, the passive scalar decreases monotonously away from the wall starting from a fixed value at the wall to the corresponding external value of the film. On the pressure side, the behavior is different, i.e. the value of the passive scalar presents a maximum, not located at the wall, indicating that the coolant distribution in the film is complex and linked to the preceding local injection process of the coolant. Such observations are confirmed by other profiles, the pressure side film being more complex than the suction side film. When comparing the meshed holes coolant distribution to the hole modeled one, differences are noticed near the walls where coolant concentrations differ. Note that both LES give the same results at  $x/c = 0.75$ . This specific location corresponds to the TE hole location at mid height (see Fig. 4.14c) indicating that the injection process in both simulations is consistent. Upstream of

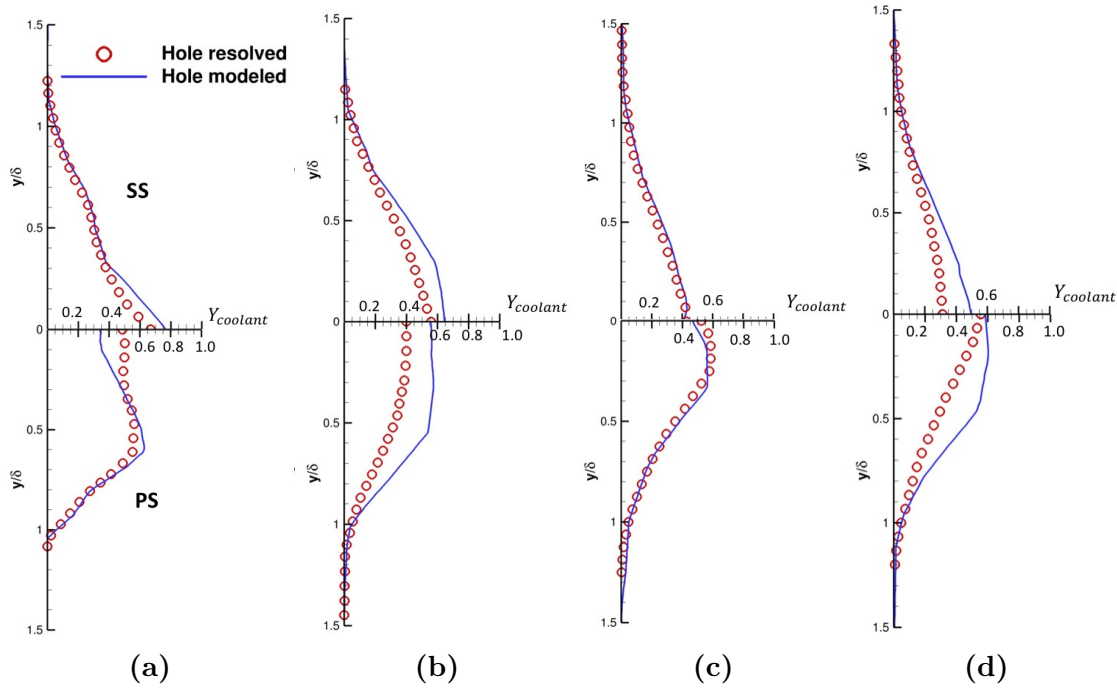


**Figure 4.14:** Profile of the coolant mass fraction for different axial positions at (a)  $x/c = 0.25$ , (b)  $x/c = 0.50$ , (c)  $x/c = 0.75$  and (d)  $x/c = 0.90$  at mid-height along NGV1. Red circles  $\circ$  represent the meshed holes LES and the solid blue line  $-$  the hole modeled LES. Pressure side (PS) is at the bottom and suction side (SS) at the top.  $\delta$  is the film thickness.

this position, the coolant injected at the LE hole location for example seems more affected and is observed to radially drift because of the swirled flow as previously shown on the vane surface temperature plots (see Fig. 4.11). Contrarily to the TE hole injection, it seems that differences of the free stream flow between LE holes will affect the modeling. Indeed, at  $x/c = 0.50$  and  $x/c = 0.90$  (see Fig. 4.14b&d), the hole modeled simulation over-estimates the value of the passive scalar if compared to the meshed holes prediction. This indicates that more coolant is present with the hole model approach. As a consequence, the coolant distribution affects the film thickness evolution plotted along the blades on Fig. 4.15 at mid-height for both NGVs and LES.

For NGV1 (see Fig. 4.15a), the film thickness increases on the pressure side due to the coolant injection by the LE and TE rows for the meshed holes LES. Between the cooling rows, the film thickness decreases due to the strong impact of the swirled flow which radially deviates the coolant. On the suction side, the swirled flow has less impact as described in Section 4.4.2 and the film thickness is only driven by the mixing between the coolant and the hot flow. Comparing the response of both NGVs, the film thickness seems more disturbed on NGV2 (see Fig. 4.15b). On the pressure side of NGV2, the thickness increases at the coolant injection positions and then decreases due to the effect of the swirled flow as previously mentioned. On the suction side, one can notice a monotonous increase of the

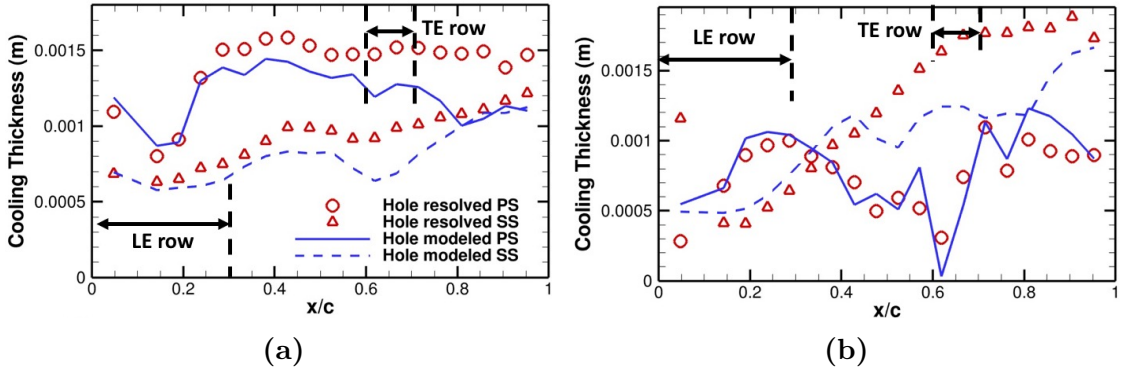


**Figure 4.15:** Film thickness along (isocontour of  $Y_{coolant} = 0.05$ ) the blades for NGV1 (a) and NGV2 (b) at mid-height. Red circles  $\circ$  represent the meshed holes LES at the pressure side. Red triangles  $\Delta$  represent the meshed holes LES at the suction side. The solid blue line  $-$  represents the hole modeled LES at the pressure side. The dashed blue line  $- - -$  represents the hole modeled LES at the suction side. Cooling row holes axial locations are indicated.

thickness without additional coolant injection, indicative of a diffusive process of the coolant fluid within the film in this region. If comparing modeling approaches, one observes that the hole modeled formalism under-estimates the film thickness evolution along both NGVs compared to the meshed holes LES.

Previously described processes taking place within the film, in its outer edge and near the injection points, can be adequately analyzed by performing a mass balance of the passive scalar concentration within the control volume corresponding to the film at mid-height as shown in Fig. 4.16. Neglecting the laminar terms in

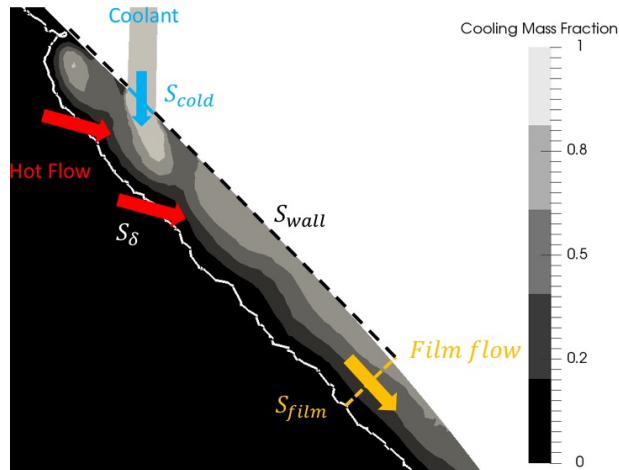


**Figure 4.16:** Control volume at mid-height to apply the mass balance in the coolant film. The control volume is delimited by the sections corresponding to the ejection exit of the coolant pipes  $S_{cold}$ , the walls  $S_{wall}$ , the thickness of the coolant  $S_{\delta}$  and the film section  $S_{film}$ .

the transport equation, the balance of the coolant mass fraction in the control

volume gives:

$$Q_{m,film} Y_{film} = \int_{S_\delta} \overline{\rho U_i Y_{coolant} n_i} dS + \int_{S_{cold}} \overline{\rho U_i Y_{coolant} n_i} dS, \quad (4.15)$$

$$\Rightarrow Y_{film} = \frac{1}{Q_{m,film}} \left( \int_{S_\delta} \overline{\rho U_i Y_{coolant} n_i} dS + \int_{S_{cold}} \overline{\rho U_i Y_{coolant} n_i} dS \right). \quad (4.16)$$

where  $Q_{m,film}$  is the mass flow rate in the coolant film,  $\rho U_i$  is the mass flux,  $n_i$  the surface normal and  $Y_{film}$  is the mass flow weighted coolant film mass fraction defined as:

$$Y_{film} = \frac{\int_0^\delta \overline{\rho U_i n_i Y_{coolant}} dn_w}{\int_0^\delta \overline{\rho U_i n_i} dn_w}, \quad (4.17)$$

where  $n_w$  is the normal coordinate from the wall and  $\bar{\bullet}$  the time average operator. As mentioned  $Y_{film}$  represents the mass flow weighted coolant mass fraction in the film thickness section  $S_{film}$  and results from the coolant passing through the film thickness section  $S_\delta$  and the coolant injected from the hole sections  $S_{cold}$ , Eq. 4.16. The latter contribution was shown to be conserved by the model, proving that  $Y_{film}$  depends only on the transport process taking place through  $S_\delta$ . Resulting  $Y_{film}$  values are plotted on Fig. 4.17 for both NGVs and both LES at mid-height. On both NGVs and for both LES,  $Y_{film}$  increases at the coolant injection posi-

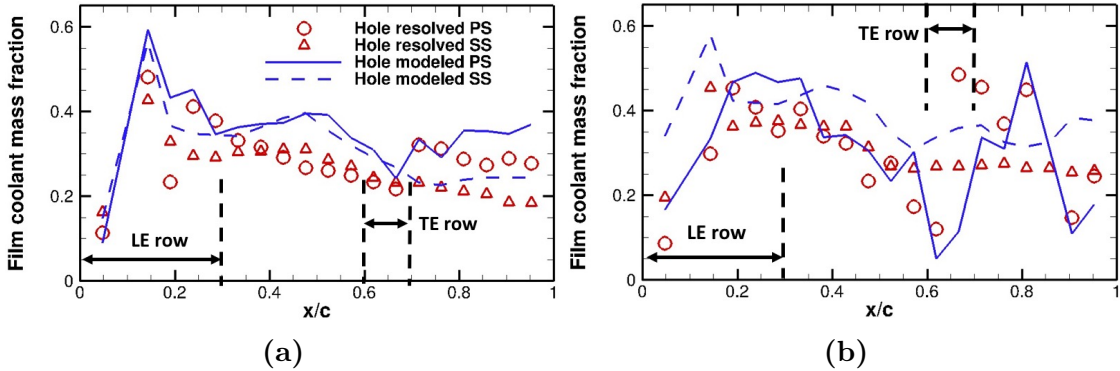


**Figure 4.17:** Coolant film mass fraction  $Y_{film}$  along NGV1(a) and NGV2(b) at mid-height. Red circles  $\circ$  represent the meshed holes LES at the pressure side. Red triangles  $\Delta$  represent the meshed holes LES at the suction side. The solid blue line  $—$  represents the hole modeled LES at the pressure side. The dashed blue line  $---$  represents the hole modeled LES at the suction side.

tions on the pressure side. On the suction side,  $Y_{film}$  decreases along the blades due to the absence of cooling holes. On both sides of NGV1 (see Fig. 4.17a), the model reproduces well the evolution of  $Y_{film}$  compared to the meshed holes LES although it over-estimates the overall levels of  $Y_{film}$  meaning that more coolant remains in the film when using the modeling approach. On both sides of NGV2 (see Fig. 4.17b), the model follows the same evolution of  $Y_{film}$  along the blade and over-estimates also the levels of coolant in the film thickness. Deviations are noticed on the pressure side at the TE coolant injection positions where levels of coolant

are locally higher in the meshed holes LES meaning that the coolant distribution around NGV2 differs at this specific position. This local discrepancy was also noticed on the profile of the isentropic Mach number of Section 4.4.1 (see Fig. 4.8).

Clearly, a key feature to reproduce observed  $Y_{film}$  is the ability of the LES to correctly predict the mixing of cold and hot flows in the near wall region. Mixing will induce a spatial evolution in the normal profile of  $Y_{coolant}$  along the wall normal direction. In that respect, the state of mixing between the hot and coolant flows can be quantified by measuring the non-uniformity of the cooling mass fraction profile along the wall normal in the film. To do so, the non-uniformity parameter  $Y'_{coolant}$  is introduced as the difference between the local value of  $Y_{coolant}$  and the spatial averaged of the profile  $\langle Y_{coolant} \rangle_S$  on  $S_{film}$  so that,

$$Y'_{coolant} = Y_{coolant} - \langle Y_{coolant} \rangle_S . \quad (4.18)$$

One can then express the integrated gaps  $\langle Y'^2_{coolant} \rangle_S$  issued by the differences between the local value and spatial mean value,

$$\langle Y'^2_{coolant} \rangle_S = \langle Y^2_{coolant} \rangle_S - \langle Y_{coolant} \rangle_S^2, \quad (4.19)$$

$$\Rightarrow \frac{\langle Y'^2_{coolant} \rangle_S}{\langle Y^2_{coolant} \rangle_S} = 1 - \frac{\langle Y_{coolant} \rangle_S^2}{\langle Y^2_{coolant} \rangle_S}. \quad (4.20)$$

The non-uniformity of the profile of  $Y_{coolant}$  is given by  $\frac{\langle Y'^2_{coolant} \rangle_S}{\langle Y^2_{coolant} \rangle_S}$  and computed with Eq. (4.20) and is equivalent to a measure of the mixing state, bounded between 0 and 1. If the mixing state equals 1, the profile of the coolant mass fraction is flat, indicating that the hot and cold flows are fully mixed within the film; otherwise, the profile is not flat meaning that the flow is not totally mixed. The evolution of the mixing state along both blades for both sides and for both LES is given on Fig. 4.18.

For both NGVs, the mixing state is seen to increase in the region of coolant injection and to decrease elsewhere. This evolution is very similar to the film thickness one (see Fig. 4.15) indicating that the film thickness  $\delta$  is linked to the mixing state. For NGV1 (see Fig. 4.18a), the mixing state of the hole modeled LES is lower than the one from the meshed holes approach on both sides. For NGV2 (see Fig. 4.18b) the mixing state is also lower if using the model but the evolution is more disturbed, presenting a minimum value at  $x/c = 0.6$  in a region with few coolant on the blade surface.

One origin of the differences is the source of the mixing which originates from the coolant flux through  $S_\delta$ . This flux of coolant through the edge of the film  $S_\delta$  appears in Eq. (4.16) and can be split into a mean and a turbulent contribution using the Reynolds decomposition and Favre averaging [120]  $\tilde{\bullet}$  so that,

$$\int_{S_\delta} \overline{\rho Y_{coolant} U_i n_i} dS = \underbrace{\int_{S_\delta} \widetilde{\rho Y_{coolant}} \tilde{U}_i n_i dS}_{\text{Mean field contribution}} + \underbrace{\int_{S_\delta} \widetilde{\rho Y''_{coolant}} U''_i n_i dS}_{\text{Resolved turbulence contribution}}, \quad (4.21)$$

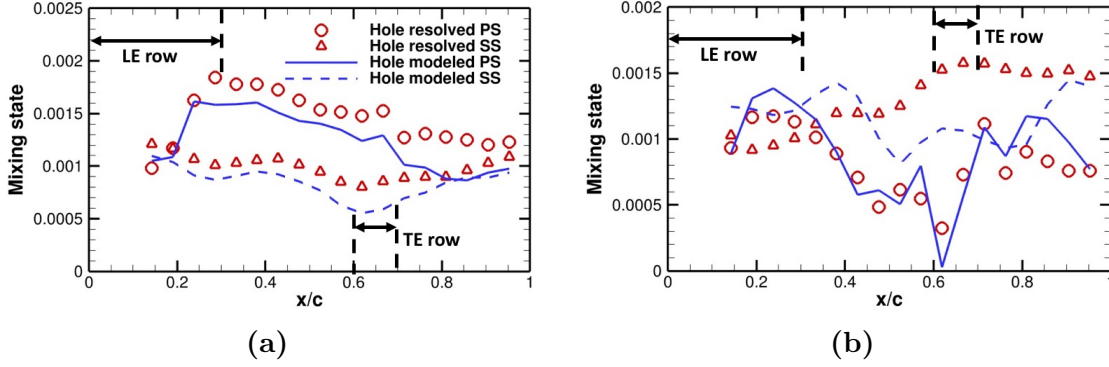


**Figure 4.18:** Mixing state at mid height along NGV1 (a) and NGV2 (b). Red circles  $\circ$  represent the meshed holes LES at the pressure side. Red triangles  $\triangle$  represent the meshed holes LES at the suction side. The solid blue line  $-$  represents the hole modeled LES at the pressure side. The dashed blue line  $- -$  represents the hole modeled LES at the suction side.

where  $\widetilde{Y''_{coolant} U''_i}$  corresponds to the resolved turbulent diffusion of  $Y_{coolant}$  and  $''$  the temporal fluctuations with respect to the Favre averaging. Since the film remains attached to the wall far from the injection holes, the direction of the flow at the edge of the film thickness can be assumed to be tangential to the wall if neglecting the normal velocity to the wall in the film thickness. As a result, the mean velocity  $\widetilde{U}_i$  is roughly orthogonal to the wall normal of the film section along the blades which indicates that the resolved turbulence contribution term dominates the mean field contribution term in Eq. (4.21). Consequently,  $Y_{coolant}$  levels originate from the turbulent mixing represented by  $\widetilde{Y''_{coolant} U''_i}$  at the edge of the film thickness section  $S_\delta$ . In the following, the cross correlations  $\widetilde{Y''_{coolant} U''_i}$  are not directly investigated but only estimated from the contribution of the turbulent velocity  $U_i^{rms}$  and the contribution of the turbulent passive scalar field  $Y_{coolant}^{rms}$ . In the following,  $U_i^{rms}$  is estimated from the turbulent kinetic energy map  $TKE$  and  $Y_{coolant}^{rms}$  is estimated from the temporal Root Mean Squared (RMS)  $Y_{rms}$  computed with  $Y_{rms} = \sqrt{\overline{Y_{coolant}^2} - \overline{Y_{coolant}}^2}$ . Both fields are displayed in Fig. 4.19 and Fig. 4.20 at mid-height for NGV1 and NGV2 for both LES. Results confirm that the activity of the  $Y_{rms}$  seems strongly correlated to the turbulent kinetic energy map  $TKE$  around the blade validating the fact that the turbulent mixing can be evaluated from  $TKE$  and  $Y_{rms}$  maps. In the meshed holes LES (see Fig. 4.19a&c), the turbulent mixing between the coolant and the hot flows takes place in the film thickness and is more important at the coolant injection locations. These maps further evidence that the turbulence is produced within the plena and pipes of both NGVs and is then propagated around the blades in the film (see Figs. 4.20a&c). On the pressure side, the turbulent kinetic energy generation occurs at the coolant injection locations. Between coolant injection rows, turbulence decreases due to the acceleration of the flow. On the suction side, the turbulence is created near the NGV and then decreases downstream. One can also notice an increase of the

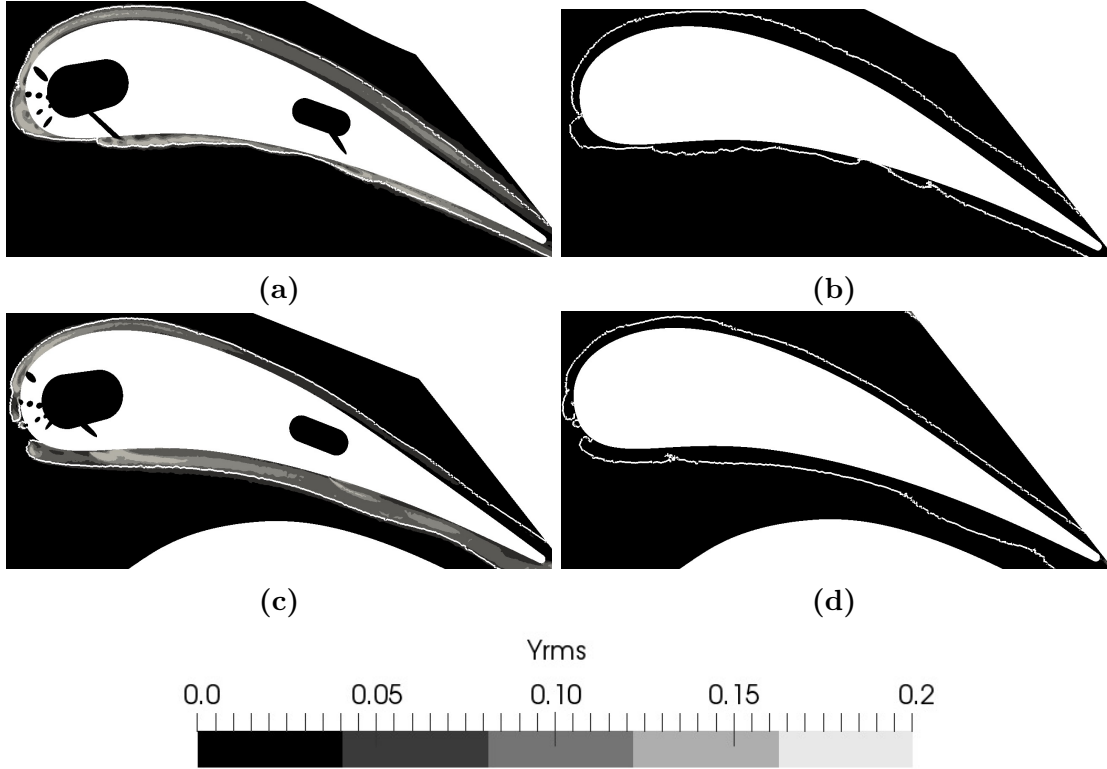


**Figure 4.19:**  $Y_{RMS}$  map at mid height on NGV1 and NGV2 at mid-height for both LES. Top (a) & (b), NGV1. Bottom (c) & (d), NGV2. Left (a) & (c), meshed holes. Right (b) & (d), hole modeled. The film thickness is represented by the white isoline.

turbulent kinetic energy level at  $x/c \approx 0.75$  for both NGVs without injection of coolant indicating a potential turbulent transition of the film at this specific position which could explain the thickening of the film on the suction side previously noticed on Fig. 4.15. The level of turbulent mixing and turbulent kinetic energy for both NGVs predicted by the hole modeled LES (see Fig. 4.19b&d) is very low compared to the meshed holes one (see Fig. 4.20b&d). Since the plena and the pipes are not meshed and instead exit velocity profiles are imposed by the model, the turbulence production term is not adequately represented on the hole modeled mesh which de-activates the associated  $Y_{rms}$  production term. These views are in agreement with the fact that the turbulent mixing of coolant taking place within the film section  $S_\delta$  is effectively almost zero in both cases confirming that more coolant remains in the film and it is only its upper mixing that is miss-represented when using the modeling approach

To conclude, the investigation of the impact of the model on the adiabatic vane surface temperature shows that the blades are slightly colder if using the model. By tracking the coolant with a passive scalar and performing a mass balance in the near wall regions of the blades, it can be deduced that the mixing is less efficient with the model. Results show that the lack of mixing in the model is due to absence of turbulent fluctuations in the coolant film, keeping the film temperature near the

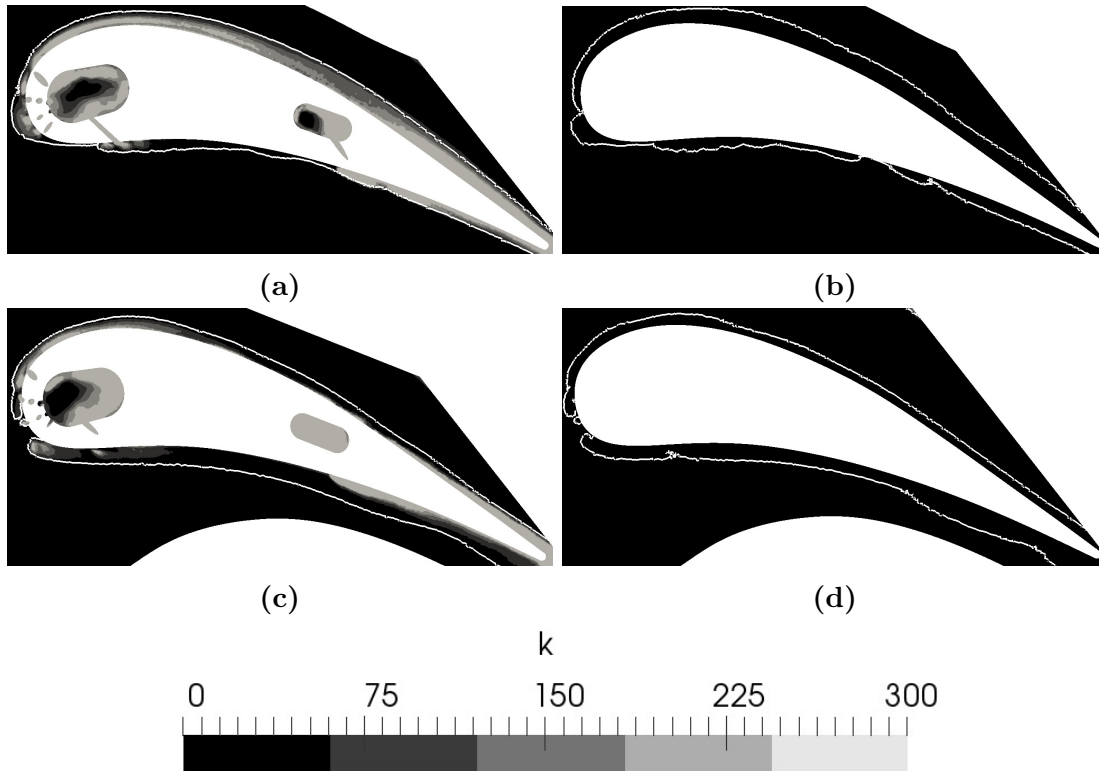


**Figure 4.20:** Turbulent kinetic energy maps  $TKE$  on NGV1 and NGV2 at mid-height for both LES. Top (a) & (b), NGV1. Bottom (c) & (d), NGV2. Left (a) & (c), meshed holes. Right (b) & (d), hole modeled. The film thickness is represented by the white isoline.

cold injected temperature. Since the pipes are not meshed and no turbulent fluctuations are injected with the model, as shown previously, the mixing is decreased.

## 4.5 Conclusion

In the present study, the applicability of a coolant injection model, initially developed in the context of multiperforated liners in the combustion chamber, to predict the surface temperature of turbine blades with Large-Eddy Simulation (LES) has been assessed. To evaluate the coolant model, a reference meshed holes LES has been performed on the Nozzle Guide Vanes (NGV) of the FACTOR project and then compared to a hole modeled LES keeping the same mesh around the blade and numerical set up. The operating points of both LES have first been checked to assure the comparability of both LES. The estimations of the CPU cost for both LES show a drastic reduction of the CPU time when the holes are modeled and not meshed. This permits to test many hole layouts for a given blade geometry in a design process. The hole modeled LES gives indeed a very close distribution of the vane surface temperature with a maximum under-estimation of 4 % compared to the meshed holes LES. Investigations of the coolant film show that the film temperature is colder in the hole modeled LES. Estimations of the mixing state show that the mixing is less efficient in the hole modeled LES compared to the meshed holes LES. Indeed, the evaluation of the turbulent mixing contribution indicates that the turbulence is produced in the pipes, which is not taken into account by the model, leading to a lack of agitation in the film, which explains the lower wall temperatures. As a result, the model needs to be improved by considering, for example, injection of synthetic turbulence at the exit pipe section in future studies.

## Part II

# Analysis of the combustor and high-pressure turbine flows

*This part of the manuscript focuses on the analysis of the flow field in the combustion chamber and high-pressure vane passage. With respect to Part I, the domain is extended to include the high-pressure turbine. In Chapter 5 two different clocking positions are investigated and heat load differences are discussed. Chapter 6 investigates the impact of the flow field in the chamber on the flow topology in the isolated high-pressure vane domain. A novel approach to create realistic unsteady inlet conditions for isolated high-pressure vanes LES is presented allowing to recover the flow field of an integrated combustion chamber-high-pressure vane simulation to a large extent. Finally an integrated combustor & high-pressure turbine simulation is performed and compared against experimental results.*



# Chapter 5

## Analysis of the chamber clocking position dependent heat load on the NGV surface

### Contents

---

5.1	Introduction . . . . .	<b>87</b>
5.2	Combustor-NGV Setup . . . . .	<b>89</b>
5.3	Results . . . . .	<b>93</b>
5.3.1	Flow field in the combustion chamber . . . . .	94
5.3.2	Flow field in the NGV passage . . . . .	108
5.4	Conclusion . . . . .	<b>124</b>

---

### 5.1 Introduction

Today, high pressure turbine components are designed to meet specific aerodynamic performance goals over a wide range of operating conditions. At the same time, hot section components of an engine need to attain a long lifetime, which is only guaranteed by the application of sophisticated cooling systems. These parts are manufactured from single crystal Ni-based superalloys [121], which due to complicated manufacturing processes belong to the most expensive components of an engine. Operating cost of gas turbine engines are thereby greatly influenced by the durability of hot section components, which are exposed to a harsh aerothermal environment causing a multitude of different failure modes such as high cycle fatigue, low cycle fatigue, hot corrosion/oxidation, creep, and thermomechanical fatigue. In the 1980s, the investigation of hot-spot phenomena, provoked by the discrete positioning of fuel injectors in the combustor caught more and more attention from the research community.

Starting from 1982, when the NASA Lewis research center established the first experimental facility to investigate the impact of hot streaks on the high-pressure

turbine [122], ten other test facilities dedicated to the investigation of combustor-turbine interactions went into service [123–126]. In 1999, Dorney et al. [127] gave a review of experimental and computational studies on the migration of hot streaks. Povey and Qureshi (2009) [128] then summarized developments and research on combustor simulators dedicated to the investigation of the impact of Inlet Temperature Distortions (ITD) on the high-pressure turbine. These studies clearly identified hot-streak phenomena as a major obstacle for further increasing the efficiency of gas turbine engines, as increasing the thermodynamic efficiency inevitably requires higher temperatures. In the past decades, efficiency driven rising Turbine Entry Temperatures (TET) and pressure ratios decreased the heat sink capacity of air bled of the latter stages of the compressor, thereby promoting the development of sophisticated cooling systems for the stator of the high-pressure turbine. Likewise, the introduction of  $\text{NO}_x$  reducing compact design lean combustion concepts in the next generation of aircraft engines entails a harsher thermal environment in the combustion chamber and therefore at the inlet of the high-pressure turbine [4]. Indeed, compared to current state of the art rich quench lean (RQL) combustion concepts, the flow field of lean combustors is characterized by higher levels of turbulence, stronger temperature non-uniformities due to a combustion process operated at lean conditions and stronger fuel injection system generated residual swirl. Such flow features adversely alter secondary flow patterns in the high-pressure turbine, leading to increased aerodynamic losses and modified heat load [128–130]. Recently, the European FACTOR<sup>1</sup> project, which is the basis for the herein presented research, was launched to investigate combustor-turbine interactions in next generation lean combustion chambers using a joint CFD and experimental approach.

In the context of efficiency driven increasing combustion chamber temperatures, a better understanding of unsteady flows is of major importance. However, the harsh aerothermal environment in combustion chambers complicates accurate measurements, which often makes simulations the only tool to gather spatially well resolved data allowing to understand interaction phenomena present in the combustion chamber. Steady state CFD simulations may however be insufficient to capture the thermal impact of locally highly unsteady flows and thereby induce the application of huge safety margins to account for such uncertainties. With increasing affordability of high performance computational resources, high fidelity Large Eddy Simulations (LES) can today be applied in the combustor and high-pressure turbine design phase and come as a credible complement to existing RANS predictions although validations are still required. This work contributes to this specific context by introducing LES based predictions and analysis to highlight thermally critical areas depending on the clocking position between combustion chamber and vanes.

---

<sup>1</sup>FACTOR (Full Aerothermal Combustor Turbine interactiOns Research) is a collaborative European research project co-funded by the European Commission within the 7th Framework Programme (2010-2016) under the Grant Agreement no265985 to investigate interactions of lean combustion chambers with the high-pressure turbine.

Results detailed hereafter have been presented at the ASME Conference 2017 (GT2017-64648) [131] and more comprehensive investigations are detailed in this chapter. First, the FACTOR test rig and the operating conditions simulated here are described. Note that the operating conditions in this chapter are different from those finally obtained at the FACTOR test rig at DLR Göttingen, as most simulations were performed before the start of the experimental campaign. The next section presents numerical methodology and LES setup. Statistical tools used here are introduced and explained in Section 2.2. Finally, in the result section, three different simulations are discussed:

- 1.) Combustion chamber only (already introduced in Chap. 3),
- 2.) Combustion chamber and NGVs in leading-edge clocking position,
- 3.) Combustion chamber and NGVs in passage clocking configuration.

Simulations are first compared in the combustor part and validated against available experimental results. In the following, the nozzle is addressed based on numerical results only. The flow field in the nozzle is discussed and clocking position dependent heat load differences are evidenced by a conjoint analysis of high order temperature moments and turbulence quantities.

## 5.2 Combustor-NGV Setup

This section informs about specific geometrical features of the FACTOR geometry and the two swirler-NGV clocking positions which are investigated in this chapter. Note that for all discussed simulations, the axial periodic numerical domain of the FACTOR test rig is retained. It therefore contains one swirler and two NGVs with an Axial Chord Length (ACL) of 40 mm, representing an  $18^\circ$  section of the full annular non-reactive test rig. To reduce the impact of boundary conditions on the zone of interest, the domain features a large entry plenum and a pressure outlet sufficiently far from the NGVs. The combustor module is identical to that previously discussed in Chapter 3. In this study, two different swirler-vane clocking positions are investigated (see Fig. 5.1a) and compared against the chamber only simulation of Chapter 3. Note that the specificity of each case is that: In the leading edge clocking position (LE), the hot-spot impinges on the NGV (see Fig. 5.1b) and in the passage clocking configuration (PA), the hot-spot travels through the NGV passage (see Fig. 5.1c) [132]. Hereafter, the NGV hit by the hot-spot in LE-clocking configuration is denominated LE1, the other is called LE2. For the PA-clocking configuration, the combustor module is turned by  $4.5^\circ$  and the NGVs are respectively named PA1 (=LE1) and PA2 (=LE2). In the simulation without vanes, i.e. from Chapter 3, the swirler is at the same position as in the LE case. Therefore the flow field on P40 is similar and not shifted as in the PA case. The NGV cooling system is not considered in this study, because the focus here is to investigate the impact of the vanes on the flow field.

As said before, the specificity of the present Chapter is the inclusion of the vanes in the simulations. In these cases, the vane inlet Reynolds number based on the vane axial chord and inlet velocity is about 106 000 while the outlet Reynolds

CHAPTER 5. ANALYSIS OF THE CHAMBER CLOCKING POSITION  
DEPENDENT HEAT LOAD ON THE NGV SURFACE

**Table 5.1:** FACTOR operating conditions [16] at the trisector test rig at the University of Florence without vanes.

	IOP	DP
Static pressure on P40 [kPa]	115	147.65
Mach number on P40 [-]	0.113	0.108
Mass flow [kg/s]	4.8	4.8
Flow split swirler [-]	65%	65%
Flow split outer cavity [-]	21%	21%
Flow split inner cavity [-]	14%	14%
Swirler inlet temperature [K]	300	531
Coolant air temperature [K]	300	300
Swirler Reynolds number [-]	168 500	111 000
Swirler Mach number [-]	0.108	0.112

number is about 424 000 for an outlet Mach number of 0.96. All simulations are performed at design point (DP) operating conditions (see Tab. 5.1). Measurement data of the FACTOR geometry without NGVs is available from a trisector test rig at the University of Florence at isothermal (IOP) and design point operating conditions [106]. Certain measurement techniques like HWA require isothermal conditions. The comparability of both operating points is discussed in [16]. While the operating points are well matched for the simulations on the chamber only domain, pressure levels are slightly lower for the simulations including the high-pressure vanes in the domain as the pressure loss over the vanes is a priori not known. The static pressure on P40 is 140325  $Pa$  for the LE case and 141877  $Pa$  for the PA case. Note that the clocking positions and operating points presented in this Chapter do not correspond to the final test configuration at the FACTOR test rig in Göttingen (see Chapter 7). The reason for this is that the FACTOR test rig in Göttingen became operational after most numerical studies were performed and that in a first experimental campaign the initially planned operating point could not be obtained.

All simulations presented here are performed using AVBP [60], a massively parallel CFD code developed by CERFACS. In this study, simulations are first converged using the Lax-Wendroff scheme [66], then a more accurate finite element two-step time-explicit Taylor Galerkin scheme (TTG4A), fourth order accurate in time and third order in space, is used for the discretization of convective terms [67]. Simulations with vanes are evaluated over a period of 40 ms (approx. four flow-through times) using the TTG4A scheme, while the averaging time of the chamber only prediction is 140 ms. This difference explains the smoother flow fields of the chamber only simulations, especially when comparing higher order statistics. To access turbulence quantities using autocorrelation [23, 38], a constant time step of  $4 \times 10^{-8}$  s, corresponding to a maximum CFL number of 0.9 is used.

When it comes to modelling, the sub grid scale (SGS) turbulent contributions

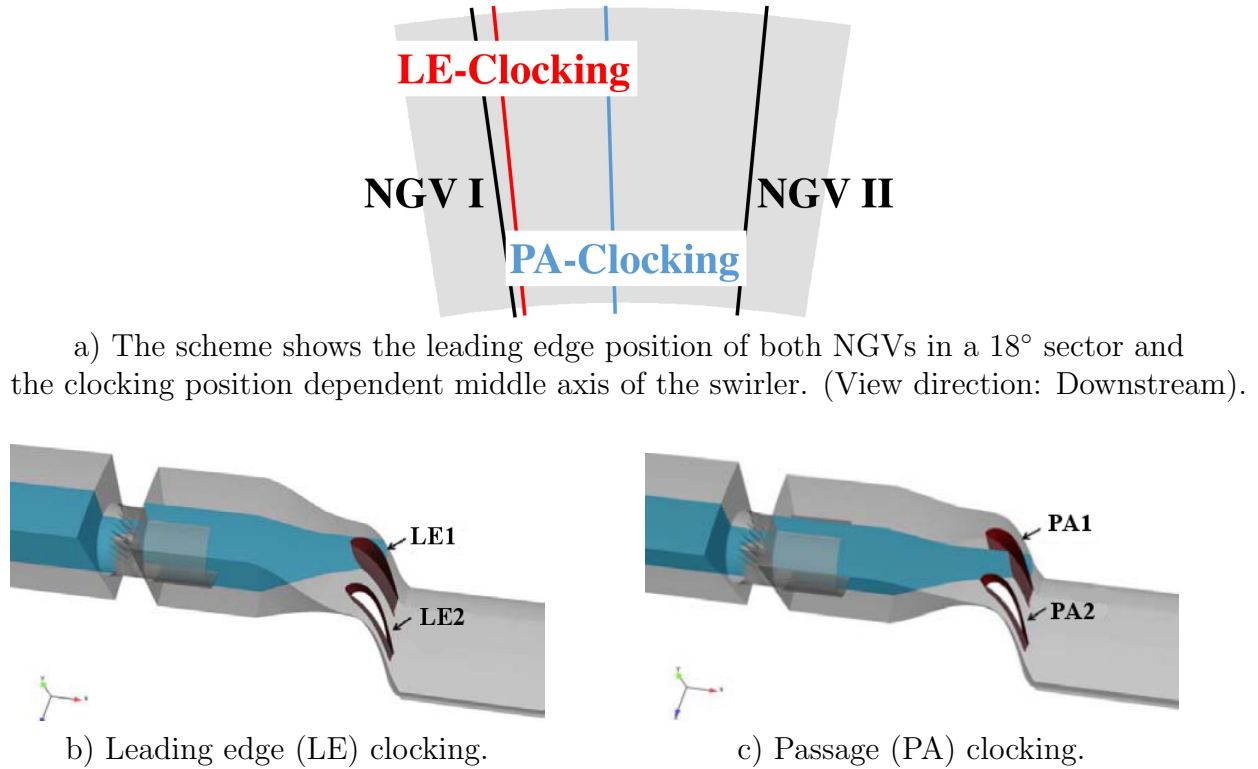


**Figure 5.1:** FACTOR geometry with leading edge and passage clocking positions [132].

are computed using the Smagorinsky model [51]. This model, originally developed for exterior flows, is one of the most robust and widely used LES SGS model. Effusion cooling systems are modeled with a homogeneous injection model [25] (see Chapter 3). The near-wall behavior is modeled by wall functions. Finally, simulations are performed using a mass flow inlet, combined with a pressure outlet using different values for chamber only and vane cases. The target pressure value on P40 is thereby controlled by the pressure imposed at the exit of the domain, which can lead to small deviations as the flow behavior in the nozzle is not a priori known.

The hybrid mesh contains 70 million cells (see Fig. 5.2) and uses prism layers around the NGV to guarantee low  $y^+$  values approaching 10 (see Fig. 5.3), whereas the rest of the domain is discretized by tetrahedral cells. A mesh independency study is included in [15] and confirms the adequacy of the presented solution. The simulation was performed on 512 cores for a computation cost of 260 khrs using Turing (IDRIS-GENCI - France). One solution is about 1 GB and for the study of the temporal evaluation 650 instantaneous solutions of the LE clocking simulation, interpolated on a coarse grid (15 Mio cells / 120 MB each), were stored. These interpolated solutions are used to perform POD/DMD analysis of the flow field. For all other purposes, solutions from the full computational grid are used.



**Figure 5.2:** Mesh on  $H/h=0.5$  from end of duct to NGVs for LE clocking.

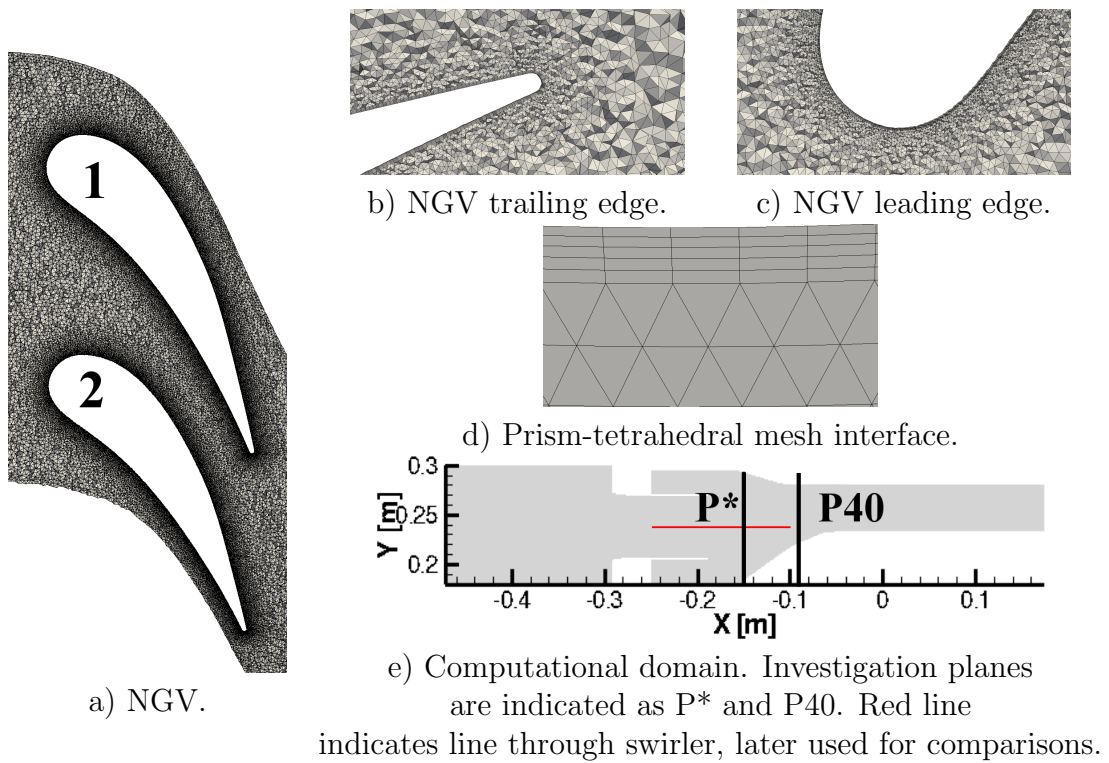


**Figure 5.3:** Different views of the computational grid in the NGV domain.

## 5.3 Results

In this section, the flow field in the combustion chamber is presented first and validated against available experimental data. Afterwards, the discussion focuses on the flow field in the nozzle addressing differences between LE and PA clocking simulations based on numerical predictions only. Interactions present between the flow in the chamber and NGV are visualized and lead to a more detailed discussion of the impact of the clocking position on the flow in the high-pressure turbine. Finally, clocking position dependent heat load differences are evidenced by a conjoint analysis of high order temperature moments in the NGV passages.

### Analysis of dominant flow features in the chamber

To introduce the discussion in this chapter, this section shows the existence of interactions between chamber and vane flow using POD. To do so, coarse grid interpolated instantaneous solutions are treated by POD as described in Section 2.2.2. In the PA clocking configuration, instantaneous solutions were not stored on coarse grids so the following addresses only the LE prediction. Features are nonetheless expected to be also present for this other configuration. Part of the activity pictured in the LES mean fields as well as in the experiments detailed in the following discussion, comes from the presence of the PVC in P40. This finding is confirmed if looking at Fig. 5.4 which shows a clear peak at 500 Hz in P40 as well as a small peak at 1000 Hz. Such a frequency spectrum indicates that the PVC still impacts the flow field on P40 which most likely influences the flow dynamics as discussed hereafter.

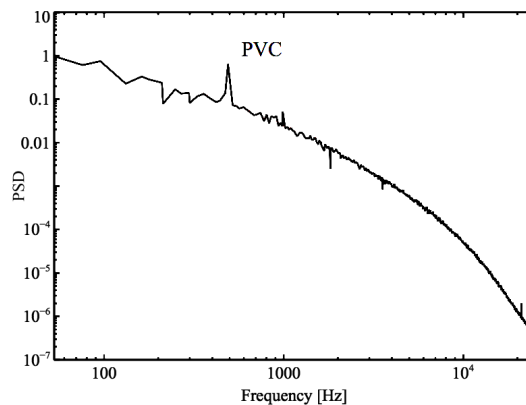


**Figure 5.4:** Frequency spectrum on P40 with marked peak at 500 Hz and 1000 Hz (PVC) calculated using a DMD on static pressure on instantaneous LES solutions.

Using POD on instantaneous pressure fields, the PVC is clearly captured by the first few POD modes, which identifies the PVC as the most energetic structure in the flow field. Indeed, the combination of specific POD modes allows the reconstruction of a turning fluid structure corresponding to the PVC in the combustor. A fast Fourier transformation (FFT) of the retained modes allows to confirm the presence of peaks at 500 Hz and 1000 Hz. Then visualizing the spatial distribution

of these modes, one observes a one armed structure at 500 Hz (see Fig. 5.5a) and a two armed structure at 1000 Hz (see Fig. 5.5b). Note that in both cases, activity can be also observed in the NGV passage, where the first POD modes highlight flow features close to the walls. This shows that flow structures in the passage are actively modulated by the strong activity in the chamber and justifies the following discussion around the flow field in the chamber and its impact on the flow in the vane passage.

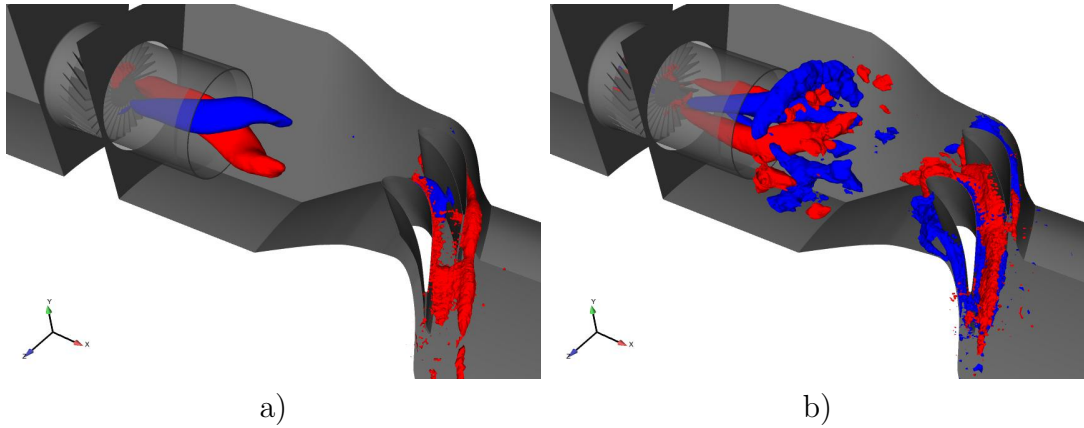


**Figure 5.5:** Visualization of individual spatial POD modes calculated on pressure with isosurface for positive (red) and negative (blue) values. a) Visualization of mode 1 with 500 Hz peak. b) Visualization of mode 3 with 1000 Hz peak.

### 5.3.1 Flow field in the combustion chamber

First, some general features of the flow field in the combustion chamber are presented and differences between simulations are explained. The leading edge (LE) and passage clocking (PA) configurations are compared to the simulation without vanes (Combustion chamber, CC only, using the homogeneous coolant injection model), which was presented in Chapter 3. To do so, the flow field is visualized on planes through the central axis of the engine, on a plane downstream of the swirler and on P40, the intersection between combustion chamber and high-pressure turbine.

In the combustion chamber the flow is dominated by the PVC (see Fig. 5.6) and its characteristic frequency of 500  $Hz$  is seen to impact large parts of the domain as stressed in the introduction and detailed later. Note that this characteristic frequency depends on the operating conditions and is found to be around 315  $Hz$  for isothermal operating conditions, presented in Chapter 3. The PVC usually features one main arm, occasionally two arms rotating with a phase difference of  $180^\circ$ . Shortly after leaving the restraining duct, the PVC breaks down and creates small vortices that propagate through the domain.

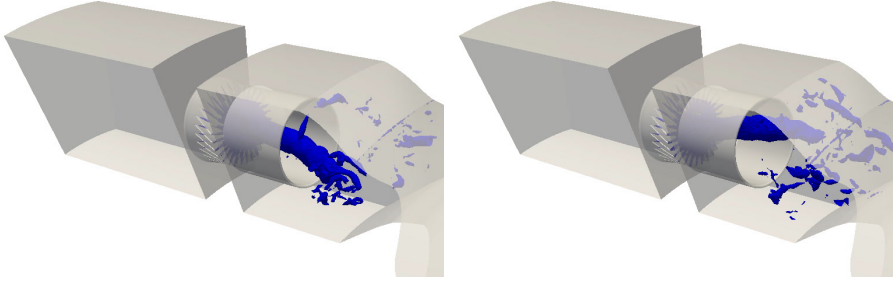


**Figure 5.6:** PVC visualized as instantaneous isosurface of pressure for the chamber only case for different time steps. The PVC is created by the swirler and breaks down shortly after leaving restraining duct.

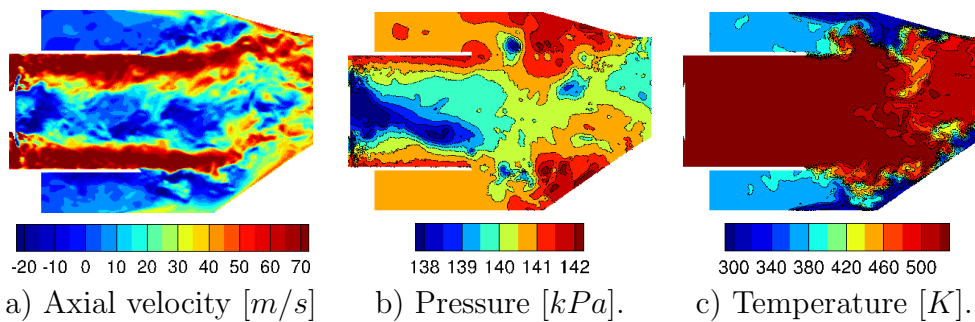


**Figure 5.7:** Central axial cross section cuts of an instantaneous flow field through the swirler from swirler to P40. (LE case, Design Point).

This specific dynamics of the flow can be visualized by instantaneous contours of axial velocity, static pressure and static temperature as shown in Fig. 5.7 at a given instant of the LE case. Note that instantaneous solutions for the other cases show a similar behavior, so a comparison is omitted at this point and the focus lies more on a qualitative discussion of flow features. In the axial velocity plot (see Fig. 5.7a), high velocities at the walls inside the duct as well as the recirculation zone in the middle of the swirler and chamber are well visible. Outside the duct, velocities are rather low. At the liners, locally increased axial velocity is caused by the coolant injection. The instantaneous pressure contour (see Fig. 5.7b) clearly shows the swirler generated PVC as a low pressure zone propagating from the swirler to the lower edge of the duct, where it breaks down, causing the wavy pattern observed in P40 (to be detailed afterwards and seen in Fig. 5.23b). Kelvin-Helmholtz instabilities at the duct edges are also visible as low pressure zones and the injection of coolant is seen to locally increase the static pressure level near the liners (see Fig. 5.7b). The instantaneous temperature field (see Fig. 5.7c) finally visualizes the mixing behavior between the hot main flow and the coolant flow injected by the effusion cooling system of the liners. Clearly, the absence of dilution holes leaves the central hot-spot largely undiluted and the coolant mostly travels along the liners.

To do a more quantitative comparison of the predictions with available time-

averaged PIV measurements, non-dimensional mean axial velocity plots of simulations at design point are discussed (see Fig. 5.8a). Quantities are non-dimensionalized here to account for the different operating points in experiment and simulation [15]. Note that PIV measurements were performed without the attached high-pressure turbine and that due to the absence of seeding particles in the coolant flow, the velocity measurement near the multiperforated liners is close to zero. In contrast to that, high axial velocities are seen in all simulations given that the homogeneous coolant injection model is applied in all cases. Due to the high rotational speed induced by the swirler, air exiting the combustor is accelerated towards the duct wall and axial velocities along the inner duct walls are rather high, whereas lower velocity values can be observed in the center. Outside of the duct, the flow is mostly stagnant. Following the duct, a recirculation zone with negative axial velocities is created. Compared to the experiment, the recirculation zone in the simulations seems slimmer, especially for the cases with vanes (Fig. 5.8c/d) which might point to one possible impact of the vanes on the upstream flow field. With the presence of vanes, velocities in the recirculation zone are higher, albeit its spatial expansion is reduced compared to the case without vanes (Fig. 5.8b vs Fig. 5.8c/d).

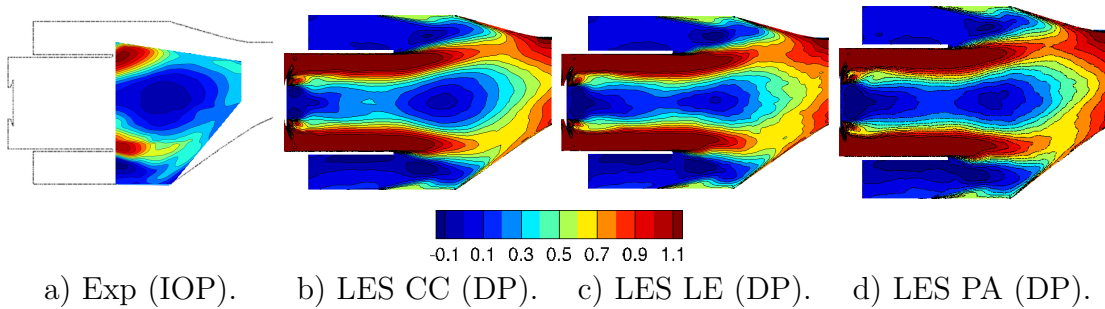


**Figure 5.8:** Central axial cross section cuts of the averaged axial velocity normalized by reference velocity (see Tab. 5.1) through the swirler from swirler to P40.  $u_{nondim} = u/u_{ref}$ ,  $u_{ref,DP} = 51.3m/s$ ,  $u_{ref,IOP} = 37.5$ . Simulations: LE / PA clocking and combustion chamber (CC) only at design point; PIV experiment at isothermal operating point.

Throughout the combustion chamber, the swirling motion induced by the fuel injection system impacts the flow field (see Fig. 5.9) and contributes to the complex flow conditions on P40. Similarly to the axial velocity field, the mean tangential velocity observed on a cross-section plane is very similar for all simulations. The presence of vanes (Fig. 5.9a vs Fig. 5.9b/c) as well as the clocking position (Fig. 5.9b vs Fig. 5.9c) seem to only slightly impact the flow field upstream of P40 and on the combustor central plane.

Note that when it comes to mean pressure fields, these differ slightly from one another due to the different losses issued by the different configurations addressed. Figure 5.10 is thus non-dimensionalized by the average pressure on P40 to allow a direct comparison of all cases. As previously mentioned, these pressure differences can be explained by the numerical approach, i.e. imposing a mass flow rate

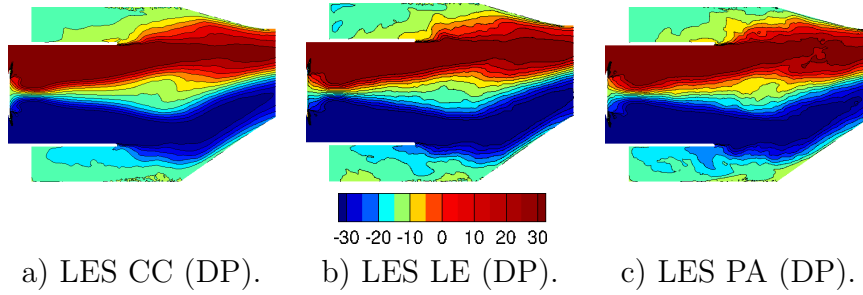


**Figure 5.9:** Central axial cross section cuts of the averaged tangential velocity [ $\frac{m}{s}$ ] field through the swirler from swirler to P40. (Design Point).

together with a pressure outlet. Pressure loss may also differ due to the imposed changes in geometry: i.e. different clockings. Despite this specific difficulty, all predictions are very similar and show lower pressure values in the middle of the duct, created by the swirling motion induced by the fuel injection system. All simulations also show increased pressure levels where coolant is injected at the liners of the combustion chamber. Small differences are visible in the shear layer, right after the duct. Here, pressure values in the LE prediction are indeed slightly higher than in the other cases indicating a different overall pressure loss in all these simulations.

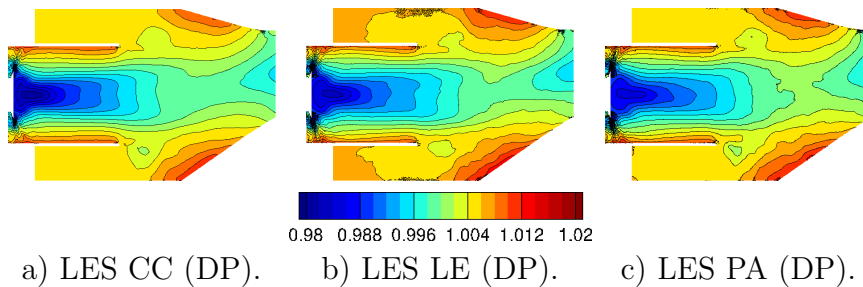


**Figure 5.10:** Central axial cross section cuts of the non-dimensional pressure field through the swirler from swirler to P40. Pressure is non-dimensionalized by average pressure on P40 (CC: 147640 Pa, LE: 140325 Pa, PA: 141877 Pa). (Design Point).

Mean temperature distributions on the cross section going through the swirler up to P40 are again seen to be very similar for all cases (see Fig. 5.11). As expected, the duct is uniformly filled with hot air injected through the swirler. After the duct, this hot air mixes with the cold air injected by the effusion cooling system. Note that the cold air does not penetrate far into the flow so that the hot-spot stays largely undiluted as seen on P40 in the following section. One minor difference is that the coolant close to the liners penetrates slightly further into the hot main flow for both cases with vanes as compared to the simulation without vanes.

Following the discussion of the general flow field, the unsteady activity of the flow can first be evaluated looking at RMS fields. To do so, the Turbulent Kinetic Energy (TKE,  $TKE = 0.5(u_{rms}^2 + v_{rms}^2 + w_{rms}^2)$ ), on the mid cross section cut going through the swirler is shown in Fig. 5.12. For all simulations, high levels

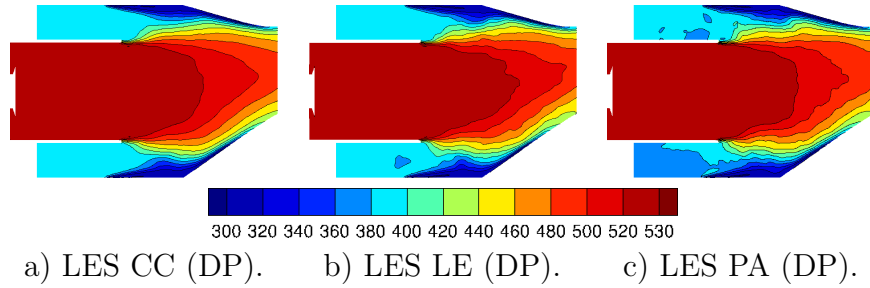


**Figure 5.11:** Central axial cross section cuts of the temperature field through the swirler from swirler to P40. (Design Point).

of turbulence can be seen right downstream of the restraining duct, where the high velocity flow inside the duct meets the rather stagnant outer flow. In the predictions with vanes (see Fig. 5.12b&c), the level of turbulence in this region is higher than in the case without vanes. Potential reasons for this are the generally higher velocities in the vane cases and the interactions imposed on the upstream flow by the vanes. Close to the swirler, in the center of the duct, the chamber only simulation shows higher turbulence levels than both other predictions. Further downstream, predictions with vanes show a region of low turbulence activity that falls together with the recirculation zone. Indeed, the recirculation zone is rather stable which explains the low turbulence levels.

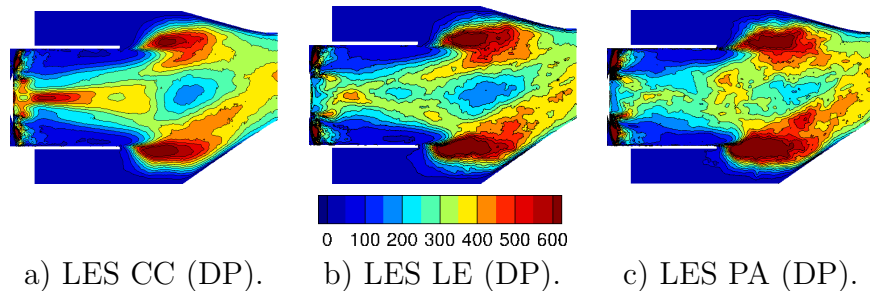


**Figure 5.12:** Central axial cross section cuts of the  $TKE [m^2/s^2]$  field through the swirler from swirler to P40. (Design Point).

More quantitative discussion of the flow field in the chamber is intended by Fig. 5.13. The focus here is the flow field in the swirler. To allow for a quantitative comparison of the three different simulations, averaged flow quantities (Axial velocity, Pressure, Temperature, TKE) along a line (marked on Fig. 5.3e) through the middle axis of the duct are presented. Experimental data is not available at this location, so the following discussion addresses the numerical predictions only. The combustor only simulation shows highest axial velocities in the swirler and also the strongest recirculation zone, as previously observed when comparing 2D plots (see Fig. 5.13a). Both simulations that include vanes are close to each other and feature a weaker recirculation zone. The static pressure increases slightly through the swirler (see Fig. 5.13b), which confirms the observation from the above 2D plots. High radial velocities inside the swirler lead to a reduced pressure in its

center. When moving towards the exit of the swirler, the rotation slows down and the pressure increases. The CC case features highest pressure values. This is, as previously mentioned, due to the simulation approach of setting a mass flow rate at the inlet and the pressure at the outlet. As the pressure drop over the domain is not known beforehand, it should be stressed that present geometrical changes (i.e. presence of vanes) can also explain observed differences. Temperature levels through the swirler are quite similar, as there is no coolant flow moving upstream through the swirler (see Fig. 5.13c). Similar observations were already reported when considering the flow field on the cross section plane going through the swirler and middle axis of the combustor. After the end of the duct, coolant mixes with the hot flow and the temperature drops. Here, the LE case shows the highest temperature values and the PA case the lowest. When entering the chamber through the swirler high values of turbulence are created at the beginning of the duct (see Fig. 5.13d). Inside the duct the chamber only case features highest turbulence values, that however decrease towards the exit of the duct, where they can be found in-between LE and PA case values. Further downstream, values increase again due to turbulence created by the shear layer at the lower edge of the duct. Here the upward movement due to the geometrical shape of the chamber (compare with Fig. 5.3e) moves the high turbulence shear regions to the observation line.

To better understand the flow field, a plane perpendicular to the swirler axis and located downstream the duct (noted  $P^*$  on Fig. 5.3e) is used to visualize the flow field. At this location, no experimental data is available, so that discussions are limited to a comparison of numerical predictions. As mentioned previously, the main flow is restrained by the duct after entering the chamber and forms a ring of high axial velocity (see Fig. 5.14). Close to the liners, high values of axial velocities are seen due to the coolant injected using the homogeneous coolant injection model discussed in Chapter 3. Inbetween liners and the central main stream, the flow is almost stagnant. Inside the central flow, low or negative velocities can be observed, corresponding to the central recirculation zone. Note that at this specific axial location, the chamber only simulation features the largest recirculation zone.

One can also note that, apart from the axial movement, the flow field is dominated by high levels of residual swirl, caused by the swirler at the entrance of the chamber and visualized by radial velocity plots (see Fig. 5.15). The radial movement is seen to be well conserved further downstream due to the presence of the confining duct and appears to be rather similar for all cases. Because of the geometrical shape of the chamber (i.e. the middle axis of the swirler is below the middle of P40) the upwards movement is seen to be stronger at this specific axial location. The LE case also features higher values of radial velocity, whereas the chamber only case shows the lowest values. With the mass flow through the system being conserved for all cases, the velocities are inversely proportional to the operating pressure of the system. Following the velocity plots downstream of the swirler, non-dimensional pressure plots are visualized on Fig. 5.16. Here, a low pressure zone is visible in the center of the combustor and, close to the liners, the pressure is higher due to the coolant injection (in agreement with Fig. 5.14). The low-pressure zone appears largest for the chamber only case. In the LE prediction,

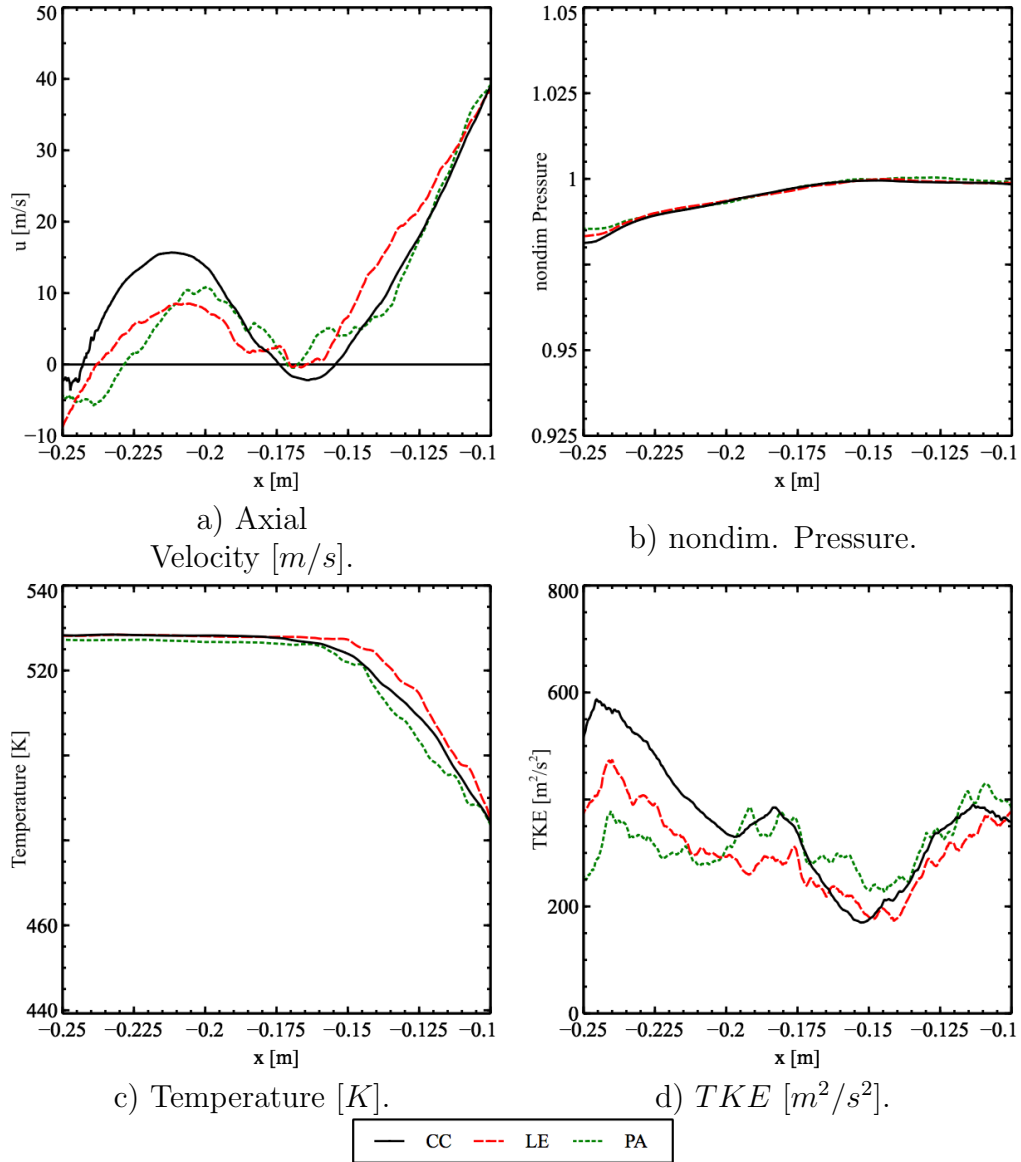


**Figure 5.13:** Flow quantities on line through center of the swirler (Red line on Fig. 5.3e).

differences between low pressure zone in the center and higher pressure zone close to the lower liner appears pronounced. The coolant injected through the liners, impacting the velocity as well as the pressure distributions in this region, is seen to locally decrease the temperature (see Fig. 5.17). In the center, the plot downstream of the swirler shows a central undiluted hot-spot as the coolant injection system does not penetrate far into the flow. The coolant stays mostly close to the liners, as also seen in plots further downstream in the following discussion. On the left side of the domain, the hot flow moves closer to the outer liner due to the rotational movement induced by the swirler.

Finally,  $TKE$  maps in  $P^*$  again show a ring shape, with low values in the cen-

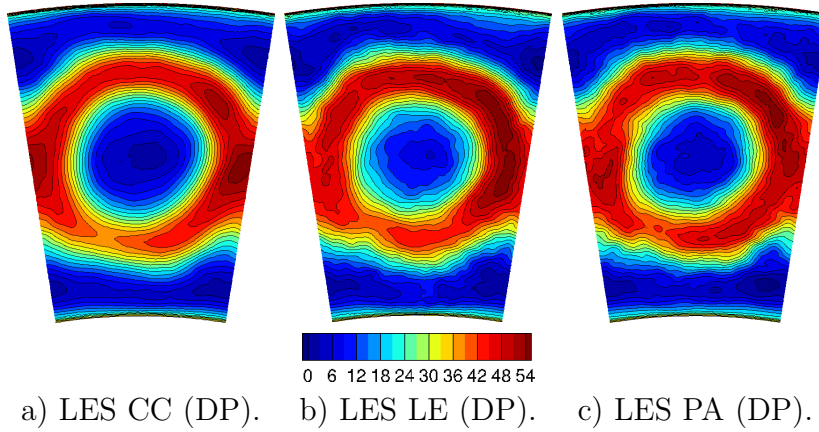


**Figure 5.14:** Axial velocity [ $m/s$ ] in chamber after swirler (noted  $P^*$  on Fig. 5.3e).

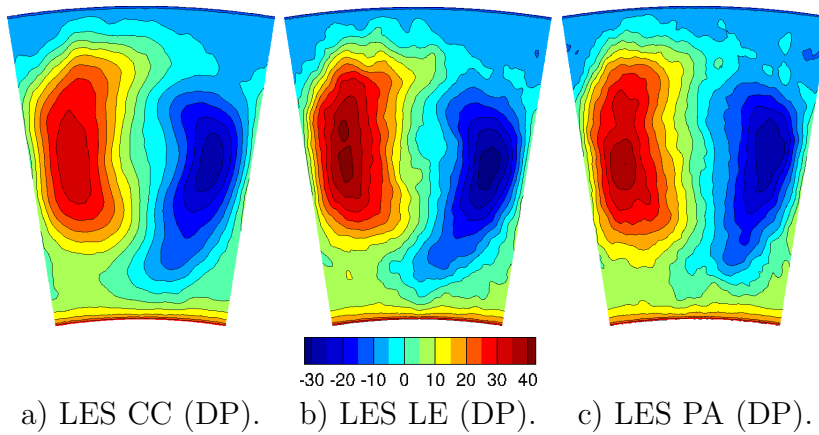


**Figure 5.15:** Radial velocity [ $m/s$ ] in chamber after swirler (noted  $P^*$  on Fig. 5.3e).

ter and close to the liners (see Fig. 5.18). In the azimuthal direction, high levels of turbulence can be observed near the periodic boundaries of the domain. Here, the rotating fluid meets the rotating flow from the neighboring swirler moving in the opposite direction. This creates a shear layer and results in higher levels of turbulence. At this specific point, both cases with vanes feature slightly higher turbulence values, again confirming the effect of this device on the combustor flow. Note also that the ring shape in the PA case is slightly more oval than round, which could be an impact of the vane passage alignment with the swirler. Higher  $TKE$  values in the cases with vanes, may be due to higher velocities, previously shown in this section. Further, increased  $TKE$  values also indicate more losses, that may contribute to the globally higher pressure losses in the cases with vanes. Besides  $TKE$ ,  $T_{rms}$  also shows activity in the flow field and is important for the following discussion.  $T_{rms}$  values are indeed high near the inner and outer liners, where the main flow mixes with the injected coolant (see Fig. 5.19). In the central region as well as directly next to the liners,  $T_{rms}$  values are low. The  $T_{rms}$  distribution is impacted by the upward movement on the left side and the downward movement on the right side - a shape later also observed on P40. Note that higher  $TKE$  levels observed in both cases with vanes (see Fig. 5.18) do not lead to increased

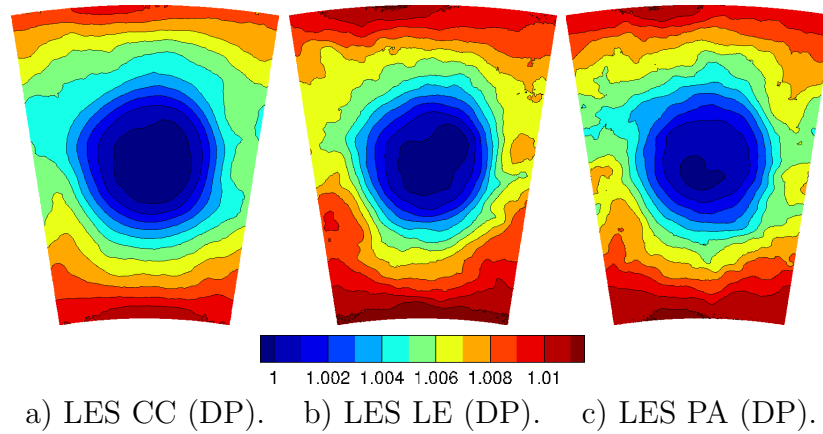


**Figure 5.16:** Non-dimensional pressure  $[-]$  in chamber after swirler (noted  $P^*$  on Fig. 5.3e). Pressure is non-dimensionalized by average pressure on P40 (CC: 147640 Pa, LE: 140325 Pa, PA: 141877 Pa).

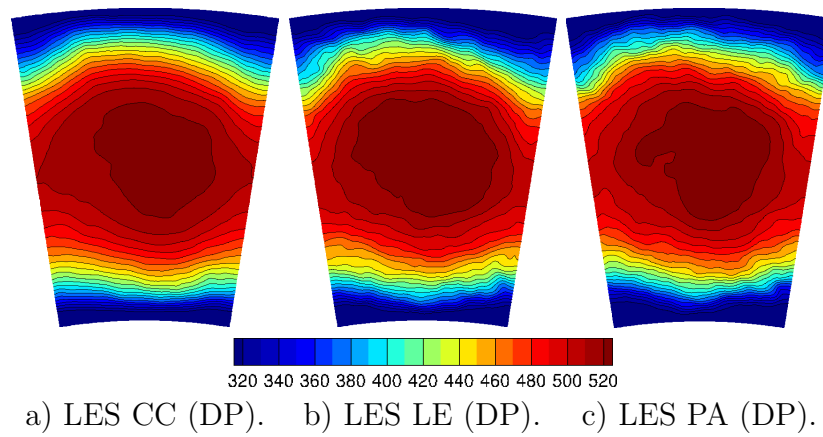


**Figure 5.17:** Temperature  $[K]$  in chamber after swirler (noted  $P^*$  on Fig. 5.3e).

values of  $T_{rms}$ .

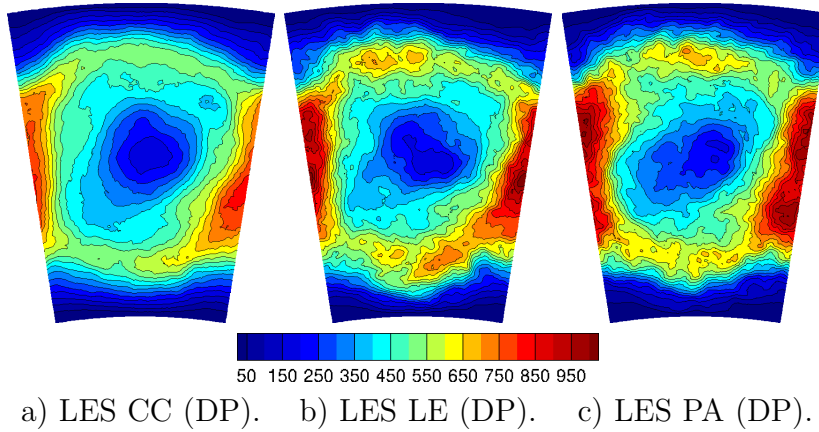


**Figure 5.18:**  $TKE$  [ $m^2/s^2$ ] in chamber after swirler (noted  $P^*$  on Fig. 5.3e).

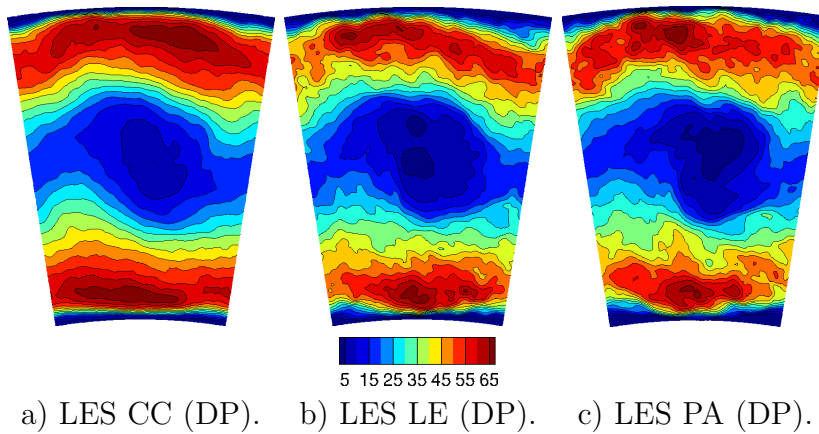


**Figure 5.19:**  $T_{rms}$  [ $K$ ] in chamber after swirler (noted  $P^*$  on Fig. 5.3e).

### Flow field in P40

Having discussed the evolution of different variables through the combustion chamber, the focus now lies on P40, the intersection plane between combustor and high-pressure turbine. At this location, measurement data, i.e. radial and tangential velocity obtained at the University of Florence allows for experimental validations. Note that the experimental data used for comparison was obtained from the UNIFI rig without attached high-pressure nozzle. Such experimental data confirms that the flow field on P40 is primarily characterized by residual swirl as well as by the presence of strong temperature fluctuations and high levels of turbulence. Once again, when compared to experimental data, mean radial and tangential velocity plots compare well with experimental results obtained by means of a 5 hole probe used to determine static/total pressure and flow angles [106] (see Fig. 5.20). Note that in the PA clocking configuration, the swirler is shifted by  $4.5^\circ$  which is the reason for the angular shift of radial and tangential velocity plots whenever compared to the LE or CC predictions. The velocities in the experiment are slightly higher than in the simulations and cases with vanes feature slightly higher velocities than the chamber only case.

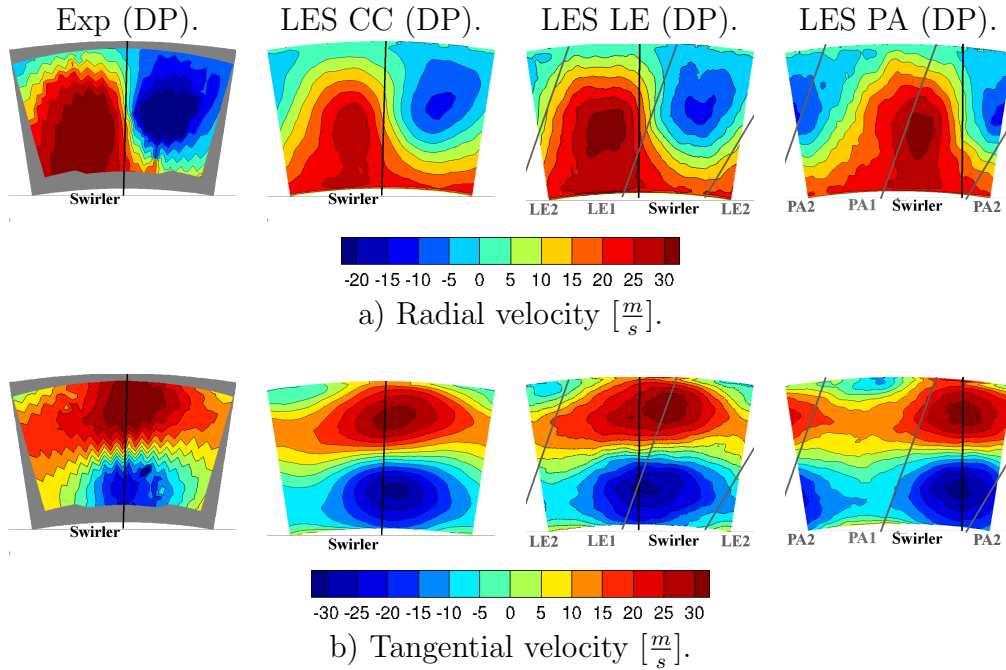


**Figure 5.20:** Radial and tangential velocity on P40. Black lines indicate middle axis of swirler and inclined grey lines indicate vane positions. View direction: Downstream. (Design Point).

Looking at total mean quantities such as total temperature and total pressure on P40, the hot-spot is seen to remain largely undiluted and very well marked due to the presence of the confining duct (see Fig. 5.21a). The temperature distribution for the PA case is similar to the LE case, albeit shifted by  $4.5^\circ$ . As previously discussed, coolant flow does not penetrate far into the main stream and the absence of dilution holes in the lean combustor demonstrator accounts for high temperatures in the middle and cold flow close to the liners. Regarding the pressure distribution, a low pressure zone linked to the residual swirl can be observed in the middle of P40 (see Fig. 5.21b) for the LE case. For the PA simulation, the low pressure zone is again shifted by  $4.5^\circ$ .

Figure 5.22 shows azimuthally averaged profiles (black lines) for the previously discussed total quantities along with the azimuthally averaged maximum (red lines) and minimum (blue lines) values that occurred over the investigation period. The azimuthal average total temperature agrees well for both cases (see Fig. 5.22a). For both predictions, azimuthally averaged temperature values fluctuate by approximately  $\pm 50$  K (difference between red and blue lines) or 12.5% over the investigated time period, with larger variations close to the inner and outer liners. These larger temperature fluctuations observed close to the liners are also mirrored in the higher RMS values in this region, which is discussed later. The envelope of maximum and minimum temperature values follows the same shape as the average temperature value with increased values in the middle of the

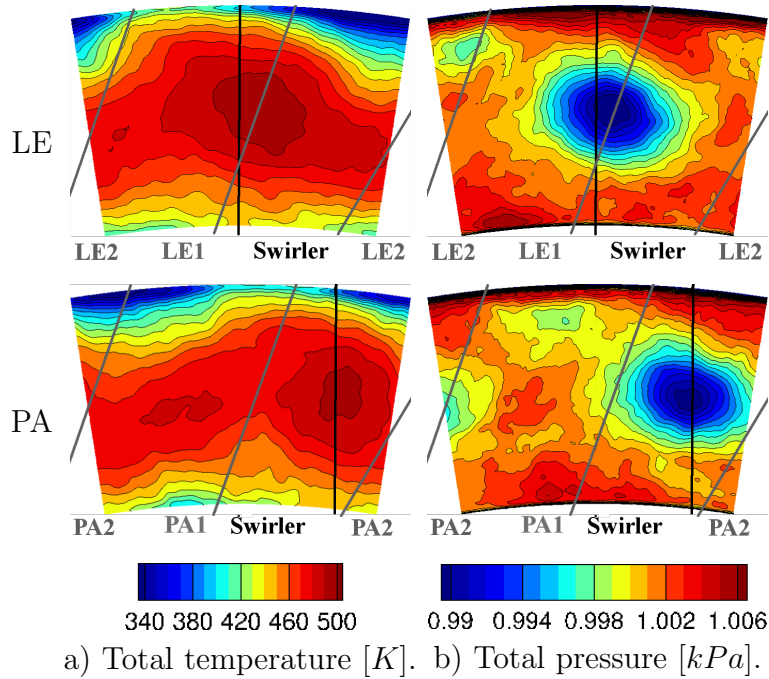


**Figure 5.21:** Total quantities on P40 for LE and PA case. Total pressure non-dimensionalized by average value on P40 (LE: 141953 Pa; PA: 143523 Pa). Black lines indicate middle axis of swirler and inclined grey lines indicate vane positions. View direction: Downstream.

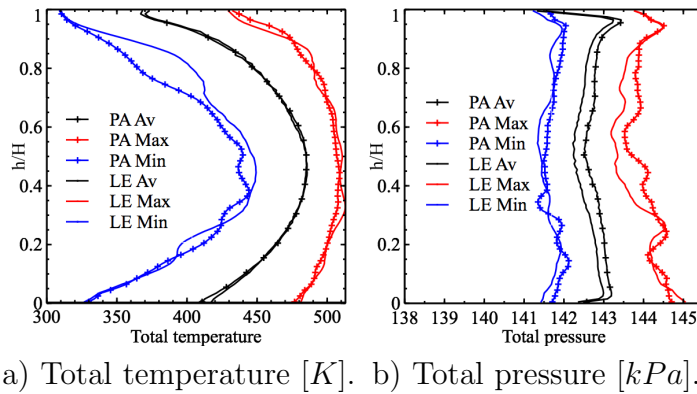


**Figure 5.22:** Azimuthal averaged profiles (minimum during investigation time, temporal average, maximum during investigation time) on P40 for PA and LE LES cases.

channel. The mean temperature is in general closer to the maximum temperature value than to the minimum temperature value which indicates a negatively skewed temperature distribution (to be discussed later). Note also that the temperature values close to the inner liner are generally higher than the values close to the outer liner which is explained by a larger coolant mass flow close to the outer liner. This again is due to the geometrical shape of the chamber (compare Fig. 5.3e): The coolant injection per surface area is equal for the inner and outer liners. However, towards the exit of the chamber, the inner radius increases, while the outer one decreases. The pressure distribution is almost flat, with somewhat reduced pressure

levels at mid-height (see Fig. 5.22b). In both simulations, pressure locally varies by  $\pm 1.5 \text{ kPa}$  (difference between red and blue lines) or around 1% over the investigated time period. Here, the LE prediction shows slightly lower total pressure values than the PA case. The shape however shows again a good agreement.

Higher order statistics are now addressed further as these have been identified as essential for the validation of high-fidelity LES. Indeed, HWA measurements of the axial velocity component at isothermal operating conditions allow for a comparison of higher order statistics, in this case  $TKE_{ax}$  ( $TKE_{ax} = 1.5u_{ax,rms}^2$ ) and turbulent time scale (see Fig. 5.23). To comply with experimental data,  $TKE_{ax}$  is calculated on the axial velocity component and values are non-dimensionalized by the average value in the experimental investigation zone (see Tab. 5.2) to allow for a direct comparison. For the calculation of  $t_{turb}$ , please see Section 2.2. Comparisons with numerical predictions at design point operating conditions are again in good agreement with the non-dimensionalized quantities obtained from experimental data. As previously observed for the mean fields, PA case predictions for  $TKE_{ax}$  and  $t_{turb}$  are shifted by  $4.5^\circ$  as compared to the other cases. As expected, isothermal operating conditions feature lower  $TKE_{ax}$  values due to lower velocities in this case. For cases with vanes,  $TKE_{ax}$  values are higher than in the case without vanes which confirms an impact of the vanes on the flow field upstream. Despite rather different 0D values,  $TKE_{ax}$  2D maps show all a similar wavy pattern created by the break down of the fuel injection system generated CRZ in the chamber (see Fig. 5.23a). In the center of P40 and in the liner region, locally persistent flow features, that coincide with the hot-spot, are present in all cases (see Fig. 5.23b). These are evidenced by longer timescale values observed close to the liners, where coolant flow migrates through the passage. Note that, the hot-spot is surrounded by a ring of short turbulent timescale values likely linked to the PVC, which indicates intense turbulence activity in this region of the flow. In the cases with vanes, the central spot of longer turbulent timescales is less marked, which is again an impact of the vanes on the flow field upstream.

	Exp (IOP).	CC only (DP).	LES LE (DP).	LES PA (DP).
$TKE_{ax} [m^2/s^2]$	93.2	262	306	311
Turbulent time scale [ $10^{-4} \text{ s}$ ]	1.597	1.389	1.074	1.051

**Table 5.2:** Average values for turbulence quantities on P40 in experimental investigation zone used for non-dimensionalization.

Before extending the discussion to the flow field in the vane passages, most important phenomena in the chamber are briefly summarized by the scheme presented in Fig. 5.24. As previously mentioned the flow in the chamber is highly swirled. This leads to the creation of shear layers (see Fig. 5.24, left) between the swirled flow from neighboring fuel injection systems. On P40, further downstream

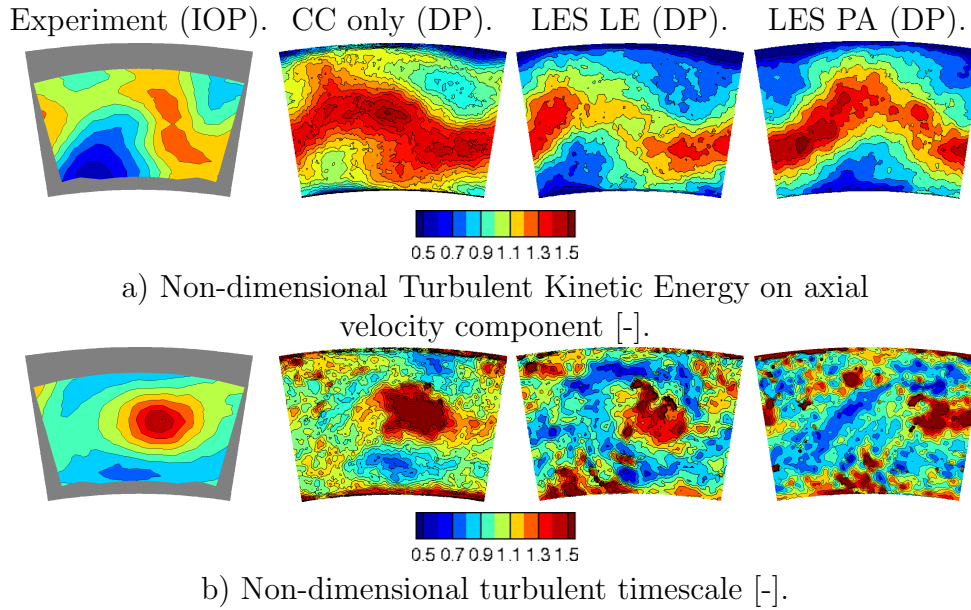


**Figure 5.23:** Non-dimensionalized flow field on P40. Comparison of design point simulation and isothermal operating point measurements. Values are non-dimensionalized by the time and space average value in the experimental investigation zone (see Tab. 5.2). View direction: Downstream.

a typical wavy pattern can then be observed (see Fig. 5.24, right). The swirling motion has an important impact on the temperature distribution (and other flow quantities). Throughout the chamber, coolant ejected through the effusion cooling system is pushed to one side (left side for the inner liner, right side for the outer liner, when looking downstream). On P40 coolant is then moved away from the wall which creates the pattern observed on P40. In the following the question of how the chamber flow field impacts the flow field in the vane passage is addressed and discussed in detail.

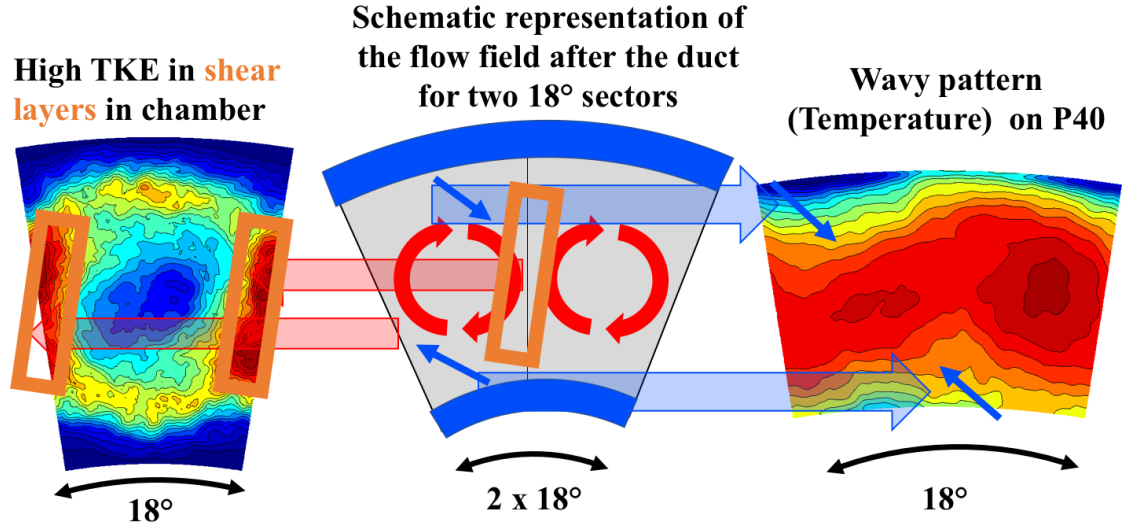


**Figure 5.24:** Schematic drawing of important flow features in the chamber. Hot rotating flow from the swirler is represented by red arrows and the injected coolant is represented in blue. The effect of the velocity field on the coolant is represented by blue arrows. (View direction: Downstream).

### 5.3.2 Flow field in the NGV passage

Having validated the flow field in the combustion chamber against available experimental data and previous simulations, the following discussion focuses on the vane flow as issued by the numerical predictions for LE and PA clocking positions. To ease understanding of the following discussion, the average temperature is here presented first on an iso-Hh=0.5 plane through chamber and vane passage (see Fig. 5.25). Hot air is seen to enter the chamber from the left-hand side of the domain. Further downstream the temperature declines only slightly due to weak mixing with coolant flow entering the chamber through the liners. In contrast to the FACTOR design, current state of the art rich-quench-lean combustion chambers feature dilution holes where cold air is injected into the chamber to change from a rich to a lean combustion regime. At the outlet of the domain, temperature for cases with vanes is lower due to the expansion in the nozzle.

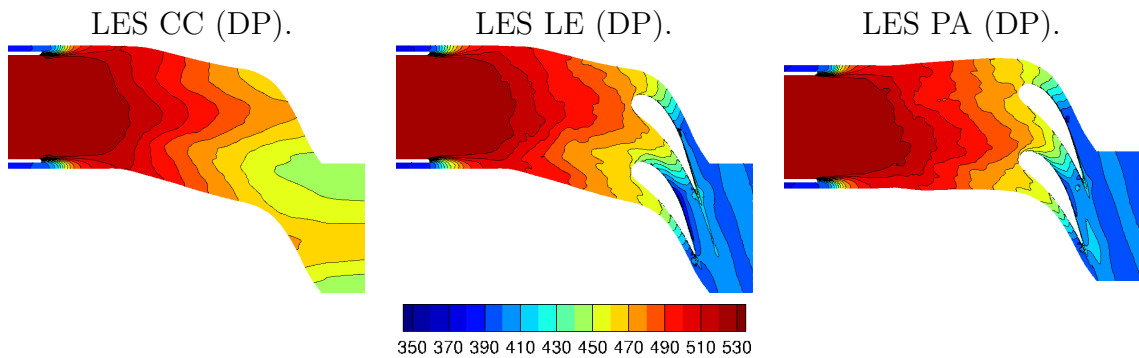


**Figure 5.25:** Average temperature [K] on Hh=0.5.

The migration of the hot streak through the vane passage is visualized in Fig. 5.26 and shows the impact of the clocking position. In the LE clocking configuration (see Fig. 5.26a), the hot spot directly hits LE1 and stays in contact with the vane while migrating through the passage. In the PA clocking case (see Fig. 5.26b), the hot spot is seen to migrate through the mid passage. For this case, the hot spot is seen to reach P41, the exit plane of the vane passage, while the isosurface of total temperature ( $T_{tot} = 470 K$ ) does not reach as far in the LE case, indicating more mixing for this configuration. In the nozzle, the flow is accelerated and also reoriented in the azimuthal direction. Comparing both simulations in terms of velocity magnitude (see Fig. 5.27a), one remarks a good correspondence between both predictions, confirming that both simulations are at approximately the same operating point. In the middle channel, minor differences are however visible and the PA clocking simulation attains slightly higher velocities at P40 and at the throat of the nozzle of the mid channel. One potential reason for this is the higher pressure difference over the nozzle in the PA case ( $\Delta P_{LE} = 83300$ ,  $\Delta P_{PA} = 84900$ ). The final and most important design difference issued by these two simulations is evidenced by the mean temperature fields presented in Fig. 5.27b. In the LE clocking configuration, the hot-spot impinges mostly on the pressure side (PS) of NGV1 (upper NGV). In the PA case, the swirler is shifted by  $4.5^\circ$ , as compared to the LE case, so that the hot streak travels through the passage.

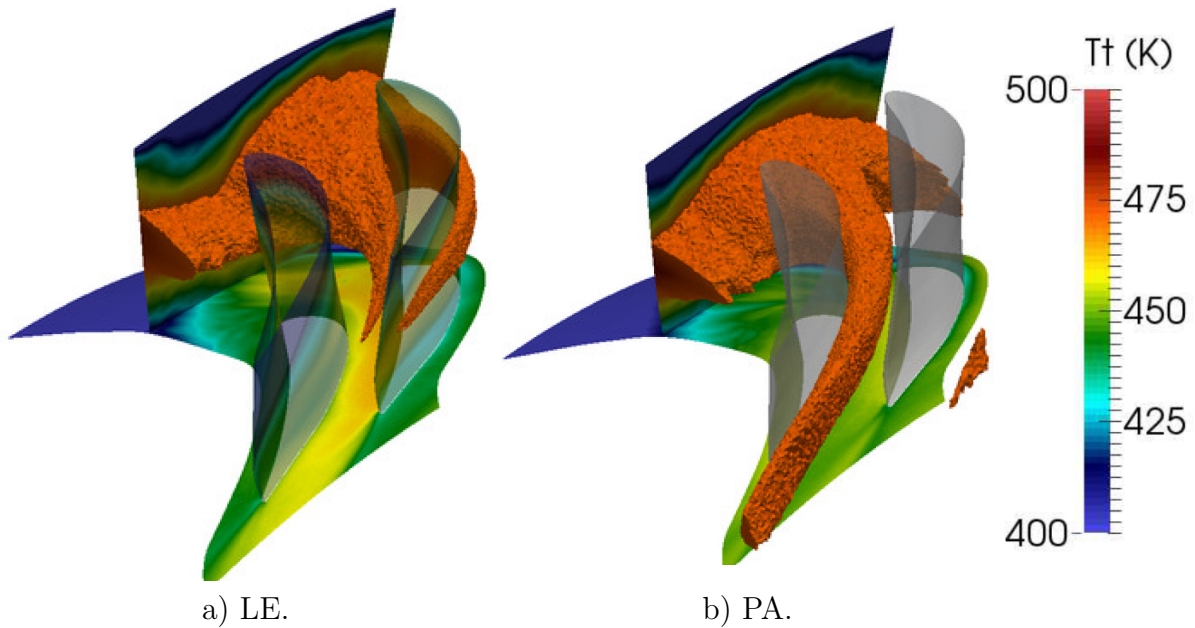


**Figure 5.26:** Visualization of the hot spot by an isosurface of total temperature ( $T_{tot} = 470 K$ ) [16].

As noted previously in the discussion of the flow field in the combustion chamber  $TKE$  fields through the vanes are quite different in both simulations (see Fig. 5.28). Two spots of lower turbulence activity are seen to migrate through the flow field and due to the  $4.5^\circ$  shift impinge on the blades at different locations in

CHAPTER 5. ANALYSIS OF THE CHAMBER CLOCKING POSITION  
DEPENDENT HEAT LOAD ON THE NGV SURFACE

the LE and PA cases. For LE clocking, the hot spot and flow activity are seen to impinge on LE1, the second is in the passage between both NGVs, closer to LE2. In the PA case, one spot of low turbulence activity is seen on the suction side of PA1 and the other is seen to impinge on the leading edge of PA2. In the PA case, the suction side of the lower NGV (PA2) is exposed to higher turbulence levels than in the LE case (LE2).

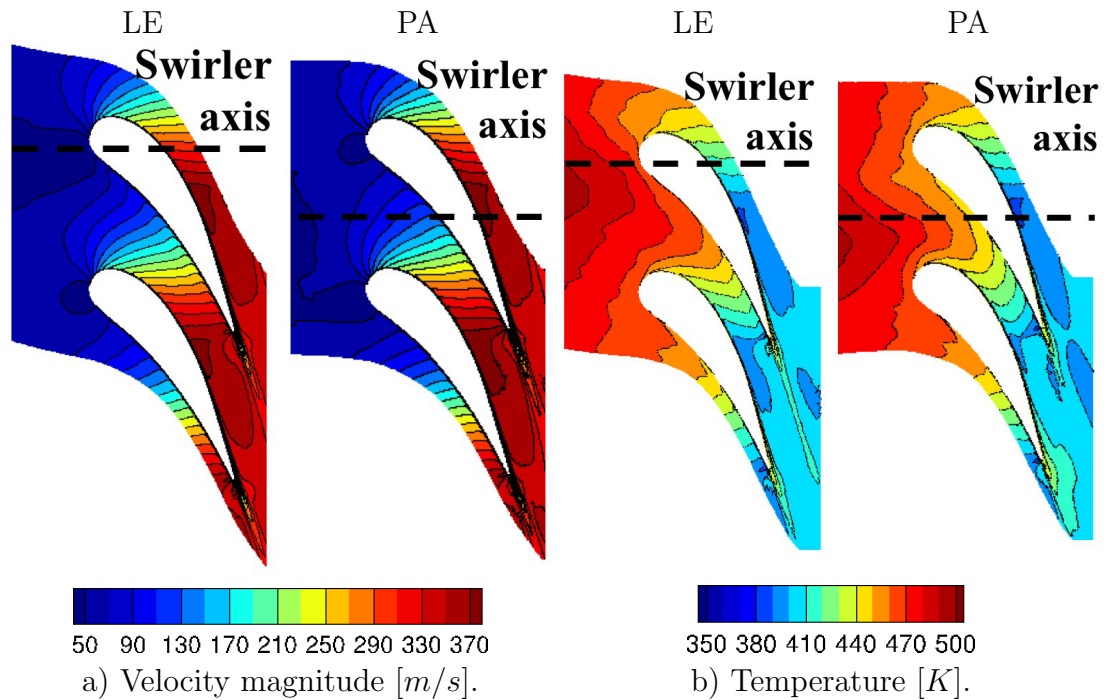


**Figure 5.27:** Mean flow field on  $h/H=0.5$  for LE and PA case. (Design point).

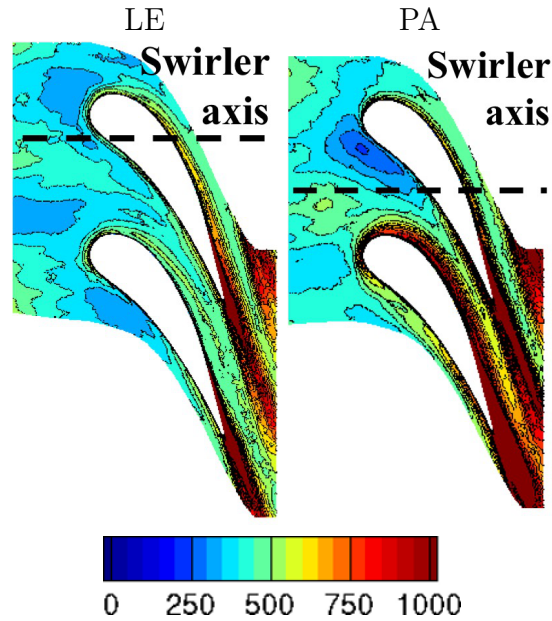


**Figure 5.28:** Mean  $TKE$  [ $\frac{m^2}{s^2}$ ] field on  $h/H=0.5$  for LE and PA case. (Design point).

A comparison of blade pressure profiles at different heights allows for a more quantitative understanding of observed differences between both predictions. On Fig. 5.29, the flow expansion through the vane passage for LE and PA cases is compared at different heights showing a generally similar pressure distribution in both cases. The stagnation pressure for LE1 at mid-height is slightly lower compared to the other vanes, which is potentially caused by the low density hot streak impinging in this region. In general, NGVs are exposed to highest temperatures at mid-chord on the leading edge (see Fig. 5.30). One also notes that, temperatures in the hub region are higher than in the shroud region. These temperature differences are due to a higher coolant to surface ratio for the shroud as compared to the hub and therefore different mixing and heat transfer. A comparison of temperature clearly identifies LE1 as the NGV exposed to the highest heat load. In the shroud region, PA1 however exhibits higher surface temperatures than the other NGVs. Close to the outer liner, temperature differences for vanes at the same position reach about  $50 K$ , whereas differences are lower for the hub region ( $\approx 25 K$ ) and in the center ( $\approx 10 K$ ). This observation is in line with the previous discussion around Fig. 5.22a): 1) Narrow bandwidth of temperature values in the middle ( $Hh=0.5$ ), 2) Higher temperature values close to the inner liner ( $Hh=0.3$ ).

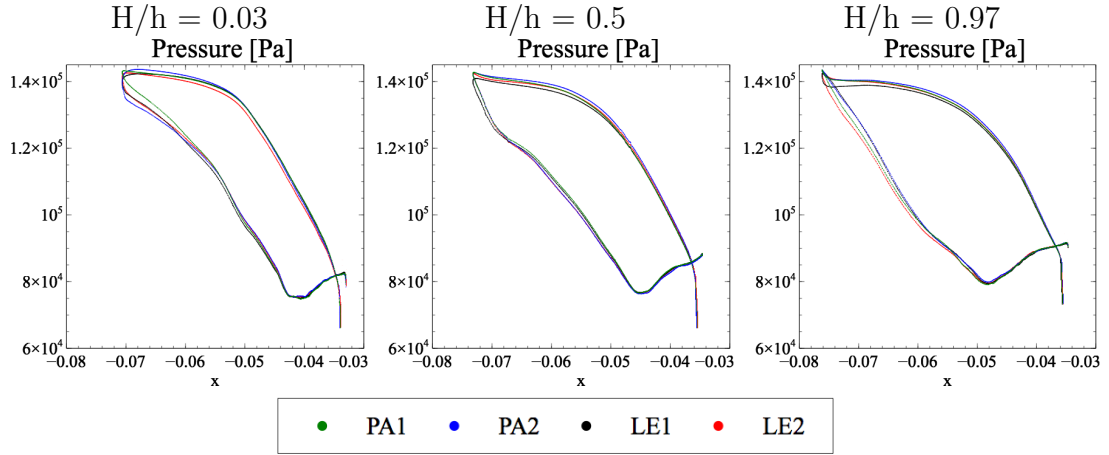


**Figure 5.29:** Pressure profiles on blades for LE and PA case at design point for different heights.

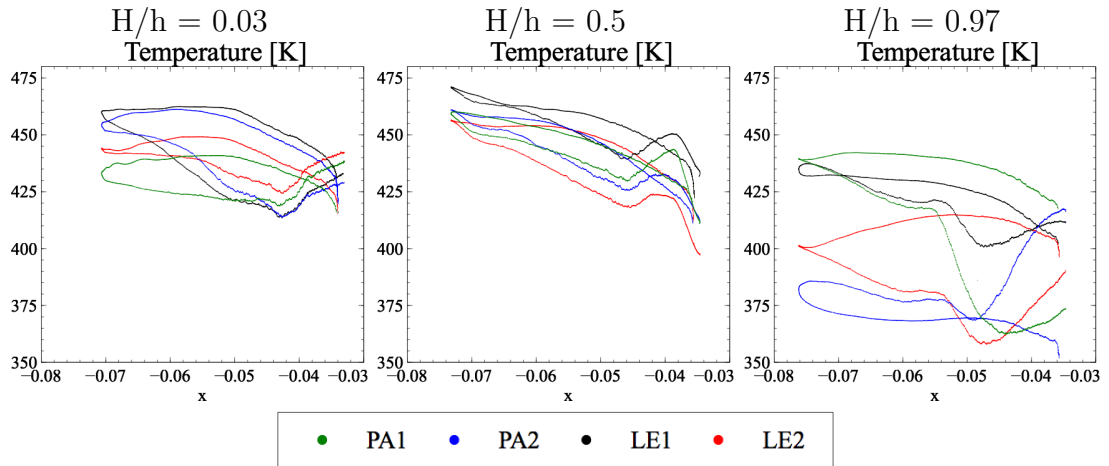


**Figure 5.30:** Temperature profiles on blades for LE and PA case at design point for different heights.

### Analysis of the flow for individual vane passages

A comparison of the flow quantities on the vane surface in the previous section yielded marked differences for the considered cases. To complement the previous discussion, the flow field in each of the high-pressure vane passage is specifically studied, to better evidence the clocking effects on the NGV flow. To do so, average values of  $T$ ,  $T_{rms}$  and  $TKE$  on consecutive planar sections along the  $x$  axis are presented in a non-dimensional form. Values are non-dimensionalized by the value on each half of P40 or respectively by the average value in the channel, as summarized in Tab. 5.3. For the comparison, each integration plane is then divided as in Fig. 5.31 to evaluate integrated values in a passage (see Fig. 5.31a), or around the blade (see Fig. 5.31b). Splitting the observation plane indeed allows for a more detailed quantitative comparison of the flow field evolution.

Having detailed the investigation method, results are presented in the follow-

	$T$ [K]	$T_{rms}$ [K]	$TKE$ [ $m^2/s^2$ ]
Channel1 LE	369	32.9	453
Channel2 LE	350	35.7	451
Channel1 PA	330	36.7	445
Channel2 PA	371	32.5	456
Vane1 LE	389	33.7	458
Vane2 LE	330	34.9	447
Vane1 PA	324	33.6	452
Vane2 PA	376	35.6	450

**Table 5.3:** Average values on first plane in vane passage used for non-dimensionalization.

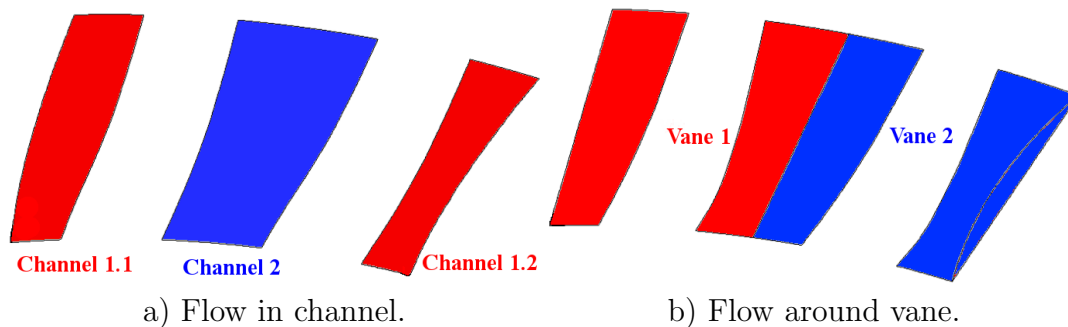


**Figure 5.31:** Distinction of channel and vane for quantitative analysis of the flow.

ing. One element at play when analyzing the mixing process between the cold and hot flow is related to the amount of turbulence entering each channel. In that respect, turbulence levels are observed to rise sharply over the nozzle due to interactions of the flow with the NGVs that redirect the flow in the azimuthal direction (see Fig. 5.32). In that respect, the vane aligned with the swirler and directly hit by the hot-spot, LE1, features higher levels of turbulence than the other vanes (see Tab. 5.3). The residual swirl core, coinciding with the hotstreak is naturally expected to be impacted by the unsteady behavior of the PVC, as shown before. When the residual swirl core impacts on LE1, high levels of turbulence are hence created explaining the previous observation. When performing a vane-wise comparison, non-dimensional  $TKE$  values show similar evolutions and spread less than in the channel-wise comparison.

Due to expansion in the nozzle, the static temperature declines in a uniform way for both simulations independently of the channel- or vane-wise evaluation (see Fig. 5.33). When considering Tab. 5.3, one notes that the average temperature of LE1 is about 60 K higher than the average temperature around LE2. In the PA clocking configuration, the difference between both vanes is slightly smaller, but still reaches 50 K. Focusing on the channel-wise averaged temperatures, one notes, as expected, higher differences in the PA case ( $\approx 40$  K) than in the LE case ( $\approx 20$  K) (see Tab. 5.3). This is due to the fact that, in the PA case, the hot streak travels through the channel in the middle of the domain, while the other channel does not transport as much of the hot air originating from the swirler.

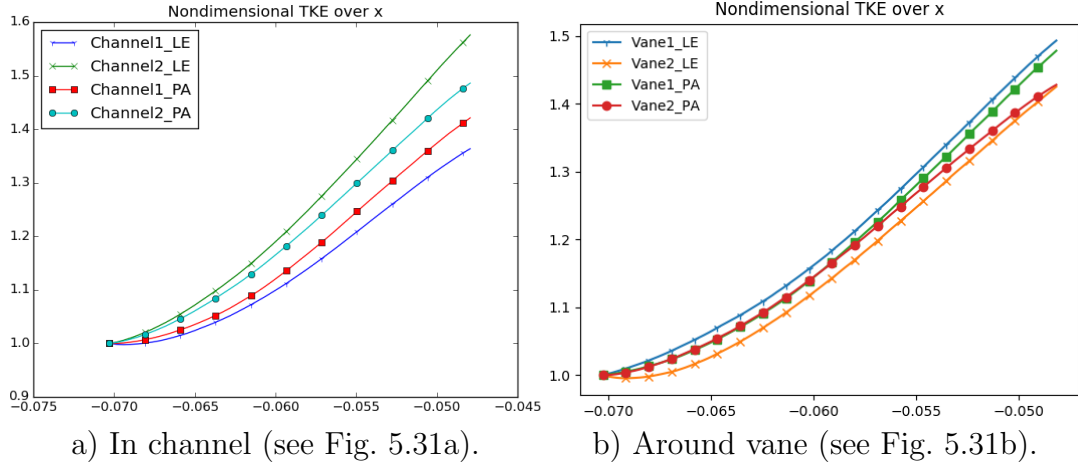


**Figure 5.32:** Evolution of non-dimensional  $TKE$  averaged on planes (see Fig. 5.31) over  $x$ .

Moving further downstream in the vane passage, the evolution between the LE case differs more for a channel-wise evaluation (see Fig. 5.33a), while it is the other way round when performing a vane-wise (see Fig. 5.33b) comparison. Here, for the vane-wise comparison, values for both vanes are rather close. If looking at

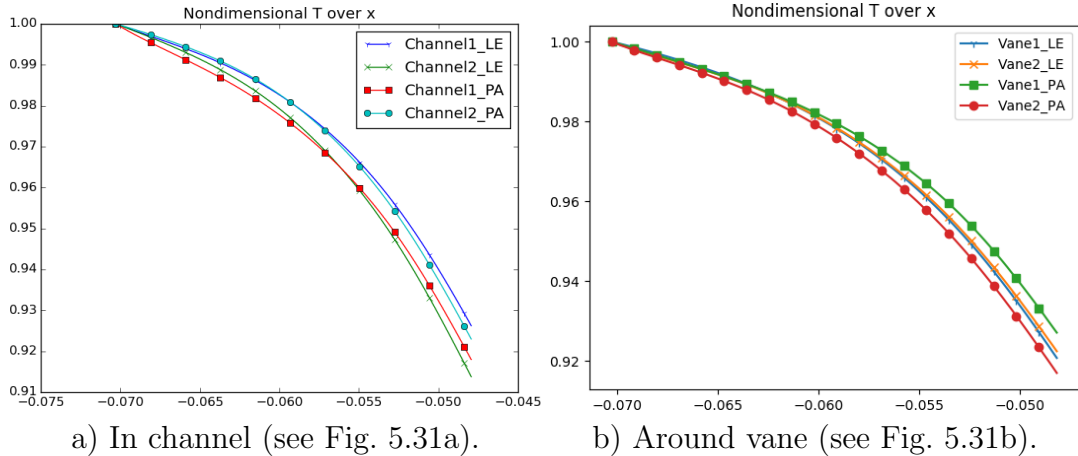


**Figure 5.33:** Evolution of non-dimensional temperature averaged on planes (see Fig. 5.31) over  $x$ .

the mixing process,  $T_{rms}$  values are seen to decrease steadily (see Fig. 5.34) due to the continuous mixing of hot and cold flow through the nozzle. When performing a channel-wise comparison of  $T_{rms}$  moving downstream from the leading edge to the trailing edge, one notes that for the LE case non-dimensional  $T_{rms}$  values diverge, while values stay closer together for the PA case (see Fig. 5.34a). LE2 (lower temperature than LE1) and PA2 (higher temperature than PA1), feature higher levels of temperature fluctuations (see Tab. 5.3). One also notes that, for both cases with high initial values,  $T_{rms}$  decreases less when moving downstream (see Fig. 5.34b).

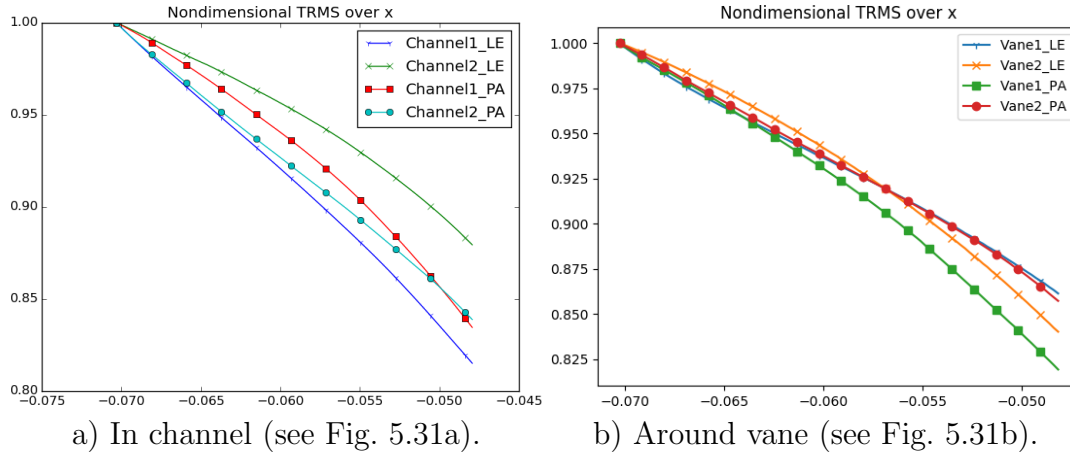


**Figure 5.34:** Evolution of non-dimensional  $T_{rms}$  averaged on planes (see Fig. 5.31) over  $x$ .

After discussing the global evolution of the quantities of interest through the NGV passage, the focus now lies on a more detailed discussion of the mean flow fields across the NGV passages for four specific observation planes (see Fig. 5.35):

- The first plane, P40, is the interface between combustion chamber and high-pressure turbine.
- The following plane (P40 + 0.5 ACL) cuts through the NGV leading edge.
- The next plane (P40 + 1 ACL) is in the middle of the vane passage,
- while the last plane (P40 + 1.5 ACL) is at the exit of the stator.

In the following, temperature moments are presented on consecutive planes through the vane passage.

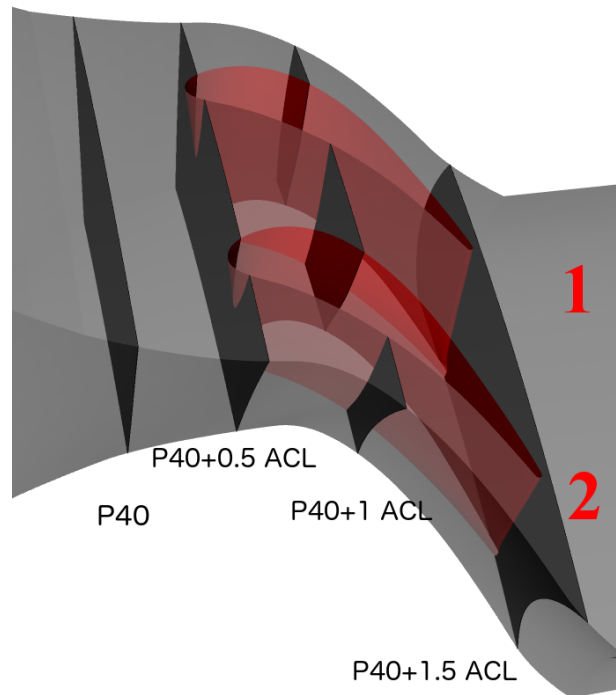


**Figure 5.35:** FACTOR NGV section with investigation planes.

### Temperature statistics on planes through the passage

The temperature field is strongly impacted by the non-uniform chamber exit flow field, e.g. by high levels of residual swirl and the well marked hot-spot. Due to geometrical factors, the flow close to the outer liner is colder than the flow close to the inner liner (see Fig. 5.36). Indeed, compared to the outer liners, there is less coolant injected through the inner liners of the chamber and the inner radius of the flow channel increases towards the high-pressure turbine, whereas the outer radius becomes smaller. Traveling through the vane passage, higher temperatures can be observed close to the NGV directly impacted by the hot streak (LE1). In the LE clocking case, rotating vortex structures coinciding with high temperature values directly impact the leading edge which slows down the rotational movement induced by the fuel injection system. Residual swirl moves coolant flow to the suction side of LE2 or respectively PA1, leading to a marked cold region in the shroud area (to be discussed later). In the LE clocking configuration the wake region after LE1 is seen to be hotter because of the hot-spot directly impinging on this vane, whereas in the PA clocking configuration a marked hot-spot remains in the middle of the passage. After the vane passage, temperatures are lower due to expansion and low values of standard deviation indicate a more homogeneous temperature distribution (see Fig. 5.38a). In the PA clocking case the rotational movement is better conserved and yields globally stronger variations in temperature throughout the passage and on the NGV surface (to be discussed later). For both configurations, the strongest temperature variations can be observed close to the liners, a region where mainly coolant air is transported through the passage

(see Fig. 5.38a). Flow regions that are more probably exposed to high temperature values can be distinguished using higher statistics. This indeed allows for a better assessment of local heat load than if only looking at mean quantities [29].

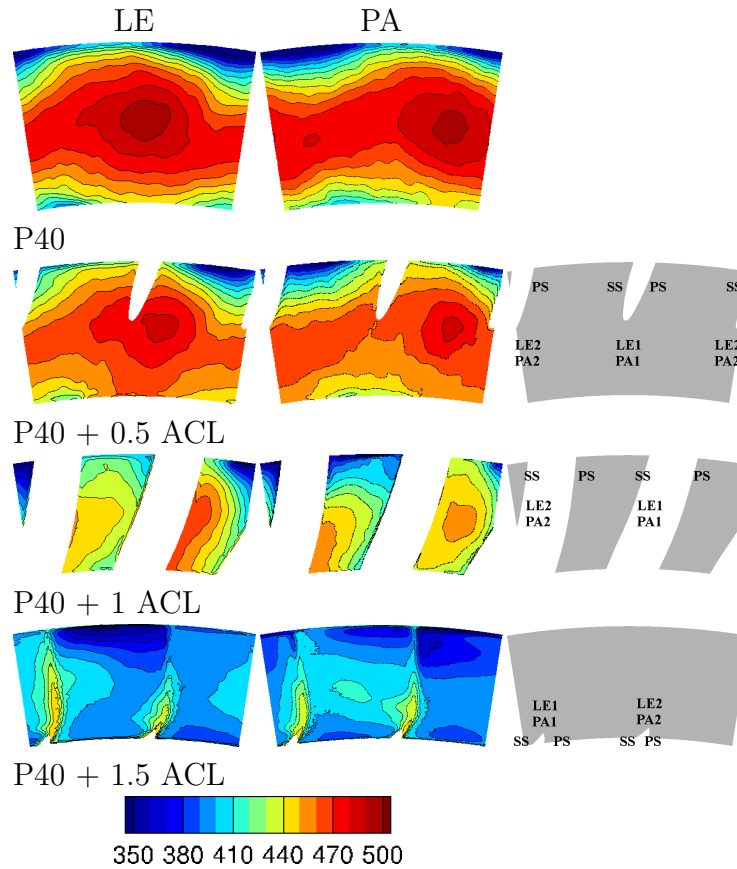
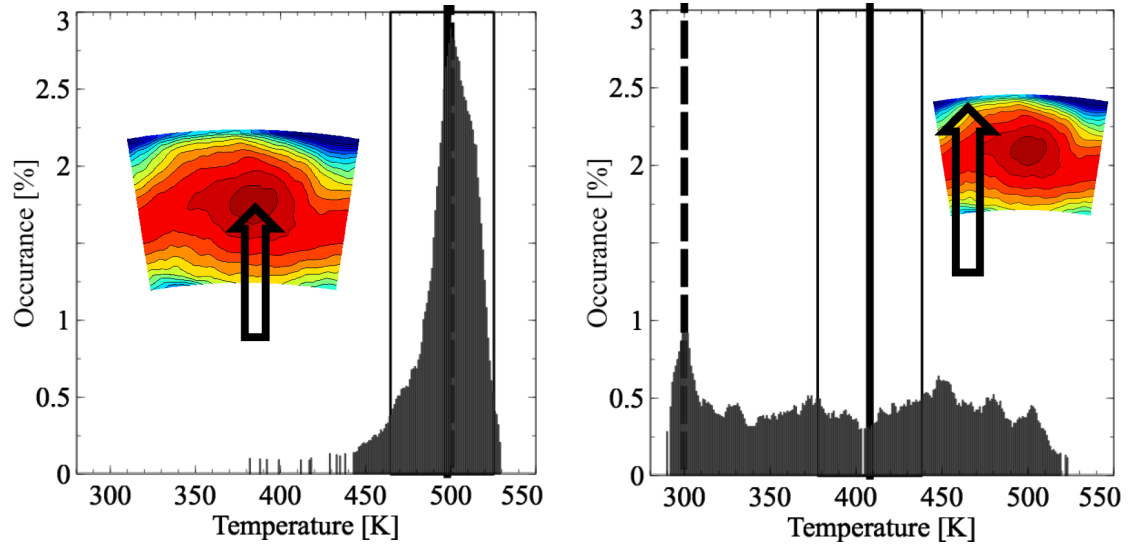


**Figure 5.36:** Evolution of static temperature on planes at successive axial positions through the NGV passage. Vane positions indicated on the right. View direction is downstream.

To illustrate the typical need for discussion on higher order temperature statistics through the vane passage, two specific points on P40 (hot-spot and liner region) are discussed in more detail. The observed temperature distributions in both regions are indeed seen to be quite different. In the hot-spot region, the temperature distribution is single peaked and narrowly arranged around a mode value that is higher than the local mean value (see Fig. 5.37a). Contrarily, close to the liner, interactions between the hot flow and the coolant flow yield a broad distribution of temperature values (see Fig. 5.37b), also indicated by high standard deviation. In this case, skewness is close to zero and kurtosis is rather low. The temperature distribution is therefore seen to be highly dependent on the location and the mean value (or even RMS) may be insufficient to evaluate what is really going on in the flow field.

The temperature distribution throughout the vane passage is mostly negatively skewed (see Fig. 5.38b), except for small regions along the upper liner on P40. The hot-spot is visible as a zone of negative skewness, indicating a high probability of



(a) Hot-spot region: Mean temperature (solid line): 495 K, Mode value (dashed line): 498 K; Standard deviation (rectangle): 20.6; Skewness: -2.04; Kurtosis: 9.23.

(b) Liner region: Mean temperature (solid line): 408 K, Mode value (dashed line): 310 K; Standard deviation (rectangle): 62.8; Skewness: 0.2; Kurtosis: 1.96.

**Figure 5.37:** Temperature distribution over time in two different points on P40 (LE case).

temperature values above the local mean value. The kurtosis plot (see Fig. 5.38c) shows a marked peak for the hot-spot, that is more significant for the LE clocking case. In the LE case the hot-spot migrates along the NGV surface at about mid-height. Low values of kurtosis, observed away from the central hot-spot and after the vane passage, indicate a flat distribution of temperature values.

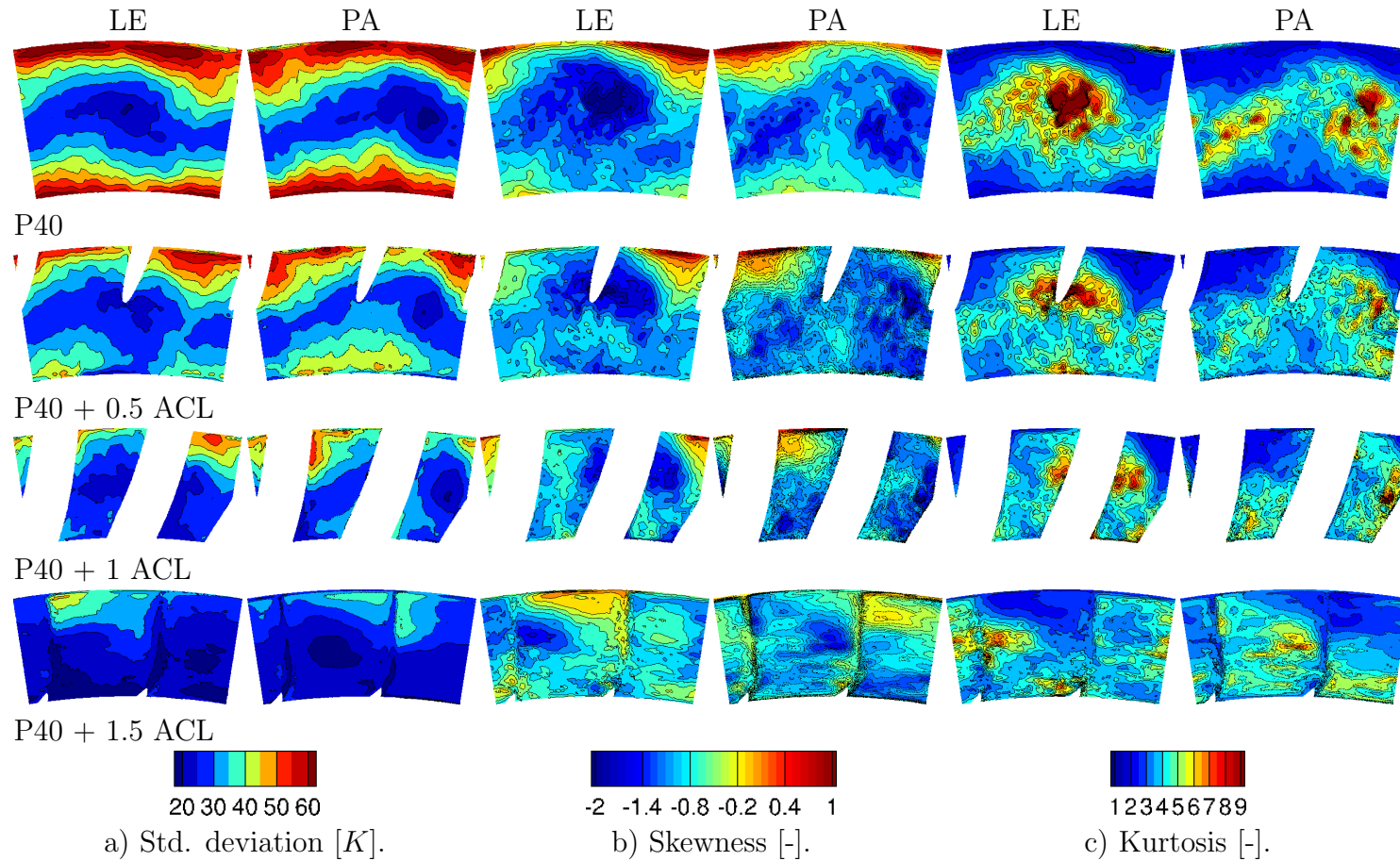


**Figure 5.38:** Evolution of statistical moments (Standard deviation, skewness, kurtosis) for static temperature on planes at successive axial positions through the NGV passage. View direction is downstream.

### Analysis of dynamic features on the NGV surface

Flow features around the NGVs are highly dependent on the flow in the chamber, especially in the presence of high levels of residual swirl as found in the FACTOR geometry. In the following findings from literature are compared with the LE case of the FACTOR geometry (for the PA case a sufficient amount of instantaneous solutions is not available). Jacobi et al. [133] investigated the impact of a highly swirled flow on secondary flow structures in the vane passage (see Fig. 5.39). To do so, they used a joint experimental and numerical approach for a can combustor geometry with two vanes. In their study, a residual swirl core is seen to propagate downstream up to the NGVs, where it impinges on the NGV's leading edge and contributes to the creation of secondary flow structures. For the FACTOR case, the PVC is seen to break down shortly after leaving the duct. This observation differentiates the two studies and can be explained, because: 1.) The swirl in the study of Jacobi et al. [133] is much more confined and 2.) FACTOR is representative of a full annular test rig, allowing for interactions with neighboring swirlers contributing to the break-down of the PVC. This last comment is important and stems from the fact that, in the study by Jacobi et al. [133] the domain is tightly confined in both lateral directions contrarily to FACTOR.

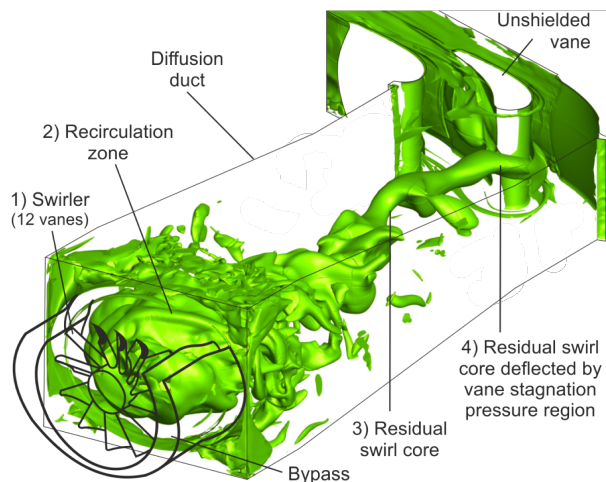


**Figure 5.39:** Residual swirl core present in the study of Jacobi et al. [133], visualized by an isosurface of total pressure.

When it comes to FACTOR and the present simulations, a mean to identify vortex structures and their activity can be obtained by use of POD. This analysis allows indeed to identify energetic flow structures. If using POD on a set of instantaneous pressure fields, one clearly identifies the PVC as the most energetic flow structure. When focussing on the NGVs, as shown in Fig. 5.41, the method identifies a link between a vortex traveling along the suction side of NGV1 and the PVC (marked as vortex Z). More importantly, this vortex looks similar to one mentioned by Jacobi et al. [133], with the important difference however that it only appears intermittently in the FACTOR simulation. Despite such differences,

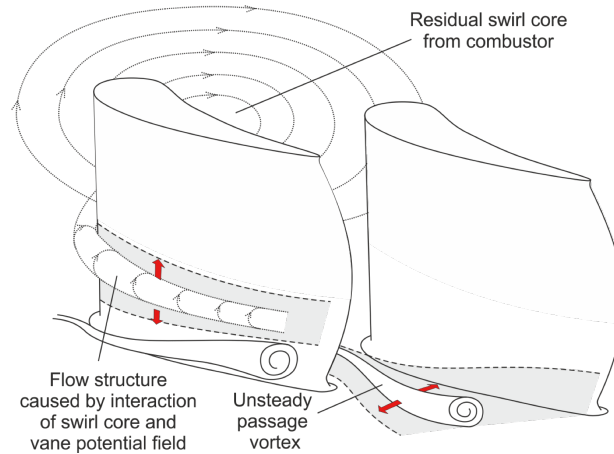


**Figure 5.40:** Schematic drawing of secondary flow structures created with the presence of vanes in a swirled flow [133].

Jacobi et al. [133] report an interesting effect due to the presence of residual swirl upstream the NGV. Indeed as seen in Fig. 5.40 (from Jacobi et al. [133]), residual swirl results in the creation of new vortical structures around the blade that can impact secondary flows usually observed around blades [133]. For FACTOR, a similar constantly present vortex structure at mid-span of the blade can be observed, when using 2D time-constant inlet boundary conditions for isolated vane simulations, as presented in the next chapter. Vortex B is modulated by the PVC, but also exists without the PVC as discussed in Chapter 6.

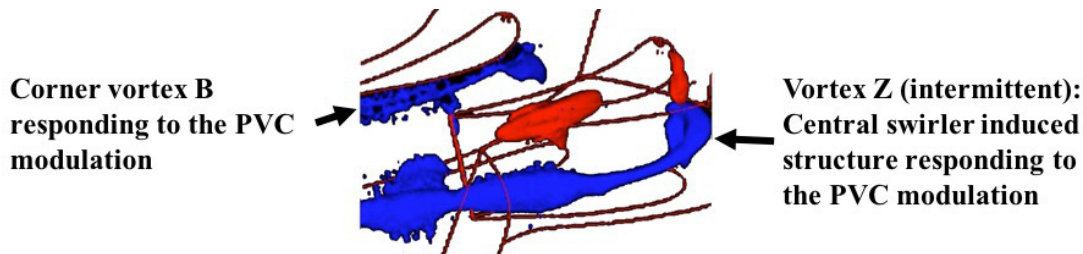


**Figure 5.41:** Visualization of the first pressure mode evidencing a PVC response on the NGV.

Using a  $Q$ -criterion isosurface on an averaged solution, persistent flow patterns on the NGV surface are evidenced. These are indeed important for the blade integrity as they impact the migration of hot and cold flows and the flow mixing in the passage. Prior to this discussion, the flow aerodynamics and more specifically the persistent secondary flow structures around each blade are detailed so as to understand their link with the observed blade wall temperature. Such vortices are commonly known and have been subject to several dedicated studies [6,133]. In an engineering context, control of secondary flow structures has ever been attempted since these are of great importance due to their impact on losses as well as the redistribution of hot and cold flows in the vane passage. Based on the obtained mean flow predictions, a vortex originating from the top mid-blade section and

moving down towards the mid-span trailing edge on the suction side is clearly evidenced (B, see Fig. 5.42). This vortex (B) is always present and can be therefore expected to have a much more important impact on the temperature distribution (to be discussed later) on the NGV surface than the previously mentioned intermittent vortex. Other vortices described on Fig. 5.42 are less dominant (smaller) and their effect on the flow field is weaker (to be discussed later). Vortex A and C are horseshoe vortices that are typically created close to the outer and inner liner wall, when the boundary layer meets the vanes [134]. These vortices wrap around the blade and are therefore present on the suction side and the pressure side of the blade. Vortex D is again a corner vortex, weaker however than vortex B.

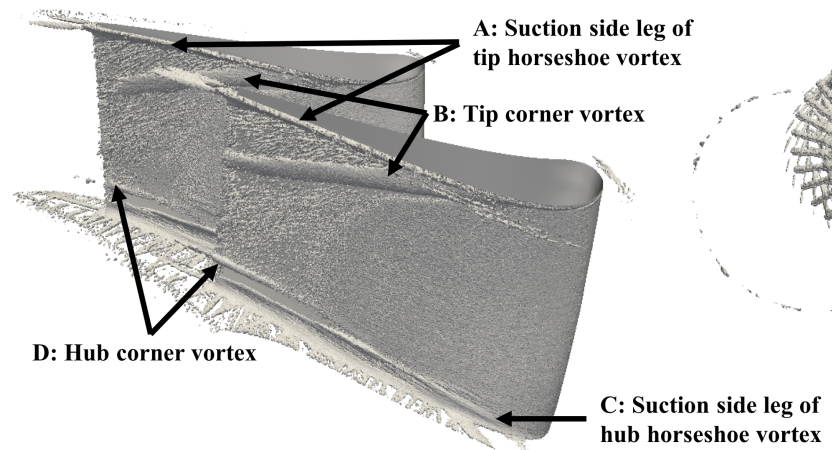


**Figure 5.42:** Secondary flow structures on NGV blade according to Wang et al. [134] (swirler visible on the right-hand side).

If looking at the blade pressure response at the PVC frequency of 500 Hz, an important flow excitation is visible on the NGV surface as evidenced on Fig. 5.43. This activity is visible on the pressure side of NGV1 as well as around the leading edge of NGV2 and can be clearly linked to the PVC given the marked amplitude at PVC frequency. Both observations (activity on PS NGV1, LE NGV2) however have a negligible impact on the NGV wall temperature distribution compared to the corner vortices (marked as B on Fig. 5.42&5.43). On both NGVs (slightly stronger on LE2), a vortex trace responding at 500 Hz is visible on the Suction Side (SS) (see Fig. 5.43, Vortex B), meaning that the PVC modulates the position of these vortices. The corner vortices on both blades are seen to contribute to the transport of coolant flow from the tip region to mid height of the NGVs, as detailed in the following. As shown in Chapter 6, the presence/absence of the PVC modulation mainly affects the wall temperature distribution caused by Vortex B, in previously mentioned areas of high activity, wall temperature stays very similar.

The impact of Vortex B on the blade wall temperature distribution is present for both, LE and PA, cases and clearly underlines the response of the above discussed vortex B to the PVC forcing. For the PA case, as previously mentioned not analyzed here due to the lack of a sufficiently large set of instantaneous solutions, the impact of the PVC is expected to be more prominent in the passage where

the hot spot travels through the stator, and less present in the other passage. The corner vortex B, modulated by the PVC in the LE case, is expected to be equally present in the PA case for both vanes, as the effect on the temperature distribution is also clearly visible in this case (to be discussed later).

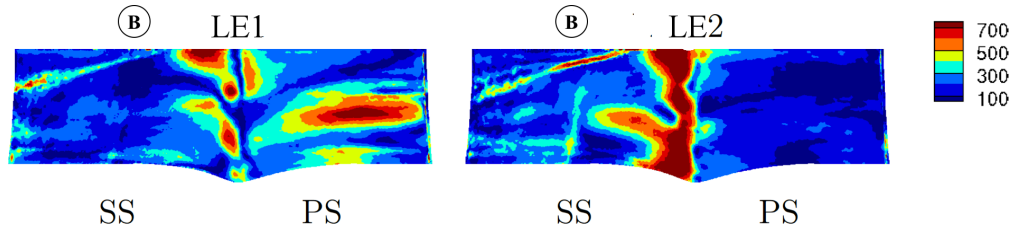


**Figure 5.43:** Pressure fluctuations [Pa] on NGV surface at PVC frequency obtained by a DMD analysis of a set of coarse grid interpolated instantaneous solutions. Trace of vortex B well visible on both NGVs suction side. (LE case, design point). SS = Suction Side, PS = Pressure Side.

Looking at DMD on wall temperature, fluctuations at the PVC frequency indicate that the coolant flow is impacted by the forcing from the PVC as evidenced by Fig. 5.44. For the PA case, not presented here, important temperature fluctuations are also present close to the upper liner and are likely to be modulated again by the PVC forcing (to be discussed later).

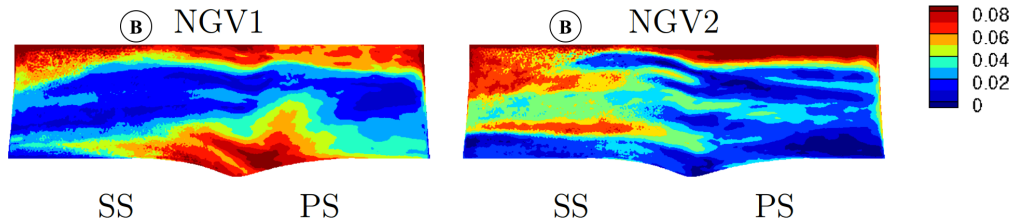


**Figure 5.44:** Temperature fluctuations relative to the local mean value on NGV surface at PVC frequency obtained by a DMD analysis of a set of coarse grid interpolated instantaneous solutions. Trace of vortex B well visible on both NGVs suction side. (LE case, design point).

To finish the discussion on the blade wall temperature (see Fig. 5.45), higher order temperature statistics on the vane surface are finally probed. For all NGVs, coolant flow can be seen to migrate from the shroud down to mid height along the suction side of the NGV (see Fig. 5.45a). This is linked to the generation of secondary flow structures naturally present with the introduction of vanes in a flow field, as discussed earlier. The effect of vortex B on the temperature distribution is strongest for LE2 and PA1. For PA2, cold air can be seen to migrate along PS and SS, again close to the upper liner. As discussed previously, the coolant to surface ratio in the high-pressure turbine is higher for the outer liner than for the inner liner, which explains higher temperatures in the hub area of the NGVs. High values of standard deviation show great temperature variations in the NGV tip region, where coolant flow migrates through the passage (see Fig. 5.45b). These variations are strongest for PA2, the NGV with an important amount of coolant flow on PS

and SS close to the outer liner. As shown earlier, these temperature fluctuations can be at least partly attributed to vortices impacted by the PVC (compare discussion around Fig. 5.44). At mid-height, where hot air hits the NGV, temperature variations are lower. On the NGV surface, skewness can be used to determine whether, temperatures are commonly above or below the local average value (see Fig. 5.45c). In general the temperature distributions on the NGV surface are negatively skewed, indicating that the most common temperatures are higher than the mean value. On LE1, a trace of negative skewness evidences the path taken by the hot air as it migrates along the surface. In this region, the heat load is likely to be underestimated if taking only the mean temperature into account for diagnostics. Equivalently, areas where mainly coolant migrates along the NGV surface exhibit slightly positive skewness, which means that the most common temperature value in this region is lower than the mean temperature value. On LE1, a marked trace in the kurtosis plot, indicating a peaked temperature distribution, appears, where the hot streak migrates along the surface (see Fig. 5.45d). Caused by vortex B on the suction side, the Kurtosis trace moves down to mid-height at the NGV trailing edge. Other NGVs do not show marked features in the Kurtosis plot. Low Kurtosis values, especially for LE2 and PA2 indicate that a broad temperature distribution is present for these vanes. When comparing LE and PA cases more globally, one observes clear differences for all relevant higher order temperature quantities on the NGV blades, which clearly justifies performing dedicated simulations for each of these cases. While the LE case is clearly exposed to higher temperature values, the PA case poses its own challenges for the blade integrity by featuring higher temperature variations on the blade. Skewness and Kurtosis are less conclusive if comparing both cases, with the exception of the marked kurtosis trace identifying the impact of the hotspot on LE1.

## 5.4 Conclusion

In this chapter, the simulation domain was extended to include the nozzle guide vanes with two different clocking positions. The flow field in the chamber is discussed first and certain features are presented in more detail:

- 1) The fuel injection system generated PVC is identified as the most dominant flow feature in the chamber.
- 2) The coolant injection system as well as the absence of dilution holes translates to a highly non-uniform temperature distribution on P40.
- 3) The geometrical shape of the chamber, i.e. compact design, contributes to high levels of residual swirl and turbulence on P40.

Upstream of P40, the presence of vanes or the clocking position are observed not to have a major qualitative impact on the flow field, despite the fact that for both cases with vanes, the pressure in the chamber is lower than in the CC case, which is due to different pressure losses. When available, a good agreement between experimental data obtained at the UNIFI test rig and the LES predictions

can be found. The activity in the chamber strongly impacts the activity further downstream in the vane passage. Here, differences in the flow field between LE and PA cases become more apparent and the temperature field on the NGV surface is seen to be strongly affected by:

- 1) Secondary flow structures.
- 2) The clocking position.
- 3) The presence of the PVC in the chamber.

This study shows the highly clocking position dependent nature of the heat load distribution on the NGVs of a high-pressure turbine and illustrates the value of using higher order statistic analysis from readily available LES data to gain further insights in the flow field. In the last part of this chapter, traces of vortices and their impact on the temperature distribution on the blade were revealed. These vortices partly respond to the forcing of the PVC in the chamber.

Finally, in the next chapter, the impact of the PVC on the flow field in the high pressure stator will be studied in more detail. This is done by first extracting the flow field on P40 from existing chamber & vane simulations and then recasting the flow field on the isolated high-pressure vane domain. One main impact of these different inlet conditions is the change of secondary flow structures, briefly discussed in this chapter, and the effect on the vane temperature distributions.

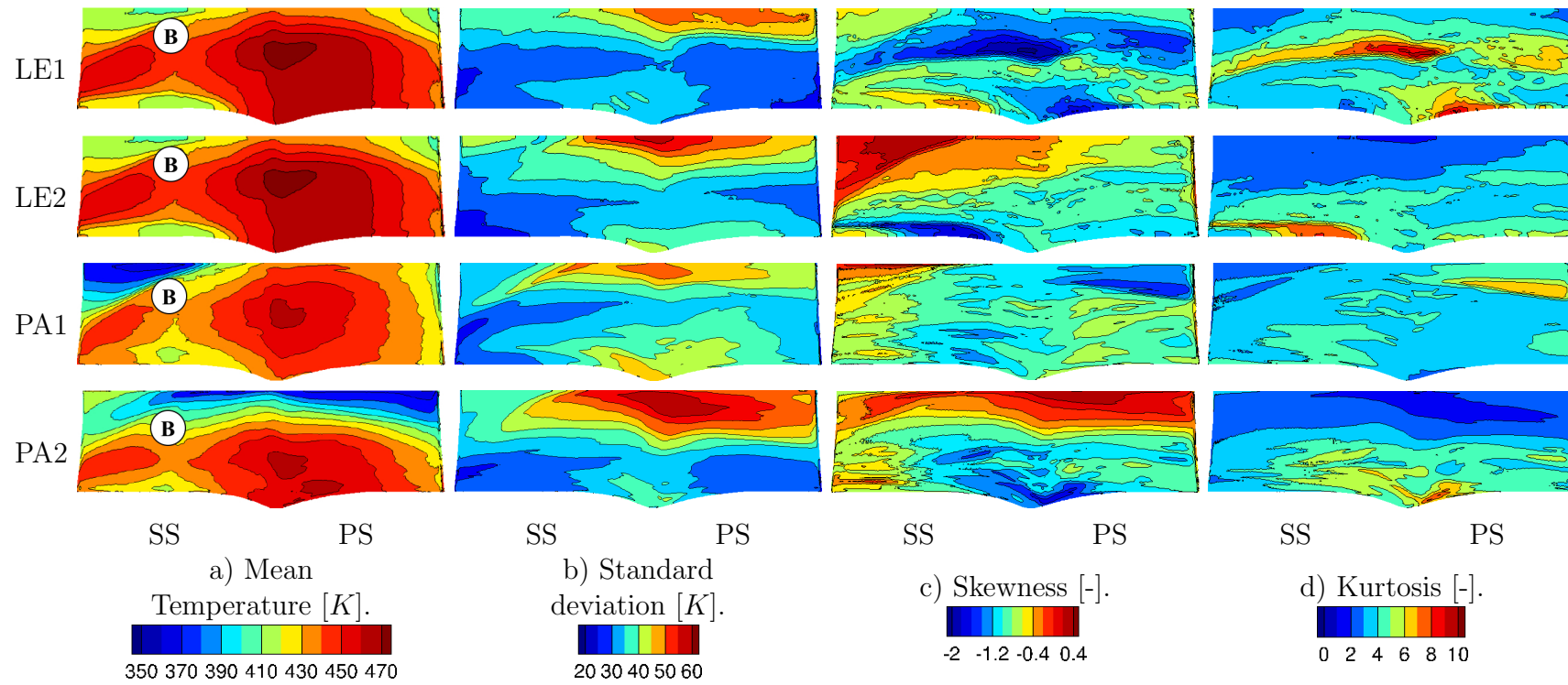


**Figure 5.45:** Temperature and high order statistical moments on NGV surface for LE and PA case. SS = Suction Side, PS = Pressure Side. (Design point).

# Chapter 6

## Towards accurate isolated stator LES

### Contents

---

6.1	Introduction . . . . .	<b>127</b>
6.2	Numerical Setup and Operating point . . . . .	<b>129</b>
6.3	Analysis of the flow field using POD . . . . .	<b>131</b>
6.3.1	Investigation of the flow field in the integrated domain	131
6.3.2	Investigation of the flow field on P40 . . . . .	132
6.4	Towards predictive LES of isolated NGVs . . . . .	<b>134</b>
6.4.1	POD reconstructed flow field in P40 . . . . .	135
6.4.2	Impact of the inflow specification on the LES prediction of an isolated NGV . . . . .	138
6.4.3	Evolution of the flow field through the vane passage . .	142
6.4.4	Impact on the high-pressure vanes . . . . .	148
6.5	Conclusions . . . . .	<b>150</b>

---

### 6.1 Introduction

Due to an inherited industrial organization, engine components are today often designed separately. Information between these components is therefore usually exchanged using 0D or radially averaged profiles at precise engine locations. This approach is of course and by nature not capable of accounting for non-uniformities in temperature and velocity distributions in the azimuthal direction which in future lean combustion chambers will be marked. Although these are expected to have an impact on the performance of the high-pressure turbine, as confirmed by the study in Chapter 5, imposing 2D profiles at the inlet of the high-pressure turbine is deemed necessary to yield potentially realistic results. However, such an approach, although conceivable in RANS, seems quite restrictive in LES and its impact on the quality of the associated predictions is not clear. Indeed, correctly

specifying inlet conditions is already known to be a crucial part of numerical simulations as the flow field at the inlet determines to a large extent the behavior of the fluid inside the computational domain. This observation is even more true in time and space resolved simulations like LES where the inlet boundary conditions should ideally provide time resolved information featuring physical turbulence as well as coherent flow structures.

High computational cost of integrated combustor & NGV simulations as well as the commonly incongruent periodicity angles between chamber and high-pressure turbines explain the interest in performing isolated high-pressure turbine simulations. Note that in the FACTOR setup, the common periodicity angle of chamber and turbine eliminates the need for an adaptation between chamber outlet to turbine inlet, which is necessary for real cases. In such a case, although geometrical specificities are removed, obtaining correct CFD predictions of isolated NGV simulations still remains tricky and the flow field at the inlet of such an isolated computational domain has to be chosen with great care.

In an industrial context, fully integrated combustor-turbine simulation as presented in Chapter 5, are still out of reach in terms of computational power and also difficult to perform between different development partners. To gain more insight in the specific context of combustor turbine interactions whenever addressed in the design process, this study proposes to evaluate the impact of the inflow specification by comparing a fully integrated combustor & NGV simulation with isolated NGV simulations. To do so, the unsteady inlet condition at the interface plane, P40 (between the combustor and the NGV of the integrated LES prediction), is reconstructed in different ways. First, data from the intersection plane of an integrated simulation is decomposed using Proper Orthogonal Decomposition (POD). The flow field is then reconstructed using different criteria and injected in isolated stator vanes LES. Compared to imposing a 1D profile, as it is standard design practice for turbines, 2D maps of temporarily varying boundary conditions reconstructed from POD are expected to allow for more realistic simulations. The objectives in this chapter are hence twofold:

- 1) Determine if the flow field of the integrated combustor-turbine simulation can be recovered in the isolated domain using the approach introduced above.

- 2) Evaluate the impact of dominant flow structures on the flow in the vane passage.

Indeed, thanks to such a modal decomposition, different flow features can be incorporated or removed from the inflow data, thereby allowing the identification of the impact of leading order features from the combustor on the NGV response. One such flow feature of interest is clearly the PVC, previously identified as the most dominant flow feature in the chamber. Despite breaking down shortly after leaving the confining duct, it is expected to impact the flow even downstream of P40, as will be shown in this chapter. Note also that despite the fact that the full combustor & NGV simulation is used and available here, the POD data-basis could also be retrieved from isolated combustor LES which is now quite common in the industry.

The POD approach used in this chapter is presented in Section 2.2.2 and the

geometry and flow field of the integrated simulation were discussed in Chapter 5. This chapter therefore specifically focuses on the impact of the flow field on P40 on isolated high-pressure vane simulations. First, the numerical and geometrical setup used for the isolated NGV LES's are detailed, followed by a discussion around the POD inflow data reconstruction in comparison to the integrated combustor + NGV reference simulation. Differences in the flow field of the standalone stator domain predictions are then evidenced by visualizations as well as the application of statistical tools.

## 6.2 Numerical Setup and Operating point

Simulations presented hereafter are all performed for the leading edge clocking position, where the swirler is aligned with the NGV leading edge, as described in Chapter 5. As in previous chapters, operating conditions correspond to the UNIFI test rig.

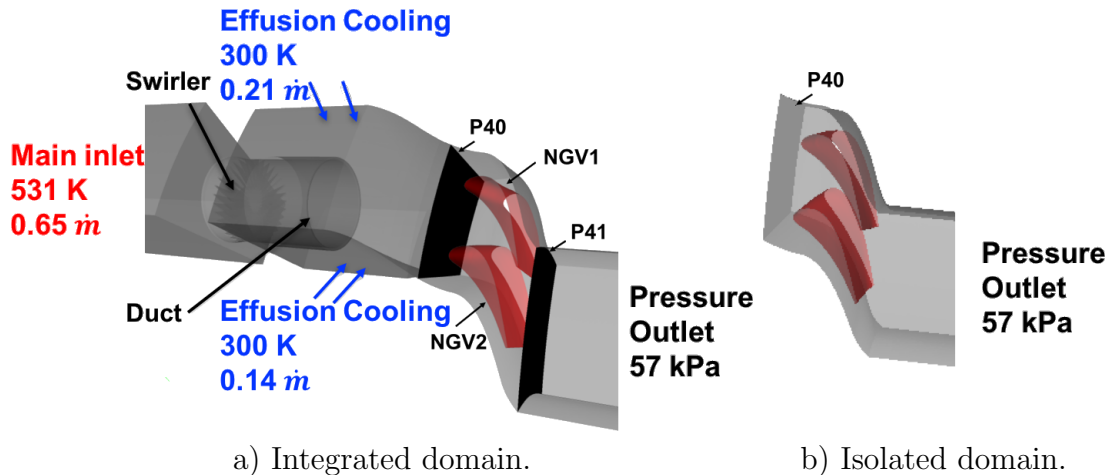


**Figure 6.1:** FACTOR domain and NGV setup.

The NGV standalone simulation domain features one  $18^\circ$  sector of the FACTOR test rig downstream of P40, therefore containing two NGV blades. Note that for these simulations, the inlet section corresponds exactly to P40. At this position and for these simulations, constant or unsteady 2D fields of mass flow and temperature are prescribed, changing every  $2e-5$  s or every 500 iterations. All other boundaries (NGVs, walls, exit) are identical to those of the integrated simulation, which were described in Chapter 5. However, unlike in Chapter 5, where the Smagorinsky [51] SGS is applied to account for SGS turbulence contributions, the WALE model [52], specifically developed for interior flows, is applied for every simulation in this chapter. This change may explain differences observed if comparing to Chapter 5 predictions, a clearer evaluation of such a change being available in Appendix A. Aside from this change and to avoid any numerical artifacts, the standalone stator simulation uses the second part of the zone-wise designed grid of the fully integrated domain downstream of P40 (see Fig. 6.1b)

and is thereby identical with that part of the grid in the integrated simulation. The high-pressure vane domain is consequently discretized by 35 M cells.

Simulations are again performed using the AVBP [60] code which is adapted to allow for the imposition of temporarily varying inlet boundary conditions. To do so, user-defined functions for an existing boundary condition are adapted to read inlet data from tables created from recast POD data. For the standalone NGV cases, the inlet boundary plane consists of around 10500 nodes and the data to be imposed comes from the integrated combustor & NGV simulation analyzed over a period of 40 ms, data in P40 being stored every 0.02 ms. This timestep size seems to be a good compromise between the size of the database and a good temporal resolution (i.e. approx. 25 times shorter than the average turbulent timescale on P40). The acquired data hence consists at most of 80 M entries and corresponds to approximately 40 characteristic flow through times of the NGV domain. From this data set, prior to the actual LES, time-dependent values for each inlet node are recalculated using certain POD modes potentially representative for certain flow features. This information is then read during the simulation and imposed at the inlet of the domain using a linear temporal interpolation to obtain the values for each node in-between the given timesteps. The number of modes used to generate the data set slightly impacts the pre-processing time, but does not affect the computation cost of the LES. Note that the approach, by construction and due to the mesh coincidence at P40, does not take into consideration the interpolation from the original 3D mesh on the 2D planar inlet mesh of the NGV only computational domain. The only approximation at the inflow therefore results from the choice in the number of POD modes used to approximate the original signal.

The POD methodology, described in Section 2.2.2, is briefly recalled to allow for a better understanding of the following discussion. POD is a methodology to find an optimal lower dimensional description of a high dimensional data set [74] by determining the optimal set of modes to represent data based on the  $L_2$  norm (energy) [75]. The data is hence represented as a set of spatial modes that are independent of time and a set of temporal modes that are independent of space. POD can also be used to recast a flow field at the inlet of a truncated domain using certain modes that represent specific flow features, as presented hereafter. To do so, POD is individually performed on the variables  $\bar{\rho}\tilde{u}$ ,  $\bar{\rho}\tilde{v}$ ,  $\bar{\rho}\tilde{w}$ ,  $\tilde{T}$ . Then different numbers of modes are used to reconstruct the inlet signal. In all cases, it is furthermore noted that all reconstructed inlet signals preserve the mean value, as the 0<sup>th</sup> POD mode that represents the mean stationary 2D field is always retained. When imposing reconstructed signals at the inflow of an AVBP simulation, the conservative Navier-Stokes variables  $\bar{\rho}\tilde{u}$ ,  $\bar{\rho}\tilde{v}$ ,  $\bar{\rho}\tilde{w}$  and the static temperature are imposed. The approach uses existing Navier-Stokes characteristic boundary conditions with a high relaxation value to ensure that imposed values are attained, i.e. partly reflective boundary conditions. All simulations are started from the same interpolated initial solution obtained from integrated combustor & NGVs simulation.

## 6.3 Analysis of the flow field using POD

As anticipated in the discussion and evidenced by the previous analysis in Chapter 5, part of the activity pictured in the LES mean fields as well as in the experiments in P40 comes from the presence of the PVC, the most energetic structure in the flow field. POD, described in Section 2.2.2 is more and more applied in research to investigate transient flow data readily available from LES [135]. This section addresses specifically this question by first analyzing the flow field data obtained from an integrated combustor + NGV simulation. Data reduction is then evaluated in light to the reference data as well as conclusions obtained from Chapter 5 prior to their use in the LES's of the NGV only predictions in Section 6.4. First POD is applied on the flow field of the entire chamber + NGV simulation, then P40 which is of interest to the next section is investigated in more detail

### 6.3.1 Investigation of the flow field in the integrated domain

Using POD on a set of instantaneous pressure fields of the entire 3D domain, the PVC is indeed clearly identified by the first few POD modes. To identify modes that carry a trace of the PVC, a fast fourier transformation (FFT) of the temporal POD modes is performed (see Fig. 6.2). Analyzing these spectra, peaks at  $500\text{ Hz}$  and  $1000\text{ Hz}$  are evidenced. Note also that the first and second temporal modes show both a peak at  $500\text{ Hz}$ , the signal however being shifted by  $\frac{\pi}{2}$ . The peak at  $1000\text{ Hz}$  is well visible in the frequency spectrum in the chamber, but less dominant downstream P40. Higher modes carry less energy and feature a broader frequency spectra, generally in a higher frequency range. Higher spatial modes are associated to smaller scale structures and after the first  $\approx 50$  modes their spatial representation can often not be directly attributed to specific flow features present in the chamber. By visualizing the first spatial modes, one observes a one armed structure in the duct associated to the modes with a  $500\text{ Hz}$  peak (see Fig. 6.3a) and a two armed structure associated to the modes with a  $1000\text{ Hz}$  peak (see Fig. 6.3b). The combination of specific POD modes furthermore allows the reconstruction of a turning fluid structure corresponding to the PVC in the chamber. Note that along with the trace in the chamber, POD also detects an impact of the PVC on the flow field in the vane passage as will be shown in this chapter. Note however that the PVC itself breaks down in the chamber and does not reach P40, as shown in Chapter 5: The rotating structure is not present in P40.

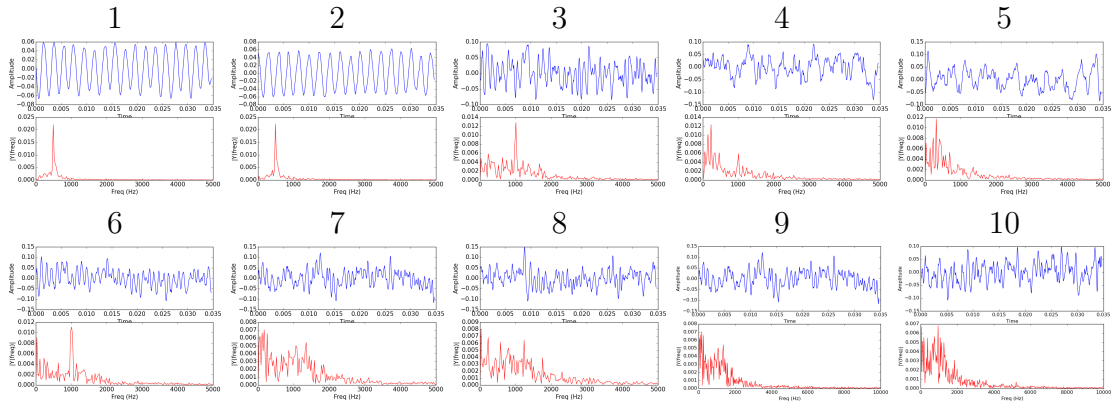


**Figure 6.2:** FFT analysis of the ten most energetic temporal POD modes of pressure in the entire domain.

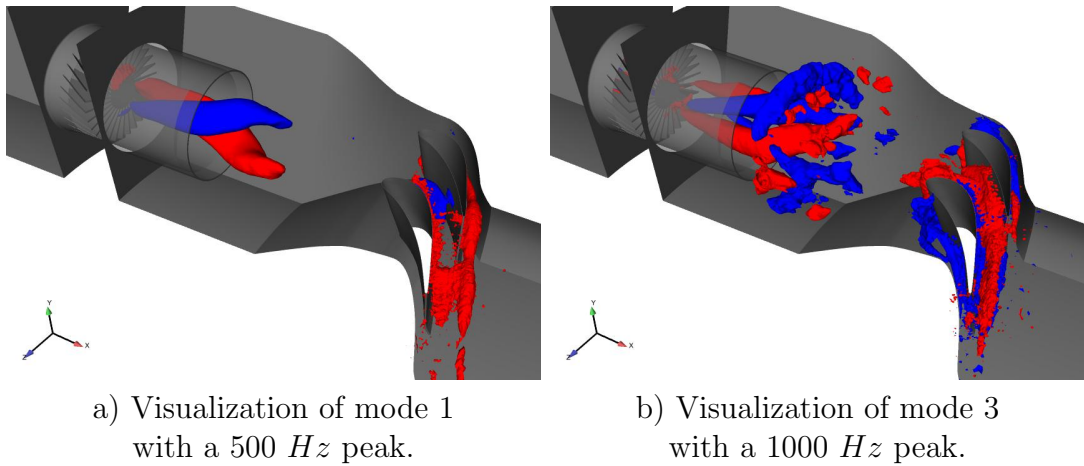


**Figure 6.3:** Visualization of spatial POD modes of pressure with isosurface for positive (red) and negative (blue) values.

### 6.3.2 Investigation of the flow field on P40

For the following discussion on standalone vane simulations, the flow field at the inlet, P40, is of great importance. It is therefore also specifically analyzed by means of POD, the difference being here the 2D nature of the treated information compared to the 3D fields detailed before. Although only temperature is detailed here, findings are similar for other flow quantities. Using only the first 2D POD mode to reconstruct the temperature field on P40, one observes that, close to the upper liner, a high fraction of  $T_{rms}$  of the fully unsteady field is retained (see Fig. 6.4, for a comparison to the total  $T_{rms}$ , please have a look at Fig. 6.8a). Analyzing the same P40 flow field, using dynamic mode decomposition (DMD, see Section 2.2.3) [76] shows that a high amplitude peak at 500  $Hz$  appears for the same region. The activity caused by the PVC at 500  $Hz$  is indeed strongest close to the upper liner and agrees well with the region highlighted by the first 2D POD mode. On the contrary, in the central region, where the hot spot migrates through the domain, the temperature activity at the PVC frequency is low. Note that here

only data from P40 was used for the analysis which yields a less dominant peak at  $500\text{ Hz}$ , than if performing the same analysis on data from the entire domain as presented in Fig. 6.2. Clearly, the conjoint analysis based on POD and DMD allows therefore to conclude that the first POD mode of the 2D data set on P40 can be associated to the PVC in the chamber which evolves mainly at  $500\text{ Hz}$ .

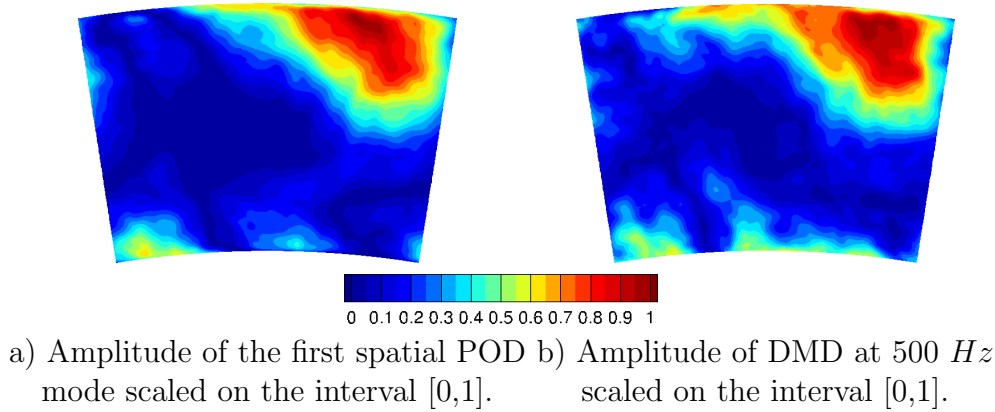


**Figure 6.4:** Spatial POD and DMD analysis of temperature on P40.

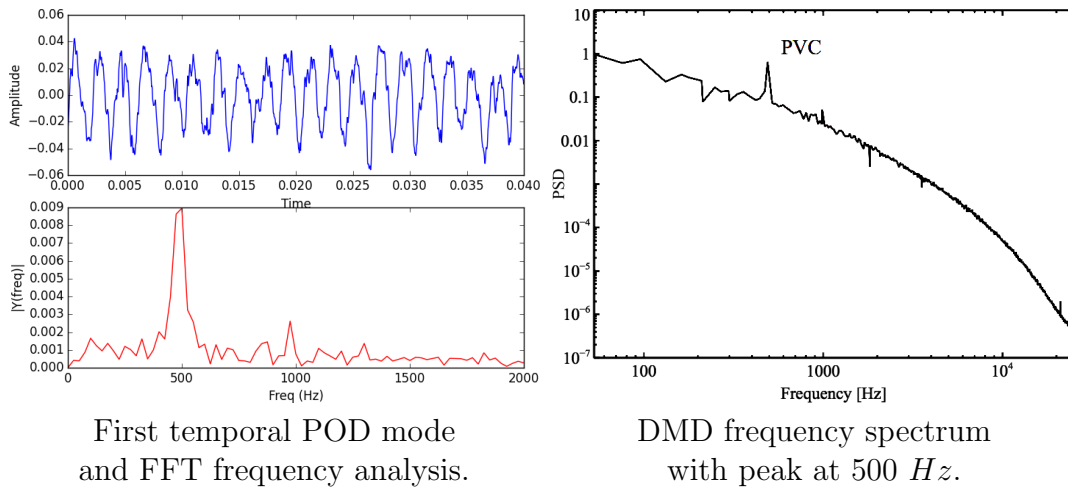


**Figure 6.5:** Temporal POD and DMD analysis of temperature on P40.

Apart from the spatial distribution and their associated frequency spectra, the energy associated with POD modes is of interest and importance for the following discussion. To analyze the energy attributed to these POD modes, the RMS value of the considered quantities depending on the number of nodes used to recalculate the temporal and spatial data of said quantities, is averaged on P40. Regarding the RMS associated with each mode, one notes, that the first ten modes together contribute already to about 50% to the total RMS of the investigated quantity (see Fig. 6.6). Note that, compared to other quantities, the first few temperature modes carry a higher fraction of the total RMS. The first modes correspond to the most dominant flow features in the domain and for the FACTOR test rig can often be associated to the PVC, as demonstrated previously in Figures 6.4 & 6.5. In general, higher modes describe smaller structures with shorter timescale and

less energy than the first modes. The question these observations raise is: What is the impact of the remaining part of the modal information on an isolated LES? That is either the PVC or purely turbulent activity.

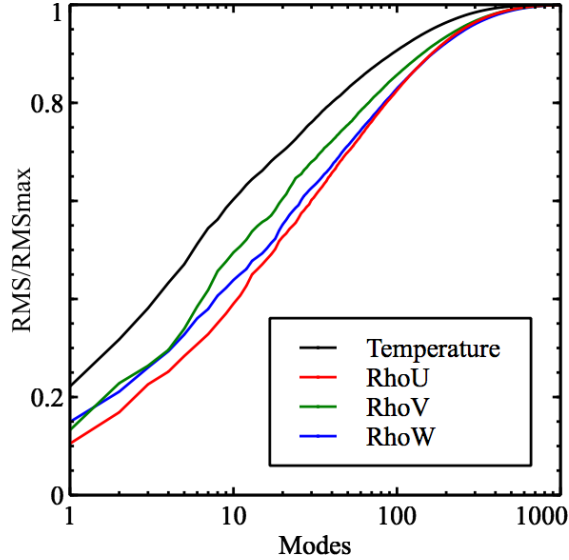


**Figure 6.6:** Ratio of spatially averaged RMS value on P40 reconstructed by different number of modes and spatially averaged RMS value on P40 using all modes for variables imposed at the inlet ( $T$ ,  $\rho u$ ,  $\rho v$ ,  $\rho w$ ).

## 6.4 Towards predictive LES of isolated NGVs

Based on the previous findings, the focus now lies on the capacity of a standalone NGV LES to recover the flow field of the integrated simulation. A second objective is to understand the impact of the various unsteady flow features found in Chapter 5 on the flow field in the high-pressure turbine. This can indeed be investigated here since this section is simulated independently from the combustion chamber. To do so, one constant and different unsteady inlet conditions are imposed on isolated NGV simulations. In the following and to guide the understanding, differences between four isolated nozzle simulations (see Tab. 6.1) are presented and compared to the fully integrated simulation:

- Case a): This case corresponds to the fully integrated reference domain. It serves as a reference for the isolated simulations.
- Case b): Here, the full unsteady data set obtained from the previous simulation is used to create a fully unsteady inlet boundary condition for the isolated NGV domain. This is done to test the ability of the approach to recreate the flow field of the coupled chamber + NGV simulation.

- Case c): In this case, all modes except for the first ten modes of the POD basis are used. The goal is to investigate to what extent the less energetic flow features impact the flow field in the isolated domain. Note that this case is presented as a counterpart to Case d).
- Case d): The first ten POD modes, representative of the PVC, which was previously identified as the most energetic coherent flow structure in the chamber, are imposed at the inlet of the high-pressure vane domain. These 10 most energetic POD modes are representative of about 50 % of energy compared to the reference simulation.
- Case e): Finally, this case uses the temporally averaged 2D flow field at the inlet of the standalone NGV simulation. Note that this last simulation is close to current standards, whenever produced in industry although here LES is applied instead of RANS.

Finally, note that average mass flow  $(\bar{\rho}\tilde{u}, \bar{\rho}\tilde{v}, \bar{\rho}\tilde{w})$  and temperature values are conserved in all cases, so the operating conditions of the vanes is not affected.

Case	Description	Domain
a)	Reference	Combustion chamber & NGVs
b)	All POD modes	Stator
c)	Without first ten modes	Stator
d)	First ten modes (PVC)	Stator
e)	Constant 2D boundary conditions	Stator

**Table 6.1:** Test cases with different inlet boundary conditions.

In the following, the impact of the different reconstruction approaches presented in Tab. 6.1 on the inlet boundary condition, P40, compared to the reference simulation is presented first. The flow field in the NGV domain will be addressed in the next section to give a macroscopic view of the different flow features present in the vane passage that are impacted by the inlet boundary condition modelization. The investigation of the flow field is then done in more depth at specific engine locations to determine the impact of previously discussed macroscopic flow features. Finally, the impact of the inlet conditions and associated changes in the flow field on the NGVs is detailed.

### 6.4.1 POD reconstructed flow field in P40

Note that the flow field on P40 and in the vane passage of the fully integrated simulation has been extensively discussed in Chapter 5. The following discussion thereby focuses first on the unsteady inlet signal as recovered in the standalone simulations when applying the approaches presented in Tab. 6.1. Note at this point that by construction and as previously explained, averaged values of imposed quantities are identical for all cases, so only RMS quantities are discussed from here on. In general, reconstructed solutions feature lower RMS values than the original

solution (see Fig. 6.7). Despite this observation, Case b), featuring all POD modes, is seen to be very close to the reference case confirming the validity of exploiting only 2D fields at the exit of the combustion chamber for the present exercise. For Case d), although containing the most energetic modes, the inlet condition reconstructed using the first ten modes features lower RMS values than the inlet condition using all other modes except the first ten (Case c). Such observations are however in agreement with the analysis of Fig. 6.6: The first ten temperature modes are representative of 60% of the energy, whereas the first ten modes only represent around 40% of the RMS for the other variables. The original wavy pattern of turbulent kinetic energy ( $TKE$ ,  $TKE = 0.5(u_{rms}^2 + v_{rms}^2 + w_{rms}^2)$ ) on P40 is nonetheless conserved in all cases using unsteady inlet boundary conditions (see Fig. 6.7). Clearly for Case e) which supposes constant inlet conditions, and therefore contains no turbulence, no pattern can be observed at the inlet.

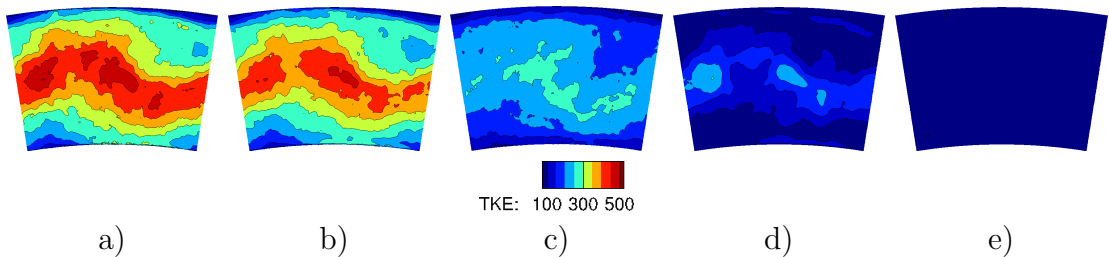


**Figure 6.7:**  $TKE$  [ $m^2/s^2$ ] on P40 retrieved from simulations. a) Reference, b) All modes, c) Without first ten modes, d) First ten modes, e) Constant.

In contrast to the above discussed  $TKE$  maps, where most activity can be observed in the center,  $T_{rms}$  maps at the inlet plane show higher activity close to the liners of the chamber (see Fig. 6.8). In the middle of P40, where the hot spot enters the high-pressure turbine, temperature fluctuations are indeed comparatively low. As previously discussed in Chapter 5, the amplitude of the temperature variations is highest close to inner and outer liners, where mainly coolant flow migrates through the domain. Here again, the reference case and the one using all modes are very close. Unlike for  $TKE$  fields, Case d) shows locally higher RMS values than Case c), which is due to locally strong contributions of low order POD modes to the local  $T_{rms}$  value (see discussion around Fig. 6.6), especially in regions close to the liners. Finally and as expected,  $T_{rms}$  is zero for the case with constant inlet boundary conditions.

To better understand the previous discussion on the  $T_{rms}$  field at the inlet, temperature PDF's on P40 obtained over 40 ms are now analyzed. The temperature PDF distribution on P40 (see Fig. 6.9) indeed shows clear differences depending on the investigated case. Using all POD modes (Case b), a small peak at 300 K is visible, which corresponds to the temperature of the coolant injected into the chamber. “All modes”, Case b), is in fact the only case that captures intermittent fluid packets at 300 K on P40. Indeed, other cases do not capture this peak, because reducing the number of modes used to calculate the inlet signal leads to less extreme temperature values (e.g. very low / very high values). For the same reason, RMS values are lower for these cases, as shown previously. It is furthermore

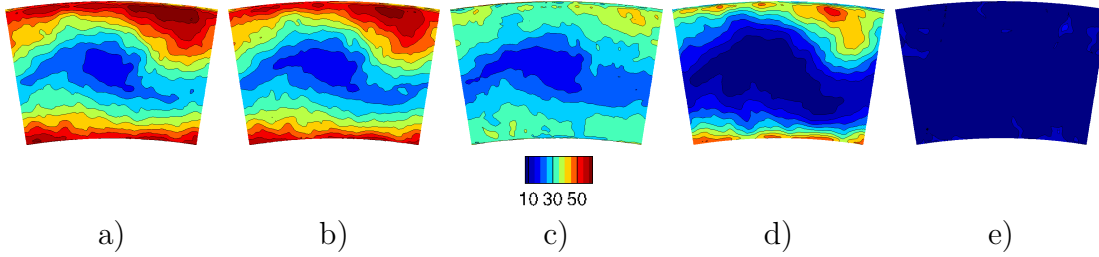


**Figure 6.8:**  $T_{rms}$  [ $K^2$ ] on P40 retrieved from simulation. a) Reference, b) All modes, c) Without first ten modes, d) First ten modes, e) Constant.

observed that degrading the signal at the inlet yields more peaked temperature distributions with fewer extreme temperature values. Note however, that for all cases the average temperature is not affected as ensured by construction. Interestingly, for Case c), using the truncated inlet signal, the temperature distribution is flatter as compared to all other cases. In fact, this case is missing the excitation of the PVC which contributes to attaining extreme temperature values observed in the other cases. Imposing only the PVC at the inlet, as in Case d), yields a rather pronounced peak at 485 K. Another consequence is that, medium temperature values, e.g. between 350 K and 450 K, occur less frequently on P40 than in the first cases (a to c). Finally, in Case e), due to the time-constant inlet condition, the PDF shape obtained corresponds to the spatial heterogeneity present in the mean temperature field imposed constant in time on P40. Since this distribution is not smooth multiple discrete values of  $T$  are attained as evidenced by the retained PDF. Clearly, the resulting PDF significantly differs from the other cases.

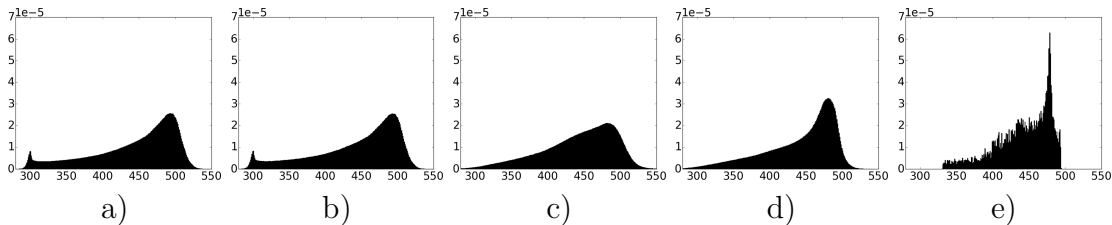


**Figure 6.9:** Temperature distribution on P40 over 40 ms (all nodes, 2000 instantaneous solutions). a) Reference, b) All modes, c) Without first ten modes, d) First ten modes, e) Constant.

Before starting with the discussion of the flow field in the NGV, a brief comparison of the mean pressure value obtained on P40 confirms that all simulations have the same operating point (see Tab. 6.2) and are thereby mutually comparable. In terms of operating conditions, recall that all simulations feature the same mass flow rate which is imposed at the inlet. At the outlet of the domain, the static pressure (87 KPa) is imposed, which due to different flow behavior in the vane passage leads to different pressure values at the inlet plane (see Tab. 6.2). Indeed, isolated simulations show generally higher pressure values than the reference case, which indicates higher losses in the passage for these cases. These losses are mainly

due to secondary flow structures and Case e), featuring the strongest secondary flow structures due to the undisturbed inlet boundary condition (to be discussed later), also features the highest pressure loss over the vane passage. Globally, differences in pressure are nonetheless rather low ( $<0.5\%$ ), so all simulations produce the same operating point, equal to that of the reference simulation. Note finally that, pressure profiles on the vane surface are also identical, they will therefore not be further detailed in this chapter.

a) Reference	b) All modes	c) Without first ten modes.	d) First ten modes.	e) Constant.
141.22	141.29	141.43	141.43	141.56

**Table 6.2:** Static pressure [ $kPa$ ] on P40.

### 6.4.2 Impact of the inflow specification on the LES prediction of an isolated NGV

In the following and to ease understanding, the discussion first addresses the impact of the inlet conditions on secondary flow structures using 3D visualisations. Secondary flow structures through the vanes are visualized based on instantaneous solutions using the Q-criterion [136] at the exact same instant in time (see Fig. 6.10).

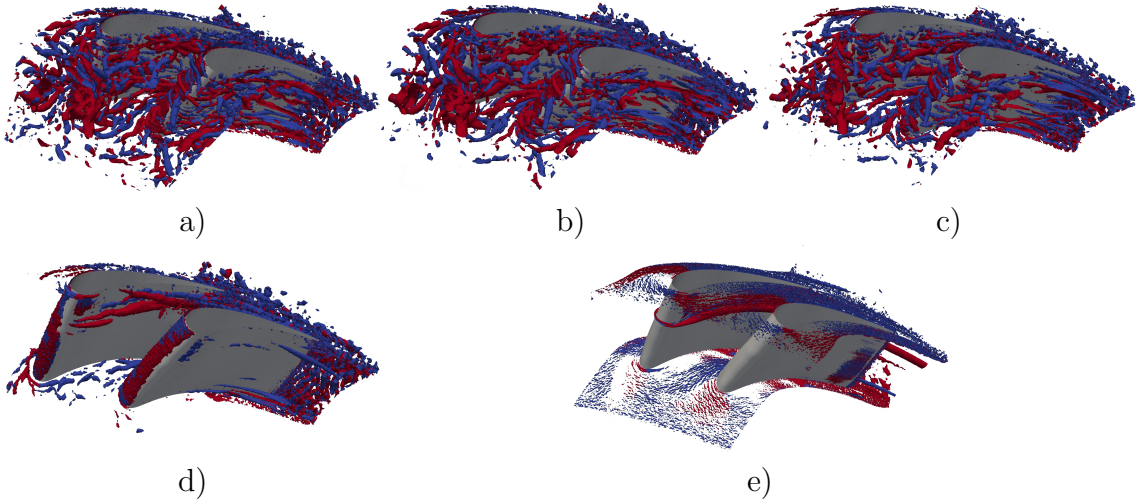


**Figure 6.10:** Visualization of vortex structures in the NGV passage using an isosurface of Q-criterion ( $10^8$ ) [136] on instantaneous solutions. To visualize the direction of the vortex rotation, red indicates positive X-Vorticity, blue indicates negative X-Vorticity. a) Reference, b) All modes, c) Without first ten modes, d) First ten modes, e) Constant. (NGV2 in foreground, NGV1 behind).

Clearly, such views show marked discrepancies depending on the inlet boundary condition. When looking at Cases a) to c), one remarks high levels of activity in the entire domain. Using the full unsteady flow fields at the inlet of the isolated

domain (see Fig. 6.10b), allows indeed to preserve all coherent flow structures as observed in the reference case. Clearly, vortice structures as in Case a) are found to be traveling from the inlet downstream to the NGVs. Most of these vortices appear however only intermittently and are thereby not visible in the averaged solution (to be discussed later). If comparing all cases with unsteady inlet conditions, Case d) is seen to have considerably less activity within the passage. As for Case e), a steady turbulence free instantaneous flow field as the one shown here is observed. Note that in this specific case with the absence of distortions at the inlet, a strong persistent vortex, present throughout the entire simulation, is formed at mid-span of the NGV impacted by the hotspot and aligned with the swirler. This specific vortex on mid-height of the blade was already addressed in Chapter 5. In the wake of the NGVs significantly less turbulent activity can be found compared to the other cases. Note that some of the vortices present in the other cases are also present over extended periods of time in these simulations and can therefore be seen in averaged solutions presented in the following.

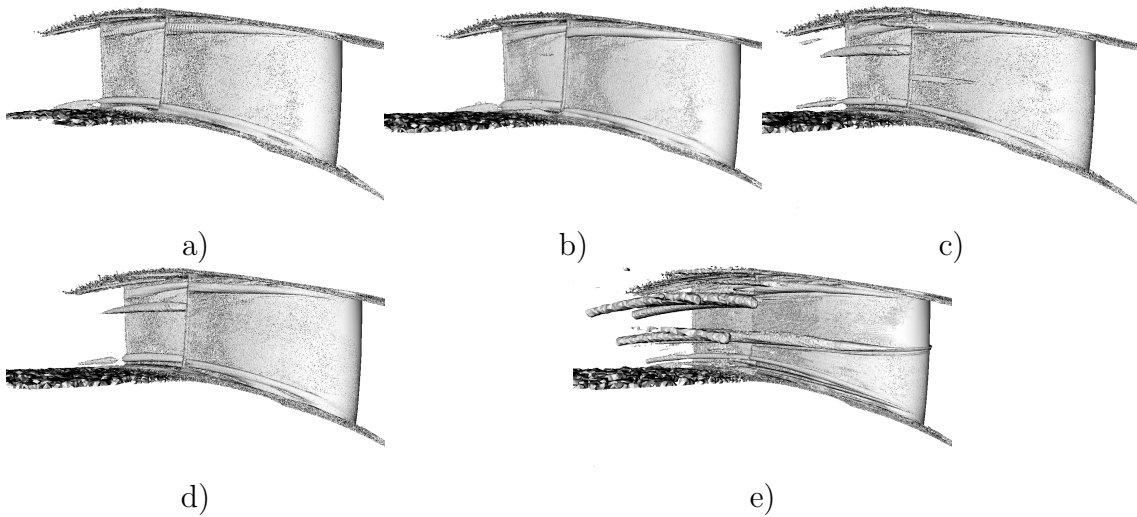


**Figure 6.11:** Visualization of vortex structures in the NGV passage using an isosurface of  $Q$ -criterion ( $10^8$ ) [136] on solutions averaged over 40 *ms*. a) Reference. b) All modes. c) Without first ten modes. d) First ten modes. e) Constant. (NGV1 in background, NGV2 foreground).

To further evidence discussed features, averaged  $Q$ -criterion isosurfaces are provided in Fig. 6.11. Applying a constant boundary condition at the inflow (Case e) results in stronger and more persistent vortex structures as these are not disturbed by the changing inlet condition. As mentioned previously, Case e) is also the case that features the highest pressure loss, so observed more dominant secondary flow structures can be seen as a reason for such an increase. In this case, a horseshoe vortex is formed at mid-height of the blade (see Fig. 6.11e). In fact, and complementary to the conventional passage vortices, an additional vortex similar to the one observed by Jacobi et al. [133] and presented in Chapter 5 appears. Note that whenever injecting POD modes, a more disturbed and unsteady flow field through the vane is created and this specific horseshoe vortex at mid height

of the blade only appears intermittently. In such cases, it is no longer visible in the mean field. For Cases c) and d), the activity imposed at the inlet is indeed strong enough to remove the horseshoe vortex whenever it is created for a limited period of time. Close to the liners however, depending on the inflow activity retained, vortices are observed to be larger than in the reference case: i.e. Cases c) and d). Finally, Cases a) and b) are very similar and show that proper secondary flow structures are preserved in the truncated domain only if using all POD modes.

In the following, the discussion focuses on changes of the temperature fields in each case linked to the differences of the inlet condition and the associated changes in the flow organisation visualized by the Q-Criterion (for more background on aerodynamics and general flow organization the reader is referred to Chapter 5 and previous work by C. Koupper [16]). The instantaneous temperature fields at mid height are first shown in Fig. 6.12. As assumed, Case a) and Case b) are in very good agreement. This explains the globally very similar behavior for both cases and shows that the methodology is able to recreate the flow of the fully integrated simulation in an isolated domain. The observation is also in line with Fig. 6.10, where clearly more activity can be observed for the first two cases. The flow field for Case d) looks however more unsteady than that of Case c) for which the PVC was removed from the inlet signal. The simulation using a constant boundary condition finally shows a very smooth temperature distribution due to the lack of activity at the inlet and induced low mixing. Comparing Cases d) (only PVC imposed) and c) (all modes except PVC) one concludes that the PVC has as an important contribution to the mixing between the hot and cold flows through the vanes.

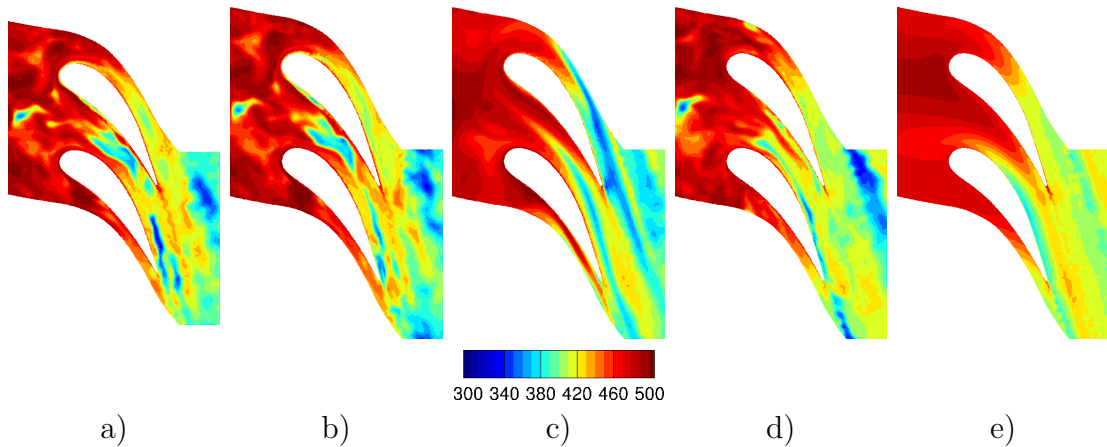


**Figure 6.12:** Instantaneous temperature [K] plot on  $Hh=0.5$  isosurface. NGV1: upper, NGV2: lower. a) Reference, b) All modes, c) Without first ten modes, d) First ten modes, e) Constant.

The consequences of above observations are evidenced by the mean temperature fields obtained for all simulations and which show marked differences (see Fig. 6.13). As previously discussed, the hotspot impinges on NGV1 (upper NGV), and again the reference simulation, Case a), and that using all POD modes, Case b), show good agreement. Simulations using a partially unsteady inlet signal,

Cases c) and d), show a rather good agreement with the reference simulation. In the wake of NGV1 (impacted by the hotspot) differences to the reference simulation become more apparent: Here both cases with reduced modes imposed at the inlet feature higher temperatures, which is caused by reduced mixing in the NGV wake. When using constant inlet boundary conditions, Case e), the lack of mixing causes even more extreme temperature values, especially in the wake of NGV1.

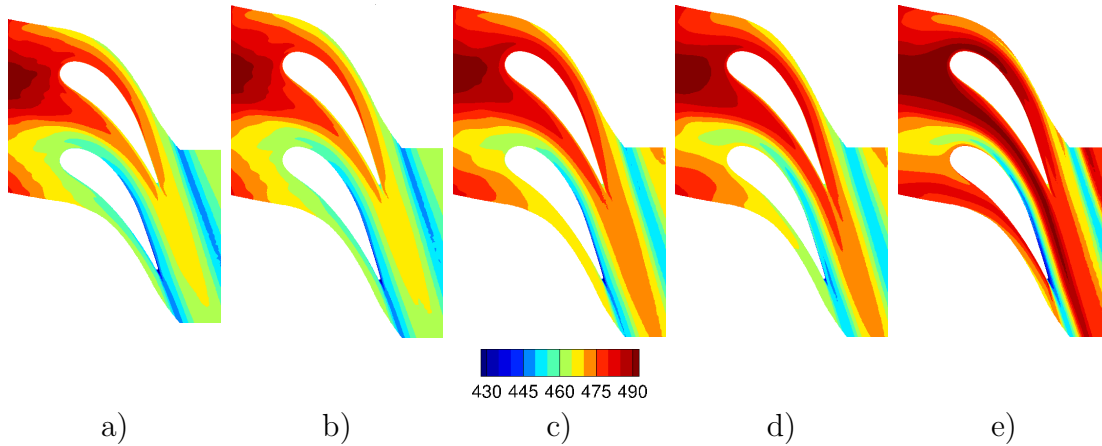


**Figure 6.13:** Average total temperature [K] plot on  $Hh=0.5$  isosurface. NGV1: upper, NGV2: lower. a) Reference, b) All modes, c) Without first ten modes, d) First ten modes, e) Constant.

If looking at the corresponding temperature RMS fields, Fig. 6.14, the hot spot region features low temperature fluctuations, which is again visible in the passage (see Fig. 6.14). NGV2 generally features lower temperatures, temperature fluctuations however are higher.  $T_{rms}$  values for Case d) show higher temperature fluctuations around NGV2, than Case c), which again points to the importance of the PVC for the mixing in the vane passage. This is also in line with the previous discussion around Fig. 6.6, where one notes that a rather high fraction of  $T_{rms}$  is represented by the first modes only. In Case e),  $T_{rms}$  values are generally rather low, although the simulation shows perceptible fluctuations in the NGV wake.

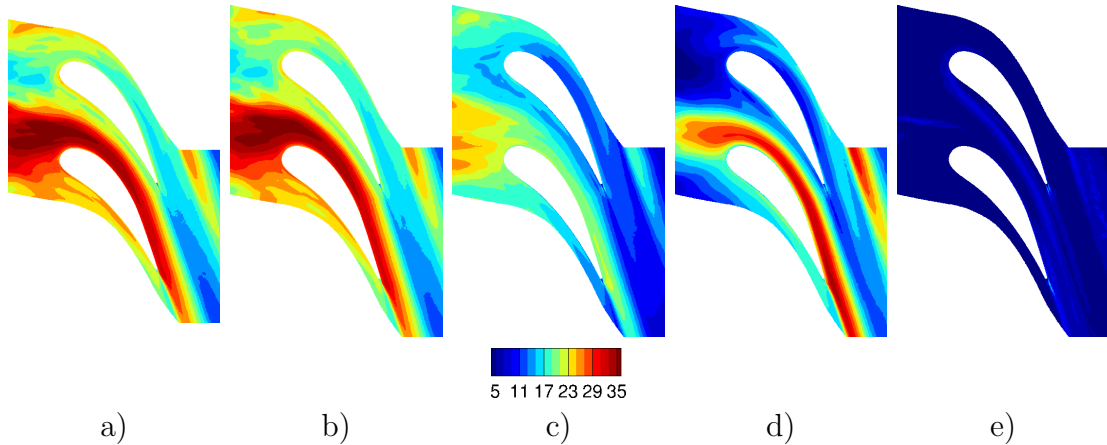


**Figure 6.14:** Average  $T_{rms}$  [ $K^2$ ] plot on  $Hh=0.5$  isosurface. NGV1: upper, NGV2: lower. a) Reference, b) All modes, c) Without first ten modes, d) First ten modes, e) Constant.

### 6.4.3 Evolution of the flow field through the vane passage

As the previous section provided a macroscopic view on the impact of the different inlet conditions specified in Tab. 6.1, this section intends to provide a closer investigation of the flow field at distinct locations in the passage, specified in Fig. 6.15.

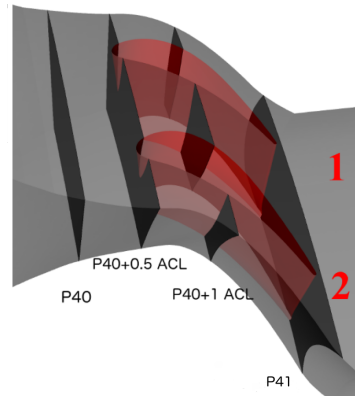


**Figure 6.15:** Observation planes used for following discussions.

The consequences of different inlet conditions are well visible on temperature fields which appear to be quite sensitive to the modifications imposed at the inlet and the associated changes of secondary flow structures. Temperature fields of Cases a) and b) 1 ACL downstream of P40 are almost identical (see Fig. 6.16). For Cases c) and d), the general flow organization is similar, temperatures however attain more extreme values, which can be attributed to a lack of mixing in both cases. In Case e) values attained are even more extreme, illustrating less mixing between hot and cold streams. The flow organization is disturbed by stronger vortices present in this case, as demonstrated earlier in the discussion around Fig. 6.11. On P41, at the exit of the nozzle, Cases a) and b) are still mostly

identical (see Fig. 6.17), which again confirms the ability of the presented approach to recover the flow field of an integrated simulation. Cases c) and d) feature slightly more extreme values than previous cases, which is due to less mixing. The case with constant inlet conditions, shows even more extreme temperature values, notably in the NGV wake where temperatures are about 20 K higher than in the reference case. Using constant boundary conditions induces considerably less mixing. Secondary flow structures also impact the temperature distribution in the vane passage. In the middle of Fig. 6.17e, cold air from the outer liner is seen to be pulled down and migrates along the NGV surface through the channel (to be discussed later). Here again, comparing Case e) with the other cases, the importance of the PVC for the mixing of hot and cold flow and also the impact of secondary flow structures becomes evident.

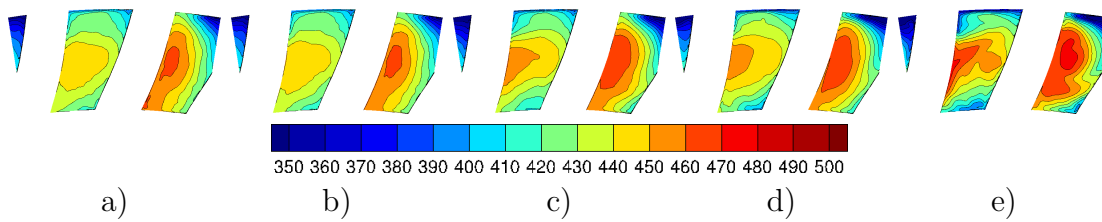


**Figure 6.16:** Average static temperature [K] on P40 + 1 ACL. a) Reference, b) All modes, c) Without first ten modes, d) First ten modes, e) Constant.

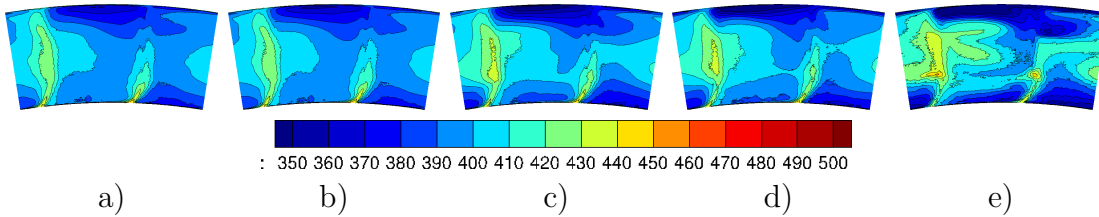


**Figure 6.17:** Average static temperature [K] on P41. a) Reference, b) All modes, c) Without first ten modes, d) First ten modes, e) Constant.

Considering temperature PDFs for all points on P41 over the entire simulation duration of 40 ms (stored every 0.02 ms) allows a more quantitative view on previous observations. Temperature values on the stator exit plane show a normal distribution (skewness=0) for reference case (Case a), all POD modes (Case b) and the case without the first ten modes (Case c) (see Fig. 6.18), which clearly shows the effects of mixing through the vane passage. Maximum hot and cold temperature values are identical for reference and all modes simulation (Cases a&b). The case using all but the first 10 modes (Case c) shows less extreme values, which is explained by the smaller bandwidth of values on P40. For the case using only the first ten modes (Case d) the temperature distribution is more skewed at the inlet if compared to the other cases (compare with Fig. 6.9), which is also conserved through the vane passage. Extreme temperature values (e.g. values below 300 K or above 450 K) reached in this simulation are however similar to the reference case, as already observed on P40. Using constant boundary conditions at the in-

let (Case e) results in a double peaked temperature distribution at the exit plane and also less extreme temperature values. Here, the lack of mixing due to the absence of an unsteady inlet condition is again evident. The two separate peaks are representative for coolant flow, mainly found close to the liners, and hot flow, mainly found around the wake of NGV1. Although not featuring the highest temperature values (not above 495 K), the right peak of the PDF indicates a higher probability to encounter high temperatures than in the other predictions. In an industrial context, using such constant inlet boundary conditions, may therefore lead to overpredicted temperatures and oversized cooling systems, as will be shown later on in this chapter.

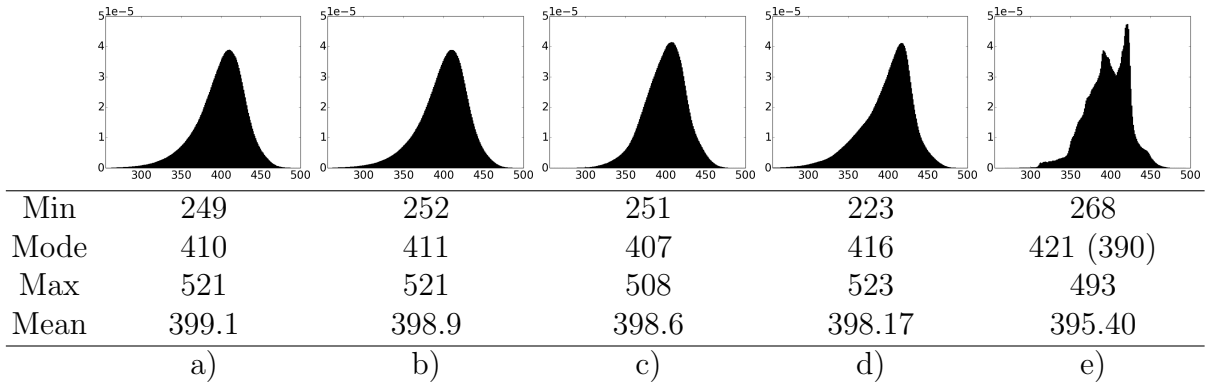


**Figure 6.18:** Temperature [K] distribution on P41 over 40 ms. a) Reference, b) All modes, c) Without first ten modes, d) First ten modes, e) Constant.

As expected and shown earlier in this chapter, higher order quantities such as  $T_{rms}$  are significantly more sensitive to the investigated modification of inlet conditions than previously discussed first order quantities. Comparing temperature fluctuations, 1 ACL downstream of P40, again shows a good agreement between Cases a) and b) (see Fig. 6.19), confirming that even higher order statistics, like  $T_{rms}$ , are well preserved by the presented methodology. For  $T_{rms}$ , the case using the first ten modes to reconstruct the inlet conditions (Case d) features higher values than the otherwise similar Case c). Considering the differences between Cases c) and d), one concludes that the PVC plays an important role in the mixing of hot and cold flow. Temperature fluctuations in the passage are to a larger extent triggered by the PVC (compare Case d) vs a), on Fig. 6.20) rather than by smaller scale turbulence (compare Case c) vs a), on Fig. 6.20). If using constant boundary conditions (Case e), temperature fluctuations stay low compared to other cases, due to the absence of changing temperatures at the inlet and globally rather constant aerodynamics that might otherwise lead to local temperature fluctuations. Further downstream, temperature fluctuations are strongest in the channel transporting the hot spot, close to the outer liner (see Fig. 6.20). This activity can, if looking at Fig. 5.38 in Chapter 5, be attributed to coolant flow migrating through the passage. At the nozzle exit, Cases a) and b) are again very close. Case d) shows more temperature fluctuations than Case c), which is in line with the fact that low order temperature modes contribute a larger share to the

$T_{rms}$  value than for the other quantities imposed ( $\rho u$ ,  $\rho v$ ,  $\rho w$ ) at the inlet (see discussion around Fig. 6.6). While high levels of turbulence do not necessarily imply high  $T_{rms}$  values, a certain level of macro scale flow motion is needed to obtain high  $T_{rms}$  values. In the case of FACTOR, such large scale flow motion is mainly triggered by the PVC. Note also that in adiabatic simulations, if no additional fluid at a different temperature is added, as is the case in the present vane simulations,  $T_{rms}$  average values decline continuously from inlet to the exit of the domain. Case c) featuring higher modes, with smaller scale, more localized flow motion cannot achieve the same level of mixing between hot and cold flow which explains the lower  $T_{rms}$  in this case. For Case e),  $T_{rms}$  values are again very low.

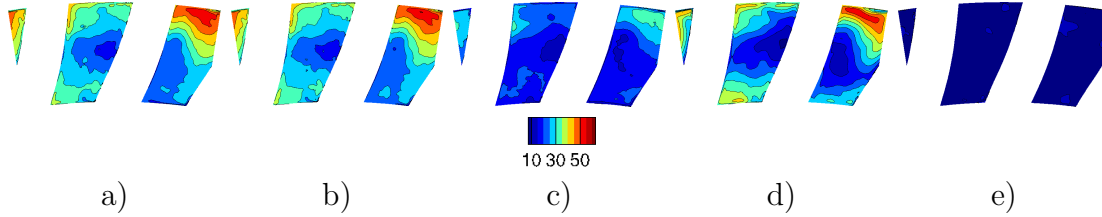


**Figure 6.19:**  $T_{rms}$  [ $K^2$ ] on P40 + 1 ACL. a) Reference, b) All modes, c) Without first ten modes, d) First ten modes, e) Constant.

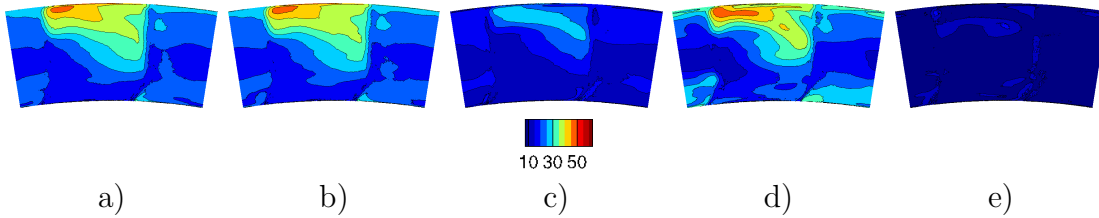


**Figure 6.20:**  $T_{rms}$  [ $K^2$ ] on P41. a) Reference, b) All modes, c) Without first ten modes, d) First ten modes, e) Constant.

To gain a global understanding of previously discussed temperature fields and PDF's, Figure 6.21 shows the evolution of integrated  $TKE$  and  $T_{rms}$  over planes through the passage. Due to interactions with the NGVs,  $TKE$  values for all simulations increase through the vane passage.  $TKE$  values for reference simulation (Case a) and that with the fully unsteady inlet signal (Case b) correspond very well. For the case using constant boundary conditions (Case e),  $TKE$  levels are naturally zero at the inlet, but due to the presence of vanes in the flow, turbulence increases through the vane passage. Whereas the simulation using all POD modes without the first ten (Case c) starts off with higher levels of  $TKE$  on P40, the simulation using the first ten modes (Case d) reaches higher  $TKE$  levels in the end. This may be explained by the unsteady inlet signal regenerated using the first ten modes featuring longer turbulent time scales than the other case, as shown in the following. In contrast to  $TKE$ ,  $T_{rms}$  values generally decrease over the vane passage due to the continuous mixing of hot and cold flow. At the exit, due to mixing, temperature differences in the flow field are less significant and the temperature is lower due to expansion. Here again, the case using all modes and

the reference case are very similar. While starting with lower initial  $T_{rms}$  value than Case c), Case d) reaches a higher value in the end, the value being quite close to that of the first two simulations. Note also that for Cases d) and e),  $T_{rms}$  values are increasing over the vane passage, while values decrease for the other cases. For Case e),  $T_{rms}$  values stay however very low.

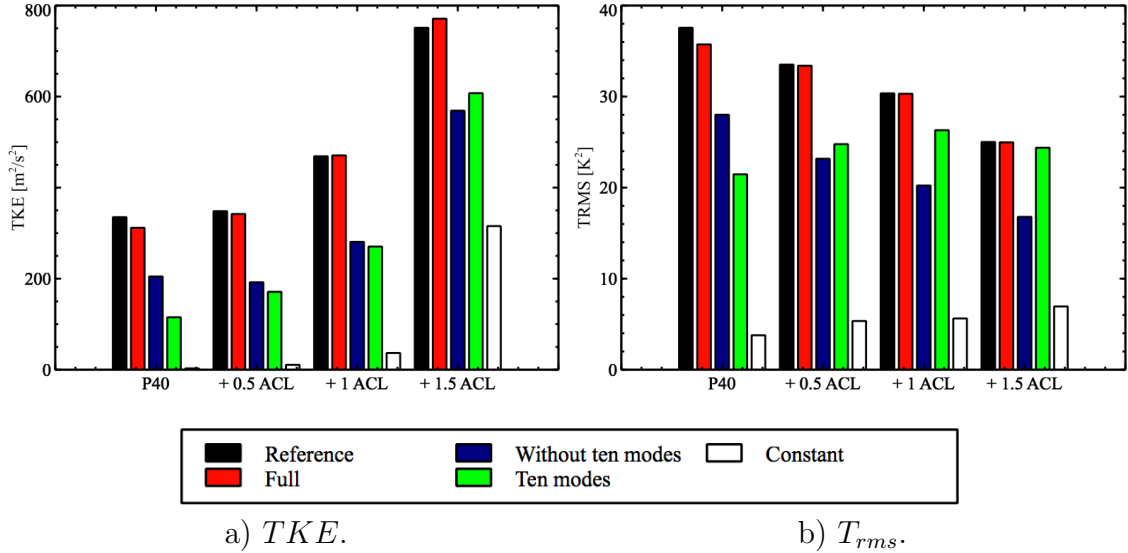


**Figure 6.21:**  $TKE$  and  $T_{rms}$  over planes through the NGV passage (see Fig. 6.15 for locations).

To better explain the evolution of  $TKE$  values on consecutive planes through the vane passage, turbulent timescales on P40 can be taken into account (see Fig. 6.22). In Case c) turbulent timescales and equivalently length scales are significantly shorter than in Case d). Turbulence thereby dissipates faster and does not produce more turbulence when interacting with the vanes which explains the evolution of TKE (growth of  $TKE$  of Case d) - first ten modes vs Case c) - without first ten modes) shown on Fig. 6.21.

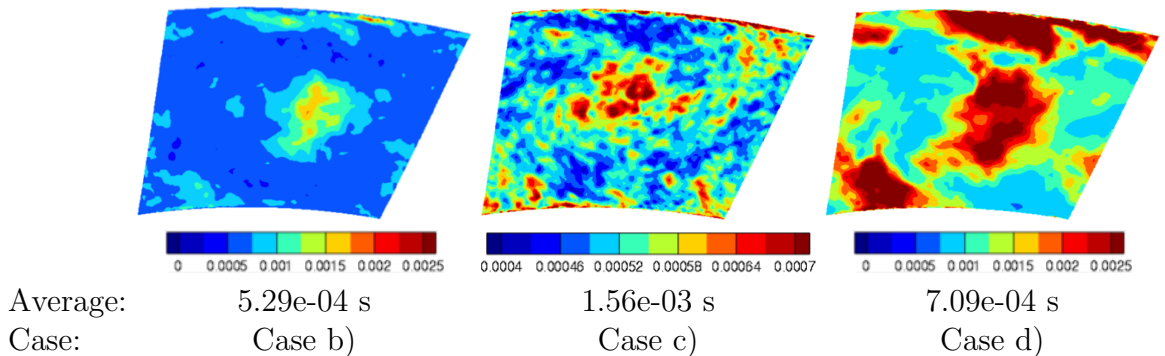


**Figure 6.22:** Turbulent timescale calculated on the axial velocity component imposed on P40. Note that the values for Case a) correspond to those of Case b) and that due to constant inlet boundary conditions for Case e) no turbulent timescale can be calculated.

From the previous discussion, at specific location in the vane passage one con-

cludes that the impact of the different inlet modeling approaches is more visible when considering higher order statistics, rather than averaged quantities. The PVC, imposed at the inlet of Case d), has one specific frequency, so the next step is to investigate for the presence of such a frequency in the flow field. As previously stated and shown in Chapter 5, the PVC breaks down within the chamber so there is no direct physical presence of the PVC in the vane passage, which is in line with results available from literature [135]. Still, a dominant flow structure at the PVC frequency considerably impacts the flow field as shown in the previous discussions. In the following, a DMD analysis is applied to investigate the presence of this activity for each case. Figure 6.23 shows the DMD spectrum obtained from an analysis of instantaneous solutions stored every  $2e-5$  s on the exit plane of the nozzle. The marked peak at  $500$  Hz, captured by the reference simulation (Case a), all modes (Case b) and 10 modes (Case d), corresponds to the PVC frequency. The simulation using 2D constant boundary conditions (Case e) shows only low levels of excitation and that using the full reconstructed inlet without the first ten modes (Case c) does show some excitation, however not at the frequency of the PVC. These findings demonstrate the following:

- Isolated vane simulations using reconstructed unsteady boundary conditions can indeed conserve most of the dynamics of the flow.
- The POD methodology is capable of extracting certain flow features and to recast them on a stand-alone high-pressure vane simulation.
- The PVC in the FACTOR geometry has a strong impact on the entire flow field, even downstream of the nozzle.

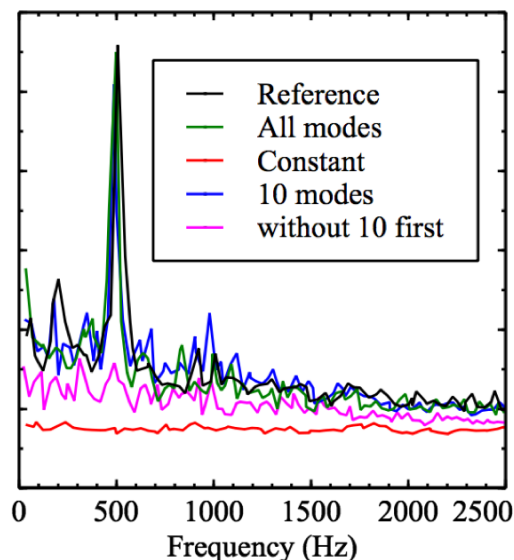


**Figure 6.23:** DMD analysis of pressure on P41.

The detailed insights provided in this section allow for a better understanding of the flow field and the differences related to the inlet modeling which distinguishes

one case from the other. In the next section the focus lies on the NGV wall and how the temperature distributions change for each of the considered cases.

#### 6.4.4 Impact on the high-pressure vanes

To finish, the impact of the different inflow specifications on the NGVs is discussed using the temperature field on the vane surface, which allows to identify the effects of the inlet conditions on the entire channel height. NGV1 is aligned with the swirler (outside of the numerical domain) and is directly hit by the hotspot (see Fig. 6.24). All simulations capture this and clearly mark NGV1 as that exposed to the highest temperatures. Note at this point that the application of the WALE SGS model instead of the Smagorinsky model used in Chapter 5 leads to differences in the temperature distribution on the NGV surface, if compared to results presented in Chapter 5. In present simulations coolant flow stays mostly close to the liner and is not pulled down towards mid height, implying an impact of the said model on secondary flow structures in the vane passage (see Appendix A for more details). The NGV surface temperature of the case using all modes (Case b) is very close to the reference case (see Fig. 6.24), demonstrating again the potential of the presented approach to improve isolated high-pressure vane simulations. Degrading the inlet signal leads to less mixing in the passage and more pronounced hot and cold regions on the blade surface. Furthermore, the reduction of excitation at the inlet promotes the creation of persistent vortex structures (see discussion around Fig. 6.11) that account for a large part of the changes of the temperature distribution on the NGV surface. In the simulation using constant boundary conditions (Case e) vortices leave a clear trace on the NGV surface as they transport coolant flow towards the middle of the channel. Temperature PDF distributions on the NGV surface over the time period of 40 ms permit again a more quantitative comparison of all cases (see Fig. 6.25). Here differences between reference case and that using all modes are stronger than in previous comparisons. In both cases extreme temperature values are however still in agreement. As previously on P41 (compare Fig. 6.18), Case c) shows a deficit of extreme temperature values (e.g. below 400 K and above 500 K), especially for the lower values. The temperature distribution shows marked peaks for constant boundary conditions simulation (Case e) which is due to the absence of mixing of hot and cold flow downstream of P40, as discussed earlier in this chapter. Due to the constant boundary conditions, this simulation also lacks extreme temperature values that occur intermittently in other cases. Here, Case e) shows the strongest differences between NGV1 and NGV2, when compared to other cases. In an industrial context, where usually at best 2D time constant inlet boundary conditions are applied, this may again lead to overestimated temperature challenges for one of the NGVs, the consequence of this being oversized cooling systems and a loss of efficiency of the engine.

When considering higher order statistics, such as RMS on the NGV surface, differences between presented cases become more apparent (see Fig. 6.26). High  $T_{rms}$  values can be observed close to the outer and inner liner, where mainly coolant flow migrates through the passage. As previously mentioned,  $T_{rms}$  values at mid height of the blade, where the hotspot migrates through the passage, are

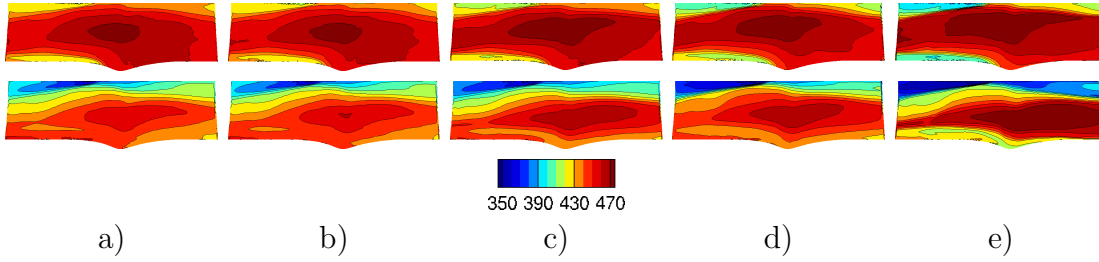


**Figure 6.24:** Average temperature [K] on NGV surface. NGV1: upper, NGV2: lower. a) Reference, b) All modes, c) Without first ten modes, d) First ten modes, e) Constant.

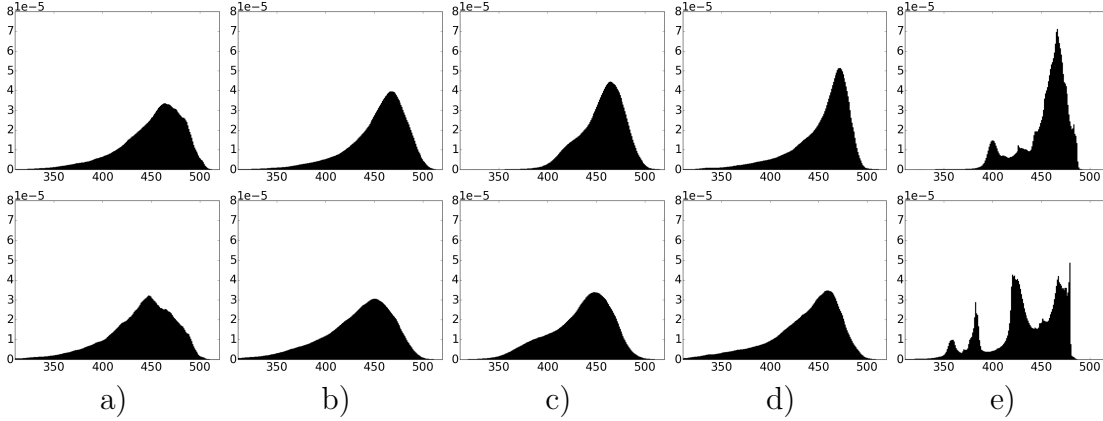


**Figure 6.25:** Temperature distribution NGVs over 40 ms. NGV1: upper, NGV2: lower. a) Reference, b) All modes, c) Without first ten modes, d) First ten modes, e) Constant.

generally lower. For Case a) and b) there is still a good agreement, however locally small differences are visible. As expected, cases with degraded inlet signal show lower  $T_{rms}$  values on the vane surface. Removing the first ten modes from the inlet signal leads to low  $T_{rms}$  values, with however generally similar distributions. Imposing only the first ten modes at the inlet, yields comparatively high  $T_{rms}$  values, especially close to the outer liner. This again underlines the importance of the PVC in mixing of hot and cold flow and also the impact of this flow structure in the high-pressure vanes domain. At the pressure side trailing edge,  $T_{rms}$  values are slightly higher than in the reference case. As previously noted, activity in Case e) is rather low which explains low values observed on the NGV surface.

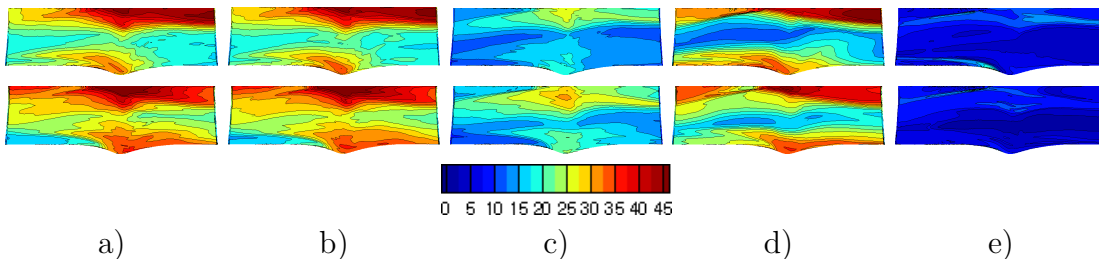


**Figure 6.26:**  $T_{rms}$  [K] on NGV surface. NGV1: upper, NGV2: lower. a) Reference, b) All modes, c) Without first ten modes, d) First ten modes, e) Constant.

## 6.5 Conclusions

The objective of this chapter was to investigate how to perform LES of isolated domains and to determine the impact of specific flow features extracted by means of POD. To do so, POD is used to perform a modal decomposition of the flow field in the integrated chamber + NGV domain. This allows to clearly identify the PVC, represented by the first few POD modes, as the most energetic flow feature in the domain. The intersection plane between chamber and NGV part is likewise analyzed by means of POD, which is then used to recreate different inlet conditions for isolated NGV simulations, using specific ranges of POD modes representative for the fully unsteady flow field or previously identified flow features, like the PVC. When imposing all POD modes retrieved from P40 of an integrated simulation, the flow field of the chamber + NGV prediction could be recovered remarkably well in the isolated NGV domain, even if considering instantaneous flow fields and higher order statistics. The presented approach may thereby point a way to perform more realistic isolated high-pressure vanes simulations without simulating the entire combustion chamber. Today, high fidelity LES of the combustion chamber are quite common and provide a source of data whose exploitation could indeed improve simulations of isolated high-pressure vanes. A further potential source of unsteady flow field data are measurements with a high spatial and temporal resolution, e.g. HWA. To allow for an application of the presented approach in an industrial design process, further work is needed to treat commonly incongruent periodicity angles between chamber and high-pressure turbine. This seems indeed quite feasible by duplication of the inlet signal for multiple vane LES.

The PVC, as the most energetic structure in the chamber strongly impacts the flow field in the high-pressure nozzle, as already explained in Chapter 5. Here it was shown, that the PVC plays an important role for the mixing between hot and cold flow. Nevertheless, differences between first order quantities for unsteady cases using all modes without the PVC (Case c) or the PVC as inlet signal (Case d) are limited. One reason for this is that these averaged quantities are identical at the inlet. Another point is that an unsteady inlet prevents the formation of strong and persistent vortices which are seen to strongly change the flow behavior in Case e) using constant inlet boundary conditions. A closer investigation of higher order quantities, available from LES, reveals however differences that can be directly contributed to the PVC:

- 1) Locally, RMS values are strongly increased, which is visible throughout the passage.
- 2) When analyzing the flow field using DMD, one can clearly identify strong flow excitation at PVC frequency. This alone may not impact the present simulations to a large extent - In a more complex simulation or in reality the strong excitation at the distinct PVC frequency may however lead to stronger changes in the flow field due to resonance effects depending on the specific geometry of vanes or cavities of the cooling system.

Comparing all cases described in this chapter leads to the conclusion that the high pressure vane domain is highly sensitive to the flow field provided at its inlet, as already mentioned in Chapter 5. Flow features identified to have a major impact

on the flow field in the vane passage, like the PVC and secondary flows, strongly depend on the modeling approach of the inlet condition. Using constant inlet boundary condition, often applied due to unavailability of transient inlet data and cost reasons, was found to yield strong vortical structures. This strongly affects the temperature field on the NGVs and also the loss prediction of such blades. A time-constant 2D inlet boundary condition, often applied in an industrial context, is found to yield harsher aerothermal conditions than predicted in the case using the fully unsteady flow field. Consequently cooling needs in industrial simulations may tend to be overpredicted, which may lead to oversized cooling systems and a loss of efficiency for the engine. The procedure shown in this chapter may point a way to produce more realistic isolated high-pressure vane simulations of industrial geometries, without the necessity of performing costly integrated simulations of chamber and high-pressure turbine.



# Chapter 7

## Combustor turbine interactions

### Contents

---

7.1	Introduction . . . . .	<b>153</b>
7.2	Experimental Setup . . . . .	<b>154</b>
7.3	Domain, Mesh and Numerical Setup . . . . .	<b>155</b>
7.4	Results . . . . .	<b>157</b>
7.4.1	Flow field in the combustor simulator . . . . .	157
7.4.2	Flow field in the high-pressure vane passage . . . . .	161
7.4.3	Flow field in the rotor . . . . .	165
7.5	Conclusions . . . . .	<b>169</b>

---

### 7.1 Introduction

Gas turbine engines feature complex geometries and the interior flow field is governed by a multitude of different physical phenomena, which renders accurate predictions of the flow field a very challenging task. Accurate measurements of the flow at nominal operating conditions are often difficult, which makes CFD a primary choice to gain insight in the flow field. The European FACTOR<sup>1</sup> project, which is the basis for the herein presented research, addresses the issue of combustor-turbine interactions and the transport of hot spots in the next generation lean combustion chambers using a joint CFD and experimental approach on a full annular non-reactive test rig [3]. The objective is to gain a better understanding of interaction phenomena in next generation compact design lean combustion engines and to improve CFD predictions. One particular numerical challenge for the simulation of multi-component turbomachinery devices is the coupling of rotating and stationary domain and also the presence of different flow regimes in combustion chamber (low Mach number) and turbine (high Mach number). Only few

---

<sup>1</sup>FACTOR (Full Aerothermal Combustor Turbine interactiOns Research) is a European research project co-funded by the European Commission to investigate interactions of lean combustion chambers with the hp-turbine.

CFD codes are available to simulate both domains simultaneously and with great accuracy. In this work, Large-Eddy Simulation (LES) predictions of combustion chamber and complete single-stage high-pressure turbine are compared with experimental results to gain insight into the interaction phenomena present between combustion chamber, stator and rotor. Experimental data obtained by means of a five-hole probe (velocity angles, static & total pressure, static & total temperature) is available on observation planes P40 (exit of the combustion chamber), P41 (exit of the stator) and P42 (exit of the rotor). The results presented herein extend on previous work published at the ASME Turbo Expo 2019 [30] and further simulations will be performed at CERFACS.

First, the test rig is introduced, followed by the presentation of the numerical approach. The result section presents predictions of an integrated LES with combustion chamber and complete single-stage high-pressure turbine as well as RANS predictions performed on the nozzle only. The results section is divided in three parts: 1. Combustion chamber, 2. High-pressure vanes, 3. Rotor, which are individually compared and discussed.

## 7.2 Experimental Setup

The FACTOR test rig installed on the NG-turb test facility at DLR Göttingen is designed as a full annular non-reactive full scale closed loop wind tunnel. The rig operates at engine representative Mach- and Reynolds number and allows continuous operation over several hours to ensure high quality measurements. 20 identical 18° sectors are each equipped with one swirler, two NGVs, three rotor blades and one strut airfoil (not simulated here). Before entering the swirler, air is heated to 530 K. The swirler is restrained by a duct to avoid early interaction with the effusion cooling system and neighboring swirlers. Coolant air is injected through multiperforated liners in the combustor simulator, the NGV blades and purge flows between the rotating and stationary parts.

The FACTOR rig allows instrumentation access at different positions in the rig (see Fig. 7.1) [17]. Measurements on P40, P41 and P42, shown hereafter, have been obtained by a 5-hole probe mounted on a traverse system that covers about 95 % of the channel height. Further measurements are available from pressure taps on two NGV blades at mid height of the channel.

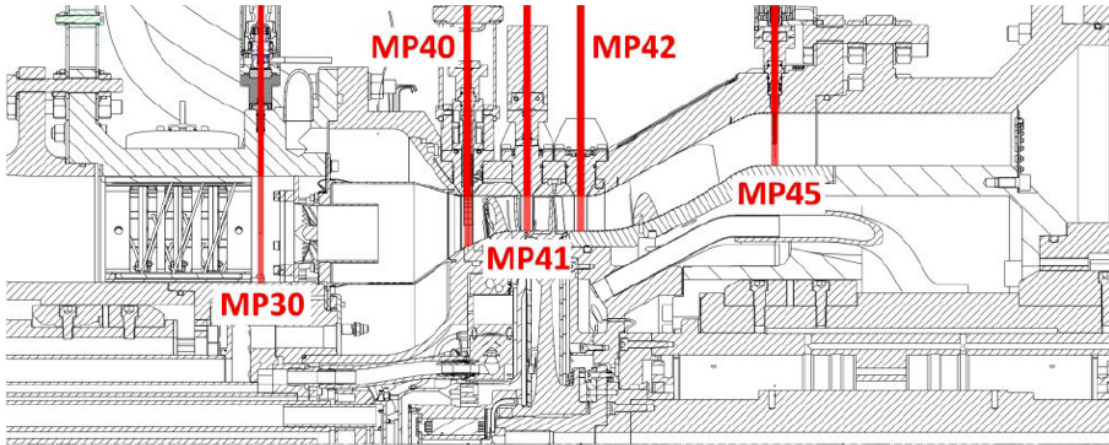


**Figure 7.1:** Measurement planes at FACTOR test rig [17].

### 7.3 Domain, Mesh and Numerical Setup

In the numerical approach one  $18^\circ$  section is simulated and the swirler is aligned with the leading edge of NGV2 (see Fig. 7.2). Inlets are defined as mass flow inlets and the outlet boundary condition is defined as a pressure outlet. Values at the main inlet are imposed using Navier-Stokes characteristic boundary conditions [56] and the pressure imposed at the outlet allows to naturally establish a radially equilibrium pressure profile [15]. Effusion cooling systems at interior and exterior liner are modeled using a heterogeneous coolant injection model (introduced in Chapter 3) [84,88]. The same model is applied on the NGVs to mimic the injection of coolant fluid on the NGV surface (investigated in Chapter 4) This approach uses a coolant distribution obtained from previous Reynolds averaged Navier Stokes (RANS) simulations of the isolated stator domain with fully featured NGV-cooling system [95]. Purge flows are included in the domain and allow for the injection of cold air at the intersection of stationary and turning parts. Walls are considered adiabatic and the near-wall behavior is modelled using wall functions based on a log law [137]. Inlet conditions are summarized in Tab. 7.1. The operating conditions finally obtained in simulations are summarized in Tab. 7.2. Note that due to an initial unintentional higher mass flow at the interior effusion cooling system, values from simulation and experiment differ. Further, as demonstrated in Appendix A, the choice sub grid scale model may yield pressure predictions that differ by 1 kPa and more.

Grids for static and rotating domain are generated separately as partly overlapping fully unstructured tetrahedral grids. The overset of both grids allows by application of the MISCOG method [139] the coupling of both computational domains. The simulation of stationary and turning part is performed using two separate instances of the AVBP code coupled by OpenPALM [140]. The static domain is discretized by 70 M cells and has been designed in accordance with a previous mesh refinement study for the FACTOR geometry [16]. At the combustion chamber liners, the mesh is refined ( $\Delta x \approx 0.25$  mm) to allow the representation of

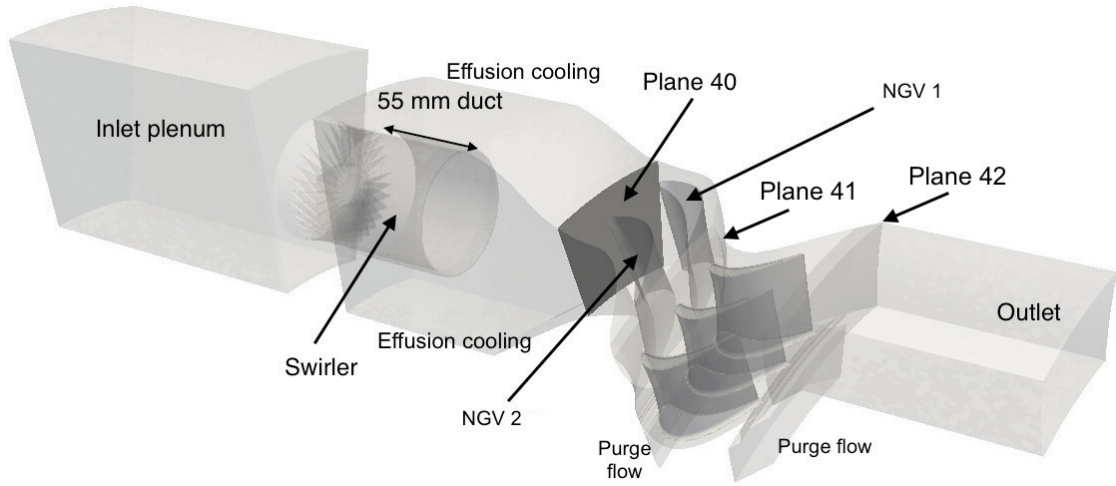


**Figure 7.2:** Numerical FACTOR domain [138].

**Table 7.1:** Inlet data for one sector of the FACTOR test rig at DLR Göttingen (Total mass flow in brackets).

Swirler mass flow	[kg/s]	0.1545 (3.09)
Effusion cooling interior liner	[kg/s]	0.0335 (0.67)
Effusion cooling exterior liner	[kg/s]	0.0475 (0.95)
Rotor front cavity purge flow	[kg/s]	0.0036 (0.072)
Rotor back cavity purge flow	[kg/s]	0.0036 (0.072)
NGV coolant feed mass flow	[kg/s]	0.018 (0.36)
Swirler air temperature	[K]	530
Coolant temperature	[K]	300
Turbine rotor RPM	[rpm]	7700

**Table 7.2:** Operating conditions for Experiment and Simulation.

		Experiment	Simulation
P40 (static = total) pressure	[kPa]	142.4	143.3
P41 total pressure	[kPa]	137.8	139.8
P42 total pressure	[kPa]	59.3	62.3
P40 (static = total) temperate	[K]	447.51	430.11
P41 total temperature	[K]	427.7	423.9
P42 total temperature	[K]	353.1	335.1

individual coolant jets on the wall. In the swirler  $y^+$  averages around 70 whereas the value ranges between 20 at the NGV leading edge and 150 at the NGV trailing edge. The rotor domain with fully meshed purge flows contains 35 M grid cells

and  $y^+$  values average around 70 for the rotor blades with lower values on leading edge and trailing edge due to refinements.

Simulations presented in this work are performed using AVBP by [60], a code developed at CERFACS to solve the filtered compressible Navier-Stokes equations for LES. The simulation is converged for 200 ms, corresponding to 20 characteristic through flow times of the combustor module, using the Lax-Wendroff scheme [66] (second order accurate in space and time). Data collected for comparison extends over 40 ms. Sub-grid scale (SGS) turbulent contributions are computed using the classical Smagorinsky model [51]. Using the classical gradient diffusion hypothesis [38] the SGS heat flux is related to the filtered temperature gradient with a SGS thermal conductivity computed with a SGS turbulent Prandtl number of 0.6. Time marching is done, respecting CFL number [94] (convection scheme) and Fourier number [70] (diffusion scheme) to guarantee linear stability. For the purpose of statistical evaluations, the time step is fixed to 4.E-8 s ( $CFL \approx 0.9$ ) during the data collection period. The computational cost for convergence of the simulation are 1 M CPU hours.

Apart from LES at CERFACS, RANS simulations were performed by different partners of the FACTOR consortium. These simulations use experimental data from P40 as inlet condition (presented in Section 7.4.1 and simulate the NGVs with fully resolved cooling system. On P41, results are compared with LES data.

## 7.4 Results

In this section, LES predictions for the fully integrated LES of combustion chamber and complete single-stage high-pressure turbine are discussed and validated against experimental data obtained at the FACTOR test rig at DLR Göttingen. First, the flow field in the combustor module, then the flow in the stator domain and at last the flow field in the rotor part, is discussed. All observation planes (P40, P41, P42) are in the stationary domain. Previous studies and validation of simulations extending over combustion chamber or combustion chamber and high-pressure vanes are similar to the flow field obtained from the fully integrated simulation of combustor and complete single-stage high-pressure turbine [24, 141]. These studies underline the importance and impact of an unsteady chamber flow field on the flow in the high-pressure turbine domain [11, 142].

### 7.4.1 Flow field in the combustor simulator

The main flow enters the combustor simulator through a swirler which creates a Processing Vortex Core (PVC), visible as a low pressure zone in Fig. 7.3a. Kelvin-Helmholtz instabilities at the duct edges are visible as low pressure zones and the injection of coolant is seen to locally increase the static pressure level near the liners. Coolant injected at the combustion chamber liners penetrates into the flow and locally mixes with hot air coming from the swirler (see Fig. 7.3b). Due to the presence of a confining duct and the absence of dilution holes in the FACTOR combustion chamber, the hot streak traveling through the chamber remains largely

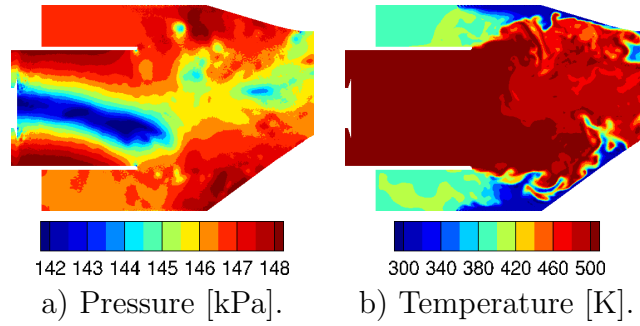


**Figure 7.3:** Central axial cross section cuts of the instantaneous flow field through the swirler from swirler to P40.

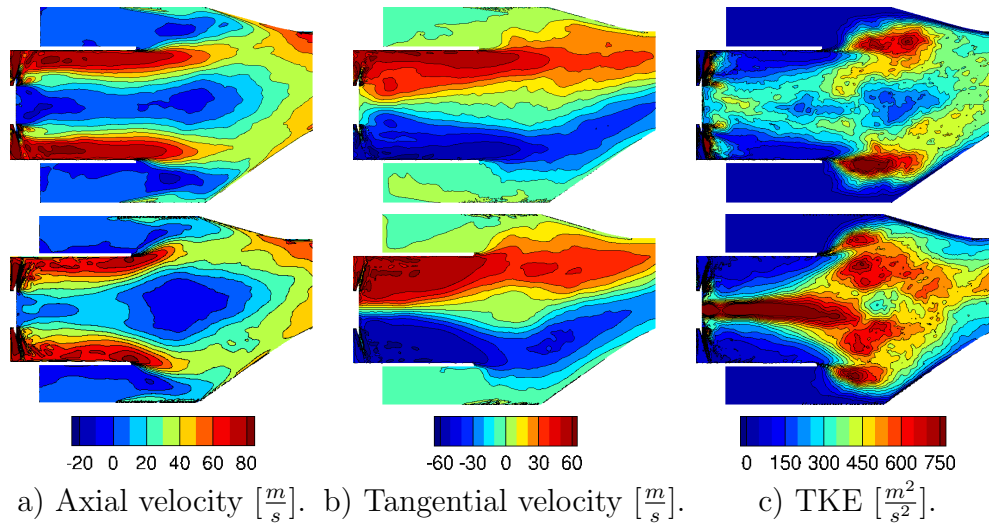
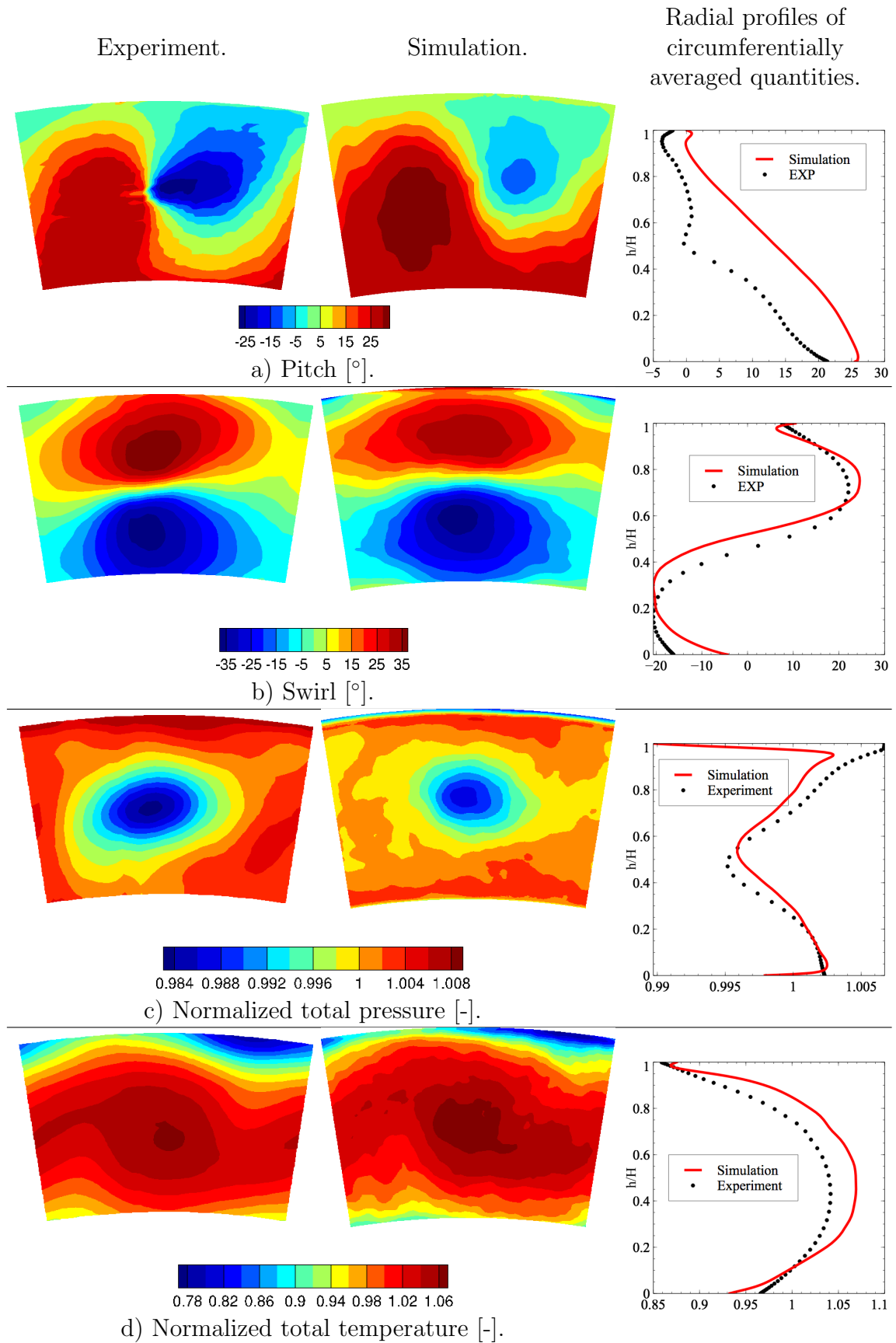


**Figure 7.4:** Central axial cross section cuts of the averaged flow field through the swirler from swirler to P40. Upper row: Combustion Chamber & NGVs (Chapter 5); Bottom row: Combustion Chamber & Hp-turbine

undiluted by the coolant air. Compared to simulations previously discussed in this manuscript (e.g. Chamber & NGV in Chapter 5) the operating pressure and temperature is lower to meet operating conditions of the test rig at DLR Göttingen. Furthermore, the application of the heterogeneous coolant injection approach locally impacts the flow field close to the combustion chamber liners. Shortly after the exit of the duct, the flow field features a central re-circulation zone, evidenced by negative axial velocity (see Fig. 7.4a). This recirculation is caused by the break down of the fuel injection system generated PVC. In the simulation with the full high-pressure turbine, the recirculation zone is larger than in previous simulations. High levels of tangential velocity (see Fig. 7.4b) induced by the swirler can be found throughout the domain and contribute to a complex flow field on P40 as well as to a redistribution of coolant flow (to be discussed later). Close to the swirler, tangential velocities are higher in the simulation with the full high-pressure turbine. In the center of the duct, as well as at the edges of the duct in the shear layer high levels of turbulent kinetic energy (TKE) can be observed (see Fig. 7.4c). In the center of the duct, high activity is created

by the PVC, whereas at the edges the shear between the stagnant flow outside the duct and the high velocity flow inside the duct is responsible for the high levels of TKE. In the simulation with only the high-pressure vanes, turbulence levels in the center of the duct are lower as compared to the other simulation. The flow field in the FACTOR combustion chamber is dominated by the PVC and excitation at the PVC frequency of 500 Hz can be found in the entire computational domain. In the following comparisons with experimental data on P40 are shown. Further comparisons to prior simulations are not discussed as too many parameters (NGV coolant injection, heterogeneous effusion cooling model, clocking position, operating point, numerical scheme, sub-grid scale model) differ with respect to the simulation discussed in this chapter.

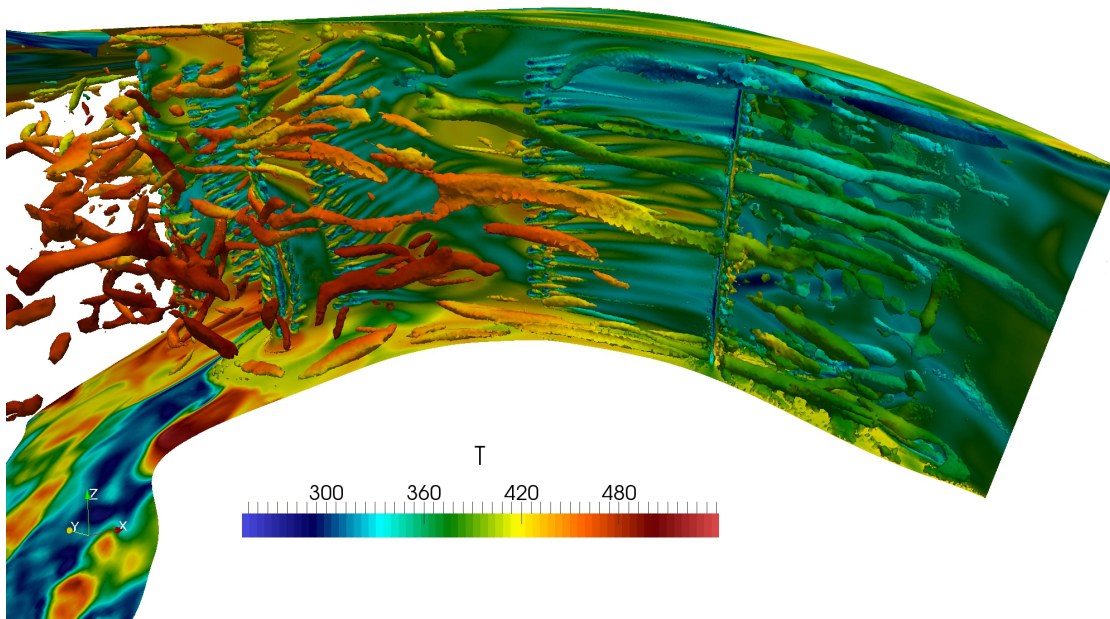
On P40, experimental data and predictions from high fidelity LES show an acceptable agreement for velocity angles and temperature (see Fig. 7.5a,b,d). The flow angles (see Fig. 7.5a,b) indicate strong residual swirl at the exit of the combustion chamber which is due to the absence of dilution holes and the compact design of the non-reactive lean combustion demonstrator. Note that on all observation planes the pitch angle shows the strongest deviation from simulations which may point to a systematic error in the measurements. The residual swirl core is visible as a low total pressure region on P40 (see Fig. 7.5c). Total pressure in the simulation is slightly higher, but shows a good qualitative agreement with the experiment. In the experiment differences between minimum and maximum pressure values are more pronounced than in the simulation. This finding together with elevated velocity angles in the experiment may point to a better conserved PVC in the experiment than in the simulation. Residual swirl impacts the temperature distribution by transporting coolant flow away from the liners to the center of the channel which creates a wavy pattern in the temperature distribution on P40 (see Fig. 7.5d). The temperature profiles on P40 agree well, except for the hub region, and show a very pronounced hot spot at channel mid height, typical for lean combustion configurations. Downstream of P40, the marked hot streak impinges on NGV2.



**Figure 7.5:** Flow field on P40 (intersection between combustion chamber and stator) for simulation and experiment. View direction: downstream.

### 7.4.2 Flow field in the high-pressure vane passage

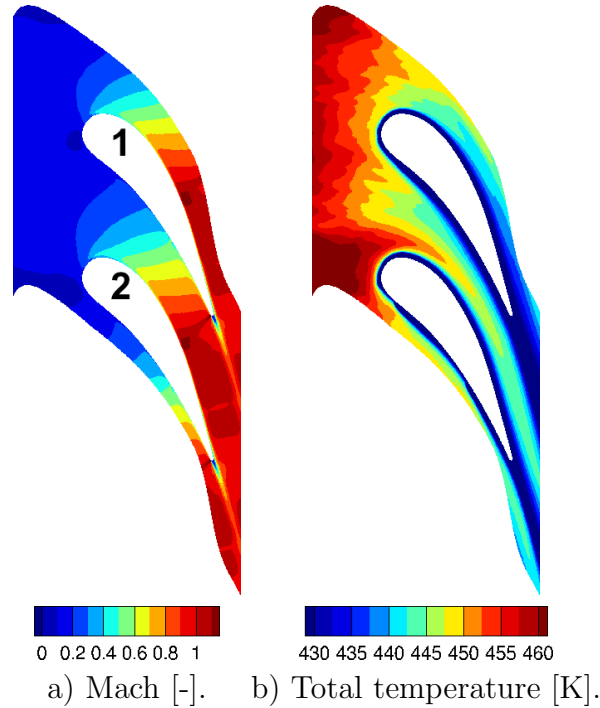
The activity in the chamber strongly impacts the flow in the high-pressure turbine [142] (see Fig. 7.6). Coherent flow structures, mainly created by the PVC, travel through the chamber and impact the NGVs. Horseshoe-vortices with a short lifespan are created at blade mid-height and are shortly afterwards transported away by the highly unsteady flow from the chamber. Corner vortices created close to hub and shroud are more persistent. In the NGV passage secondary flow structures are seen to impact the temperature distribution on the NGV surface by transporting cold air away from the liners over the NGV surface and by influencing the trajectory of coolant jets.



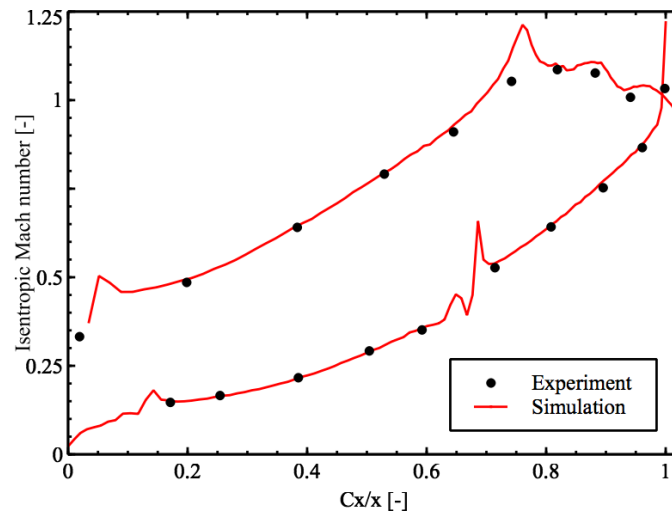
**Figure 7.6:** NGVs and  $q$ -criterion [136] of an instantaneous solution colored by static temperature.

Fig. 7.7a shows the acceleration of the flow in the nozzle and the formation of a shock at the NGV trailing edge. Although  $Mach=1$  is reached, the passage is not entirely choked. The hot spot is clearly centered on NGV2 (see Fig. 7.7b) and the coolant injected on the NGV surface is seen to stay close to the NGVs. Finally, isentropic Mach numbers calculated using the average total pressure on P40 and pressure taps at around mid-height of the channel ( $h/H \approx 0.5$ ) agree well with experimental results (see Fig. 7.8). Note that the pressure taps are placed on two different NGVs and the pressure for the simulation is obtained accordingly. Note also that the spike in the isentropic Mach number plot (see Fig. 7.8) is due to the shock hitting the next NGVs suction side.

When comparing the NGV temperature distribution for different simulations (see Fig. 7.9), temperature predictions differ close to the cooling system injection holes. This is explained by the fact that in both RANS simulations the coolant system was fully resolved, whereas in the LES it was modeled. In Chapter 4 the modeling approach was discussed and compared to a simulation with fully resolved



**Figure 7.7:** Average flow field at channel mid height in the high-pressure vane passage. Hot spot impinges on NGV2.



**Figure 7.8:** Isentropic mach number on NGV surface at mid height of the channel.

coolant injection system. In simulations with fully resolved coolant system, interactions between main flow and coolant flow occur and the coolant jets generally penetrate further into the flow. If using the model, coolant jets penetrate less far into the flow and coolant stays closer to the wall. This modeling impact is again visible on P41. Simulations commonly show that the area close to lower and upper liner is not reached by coolant injected from the NGV coolant system. Globally RANS predicts higher temperature values than the LES performed at CERFACS.

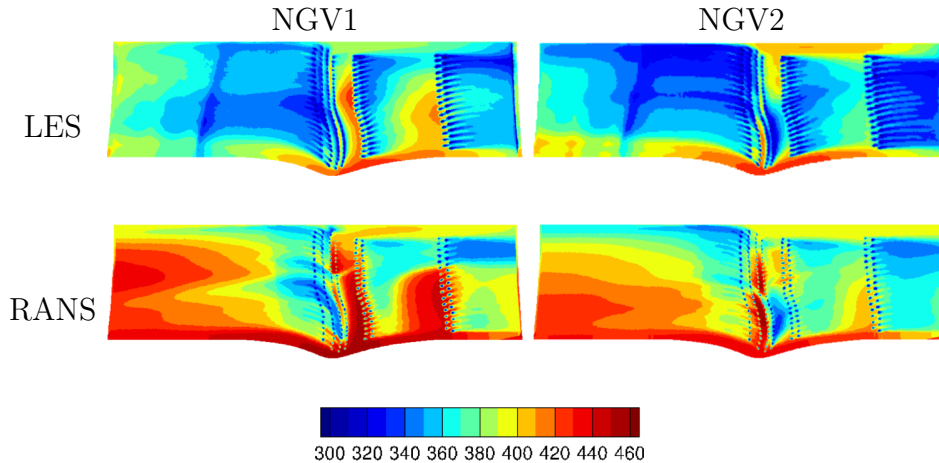


**Figure 7.9:** Flow field on P41 (after stator) for simulations and experiment. View direction: downstream.

On P41, LES results can be compared to measurement data and RANS simulations. Note that the RANS simulation does not simulate the combustion chamber, but uses experimental data on P40 as inlet conditions. When comparing the Pitch angle on P41 (see Fig. 7.10a) one notes rather high pitch angle values in the experiment close to the upper liner. This potentially indicates a systematic error with the measurements in this region. Such high pitch angles are unlikely close to the upper wall as it would indicate a strong upwards movement. In the passage clocking measurement campaign as well as in other simulations pitch angles measured are lower and more coherent with one another. Between numerical results there is generally a good agreement. Locally high pitch values are due to secondary flow structures previously discussed in this section. Plots of the Swirl angle (see Fig. 7.10b) typically show two distinct structures, due to the two NGVs in the investigation window. Here again numerical results seem somewhat more similar among themselves. If looking at azimuthally averaged profiles CERFACS LES corresponds best to the experiment in the upper half of the channel (see Fig. 7.10b). Total pressure plots clearly show the NGV wake as a low pressure zone (see Fig. 7.10c). Whereas wake positions show a reasonably good agreement, the pressure difference between wake region and channel is more pronounced in the simulation. On total temperature plots (see Fig. 7.10d), the NGV wakes are again visible, in this case due to the coolant injected to cool the NGVs. The total temperature plot shows that the hot spot migrates mostly through one passage (see Fig. 7.10d), whereas an important part of the coolant fluid injected by the effusion cooling system of the exterior liner migrates through the upper half of the second passage. The redistribution of coolant fluid is provoked by the residual swirl present in the entire compact design chamber and already visible on P40 (see Fig. 7.5d). Note that in RANS simulation, the coolant system is fully resolved. In the LES, the NGV coolant system consisting of 342 coolant injection holes is not resolved, but coolant is directly injected through discrete surface patches on the NGV surface. A previous study [95] shows that this may lead to underpredicted

mixing between coolant flow and main flow which explains colder NGV wakes in the simulation. In the shroud area the total temperature profile of the simulation agrees well with the experiment, whereas over the rest of the channel, total temperature values are higher. When comparing total temperature profiles, there is a rather good agreement between LES and experiment (see Fig. 7.11d).

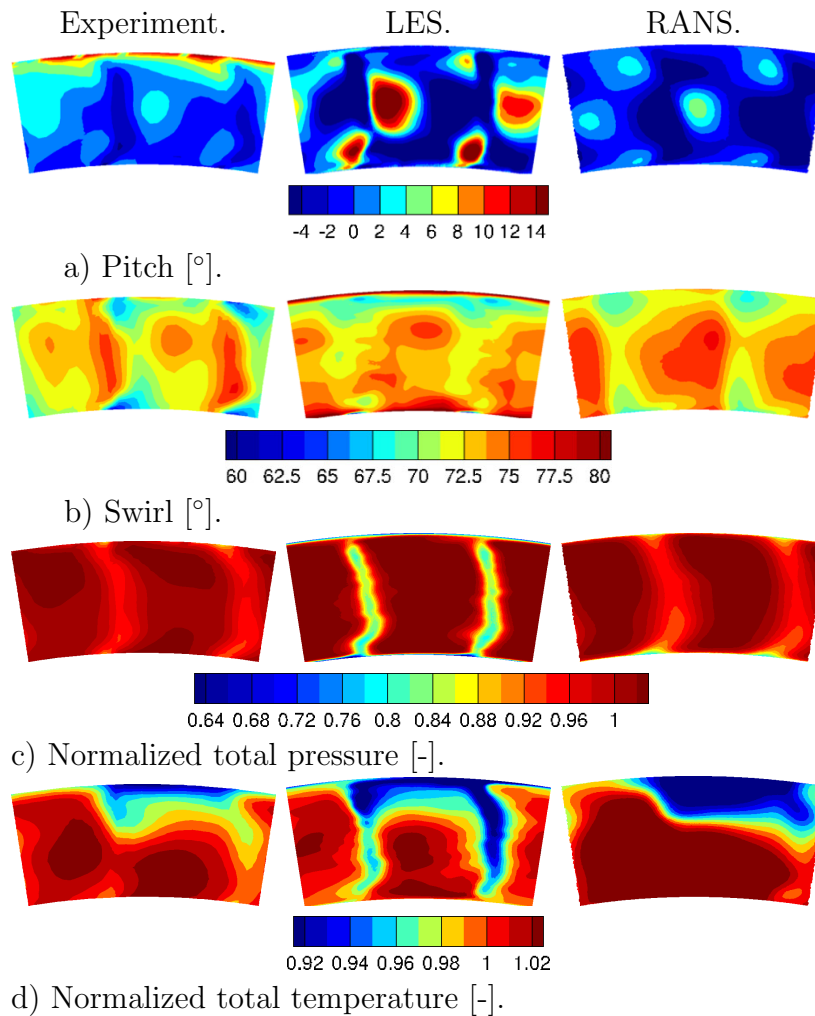


**Figure 7.10:** Flow field on P41 (after stator) for simulations and experiment. View direction: downstream.

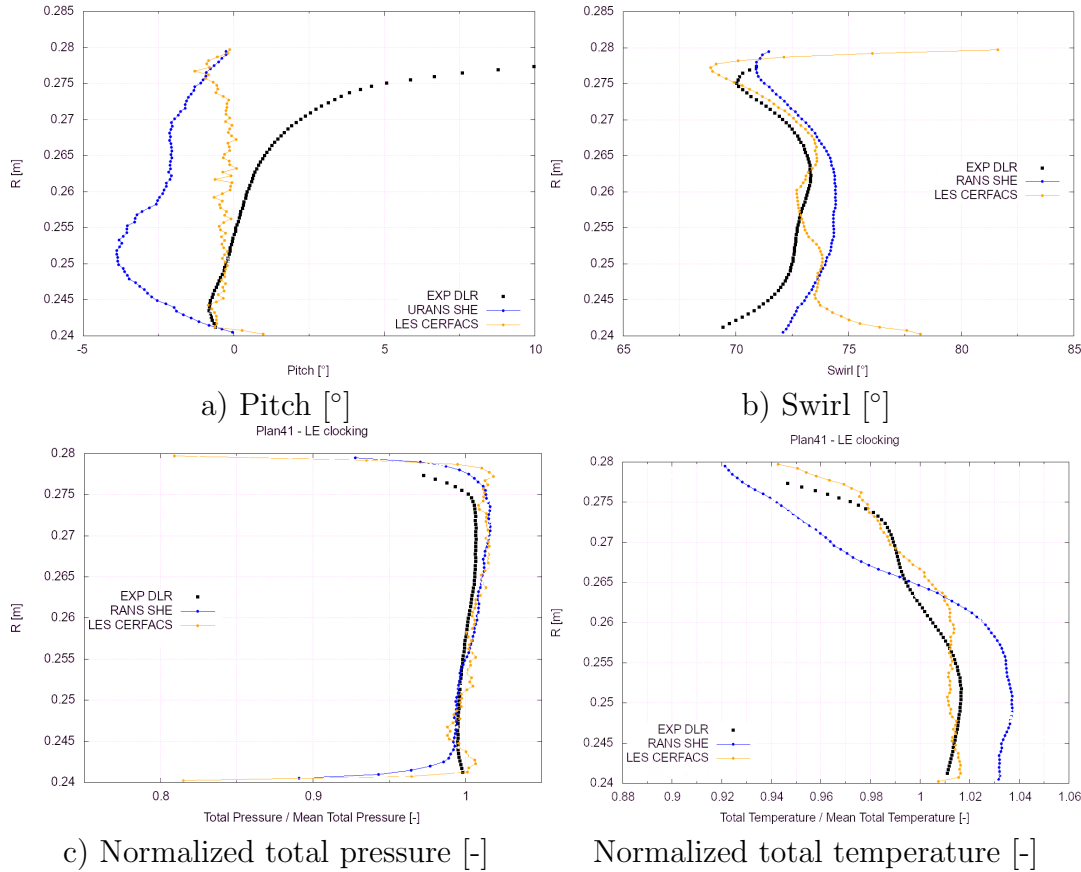


**Figure 7.11:** Azimuthally averaged profiles on P41 (after stator) for simulations and experiment.

### 7.4.3 Flow field in the rotor

The flow field in the rotating domain is highly unsteady (see Fig. 7.12). In the blade passage dominant vortex structures originating from tip and hub of the rotor blade impact the flow in the passage and have visible effects on P42 (to be discussed later). The rotor blade pressure side is generally exposed to higher temperatures than the blade's suction side.

Visualizing the rotor flow field at channel mid height allows to get a global view of the flow in the rotor before comparing flow fields on P42, at the rotor exit. Each  $18^\circ$  section simulated in this context contains three rotor blades. In average the flow field is identical for each passage. The flow is decelerated from  $\text{Mach} \approx 1$  to  $\text{Mach} \approx 0.3$  (see Fig. 7.13a). Temperature levels over the rotor drop by about 100 K (see Fig. 7.13b).

LES predictions on plane P42, situated after the exit of the rotor and the coolant flow injection, show a good agreement to experimental results (see Fig. 7.14). The agreement is a major improvement as compared to results from RANS/U-RANS simulations [18] that are very limited in their capacity to correctly predict instationary behavior that strongly influences the flow field in the high-pressure turbine. Effects of the rotor are azimuthally averaged and 2D plots (see Fig. 7.14)

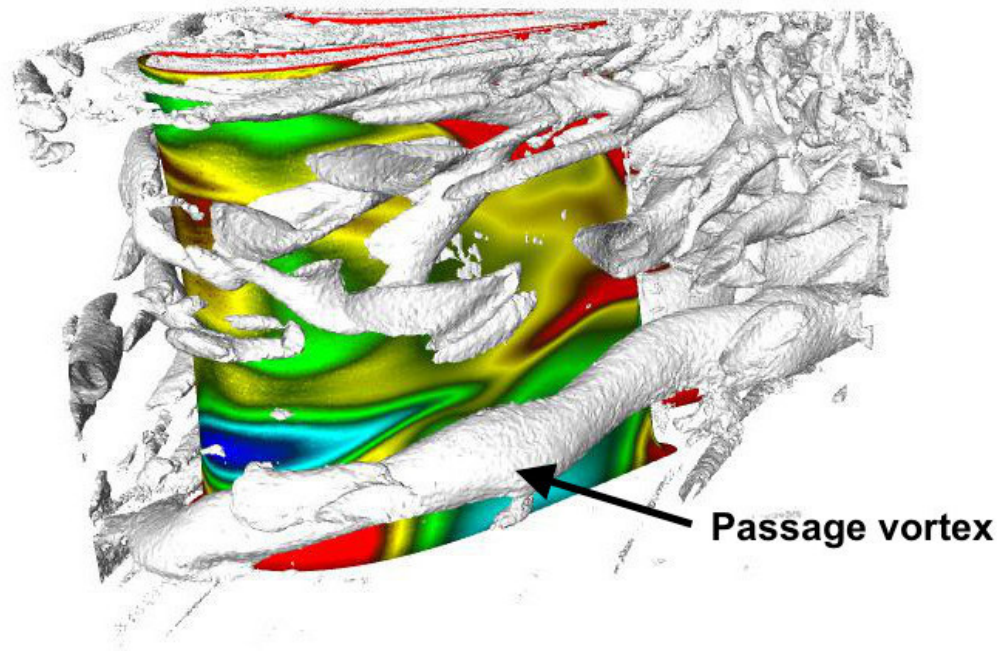


**Figure 7.12:** Vortex structures in rotor domain visualized by isosurface of  $Q$ -criterion and blade surface temperature [K] for one instantaneous solution. View on suction side of rotor 1.

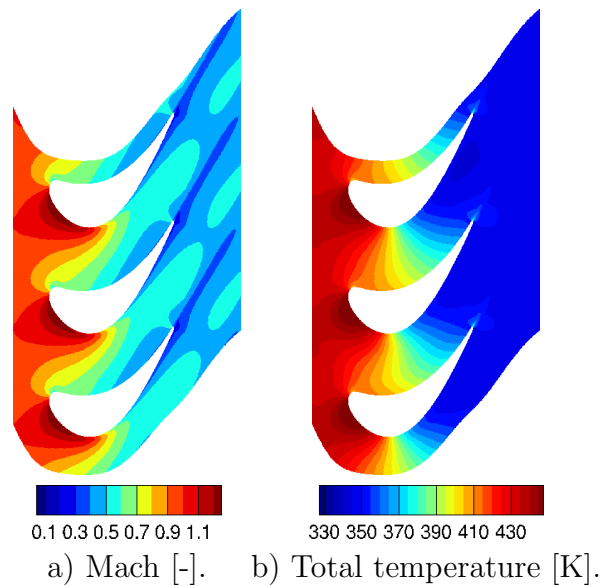


**Figure 7.13:** Average flow field at channel mid height in the high-pressure vane passage. Hot spot impinges on NGV2.

show a pattern of two similar structures that is created by the two NGV blades. Flow angles in the simulation only deviate by a few degrees from the experiment (see Fig. 7.14a,b). In the tip region differences are more important which may be due to the small tip clearance that is expensive to resolve in simulations. Tip vortices, created in this region are sensitive to small changes in the flow field and

may thereby behave different in the simulation. Passage and tip vortices induce losses that are visible in the swirl profile (see Fig. 7.14b) and also as lower total pressure values close to upper and lower liner (see Fig. 7.14c). The total pressure distribution is very close to experimental data. Whereas aerodynamics show few variance in radial direction, temperature distribution is more irregular (see Fig. 7.14d). This can be attributed to the redistribution of coolant flow due to high levels of swirl in the chamber, already observed on planes P40 and P41. In the hub region the total temperature profile corresponds better than in the shroud region which can again be attributed to the impact of secondary flow structures originating from the tip of the rotor blades. In the simulation, which covers a larger radial extent than the experiment, cool air injected at the seals of the rotor is seen to migrate along the inner liner.

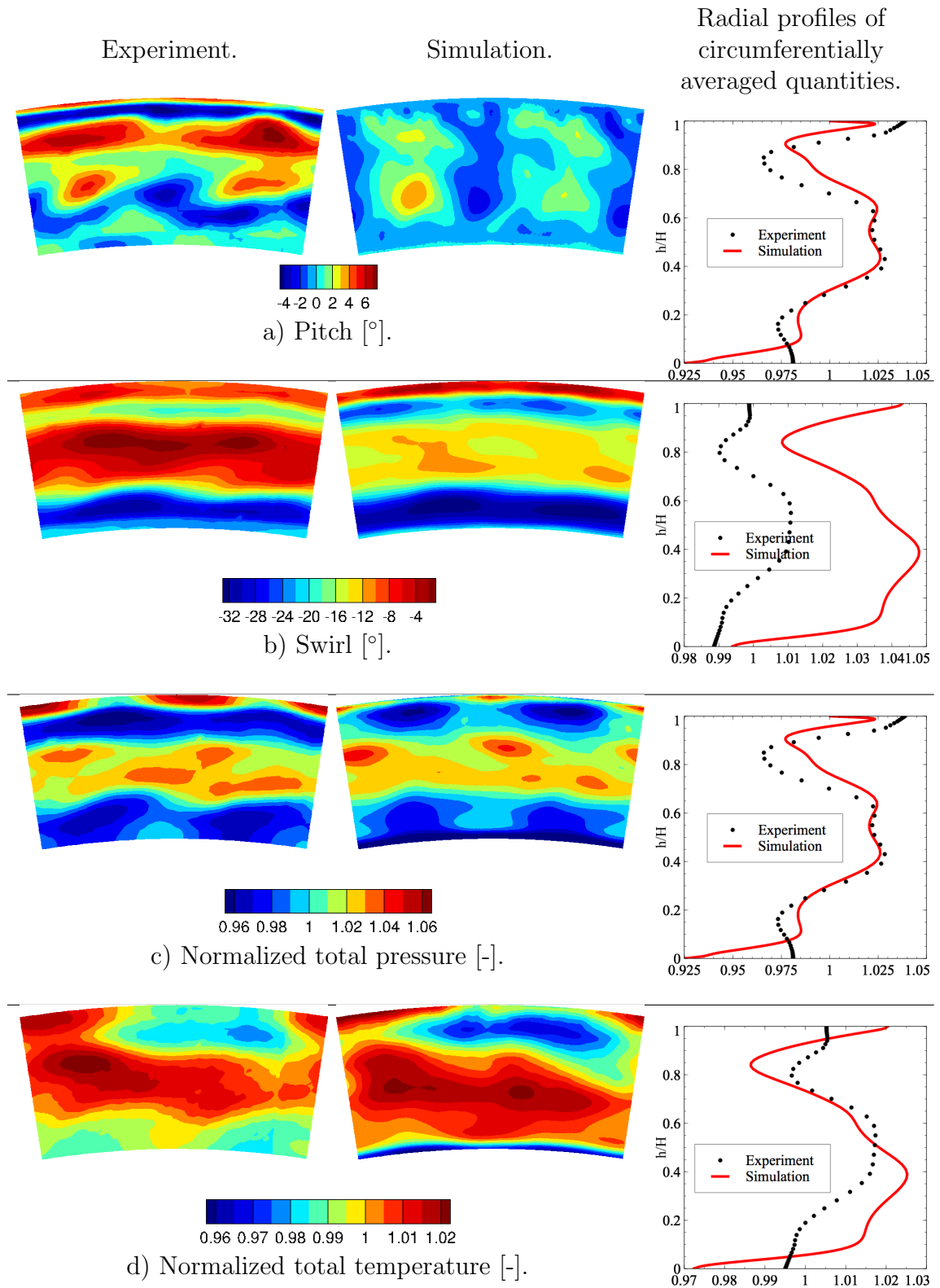


**Figure 7.14:** Flow field on P42 (after rotor) for simulation and experiment. View direction: downstream.

## 7.5 Conclusions

Next generation compact design lean combustion engines feature higher levels of distortions (temperature, swirl, turbulence) at the exit of the combustion chamber as current state of the art engines. These flow features adversely alter the flow field in the high-pressure turbine. To adequately address challenges associated with a harsher aerothermal environment in the chamber, interaction phenomena between chamber and high-pressure turbine will have to be taken into account in the design phase of next generation engines. First results from a high fidelity LES of the FACTOR combustion chamber and complete single-stage high-pressure turbine are presented and compared to experimental data on different observation planes (P40, P41, P42) as well as to pressure measurements on the NGV surface. In general there is a good agreement between simulation and experiment. Flow field predictions in the high-pressure turbine show a great improvement over RANS simulations, that only model the unsteady behavior of the flow field. Certain differences observed in the simulation on P41 may be contributed to the NGV coolant injection model, that leads to less mixing between main flow and coolant than a fully resolved coolant system. Previous simulations showed that secondary flow structures are highly sensitive to minor changes in the flow field and numerical parameters. This may explain the discrepancy of flow angles between simulation and experiment observed on P41 and P42. The simulation may be further improved by application of higher order numerical schemes and local adaptations of the computational grid.



# General Conclusions and Perspectives

## Conclusions

The FACTOR project driven by a consortium of several European engine manufacturers and research institutions is a new milestone for the development of next generation lean combustion engines. Unprecedented measurement data has been obtained and various numerical simulations have been validated. CERFACS contributes to the project by performing high-fidelity Large Eddy Simulations in order to improve the understanding of the highly unsteady flow physics present in the FACTOR lean combustor demonstrator and also in the next generation of aircraft engines. Main outcomes of this work are:

### Cooling systems for gas turbines

- **Combustion chamber:** A homogeneous and a novel heterogeneous coolant injection model to account for effusion cooling systems at the combustion chamber liners were tested and validated against experimental data obtained at the University of Florence. The shallow injection angle used in the homogeneous injection model yields a closed high-velocity coolant film close to the liners. The heterogeneous injection model is able to model individual jets which increases the penetration of coolant in the main flow. The heterogeneous injection model was retained for subsequent simulations and further improvements of this model were developed at CERFACS in the thesis of R. Bizzari [27].
- **High-pressure vanes:** The heterogeneous coolant injection model, although originally designed for the application in combustion chambers, can be used to model the coolant injected by the high-pressure vane coolant system. The simulation with the coolant injection model yields results similar to a simulation with fully resolved coolant system. Using the model, the coolant tends to stay closer to the NGV walls, whereas the jet penetration is larger for the fully resolved simulation. The lack of injection velocity fluctuations may explain part of the difference between both simulations. Taking such fluctuations into account may be a way to improve the coolant injection model for the application of modeling the coolant system of NGVs.

## Analysis in Combustion Chamber and High-pressure vanes

- The presence of vanes does not significantly impact the flow field in the chamber. Due to the heterogeneous flow field on P40 (residual swirl, marked hot spot), the flow field in the vane passage is quite different depending on the clocking position. The analysis of higher order statistical data, directly available from LES, allows to extract additional information from the simulation. The path of the hot-streak can be determined and thermally critical areas can be discovered by a conjoint analysis of local velocity and turbulence levels.
- A novel approach of improving isolated component simulations by imposing realistic time-resolved inlet boundary conditions was tested on an isolated high-pressure vanes geometry and compared against an integrated simulation featuring combustor and high-pressure vanes domain. Injecting the fully unsteady flow field obtained from the integrated simulation allows to a large extent to recover the flow field of the isolated simulation. Degrading the inlet signal impacts the flow due to reduced mixing and more persistent secondary flow structures that alter the temperature distribution on the NGVs.
- High-fidelity LES of combustor with attached single-staged high-pressure turbine were performed and results are presented in Chapter 7. Numerical predictions obtained in course of this study are close to experimental results obtained at the full annular test rig at DLR Göttingen. Predictions, especially on P42 show improvements over RANS results.

## Perspectives

The results obtained on the different topics addressed in this manuscript evidenced various possible work perspectives. First, the potential added value of performing high-fidelity LES on chamber + high-pressure turbine devices to further improve flow predictions in an industrial design process as well as in a research environment has clearly been highlighted. Further work in this environment is under way at CERFACS and different research partners.

- The novel coolant injection model applied in this work clearly showed it's potential to improve predictions of turbomachinery simulations and in future will allow for a more detailed design of sophisticated cooling systems.
- Investigating coupled chamber + vane simulations allows to better understand interactions between both engine components and the impact of the chamber on secondary flow structures which will be marked in future engines. The continuous increase of high-performance computing power will render such simulations more common in future research. This will allow further insight in complex aerothermal conditions present in turbomachinery devices.
- Advanced statistical methods to analyze time-resolved 3D data of the flow readily available from LES proved to allow for further insights in the flow field

for turbomachinery applications. Indeed, these allow to identify thermally stressed parts of the blade, e.g the trace of the hot spot. Results shown in this work are very promising and research on this topic will be continued at CERFACS.

- From a purely numerical point of view further developments of the LES methodology may lead to further insights and more accurate predictions of the flow field. Typically, wall modeled LES are used due to the high computational cost of wall resolved LES at high Reynolds numbers. Here, numerical results in the high-pressure turbine were found to be very dependent on the chosen SGS-model, which still leaves room for further investigations on the applicability of standard wall models in a turbomachinery context.
- Extracting specific flow features by means of POD analysis and recasting them at the inlet of isolated simulations allows the isolated investigation of the impact of dominant flow features in the computational domain. The methodology can make use of experimental as well as numerical data and may be a way for improving high fidelity predictions of isolated components. For high-pressure vanes, the approach already showed it's potential, but for more general applications several challenges still remain to be addressed (data availability, data treatment, in-congruent source data). At CERFACS, work on such approaches continues and is currently extended by using spectral POD, allowing to extract modes that oscillate at one specific frequency.

Future challenges in terms of environmental restrictions and economic cost reduction targets will continue to drive future development for aircraft engines. One crucial point to improve engine performance is a better understanding of interaction phenomena present between different components requiring a greater degree of high fidelity, coupled modeling. Performing such coupled simulations is now definitely in reach of high-performance computing centers as demonstrated in this work.



# Appendix A

## Impact of Sub grid Scale models on the flow field in the combustion chamber and nozzle

### A.1 Introduction

Turbulent flows contain a wide range of excited length and time scales, without a real separation of scales. Navier-Stokes equations fully describe the motion of viscous fluids [143]. However, in the context of LES, the application of filtering results in unclosed terms that contain the influence of sub-grid scale phenomena. SGS models try to estimate effects of small scale physical processes not adequately resolved on the computational grid. To do so, SGS models remove energy from the resolved scales, mimicking the drain that is associated with the energy cascade (see Fig. A.1) [39]. The issue of SGS turbulence modeling was first addressed by Smagorinsky in the 1960s [51] with the introduction of LES methods to model meteorologic phenomena. The Smagorinsky model was developed for external flows and computes the correct amount of viscous dissipation in homogeneous isotropic turbulence. The model has deficits for wall bounded flows which lead to the introduction of WALE [52] and Sigma [53] model. All three models are implemented in the AVBP code and investigated in this chapter.

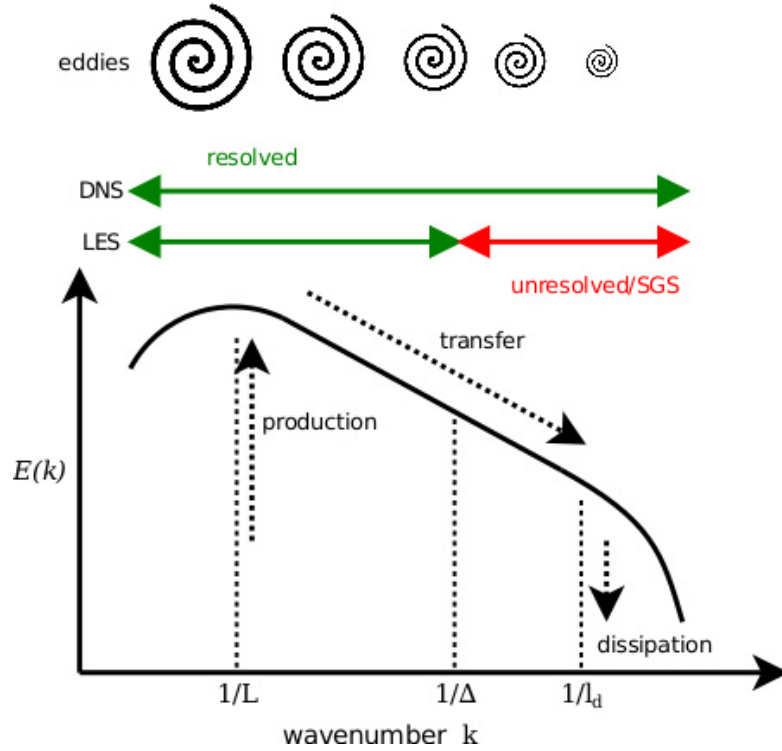


**Figure A.1:** Energy cascade [144].

Numerical setup, operating conditions and details about the flow field in the FACTOR test rig are given in Chapter 5. In this chapter the LE clocking position is investigated. In this chapter, different SGS models are presented. In the results section, the impact of previously described SGS models on the flow field in combustion chamber and in the vane passage, where the impact of SGS models is most visible, is discussed.

## A.2 Results

This section focuses on the differences in the flow field prediction obtained using different SGS models (Smagorinsky, WALE and Sigma) on the LE case (described in Chapter 5. For a better understanding of the flow field, chapter 5.3.1, which contains an extensive discussion thereof, can be consulted.

### A.2.1 Flow field in the combustion chamber

The evolution of temperature, pressure and TKE, presented in Fig. A.2 globally shows the behavior of the averaged flow field and allows a quantitative comparison of the three investigated SGS models. Differences can be observed, where wall interactions have a strong impact on the flow (swirler, vane passage). Before mixing with air in the combustion chamber the temperature is close to 531 K, then drops due to mixing with coolant flow (see Fig. A.2a). In the swirler the temperature

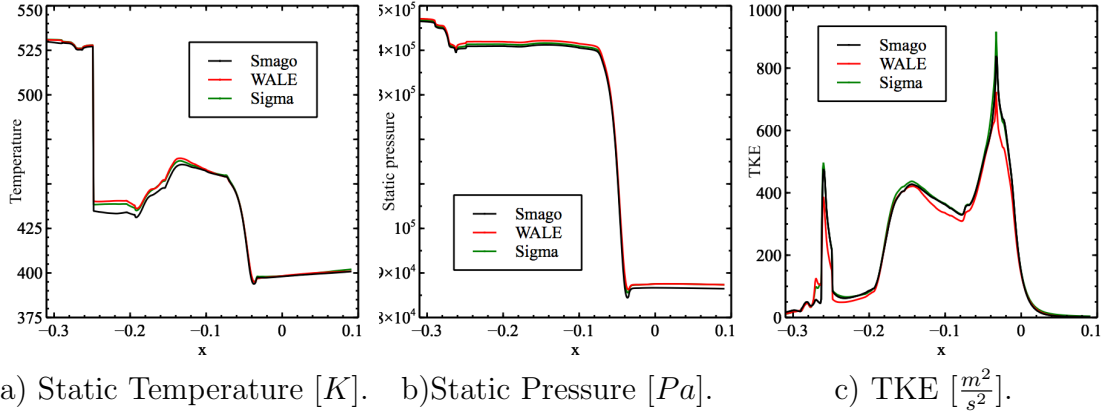


**Figure A.2:** Spatially averaged values of converged averaged flow fields on successive axial planes for different SGS models.

for Sigma/ WALE is higher than in the Smagorinsky simulation.

Through the vane passage the temperature drops due to expansion. The static pressure decreases throughout the domain, especially through the vane passage, where the flow is accelerated (see Fig. A.2b). On the TKE plot (see Fig. A.2c), a high peak can be observed when the flow travels through the swirler and also when the flow through the duct mixes with rather stagnant flow after leaving the duct. In the high pressure vane passage, the Sigma model shows the highest peak of TKE.

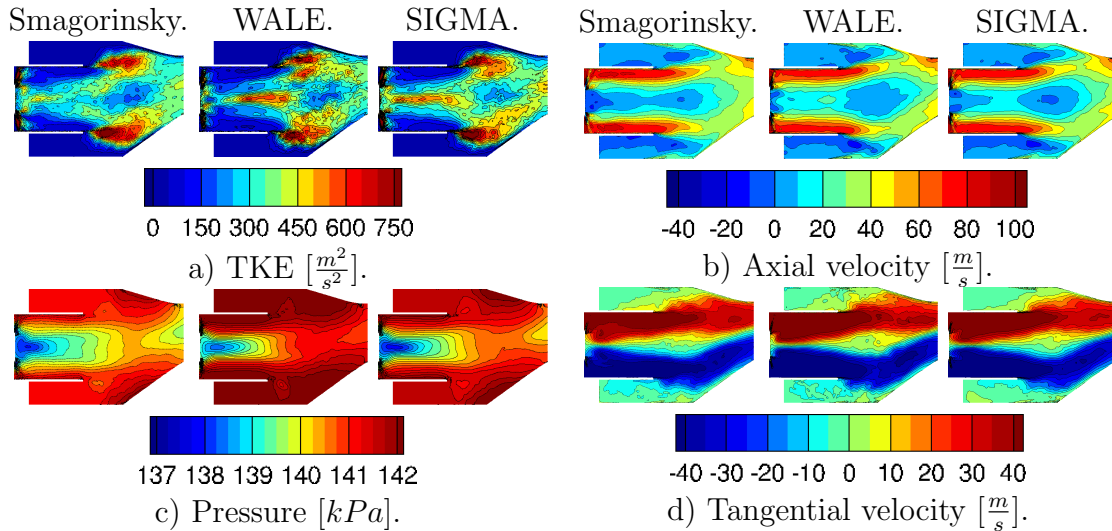


**Figure A.3:** Comparison of SGS on mid-cut through domain.

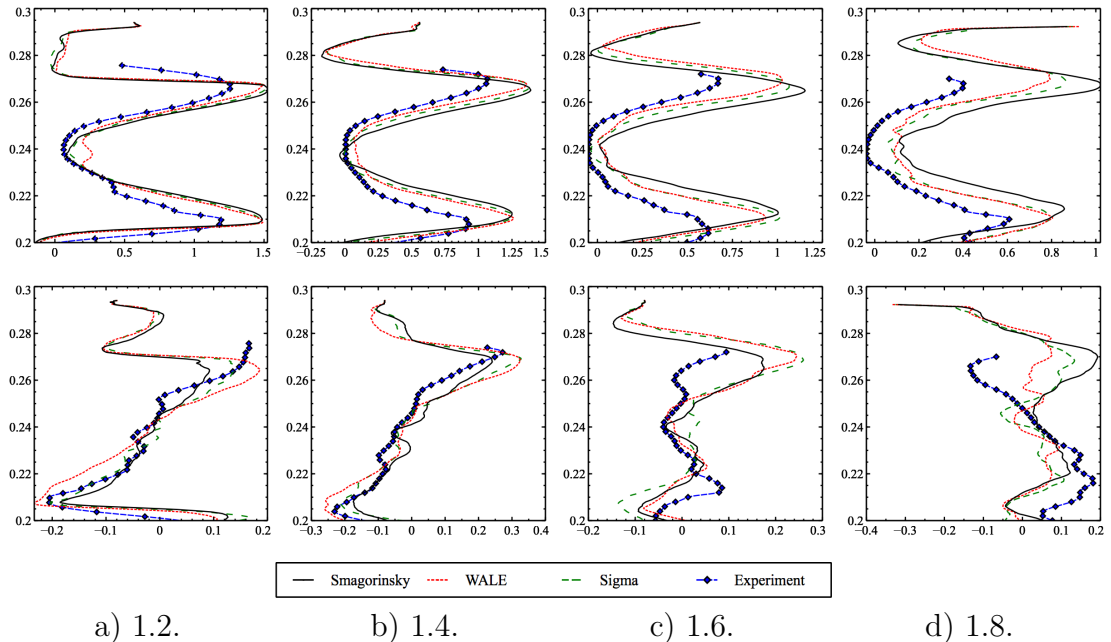
The TKE plot (see Fig. A.3a) shows clear differences depending on the SGS modeling approach. In WALE and Sigma simulations, high levels of TKE are visible in the middle of the duct. In the Smagorinsky simulation this turbulence is dissipated and turbulence levels in the middle of the duct are low. The shear layer at the duct edges has a rounder shape and covers a larger area than if using

## APPENDIX A. IMPACT OF SUB GRID SCALE MODELS ON THE FLOW FIELD IN THE COMBUSTION CHAMBER AND NOZZLE

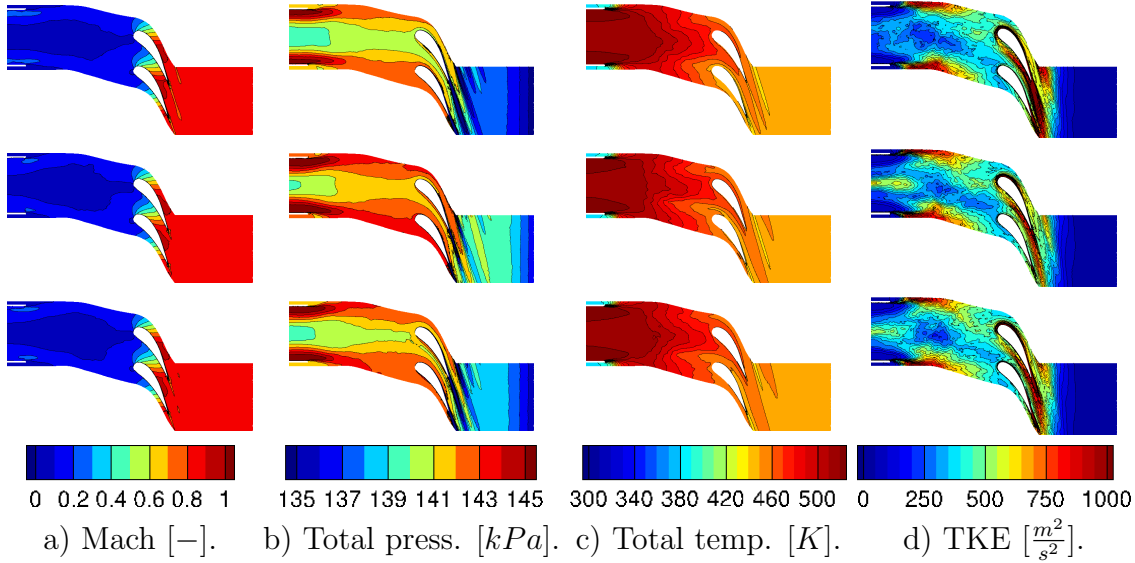
other modeling approaches. Axial velocity plots (see Fig. A.3b) show that the central re-circulation zone is not captured using the WALE model, but if applying Smagorinsky or Sigma. Due to the swirling motion in the duct, low pressure levels are observed in the middle of the duct (see Fig. A.3c). In WALE the pressure gradient from swirler to the exit of the combustion chamber is higher than in other simulations. Likewise, the pressure level predicted by this model is increased as compared to both other cases. The flow field in the combustion chamber is dominated by a swirling motion induced by the fuel injection system (see Fig. A.3d). Throughout the duct and also in the combustion chamber tangential velocities from the WALE model prediction are higher than for both other models.

Fig. A.4 allows for a more qualitative comparison of flow field predictions obtained by three different sub-grid models including a comparison to experimental data obtained from PIV measurements at isothermal operating conditions. The axial velocity plots (see Fig. A.4a) show a typical profile for swirling flows (two velocity peaks and a low velocity zone in the center). Applying the Smagorinsky model leads to the highest velocity predictions and the Sigma model is again in-between WALE and Smagorinsky. Unlike the WALE model, Smagorinsky and Sigma capture a recirculation zone, which is also confirmed by experiments. Further away from the duct, the differences between models become more significant.

Radial velocity plots indicate the rotational velocity at increasing distances from the duct (see Fig. A.4b). Shortly after the duct there is a good agreement of simulations to experimental data. Further away from the duct predictions from different SGS models and experimental results diverge.



**Figure A.4:** Averaged axial (upper) and radial (lower) velocity profiles on lines through domain for simulations (DP) and PIV-experiment (IOP). Velocities are non-dimensionalized by the reference velocity (see Tab. 5.1). Distance from the exit of the duct is non-dimensionalized by the diameter of the swirler (63 mm).



**Figure A.5:** Average flow field for Smagorinsky (upper), WALE (middle) and SIGMA (lower) on iso  $H/h=0.5$  through domain. (Design Point).

The Mach number on the  $H/h=0.5$  isosurface through the domain (see Fig. A.5a) is mostly insensitive to changes of the SGS model. In the combustion chamber, the hot-streak is visible as a low Mach zone. Through the passage, the Mach number steadily increases and reaches up to  $Mach=0.9$ . Regarding the total pressure distribution (see Fig. A.5b), higher levels can be seen for the WALE model. The prediction from the Smagorinsky model yields pressure levels about 500 Pa lower than that from the WALE model and the Sigma model lies in-between. Qualitatively pressure distributions are similar. The hot-streak impinges on NGV1 (upper NGV) (see Fig. A.5c). The Smagorinsky simulation shows slightly higher temperature values. Furthermore, the model predicts a flow separation at the trailing edge of NGV1, not predicted by the other models. The TKE plots (see Fig. A.5d) show high levels of turbulence at the shear layer after the duct and also through the vane passage. As already observed before (see Fig. A.3), WALE and Sigma predict higher levels of turbulence in the middle of the duct. Through the vane passage, TKE levels in the Smagorinsky model increase stronger as compared to both other predictions. Close to the upper liner the Mach field is similar for all SGS models and does not show a marked trace related to the hot spot (see Fig. A.6a). For the Smagorinsky model, total pressure close to the upper liners shows marked low pressure regions - possibly due to different secondary flow patterns (see Fig. A.6b). The total temperature distribution close to the upper liner shows marked differences depending on the SGS modeling approach and also impacts the temperature distribution on the NGV surface. In WALE and Sigma simulations, higher temperatures can be observed in the upper passage (see Fig. A.6c). TKE close to the upper liners is lower than at mid height (see Fig. A.6d) and no traces of turbulence created by the shear layer at the duct edges are visible.

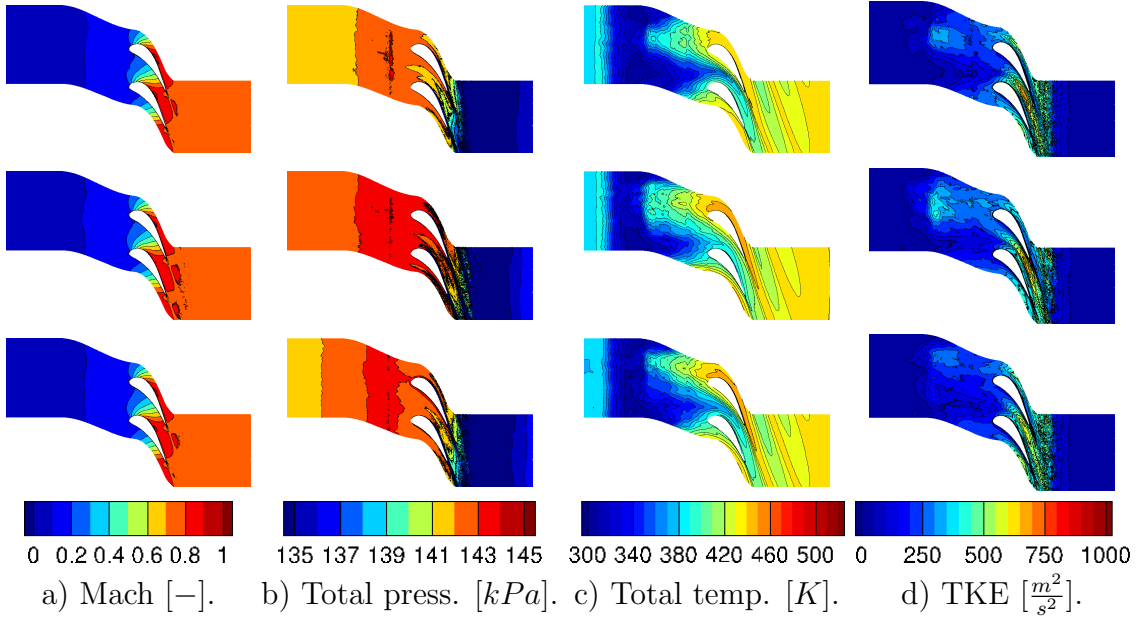


**Figure A.6:** Average flow field on iso  $H/h=0.97$  for Smagorinsky (upper), WALE (middle) and SIGMA (lower) through domain. (Design Point).

## A.2.2 Flow field on P40

In the axial velocity plot (see Fig. A.7a), highest velocity values can be observed close to the upper liner, possibly due to the application of a homogeneous coolant injection model to simulate the effusion cooling system [141]. The Mach number at the exit of the combustion (see Fig. A.7b) is slightly higher for the Smagorinsky model and lowest if applying WALE. Plots of total temperature show the central hot spot (see Fig. A.7c) which due to the absence of dilution holes remains mainly undiluted by coolant. Applying the Smagorinsky model, coolant flow from the upper liner penetrates further into the domain than in other modeling approaches.

On P40, the most significant difference can be seen in the total pressure plots (see Fig. A.7d), where the WALE model predicts pressure levels about 1000 Pa higher than the other modeling approaches. Higher total pressure levels can be observed close to the liners, where mainly coolant flow migrates along the passage and the low total pressure region in the middle of P40 is due to the hot spot.

Applying the WALE model yields lower values of TKE than if applying the other SGS models (see Fig. A.8). The Smagorinsky model, which is usually known to be too dissipative shows higher levels of turbulence, which may indicate that more turbulence is created in the shear layer after the restraining duct as compared to other SGS models.

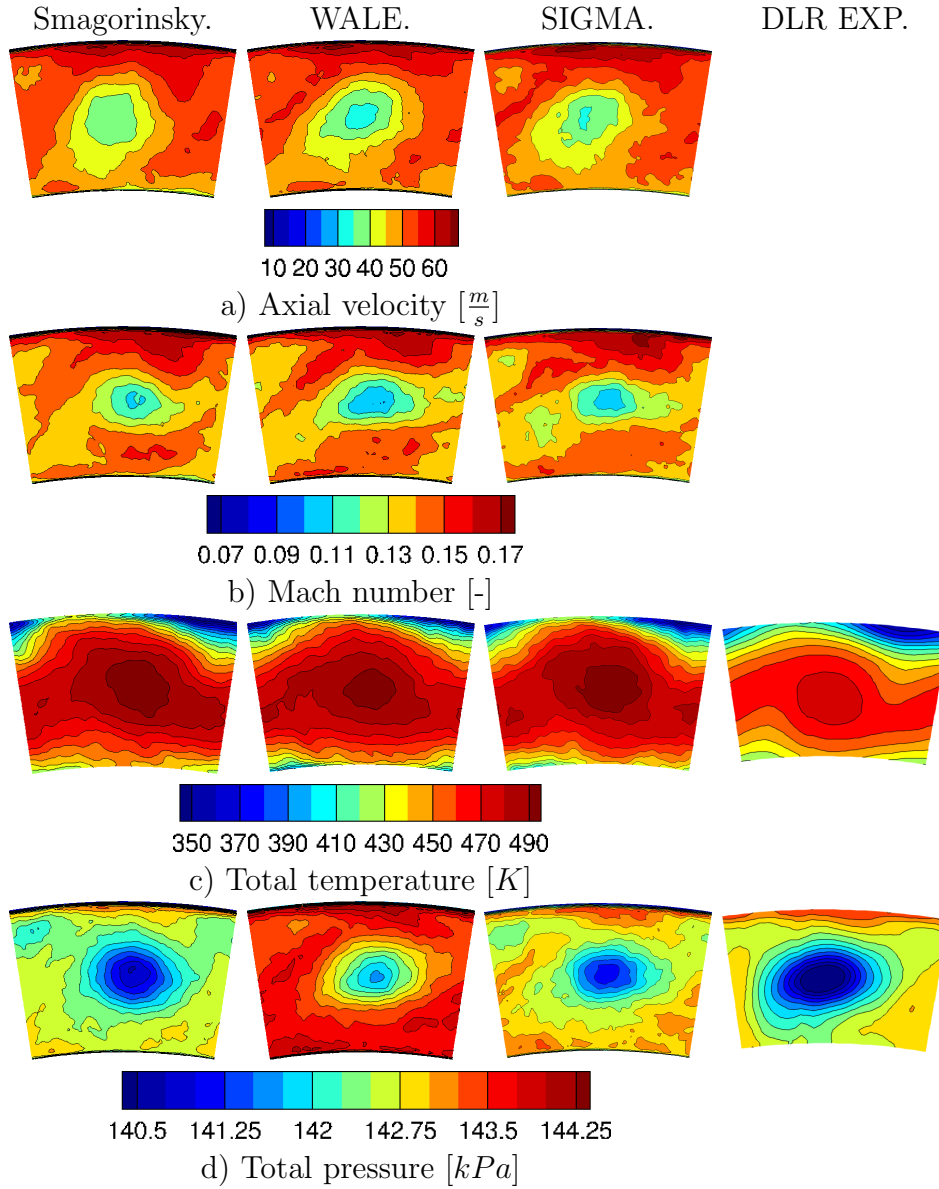


**Figure A.7:** Averaged flow field on P40 for Smagorinsky, WALE and Sigma model and experimental data.

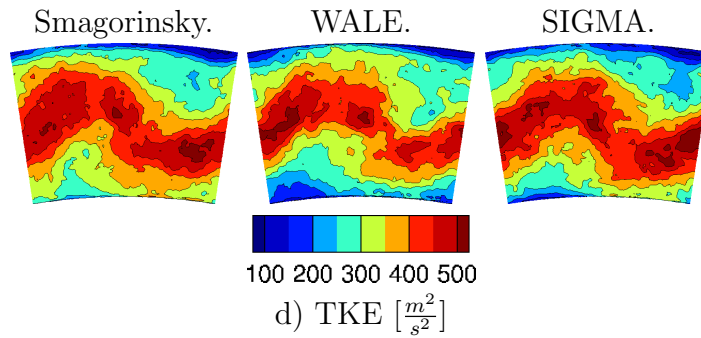


**Figure A.8:** Averaged flow field on P40 for Smagorinsky, WALE and Sigma model and experimental data.

### A.2.3 Flow field on P41

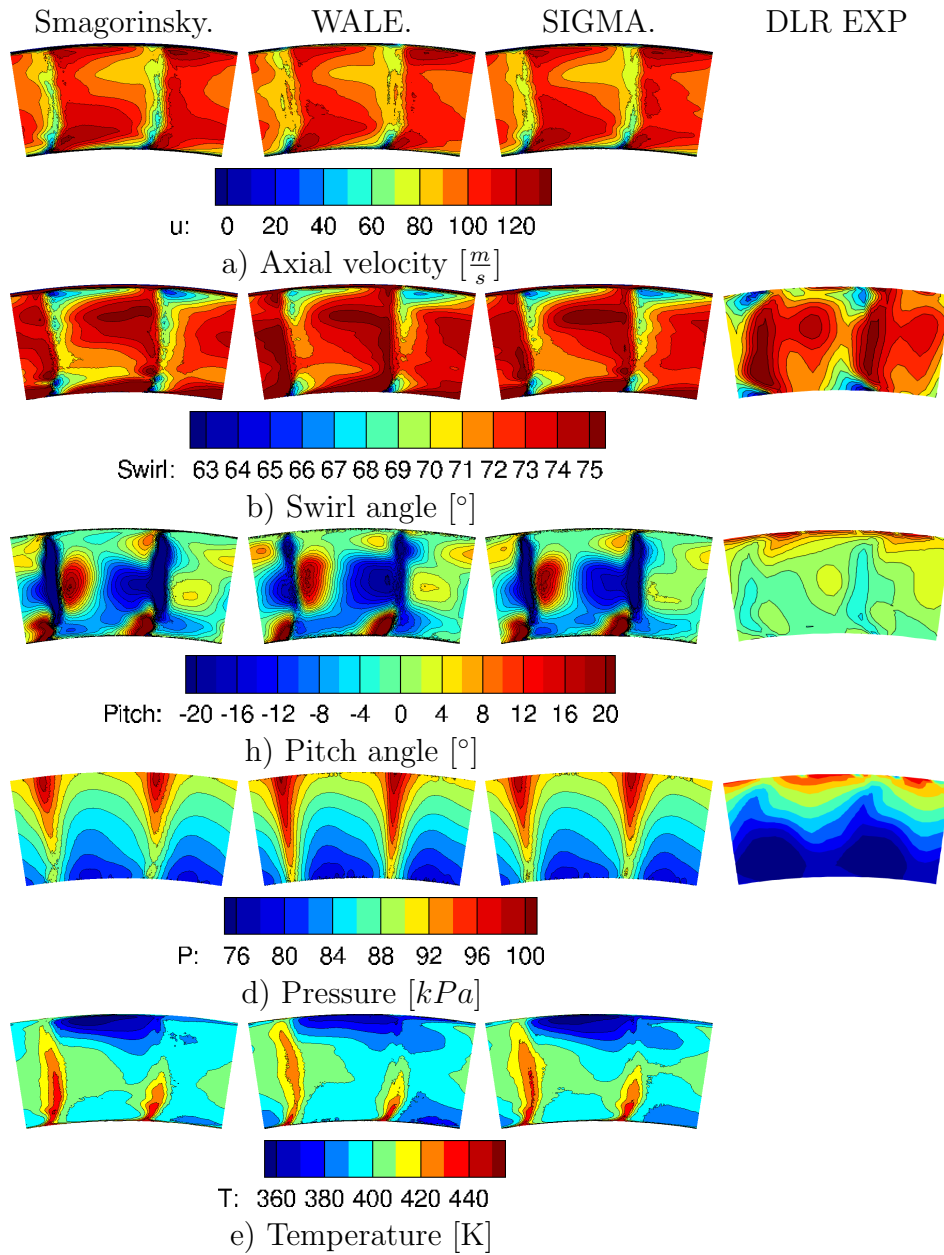


**Figure A.9:** Averaged flow field on P41 for Smagorinsky, WALE and Sigma model and experimental data.

Fig. A.9 shows the flow field on P41, after the nozzle. In all plots, the wake after the NGVs is clearly visible and the different SGS models predict similar results. The velocity field (see Fig. A.9a-c) shows differences close to upper and lower liners near the wake of the NGV, which are caused by the different behavior of secondary flow structures in the nozzle. Experimental investigations allow for a direct comparison of flow angles on P41 and show clear differences as compared to the simulations (see Fig. A.9b,c). In the experiment residual swirl on P41 seems to be considerably weaker than predicted in the simulation.

Pressure plots show a radial equilibrium pressure distribution and are slightly higher in the simulation than in the experiment (see Fig. A.9d). In the temperature plots (see Fig. A.9e), the NGV wakes are well visible as hot temperature zones. The Smagorinsky and Sigma model show higher values which may indicate more mixing in the WALE simulation.

The turbulence levels in the NGV wake are lower using the WALE model, than in both other models (see Fig. A.10).

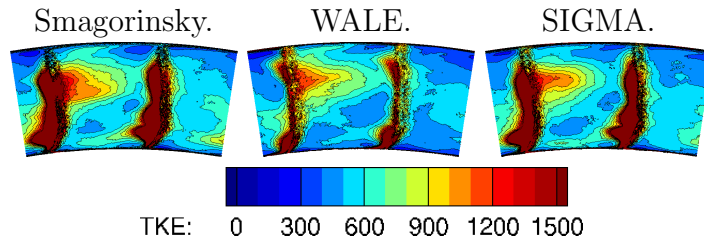


**Figure A.10:** TKE [ $\frac{m^2}{s^2}$ ] on P41 for Smagorinsky, WALE and Sigma model and experimental data.

#### A.2.4 Impact on the stator

After discussing general differences of the flow field in the combustion chamber, the focus now lies on the impact of SGS models on flow features in the high-pressure vane passage. Secondary flows, such as vortices are strongly impacted by the SGS modeling approach (see Fig. A.11). Using the Smagorinsky model (see Fig. A.11a), the tip vortex moves further down on the suction side of both NGVs, whereas the same stays mostly close to the upper liner if applying the WALE model (see Fig. A.11b). The Sigma model yields results in-between both modeling approaches.

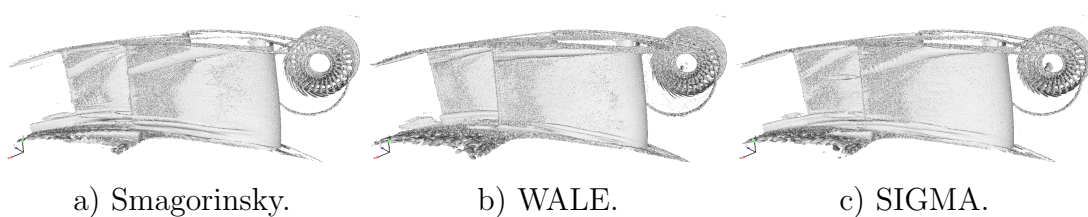


**Figure A.11:** Q-criterion ( $1E+8$ ) of averaged solutions visualizes secondary flow structures on the NGV suction side.

NGV1 is impacted by the hot spot and experiences globally higher temperature values than NGV2. In the Smagorinsky simulation, the temperature field on both NGV surfaces (see Fig. A.12a) shows the migration of coolant flow from the top liner to mid height of the trailing edge of the NGV. On the suction side, a separation of the hot flow, possibly due to detachment - reattachment is visible which is not found in other models. Temperature predictions by the WALE simulation seem to be rather smooth. The Sigma model results are in-between

APPENDIX A. IMPACT OF SUB GRID SCALE MODELS ON THE FLOW FIELD IN THE COMBUSTION CHAMBER AND NOZZLE

Smagorinsky and WALE predictions. Significant differences can be observed for the wall shear stress, where the Smagorinsky model predicts values up to twice as high as the other models, whose results are quite similar (see Fig. A.12b). For the LES prediction using the Smagorinsky model, the wall shear stress plot shows a marked trace in the shroud area on the suction side caused by a corner vortex also observed in Fig. A.11a. Non-dimensional wall distance plots show important differences between the Smagorinsky predictions and those by WALE or Sigma models, which were specifically developed for wall bounded flows (see Fig. A.12c). In the Smagorinsky model,  $y^+$  values and thereby also the velocity prescribed by the wall model are higher than for WALE and Sigma, whose predictions are very close.

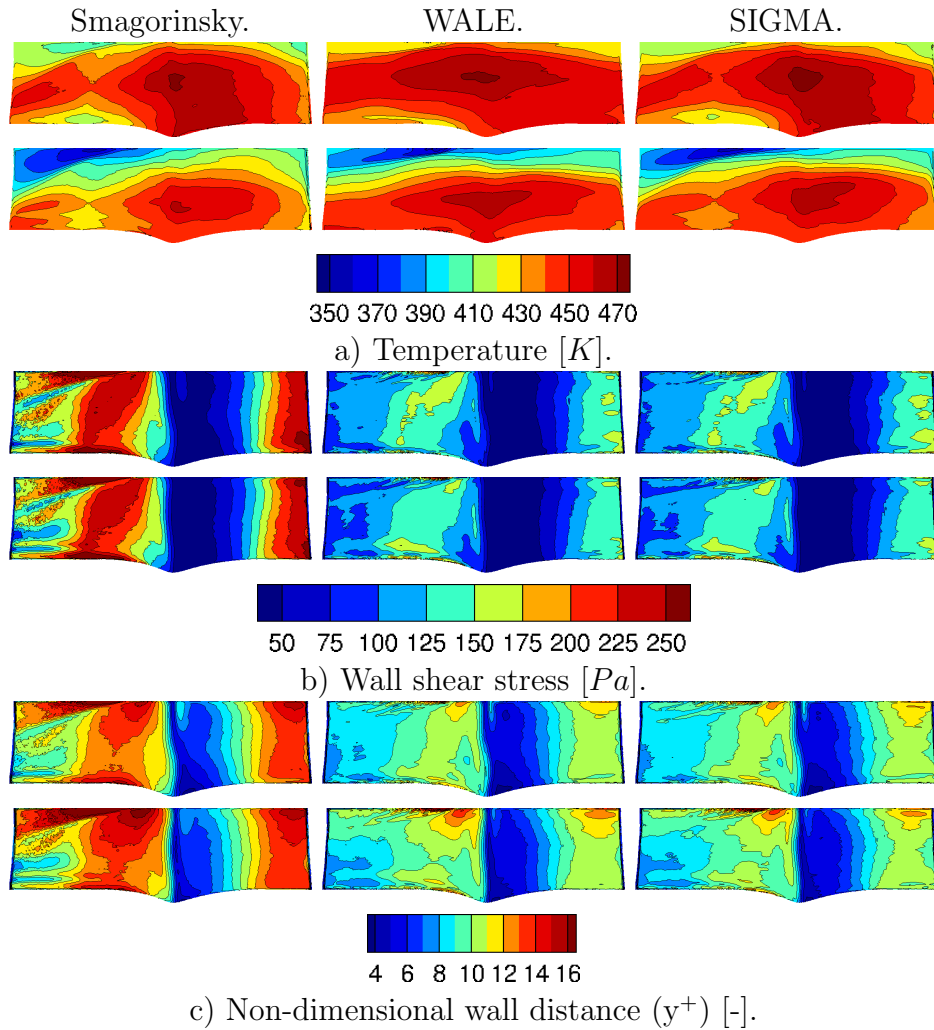
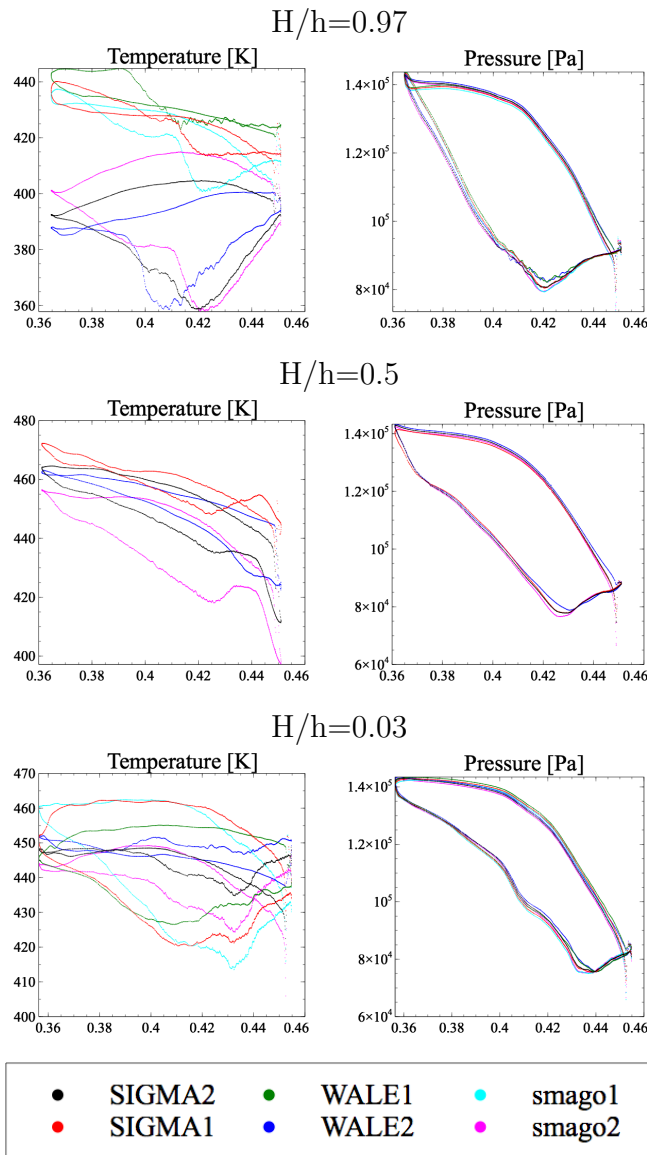


**Figure A.12:** Comparison of SGS models on the NGV surface.

Figure A.13 allows a detailed comparison of different temperature and pressure on the surface of the NGV. Regarding the temperature distribution, differences between NGV1 and NGV2 are more important than those due to the SGS modeling approach (see Fig. A.13a). Highest temperatures can be observed at  $H/h=0.5$ , where the hot spot impinges on the surface. In the near-wall region, coolant

flow migrates along the liners and temperatures are generally lower. The stagnation zone shows high levels of pressure, as well as the NGV pressure side (see Fig. A.13b). Lower pressure levels can be observed on the suction side, where the differences between the simulations are most significant. If applying the WALE model, pressure levels on the NGV surface are higher. Close to the upper liner, pressure differences between NGV PS and SS are more significant than in the hub region.



a) Temperature [K].      b) Pressure [kPa].

**Figure A.13:** Bladeprofiles at different heights.

### A.3 Conclusions

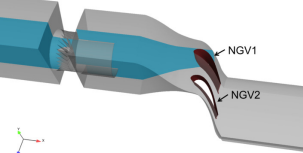
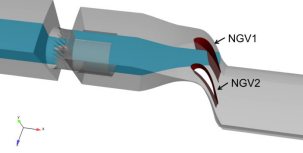
Three different eddy viscosity models (Smagorinsky, WALE, Sigma) to estimate sub grid scale turbulence contributions are tested on the geometry of the engine representative FACTOR test rig and validated against experimental data. Differences in the flow field are seen after the fuel injection system and become more significant in the high pressure vane passage. Unlike other models, the WALE model does not predict a strong re-circulation zone after the swirler, which is evidenced by PIV measurements. Pressure loss in the WALE simulation is higher compared to Smagorinsky or Sigma. In the high pressure vane passage, impact of SGS modeling on secondary flow patterns is visible. In the Smagorinsky simulation corner vortices transport significant amounts of coolant air from the upper liner down to mid height of the vane at the trailing edge. Other SGS models predict weaker vortices and the flow field seems smoother. Modeling differences are most significant on the suction side of the NGVs. Globally, the Sigma model is between predictions from Smagorinsky and WALE.

# Appendix B

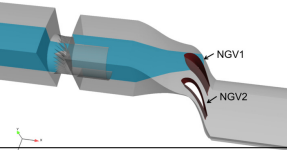
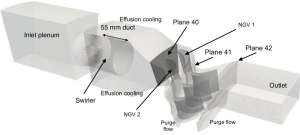
## Simulations of interest

This Appendix summarizes all LES performed during the FACTOR project. Pioneering work of C. Koupper [16] was mostly dedicated to the design of the combustor module (see Tab. B.1). Many simulations were performed to determine the geometry of the duct that restrains the fuel injection system generated processing vortex core. Further simulations investigated the sensitivity of the flow to the walls if the rig is constructed as a three sector configuration (UNIFI rig) as compared to the Full annular rig at the DLR Göttingen.

Simulations performed in this present work were performed to address remaining open questions from the thesis of C. Koupper (see Tab. B.2). Most of the original simulations were performed at operating conditions of the UNIFI test rig without NGVs.

Geometry	Case	Duct	Operating point	Mesh nodes	Mesh cells	Scheme	SGS model	Physical time [ms]	Timestep [s]
	1	D45	DP	2.2M	12.7M	TTGC	Smagorinsky	360	$2.3 \cdot 10^{-7}$
	2	D45	IOP	2.2M	12.7M	TTGC	Smagorinsky	143	$2.3 \cdot 10^{-7}$
	3	D45	DP	2.2M	12.7M	TTGC	Smagorinsky Dynamic	143	$2.3 \cdot 10^{-7}$
	4	D45	DP	6.5M	38.3M	TTGC	Smagorinsky	159	$2.3 \cdot 10^{-8}$
	5	D45	DP	5.2M	29.1M	TTGC	Smagorinsky	149	$5.8 \cdot 10^{-8}$
	6	D00	DP	Coarse: 2.7M	15.8M	TTGC	Smagorinsky	154	$6.5 \cdot 10^{-8}$
	7	D00	DP	Medium: 6.0M	34.2M	TTGC	Smagorinsky	155	$4.4 \cdot 10^{-8}$
	8	D00	DP	Fine: 12.2M	68.5M	TTGC	Smagorinsky	155	$3.7 \cdot 10^{-8}$
	9	D00	DP	Medium: 6.0M	34.2M	TTGC	WALE	157	$4.4 \cdot 10^{-8}$
	10	D00	IOP	Medium: 6.0M	34.2M	TTGC	Smagorinsky	145	$4.4 \cdot 10^{-8}$
	11	D55	DP	8.9M	51.0M	TTGC	Smagorinsky	144	$4.3 \cdot 10^{-8}$
	12	D55 LE	DP	13.7M	71.0M	TTG4A	Smagorinsky	50.3	$3.2 \cdot 10^{-8}$
	13	D55 PA	DP	13.7M	71.0M	TTG4A	Smagorinsky	49.5	$3.2 \cdot 10^{-8}$

**Table B.1:** Summary of all LES performed on the FACTOR configuration in the work of C. Koupper (reproduced from [16]).

Geometry	Case	Operating point	Coolant model liner / NGV	P40 Inlet	Mesh cells	Scheme	SGS model	Physical time [ms]	Timestep [s]	Results in
	1	DP <sub>UNIFI</sub>	Homogeneous / -	-	51M	TTGC	Smagorinsky	100	$7.5 \cdot 10^{-7}$	3
	2	DP <sub>UNIFI</sub>	Heterogeneous / -	-	55M	TTGC	Smagorinsky	100	$6.5 \cdot 10^{-7}$	3
	3	IOP <sub>UNIFI</sub>	Homogeneous / -	-	51M	TTGC	Smagorinsky	100	$7.5 \cdot 10^{-7}$	3
	4	IOP <sub>UNIFI</sub>	Heterogeneous / -	-	55M	TTGC	Smagorinsky	100	$6.5 \cdot 10^{-7}$	3
	5	DP <sub>UNIFI</sub>	Homogeneous	-	71M	TTG4A	Smagorinsky	100	$4.0 \cdot 10^{-8}$	5, A
	6	DP <sub>UNIFI</sub>	Homogeneous / -	-	71M	TTG4A	WALE	100	$4.0 \cdot 10^{-8}$	A
	7	DP <sub>UNIFI</sub>	Homogeneous / -	-	71M	TTG4A	Sigma	100	$4.0 \cdot 10^{-8}$	A
	8	DP <sub>UNIFI</sub>	- / Modeled	-	71M	TTG4A	Smagorinsky	100	$4.0 \cdot 10^{-8}$	4
	9	DP <sub>UNIFI</sub>	- / Resolved	-	71M	TTG4A	Smagorinsky	100	$4.0 \cdot 10^{-8}$	4
	10	DP <sub>UNIFI</sub>	- / -	Full	35M	TTG4A	Smagorinsky	40	$4.0 \cdot 10^{-8}$	6
	11	DP <sub>UNIFI</sub>	- / -	constant	35M	TTG4A	Smagorinsky	40	$4.0 \cdot 10^{-8}$	6
	12	DP <sub>UNIFI</sub>	- / -	PVC	35M	TTG4A	Smagorinsky	40	$4.0 \cdot 10^{-8}$	6
	13	DP <sub>UNIFI</sub>	- / -	Rest	35M	TTG4A	Smagorinsky	40	$4.0 \cdot 10^{-8}$	6
	14	DP <sub>DLR</sub>	Heterogeneous / Modeled	-	110M	TTG4A	Smagorinsky	100	$4.0 \cdot 10^{-8}$	7

**Table B.2:** Summary of the all LES performed on the FACTOR configuration.



# Appendix C

## Publications

Seven publications derive from this PhD work and are reproduced hereafter for personal and non-commercial use. The published versions can be downloaded directly on the editors' websites.

First, the following two publications present research on coolant systems investigated in Part I (Chapter 3 & Chapter 4):

[a] Thomas, M., Dombard, J., Duchaine F., Gicquel, L., and Koupper, C. "Comparison of heterogeneous and homogeneous coolant injection models for Large Eddy Simulation of multiperforated liners present in a combustion chamber". In: ASME Turbo Expo 2017: Turbine Technical Conference and Exposition. GT2017-64622. 2017

[b] Harnieh M., Thomas M., Bizzari R., Dombard J., Duchaine F., and Gicquel L. "Assessment of a coolant injection model on cooled high-pressure vanes with large-eddy simulation," In: *Flow, Turbulence and Combustion* 104, 643 - 672 (2020).

Second, high order statistical tools are applied on the entire flow field of integrated LES of combustor with attached high-pressure vanes. This research was presented at the ASME 2017 conference and the topic is further detailed in Chapter 5:

[c] Thomas, M., Dombard, J., Duchaine F., Gicquel, L., and Koupper, C. "Advanced statistical analysis estimating the heat load issued by hot streaks and turbulence on a high-pressure vane in the context of adiabatic large eddy simulations". In: ASME Turbo Expo 2019: Turbine Technical Conference and Exposition. GT2017-64648. 2017

Third, one publication compares the flow field of the full annular FACTOR test rig with LES of combustion chamber and attached single staged high-pressure turbine:

[d] Thomas, M., Dombard, J., Duchaine F., Gicquel, L., and Koupper, C. "Large-Eddy Simulation of combustor and complete single-stage high-pressure turbine of the FACTOR test rig". In: ASME Turbo Expo 2019: Turbine Technical Conference and Exposition. GT2019-91206. 2019

Fourth, one publication addresses the issue of boundary conditions in isolated component simulations:

[e] Thomas, M., Dombard, J., Duchaine F., Gicquel, L., and Koupper, C. "Impact of realistic inlet condition on LES predictions of isolated high pressure vanes". In: 12th International ERCOFTAC Symposium on Engineering Turbulence Modelling and Measurements. ETMM2018 - 110. 2018

Finally, the following paper, related to the FACTOR project was published in collaboration with other researchers at CERFACS and is not discussed in this manuscript:

[f] Martin, B, Thomas, M., Dombard, J., Duchaine F. and Gicquel, L. "Analysis of sand particle ingestion and erosion in a turbomachine using Large-Eddy Simulation". In: ASME Turbo Expo 2019: Turbine Technical Conference and Exposition. GT2019-91215. 2019

**GT2017-64622**

**COMPARISON OF HETEROGENEOUS AND HOMOGENEOUS COOLANT  
 INJECTION MODELS FOR LARGE EDDY SIMULATION OF MULTIPERFORATED  
 LINERS PRESENT IN A COMBUSTION SIMULATOR**

**Martin Thomas\***  
**Antoine Dauptain**  
**Florent Duchaine**  
**Laurent Gicquel**  
 CFD Team CERFACS  
 Toulouse, France  
 thomas@cerfacs.fr

**Charlie Koupper**  
 Safran Helicopter Engines  
 Bordes, France

**Franck Nicoud**  
 Université de Montpellier  
 Montpellier, France

**ABSTRACT**

*With the goal of increasing the thermodynamic efficiency of aircraft engines, the temperature in the combustion chamber has risen to the point where the gas temperature is above the melting point of materials used in the chamber and cooling systems are mandatory. Today, most of the existing lean burn combustors rely on multiperforated liners to keep hot gases away from the walls. However, resolving all holes of the combustor in the CFD design phase remains beyond currently available computational resources, so the effusion cooling system is often modeled by homogeneously injecting air on the whole surface of the liner, especially in the context of Large Eddy Simulation (LES) based CFD. This paper investigates a novel approach to simulate the effect of jets emitted from discrete holes on the flow inside a combustion chamber. In this new modeling approach, jet diameters are treated to be resolvable by the grid while conserving the correct mass and momentum flow rate. LES are performed on the combustion simulator of the engine representative FACTOR test rig at two different operating points and compared to measurement data as well as previous simulations obtained using a homogeneous air injection modeling on liners. The new approach shows globally similar results as the well validated homogeneous injection model and is applicable on realistic industrial geometries at a negligible level of additional cost (+0.3%).*

**NOMENCLATURE**

**Acronyms**

CFL	Courant-Friedrichs-Lewis condition
DP	Design Point
FACTOR	Full Aerothermal Combuster Turbine interactions Research
HWA	Hot wire anemometry
IOP	Isothermal Operating Point
LES	Large Eddy Simulation
NGV	Nozzle Guide Vane
P40	Intersection between Combustion Chamber and high-pressure turbine
PIV	Particle Image Velocimetry
SGS	Sub-Grid Scale
TKE	Turbulent Kinetic Energy

**Symbols**

$A$	Area	$jet$	Jet
$D$	Diameter	$mod$	Model
$E$	Enlargement	$n$	Normal
$U$	Velocity	$num$	Numerical
$\alpha$	Injection angle	$t$	Tangential
$\sigma$	Porosity	$\infty$	Free stream

\*Address all correspondence to this author.

## INTRODUCTION

To reduce the specific fuel consumption of aircraft, the thermal efficiency of engines has been increased and the temperature in the combustion chamber has risen to a point where cooling of hot engine components is mandatory. Today, engine manufacturers are striving for a longer lifespan of engine components and higher performance. This means harsher thermal environments in future engines. Small combustor systems, as applied in helicopter engines or resulting from current downsizing trends, with an inherently high surface to volume ratio, suffer from the decreasing heat sink capacity of air bled from compressors whose pressure ratio increases to meet even higher performance goals [1]. Introducing lean combustion technologies to reduce NO<sub>x</sub> emissions poses new challenges for the cooling design, because the coolant mass flow is reduced in favor of the combustion process. Likewise the absence of dilution holes reduces the capability of mixing hot and cold gases, and leads to a higher degree of swirl and temperature non-uniformities at the exit of the combustion chamber. In the past decades, full coverage film cooling where cool air is injected through a multitude of submillimetric angled perforations, has emerged as the most efficient technology to keep combustor surface temperatures at acceptable levels [2]. Liners are cooled by convection on the cold-air side and hot gases are kept away from the walls by a coolant film which forms a thermal barrier on the hot side. The goal of the liner cooling design is to maintain integrity of solid parts while using the least amount of air possible to conserve air for emission control. The design of multiperforated liners has a strong impact on the entire flow field and on the temperature profiles at the exit of the combustion chamber.

Since experimental investigations are costly and data acquisition in the rough thermal environment of an aircraft engine is difficult, CFD has evolved as a major tool to investigate and design engines. Present-day high performance computing systems render CFD possible to perform time-resolved LES of entire combustor geometries. However, as of today resolving all effusion cooling holes is still beyond available computational resources, so that different modeling approaches have been introduced.

Research on liner cooling technologies started in the 1960s [3], about 20 years after the first jet engines were applied to aircraft. Facing increasing combustion temperatures surpassing the thermal limits of high temperature alloys, Colladay (1970) [4] was the first to point out the necessity to exploit the heat sink capacity of coolant air prior to injection to dissipate excess heat from the combustion of fuel. Together with advances in manufacturing technologies, this led to the large scale introduction of angled multiperforation cooling systems on combustion chamber liners. Crawford et al. (1980) [5] performed one of the first numerical investigations of effusion cooling systems by modeling discrete holes in a 2D boundary layer code. Hunter (1998) [6] presented a near wall source term model where mass is injected

in the boundary layer close to the wall. Heidmann and Hunter (2001) [7] showed that a uniform near wall source term better corresponds to experimental results. More recently, Burdet et al. (2007) [8] used correlations tuned with experimental data to calculate jet trajectories and Voigt et al. (2012) [9] proposed an effusion cooling model including conjugate heat transfer via additional source terms in the solid while giving an overview on past modeling approaches for liner cooling. Finally, Mazzei et al. (2016) [10] compared a homogeneous injection model with a model using point mass sources within single cells performing a scale adaptive simulation and found an encouraging agreement between simulations and experimental data. The latter model indeed showed a better agreement for wall heat transfer.

Most of past research in the area of effusion cooling systems focused on simple geometries and used Reynolds-Averaged Navier-Stokes (RANS) simulations as numerical methodology. Time resolved simulations of the effusion cooling system in the highly turbulent flow field of an engine representative lean-combustor simulator can give new insights into interactions between jets and mean flow field as well as contribute to an improved liner cooling design. Mendez and Nicoud (2008) [11] developed a LES targeted homogeneous adiabatic model for industrial geometries, which conserves wall fluxes and reproduces the flow field inside the combustion chamber. The model is local and does not rely on global parameters derived from the flow field. Lahbib (2015) [12] presented a new LES targeted perforation model, which relies on mesh-resolvable jets entering the domain from discrete surface areas on the liners. Both models were designed to be applicable to real engine geometries with a large number of cooling holes without adding high computational cost.

This work presents a comparison between the homogeneous and the heterogeneous coolant injection model applied to the liner treatment of the combustion chamber simulation of the FACTOR<sup>1</sup> test rig.

The structure of this article is as follows. First, the two previously mentioned coolant injection models are presented. In the following, the general setup, the FACTOR combustion chamber simulation and operating conditions are described. The next section discusses the prediction differences between both models. These are evidenced by comparing 2D plots and radial averaged profiles. A final conclusion summarizes the results and gives an outlook on future work.

## EFFUSION COOLING

This section briefly introduces the working principles of effusion cooling systems (see Fig. 1) and presents the two modeling approaches used in this work. To reduce the temperature

---

<sup>1</sup>FACTOR (Full Aerothermal Combuster Turbine interactiOns Research) is a European research project to investigate interactions of lean combustion chambers with the high-pressure turbine.

of combustion chamber walls, cool air is injected through a multitude of angled perforations to create a coolant film on the inner side of the liners. The performance of the effusion cooling system mostly depends on its capability to create a closed coolant film under different operating conditions. Main influencing parameters for the cooling efficiency are the injection angle  $\alpha$ , porosity  $\sigma$  and hole shape [2].

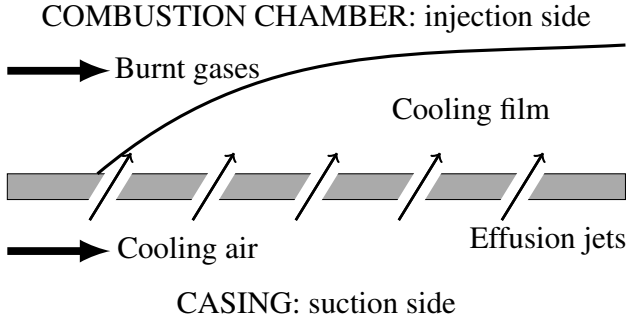


**FIGURE 1:** Schematic drawing of an effusion cooling system.

The porosity  $\sigma$  is defined as the hole surface  $A_{holes}$  over the plate surface  $A_{plate}$ ,

$$\sigma = \frac{A_{holes}}{A_{plate}} = \frac{\sum^{holes} (\pi D^2 / (4 \cos(\alpha)))}{A_{plate}}. \quad (1)$$

The injection angle  $\alpha$  is defined as,

$$\alpha = \tan^{-1} \left( \frac{U_n}{U_t} \right), \quad (2)$$

where  $U_n$  is the wall normal velocity component and  $U_t$  is the wall tangential velocity component. Injection holes typically have a diameter  $D < 1$  mm and shallow injection angles of  $\sim 20^\circ$ . Increasing the number of holes, while decreasing the hole diameter allows to use available coolant air more efficiently, as jets penetrate less into the main flow so coolant stays closer to the walls. However, small holes pose problems in the manufacturing process and are more likely to be clogged [1].

### Homogeneous injection model

The adiabatic homogeneous injection model [11] was developed to simulate the global impact of an effusion cooling system on the mean flow in complex industrial geometries. The model is local and does not rely on correlations or parameters which require information from other parts of the domain. For the surface

grid resolution, there are no additional requirements imposed by this model. The basic principle of the model is to inject coolant air on the entire plate surface. Wall tangential velocity  $U_t$  is conserved, whereas the wall normal velocity  $U_n$  is corrected to conserve the mass flow rate:

$$\rho U_n^{mod} = \rho U_n^{jet} / \sigma, \quad (3)$$

$$\rho U_t^{mod} = \rho U_t^{jet}. \quad (4)$$

The model injection angle  $\alpha^{mod}$  as compared to the original injection angle  $\alpha$  is defined as follows,

$$\tan(\alpha^{mod}) = \sigma \tan(\alpha). \quad (5)$$

### Heterogeneous injection model

The heterogeneous injection model (see Fig. 2) is designed to simulate the impact of an effusion cooling system on the entire flow field of a combustion chamber at a reasonable level of CPU cost [12]. To resolve jets by the grid, the jet geometry is adapted and the wall normal velocity  $U_n$  is reduced to maintain the correct mass flow rate for each hole. Using these modeled perforations, the wall tangential velocity  $U_t$  is corrected to conserve the axial momentum of the cooling film. Velocity profiles are prescribed on discrete surface areas and are no more uniform as in the homogeneous model. In regions with insufficient mesh resolution, the model adapts the holes to the point where a homogeneous injection is applied onto the entire plate surface.

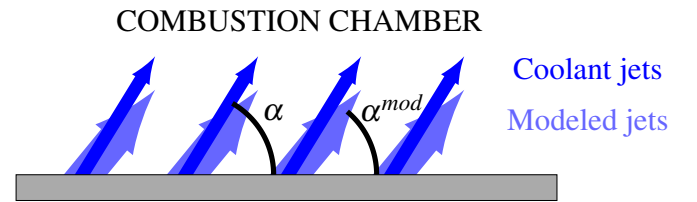


**FIGURE 2:** Schematic drawing of the heterogeneous injection model.

For the new model, the main influencing parameters are the enlargement  $E = 3$  [12], describing the minimum number of cell length per hole and the local grid resolution (here: 0.25 mm). For a coarse grid, jet diameters are enlarged up to a homogeneous representation (see Fig. 3a), whereas jets are represented with the correct diameter in regions where the grid is fine enough (see Fig. 3b).

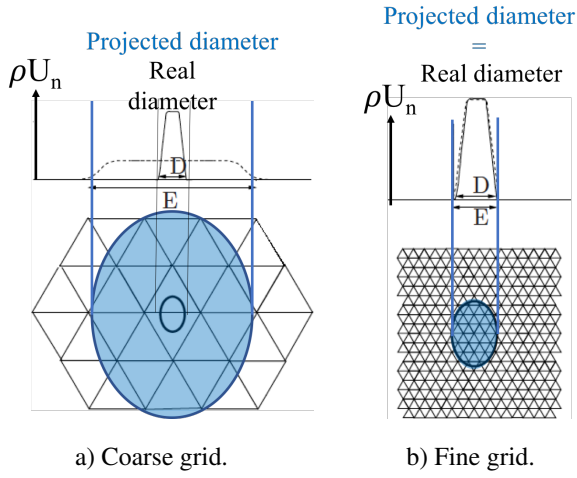


**FIGURE 3:** Widening of cooling holes as a function of local grid resolution (adapted from [12]).

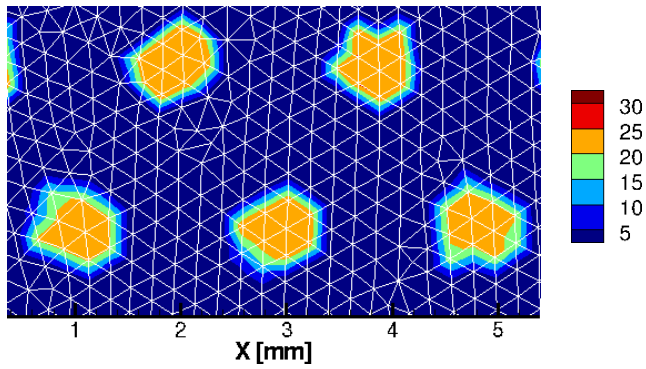


**FIGURE 4:** Injected axial momentum  $\rho U$  [ $\frac{kg}{m^2s}$ ] prescribed at the boundary for five jets arranged in a staggered pattern.

For the current study a surface grid size of 0.25 mm for the liner region was chosen, so that jet diameters are enlarged by a factor of 1.5 to be represented by at least three characteristic cell lengths (see Fig. 4). Note also that, for shallow injection angles, the model takes the elliptical hole shape into account. The numerical porosity  $\sigma_{num}$ , ranging from 1 for very fine meshes (fully resolved jets) to  $1/\sigma$  for very coarse meshes (homogeneous injection), is defined as the numerical hole surface  $A_{holes}^{num}$  over the real hole surface  $A_{holes}$ , i. e. :

$$\sigma_{num} = \frac{A_{holes}^{num}}{A_{holes}}, \quad (6)$$

becoming a local parameter. To conserve the axial momen-

tum of the cooling film using such adapted perforations, the wall tangential velocity  $U_t$  is fixed, whereas the wall normal velocity is multiplied by the factor  $1/\sigma_{num}$ , that is,

$$\rho U_n^{mod} = \rho U_n^{jet} / \sigma_{num}, \quad (7)$$

$$\rho U_t^{mod} = \rho U_t^{jet}. \quad (8)$$

Hence, the model injection angle  $\alpha^{mod}$  can be evaluated using,

$$\sigma_{num} \tan(\alpha^{mod}) = \tan(\alpha). \quad (9)$$

Note that this hypothesis may require adaptation to ensure the proper jet momentum representation and will be the subject of dedicated developments and analysis.

## SETUP

This section introduces the FACTOR geometry, the operating conditions and the mesh used for the simulations. The axial periodic domain [13] features  $1/20$  or  $18^\circ$  of the full annular non-reactive FACTOR test rig (see Fig. 5).

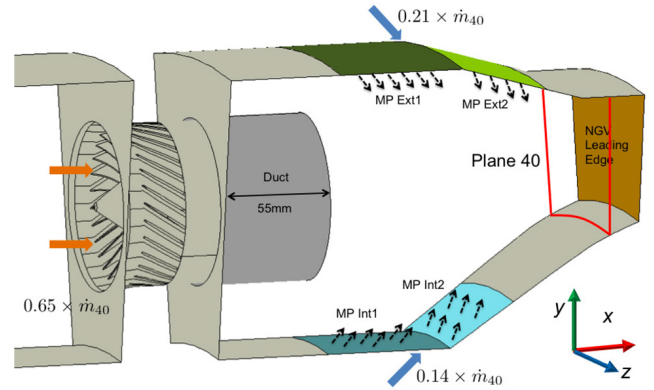


**FIGURE 5:** FACTOR combustion chamber [13].

The main flow is constrained by a 63 mm diameter duct of 55 mm length to preserve the swirler generated vortex and avoid early interactions with coolant flow and neighboring swirlers. The swirler consists of 30 flat vanes with a length of 20.5 mm around a central hub of a diameter of 22 mm. Cavity flows feeding the effusion cooling system are not simulated and coolant air is directly injected through the liners. All walls are considered to be adiabatic.

Simulations are performed at isothermal operating conditions, where hot wire anemometry (HWA) as well as particle image velocimetry (PIV) measurement data is available [14, 15]. A second, non-isothermal operating point, called design point (DP), allows for comparison of coolant distribution on P40 using temperature measurements. PIV measurements used an acquisition rate of 12 Hz over 30 s. Only the mainstream was seeded with particles, which creates a blind zone close to the walls [16]. HWA was performed on 281 points on P40 (see Fig 5) at an acquisition frequency of 20 kHz over a measurement period of 5 s. The data has been acquired on a trisector test rig at the University of Florence. Isothermal operating (IOP) conditions for measurements and simulations (see Tab. 1) have been derived from Koupper (2015) [16] to meet most important dimensionless quantities of the hot design point (DP) of the FACTOR test rig.

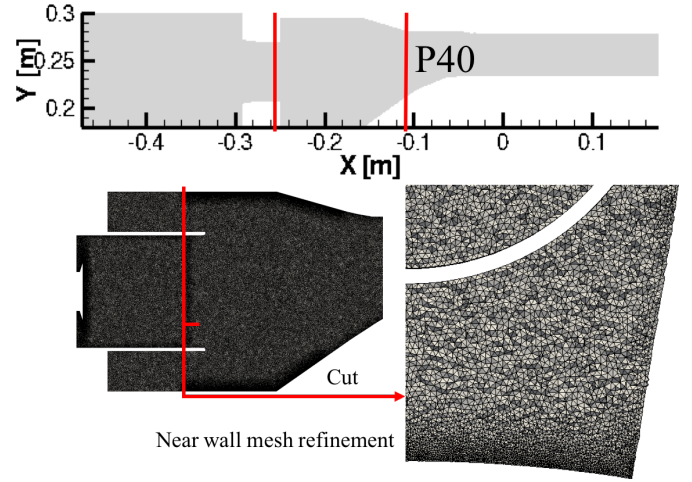


**FIGURE 6:** Computational domain and local views of the grid.

**TABLE 1:** FACTOR operating conditions [16].

	IOP	DP
Static pressure on P40 [kPa]	115	147.65
Mass flow [kg/s]	4.8	4.8
Flow split swirler [-]	65%	65%
Flow split outer cavity [-]	21%	21 %
Flow split inner cavity [-]	14%	14 %
Swirler inlet temperature [K]	300	531
Swirler Reynolds number [-]	168 500	111 000
Swirler Mach number [-]	0.108	0.112
Effusion cooling Reynolds number [-]	2340	2340

The fully unstructured tetrahedral grid contains about 50 million cells (see Fig. 6). The near wall region for the effusion cooling system is refined. To avoid influence from the boundary on the flow region of interest, the domain consists of a large entry plenum in front of the swirler and an exit sufficiently far away from P40 (see Fig. 6).

The effusion cooling system consists of four different panels (see Tab. 2). All effusion cooling holes have a diameter of  $D=0.5$  mm and are arranged in a staggered pattern. Depending on the porosity of the real geometry, the modeling parameters differ for each surface (see Tab. 2).

## NUMERICAL METHODOLOGY

Simulations presented in this work are performed using AVBP, a massively parallel CFD code developed at CERFACS and IPFEN. The code is based on a fully explicit cell-vertex formulation and solves the compressible Navier-Stokes equations for conservative variables on unstructured or hybrid grids. AVBP

**TABLE 2:** Geometrical and modeling parameters of the effusion cooling system.

Panel	Number of rows	Holes/ Row	$\alpha$	$\sigma$	Mass flow [kg/s]	Mass flow [%]	$\alpha_{hom}$	$\alpha_{het}$	$\sigma_{num}$
Ext 1	50	630	60°	0.0773	0.624	13	7.6°	47.3°	1.60
Ext 2	24	850	30°	0.115	0.384	8	3.8°	19.9°	1.60
Int 1	58	416	60°	0.0957	0.48	10	9.4°	47.5°	1.59
Int 2	21	460	30°	0.104	0.192	4	3.5°	19.3°	1.61

is dedicated to LES and has been used and validated for a wide range of different applications [17–19]. The code has been extensively used in effusion jets [11, 20] as well as jets in cross flow configurations [21]. Simulations are first converged using the Lax-Wendroff scheme [22], then the more accurate TTGC scheme [23], which provides third order accuracy in time and space, is chosen. This scheme ensures low diffusion and dispersion properties [24] and is therefore adequate for high fidelity simulations. Diffusive terms are discretized using a vertex centered formulation close to the Galerkin finite element method [25]. Time marching is done, respecting CFL (convection scheme) and Fourier (diffusion scheme) numbers to guarantee linear stability. Colin-type artificial viscosity [26] is added to dampen potential numerical oscillations naturally present with the used schemes. Sub grid scale (SGS) turbulent contributions are computed using the Smagorinsky model [27]. Using the classical gradient diffusion hypothesis [28] the SGS heat flux is related to the filtered temperature gradient with a SGS thermal conductivity computed with a SGS turbulent Prandtl number of 0.6. Effusion cooling systems are modeled using a homogeneous [11] and a heterogeneous [12] injection model. The application of Navier-Stokes Characteristic Boundary Conditions (NSCBC) [29] allows to naturally establish a radial equilibrium pressure profile at the outlet [30]. To prevent reflections from the outlet, a sponge layer [31] adds additional dissipation close to the exit of the domain. To access turbulence quantities using autocorrelation [28, 32], a constant time step of  $7 \times 10^{-8}$  s, corresponding to a CFL number [33] of 0.9 is used for the simulation. The near-wall velocity gradient is calculated using wall functions [18]. Finally, solutions are evaluated over a period of five flow through times of the combustor module using the TTGC scheme.

## RESULTS

This section compares the impact of the two different effusion cooling models on the flow field. Globally, both models lead to similar results, however differences in the near wall region are visible. Differences close to the wall are due to coolant jets modeled in the heterogeneous approach penetrating further into the domain than the coolant injected in the homogeneous approach. The additional computational cost of 0.3 % for applying the heterogeneous injection model confirms that use of this new model has a negligible impact on the overall cost of these LES.

### Mean field comparison and validations

First, the main quantities of both simulations are compared on a longitudinal plane through the hub of the swirler which is perpendicular to P40. Both simulations show a similar pressure distribution (see Fig. 7a). The low pressure zone after the swirler is due to the recirculation zone generated by the swirler.

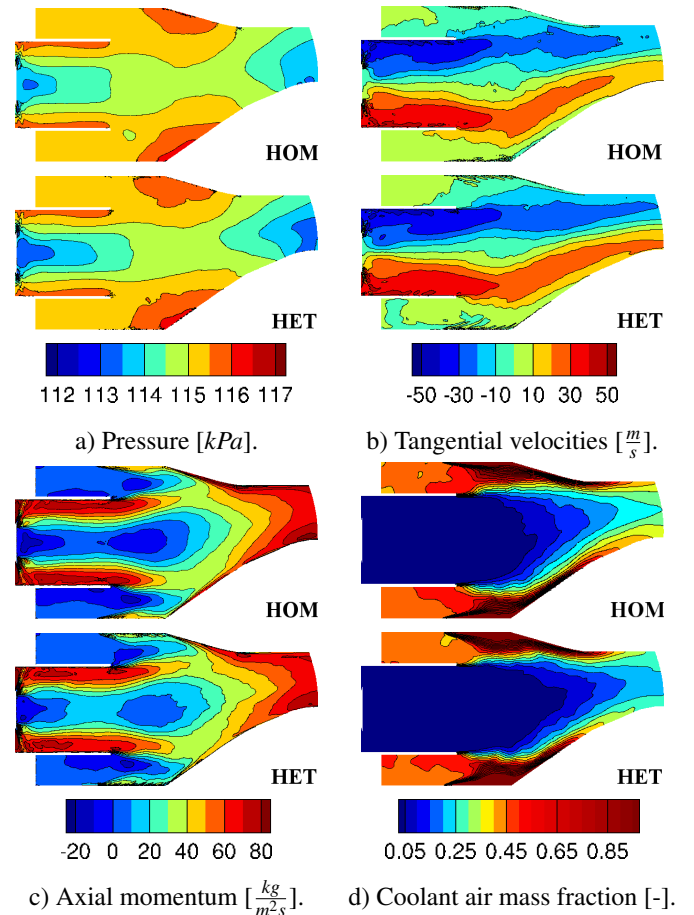


**FIGURE 7:** Cross sections through domain for homogeneous (upper) and heterogeneous (lower) injection model.

After the duct, the vortex is no longer confined and breaks down, creating recirculation zones at the edges of the duct and in the center. The tangential velocities for both simulations are similar (see Fig. 7b). Both show a clear separation of fluid moving perpendicularly to the plane of observation in the middle of the domain. In the simulation using the heterogeneous injection model, due to the steeper injection angle, flow features are moved away from the multiperforated walls as compared to the homogeneous injection model. Near the inner liner, where the inclination of the plate is stronger than for the exterior panel, there is a noticeable difference in the flow field (see Fig. 7c), also seen from the axial velocity plots on P40 (see Fig. 10, to be discussed later). The coolant distribution clearly shows the effect of the heterogeneous model on the flow (see Fig. 7d). Using the heterogeneous model, the coolant mixes more with the flow and reaches further into the domain than in the homogeneous modeling approach, where the coolant moves closer along the liner at higher speeds.

In the following, mean field visualizations yield by the two LES predictions are compared and gauged to experimental data. To do so, a longitudinal plane going through the central hub of the swirler is chosen (see Fig. 8). Velocity contours of the axial (Fig. 8a) and transversal velocity (Fig. 8b) show good agreement between both simulations and experiments indicating effects of this modeling. Indeed, both models capture the central re-circulation zone found in experiment (see Fig. 8a). Along the inner liner walls one notes that, the axial velocity in the homogeneous modeling approach is higher than in the heterogeneous approach or in the experiments. Differences between both modeling approaches are most evident close to the wall, but also in the middle of the cross section where the experimental results lie in-between those obtained from both LES predictions (see Fig. 9). Further away from the swirler, the velocities measured in the experiment are lower than those obtained from the simulations (see Fig. 9). Because of the higher inclination of the inner liner compared to the outer liner, the differences in the injection models are more obvious along the interior walls. The high velocity along the walls in the simulation using the homogeneous injection model is due to the shallow injection angle ( $< 5^\circ$ ) as compared to the real injection angle of  $60^\circ$  (see Tab. 2, Fig. 5). Using the heterogeneous model fluid is injected at a steeper angle to the surface and coolant goes further into the domain. The radial velocity components issued by both simulations are very similar (see Fig. 8b). Since the PIV measurement does not capture the upward movement of the coolant flow injected at the inner liner, as in the experiment only the main flow was seeded with particles, the PIV data shows velocities close to zero in the region near the liners.

Having assessed the mean chamber flow field, the remaining part of this section focuses on the maps and profiles for P40. Overall both models show a similar flow distribution in P40. Looking at 2D maps of coolant mass fraction in the P40 plane, Fig. 11, one observes: Using the heterogeneous injection model, coolant is arranged in a rounder shape which might indicate a better conserved processing vortex core. Along the walls, especially on the interior liner, the coolant distribution is more uniform using the homogeneous injection model.

Focusing now on the velocity field in P40, where hot wire anemometry data covering about 60 % of P40 is available for isothermal operating conditions, a direct comparison, Fig. 10, results in the following observations: First, both simulations compare well with experimental results. In the simulation using the homogeneous injection model, there is a higher axial velocity near walls, notably along the interior liners (see Fig. 10a). Figure 11 shows that the high velocities on the interior walls are mainly due to coolant injected through the interior liners. Using the homogeneous injection model a robust cooling film is created along the liners. This film can hardly be disturbed or penetrated, so there is less mixing with the surrounding flow. Inject-

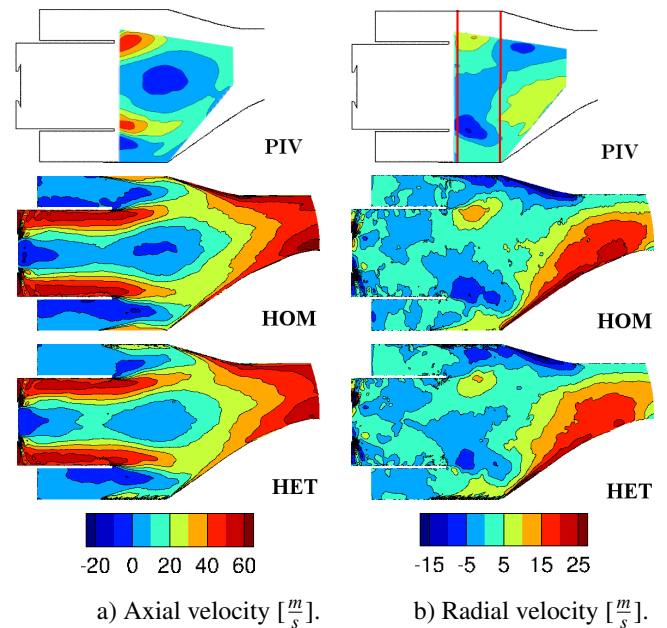


**FIGURE 8:** Velocity on cross section (Upper: PIV, Middle: Homogeneous, Lower: Heterogeneous; Red lines indicate vertical profiles in Fig. 9). (Isothermal Operating Point).

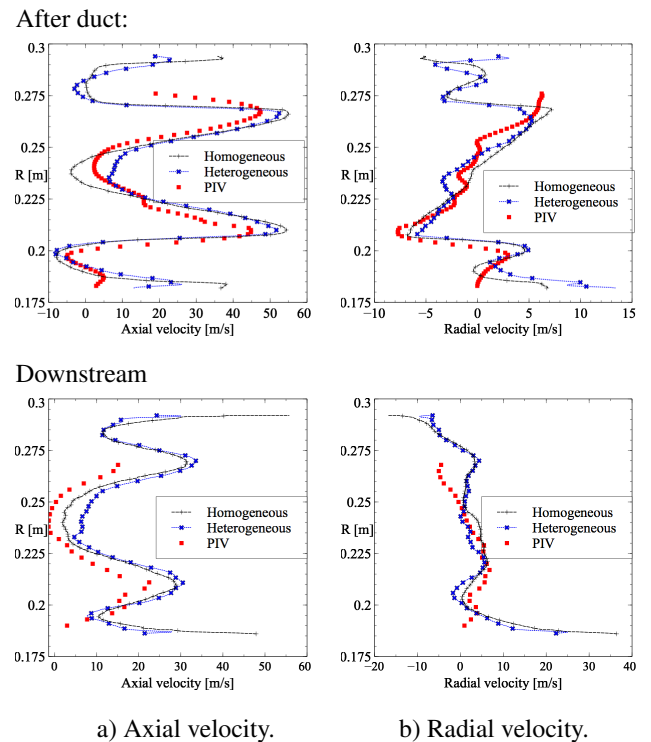


**FIGURE 9:** Vertical profiles of velocity components (Positions indicated in Fig. 8), Upper: after duct, Lower: Downstream.

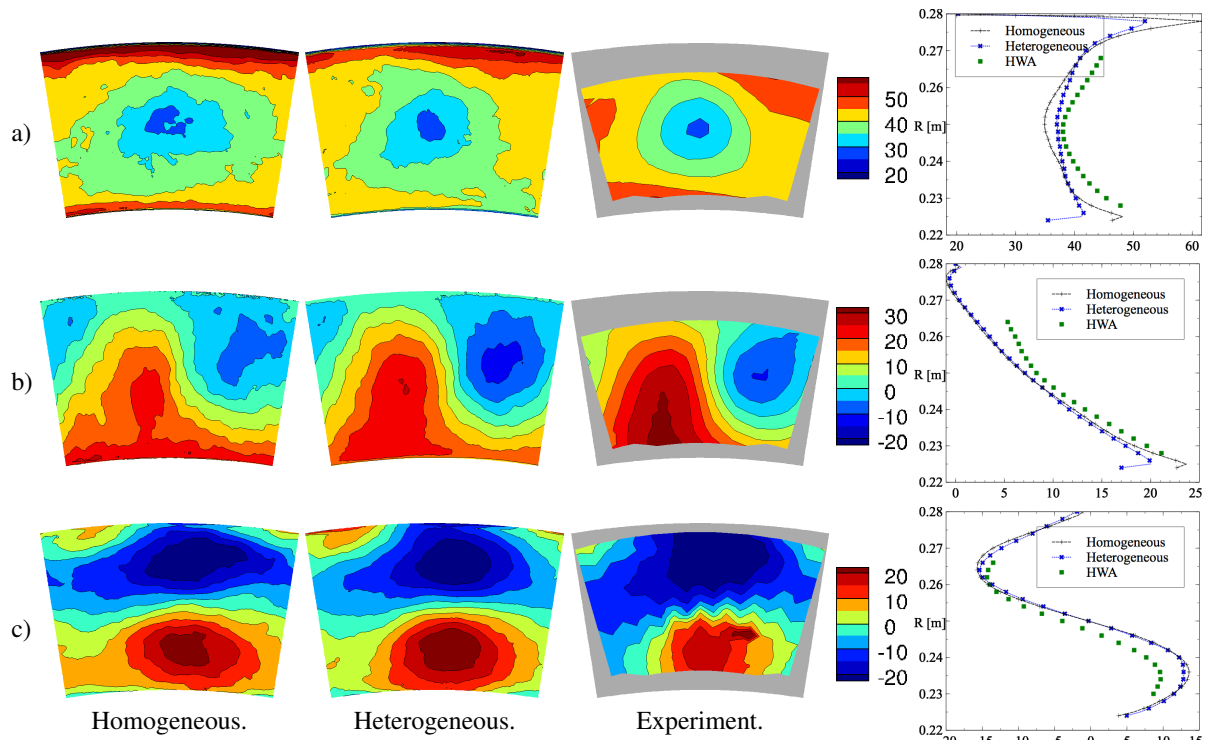


**FIGURE 10:** Velocity plots and circumferentially averaged profiles on P40. a) Axial velocity [ $\frac{m}{s}$ ]. b) Radial velocity [ $\frac{m}{s}$ ]. c) Tangential velocity [ $\frac{m}{s}$ ]. View direction: Downstream. (Isothermal Operating Point).

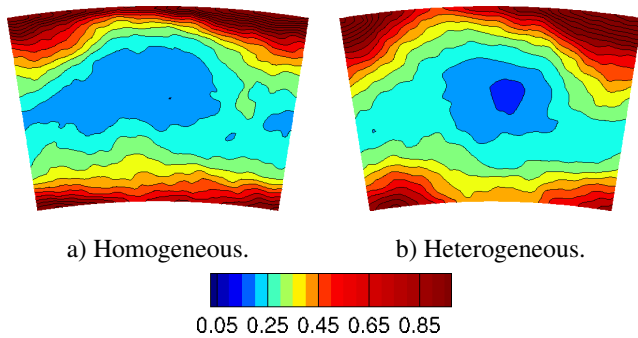


**FIGURE 11:** Coolant air mass fraction on P40. View direction: Downstream. (Isothermal Operating Point).

ing the coolant through discrete surfaces results in more mixing between coolant flow and main flow. On the interior liner, where the change of inclination is stronger as compared to the exterior combustion chamber walls, the injected coolant mixes with the flow. Finally, it is noticeable that, in the central zone covered by the measurement, the velocity in the experiment is higher than in the simulations, indicating that the velocity along the walls is probably too high in both simulations (see Fig. 10a). Regarding

the radial velocity plots (see Fig. 10b), one observes that the heterogeneous model is in better agreement with the experiments than the homogeneous injection model. For the tangential velocity components (see Fig. 10c), there is a good agreement between both models. Evaluating in the following, velocity profiles at design point operating conditions (see Fig. 12) where velocity measurements from a 5 hole pressure probe are available leads to similar observations. Again both models show a good agreement with each other. In the liner region, due to the shallow injection angle, the axial momentum predicted by the homogeneous injection model is higher than in the simulation using the heterogeneous model (see Fig. 12a). Radial and tangential velocities show a good agreement between both models and capture the velocities measured in the experiment (see Fig. 12b,c). Globally, the flow field comparing design and isothermal operating point is similar.

### Turbulence

After discussing general flow features, this section focuses on turbulence, comparing both models. Figure 13 shows the impact of the effusion cooling modeling on the recirculation zones after the duct by plotting the turbulent kinetic energy. Using the heterogeneous model these zones are flattened as compared to

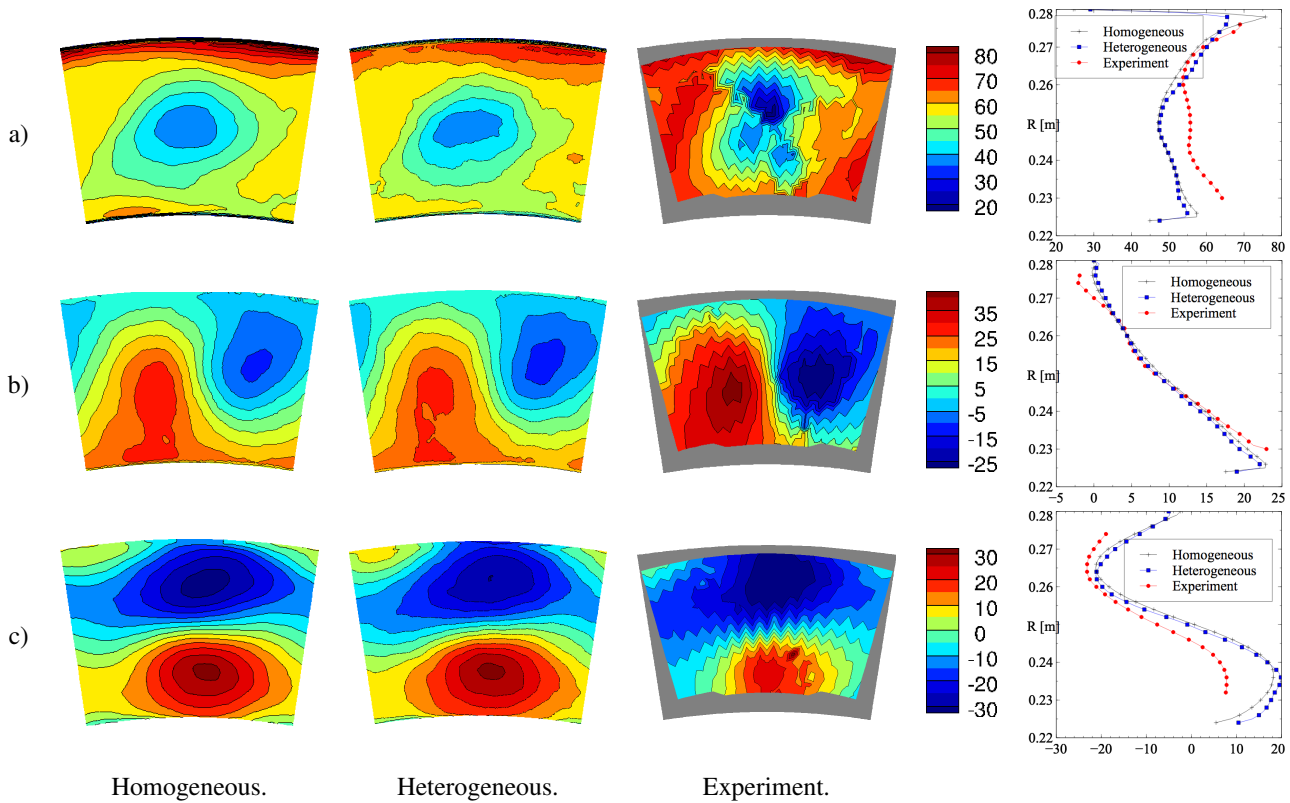


**FIGURE 12:** Velocity on P40. a) Axial momentum  $[\frac{kg}{m^2s}]$ . b) Radial velocity  $[\frac{m}{s}]$ . c) Tangential velocity  $[\frac{m}{s}]$ . View direction: Downstream. (Design Point).

the homogeneous approach. Furthermore, higher levels of turbulent kinetic energy migrate through the domain and reach P40, as also seen from Fig. 14.

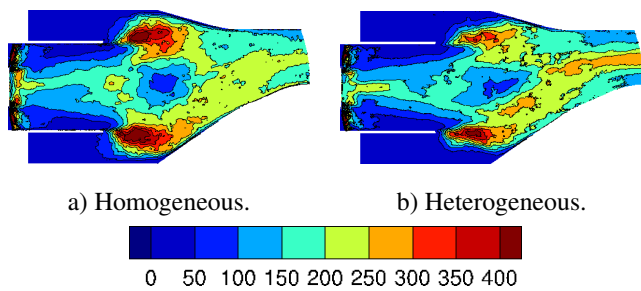


**FIGURE 13:** Plots of turbulent kinetic energy  $[\frac{m^2}{s^2}]$  on cross sections through domain. (Isothermal Operating Point).

Both models obtain a similar pattern of turbulent kinetic energy (TKE) on P40 (see Fig. 14a). The wave-like shape is caused by the PVC breaking down shortly after leaving the duct. For the

heterogeneous model the average TKE on P40 is slightly higher than the value obtained using the homogeneous injection model (see Tab. 3). This might be due to traces of the PVC being better preserved using the heterogeneous model. Notably, the upper right corner of P40, favored by coolant flow (see Fig. 11), shows lower values for TKE in the simulation using the heterogeneous injection model. Plots of turbulent timescale both capture the largely undiluted (see Fig. 11) core of the PVC as a region with large turbulent timescales (see Fig. 14b). Position and magnitude are comparable between simulations and experiment, although in the experiment access to longer acquisition time and fewer probe positions yields fields that are more uniform on P40. The frequency spectrum obtained by Dynamic Mode Decomposition [34] of a set of instantaneous 2D solutions on P40 (see Fig. 15), shows similar values for both simulations. Both capture the PVC at a frequency of 315 Hz. However the PVC signal is stronger in the simulation using the heterogeneous injection model, possibly because of better conserved traces of the PVC. The decay of turbulent kinetic energy is indicated by Kolmogorov's -5/3 law [35]. Calculating the turbulent kinetic energy on the axial velocity component available from HWA measure-

**TABLE 3:** Average values for turbulent quantities on P40.

	TKE [ $\frac{m^2}{s^2}$ ]	Turbulent timescale [ $10^{-4}s$ ]
Homogeneous	176	1.39
Heterogeneous	188	1.42
Experiment		1.59

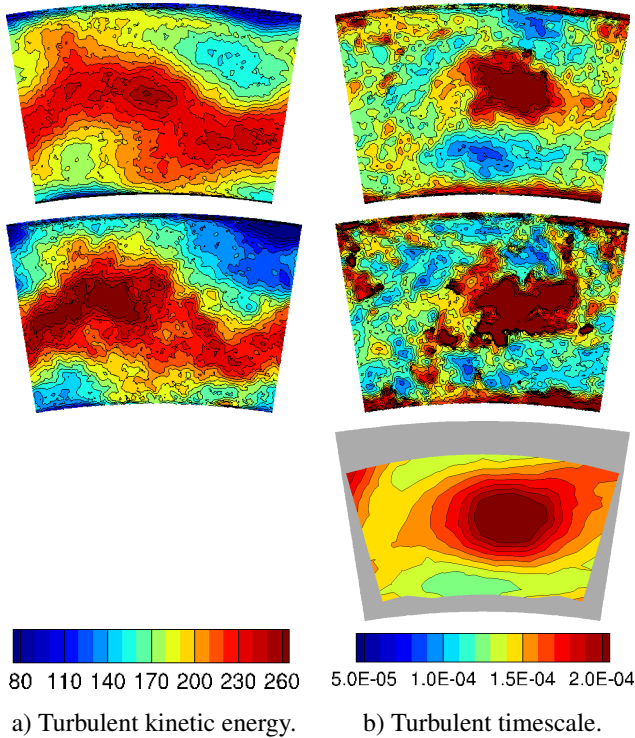


**FIGURE 14:** Turbulent kinetic energy [ $\frac{m^2}{s^2}$ ] and turbulent timescale [ $s$ ] for homogeneous (upper) and heterogeneous (middle) injection model. Turbulent timescale for experiment (lower) are displayed for comparison. View direction: Downstream. (Isothermal Operating Point).

ments allows a direct comparison of higher order LES quantities with experimental data (see Fig. 16). On P40 experimental data and 2D maps obtained from both LES's show good agreement and the previously discussed wavy shape, caused by vortex breakdown is again visible. The longer acquisition period of 5 s in the experiment as compared to 50 ms in the simulations also explains the smoother shape of second order quantities in the experiment.

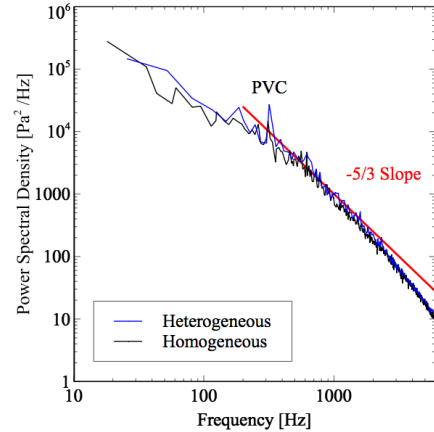


**FIGURE 15:** Power spectral density of pressure for homogeneous and heterogeneous injection model from Dynamic Mode Decomposition of 2D solutions on P40.

### Temperature

Studying the temperature field at the design point operating conditions allows to approximately investigate the coolant distribution on P40 (see Fig. 17), neglecting temperature changes caused by aerodynamic effects. Due to the absence of dilution holes in the chamber design, the temperature distribution is highly non-uniform and a well marked hotspot can be observed in the middle of P40. In the simulation using the heterogeneous injection model (see Fig. 17b)) coolant from the upper liner penetrates further into the domain compared to the simulation using the homogeneous injection model (see Fig. 17a)).

### CONCLUSION

In this study, two industrial scale applicable LES effusion cooling models are compared and evaluated against experimental data obtained from an engine representative lean combustion simulator test rig. The heterogeneous injection model can be applied to realistic gas turbine engines in the design process at a reasonable level of additional cost (+0.3 %, determined over a simulation time of 6 ms). The model offers a great flexibility as it adapts to the local mesh-resolution. Especially in cases with big injection angles, the heterogeneous model better captures the impact of angled effusion cooling systems on the flow field. Globally, the new model leads to similar results as the well-validated homogeneous injection model. In the near wall region, the application of the heterogeneous injection model leads to more realistic representation of the cooling film. Fully resolved computations of effusion cooling systems in realistic combustor geometries remaining unaffordable for the next decades, the heterogeneous injection model investigated in this work provides a good approximation on the way to more realistic engine combustor simulations. Accurately determining the performance of

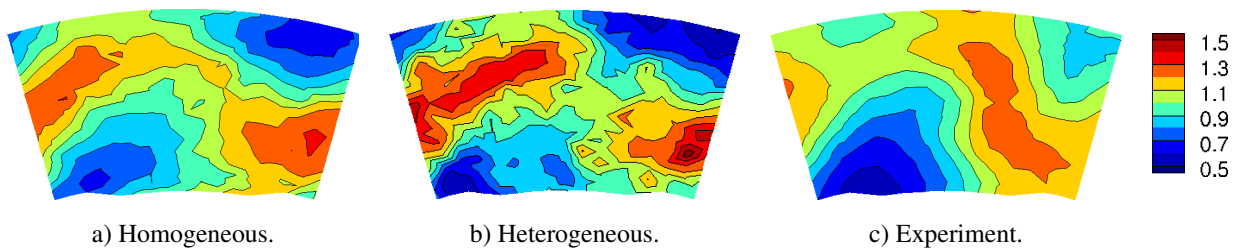


FIGURE 16: Non-dimensionalized TKE on P40 calculated on axial velocity component. View direction: Downstream. (IOP).

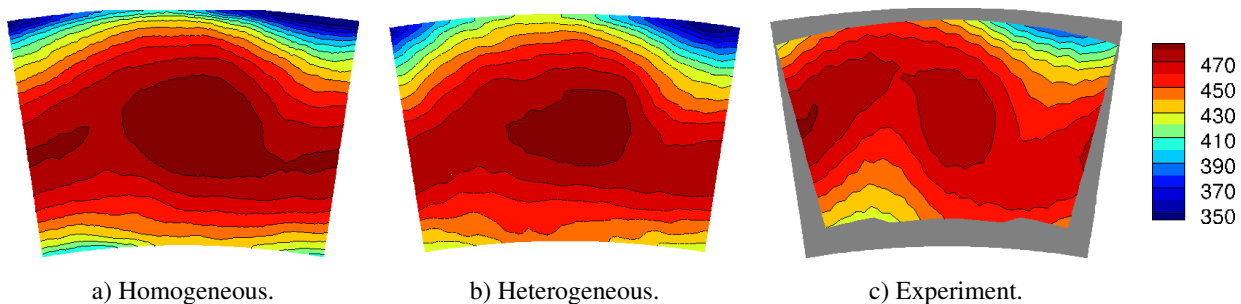


FIGURE 17: Temperature [K] on P40 for design point. View direction: Downstream.

liner cooling systems is a crucial part in the development of next generation lean combustion chambers as it plays an important role for liner lifetime and engine efficiency. Upon availability of measurement data from the full angular FACTOR test rig at new operating conditions, this data will be used to further validate the heterogeneous injection model as well as to investigate the impact of the effusion cooling system on thermal loads of the high-pressure turbine. In terms of model development, further work regarding jet velocity profiles and jet penetration depth is required. Although the generic problem of one jet in a cross flow, upon which most simple modeling approaches are based on, is well investigated, the case of a jet array in the complex flow field of a lean combustion chamber is still a very new field of research. Multi-jet interactions are still not well understood and the insufficient accuracy of currently applied models requires the use of huge safety factors in cooling system design.

#### ACKNOWLEDGMENT

The authors wish to gratefully acknowledge FACTOR (Full Aerothermal Combustor-Turbine interactiOns Research) Consortium for the kind permission of publishing the results herein. FACTOR is a Collaborative Project co-funded by the European Commission within the Seventh Framework Programme (2010-2017) under the Grant Agreement n° 265985. This work was granted access to the HPC resources of IDRIS under the allocation 2016 - 2b7525 made by GENCI.

#### REFERENCES

- [1] Wadia, A. R., 1988. "Advanced combustor linear cooling technology for gas turbines". *Defence Science Journal*, **38**(4), pp. 363–380.
- [2] Lefebvre, A. H., and Ballal, D. R., 2015. *Gas Turbine Combustion*, Vol. 1. CRC Press.
- [3] Goldstein, R. J., 1971. "Film cooling". *Advances in heat transfer*, **7**, pp. 321–379.
- [4] Colladay, R., Esgar, J., and Kaufman, A., 1970. "An analysis of the capabilities and limitations of turbine air cooling methods". *Washington, D.C.: National Aeronautics and Space Administration*.
- [5] Crawford, M., Kays, W., and Moffat, R., 1980. "Full-coverage film cooling part II: heat transfer data and numerical simulation". *Journal of engineering for power*, **102**(4), pp. 1006–1012.
- [6] Hunter, S. D., 1998. "Source term modeling of endwall cavity flow effects on gaspath aerodynamics in an axial flow turbine". *Ph.D.Thesis, University of Cincinnati*.
- [7] Heidmann, D., and Hunter, D., 2001. "Coarse Flows Grid Using Modeling Volumetric of Turbine Source Film Terms Cooling". *NASA-TM/2001-210817*(May).
- [8] Burdet, A., Abhari, R. S., and Rose, M. G., 2007. "Modeling of Film Cooling - Part II: Model for Use in Three-Dimensional Computational Fluid Dynamics". *Journal of Turbomachinery*, **129**(2), p. 221.
- [9] Voigt, S., Noll, B., and Aigner, M., 2012. "Development of

- a Macroscopic CFD Model for Effusion Cooling Applications”. *Proceedings of ASME Turbo Expo 2012*, pp. 1–9.
- [10] Mazzei, L., Picchi, A., Andreini, A., Facchini, B., and Vitale, I., 2016. “Unsteady CFD Investigation of Effusion Cooling Process in a Lean Burn Aero-Engine Combustor”. In *ASME Turbo Expo 2016: Turbomachinery Technical Conference and Exposition, American Society of Mechanical Engineers*, pp. V05BT17A008–V05BT17A008.
- [11] Mendez, S., and Nicoud, F., 2008. “Adiabatic Homogeneous Model for Flow Around a Multiperforated Plate”. *AIAA Journal*, **46**(10), pp. 2623–2633.
- [12] Lahbib, D., 2015. “Modelisation aerodynamique et thermique des multiperforations en LES”. *Ph.D. Thesis, Université de Montpellier*.
- [13] Koupper, C., Cacioli, G., Gicquel, L., Duchaine, F., Bonneau, G., Tarchi, L., and Facchini, B., 2014. “Development of an Engine Representative Combustor Simulator Dedicated to Hot Streak Generation”. *Journal of Turbomachinery*, **136**(11), p. 111007.
- [14] Koupper, C., Gicquel, L., Duchaine, F., Bacci, T., Facchini, B., Picchi, A., Tarchi, L., and Bonneau, G., 2015. “Experimental and Numerical Calculation of Turbulent Timescales at the Exit of an Engine Representative Combustor Simulator”. *Journal of Engineering for Gas Turbines and Power*, **138**(2), p. 021503.
- [15] Bacci, T., Facchini, B., Picchi, A., Tarchi, L., Koupper, C., and Champion, J.-I., 2015. “Turbulence Field Measurements At the Exit of a Combustor Simulator”. *ASME Turbo Expo*, pp. 1–14.
- [16] Koupper, C., 2015. “Unsteady multi-component simulations dedicated to the impact of the combustion chamber on the turbine of aeronautical gas turbines”. *Ph.D. Thesis, Université de Toulouse*.
- [17] Moureau, V., Lartigue, G., Sommerer, Y., Angelberger, C., Colin, O., and Poinso, T., 2005. “Numerical methods for unsteady compressible multi-component reacting flows on fixed and moving grids”. *Journal of Computational Physics*, **202**(2), pp. 710–736.
- [18] Schmitt, P., Poinso, T., Schuermans, B., and Geigle, K. P., 2007. “Large-eddy simulation and experimental study of heat transfer, nitric oxide emissions and combustion instability in a swirled turbulent high-pressure burner”. *Journal of Fluid Mechanics*, **570**, pp. 17–46.
- [19] Schoenfeld, T., and Rudgyard, M., 1999. “Steady and unsteady flow simulations using the hybrid flow solver AVBP”. *AIAA Journal*, **37**(11), pp. 1378–1385.
- [20] Mendez, S., and Nicoud, F., 2008. “Large-eddy simulation of a bi-periodic turbulent flow with effusion”. *Journal of Fluid Mechanics*, **598**, pp. 27–65.
- [21] Baya Toda, H., Cabrit, O., Truffin, K., Bruneaux, G., and Nicoud, F., 2014. “Assessment of subgrid-scale models with a large-eddy simulation-dedicated experimental database: The pulsatile impinging jet in turbulent cross-flow”. *Physics of Fluids*, **26**(7), jul, p. 075108.
- [22] Lax, P., and Wendroff, B., 1960. “Systems of conservation laws”. *Communications on Pure and Applied Mathematics*, **13**(2), pp. 217–237.
- [23] Colin, O., and Rudgyard, M., 2000. “Development of High-Order Taylor-Galerkin Schemes for LES”. *Journal of Computational Physics*, **162**(2), pp. 338–371.
- [24] Lamarque, P. M. N., 2007. “Schémas numériques et conditions limites pour la simulation aux grandes échelles de la combustion diphasique dans les foyers d’hélicoptère”. *PhD thesis, Université de Toulouse - MeGeP - Dynamique des Fluides*.
- [25] Colin, O., Benkenida, A., and Angelberger, C., 2003. “3D Modeling of Mixing, Ignition and Combustion Phenomena in Highly Stratified Gasoline Engines”. *Oil & Gas Science and Technology*, **58**(1), pp. 47–62.
- [26] Colin, O., 2000. “Large eddy simulation of evaporating sprays in complex geometries using Eulerian and Lagrangian methods”. *PhD thesis, INSA de Rouen*.
- [27] Smagorinsky, J., 1963. “General circulation experiments with the primitive equations: I. the basic experiment”. *Monthly weather review*, **91**(3), pp. 99–164.
- [28] Pope, S. B., 2001. *Turbulent Flows*. Cambridge University Press.
- [29] Poinso, T. J., and Lele, S. K., 1992. “Boundary Conditions for Direct Simulation of Compressible Viscous Flows”. *Journal of Computational Physics*, **101**, pp. 104–129.
- [30] Koupper, C., Poinso, T., Gicquel, L., and Duchaine, F., 2014. “Compatibility of Characteristic Boundary Conditions with Radial Equilibrium in Turbomachinery Simulations”. *AIAA Journal*, **52**(12), pp. 2829–2839.
- [31] Israeli, M., and Orszag, S. A., 1981. “Approximation of Radiation Boundary Conditions”. *Journal of Computational Physics* **41.1**, **20**, pp. 115–135.
- [32] Koupper, C., Gicquel, L., Duchaine, F., Bacci, T., Facchini, B., Picchi, A., Tarchi, L., and Bonneau, G., 2015. “Experimental and Numerical Calculation of Turbulent Timescales at the Exit of an Engine Representative Combustor Simulator”. *Journal of Engineering for Gas Turbines and Power*, **138**(2), p. 021503.
- [33] Courant, R., Friedrichs, K., and Lewy, H., 1928. “Über die partiellen Differenzgleichungen der mathematischen Physik”. *Mathematische Annalen*, **100**(1), pp. 32–74.
- [34] Schmid, P. J., 2010. “Dynamic mode decomposition of numerical and experimental data”. *Journal of Fluid Mechanics*, **656**, pp. 5–28.
- [35] Kolmogorov, A. N., 1941. “The local structure of turbulence in incompressible viscous fluid for very large reynolds numbers”. In *Dokl. Akad. Nauk SSSR, Vol. 30*, JSTOR, pp. 301–305.



# Assessment of a Coolant Injection Model on Cooled High-Pressure Vanes with Large-Eddy Simulation

M. Harnieh<sup>1</sup>  · M. Thomas<sup>1</sup> · R. Bizzari<sup>1</sup> · J. Dombard<sup>1</sup> · F. Duchaine<sup>1</sup> · L. Gicquel<sup>1</sup>

Received: 22 February 2019 / Accepted: 9 October 2019 /  
© Springer Nature B.V. 2019

## Abstract

The high-pressure turbine blades are the components of the aero-engines which are the most exposed to extreme thermal conditions. To alleviate this issue, the blades are equipped with cooling systems to ensure long-term operation. However, the accurate prediction of the blade temperature and the design of the cooling system in an industrial context still remains a major challenge. Potential improvement is foreseen with Large-Eddy Simulation (LES) which is well suited to predict turbulent flows in such complex systems. Nonetheless, performing LES of a real cooled high-pressure turbine still remains expensive. To alleviate the issues of CPU cost, a cooling model recently developed in the context of combustion chamber liners is assessed in the context of blade cooling. This model was initially designed to mimic coolant jets injected at the wall surface and does not require to mesh the cooling pipes leading to a significant reduction in the CPU cost. The applicability of the model is here evaluated on the cooled Nozzle Guide Vanes (NGV) of the Full Aerothermal Combustor Turbine interactions Research (FACTOR) test rig. To do so, a hole modeled LES using the cooling model is compared to a hole meshed LES. Results show that both simulations yield very similar results confirming the capability of the approach to predict the adiabatic film effectiveness. Advanced post-processing and analyses of the coolant mass fraction profiles show that the turbulent mixing between the coolant and hot flows is however reduced with the model. This finding is confirmed by the turbulent map levels which are lower in the modeled approach. Potential improvements are hence proposed to increase the accuracy of such methods.

**Keywords** Large-eddy simulation · Blade cooling · Film cooling · Modeling

## 1 Introduction

To comply with new environmental regulations, the thermal efficiency of gas turbines has been improved by increasing the temperature at the exit of the combustion chamber. As a result, the thermal load on Nozzle Guide Vanes (NGV) has significantly increased. Indeed,

---

✉ M. Harnieh  
harnieh@cerfacs.fr

<sup>1</sup> CERFACS - 42, Av. Gaspard Coriolis, 31057 Toulouse Cedex 1, France

the combustion temperatures in current burners surpass the thermal stress limits of the blade material. This makes necessary the introduction and use of sophisticated cooling systems inside and around blades. One efficient solution collects cold air from the compressor and re-injects it around the NGVs through cooling pipes. A scheme of typical engine cooled turbine blade is provided in Fig. 1. In such an arrangement, the coolant forms a protective film around the blade which limits the blade temperature. However, the turbulence generated in the flow will affect the mixing between the coolant and the hot flow impacting the film integrity and thereby its film effectiveness. The numerical prediction of the film effectiveness on cooled industrial vanes remains a challenge today due to geometry complexity as well as high number of coolant holes. Reynolds Average Navier-Stokes (RANS) simulations have been used in the past decades to predict the thermal load on blades. Due to the size and the number of cooling holes, big efforts are needed to mesh the cooling system. To limit this effort, film cooling models have been implemented in RANS [1–3]. The aim of these models is to inject the coolant flow on the wall without meshing the cooling pipes. However if implemented in the context of RANS, the predictions still suffer from a lack of accuracy to predict mixing [4–6] and obtained film effectivenesses remain highly sensitive to RANS closure as well as to the mesh resolution. To alleviate this issue, one solution is to perform Large-Eddy Simulations (LES) which resolve the most energetic turbulent structures on the mesh [7, 8]. Indeed, LES is more and more used to study the flows in academic and complex geometries in the literature [9–11]. These studies have shown the capacity of LES to predict the aerodynamics of the flow for turbomachinery configurations. When extended to cooled configurations, few LES studies have been reported. Such high-fidelity simulations were

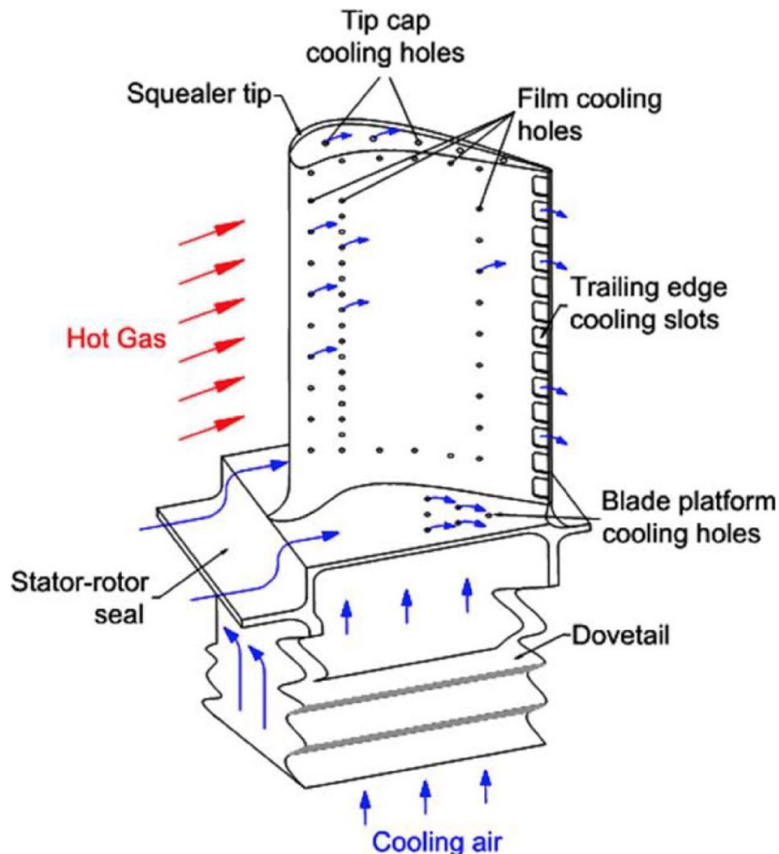


**Fig. 1** Scheme of a cooled turbine vane extracted from [23]

only performed on isolated cooling systems of academic vanes featuring a limited span-wise extent [12–14]. Very few LES studies representing full span-wise extent of 3D cooled turbine vanes have been reported in the literature [6, 15]. Indeed, resolving the entire NGV cooling system in LES requires a large number of cells to compute the flow in the cooling system. The same situation has been encountered for the modeling of multiperforated plates of aeronautical combustion chamber liners. To limit the associated computational cost, Mendez and Nicoud [16] have proposed a homogeneous model with the objective to inject the coolant homogeneously on the wall conserving the integrated mass flow rate and tangential momentum flux over the wall. In this homogenisation process, the dynamic of the jets is lost and the mixing with the hot flow is under-estimated. While addressing this specific weakness, Bizzari et al. [17] have proposed a thickened hole LES model so as to take into account the position of perforations as well as the capacity of the local mesh resolution to properly represent the jets. In this approach, the cooling system is not meshed but projected on the surface of the blades allowing to save significant CPU resources and human work to set up CAD and associated meshes. This new modeling approach provides better results compared to the homogeneous model, reproducing the dynamics of the jets if increasing the mesh resolution [18, 19]. The aim of the present work is to evaluate this new modeling approach in the specific context of cooled industrial turbine vanes. To assess the model, two simulations are carried out on the NGVs of the European project FACTOR (Full Aerothermal Combustor Turbine interactiOns Research) [20], experimentally studied at the DLR (Germany) [21] and at UNIFI (Italy) [22]. The rig features a full annular non-reactive lean combustion demonstrator with one high-pressure turbine stage. At the exit of the combustor, the flow field features high levels of swirl, turbulence and temperature non-uniformities approaching realistic conditions of industrial configurations. The blades are cooled by a cold flow coming from internal plena and exiting through 171 holes on each vane. First, a fully meshed configuration is considered including the cooling system: i.e. the plena and the holes. Then, a second computation using the thickened hole model which does not consider the internal feeding plena is produced. Comparisons of both predictions are then detailed in an attempt to assess the capacity of the hole modeled approach for real applications.

The discussion around this specific objective is organized as follows. First, the modeling of the coolant injection process is introduced in Section 2. Details on the numerical set up, computational domains and LES modeling are presented in Section 3. Finally, comparisons between the hole meshed and modeled predictions are exposed in Section 4 including a detailed analysis of the mixing process taking place in the film in both simulations. From this investigation, potential improvements of the model are proposed in the conclusion as a path for its use in the context of industrial applications.

## 2 Coolant Injection Modeling

The coolant model, already described in Bizzari et al. [17] has initially been developed in the context of the combustion chamber. In the following, the coolant model is adapted and presented in the specific context of NGV cooling. To do so, the geometric parameters of the cooling holes are first presented. Next, the assumptions and mathematical details of the model are introduced. Finally, the validity of the model in this specific context is discussed.

The geometric parameters of the holes used in the model are shown on Fig. 2. Note that this specific configuration contains only cylindrical holes. The hole surfaces are assumed to be ellipsoidal and defined by the minimum diameter  $D$ , the hole surface  $S_{hole}$  and the

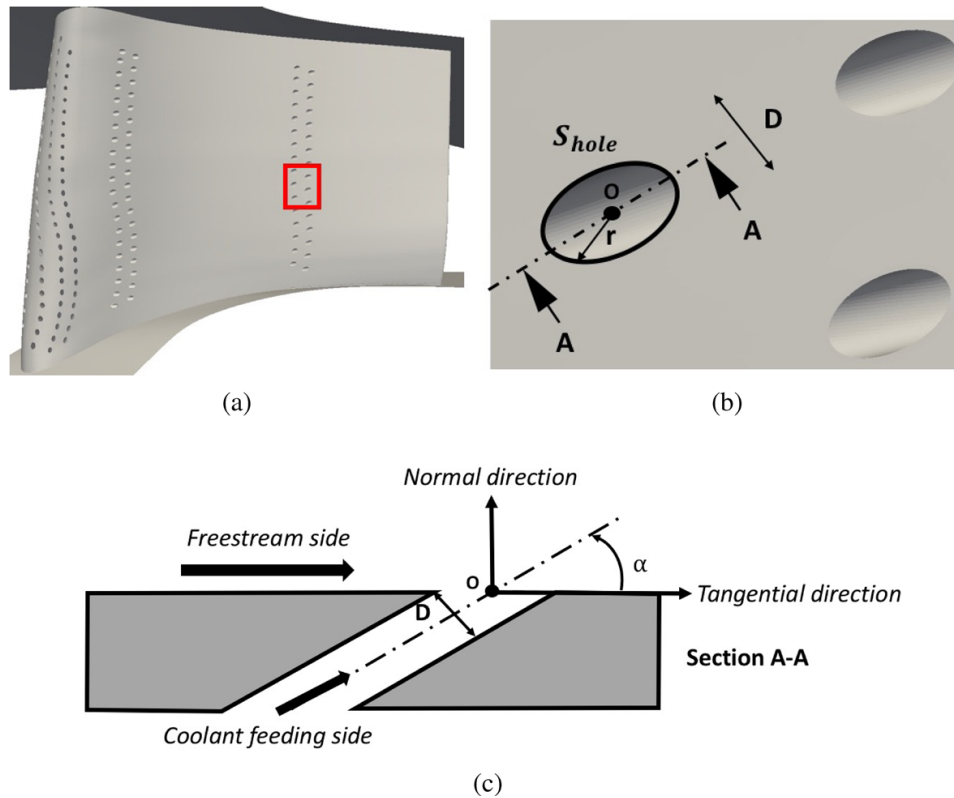


**Fig. 2** Geometric definitions of the holes. Example of the pressure side view of a cooled NGV (a). Normal blade view in the red square (b) and view of the A-A cut (c).  $O$  is the center of the hole,  $D$  the minimum diameter of the hole,  $r$  the local radial coordinate defined on the hole surface  $S_{hole}$  and  $\alpha$  the inclination angle to the wall

inclination angle to the blade surface  $\alpha$ , Fig. 2a and b. A local radial coordinate  $r$  is defined on the hole surface from the center  $O$ . The normal direction is defined at the center of the hole and the tangential direction is chosen to be aligned with the projection of the perforation axis vector on the wall, Fig. 2c.

The main idea of the model is to directly inject the coolant on the wall surface without representing the cooling pipes using an equivalent boundary condition. In the following, each hole is independently considered and then the contribution in terms of boundary fluxes of each hole will be added. The injection of the coolant on the wall is represented by an axis-symmetric normalized distribution function  $f(r)$  centered on the hole center and defined on the total surface of the blade  $S_{tot}$  to geometrically identify the considered hole extent. This specific function is expressed as,

$$f(r) = 0.5 \left( 1 - \tanh \left( \frac{r - 0.5D_{num}}{\beta \Delta x} \right) \right), \quad (1)$$

where  $\Delta x$  is the local mesh size,  $D_{num}$  is the thickened numerical diameter used in the model and  $\beta$  a numerical constant to limit the sharpness of the distribution function on the mesh to avoid numerical stability issues. Bizzari et al. [17] shows that  $\beta = 0.1$  is a correct value to represent the distribution function on such meshes to avoid numerical problems of stability. A 1D plot of the distribution function  $f(r)$  is provided in Fig. 3. The numerical diameter  $D_{num}$  depends on the thickening factor  $\Gamma$  following,

$$D_{num} = \Gamma D. \quad (2)$$

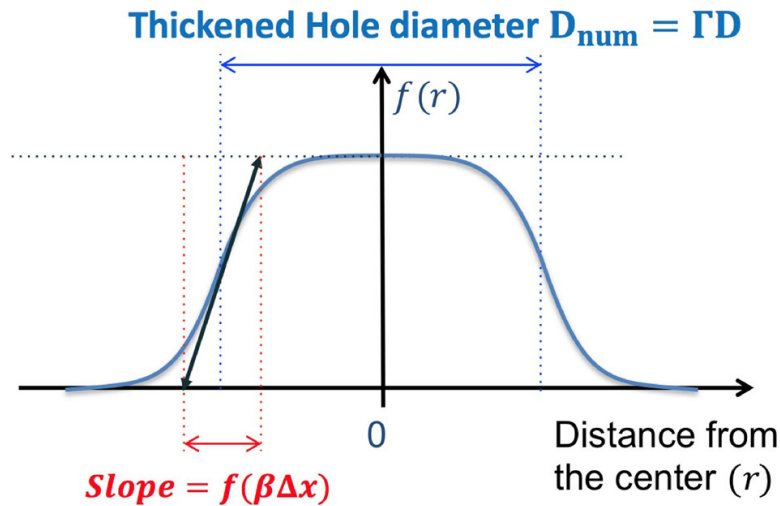


**Fig. 3** Plot of the distribution function  $f(r)$  across a hole of diameter  $D$

The thickening factor  $\Gamma$  allows to extend the hole diameter if the hole is under-resolved, i.e.,  $\frac{D}{\Delta x} < 3$  and is then expressed as,

$$\Gamma = \text{Max} \left( \frac{3\Delta x}{D}, 1 \right). \tag{3}$$

This way, the radial extent of the distribution function covers the numerical diameter of the hole  $D_{num}$ . The normal and tangential velocity profiles to be imposed by the model on the blade surface, respectively noted  $V_n^{model}$  and  $V_t^{model}$ , are assumed to be independent in time and to follow the expressions,

$$V_n^{model} = A_n f(r), \tag{4}$$

$$V_t^{model} = A_t f(r), \tag{5}$$

where  $A_n$  and  $A_t$  are constant of the model. Note that the distribution function  $f(r)$  is used to impose the shape of the velocity profiles on the blade surface issued by the considered hole.

The model is built to conserve the mass and tangential momentum fluxes of the physical jet through the considered hole section  $S_{hole}$ . To do so, the model parameters  $A_n$  and  $A_t$  are determined following the conservation of the previous cited fluxes through the total surface of the blade  $S_{tot}$  containing only the considered hole between the physical and modeled jet,

$$\int_{S_{tot}} \rho V_n^{model} dS = \int_{S_{hole}} \rho V_n^{jet} dS, \tag{6}$$

$$\int_{S_{tot}} \rho V_n^{model} V_t^{model} dS = \int_{S_{hole}} \rho V_n^{jet} V_t^{jet} dS, \tag{7}$$

where  $V_n^{jet}$  and  $V_t^{jet}$  are the normal and tangential velocity profiles of the real jet if known and  $\rho$  is the density assumed uniform. Injecting the expressions of the modeled velocity profile in the conservation equations gives,

$$A_n \int_{S_{tot}} f(r) dS = \int_{S_{hole}} V_n^{jet} dS, \tag{8}$$

$$A_n A_t \int_{S_{tot}} f^2(r) dS = \int_{S_{hole}} V_n^{jet} V_t^{jet} dS, \tag{9}$$

resulting in expressions for  $A_n$  and  $A_t$ ,

$$A_n = \frac{\langle V_n^{jet} \rangle_{S_{hole}} S_{hole}}{\int_{S_{tot}} f(r) dS}, \quad (10)$$

$$A_t = \langle V_t^{jet} \rangle_{S_{hole}} \frac{\int_{S_{tot}} f(r) dS}{\int_{S_{tot}} f^2(r) dS}, \quad (11)$$

where  $\langle \bullet \rangle_S$  is the spatial average on section  $S$ . Note that the temperature profile is kept uniform on the hole extent. To apply the model in the context of turbine blades, one must know a priori the mass flow rate of each hole  $Q_{m,hole}$  to retrieve the surface averaged normal velocity and the jet angle to retrieve the surface averaged tangential velocity. The jet angle is assumed to be equal to the geometric angle  $\alpha$  of the hole leading to the following expressions of the spatial averages of the velocity profiles,

$$\langle V_n^{jet} \rangle_{S_{hole}} = \frac{Q_{m,hole}}{\rho S_{hole}}, \quad (12)$$

$$\langle V_t^{jet} \rangle_{S_{hole}} = \frac{Q_{m,hole}}{\rho S_{hole} \tan(\alpha)}. \quad (13)$$

Such a modeling approach was originally proposed in the context of multi-perforated liners which operate in conditions that are different from the ones encountered for NGV flows so deviations are expected between hole meshed and hole modeled simulations. Indeed the model assumes that the velocity profile is axi-symmetric and stationary. Density as well as temperature are assumed to be uniform on the hole section which differs from real cooling hole features present in turbines [24]. In terms of flow characteristic and response in the specific context of jets in cross flows, the operating condition of the jet issued by the cooling system is usually determined by use of the blowing and momentum ratios respectively noted  $M$  and  $J$  and following,

$$M = \frac{\langle \rho V \rangle_{S_{hole}}}{\rho_\infty V_\infty}, \quad (14)$$

$$J = \frac{\langle \rho V^2 \rangle_{S_{hole}}}{\rho_\infty V_\infty^2}. \quad (15)$$

where  $\infty$  refers to the local free-stream condition. For combustion chamber liners typical values are  $1 < M < 20$  and  $30 < J < 90$  [25] while for blade cooling systems, typical values are around 0.5 - 2 for both  $M$  and  $J$  [26]. Inter-hole distances are also quite different, the overall number of holes and their proximity strongly impacting the resulting film cooling dynamics. Differences in flow responses as well as model sensitivities will thus arise depending on the context of use. One objective of the following discussion is to highlight such changes and their potential importance in the context of a hole modeled LES of NGVs.

### 3 Computational Domain, Mesh and LES Modeling

In this section, the geometry, the mesh, the numerical set up and LES modeling are introduced. Next, the resulting velocity profiles on the hole surfaces issued from the model is detailed and then compared to a hole meshed LES to highlight potential differences in terms of coolant injection.

The configuration addressed for the study focuses on the high pressure vane section of the FACTOR test rig [20–22]. A view of the high pressure vanes used in the FACTOR test rig is provided in Fig. 4. The Axial Chord Length of the vane hereafter noted  $c$  is 40 mm, Fig. 4a. To generate the coolant film around the vanes, 171 coolant holes of 0.8 mm diameter are drilled in the NGV wall. The coolant holes are mainly located on the pressure side of the vane and split in two regions, Fig. 4b. The first region lies near the leading edge of the vane (between  $x/c = 0$  and  $x/c = 0.3$ ) and this specific set of holes is hereafter denoted as the leading edge (LE) rows. A second set of holes is located upstream the trailing edge (between  $x/c = 0.6$  and  $x/c = 0.7$ ) on the pressure side and will be identified as the trailing edge (TE) rows in the remaining part of the text. The coolant flow is supplied by two coolant feeding plena for each NGV hereafter denoted *LE plena* and *TE plena*. The operating conditions of the vanes are given by non-dimensional numbers at the trailing edge axial plane and corresponds to a Mach number of 0.93 and a Reynolds number based on the axial chord length of 430,000.

For all computations discussed hereafter, the computational domain retained represents a  $18^\circ$  periodic sector ( $1/20^{th}$  of the full annular domain) of the high-pressure nozzle section containing two NGVs respectively denoted as NGV1 and NGV2 as displayed in Fig. 5. NGV1 is arbitrary chosen to be positioned before NGV2 in the clockwise direction if looking downstream. The domain is axially limited by the turbine inlet plane ( $P40$ ) which is well numerically and experimentally characterized and located 17 mm upstream the blades ( $0.425c$ ). A second axial plane denoted  $P41$  is defined and is located at an axial distance of  $1.5c$  downstream the axial plane  $P40$ . The inlets of the coolant flow correspond to the inlets of the coolant feeding plena. The outlet is located  $6c$  downstream the blades to avoid interactions between the flow in the region of interest with the outlet boundary.

All simulations rely on the resolution of the compressible LES equations [27, 28] for which subgrid scale turbulent closure relies on the WALE model published in [29]. Note that for the discussed predictions all walls are treated using an adiabatic logarithmic law

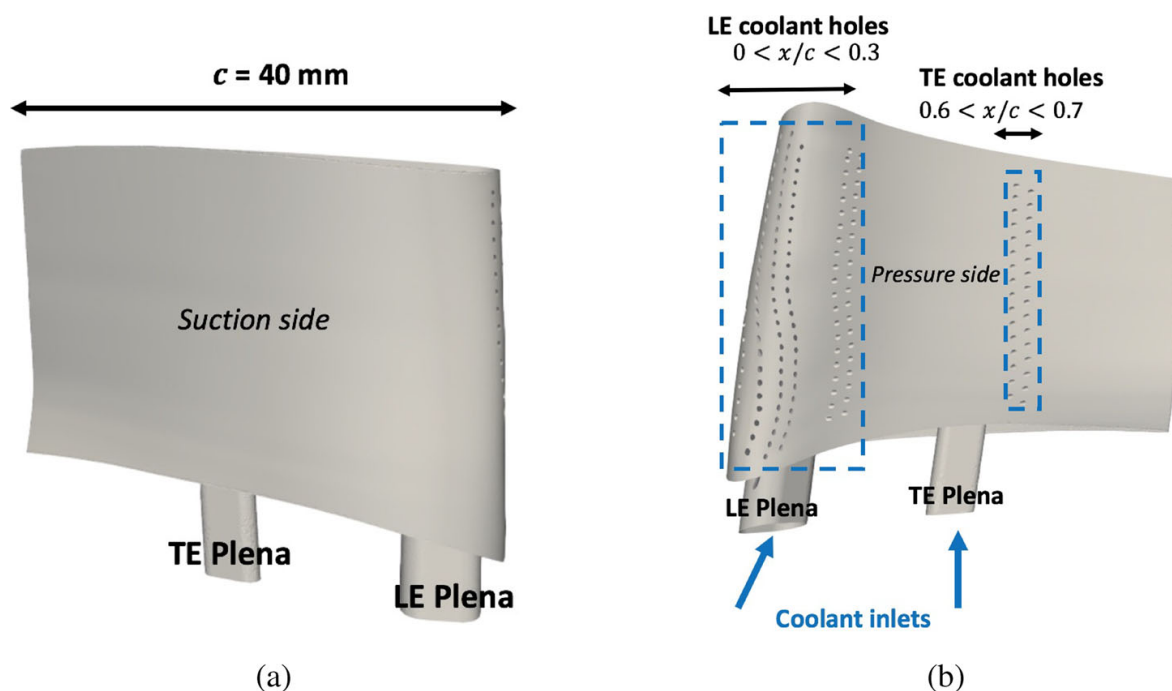


**Fig. 4** Design of the cooled high pressure vanes used in the FACTOR project. Views of the suction side (a) and pressure side (b)

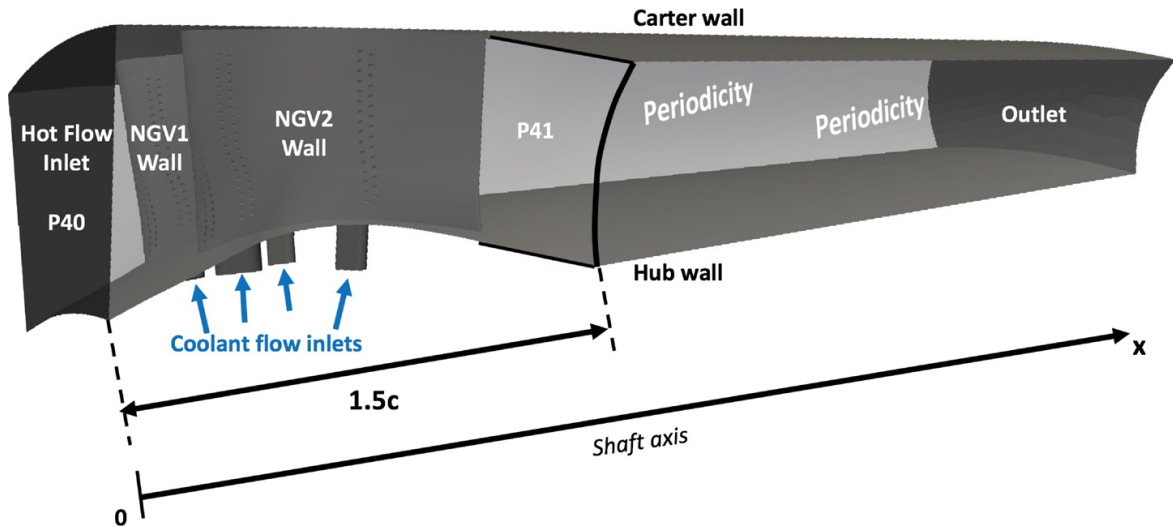


Fig. 5 Computational domain and positions of the axial planes *P40* and *P41*

of the wall to alleviate the overall cost imposed by a wall resolved LES and reproduce an industrial context as most likely encountered for such LES [10, 11, 30].

Inflow and outflow boundary conditions are specified using the Navier-Stokes Characteristic Boundary Condition (NSCBC) formalism [31, 32]. The inlet boundary condition is extracted from a time-averaged LES of an integrated computation where the combustion chamber and uncooled NGVs are considered [33]. The corresponding 2D time-averaged maps of the mass flow distribution  $\rho U_i$  and static temperature  $T$  are extracted at the plane *P40* and imposed at the inlet of the computational domain featuring a stationary field, a hot spot of temperature aligned on NGV1 and a swirled flow as shown on Fig. 6. Note that to purely evaluate the impact of the model on the mixing process, no freestream turbulence is injected at the inlet of the computational domain. The coolant mass flow rates  $Q_{m1}$  and  $Q_{m2}$  are respectively imposed at the inlet of the two plena for both NGVs at a temperature  $T_{cold} = 300$  K and to correspond to the targeted operating point of the system, Table 1.

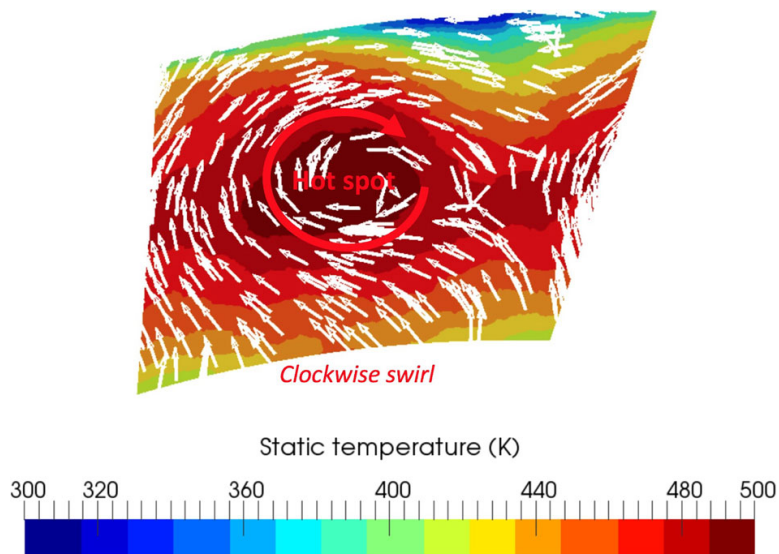


Fig. 6 2D temperature map including a hot spot and swirled flow imposed at the inlet boundary condition. Arrows evidence the swirled flow

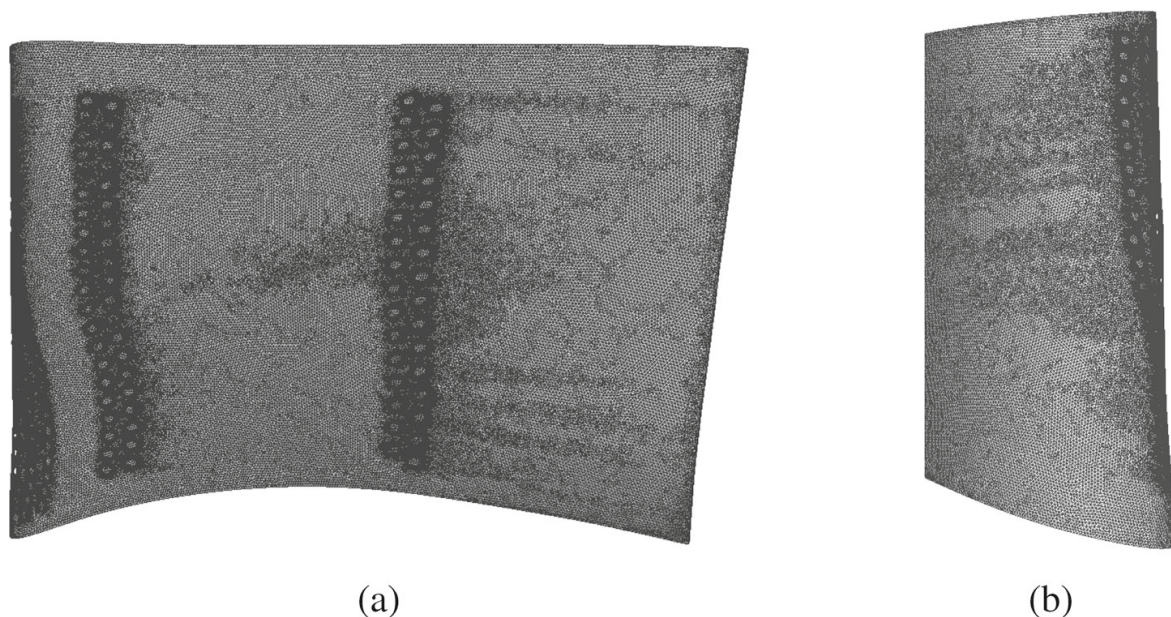
**Table 1** Boundary conditions used in the hole meshed LES

Patch	Variable	Spatial mean value
Inlet	$Q_m$	0.240 kg.s <sup>-1</sup>
•	$T_{inlet}$	455 K
Plena LE NGV1 & NGV2	$Q_{m1}$	0.012 kg.s <sup>-1</sup>
Plena TE NGV1 & NGV2	$Q_{m2}$	0.006 kg.s <sup>-1</sup>
•	$T_{cold}$	300 K
Outlet	$P_{outlet}$	87,000 Pa
Wall		Adiabatic wall law

Equivalently, at the outlet, the surface averaged static pressure is imposed to reach the operating point of the blades and the radial equilibrium is naturally obtained using the specific 3D NSCBC outlet boundary condition accounting for transversal terms [34, 35].

Finally, integration of the modeled equations is obtained by use of the finite element numerical explicit scheme, TTG4A, 3<sup>rd</sup> order in space and 4<sup>th</sup> order in time [36].

For the above discussed conditions, two LES are produced: (a) a so-called hole meshed LES and (b) a hole modeled LES. For the first one, the entire computational domain is considered: i.e. including the vane and the different internal cooling systems. The corresponding mesh is composed of 73 million of tetrahedra with 35 million elements needed to discretize the cooling system. Special refinement of the surface mesh at the cold flow injection is performed to discretize the diameter of holes with around 13–15 points. However, to ensure that the locally strong gradients induced by the injection of the coolant are properly captured by the meshes, an adaptive mesh refinement process has been applied to refine the mixing regions between main flow and coolant jets. The mesh refinement process is based on the mmg3d library [37]. The metric used to perform the automatic refinement is based on the entropy source terms, i.e. where aero-dynamic losses take place [38–40]. Since coolant jets are expected to generate aero-dynamic losses, the surface mesh is then refined along the coolant jet trajectories as shown on the surface mesh of NGV1 on Fig. 7. The impact of the

**Fig. 7** Surface mesh on the pressure side (a) and near the leading edge (b) of NGV1

mesh adaptation process on resolved turbulence in the film regions of the vanes is addressed in Appendix 1. For the final mesh used in this study, turbulence is quite resolved in the film regions to capture fine patterns of temperature on the vane surfaces. Note nevertheless that such a mesh resolution does not result in a purely academic LES in the sense that it does not respect all the required mesh resolutions of an academic problem [7]. Using 15 points to discretize the diameter of each hole and the use of a wall modeled approach is a good compromise to deal with the capacity of the mesh to capture flow dynamics while limiting its CPU cost. The second prediction refers as the hole modeled simulation, uses the same mesh than the hole meshed LES mesh without including plena and the pipes connecting the internal flow to the main flow. The resulting cell number is therefore 38 million cells and corresponds to the vane mesh of the hole meshed simulation. It is worth to note that the projected holes are sufficiently resolved as described previously. As a result, the value of the thickening factor in Eq. 2 is  $\Gamma = 1$  meaning that the modeled holes are not thickened in this context. These changes in cell count result in different CPU costs presented in Table 2 for one flow through time defined as the time taken by a fluid particle generated at the inlet to reach the outlet following a streamline.

One requirement behind the hole modeled approach is the knowledge of mass flow distribution issued by each hole to be considered by the model. For the hole modeled LES, the distribution of the coolant mass flow rate is deduced from the hole meshed LES to limit sources of differences to the proposed modeling procedure.

Deviations in terms of velocity profile injected between the two modeling approaches are now discussed. In the hole meshed LES, the exiting jet profile is potentially unsteady and non axi-symmetric through one specific hole contrarily to the hole modeled approach. This non axi-symmetry and unsteady activity is confirmed by Figs. 8 and 9. In both cases, the 2D maps of the time-averaged normal profile of coolant mass flux are extracted for both predictions: i.e.  $\rho U_i n_i$  where  $n_i$  is the hole normal at the exit section of one specific hole of NGV1. In the hole meshed LES, the mass flux profile is not axi-symmetric and presents a sheared flow pattern (Fig. 8a) in contrast to the hole modeled LES (Fig. 8b). The unsteady activity is evidenced through the profile of the turbulent kinetic energy  $k$  shown for both cases on Fig. 9. For the hole meshed prediction (Fig. 9a), the turbulence intensity is around 5% and located in the sheared region of the profile, a feature that is not taken into account by the hole modeled approach (Fig. 9b). These different treatments of the coolant injection flow topology between a hole meshed and a hole modeled LES are expected.

The remaining question is to what extent the coolant model impacts the prediction and the development of the coolant film in comparison with the reference simulation. This specific question is the main subject of the remaining discussion which focuses on the qualification of the modeling and the impact on the temperature of the NGV walls.

**Table 2** Summary of the LES mesh sizes and associated CPU costs for one convective time

Case	Number of cells	CPU cost (CPUH)
Hole meshed LES	$73.10^6$	10,000
Hole modeled LES	$38.10^6$	3000

Computations were performed with the High Performance Computing (HPC) resources of IDRIS on the Blue Gene machine TURING

Further information on the machine can be found on <http://www.idris.fr/eng/turing/>

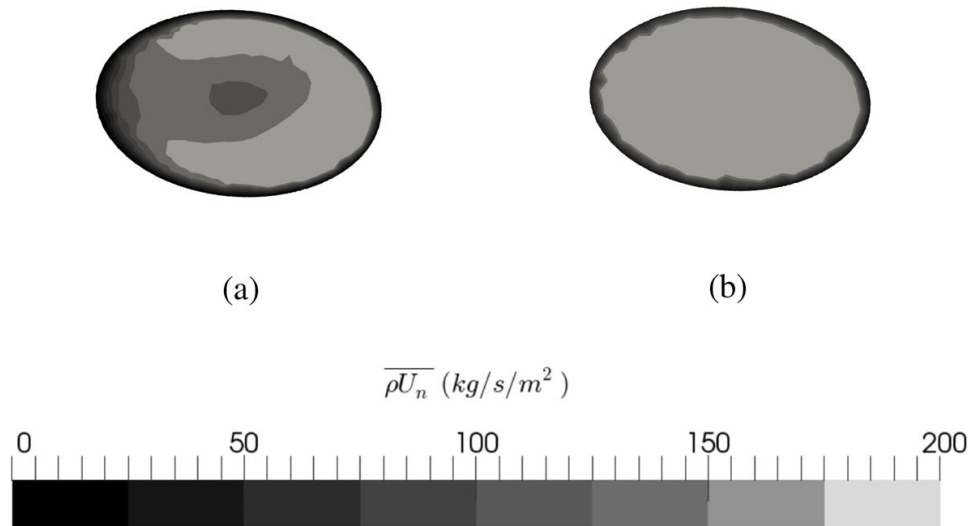


**Fig. 8** Time-averaged normal profiles of the mass flux  $\rho U_i n_i$  at the ejection section of a hole located in the last row of holes at mid height of NGV1 for the hole meshed **(a)** and hole modeled **(b)** LES

### 4 Results

In this section, detailed comparisons of both LES predictions are proposed so as to qualify the capacity of the hole modeled approach to reproduce accurately the coolant injection for complex NGV simulations. First, obtained operating conditions and flow organization issued by both LES are studied to ensure the comparability. Then, the effect of the model on adiabatic film effectiveness is investigated. Finally, the film evolution is more specifically addressed in both cases with emphasis on the capacity of both simulations to reproduce the mixing process taking place between the hot and cold flow in the near wall flow.

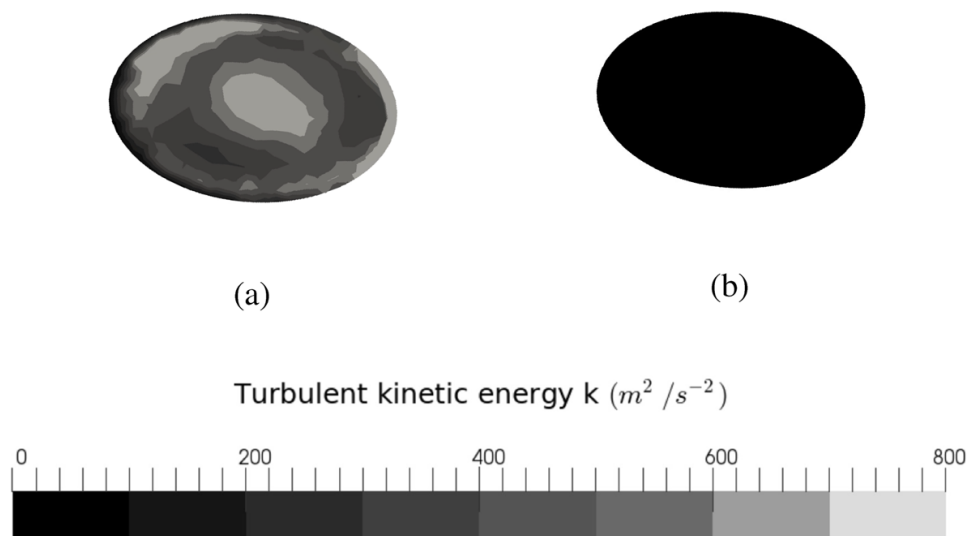


**Fig. 9** Turbulent kinetic energy  $k$  at the ejection section of a hole located in the last row of holes at mid height of NGV1 for the hole meshed **(a)** and modeled **(b)** LES

#### 4.1 Mean flow operating conditions and flow organization

Wall temperature around a complex NGV geometry is the result of multiple factors that are tightly coupled. For uncooled NGVs and under adiabatic wall conditions, the wall temperature is governed by the aero-dynamics of the flow induced by the presence of the blade and the impact of the hot spot. For anisothermal case: i.e. with cooling, the wall temperature is induced by more complex phenomena and results from the mixing occurring between the hot and cold stream as well as the associated aero-dynamics response of the flow dictated by the operating point of the blade. In the case of film cooling, the discrete nature of the cold stream injection all around the blade boundary layer clearly hinders the analysis. As a consequence and prior to a deeper analysis of the hole modeled approach, a verification of the overall operating condition provided by the two simulations is mandatory.

This specific point is addressed in Table 3 by considering the mass flow rates going through the system, the total temperature  $T_t$  and pressure  $P_t$  at the plane  $P40$ , corresponding to the inlet of the domain to ensure that both LES ingest the same flow. To evaluate the impact of the model on the losses, the drop of total variables between the axial planes  $P40$  and  $P41$  is also evaluated from the total enthalpy loss coefficient  $\xi_{ht}$  as well as from the total pressure loss coefficient  $\xi$ . For both cases, the total enthalpy loss coefficient  $\xi_{ht}$  is defined as,

$$\xi_{ht} = \frac{T_{t40} - T_{t41}}{0.5 \langle V_{41}^2 \rangle_S}, \quad (16)$$

where  $T_{t40}$  and  $T_{t41}$  are respectively the mass flow averaged total temperature on the axial planes  $P40$  and  $P41$  and  $0.5 \langle V_{41}^2 \rangle_S$  is the surface averaged kinetic energy on  $P41$ . The total pressure loss coefficient  $\xi$  is defined as,

$$\xi = \frac{P_{t40} - P_{t41}}{P_{41} - P_{41}}, \quad (17)$$

where  $P_{t40}$  and  $P_{t41}$  are respectively the mass flow averaged total pressure on the axial planes  $P40$  and  $P41$  and  $P_{41}$  the surface averaged of the static pressure on the axial plane  $P41$ . The swirl number  $S_{w,S}$  is also computed between planes  $P40$  and  $P41$  to ensure that the transport of the swirled flow is equivalent between both LES. For this quantity, the definition from [41] is retained,

$$S_{w,S} = \frac{1}{(R_{carter} - R_{hub})} \frac{\int_S \overline{\rho U_x U_\theta} dS}{\int_S \overline{\rho U_x^2} + (\overline{P} - \langle \overline{P} \rangle_S) dS}, \quad (18)$$

**Table 3** Hot and cold mass flow rates for both LES and total pressure  $P_t$  and total temperature  $T_t$  at the inlet of the domain ( $P40$ ) and drop between the planes 41 and 40

Case	Hole meshed LES	Hole modeled LES
Hot mass flow rate (kg.s <sup>-1</sup> )	0.240	0.240
Cold mass flow rate (kg.s <sup>-1</sup> )	0.018	0.018
$T_{t40}$ (K)	443	443
$P_{t40}$ (Pa)	149738	149619
$S_{w,40}$	0.19	0.19
$\xi_{ht}$	≈ 0	≈ 0
$\xi$	0.072	0.070
$S_{w,41}$	21.2	20.3

where  $\overline{U_x}$  is the time-averaged of the axial velocity component,  $\overline{U_\theta}$  the angular velocity component and  $\overline{P}$  the static pressure.  $R_{carter}$  and  $R_{hub}$  are respectively the radius of the hub and carter. Numbers confirm that both simulations inject the same mass flow rate for hot and cold streams and same total temperature. Since the coolant mass flow represents only 7.5% of the total mass flow and no work is enforced on the fluid, the total enthalpy is conserved between  $P40$  and  $P41$  which leads to  $\xi_{ht} \approx 0$ . The total pressure at the inlet is not directly imposed by the boundary conditions but it is the result of the losses produced within the domain. In that case, the difference at the inlet between the two LES is negligible assuring same flow injection at the inlet of the domain for both LES. The total pressure loss coefficient representative of the losses present in both simulations is found to be slightly more important for the hole meshed LES. The swirl number increases between  $P40$  and  $P41$  showing that the swirled flow is strengthened by the expansion through the passage of the blades. Since the values at  $P40$  and  $P41$  between the two LES are very similar, the transport of the swirled flow through the blades can be considered equivalent between the two LES. Although such small differences appear, the impact of the blades on the flow can be considered equivalent between the hole meshed and modeled LES.

The operating point of the vanes for both LES is now studied by investigating the flow expansion through the flow passage from the isentropic Mach number obtained using,

$$Ma_{is} = \sqrt{\frac{2}{\gamma - 1} \left[ \left( 1 + \frac{P_{stagn}}{\overline{P}} \right)^{\frac{\gamma-1}{\gamma}} - 1 \right]}, \quad (19)$$

where  $\overline{P}$  is the time-averaged pressure on the blade surface,  $P_{stagn}$  the pressure at the stagnation point and  $\gamma$  the local heat capacity ratio. The flow expansion is first validated by comparing the hole meshed LES to experimental results on Fig. 10. Note that in the experiment, the pressure probes are located on the pressure side of NGV1 and suction side of NGV2. To compare the LES with the experimental results, the pressure is extracted on the blade walls from the simulation at the same positions as in the experiment. A very good

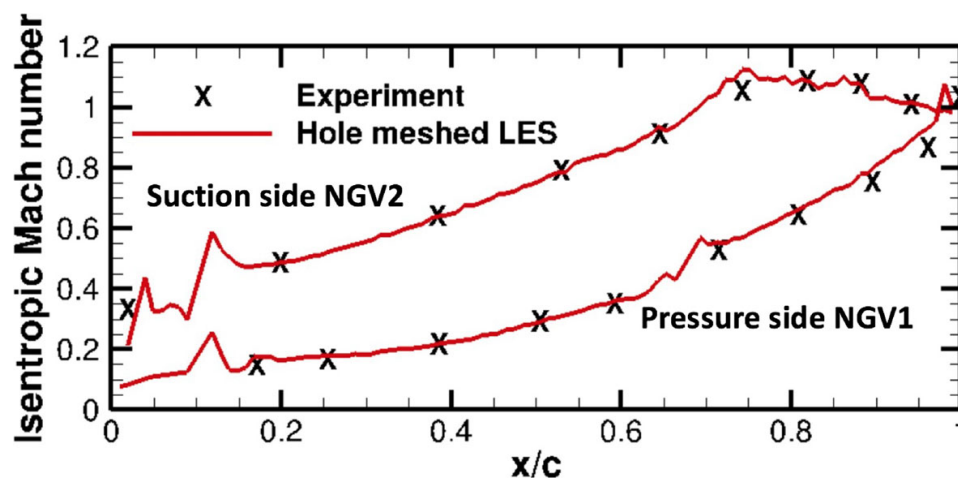


**Fig. 10** Isentropic Mach number at mid-height of the vanes for the LES prediction (red solid line) and experimental results (black crosses). Pressure side of NGV1 at bottom and suction side of NGV2 at top

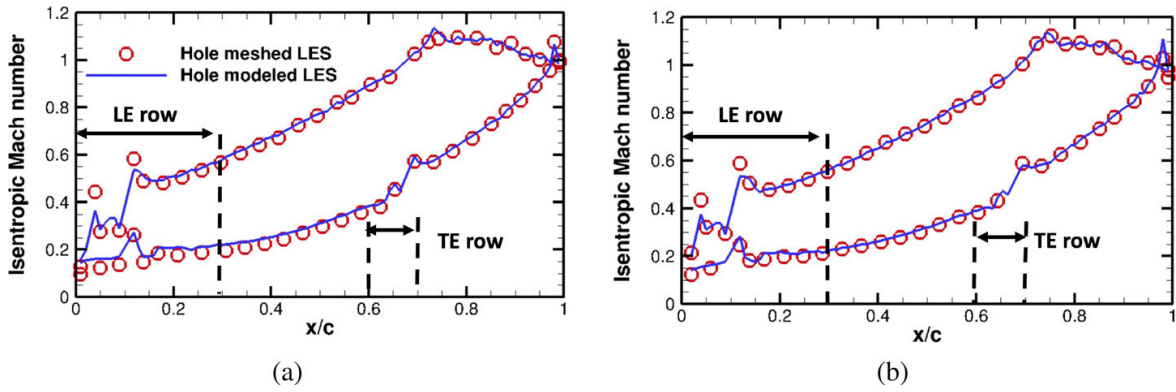


**Fig. 11** Isentropic Mach number along NGV1 (a) and NGV2 (b) at mid-height of the vanes. Red circles  $\circ$  represent the hole meshed LES and solid blue lines  $\text{—}$  represent the hole modeled LES. Axial extent of coolant hole positions is indicated

agreement is found between the LES prediction and the experiment validating the flow expansion through the vanes in the hole meshed LES. On the suction side, the flow strongly accelerates and passes in a transonic regime at  $x/c = 0.75$ . On the pressure side, discontinuities observed near  $x/c = 0.1$  and  $x/c = 0.7$  correspond to the local acceleration of the flow due to coolant ejection. To check the impact of the model on the flow expansion, the hole meshed LES is compared to the hole modeled LES on Fig. 11. For both NGVs, the model reproduces well the flow expansion. Nevertheless, a slight deviation is observed in

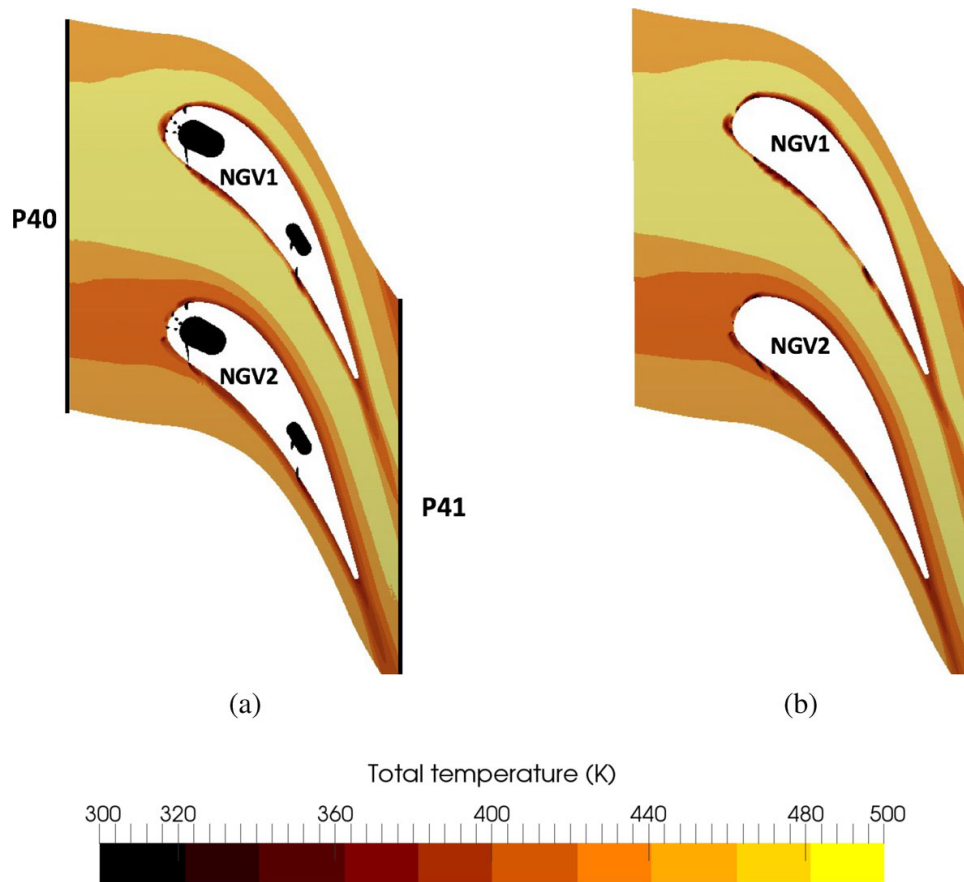


**Fig. 12** Time-averaged total temperature fields at mid-height of the vanes. **a** hole meshed and **b** hole modeled LES

the regions where the coolant is ejected. Note that since the jet velocity profile injected with the hole model differs from the one obtained in the hole meshed LES, this slight deviation was expected.

After validation of the operating point of the vanes, the mean flow organization within the computational domain of both simulations is studied by looking at the mean total temperature field at mid-height of the vanes and shown on Fig. 12. For both predictions, NGV1 is impacted by the hot spot. The cold flow issued from NGV1 cooling system is expected to picture stronger gradients of total temperature than NGV2. Aside from this inflow difference between NGV1 and NGV2, total temperature maps appear very similar for both simulations except in the region of the cooling flow near the blade surfaces. Nonetheless, coolant jets evidenced by cold temperature defined between 300 and 320 K are observed to be more marked in the hole modeled LES compared to the hole meshed LES. This indicates a potential impact of the model in the film region.

To assess the hot spot transport between planes  $P40$  and  $P41$ , the mass flow averaged mean total temperature field is further azimuthally mass-flow averaged on the axial planes  $P40$  and  $P41$  and resulting in radial profiles plotted on Fig. 13. At plane  $P40$ , no difference is noticed between both LES confirming that the inflow imposed is the same. In plane  $P41$ , the profiles appear very similar and differences appear near the carter (top section of the curves), between  $0.6 < h/H < 0.8$  showing a weak impact of the model on the migration of the hot spot through the NGVs.

Overall, verification of the mean operating point, flow expansion and flow topology are found to be equivalent for both LES with only minor differences attributed to the different

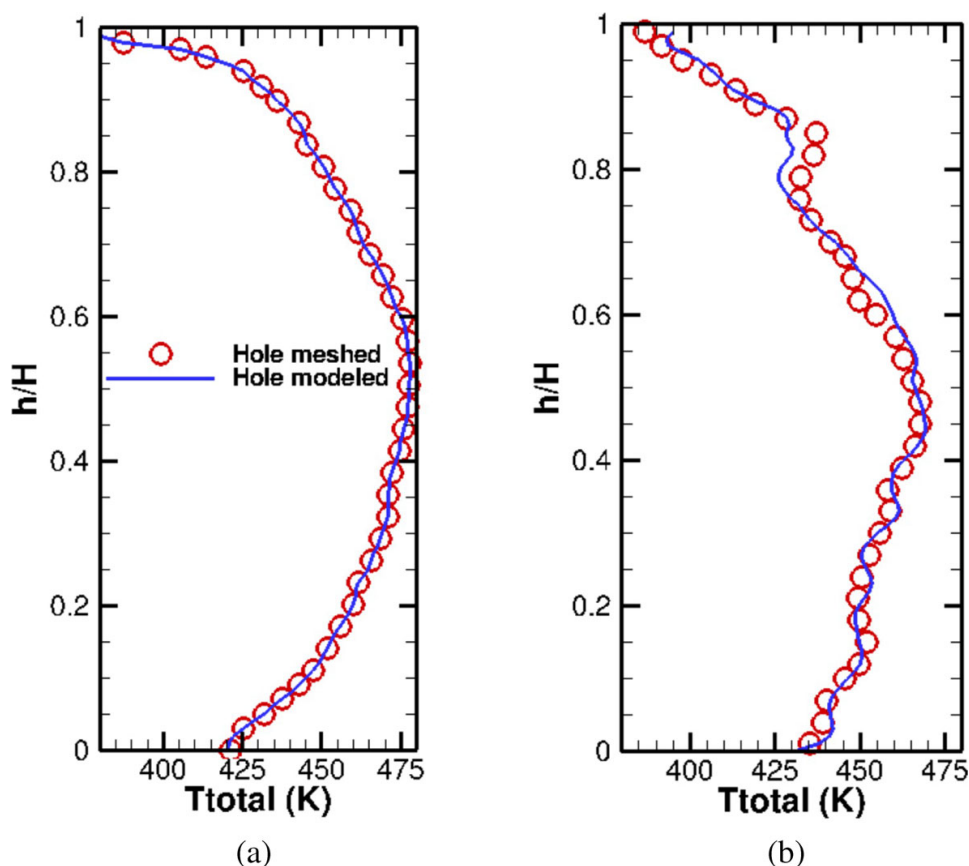


**Fig. 13** Radial total temperature profiles at the axial plane  $P40$  (a) and  $P41$  (b). Red circle  $\circ$  represents the hole meshed LES and solid blue line — the hole modeled LES. Radial coordinate  $h$  normalized by the height of the vanes  $H$

coolant injection approaches. These findings underline the impact of modeling but at the same time highlight the suitability of the proposed approach for more efficient LES use on such problems. Verification is however still needed. Since the objective is to predict adiabatic film effectiveness of film cooling design strategies, adiabatic film effectiveness profiles on both NGVs are addressed in the following section.

## 4.2 Adiabatic film effectiveness predictions

The adiabatic film effectiveness  $\eta$  is obtained from the skin temperature maps following,

$$\eta = \frac{T_{hot} - \overline{T_{skin}}}{T_{hot} - T_{coolant}}, \quad (20)$$

where  $\overline{T_{skin}}$  is the time-averaged of the local skin temperature,  $T_{coolant}$  the coolant temperature taken at 300 K and  $T_{hot}$  the spatial and time-averaged total temperature on the axial plane  $P40$ . The impact of the model on the adiabatic film effectiveness is assessed by comparing the profiles obtained on unwrapped blade surfaces from the two LES predictions in Fig. 14. A good agreement between the two LES predictions for both NGVs is confirmed. Indeed, with both approaches all macroscopic features are present and equivalently positioned around the two blades. Features only locally deviate and express in terms of small local  $\eta$  variations and associated spatial extents. As anticipated, NGV1 profile, Fig. 14a and b, seems strongly influenced by the swirled flow. For this blade, the swirled flow radially deviates the cold flow on the blade surface for both approaches in the interval between

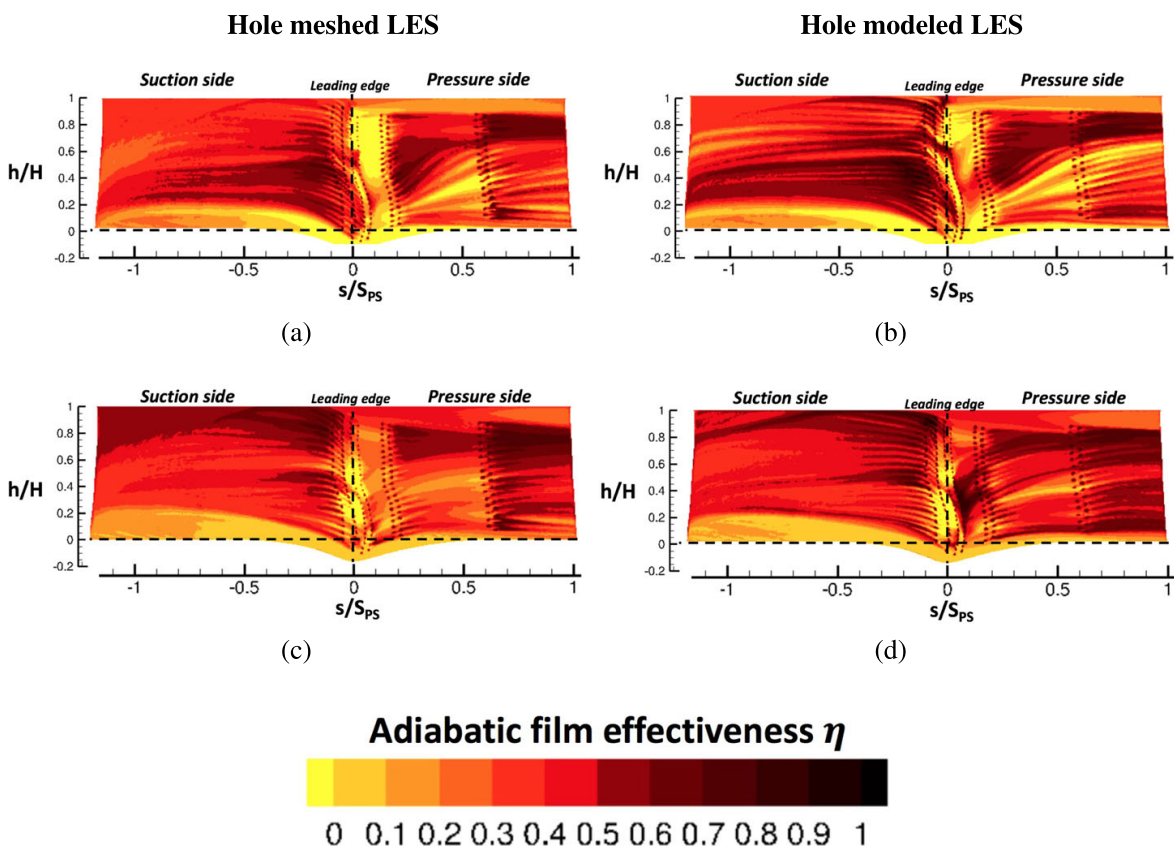


**Fig. 14** Time-averaged adiabatic film effectiveness  $\eta$  on both NGVs for both LES. Top (a) & (b), NGV1. Bottom (c) & (d), NGV2. Left (a) & (c), hole meshed. Right (b) & (d), hole modeled. Radial coordinate  $h$  normalized by the height of the vanes  $H$  and curvilinear coordinate  $s$  normalized by the total curvilinear distance on the pressure side  $S_{PS}$

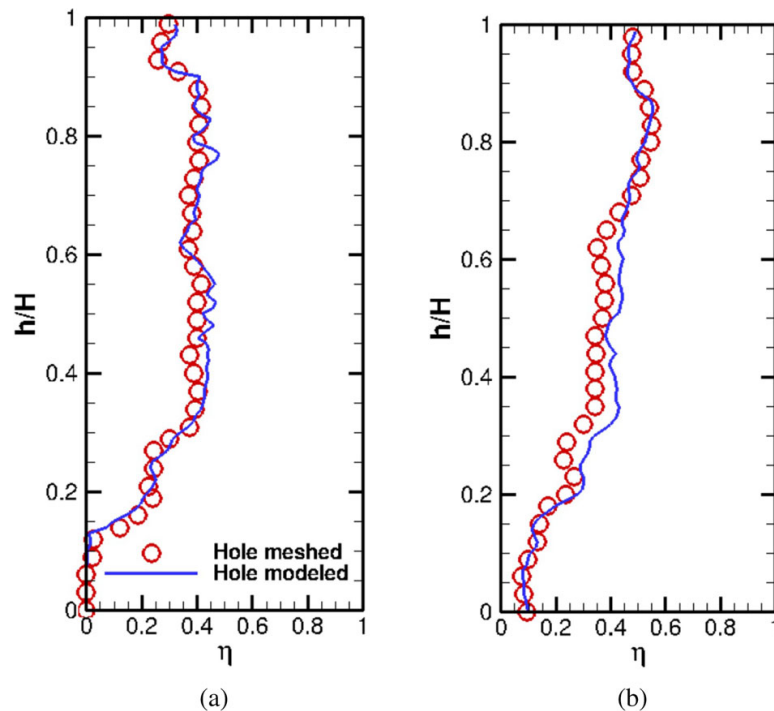


**Fig. 15** Radial profiles of adiabatic film effectiveness  $\eta$  for NGV1 (a) and NGV2 (b). Red circle  $\circ$  represents the hole meshed LES and solid blue line  $\text{—}$  the hole modeled LES

$s/S_{PS} = 0.2$  and  $s/S_{PS} = 0.6$ . This effect is stronger on the pressure side of NGV1 because of the impact of the hot spot. The effect is clearly weaker on NGV2, Fig. 14c and d. If focusing on profile obtained with the hole modeled LES, the patterns remain similar to the hole meshed predictions but peak values are more pronounced with the proposed model. The deviation induced by the swirled flow seems not to be impacted by the model for both NGVs. Locally, the traces of the cold jets, evidenced by the color map delimited by the isolines  $\eta = 0.8$  and  $\eta = 1$  on the blade surfaces, appear more marked for the hole modeled LES indicating that the mixing process with the hot flow is less efficient. To quantify the impact of the model on the adiabatic film effectiveness distribution, the radial profiles of  $\eta$  for both NGVs are plotted on Fig. 15. A very good agreement is found between the two simulations. Nevertheless, profiles exhibits more peak values in the hole modeled LES. Indeed for NGV1, both approaches are very close and peaks that are locally accentuated indicative of local cool or hot streams. The difference is more important for NGV2 with a maximum deviation around 10% and for a larger radial extent. For both NGVs, use of a hole modeled approach induces an efficiency that is slightly higher at mid-height with no impact near the top and bottom walls. Indeed, the hole modeled approach does not fully recover the hole meshed approach indicating that the coolant film region is partially impacted. Since fundamental differences are present when using a hole modeled approach, such differences were expected compared to a fully meshed approach. In that respect, results also confirm that such an approach remains attractive while mixing process between the coolant film and the external hot stream clearly differ. To find the origin of such defect near wall films are specifically investigated in the next section.

### 4.3 Investigation of the film cooling mixing

A key feature differentiating the predictions of the hole meshed LES from the modeled one is the coolant film development around the NGVs. To quantify and address this specific

region of the flow, the coolant is traced in both simulations using the passive scalar hypothesis. Indeed, injecting such a scalar, noted  $Y_{coolant}$ , through the jet orifices eases the analysis of the coolant films and it is not affected by compressible effects, viscous work or the non-uniformity of fields imposed at the inlet contrary to the static and total temperatures. To track the coolant fluid,  $Y_{coolant}$  is imposed at 1 at the inlets of the cooling system, 0 at the inlet of the main flow and no diffusion of  $Y_{coolant}$  is assured through walls.  $Y_{coolant}$  is then transported by the flow through convection-diffusion equation and the retained diffusivity coefficient  $D_{coolant}$  being the one of air. From such an approach, one directly accesses the hot versus cold proportions of the fluid with  $Y_{hot} = 1 - Y_{coolant}$ . Such a passive scalar furthermore provides access to a clear vision of the film topology. As shown in Section 4.2, the swirled flow injected at the inlet impacts the coolant distribution on the vane surfaces by introducing a radial migration of the cold flow. This migration is identical in the two LES predictions. Thus, following investigations focus near mid-height plane of the vanes. The impact of the model on the instantaneous coolant jet topology is first studied by comparing the coolant temperature iso-surface obtained from LES predictions near the leading edge of NGV1 on Fig. 16. Clearly, the model reproduces well the coolant trajectories as well as jet penetrations. In the hole meshed LES, Fig. 16a, spatial fluctuations of the iso-surface are observed and originate from turbulent fluctuations generated in the coolant pipes [42, 43]. The iso-surfaces issued from the hole modeled LES, Fig. 16b, are smoother and more coherent compared to the hole meshed due to the lack of turbulent fluctuations injected at the blade surface with the model. In the following, the time-averaged film cooling topology is discussed. The mean coolant film topology near the leading edge of NGV1 is displayed at mid-height in Fig. 17 for both predictions. For the hole meshed as well as the hole modeled predictions, the coolant directly injected by the inlet plenum and through the cooling pipes appears to produce a coolant film along the blades. After a local perturbation of the hot flow near the exit of each pipe, the coolant re-attaches on the wall in both simulations. The topology of the coolant distribution seems however more diffused in the hole meshed LES indicating a difference of mixing between the two approaches. This impact seems also more important on the pressure side on the NGV. At the leading edge of the vane, jet angles are observed to differ between the two simulations. To illustrate the difference of coolant distribution between the two simulations, the profile of  $Y_{coolant}$  is plotted along the wall normal distance on both sides of NGV1 at different axial positions at mid-height of the vanes on Fig. 18. Note that profiles are normalized by the mean local film thickness  $\delta$  defined as the normal distance from the wall up to the position where  $\overline{Y_{coolant}} = 0.05$  where  $\overline{\bullet}$  is the time average operator. Both predictions remain equivalent and the impact of modeling remains

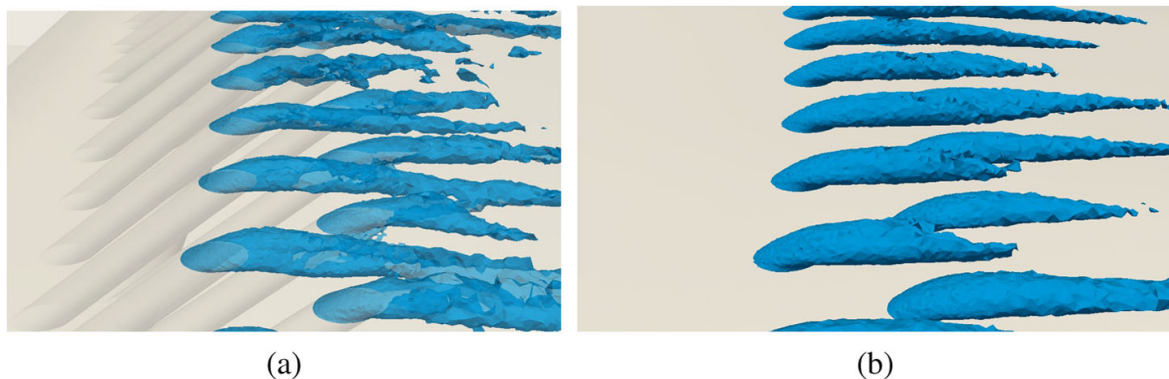


**Fig. 16** Instantaneous isosurface of the coolant temperature to evidence the coolant injection near the surface blade of NGV1 in the hole meshed case (a) and hole modeled case (b)

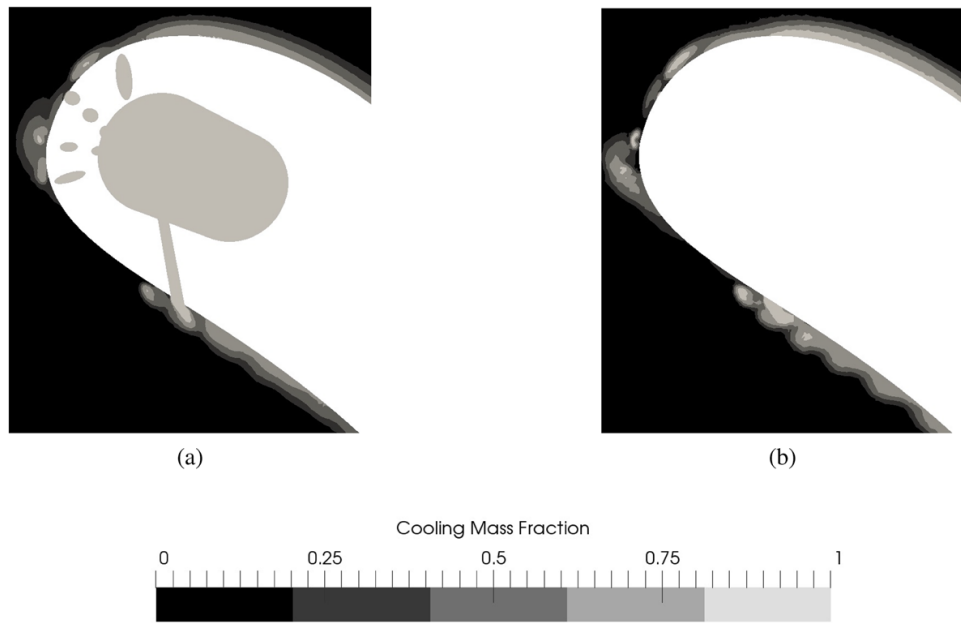


**Fig. 17** Cooling mass fraction near the leading edge of NGV1 at mid-height

localized in the film. From Fig. 18a, at  $x/c = 0.25$ , on the suction side, the passive scalar decreases monotonously away from the wall starting from a fixed value at the wall to the corresponding external value of the film. On the pressure side, the behaviour is different, i.e. the value of the passive scalar presents a maximum, not located at the wall, indicating that the coolant distribution in the film is complex and linked to the preceding local injection

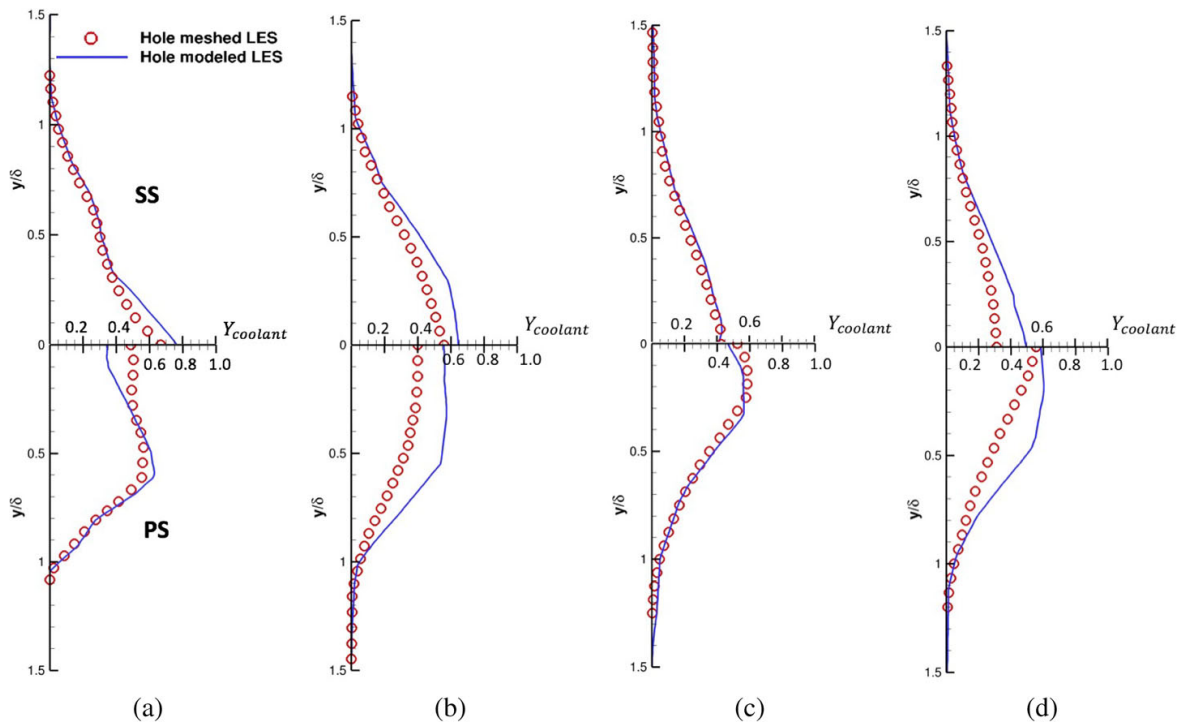


**Fig. 18** Profile of the coolant mass fraction for different axial positions at **a**  $x/c = 0.25$ , **b**  $x/c = 0.50$ , **c**  $x/c = 0.75$  and **d**  $x/c = 0.90$  at mid-height along NGV1. Red circles  $\circ$  represent the hole meshed LES and the solid blue line  $\text{—}$  the hole modeled LES. Pressure side (PS) is at the bottom and suction side (SS) at the top.  $\delta$  is the film thickness

process of the coolant. Such observations are confirmed by the other profile positions, the pressure side film being more complex than the suction side film. When comparing the hole meshed distribution to the hole modeled one, differences are noticed near the walls where coolant concentrations differ while both LES recover the same value when  $y$  approaches  $\delta$ . Note that both LES give the same results at  $x/c = 0.75$ , Fig. 18c. It is important to recall that this specific station is located near the coolant holes located at  $x/c = 0.7$ . In this region, the coolant distribution is then mainly dictated by the coolant mass flux injected through the holes which is consistent in both simulations. At  $x/c = 0.50$  and  $x/c = 0.90$  (Fig. 18b and d), the hole modeled simulation over-estimates the value of the passive scalar if compared to the hole meshed. This indicates that the coolant concentration is locally higher in the film with the hole modeled approach. As a consequence the coolant model is expected to affect the film thickness evolution plotted along the blades on Fig. 19 at mid-height of the vanes. For NGV1 (Fig. 19a), the film thickness increases on the pressure side due to the coolant injection by the LE and TE rows for the hole meshed LES. Between these cooling holes, the film thickness decreases due to the strong impact of the swirled flow which radially deviates the coolant. On the suction side, the swirled flow has less impact as described in Section 4.2 and the film thickness is only driven by the mixing process between the coolant and the hot flow. Comparing the response of both NGVs, the film thickness seems more disturbed on NGV2 (Fig. 19b). On the pressure side of NGV2, the thickness increases at the coolant injection positions and then decreases due to the effect of the swirled flow as previously mentioned. On the suction side, one can notice a monotonous increase of the thickness indicative of a diffusive process of the coolant fluid within the film in this region. If comparing modeling approaches, one observes that the hole modeled formalism underestimates the film thickness evolution along both NGVs compared to the hole meshed LES. From the studied profiles, the axial evolution of the quantity of coolant in the film along the vane can be evaluated using the mass flow weighted film coolant fraction  $Y_{film}$  defined as,

$$Y_{film}(x) = \frac{\int_0^\delta \rho U_i n_i Y_{coolant} dn}{\int_0^\delta \rho U_i n_i dn}, \tag{21}$$

where  $n$  is the normal coordinate from the wall and  $n_i$  the normalized vector tangential to the wall. Resulting profiles of  $Y_{film}$  are plotted on Fig. 20 for both LES at mid-height of the vanes. On both NGVs and for both LES,  $Y_{film}$  increases at the coolant injection positions on the pressure side. On the suction side,  $Y_{film}$  decreases along the blades due to the

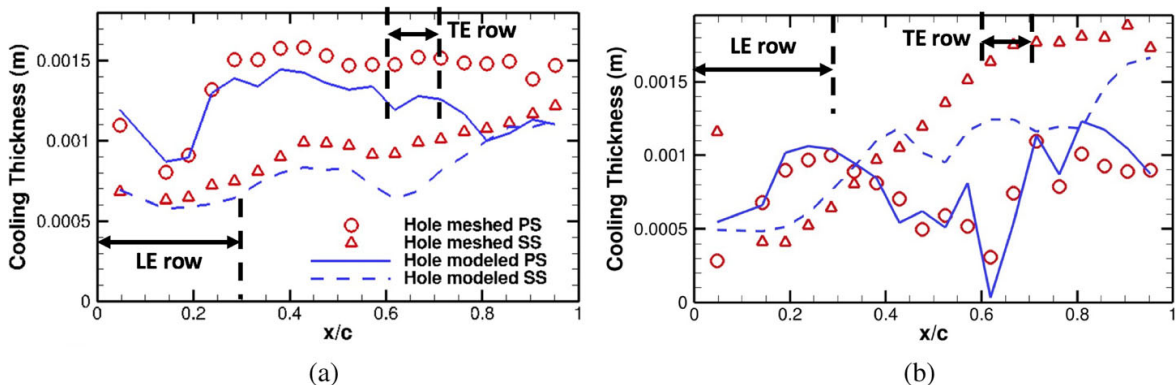


**Fig. 19** Film thickness along the blades for NGV1 (a) and NGV2 (b) at mid-height. Red circles  $\circ$  represent the hole meshed LES at the pressure side. Red triangles  $\Delta$  represent the hole meshed LES at the suction side. The solid blue line  $\_$  represents the hole modeled LES at the pressure side. The dashed blue line  $\_ \_$  represents the hole modeled LES at the suction side. Cooling row axial locations are indicated

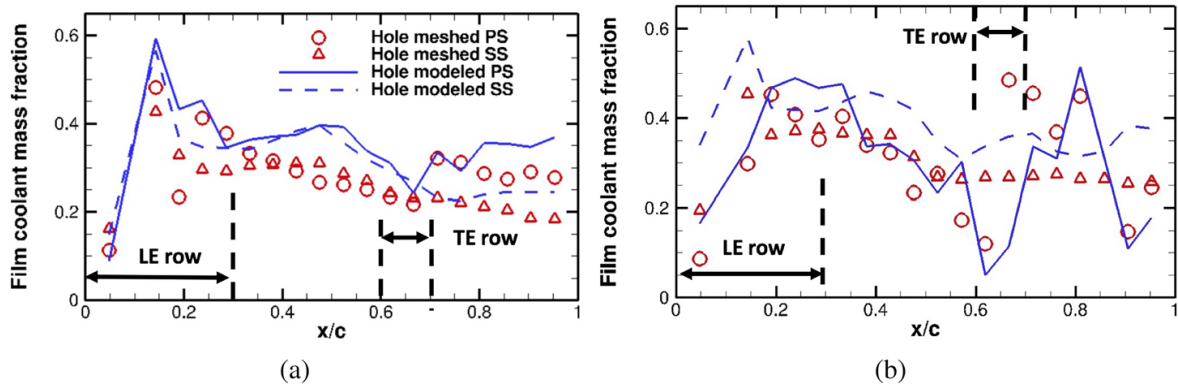


**Fig. 20** Film coolant mass fraction  $Y_{film}$  along NGV1 (a) and NGV2 (b) at mid-height. Red circles  $\circ$  represent the hole meshed LES at the pressure side. Red triangles  $\triangle$  represent the hole meshed LES at the suction side. The solid blue line  $\_$  represents the hole modeled LES at the pressure side. The dashed blue line  $-\ -$  represents the hole modeled LES at the suction side

absence of cooling holes. On both sides of NGV1 (Fig. 20a), the model reproduces well the evolution of  $Y_{film}$  compared to the hole meshed LES and over-estimates the levels of  $Y_{film}$  meaning that more coolant remains in the film thickness. On both sides of NGV2 (Fig. 20b), the model follows the same evolution of  $Y_{film}$  along the blade and over-estimates also the levels of coolant in the film thickness. Local differences are noticed on the pressure side at the TE coolant injections where levels of coolant are locally higher in the hole meshed LES meaning that the coolant distribution around NGV2 differs at this specific position. Consequently, the model slightly over-estimates levels of coolant present in the film region.

To investigate the axial evolution of  $Y_{film}$  in the coolant film, previously described processes taking place within the film, in its outer edge can be adequately analyzed by performing a mass balance of the passive scalar concentration within the control volume corresponding to the film region at mid-height as shown on Fig. 21. Since the control volume is applied at mid-height of the blades, the radial contribution of the coolant mass flux

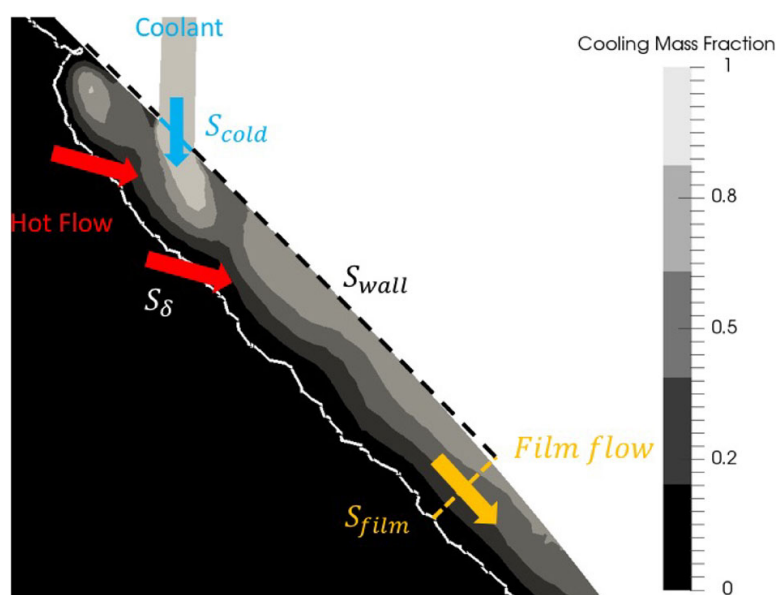


**Fig. 21** Control volume  $V_{film}$  at mid-height used in the study. The control volume is delimited by the sections corresponding to the ejection exit of the coolant pipes  $S_{cold}$ , the walls  $S_{wall}$ , the thickness of the coolant  $S_{\delta}$  and the film section  $S_{film}$

is then not taken into account in the balance. Neglecting the laminar diffusive terms, the balance of the coolant mass fraction in the control volume gives:

$$\int_{S_{film}(x)} \overline{\rho U_i Y_{coolant} n_i} dS = - \int_{S_{cold}(x)} \overline{\rho U_i Y_{coolant} n_i} dS - \int_{S_\delta(x)} \overline{\rho U_i Y_{coolant} n_i} dS, \quad (22)$$

where  $\rho U_i$  is the surface mass flux and  $n_i$  the surface normal pointing out of the control volume. The term in the LHS of Eq. 22 represents the coolant mass flux through  $S_{film}$ . The first term in the RHS represents the coolant mass flux from the coolant pipes and will be replaced hereafter by  $Q_{m,cold}$ . Finally, the second term represents the mass flux through the edge of the coolant film. Since the control volume  $V_{film}$  is built from the time-averaged coolant mass fraction field, the time-averaged operator can switch with spatial integration in Eq. 22 which gives,

$$\int_{S_{film}(x)} \overline{\rho U_i Y_{coolant} n_i} dS = Q_{m,cold}(x) - \int_{S_\delta(x)} \overline{\rho U_i Y_{coolant} n_i} dS. \quad (23)$$

The film coolant mass fraction  $Y_{film}$  can appear in the balance by combining Eq. 21 with Eq. 23 which yields,

$$Y_{film}(x) = \frac{1}{Q_{m,film}(x)} \left( \underbrace{Q_{m,cold}(x)}_{\text{Coolant pipe contribution}} - \underbrace{\int_{S_\delta(x)} \overline{\rho U_i Y_{coolant} n_i} dS}_{\text{Hot flow contribution}} \right), \quad (24)$$

where  $Q_{m,film}$  is the mass flow rate in the coolant film. As a result, one origin of the axial evolution of  $Y_{film}$  is the source of the mixing process which originates from the coolant flux through  $S_\delta$ . This flux can be split into a mean and turbulent contributions using the Reynolds decomposition and Favre averaging [44]  $\tilde{\cdot}$  so that,

$$\int_{S_\delta(x)} \overline{\rho Y_{coolant} U_i n_i} dS = \underbrace{\int_{S_\delta(x)} \overline{\rho Y_{coolant} \tilde{U}_i} n_i dS}_{\text{Mean field contribution}} + \underbrace{\int_{S_\delta(x)} \overline{\rho Y_{coolant}'' U_i''} n_i dS}_{\text{Resolved turbulence contribution}}, \quad (25)$$

where  $\overline{Y_{coolant}'' U_i''}$  corresponds to the resolved turbulent mass flux of  $Y_{coolant}$  and  $''$  the temporal fluctuations with respect to the Favre averaging. Since the film remains attached to

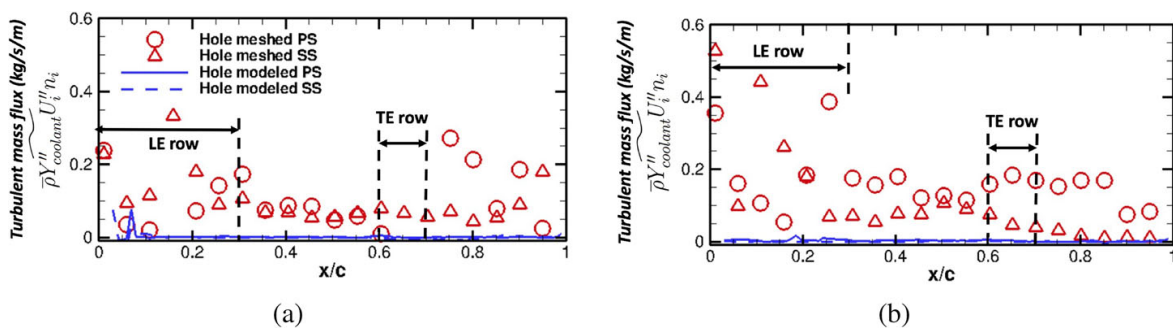


**Fig. 22** Axial evolution of turbulent mass flux  $\overline{\rho Y_{coolant}'' U_i''} n_i$  through the edge of the film  $S_\delta$  at mid-height of NGV1 (a) and NGV2 (b). Red circles  $\circ$  represent the hole meshed LES at the pressure side. Red triangles  $\Delta$  represent the hole meshed LES at the suction side. The solid blue line  $\_$  represents the hole modeled LES at the pressure side. The dashed blue line  $\_ \_$  represents the hole modeled LES at the suction side

the wall far from the injection holes, the direction of the flow at the edge of the film thickness can be assumed to be tangential to the wall if neglecting the normal velocity to the wall in the film thickness. As a result, the mean velocity  $\widetilde{U}_i$  is roughly orthogonal to the normal of the film section along the blades which indicates that the resolved turbulence contribution term dominates the mean field contribution term in Eq. 25. Consequently,  $Y_{film}$  levels originate from the turbulent mass flux  $\widetilde{\overline{\rho Y''_{coolant} U_i''}}$  through the edge of the film thickness section  $S_\delta$ . The impact of the model on the local value of the turbulent mass flux along  $S_\delta$  on both NGVs is provided at mid-height of the vanes in Fig. 22. Clearly, turbulent mass flux is reduced in the hole modeled LES compared to the hole meshed LES for both NGVs. In the hole meshed LES, Fig. 22a and b,  $\widetilde{\overline{\rho Y''_{coolant} U_i''} n_i}$  increases with the axial positions where the coolant is ejected, i.e, for  $0 < x/c < 0.3$  and  $0.6 < x/c < 0.7$ . This means that turbulent mass flux mainly occurs in the regions of coolant injection. Out of these axial positions, levels of  $\widetilde{\overline{\rho Y''_{coolant} U_i''} n_i}$  decrease. Note that levels of  $\widetilde{\overline{\rho Y''_{coolant} U_i''} n_i}$  remain strictly positive all along the coolant film. From Eq. 24, this shows that turbulent mass flux decreases levels of  $Y_{film}$  confirming previous observations. To find the origin of such deviations between the two LES predictions, turbulent activity in the film region is evaluated by investigating the turbulent kinetic energy map  $k$  as well as the temporal Root Mean Squared (RMS)  $Y_{rms}$ . Turbulent fields are extracted at mid-height of the vanes and displayed in Figs. 23 and 24

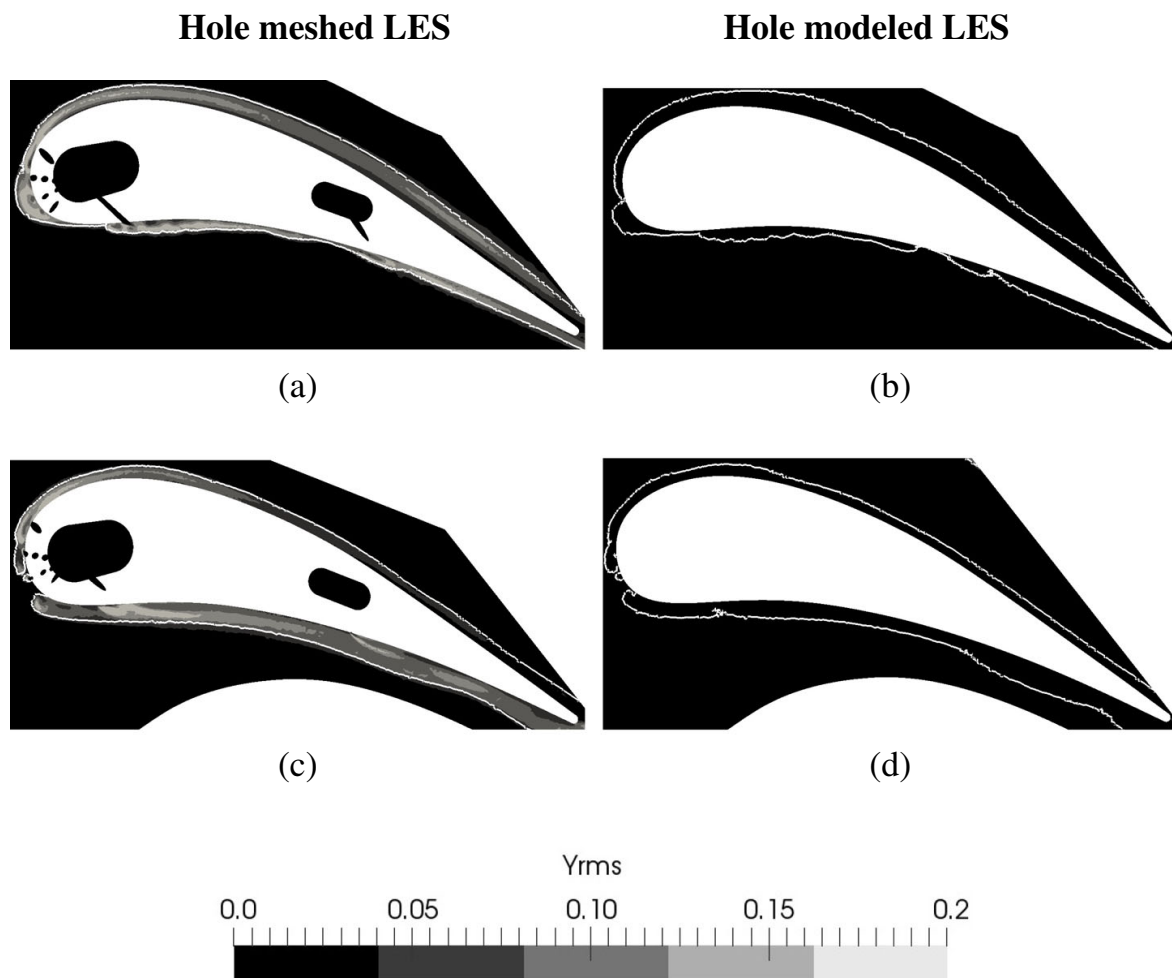


**Fig. 23**  $Y_{RMS}$  map at mid height on NGV1 and NGV2 at mid-height for both LES. Top (a) & (b), NGV1. Bottom (c) & (d), NGV2. Left (a) & (c), hole meshed. Right (b) & (d), hole modeled. The film mean thickness is represented by the white isoline

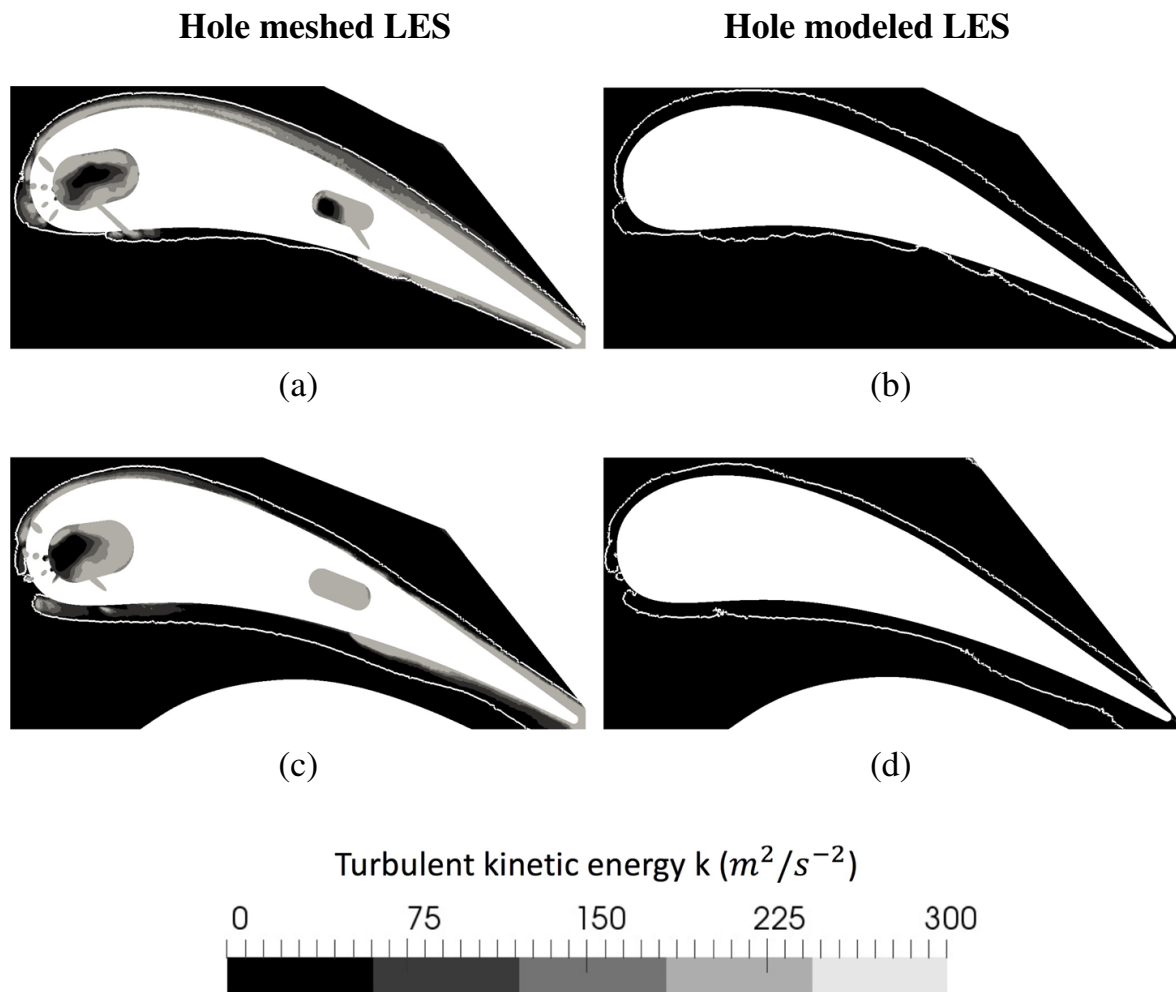


**Fig. 24** Turbulent kinetic energy maps  $k$  on NGV1 and NGV2 at mid-height for both LES. Top (a) & (b), NGV1. Bottom (c) & (d), NGV2. Left (a) & (c), hole meshed. Right (b) & (d), hole modeled. The mean film thickness is represented by the white isoline

for NGV1 and NGV2 for both LES predictions. Results confirm that turbulent activity in the coolant film of both NGVs is reduced in the hole modeled LES compared to the hole meshed LES. Indeed, in the hole meshed LES (Fig. 23a and c), the turbulent mixing between the coolant and the hot streams takes place in the film thickness and is higher at the coolant injection locations. These maps evidence that turbulence is produced within the plena and pipes of both NGVs and is then propagated around the blades in the film thickness (Fig. 24a and c). On the pressure side, the turbulent kinetic energy occurs at the coolant injections. Between the hole rows, the turbulence decreases due to the acceleration of the flow where turbulent structures are stretched and dissipated. On the suction side, the turbulence is created near the NGV and then decreases downstream. One can also notice an increase of the turbulent kinetic energy level at  $x/c \approx 0.75$  for both NGVs without injection of coolant indicating a potential turbulent transition of the film at this specific position which could explain the thickening of the film on the suction side previously noticed on Fig. 19. The level of turbulent mixing and turbulent kinetic energy for both NGVs predicted by the hole modeled LES (Fig. 23b and d) is very reduced compared to the hole meshed (Fig. 24b and d). Since the plena and the pipes are not meshed and with the stationary velocity profile imposed by the model, the turbulence production term is not represented on the hole

modeled mesh which de-activates the associated  $Y_{rms}$  production term. The coolant turbulent mixing within the film thickness section  $S_\delta$  is effectively almost zero with the model confirming that more coolant remains in the film thickness with the hole modeled approach if compared to the hole meshed LES.

To conclude, the investigation of the impact of the model on the adiabatic film effectiveness profiles shows that the blades are slightly colder if using the model. By tracking the coolant with a passive scalar and performing a mass balance in the near wall regions of the blades, it can be deduced that the mixing is less efficient with the model. Results show that the lack of mixing in the model is due to absence of turbulent fluctuations in the coolant film, keeping the film temperature near the cold injected temperature. Since the pipes are not meshed and no turbulent fluctuations are injected with the model, as shown in Section 3, the film region suffers from a lack of turbulent activity which reduces the associated turbulent mixing.

## 5 Conclusion

In the present study, the applicability of a coolant injection model to predict the skin temperature of turbine blades with Large-Eddy Simulation (LES) has been assessed. The model was derived from an existing coolant injection model designed for modeling the injection of coolant in the context of the combustion chamber and adapted to turbine blades. To evaluate the coolant model, a reference hole meshed LES has been performed on the Nozzle Guide Vanes of the FACTOR project and then compared to a hole modeled LES keeping the same mesh around the blade and numerical set up. The operating points of both LES have first been checked to ensure their comparability. The estimations of the CPU cost for both LES show a drastic reduction of the CPU cost when the hole model approach is used. Results are very encouraging. The hole modeled LES gives a very close distribution of the adiabatic film effectiveness compared to the hole meshed LES. Investigations of the coolant film show that the film effectiveness is slightly higher in the hole modeled LES. By tracking the coolant with a passive scalar and performing a mass balance in the film thickness, the coolant mass fraction distribution in the coolant film is shown to be impacted by the turbulent mass flux at the edge of the coolant film. The turbulent mass flux is shown to be strongly reduced in the hole modeled approach. Indeed, the evaluation of the turbulent maps indicates that the turbulence is produced in the pipes which is not taken into account with the model and then leads to a lack of agitation with the model. As a result, the model needs to be improved to recover the agitation between the hot and cold flows. Naturally, one possibility is to inject synthetic turbulence at the exit pipe section with the model which needs to be tested in future studies.

**Acknowledgements** The authors wish to gratefully acknowledge FACTOR (Full Aerothermal Combustor-Turbine interactions Research) Consortium for the kind permission of publishing the results herein. FACTOR is a Collaborative Project co-funded by the European Commission within the Seventh Framework Programme (2010- 2017) under the Grant Agreement 265985. This work was granted access to the HPC resources of IDRIS under the allocation 2018 - A0042A06074 made by GENCI.

## Compliance with Ethical Standards

**Conflict of interests** The authors declare that they have no conflict of interest.

## Appendix 1: Sensitivity of Resolved Turbulence and Wall Temperature to Mesh Adaptation Process

In the present study, a mesh adaptation process has been performed to accurately refine the regions of mixing between the hot and coolant streams. To do so, an user-defined mesh is first created. Then, an automatic mesh adaptation is performed based on the entropy source terms obtained from the user-defined mesh to identify regions of strong velocity and temperature gradients and refine these regions. The properties of the two meshes are summarized in Table 4. To only refine the freestream and the near wall flow regions of the vanes, the mesh in the cooling system including coolant pipes and plena is frozen during the mesh adaptation process. As a result, the number of cells only increases in the freestream region by 52%. To localize the refined regions, a view of the two meshes at mid-height of the vanes are provided on Fig. 25. The mesh is observed to be mainly refined in the near wall flow region of the vanes. The impact of the mesh adaptation on resolved turbulence is now addressed. To quantify the resolution of turbulence on mesh, the criteria of Pope [45] is studied through the evaluation of  $M_E$  defined so that,

$$M_E = \frac{k_{res}}{k_{res} + k_{sgs}}, \quad (26)$$

where  $k_{sgs}$  is the sub-grid turbulent kinetic energy,  $k_{res} = 0.5(u_{rms}^2 + v_{rms}^2 + w_{rms}^2)$  is the resolved turbulent kinetic energy and  $u_{rms}$ ,  $v_{rms}$ ,  $w_{rms}$  are the RMS of velocity fields. For the above relation, a closure for  $k_{sgs}$  is needed. To close  $k_{sgs}$ , the following relation is used [46]:

$$\nu_t = C_m V^{\frac{1}{3}} \sqrt{k_{sgs}}, \quad (27)$$

where  $\nu_t$  is the turbulent viscosity,  $V$  the node volume and  $C_m$  a constant of the model. To operate suitability of LES, near 80% of the turbulence should be resolved on mesh according to Pope [45]. The map of  $M_E$  is provided at mid-height of the vanes on Fig. 26 for the two meshes. To evidence the regions where more than 80% of turbulence is resolved on mesh, an iso-line equal to  $M_E = 0.8$  is added to Fig. 26. For the user-defined mesh, Fig. 26a, turbulence in the film region of the vanes is clearly under-resolved. Nevertheless in the wakes of the vanes, turbulence is observed to be sufficiently resolved. For the adapted mesh, Fig. 26b, the resolution of turbulence is clearly improved in the film region and locally reaches 80% of the overall turbulence. The resolution of turbulence is also improved in the wakes of the vanes. In the coolant pipes, a good resolution of turbulence is also observed featuring more than 80% of resolution. The impact of the increasing mesh resolution on the prediction of time-averaged adiabatic wall temperature is shown on Fig. 27. For the user-defined mesh, Fig. 27a, a large range of temperature is observed on the vane surfaces and local patterns of hot and cold temperature are observed. For the adapted mesh, Fig. 27b, the wall temperature is more segregated compared to the user-defined mesh. Indeed, finer

**Table 4** Number of cells for the user-defined mesh and adapted mesh

	User-defined mesh	Adapted mesh
Number of cells (millions)	60	73 (+ 21%)
Number of cells in the cooling system (millions)	35	35 (+ 0%)
Number of cells in the freestream region (millions)	25	38 (+ 52%)

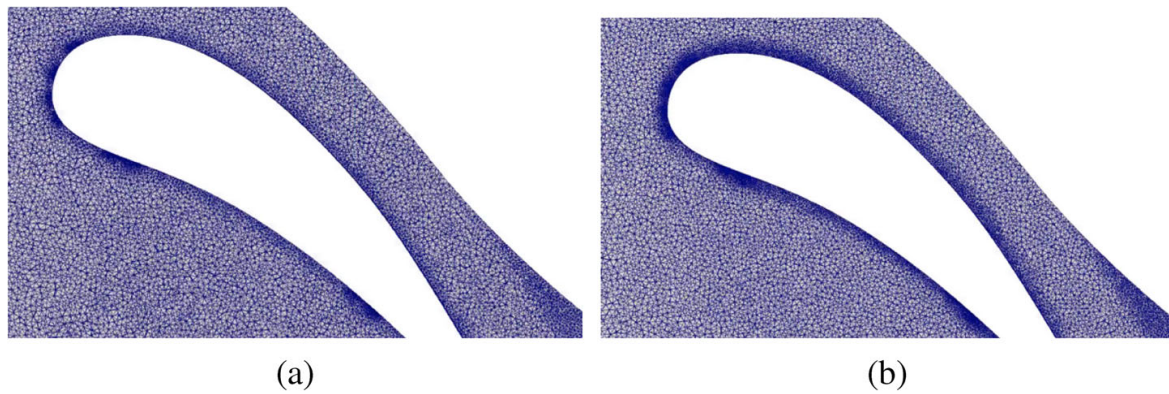
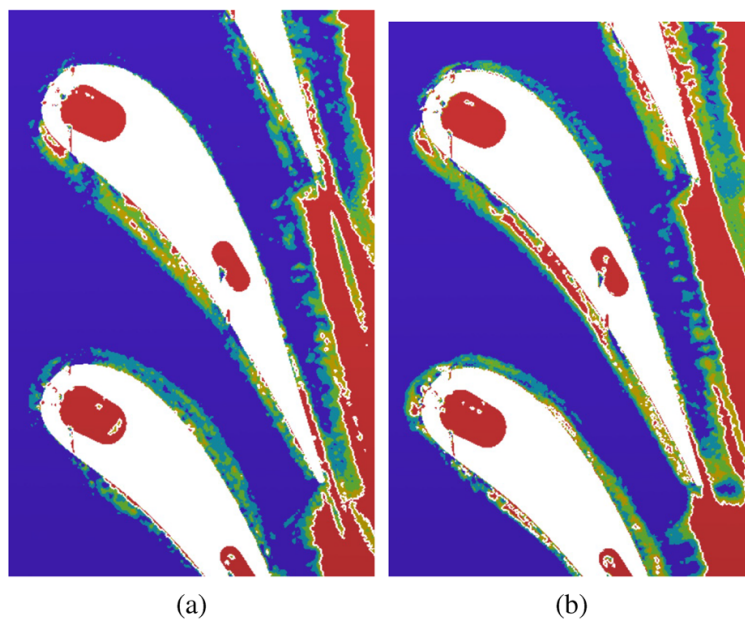


**Fig. 25** View of user-defined mesh **(a)** and adapted mesh **(b)** at mid-height of NGV1

patterns of hot and cold temperatures are observed on the vane surfaces because a finer turbulence is resolved on the adapted mesh.

As a consequence of the previous discussion, the mesh adaptation process has improved the resolution of turbulence in the film region of the vanes. Although turbulence resolution



$$\frac{k_{res}}{k_{res} + k_{sgs}}$$



**Fig. 26**  $M_E$  map at mid-height of the vanes. White iso-line represents  $M_E = 0.8$ . User-defined mesh **(a)** and adapted mesh **(b)**

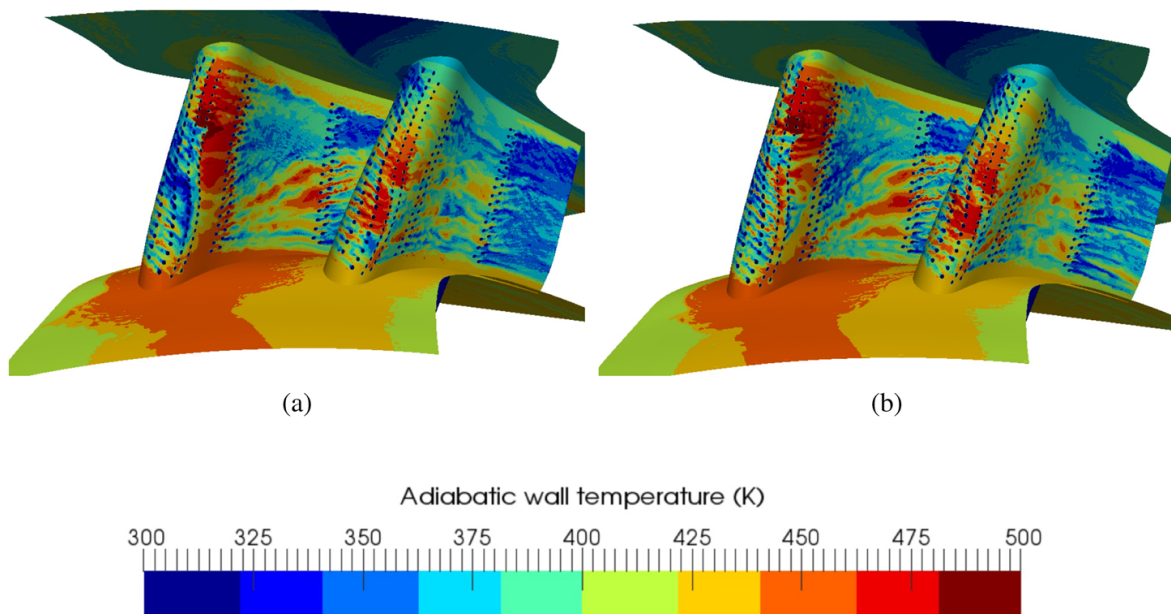


**Fig. 27** Impact of mesh adaptation on adiabatic wall temperature. User-defined mesh (a) and adapted mesh (b)

remains locally inferior to 80% around the vanes, the adapted mesh allows to capture very fine patterns of hot and cold temperature on the vane surfaces.

## References

1. Andrei, L., Innocenti, L., Andreini, A., Facchini, B., Winchler, L.: Film cooling modeling for gas turbine nozzles and blades: validation and application. *J. Turbomach.* **139**, 011004–011004–9 (2016). <https://doi.org/10.1115/1.4034233>
2. Andreini, A., Da Soghe, R., Facchini, B., Mazzei, L., Colantuoni, S., Turrini, F.: Local source based cfd modeling of effusion cooling holes: validation and application to an actual combustor test case. *J. Eng. Gas Turbines Power.* **136**(1), 011506–011506–11 (2013). <https://doi.org/10.1115/1.4025316>
3. auf dem Kampe, T., Völker, S.: A model for cylindrical hole film cooling—part ii: model formulation, implementation and results. *J. Turbomach.* **134**(6), 061011 (2012)
4. Dickhoff, J., Kusterer, K., Bhaskar, S.K., Bohn, D.: Cfd simulations for film cooling holes: comparison between different isotropic and anisotropic eddy viscosity models (51081) v05AT12a008 (2018). <https://doi.org/10.1115/GT2018-75543>
5. Dyson, T.E., Bogard, D.G., Bradshaw, S.D.: Evaluation of cfd simulations of film cooling performance in the showerhead region of a turbine vane including conjugate effects (45233), 1977–1986 (2012). <https://doi.org/10.1115/IMECE2012-88386>
6. Ravelli, S., Barigozzi, G.: Comparison of rans and detached eddy simulation modeling against measurements of leading edge film cooling on a first-stage vane. *J. Turbomach.* **139**(5), 051005 (2017)
7. Sagaut, P.: *Large Eddy Simulation for Incompressible Flows*. Scientific Computation Series. Springer, Berlin (2000)
8. Tucker, P.: Computation of unsteady turbomachinery flows: part 1 progress and challenges. *Prog. Aerosp. Sci.* **47**(7), 522–545 (2011)
9. Pichler, R., Sandberg, R.D., Laskowski, G., Michelassi, V.: High-fidelity simulations of a linear hpt vane cascade subject to varying inlet turbulence. In: *Turbo Expo: Power for Land, Sea, and Air*, 50787, pp. V02AT40A001 (2017)
10. Tucker, P.: Computation of unsteady turbomachinery flows: part 2 LES and hybrids. *Prog. Aerosp. Sci.* **47**(7), 546–569 (2011)
11. Tyacke, J.C., Tucker, P.G.: Future use of large eddy simulation in aero-engines. *J. Turbomach.* **137**(8), 081005 (2015)

12. Aillaud, P., Duchaine, F., Gicquel, O., Koupper, C., Staffelbach, G.: Large eddy simulation of trailing edge cutback film cooling: impact of internal stiffening ribs on the adiabatic effectiveness. In: 7th European Conference for Aeronautics and Aerospace Sciences (EUCASS 2017), vol. CD. Milan, Italy (2017)
13. Duchaine, F., Corpron, A., Pons, L., Moureau, V., Nicoud, F., Poinsot, T.: Development and assessment of a coupled strategy for conjugate heat transfer with large eddy simulation: application to a cooled turbine blade. *Int. J. Heat Fluid Flow* **30**(6), 1129–1141 (2009)
14. Grosnickel, T., Duchaine, F., Gicquel, L., Koupper, C.: Large-eddy simulation of the flow developing in static and rotating ribbed channels. In: ASME Turboexpo 2019, pp. GT2019–90370. Phoenix, AZ, USA (2019)
15. Ling, Z., Guoliang, W.: Large eddy simulation on compound angle film cooling of turbine blades. In: IEEE 2011 10th International Conference on Electronic Measurement & Instruments, vol. 1, pp. 282–287. IEEE (2011)
16. Mendez, S., Nicoud, F.: Adiabatic homogeneous model for flow around a multiperforated plate. *AIAA J.* **46**(10), 2623–2633 (2008)
17. Bizzari, R., Lahbib, D., Dauptain, A., Duchaine, F., Gicquel, L., Nicoud, F.: A thickened-hole model for large eddy simulations over multiperforated liners. *Flow Turbul. Combust.* **101**(3), 705–717 (2018). <https://doi.org/10.1007/s10494-018-9909-3>
18. Bizzari, R.: Aerodynamic and Thermal Modelling of Effusion Cooling in LES. Phd thesis, Université Fédérale de Toulouse, INPT - Ecole doctorale MEGeP (2018)
19. Bizzari, R., Férand, M., Dauptain, A., Staffelbach, G., Richard, S., Mueller, J.D., Ogier, T., Exilard, G., Nicoud, F.: Mesh local refinement to enhance effusion cooling models; invited conference. In: ERCOF-TAC (ed.) 12th International Symposium on Engineering Turbulence Modelling and Measurements (ETMM12). Montpellier (France) (2018)
20. Battisti, C., Kost, F., Atkins, N., Playford, W., Orain, M., Caciolli, G., Tarchi, L., Mersinligil, M., Raffel, J.: Full aerothermal combustor turbine interaction research. In: Proceedings of 2nd EASN WORKSHOP on Flight Physics (2012)
21. Krumme, A., Tegeler, M., Gattermann, S.: Design, integration and operation of a rotating combustor-turbine-interaction test rig within the scope of ec fp7 project factor. In: Proceedings of 13th European Conference on Turbomachinery Fluid Dynamics & Thermodynamics ETC13, pp. 1–13 (2019)
22. Bacci, T., Caciolli, G., Facchini, B., Tarchi, L., Koupper, C., Champion, J.L.: Flowfield and temperature profiles measurements on a combustor simulator dedicated to hot streaks generation. In: ASME Turbo Expo 2015: Turbine Technical Conference and Exposition, pp. V05CT17A001–V05CT17A001. American Society of Mechanical Engineers (2015)
23. Han, J.C., Rallabandi, A.: Turbine blade film cooling using psp technique. *Frontiers in Heat and Mass Transfer (FHMT)* **1**(1), 1–21 (2010)
24. Peet, Y., Lele, S.: Near field of film cooling jet issued into a flat plate boundary layer: Les study. *Proceedings of the ASME Turbo Expo* **4** (2008). <https://doi.org/10.1115/GT2008-50420>
25. Bizzari, R., Lahbib, D., Dauptain, A., Duchaine, F., Richard, S., Nicoud, F.: Low order modeling method for assessing the temperature of multi-perforated plates. *Int. J. Heat Mass Trans.* **127**(Part B), 727–742 (2018). <https://doi.org/10.1016/j.ijheatmasstransfer.2018.07.059>
26. Han, J.C., Ekkad, S.: Recent development in turbine blade film cooling. *Int. J. Rotating Mach.* **7**(1), 21–40 (2001)
27. Garnier, E., Adams, N., Sagaut, P.: Large eddy simulation for compressible flows (2009). <https://doi.org/10.1007/978-90-481-2819-8>
28. Poinsot, T., Veynante, D.: Theoretical and Numerical Combustion, 3rd edn. [www.cerfacs.fr/elearning](http://www.cerfacs.fr/elearning) (2011)
29. Nicoud, F., Ducros, F.: Subgrid-scale stress modelling based on the square of the velocity gradient tensor. *Flow Turbul. Combust.* **62**(3), 183–200 (1999)
30. Gourdain, N., Gicquel, L., Montagnac, M., Vermorel, O., Gazaix, M., Staffelbach, G., Garcia, M., Bousuge, J., Poinsot, T.: High performance parallel computing of flows in complex geometries: I. methods. *Comput. Sci. Disc.* **2**, 015003 (2009)
31. Odier, N., Sanjosé, M., Gicquel, L., Poinsot, T., Moreau, S., Duchaine, F.: A characteristic inlet boundary condition for compressible, turbulent, multispecies turbomachinery flows. *Comput. Fluids* **178**, 41–55 (2018). <https://doi.org/10.1016/j.compfluid.2018.09.014>
32. Poinsot, T., Lele, S.: Boundary conditions for direct simulations of compressible viscous flows. *J. Comput. Phys.* **101**(1), 104–129 (1992). [https://doi.org/10.1016/0021-9991\(92\)90046-2](https://doi.org/10.1016/0021-9991(92)90046-2)
33. Thomas, M., Duchaine, F., Gicquel, L., Koupper, C.: Advanced statistical analysis estimating the heat load issued by hot streaks and turbulence on a high-pressure vane in the context of adiabatic large eddy

- simulations. In: ASME Turbo Expo 2017: Turbomachinery Technical Conference and Exposition, pp. V02BT41A041–V02BT41A041. American Society of Mechanical Engineers (2017)
34. Granet, V., Vermorel, O., Leonard, T., Gicquel, L., Poinso, T.: Comparison of nonreflecting outlet boundary conditions for compressible solvers on unstructured grids. *AIAA J.* **48**(10), 2348–2364 (2010)
  35. Koupper, C., Poinso, T., Gicquel, L., Duchaine, F.: Compatibility of characteristic boundary conditions with radial equilibrium in turbomachinery simulations. *AIAA J.* **52** (2014). <https://doi.org/10.2514/1.J052915>
  36. Donea, J., Huerta, A.: *Finite Element Methods for Flow Problems*. Wiley, New York (2003)
  37. Dapogny, C., Dobrzynski, C., Frey, P.: Three-dimensional adaptive domain remeshing, implicit domain meshing, and applications to free and moving boundary problems. *J. Comput. Phys.* **262**, 358–378 (2014). <https://doi.org/10.1016/j.jcp.2014.01.005>. <http://www.sciencedirect.com/science/article/pii/S0021999114000266>
  38. Harnieh, M., Gicquel, L., Duchaine, F.: Large eddy simulations of a highly loaded transonic blade with separated flow - invited conference. In: *Turbomachinery Technical Conference and Exposition 2018*, pp. GT2018–75730. ASME International Gas Turbine Institute, Oslo (2018)
  39. Jin, Y., Du, J., Li, Z., Zhang, H.: Second-law analysis of irreversible losses in gas turbines. *Entropy* **19**(9), 470 (2017). <https://doi.org/10.3390/e19090470>
  40. Safari, M., Sheikhi, M.R.H., Janbozorgi, M., Metghalchi, H.: Entropy transport equation in large eddy simulation for exergy analysis of turbulent combustion systems. *Entropy* **12**(3), 434–444 (2010). <https://doi.org/10.3390/e12030434>
  41. Koupper, C., Caciolli, G., Gicquel, L., Duchaine, F., Bonneau, G., Tarchi, L., Facchini, B.: Development of an engine representative combustor simulator dedicated to hot streak generation. *J. Turbomach.* **136**(11), 111007–111007–10 (2014)
  42. Fric, T.F., Roshko, A.: Vortical structure in the wake of a transverse jet. *J. Fluid Mech.* **279**, 1–47 (1994)
  43. New, T., Lim, T., Luo, S.: Elliptic jets in cross-flow. *J. Fluid Mech.* **494**, 119–140 (2003)
  44. Favre, A.: Statistical equations of turbulent gases. In: *Problems of Hydrodynamics and Continuum Mechanics*, pp. 231–266. SIAM, Philadelphia (1969)
  45. Pope, S.B.: *Turbulent Flows*. Cambridge University Press, Cambridge (2000)
  46. Smagorinsky, J.: General circulation experiments with the primitive equations: 1. The basic experiment. *Mon. Weather Rev.* **91**, 99–164 (1963)

**Publisher's Note** Springer Nature remains neutral with regard to jurisdictional claims in published maps and institutional affiliations.

**GT2017-64648**

**DRAFT: ADVANCED STATISTICAL ANALYSIS ESTIMATING THE HEAT LOAD  
ISSUED BY HOT STREAKS AND TURBULENCE ON A HIGH-PRESSURE VANE IN  
THE CONTEXT OF ADIABATIC LARGE EDDY SIMULATIONS**

**Martin Thomas\*, Florent Duchaine, Laurent Gicquel**  
CFD Team CERFACS  
Toulouse, France  
thomas@cerfacs.fr

**Charlie Koupper**  
Safran Helicopter Engines  
Bordes, France

**ABSTRACT**

*The next generation of lean combustion engines promises to further decrease environmental impact and cost of air traffic. Compared to the currently employed Rich Quench Lean (RQL) concept, the flow field at the exit of a lean combustion chamber is characterized by stronger variations of velocity as well as temperature and higher levels of turbulence. These specific features may have a substantial impact on the aerothermal performance of the high-pressure turbine and thereby on the efficiency of the entire engine. Indeed, high levels of turbulence in the Nozzle Guide Vane (NGV) passages locally impact the heat flux and result in globally over dimensioned cooling systems of the NGV. In this study, Large Eddy Simulations (LES) are performed on an engine representative lean combustion simulator geometry to investigate the evolution of turbulence and the migration of hot streaks through the high-pressure turbine. To investigate the impact of non-uniform stator inlet conditions on the estimated thermal stress on the NGVs, adiabatic LES predictions of the lean combustor NGV FACTOR configuration are analyzed through the use of high statistical moments of temperature and two point statistics for the assessment of turbulent quantities. Relations between temperature statistical features and turbulence are evidenced on planes through the NGV passage pointing to the role of mixing and large scale features along with marked wall temperatures that locally can largely differ from obtained mean values.*

**NOMENCLATURE**

**Acronyms**

ACL	Axial Chord Length
CFD	Computational Fluid Dynamics
CFL	Courant-Friedrichs-Lewis condition
FACTOR	Full Aerothermal Combuster Turbine interactions Research
ITD	Inlet temperature distortions
LES	Large Eddy Simulation
LPP	Lean Partially Premixed
NGV	Nozzle Guide Vane
P40	Intersection plane between combustion chamber and stator
PS	Pressure side
RANS	Reynolds Averaged Navier-Stokes
RMS	Root Mean Square
RQL	Rich Quench Lean
SS	Suction side

---

\*Address all correspondence to this author.

## Symbols

$i, j$	Counter
$K$	Kurtosis
$N$	Number of instantaneous solutions
$N_0$	Solution number of first zero crossing of $R_{uu}$
$R$	Autocorrelation coefficient
$S$	Skewness
$t$	Time
$t_{turb}$	Turbulent timescale
$T$	Temperature
$u$	Axial velocity
$V$	Velocity
$y^+$	Non-dimensional wall distance
$\rho$	Density
$\tau$	Time lag
$\Delta t$	Time step
$\sigma$	Standard deviation

## Subscripts

$r$	Radial
$t$	Tangential
$x$	Axial

## Superscripts

$-$	Averaged quantity
$'$	Fluctuating Quantity

## INTRODUCTION

Facing stricter emission regulations,  $\text{NO}_x$  reducing lean combustion concepts will have to be introduced in the next generation of aircraft engines. Indeed, this new technology seems to be a good solution for a more compact combustor design and to drastically reduce  $\text{NO}_x$  emission. Lean partially premixed (LPP) combustors are operated close to the lean blowout limit. The combustion process is stabilized by a recirculation zone induced by a swirl motion. This swirl is produced by a strong vortex generated by the fuel injection system, which provides the combustion chamber with a homogeneous fuel-air mixture over a wide range of operating conditions [1]. Compared to currently employed Rich Quench Lean (RQL) combustion chambers, particularities of the new concept are higher levels of swirl, turbulence and temperature non-uniformities at the exit of the combustion chamber. These features adversely alter secondary flow patterns in the high-pressure turbine, leading to an increase in aerodynamic losses [2–4].

Today, driven by the need to increase the engine thermal efficiency, the combustor exit temperature reached up to 2000 K, a level well superior to the melting point of alloys used in high-pressure turbines. At the turbine inlet, the Inlet Temperature Distortions (ITD), due to the discrete positioning of fuel injectors and high levels of turbulence locally may result in an increased heat flux on walls of the high-pressure turbine and

result in globally over-dimensioned NGV cooling systems. As an example and to stress the critical aspects of such distributions, Bogard and Thole (2006) [5] state that decreasing temperatures by just 25 K can double the life time for certain parts of the engine.

Since gas turbines have been first applied to aircraft in the 1940s, there was a rapid development of new technologies to meet the increasing demand for performance and efficiency. Because of issues induced by the increasing burnt gas temperature, Combustor / turbine interactions have been very early on identified and investigated. In the 80s, first experimental research facilities were established at the NASA Lewis research center to investigate the impact of hot streaks on the high-pressure turbine [6]. Dorney et al. [7] (1999) gave a review of experimental and computational studies on the migration of hot streaks. Povey and Qureshi (2009) [4] summarized developments and research on combustor simulators dedicated to the investigation of the impact of ITD on the high-pressure turbine. Most of past research focuses on RQL architectures which possess an inherently different flow field than future LPP combustors. The impact of NGVs on the combustor flow field is a very recent area of research and the FACTOR test rig is one of the first to address this issue. In parallel, the first attempt to conduct Large Eddy Simulation (LES) of a combustion chamber and its stator was produced by Roux et al. (2008) [8]. More recently Koupper et al. (2016) [9] presented first LES of combustor-turbine interactions for a lean combustion chamber, the FACTOR<sup>1</sup> test rig. Today's industrial standard is to design combustion chamber and turbine separately and to exchange information, usually radially averaged profiles of the combustor exit quantities, on the interface between the combustion chamber and the stator. This however, does not take into account the huge fluctuations present at the exit of LPP combustion chambers. This combined with the lack of experience with LPP combustors leads to the application of huge safety margins, to account for uncertainties not yet investigated by experiments or simulations.

The current study expands on previous research by Koupper et al. (2016) [9] on combustor turbine interactions issued by the analysis of LES predictions obtained for the FACTOR geometry, taking time resolved information into account. Exploiting the temporal information available from LES data by means of statistical analysis allows to estimate the thermal loads the high-pressure turbine is exposed to in the context of adiabatic simulations. To complement such analysis, use of high order statistics of temperature allows describing the Probability Density Function (PDF), which characterizes the temperature

<sup>1</sup>FACTOR (Full Aerothermal Combustor Turbine interactions Research) is a European research project to investigate interactions of lean combustion chambers with the high-pressure turbine

distribution in each point of the domain. This type of analysis can be used to determine where the mode value is situated in relation to the local mean, revealing locations with important temperature fluctuations that can locally surpass the thermal resistance of the NGV. Besides the local value of temperature, turbulence is the main quantity determining the local convective heat flux on the NGV surface. Using two-point statistical functions on the axial velocity component one can reveal large scale flow structures as well as smaller turbulent activity present in the flow field and not visible if solely using the evaluation of instantaneous or averaged flow fields.

This article first introduces the statistical tools devised throughout the paper followed by a description of the geometry of the FACTOR test rig. The next section introduces the LES setup, operating conditions and numerical methodology. Finally, the flow field is discussed and impacts on the NGV thermal heat load are shown by means of a statistical analysis of high order moments and flow quantities on the NGV surface.

### Statistical methodology

In this section, statistical tools used in this work are introduced and explained. The main prerequisite for such kind of statistical analysis is the availability of sufficiently long statistically stationary data. Over this duration a sufficiently high number of 3D or interpolated 2D flow fields is stored at a constant time-interval. Although a statistical context calls for a continuous mathematical representation, operations are here described in their discrete form. Note also that all quantities are one point statistics and refer to a unique location denominated by the vector  $x$ . In this one point statistics context, describing the shape of probability density functions (PDF) of temperature allows qualifying the relation between inlet temperature distortions (ITD) on P40 and temperature distributions on the adiabatic NGV surface. The first statistical moment, the mean  $\bar{T}(x)$ , of a quantity  $T(x)$  defines the average of a quantity over a number  $N$  of discrete realizations:

$$\bar{T}(x) = \frac{1}{N} \sum_{i=1}^N T_i(x). \quad (1)$$

The standard deviation  $\sigma(x)$ , describes how far values are spread from the mean:

$$\sigma(x) = \sqrt{\frac{1}{N} \sum_{i=1}^N (T_i(x) - \bar{T}(x))^2}. \quad (2)$$

Skewness  $S(x)$ , the third statistical moment, is a measure for the asymmetry of a PDF, indicating whether the most probable value

(mode value) is lower (positive Skewness) or higher (negative Skewness) than the mean:

$$S(x) = \frac{1}{N} \sum_{i=1}^N \left( \frac{T_i(x) - \bar{T}(x)}{\sigma(x)} \right)^3. \quad (3)$$

The Skewness of symmetric distributions (e.g. Gaussian) is 0, but the reverse is not true. For single peaked PDFs, the Skewness can be interpreted as the distance of the mode value to the mean. Kurtosis, the fourth statistical moment, indicates how "peaked" the signal is around the mean value. For a Gaussian PDF the Kurtosis value is  $K = 3$ . Distributions with a sharper peak have higher Kurtosis values and those which are flatter show lower values of Kurtosis. The fourth order statistical moment  $K(x)$  is calculated by:

$$K(x) = \frac{1}{N} \sum_{i=1}^N \left( \frac{T_i(x) - \bar{T}(x)}{\sigma(x)} \right)^4. \quad (4)$$

One point statistics allow to investigate distribution properties for a single variable. For a more detailed discussion of PDF used to describe turbulent flows, the reader is referred to Tennekes et al. (1972) [10].

To investigate turbulent timescales which have a major impact on the heat flux on the NGV surface, the application of two point statistical analysis becomes mandatory. In this work, autocorrelation is used to calculate turbulent timescales  $t_{urb}(x)$  from a set of instantaneous CFD predictions stored at constant time intervals over a statistically significant time period covering multiple flow-through times [11, 12]. First, the axial velocity component  $u_i(x)$  is decomposed in a mean  $\bar{u}(x)$  and a fluctuating part  $u'_i(x)$ :

$$u'_i(x) = u_i(x) - \bar{u}(x), \quad (5)$$

where the discrete mean value  $\bar{u}(x)$  is calculated as described by Eq. (1). The next step is to approximate the root mean square (RMS) value  $u_{RMS}(x)$  of  $u(x)$ :

$$u_{RMS}(x) = \sqrt{\frac{1}{N} \sum_{i=1}^N (u_i(x) - \bar{u}(x))^2}. \quad (6)$$

The autocorrelation coefficient  $R_{uu}$  is then calculated for different time lags  $\tau = \Delta t \times j$  and normalized by  $u_{RMS}(x)^2$ :

$$R_{uu}(x, \Delta t \times j) = \frac{\frac{1}{N} \sum_{i=1}^N u'_i(x) u'_{i+j}(x)}{u_{RMS}(x)^2}, \quad (7)$$

where  $j$  is a counter variable and  $\Delta t$  the time step size. Provided that the available data set is long enough  $R_{uu}(x, \Delta t \times j)$  depends only on the time lag  $\tau = \Delta t \times j$  and not on the choice of a specific solution  $i$ . The turbulent timescale  $t_{turb}$  for each point can then be calculated by:

$$t_{turb}(x) = \Delta t \sum_{j=1}^{N_0} R_{uu}(x, \Delta t \times j), \quad (8)$$

where  $N_0$  is the solution where the discrete autocorrelation coefficient  $R_{uu}(x, \Delta t \times j)$  equals 0 [13], meaning that the signal is not correlated anymore.

### FACTOR COMBUSTOR-NGV SETUP

The axial periodic numerical domain of the FACTOR test rig contains one swirler and two uncooled NGV with an Axial Chord Length (ACL) of 40 mm, representing a 18° section of the full angular non-reactive test rig. To reduce the impact of boundary conditions on the zone of interest, the domain features a large entry plenum and a pressure outlet sufficiently far from the NGVs (see Fig. 1a). To avoid early interactions of the swirler generated vortex with neighboring swirlers and the effusion cooling system, the main flow is restrained by a 55 mm duct of 63 mm diameter (see Fig. 1b). The swirler consists of 30 flat vanes with a length of 20.5 mm around a central hub of diameter 22 mm. The main flow traveling through the swirler at a temperature of 531 K is used to simulate combustion-generated temperature non-uniformities (hot streaks). Cavity flows are not simulated and coolant air (300 K) is directly injected through the liners as shown in Fig. 1b. The exit Reynolds number based on the NGV chord length (64 mm), calculated according to [14] is  $Re_{2th} = 742000$  ( $Ma_2 = 0.86$ ). Due to the absence of dilution holes in the FACTOR geometry, the hot streak remains largely undiluted by the coolant air, which mostly travels along the liners of the combustion chamber. In this study, the leading edge clocking position is investigated (see Fig. 1c) [9]. Operating conditions for the FACTOR test rig were chosen to be representative for a large envelop of different turbomachinery applications (see Tab. 1). Isothermal operating conditions for measurements were defined such that most non-dimensional quantities are met [15]. At isothermal operating conditions PIV measurements allow for a comparison of the flow field on a cross-section and HWA investigations allow to compare higher statistical quantities on P40. For design point operating conditions pressure, velocity and temperature measurements are available on P40. Note that the test rig in its current set up does not contain NGVs, which slightly impacts the flow field in combustion chamber and P40 [9]. Measurements have been performed at a trisector test rig at the University of Florence.

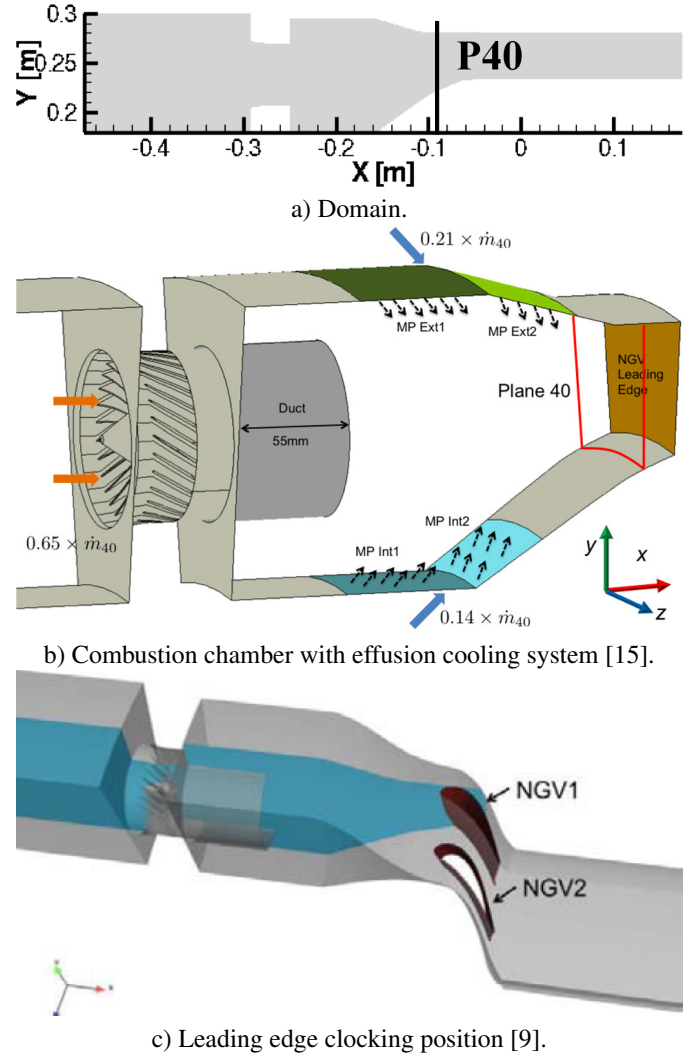


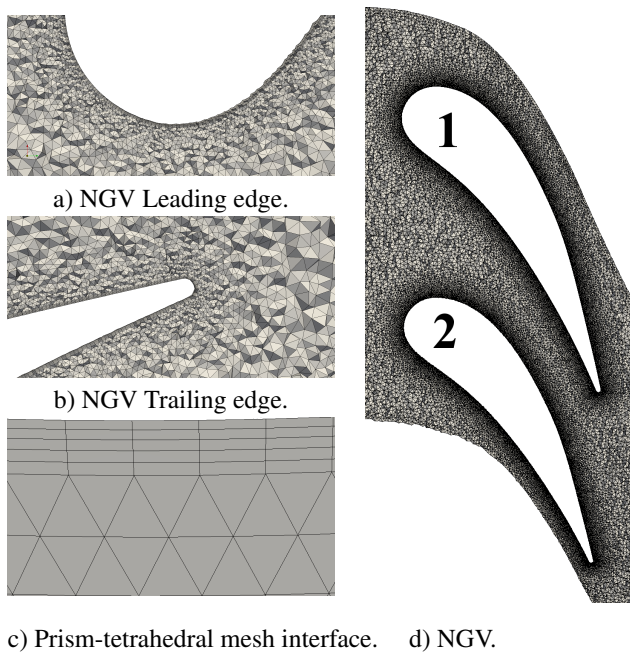
FIGURE 1: FACTOR geometry.

### NUMERICAL METHODOLOGY

Simulations presented in this work are performed using AVBP, a massively parallel CFD code developed at CERFACS and IPFEN. The code is based on a fully explicit cell-vertex formulation and solves the compressible Navier-Stokes equations for conservative variables on hybrid or unstructured meshes. AVBP is dedicated to LES and has been used and validated for a wide range of different applications [16–18]. Simulations are first converged using the Lax-Wendroff scheme [19], then a more accurate finite element two-step time-explicit Taylor Galerkin scheme (TTG4A), fourth order accurate in time and third order in space, is used for the discretization of convective terms [20]. This scheme ensures low diffusion and dispersion properties [21] and is therefore adequate for high fidelity simu-

**TABLE 1:** FACTOR operating conditions [15].

	IOP	DP
Static pressure on P40 [kPa]	115	147.65
Mass flow [kg/s]	4.8	4.8
Flow split swirler [-]	65%	65%
Flow split outer cavity [-]	21%	21 %
Flow split inner cavity [-]	14%	14 %
Swirler inlet temperature [K]	300	531
Coolant air temperature [K]	300	300
Swirler Reynolds number [-]	168 500	111 000
Swirler Mach number [-]	0.108	0.112

**FIGURE 2:** Mesh.

lations. Diffusive terms are discretized using a vertex centered formulation close to the Galerkin finite element method [22]. Time marching is done, respecting CFL (convection scheme) and Fourier (diffusion scheme) numbers to guarantee linear stability. To access turbulence quantities using autocorrelation [11, 12], a constant time step of  $4 \times 10^{-8}$  s, corresponding to a CFL number [30] of 0.9 is used for the simulation. Colin-type artificial

viscosity [24] is added to dampen potential numerical oscillations naturally present with the used schemes. Sub grid scale (SGS) turbulent contributions are computed using the Smagorinsky model [25]. Using the classical gradient diffusion hypothesis [12] the SGS heat flux is related to the filtered temperature gradient with a SGS thermal conductivity computed with a SGS turbulent Prandtl number of 0.6. Effusion cooling systems are modeled using a homogeneous [26] injection model. The application of Navier-Stokes Characteristic Boundary Conditions [27] allows to naturally establish a radial equilibrium pressure profile at the outlet [28]. To prevent reflections from the outlet, a sponge layer [29] adds additional dissipation close to the exit of the domain. The near-wall velocity gradient is calculated using wall functions [17]. Finally, solutions are evaluated over a period of five flow through times of the combustor module using the TTGC scheme. The simulation was performed on 512 cores for a computation cost of 260 khrs using Turing (IDRIS-GENCI - France). One solution is about 1 GB, for temporal evaluations 650 solutions, interpolated on a coarse grid (15 Mio cells / 120 MB each), were stored. The hybrid mesh contains 70 million cells (see Fig. 2) and uses prislayers around the NGV to guarantee low  $y^+$  values approaching 10, whereas the rest of the domain is discretized by tetrahedral cells.

## RESULTS

This section discusses the results obtained if applying the described statistical analysis to temperature and turbulent timescales on a set of instantaneous LES solutions for the combustor-NGV-leading edge clocking position. Primary focus is here dedicated to this specific combustor-turbine configuration and the evaluation of temperature PDFs combined with turbulence, because previous investigations by Koupper et al. (2016) [9] focused on the mean quantities for different clocking positions.

First the flow field in the combustion chamber is presented and validated with experimental measurements. Following, an analysis of the high statistical moments of temperature is shown, completed by a discussion of turbulence quantities in the NGV passage and their impact on the adiabatic NGV surface temperatures.

### Flow field in the combustion chamber and the NGV passage

To better understand the following investigations of temperature and turbulence in the NGV passage, some general features of the flow field within the combustor are presented first. Cross-section cuts through the central axis visualize general aspects of the flow field. This is followed by a presentation of mean quantities on P40, the intersection between combustion chamber and high-pressure turbine, and mean fields on an isoradius-cut show-

ing the flow field evolution through the NGV passage.

**Flow field in the combustion chamber.** The flow field features a huge central re-circulation zone (annotated as A on Fig. 3), visible in PIV visualizations (see Fig. 3b) and well captured by the simulation (see Fig. 3a), which is caused by the break down of the fuel injection system generated vortex. Note that for the PIV measurements (see Fig. 3b) at isothermal operating conditions only the mainstream was seeded with particles, which leads to blind zones close to the liners, where coolant air is injected. Smaller re-circulation zones (marked as A on Fig. 4) at the edges of the duct are evidenced by high values of turbulent kinetic energy (see Fig. 4a), which decay before reaching P40. An important proportion of air (referenced as B on Fig. 4b) travels just along the liners of the combustion chamber, evidenced by high levels of axial momentum. Temperature plots of the central axis cross-section (see Fig. 4c) show that the main flow remains largely undiluted by the coolant which mostly stays close to the walls. The swirling motion (see Fig. 4d) generated by the fuel injection system is strong throughout the domain and contributes to the complex flow field at the inlet of the stator. The dynamics of the flow is visualized by instantaneous contours of static pressure and static temperature for one instantaneous solution. The instantaneous pressure contour clearly (see Fig. 5a) shows the fuel injection system generated PVC (identified as A on Fig. 5) as a low pressure zone propagating from the swirler to the edge of the duct, where it breaks down, causing the wavy pattern observed in P40 (see Fig. 9a) and to be discussed later. Kelvin-Helmholtz instabilities (annotated as B on Fig. 5) at the duct edges are visible as low pressure zones and the injection of coolant is seen to locally increase the static pressure (see C on Fig. 5) level near the liners. The instantaneous temperature field (see Fig. 5b) visualizes the mixing behavior between the hot main flow and the coolant flow injected by the effusion cooling system of the liners. Clearly, the absence of dilution holes leaves the central hot spot largely undiluted and the coolant mostly travels along the liners.

**Flow field in P40.** After describing the mean flow field on a cross section through the combustor simulator, the focus now lies on P40, the intersection between combustion chamber and stator. Along the upper liner, high values of axial momentum (see Fig. 6a) indicate a high velocity flow of coolant air originating from the effusion cooling system (see Fig. 7d). The high momentum of this flow is the main reason explaining why the flow section remains undiluted throughout the NGV passage as discussed later. In the middle, low axial momentum and low Mach number show that in the hot flow region, comparatively few mass is transported (see Fig. 6). This is also shown by non-dimensionalized total pressure plots which compare well between experiment and simulation (see Fig. 7a). The rotational

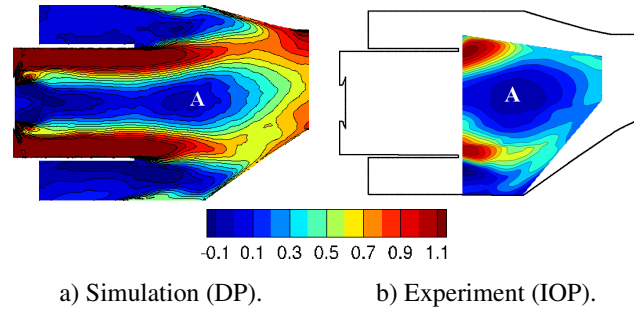


**FIGURE 3:** Central axial cross section cuts of the averaged axial velocity normalized by reference velocity (see Tab. 1) through the swirler from swirler to P40.

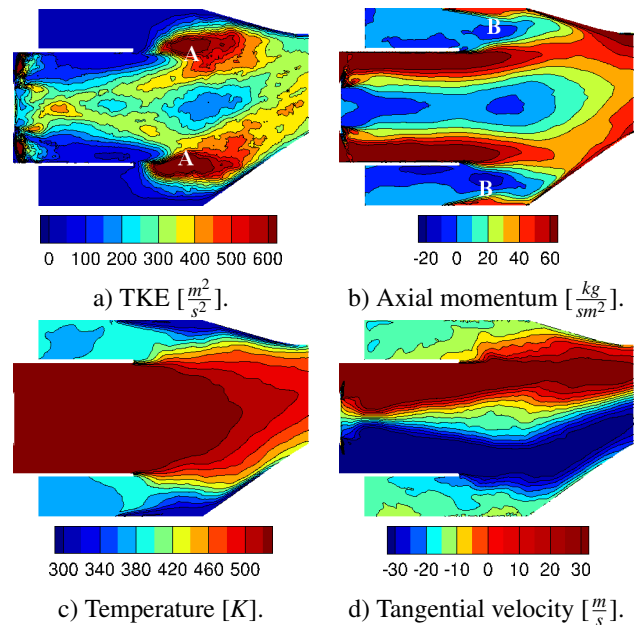


**FIGURE 4:** Central axial cross section cuts of the averaged flow field through the swirler from swirler to P40. (Design Point).

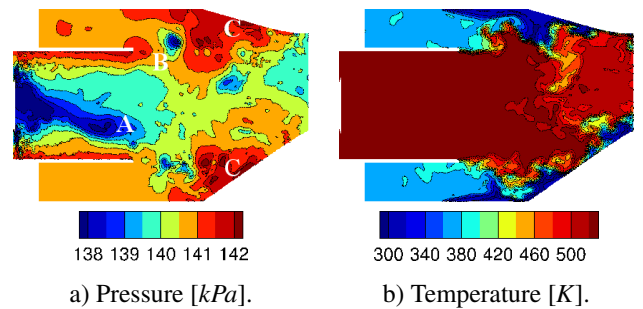


**FIGURE 5:** Central axial cross section cuts of an instantaneous flow field through the swirler from swirler to P40. (Design Point).

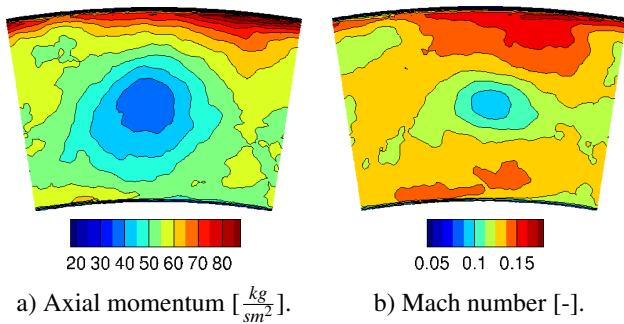


**FIGURE 6:** Averaged flow field on P40. View direction: Downstream. (Design Point).

movement shown in Fig. 7b and 7c, is caused by residual swirl from the fuel injection system generated vortex and is coherent with the results obtained from simulations. The stronger swirl in the experiment is explained by the absence of NGVs slowing down the rotation in the simulation. Average temperature plots on P40 show a highly non-uniform temperature distribution (see Fig. 7d). Close to the walls, the effusion cooling system strongly reduces the temperature compared to the middle, where the hot streak remains undiluted due to the absence of dilution holes in the FACTOR geometry. The boundary layer shows a high standard deviation for the temperature (see Fig. 8a), indicating a strong mixing between hot and cold flow along the wall. Comparatively values of temperature standard deviation remain low around mid-height pointing out a continuous flow of hot air in the center (see Fig. 8a). Negative Skewness in the middle of P40 (see Fig. 8b) results from a high probability of hot temperature, due to the hot spot, that are higher than the local average. The top region is instead favored by the cold flow injected by the effusion cooling system. The map of Kurtosis shows a well marked high value peak in the center, corresponding to the hot spot, which is largely undiluted by coolant (see Fig. 8c).

On P40, the turbulent kinetic energy shows a wave-like structure originating from the vortex breaking down after leaving the duct (see Fig. 9a). The evaluation of two point statistics, in this case the turbulent timescales on P40 (see Fig. 9b), reveals high values in the center and in the corners. Both show a good qualitative agreement to results obtained from experiments at isothermal operating conditions. By comparing with the temperature distribution on P40 (see Fig. 7d), the high timescale value in the middle can be attributed to the hot spot, whereas high values at corners are due to the coolant flow. In both cases, high values indicate a low level of mixing and larger local flow structures. Such time-scale maps also reveal flow patterns not visible from the evaluation of temperature data, but important for the estimation of the heat load on the NGV surface. In P40, low levels of TKE coincide with longer turbulent timescales. Regions with constantly high temperature and at the same time high levels of

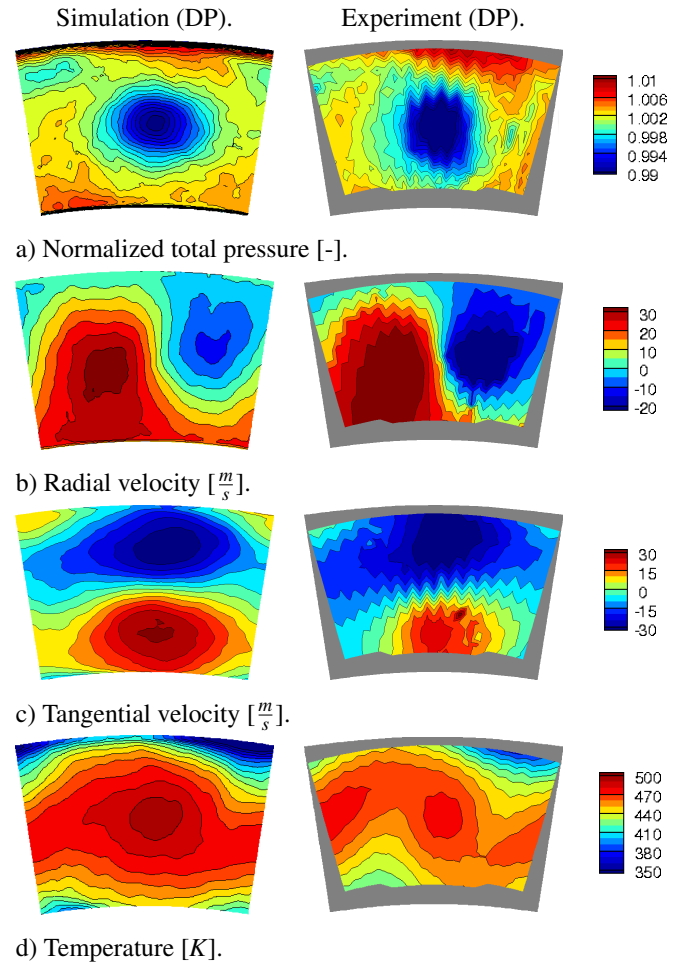


**FIGURE 7:** Flow field on P40. View direction: Downstream. (Design Point).

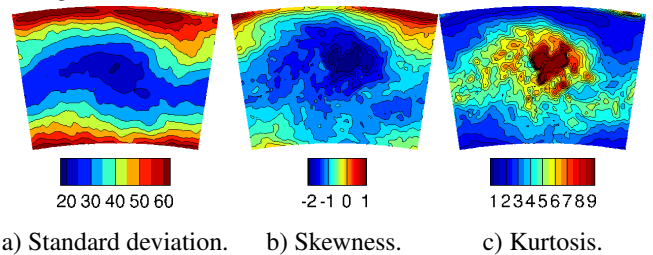


**FIGURE 8:** Statistical moments of temperature on P40. View direction: Downstream. (Design Point).

turbulent kinetic energy result in a locally persistent feature and a potentially increased heat load on the NGV surface, if these highly correlated temperature / turbulence spots are preserved and hit the NGV.

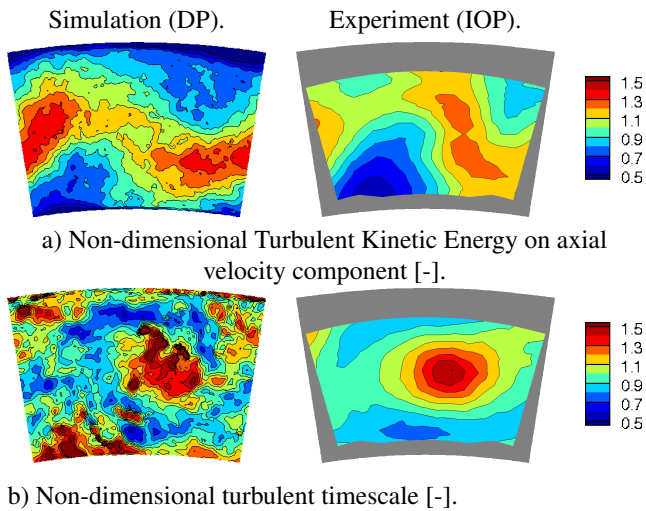


**FIGURE 9:** Non-dimensionalized flow field on P40. Comparison of design point simulation and isothermal operating point measurements. Values are non-dimensionalized by the average value in the experimental investigation zone. View direction: Downstream.

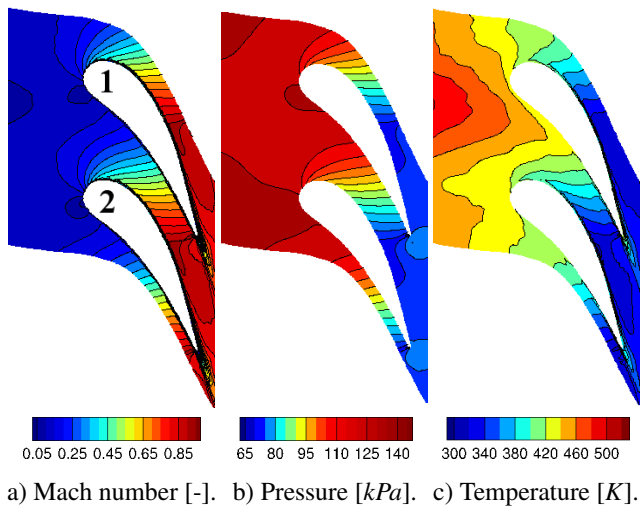


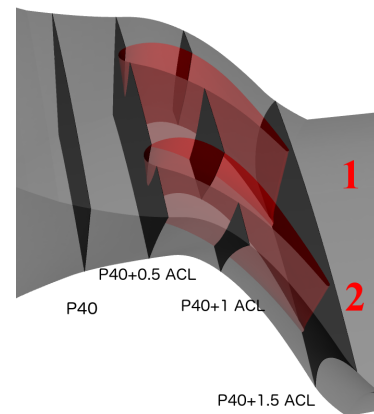
**FIGURE 10:** Flow field on an isoradius cut ( $h/H \approx 0.5$ ) in the NGV passage. Upper: NGV 1, Lower: NGV 2.

**Flow field in the NGV passage.** Before investigating the evolution of the flow field through the NGV passage using the above detailed statistical tools, this section describes the flow field in the NGV passage. Although the flow reaches Mach=1 in large parts of the passage, it is not completely choked (see Fig. 10a). Due to the expansion, the pressure drops and the fluid is accelerated (see Fig. 10b). The temperature field shows how

the hot spot impinges mostly on the pressure side of NGV 1 (see Fig. 10c). Due to the non-uniformities present at the stator inlet plane, P40, the flow field in the passage shows different evolutions if comparing both passages, especially regarding the temperature.

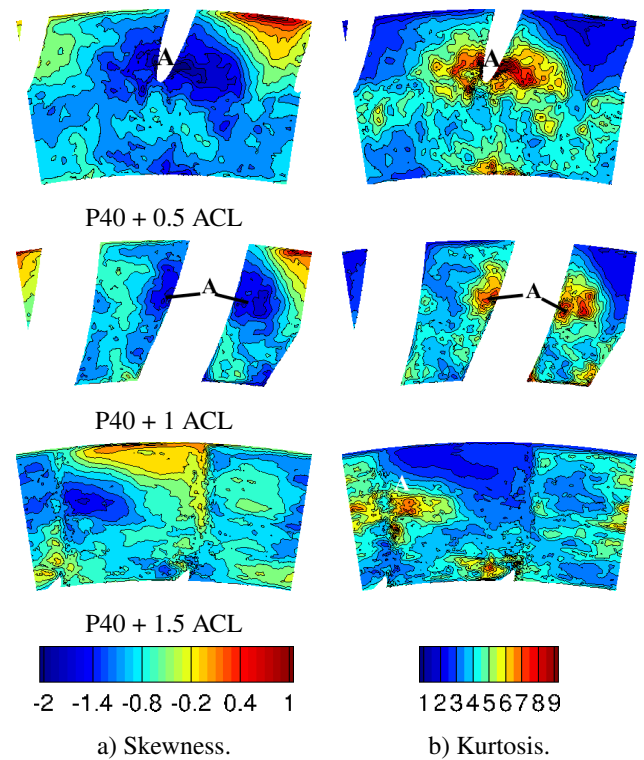
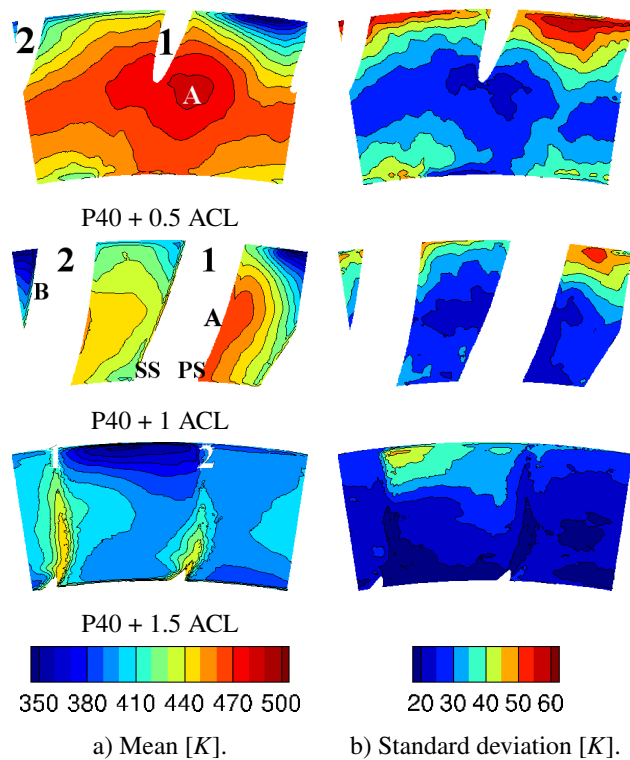
### Flow field evolution through NGV passage

Figure 11 depicts the planes used for the following investigation. The first plane, P40, is the intersection between the combustion chamber and the high-pressure turbine. The following plane (P40 + 0.5 ACL) is used to investigate the impingement of the hot streak on the NGV leading edge. P40 + 1 ACL is situated in between leading edge and trailing edge (P40 + 1.5 ACL).



**FIGURE 11:** FACTOR NGV section with investigation planes.

**Evolution of high statistic moments of temperature through the NGV passage.** Traveling through the NGV passage, the hot spot (marked as A on Fig. 12) migrates along the pressure side of NGV 1. The rotational movement, induced by the swirler (see Fig. 7b), moves coolant (see B on Fig. 12) from the upper wall to the suction side of NGV 2. Due to expansion in the stator the temperature decreases in the NGV passage. The standard deviation shows that the mixing of hot and cold fluids reduces while traveling through the NGV passage. Skewness and Kurtosis plots (see Fig. 13) better show the center of the hot spot (identified as A on Fig. 13) than lower statistical moments like the mean value. High values of Kurtosis signify a strong peak in the PDF, meaning that the hot spot remains undiluted throughout the NGV passage (see Fig. 13b). Away from the center of P40, Kurtosis values are decreasing, indicating a strong mixing between hot and cold flows due to secondary flow structures.



**FIGURE 12:** Evolution of statistical moments (Mean, Standard deviation) for static temperature on planes at successive axial positions through the NGV passage. View direction is downstream.

**FIGURE 13:** Evolution of statistical moments (Skewness, Kurtosis) for static temperature on planes at successive axial positions through the NGV passage. View direction is downstream.

### Evolution of turbulence through the NGV passage.

The highest thermal load on the NGV surface occurs where high temperature and fast turbulent flows coincide. Such regions with locally strongly increased Nusselt number are prone to thermal material failure and are responsible for mostly over-dimensioned cooling systems for the entire NGV. To find such regions in purely adiabatic simulations, values for turbulent kinetic energy and turbulent timescale can be taken into account.

Until hitting the leading edge turbulence intensity in the flow decays. At  $P40 + 0.5$  ACL the hot spot impinges on the leading edge (annotated as A on Fig. 14), which locally strongly increases levels of TKE (see Fig. 14a), and thereby also heat flux. Low values of TKE on the top right and bottom left corner are due to coolant flow moved by the rotational movement of the fluid. Throughout the NGV passage TKE increases, meaning that despite reduced temperatures due to expansion, the heat load on the NGVs would not be negligible. Higher levels of TKE occur mainly at the boundary of the NGV and at the wake. A large part of the rise in turbulent kinetic energy can be attributed to secondary flow structures, such as vortices, partly triggered by the non-uniformities present at the stator inlet, P40. The increase of TKE is to be avoided, as firstly, it reduces the energy

of the main flow and thereby the useful work done by the fluid in the high-pressure turbine, and secondly it strongly increases the heat flux on the NGV surface, reducing component lifetime and making sophisticated cooling systems necessary.

Large coherent flow structures visualized by the turbulent timescale (see Fig. 14b) using two-point statistical functions, interestingly, highlight different flow features than those observed in the evaluation of high order temperature statistics (see Fig. 12,13). The hot spot, marked by high values of Kurtosis (see A on Fig. 13) is slightly more centered and thereby does not completely coincide with the peak of turbulent timescale identified as B on Fig. 14. Notably, regarding the evolution of large coherent structures through the NGV passage, the central high value peak detaches from the NGV surface as opposed to the hot streak which travels along the NGV surface.

**Thermal load on NGV.** NGV 1, in this configuration directly hit by the hot spot experiences a higher heat load, especially in the leading edge area (marked as A on Fig. 15a). On the suction side, vortices concentrate the hot fluid in the mid-

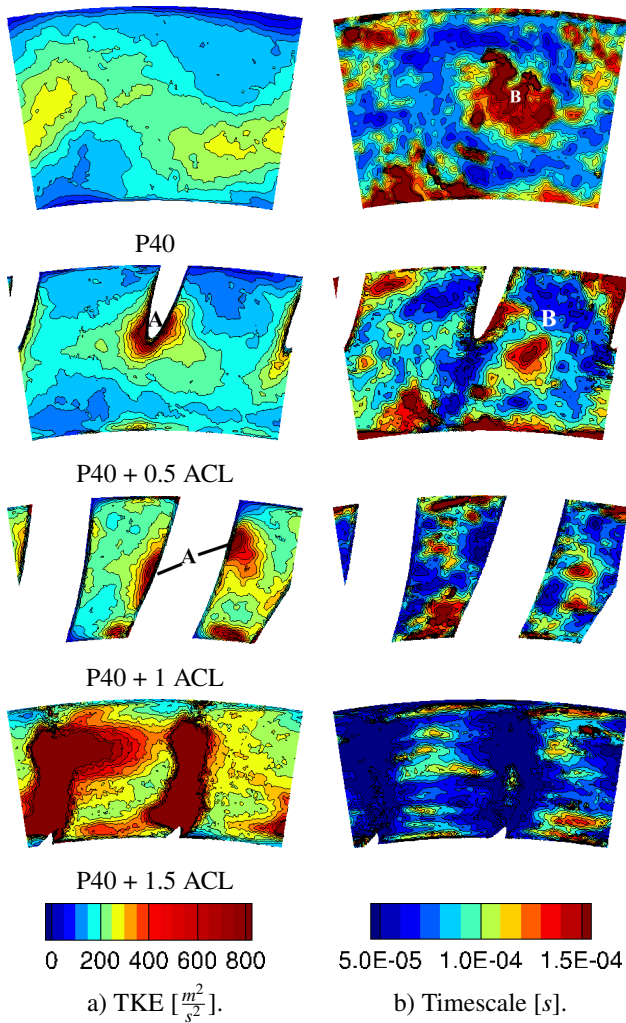


**FIGURE 14:** Evolution of turbulent kinetic energy and timescale on planes at successive axial positions through the NGV passage. View direction is downstream.

dle of the NGV (see B on Fig. 15). Low values of standard deviation coinciding with high mean values reveal that in this region, the NGV is constantly exposed to a harsh thermal environment. High values of standard deviation in the top region of the pressure side show mixing of wall bounded coolant flow and hot main flow due to secondary flow structures. The Skewness plot of the temperature for NGV 1 indicates negative values on a large part of the surface, meaning that in these areas the most probable temperature value is higher than the mean temperature value. A high value of Kurtosis shows where the hot spot mainly impinges on the NGV surface (annotated as C on Fig. 15). Kurtosis and Skewness indicate that the hot fluid mainly travels along suction side.

The pressure side of NGV 2 is also hit by the hot spot, whereas the tip region on the suction side features a cold zone due to coolant flow (identified as D on Fig. 15) migrating along the NGV, because of secondary flow structures and residual swirl on P40 (see Fig. 7b). The standard deviation shows high values near the tip, similar to NGV 1, indicating temperature fluctuations triggered by vortices in the NGV passage. Lower values of standard deviation indicate a continuously high heat load on the lower part of the NGV, where the hot spot impinges. The large slightly positive Skewness region in the upper part reveals a region where the adiabatic surface temperature is likely to be lower than the mean. This flow pattern is caused by coolant flow migrating on the NGV surface. In the hub region on the suction side segregated zones are visible on the Skewness and Kurtosis plot, indicating an area constantly exposed to high levels of temperature. In the hub region of both NGVs, segregated zones are visible in the Skewness and Kurtosis plots. These features are caused by horse-shoe vortices on both NGVs.

## CONCLUSION

LES on an engine representative lean combustion simulator with adjoint stator are performed to investigate the evolution of temperature and turbulence through the passage of the NGVs. A set of instantaneous solutions over a statistically significant time period of multiple flow through times is evaluated using statistical tools such as autocorrelation on the axial velocity component to access turbulent time scales and high statistic moments of the temperature variable to visualize local temperature distributions. Calculating high statistic moments of temperature allows to highlight regions where the most probable temperature value strongly differs from the average temperature, locally imposing higher levels of thermal stress than estimated if only taking mean values into account. Evaluating the axial velocity component using autocorrelation functions allows to find coherent flow structures, not visible in instantaneous or averaged solutions. The statistical methodology presented here can be used to estimate heat load in the context of adiabatic LES simulations. The results presented in this work show strong differences in the thermal load the NGV is exposed to depending on its position relative to the swirler. The NGV directly hit by the hot spot is exposed to higher temperatures, but also higher levels of turbulence, which translates into increased thermal stress. Due to the absence of dilution holes in lean combustion chambers, the hot spot remains mostly undiluted, until impinging on the NGV. Performing integrated LES of a combustor-turbine geometry and calculating high statistical moments of temperature allows to better quantify the heat load the high-pressure turbine is exposed to. With the introduction of LES in the industrial design process, taking the full data of time-resolved LES predictions into account, permits to gather new insights at no additional cost. The impact of the cooling system on wall temperatures and on the flow field will be subject to further dedicated studies.

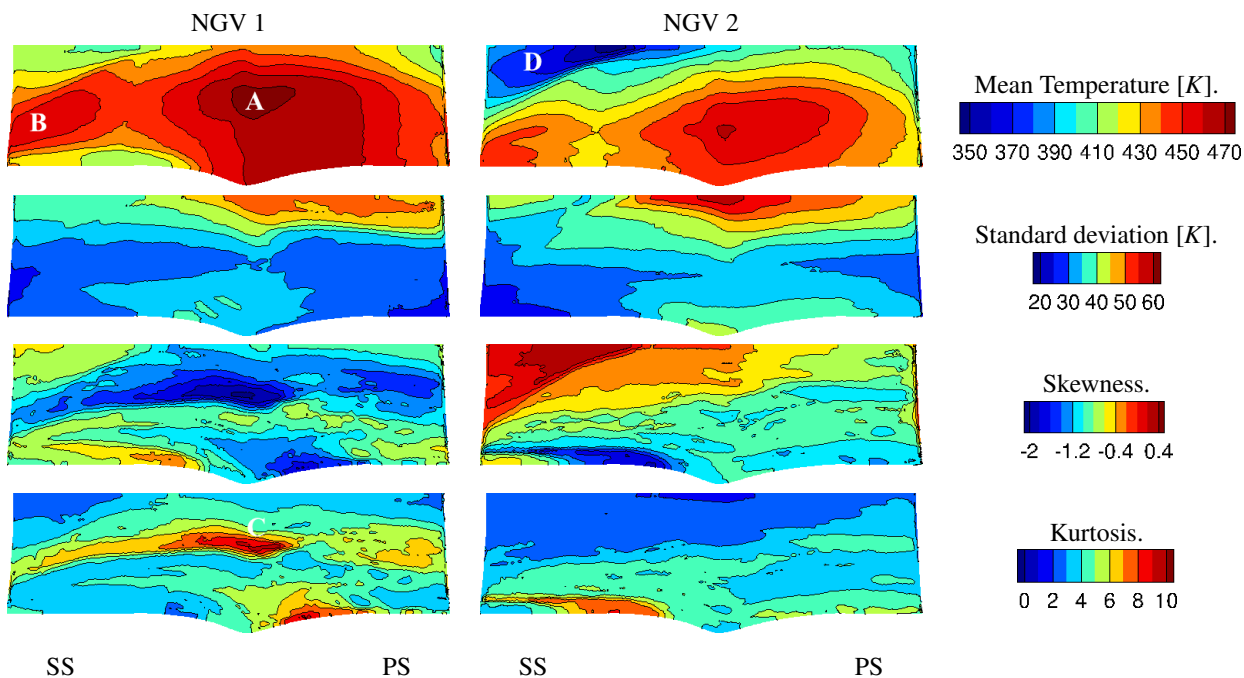


FIGURE 15: Temperature and high order statistical moments on NGV surface.

## ACKNOWLEDGMENT

The authors wish to gratefully acknowledge FACTOR (Full Aerothermal Combustor-Turbine interactions Research) Consortium for the kind permission of publishing the results herein. FACTOR is a Collaborative Project co-funded by the European Commission within the Seventh Framework Programme (2010-2017) under the Grant Agreement n° 265985. This work was granted access to the HPC resources of IDRIS under the allocation 2016 - 2b7525 made by GENCI.

## REFERENCES

- [1] Lefebvre, A. H., and Ballal, D. R., 2015. *Gas Turbine Combustion*, Vol. 1. CRC Press.
- [2] Cha, C. M., Ireland, P. T., Denman, P. A., and Savarianandam, V., 2012. "Turbulence Levels Are High At the Combustor-Turbine Interface". *Proceedings of ASME Turbo Expo 2012*, pp. 1–20.
- [3] Hermanson, K. S., and Thole, K. a., 2000. "Effect of Inlet Conditions on Endwall Secondary Flows". *Journal of Propulsion and Power*, **16**(2), pp. 286–296.
- [4] Povey, T., and Qureshi, I., 2009. "Developments in Hot-Streak Simulators for Turbine Testing". *Journal of Turbomachinery*, **131**(3), p. 31009.
- [5] Bogard, D. G., and Thole, K. A., 2006. "Gas Turbine Film Cooling". *Journal of propulsion and power*, **22**(2), pp. 249–270.
- [6] Schwab, J. R., Stabe, R. G., and Whitney, W. J., 1983. "Analytical and Experimental Study of Flow Through and Axial Turbine Stage with a Nonuniform Inlet Radial Temperature Profile". *19th AIAA/SAE/ASME Joint Propulsion Conference*.
- [7] Dorney, D. J., Gundy-Burlet, K. L., and Sondak, D. L., 1999. "A Survey Of Hot Streak Experiments And Simulations". *International Journal of Turbo and Jet Engines*, **16**(1), pp. 1–16.
- [8] Roux, S., Cazalens, M., and Poinot, T., 2008. "Outlet-Boundary-Condition Influence for Large Eddy Simulation of Combustion Instabilities in Gas Turbines". *Journal of Propulsion and Power*, **24**(3), pp. 541–546.
- [9] Koupper, C., Gicquel, L., and Duchaine, F., 2016. "Large Eddy Simulations of the combustor turbine interface: Study of the potential and clocking effects". *ASME Turbo Expo 2016: Turbomachinery Technical Conference and Exposition. American Society of Mechanical Engineers*.
- [10] Tennekes, H., and Lumley, J. L., 1972. *A first course in turbulence*. MIT press.
- [11] Koupper, C., Gicquel, L., Duchaine, F., Bacci, T., Facchini, B., Picchi, A., Tarchi, L., and Bonneau, G., 2015. "Experimental and Numerical Calculation of Turbulent Timescales at the Exit of an Engine Representative Combustor Simula-

- tor”. *Journal of Engineering for Gas Turbines and Power*, **138**(2), p. 021503.
- [12] Pope, S. B., 2001. *Turbulent Flows*. Cambridge University Press.
- [13] Nix, A., Smith, A., Diller, T., Ng, W., and Thole, K., 2002. “High intensity, large length-scale freestream turbulence generation in a transonic turbine cascade”. In *ASME Turbo Expo 2002: Power for Land, Sea, and Air*, American Society of Mechanical Engineers, pp. 961–968.
- [14] Gomes, R. A., and Niehuis, R., 2011. “Film Cooling Effectiveness Measurements With Periodic Unsteady Inflow on Highly Loaded Blades With Main Flow Separation”. *Journal of Turbomachinery*, **133**(2), p. 021019.
- [15] Koupper, C., 2015. “Unsteady multi-component simulations dedicated to the impact of the combustion chamber on the turbine of aeronautical gas turbines”. *PhD thesis. Universite de Toulouse - MeGeP - Dynamique des Fluides, France*.
- [16] Moureau, V., Lartigue, G., Sommerer, Y., Angelberger, C., Colin, O., and Poinso, T., 2005. “Numerical methods for unsteady compressible multi-component reacting flows on fixed and moving grids”. *Journal of Computational Physics*, **202**(2), pp. 710–736.
- [17] Schmitt, P., Poinso, T., Schuermans, B., and Geigle, K. P., 2007. “Large-eddy simulation and experimental study of heat transfer, nitric oxide emissions and combustion instability in a swirled turbulent high-pressure burner”. *Journal of Fluid Mechanics*, **570**, pp. 17–46.
- [18] Schoenfeld, T., and Rudgyard, M., 1999. “Steady and unsteady flow simulations using the hybrid flow solver AVBP”. *AIAA Journal*, **37**(11), pp. 1378–1385.
- [19] Lax, P., and Wendroff, B., 1960. “Systems of conservation laws”. *Communications on Pure and Applied mathematics*, **13**(2), pp. 217–237.
- [20] Colin, O., and Rudgyard, M., 2000. “Development of high-order taylor-galerkin schemes for LES”. *Journal of Computational Physics*, **162**(2), pp. 338 – 371.
- [21] Lamarque, P. M. N., 2007. “Schémas numériques et conditions limites pour la simulation aux grandes échelles de la combustion diphasique dans les foyers d ’ hélicoptère”. *PhD thesis. Universite de Toulouse - MeGeP - Dynamique des Fluides, France*.
- [22] Colin, O., Benkenida, A., and Angelberger, C., 2003. “3D Modeling of Mixing, Ignition and Combustion Phenomena in Highly Stratified Gasoline Engines”. *Oil & Gas Science and Technology*, **58**(1), pp. 47–62.
- [23] Hirsch, C., 2007. *Numerical computation of internal and external flows: The fundamentals of computational fluid dynamics*. Butterworth-Heinemann.
- [24] Colin, O., 2000. “Large eddy simulation of evaporating sprays in complex geometries using eulerian and lagrangian methods”. *PhD thesis, INSA de Rouen*.
- [25] Smagorinsky, J., 1963. “General circulation experiments with the primitive equations: I. the basic experiment\*”. *Monthly weather review*, **91**(3), pp. 99–164.
- [26] Mendez, S., and Nicoud, F., 2008. “Adiabatic Homogeneous Model for Flow Around a Multi-perforated Plate”. *AIAA Journal*, **46**(10), pp. 2623–2633.
- [27] Poinso, T. J., and Lele, S. K., 1992. “Boundary Conditions for Direct Simulation of Compressible Viscous Flows”. *Journal of Computational Physics*, **101**, pp. 104–129.
- [28] Koupper, C., Poinso, T., Gicquel, L., and Duchaine, F., 2014. “Compatibility of Characteristic Boundary Conditions with Radial Equilibrium in Turbomachinery Simulations”. *AIAA Journal*, **52**(12), pp. 2829–2839.
- [29] Israeli, M., and Orszag, S. A., 1981. “Approximation of Radiation Boundary Conditions”. *Journal of Computational Physics* **41.1**, **20**, pp. 115–135.
- [30] Courant, R., Friedrichs, K., and Lewy, H., 1928. “Über die partiellen differenzgleichungen der mathematischen physik”. *Mathematische annalen*, **100**(1), pp. 32–74.
- [31] Meher-homji Cyrus B., G. G., 1998. “Gas turbine blade failures - causes, avoidance and troubleshooting”. *27th Turbomachinery Symposium*, **2**.

# IMPACT OF REALISTIC INLET CONDITION ON LES PREDICTIONS OF ISOLATED HIGH PRESSURE VANES

*M. Thomas*<sup>1</sup>, *F. Duchaine*<sup>1</sup>, *L. Gicquel*<sup>1</sup> and *C. Koupper*<sup>2</sup>

<sup>1</sup> *CERFACS*

<sup>2</sup> *Safran Helicopter Engines*

[thomas@cerfacs.fr](mailto:thomas@cerfacs.fr)

## Abstract

Next generation lean combustion gas turbine engines feature a harsher aerothermal environment if compared to current state of the art engine technologies. Higher levels of swirl, turbulence and temperature non-uniformities at the exit of the combustion chamber directly impact the high-pressure turbine, which in industrial design practice is usually simulated separately using 1D time averaged profiles as inlet condition for the turbine. The definition of inlet boundary conditions for stand-alone high fidelity stator simulations is however crucial to obtain meaningful Large Eddy Simulation (LES) predictions and 1D time averaged profiles are most likely inappropriate. This work investigates this specific point and compares different approaches. To do so, an integrated simulation of a combustion chamber and its high pressure vanes is performed first and serves as a reference for stand-alone stator vane simulations performed afterwards using inlet boundary conditions retrieved from the first simulation. As shown hereafter use of instantaneous flow fields from the reference simulation allows to a large extent to recover the correct flow field, which is a huge improvement over simulations using 2D constant boundary conditions, with or without synthetic turbulence [1]. Differences between the fully integrated simulation and that using constant boundary conditions are principally due to the lack of mixing and strong persistent vortex structures in the stand-alone high pressure turbine simulation using constant boundary conditions. Changes of secondary flow patterns are also seen to impact the temperature distribution on the nozzle guide vane (NGV) walls.

## Introduction

Recent changes, from conventional rich-quench lean combustor design to NO<sub>x</sub>-reducing lean combustion chambers where the cooling air is diminished to favor the chamber fuel and air premixing process, significantly impact the combustor exit flowfield. Indeed at the exit of the burner and prior to its entrance through the turbine stage, the flow exhibits large hot spots with strong residual swirl which impacts the aerothermal

performance of the device. To investigate such issues and construct reliable CFD tools, the FACTOR<sup>1</sup> EU project gathered multiple European engine manufacturers and research laboratories around two state-of-the-art experiments: a trisector combustor studied at UNIFI [2] and a full annular combustor equipped with its turbine stage located at DLR Göttingen [3]. In this context, advanced Large Eddy Simulations (LES) and associated analyses [4] confirmed the designs and the importance of combustor-turbine interactions in such new engines. Due to these couplings, it was also found that performing an isolated high pressure vane LES remains a challenge [5]. Indeed, the definition of numerical boundary conditions in LES of complex industrial geometries is known to strongly impact the predictions of simulations. In LES, information for all resolved scales of turbulence should be provided at the inlet. However, this information is often not available. Imposing synthetic turbulence at the inlet of the high pressure turbine, as demonstrated by Duchaine et al. [1], is one possibility to obtain more realistic flow predictions. In such geometries, turbulence is however highly complex, which limits the applicability of such approaches. In fact, specific methods are needed to properly take into account the missing interaction present in an integrated LES considering at once the combustor and the turbine stage. The objective of the current investigation is hence twofold: 1/ propose a method that allows stand-alone LES of high pressure vanes on the basis of stand-alone combustor simulations and 2/ complement the proposed strategy with an analysis that identifies the flow features that need to be considered and assess their respective effects on the stand-alone high pressure vane LES predictions.

In the present work and to investigate combustor-turbine interaction phenomena, an integrated LES of a combustion chamber and its high-pressure vanes is performed first to serve as a reference for later comparisons. Thanks to the obtained data an extensive analysis of the flow field at the exit of the chamber

<sup>1</sup>FACTOR (Full Aerothermal Combustor Turbine interactions Research) is a collaborative European research project co-funded by the European Commission within the 7th Framework Programme (2010-2017) under the Grant Agreement no265985 to investigate interactions of lean combustion chambers with the high-pressure turbine.

is conducted using Proper Orthogonal Decomposition (POD) [6]. Links between dominant flow features in the combustion chamber and at the interface plane between combustion chamber and turbine can hence be established. This data is then used to feed multiple isolated high-pressure vane simulations, one with recast instantaneous flow fields and a second with a 2D field of time-averaged data imposed at the inflow. The goal of such isolated LES's is to qualify a methodology to test multiple high-pressure turbine designs using the same data set and thereby to avoid multiple simulations of the combustion chamber for the purpose of turbine design optimization. Clearly, depending on the strategy adopted predictions will differ as discussed hereafter.

In the following, computational domain, setup and numerical parameters are described. The next part is dedicated to the presentation of the flow field in the FACTOR test rig. Finally, simulations using reconstructed or constant boundary conditions are compared with the reference case, focusing first on aerodynamic, then on thermal aspects.

## Geometry and numerical Setup

The axial periodic numerical domain of the FACTOR test rig contains one swirler and two NGVs, representing a  $18^\circ$  section of the full annular non-reactive test rig (see Fig. 1). To avoid early interactions of the swirler generated vortex with neighboring swirlers and the effusion cooling system, the main flow is restrained by a duct. Hot combustion gases are simulated by injecting hot air (531 K, 0.156 kg/s per sector) through the swirler and cold air (300 K, 0.084 kg/s per sector) is injected through multiperforated liners. The swirler is aligned with NGV1, which is impacted by the hot spot. The grid is designed in separate blocks

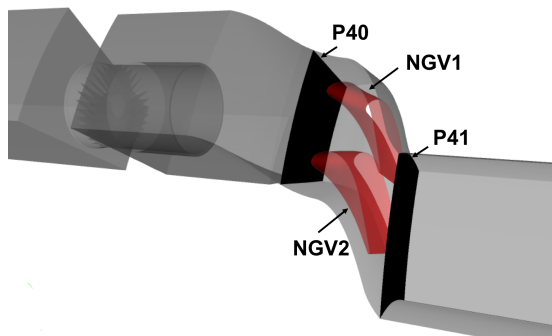


Figure 1: FACTOR Geometry.

to guarantee identical meshes in the stator section for the integrated and the stand-alone simulation. In total, the grid contains about 70 million elements, of which about 35 million are used to discretize the stator vanes. Prism layers are used around the NGV to guarantee low  $y^+$  values approaching 10, whereas the rest of the domain is discretized by tetrahedral cells. Simulations

presented in this work are performed using AVBP [7], a code developed at CERFACS and IFPEN to solve the filtered compressible Navier-Stokes equations for LES. The reference simulation is first converged using the Lax-Wendroff scheme [8], then a more accurate finite element two-step time-explicit Taylor Galerkin scheme (TTG4A), fourth order accurate in time and third order in space, is used for the discretization of convective terms [9]. This scheme ensures low diffusion and dispersion properties [10] and is therefore adequate for high fidelity simulations. Diffusive terms are discretized using a vertex centered formulation close to the Galerkin finite element method [11]. Sub grid scale (SGS) turbulent contributions are computed using the WALE model [12], which was developed specifically for interior flows to recover correct near wall behaviour. Using the classical gradient diffusion hypothesis [13] the SGS heat flux is related to the filtered temperature gradient with a SGS thermal conductivity computed with a SGS turbulent Prandtl number of 0.6. Time marching is done, respecting CFL [14] (convection scheme) and Fourier [15] (diffusion scheme) numbers to guarantee linear stability.

For the integrated simulation, mass flow ( $\rho_{in}$ ,  $\rho_{out}$ ,  $\rho_{wall}$ ) and temperature are defined at the 2D-inlet plane, coolant air is homogeneously injected [16] at the liners of the combustion chamber and the exit is defined as a pressure outlet. For the isolated stator vane simulation, mass flow and temperature are imposed at each inlet node, changing every 500 iterations ( $= 2e-5$  s), corresponding to an acquisition frequency of 50 kHz, to follow the stored instantaneous flow fields obtained from the reference computation (see Fig. 2). The inlet data is stored for all nodes and instants in different tables for each variable that are read at the initialization of the stand-alone simulations. The approach uses existing Navier-Stokes characteristic boundary conditions with a high relaxation parameter value to ensure that imposed values are attained, i.e. partly reflective boundary conditions.

During the simulation of the integrated domain, instantaneous solutions are stored on P40, the intersection plane of combustion chamber and high-pressure turbine, at a frequency of 50 kHz over a period of 40 ms, yielding a data set of 2000 solutions. The acquisition frequency is sufficiently high to capture all important flow features and constitutes a good compromise between amount of data and accuracy. Combustion chamber simulations take 100 ms to 200 ms to converge and usually provide enough data to converge the simulation in the stator. Isolated stator vane simulations are started using an instantaneous solution of the integrated simulation.

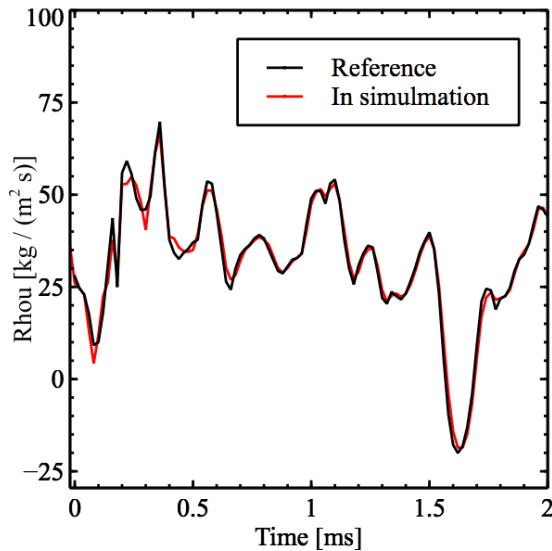


Figure 2: RhoU on one inlet node of the stand-alone stator domain over the first 2 ms of the simulation.

## Results and Discussion

First, some general flow features of this next generation lean combustion chamber are introduced and the flow field obtained in the reference simulation is validated with experimental data. Following, differences between the stand-alone stator simulations are discussed, first with a focus on aerodynamics, then on thermal aspects.

### Flow field in the combustion chamber

Due to the absence of dilution holes and the presence of a confining duct in the FACTOR geometry, the hot streak remains largely undiluted by the coolant air, which mostly travels along the liners. The flow field features a central re-circulation zone, caused by the break down of the fuel injection system flow generating a Processing Vortex Core (PVC) (see Fig. 3), which is clearly identified by the first POD mode as the most energetic structure in the flow field. At the exit of the combustion chamber (plane P40) high levels of turbulence (Turbulence intensity up to 20 %), residual swirl and temperature non-uniformities can be observed. Certain flow features in the stator domain appear at the PVC frequency and can thereby be linked directly to the PVC in the chamber.

On P40, turbulent kinetic energy shows a wavy pattern caused by the residual swirl motion (see Fig. 4a). Turbulent timescales calculated from auto correlation of the axial velocity component are highly non-uniform on P40 (see Fig. 4b) [17]. LES predictions show good qualitative agreement with experimental data calculated from hot wire anemometry measurements in isothermal conditions [17]. In the center re-

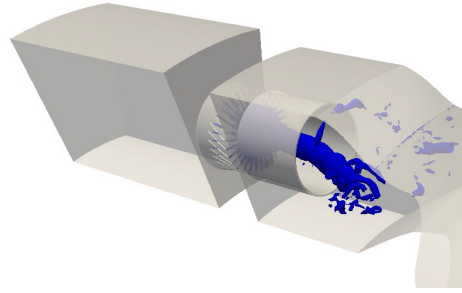


Figure 3: PVC visualized as isosurface of pressure. The PVC is created by the swirled flow and breaks down shortly after leaving restraining duct.

gion (hot spot) and close to the liners (coolant flow) larger turbulent timescales can be observed. The non-uniformity of turbulent timescales on P40 evidences a highly complicated and in-homogeneous flow field that cannot adequately be reproduced by constant boundary conditions or by injection of synthetic turbulence. Large turbulent timescales indicate coherent flow structures, in this case, coinciding with the hot spot and impacting the flow field further downstream in the high-pressure vane passage. Further discussion and experimental validation of FACTOR can be found in [2, 18].

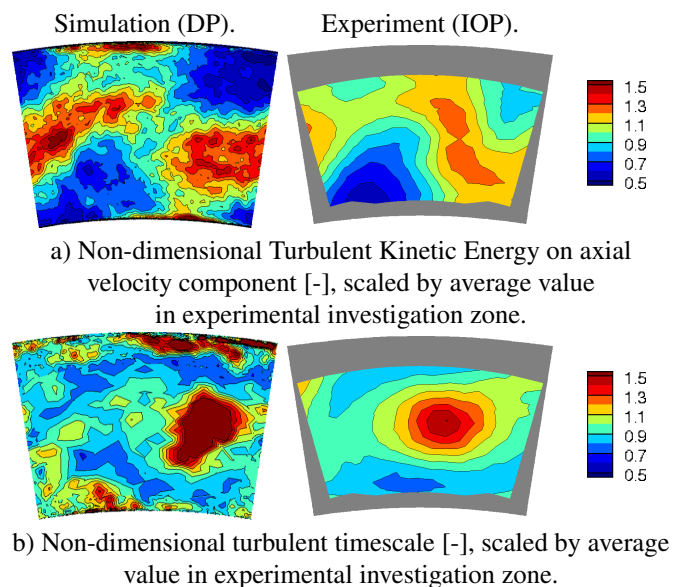


Figure 4: Non-dimensionalized flow field on P40. Comparison of design point simulation and isothermal operating point measurements. Values are non-dimensionalized by the average value in the experimental investigation zone. View direction: Downstream.

### Impact of inlet boundary conditions on the flow field in the stator

Imposing unsteady inlet conditions for the isolated stator vane simulation using previously stored in-

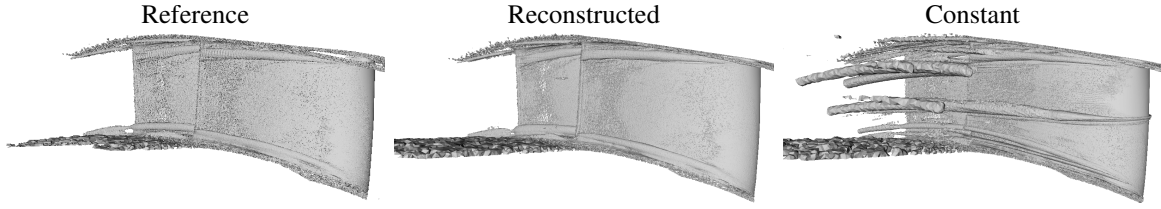


Figure 5: Q-criterion isosurface ( $1e+8$ ) on averaged solutions visualizes vortex structures (NGV1 in foreground).

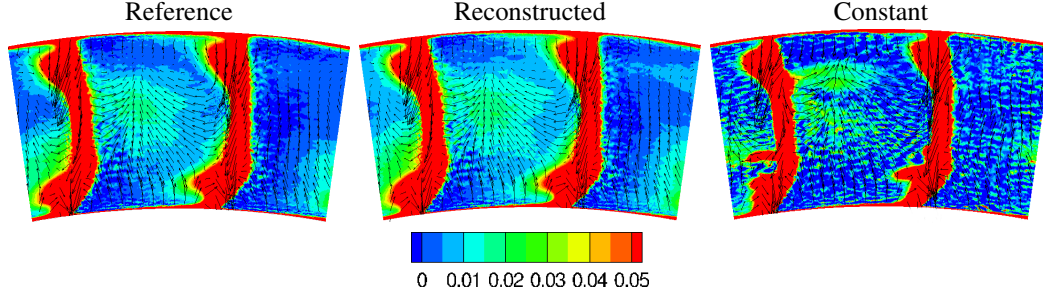


Figure 6: Pressure loss coefficient ( $p_{loss} = \frac{P_{tot,P40} - P_{tot,P41}}{P_{stat,P41}}$ ) with vector arrows of secondary flow on stator exit plane.

stantaneous solutions, allows to a large extent to recover the flow field of the reference simulation in the vanes. Contrarily, the isolated NGV simulation using constant 2D boundary condition predicts a different aerothermal environment, mainly due to more persistent secondary flow structures visualized by the Q-criterion [19] (see Fig. 5). In the simulation using constant inlet boundary conditions, a horseshoe vortex forms at mid height leading edge of the NGV hit by the hot spot. In other simulations the flow field is more disturbed, so that strong vortices triggered by certain events in the chamber only appear intermittently and are thereby not visible in the averaged solution.

Secondary flow structures impact the losses through the high-pressure vanes and the velocity field on the exit plane (plane P41). On Fig. 6, the NGV wake and the near wall zone are clearly identified as zones of high pressure loss ( $p_{loss} = \frac{P_{tot,P40} - P_{tot,P41}}{P_{stat,P41}}$ ). The hot spot traveling through the mid passage is visible with a locally increased pressure loss. In the same passage, arrows visualizing secondary flow structures evidence a counter-rotating vortex pair close to the upper liner. The reference simulation and that using the reconstructed inlet conditions are very similar, whereas some differences are visible when using constant boundary conditions. Pressure loss in the mid passage is concentrated to smaller regions. Close to the hub, the NGV wake loss zone of the constant inlet simulation reaches further into the flow than it does in both other cases, which is caused by a persistent vortex on the suction side of NGV1 (see also Fig. 5).

After analysis of losses on the exit plane the focus now lies on frequency spectra. A dynamic mode decomposition of instantaneous pressure fields at the stator exit allows to analyze the frequency spectrum in the flow field (see Fig.7). Using the reconstructed in-

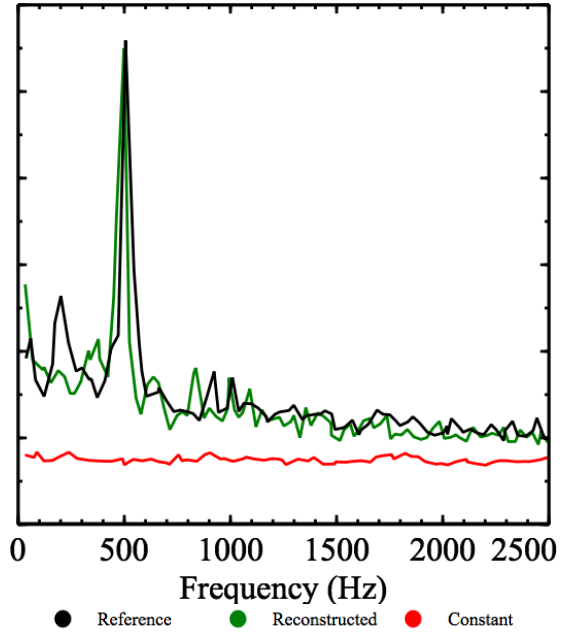


Figure 7: DMD frequency spectrum of pressure on stator exit plane.

let boundary condition, a peak can be found at 500 Hz, which corresponds to the PVC frequency in the chamber and demonstrates the ability of the presented approach to conserve the dynamics present in the combustion chamber in a stand-alone vane LES. In contrast, the frequency spectrum at the stator exit of the simulation using constant inlet boundary conditions only contains noise. The marked peak at the PVC frequency confirms the importance of this feature on the entire flow field.

After discussion of aerodynamic aspects, the focus of the following part is the impact on the tempera-

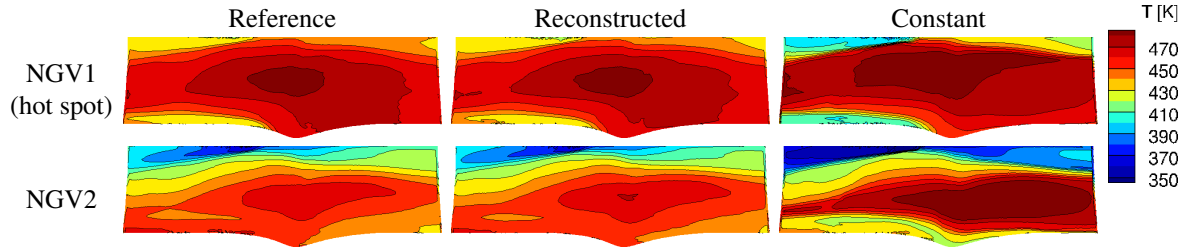


Figure 8: Time-averaged temperature on unwrapped NGV surface.

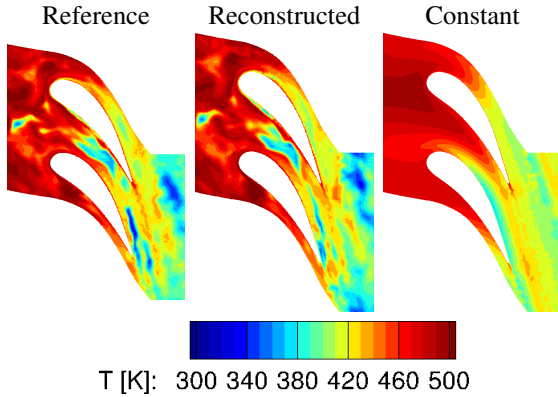


Figure 9: Instantaneous temperature plot on  $H/h=0.5$  iso-surface 35 ms after start of isolated simulation. NGV1: upper, NGV2: lower.

ture field. Visualizations of instantaneous temperature fields at mid-height through the stator show a great similarity between reference and reconstructed simulations at the same time instant (see Fig. 9). The simulation using constant boundary conditions however shows a very smooth temperature distribution due to the lack of activity at the inlet inducing less mixing.

Radial profiles of temperature mean, maximum and minimum values give an insight on the temperature field in the middle of the stator passage, one axial chord length (4 cm) downstream of P40 (see Fig. 10). Mean values of reference simulation and isolated stator simulation with reconstructed inlet conditions show a good correspondence. The simulation using constant boundary conditions shows higher mean values at mid-height of the channel and lower values close to the liners. Except for the liner regions, maximum values of the same simulation are close to the mean value, which shows that cold air rarely reaches the center region. These findings indicate a very peaked temperature distribution in the central part of the channel. A low level of mixing for the constant boundary condition simulation is further evidenced by a small variation between maximum and minimum values of the radially averaged profile as compared to the other simulations.

The different thermal environment and flow dynamics presented before impact temperature distributions on the NGV surface. Stronger vortices in the

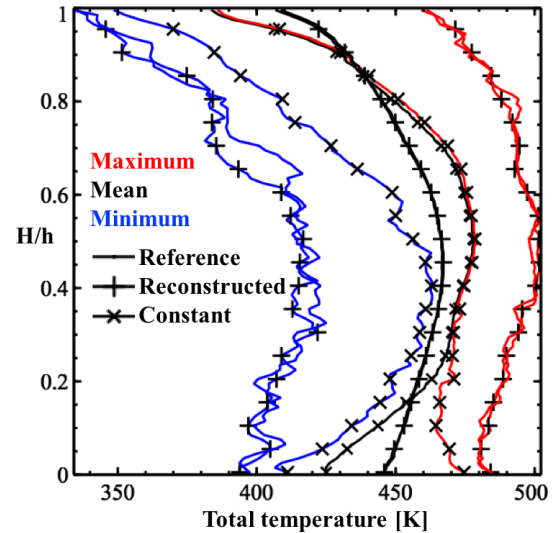


Figure 10: Temperature profiles midway through the stator domain ( $P40 + 1$  Axial chord length).

constant inlet simulation (see Fig. 5) are indeed seen to transport coolant flow away from the liners across the NGV (see Fig. 8). As a result of the missing unsteady inlet information, less mixing of the hot flow in the center with the coolant flow close to the liners leads to wrong overall temperature patterns and more extreme temperature predictions on the surface of the NGVs as compared to the reference simulation (see Fig. 8). Close to the liners, the constant boundary condition simulation underpredicts the temperature by up to 20 K with respect to the reference simulation, whereas at channel mid-height, where the hot spot impinges on the blade, temperature values are overpredicted by 15 K as compared to the integrated simulation. Cold and hot zones on the NGV surface created due to the absence of sufficient activity at the inlet are well visible on the NGV wall temperature distribution plots (see Fig. 11). For the constant inlet case, several marked peaks of temperature distribution on the NGV surface point to the lack of mixing of hot and cold flow through the turbine passage. Imposing an unsteady flow field at the inlet allows to recover the temperature pattern of the reference simulation on the NGV surface. Shape and magnitude of the NGV temperature distributions of the reconstructed inlet bound-

any case and the reference case are indeed very similar confirming the need for the proper specification of the inflow of such geometries.

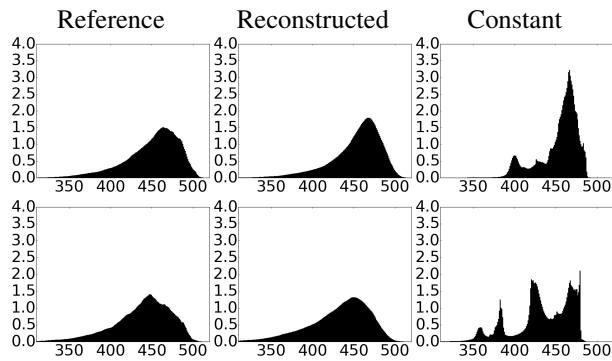


Figure 11: Temperature distribution (percentage of occurrence) on NGV for all surface points on solutions stored every  $2e-5s$ . (NGV1: upper row, NGV2: lower row).

## Conclusions and Outlook

LES of an integrated lean combustion chamber with its high-pressure vanes has been performed and compared to isolated high-pressure vanes simulations to evaluate the effect of imposing different inlet conditions. When imposing the fully unsteady flow field obtained from the integrated simulation, the flow field in the stator can be recovered to a large extent. Imposing 2D constant inlet boundary conditions, has a strong impact on the flow field. Mixing is considerably reduced and persistent vortex structures are created that strongly alter the temperature distribution on the vanes. Temperature predictions on the NGV surface are more extreme than in the reference simulation. Flow dynamics is in such cases not adequately reproduced if imposing constant inlet conditions. The herein presented methodology based on the information gathered from a combustor LES allows to test multiple different turbine designs by feeding isolated high-fidelity simulations with realistic inlet conditions.

## Acknowledgments

The authors wish to gratefully acknowledge FACTOR (Full Aerothermal Combustor-Turbine interactions Research) Consortium for the kind permission of publishing the results herein. FACTOR is a Collaborative Project co-funded by the European Commission within the Seventh Framework Programme (2010- 2017) under the Grant Agreement n° 265985. This work was granted access to the HPC resources of IDRIS under the allocation 2016 - 2b7525 made by GENCI.

## References

[1] F. Duchaine, J. Dombard, L. Y.M. Gicquel, and C. Koupper. On the importance of inlet boundary conditions for aerother-

mal predictions of turbine stages with large eddy simulation. *Computers and Fluids*, 154:60–73, 2017.

- [2] Antonio Andreini, Tommaso Bacci, Massimiliano Insinna, Lorenzo Mazzei, and Simone Salvadori. Modelling strategies for the prediction of hot streak generation in lean burn aeroengine combustors. *Aerospace Science and Technology*, (May), 2018.
- [3] Charlie Koupper, Gianluca Caciolli, Laurent Gicquel, Florent Duchaine, Guillaume Bonneau, Lorenzo Tarchi, and Bruno Facchini. Development of an Engine Representative Combustor Simulator Dedicated to Hot Streak Generation. *Journal of Turbomachinery*, 136(11):111007, 2014.
- [4] Charlie Koupper, Guillaume Bonneau, Laurent Gicquel, and Florent Duchaine. Large eddy simulations of the combustor turbine interface: Study of the potential and clocking effects. In *ASME Turbo Expo 2016: Turbomachinery Technical Conference and Exposition*, 2016.
- [5] Gaofeng Wang, Dimitrios Papadogiannis, Florent Duchaine, Nicolas Gourdain, and Laurent Y M Gicquel. Towards Massively Parallel Large Eddy Simulation of Turbine. pages 1–14, 2013.
- [6] Anindya Chatterjee. An introduction to the proper orthogonal decomposition. *Current science*, pages 808–817, 2000.
- [7] Thilo Schoenfeld and Michael Rudgyard. Steady and unsteady flow simulations using the hybrid flow solver AVBP. *AIAA Journal*, 37(11):1378–1385, 1999.
- [8] Peter Lax and Burton Wendroff. Systems of conservation laws. *Communications on Pure and Applied mathematics*, 13(2):217–237, 1960.
- [9] Olivier Colin and Michael Rudgyard. Development of high-order taylor-galerkin schemes for les. *Journal of Computational Physics*, 162(2):338 – 371, 2000.
- [10] Nicolas Lamarque. Schémas numériques et conditions limites pour la simulation aux grandes échelles de la combustion diphasique dans les foyers d ’ hélicoptère. *PhD thesis. Université de Toulouse - MeGeP - Dynamique des Fluides*, 2007.
- [11] O Colin, A Benkenida, and C Angelberger. 3D Modeling of Mixing , Ignition and Combustion Phenomena in Highly Stratified Gasoline Engines. *Oil I& Gas Science and Technology*, 58(1):47–62, 2003.
- [12] F. Ducros, F. Nicoud, and T. Poinso. Wall-adapting local eddy-viscosity models for simulations in complex geometries. *Conference on Numerical Methods in Fluid Dynamics*, pages 1–7, 1998.
- [13] Stephen B Pope. *Turbulent Flows*. Cambridge University Press, 2001.
- [14] Richard Courant, Kurt Friedrichs, and Hans Lewy. Über die partiellen Differenzgleichungen der mathematischen Physik. *Mathematische annalen*, 100(1):32–74, 1928.
- [15] C Hirsch. *Numerical Computation of Internal and External Flows*. Butterworth-Heinemann, 2007.
- [16] S. Mendez and F. Nicoud. Adiabatic Homogeneous Model for Flow Around a Multiperforated Plate. *AIAA Journal*, 46(10):2623–2633, 2008.
- [17] Charlie Koupper, Laurent Gicquel, Florent Duchaine, Tommaso Bacci, Bruno Facchini, Alessio Picchi, Lorenzo Tarchi, and Guillaume Bonneau. Experimental and Numerical Calculation of Turbulent Timescales at the Exit of an Engine Representative Combustor Simulator. *Journal of Engineering for Gas Turbines and Power*, 138(2):021503, 2015.
- [18] Martin Thomas, Laurent Gicquel, and Charlie Koupper. Comparison of heterogeneous and homogeneous coolant injection models for Large Eddy Simulation of multiperforated liners present in a combustion simulator. *ASME Turbo Expo 2017: Turbomachinery Technical Conference and Exposition*, 2017.
- [19] Jinhee Jeong and Fazle Hussain. On the identification of a vortex. *Journal of Fluid Mechanics*, 285(-1):69, 1995.

**GT2019-91206**

**LARGE EDDY SIMULATION OF COMBUSTOR AND COMPLETE SINGLE-STAGE  
HIGH-PRESSURE TURBINE OF THE FACTOR TEST RIG**

**Martin Thomas\***  
**Jerome Dombard**  
**Florent Duchaine**  
**Laurent Gicquel**  
CERFACS

42 Avenue Gaspard Coriolis  
31100 Toulouse, France  
Email: thomas@cerfacs.fr

**Charlie Koupper**

Safran Helicopter Engines  
64511 Bordes, France

**ABSTRACT**

*Development goals for next generation aircraft engines are mainly determined by the need to reduce fuel consumption and environmental impact. To reduce  $NO_x$  emissions lean combustion technologies will be applied in future development projects. The more compact design and the absence of dilution holes in this type of engines shortens residence times in the combustion chamber and reduces mixing which results in higher levels of swirl, turbulence and temperature distortions at the exit of the combustion chamber. For these engines interactions between components are more important, so that the traditional engine design approach of component-wise optimization will have to be adapted. To study new lean burn architectures the European FACTOR project investigates the transport of hot streaks produced by a non-reactive combustor simulator through a single stage high-pressure turbine. In this work high-fidelity Large Eddy Simulation (LES) of combustor and complete high-pressure turbine are discussed and validated against experimental data. Measurement data is available on P40 (exit of the combustion chamber), P41 (exit of the stator) and P42 (exit of the rotor) and generally shows a good agreement to LES data.*

**KEYWORDS**

LES, Combustor-turbine interaction, turbomachinery, FACTOR

**Nomenclature**

CFD	Computational Fluid Dynamics
CFL	Courant-Friedrichs-Lewis condition
DLR	Deutsches Luft- und Raumfahrtzentrum
FACTOR	Full Aerothermal Combuster Turbine interactiOns Research
LES	Large Eddy Simulation
MISCOG	Multi Instance Solvers Coupled via Overlapping Grids
NGV	Nozzle Guide Vane
NO	Nitrogen Oxide
P40	Exit plane of the Combustion Chamber
P41	Exit plane of the stator
P42	Exit plane of the rotor
PVC	Processing Vortex Core
RANS	Reynolds Averaged Navier-Stokes
RPM	Rotation per Minute
SGS	Sub-Grid Scale

---

\*Address all correspondence to this author.

## INTRODUCTION

Over the last decades, the performance of aircraft engines has been improved significantly by increasing the combustion temperatures and the efficiency of individual components. New technological developments in future aircraft engines are mainly driven by the requirement to diminish fuel consumption in order to reduce environmental impact and operating cost. Development of new engines today is due to inherited organization structures commonly done by groups of different design teams focussing on the optimization of individual engine components. This partly neglects interaction phenomena between engine components and leads to the application of high safety margins. For the next generation of aircraft engines one of the main design targets is the reduction of  $\text{NO}_x$  emissions [1]. This will lead to the application of lean premixed combustion technologies, that will allow for a more compact engine design. The compact design as well as the absence of dilution holes entails a harsher aerothermal environment at the exit of the combustion chamber as compared to current state of the art Rich Quench lean technologies. Increased levels of swirl, turbulence, temperature non-uniformities at the exit of the combustion chamber adversely alter secondary flow patterns in the high-pressure turbine, leading to higher aerodynamic losses [2–4]. Hot streaks produced by the discrete positioning of the fuel injection system are less extensively mixed when traveling through the combustion chamber and directly impact on the high-pressure turbine at the exit of the chamber. Because of issues induced by the increasing burnt gas temperature, Combustor / turbine interactions have been very early on identified and investigated. In the 80s, first experimental research facilities were established at the NASA Lewis research center to investigate the impact of hot streaks on the high-pressure turbine [5]. Dorney et al. [6] (1999) gave a review of experimental and computational studies on the migration of hot streaks. Povey and Qureshi (2009) [4] summarized developments and research on combustor simulators dedicated to the investigation of the impact of inlet temperature distortions on the high-pressure turbine. Most of past research focuses on Rich Quench Lean architectures which possess an inherently different flow field than future lean partially premixed combustors. To develop this new type of engines, manufacturers will have to address interaction phenomena between individual components.

Gas turbine engines feature complex geometries and the interior flow field is governed by a multitude of different physical phenomena, which renders accurate predictions of the flow field a very challenging task. Accurate measurements of the flow at nominal operating conditions are often difficult, which makes CFD a primary choice to gain insight in the flow field. The European FACTOR<sup>1</sup> project, which is the basis for the herein

presented research, addresses the issue of combustor-turbine interactions and the transport of hot spots in the next generation lean combustion chambers using a joint CFD and experimental approach on a full annular non-reactive test rig [7]. The objective is to gain a better understanding of interaction phenomena in next generation compact design lean combustion engines and to improve CFD predictions. One particular numerical challenge for the simulation of multi-component turbomachinery devices is the coupling of rotating and stationary domain and also the presence of different flow regimes in combustion chamber (low Mach number) and turbine (high Mach number). Only few CFD codes are available to simulate both domains simultaneously and with great accuracy. In this work, Large-Eddy Simulation (LES) predictions of combustion chamber and complete single-stage high-pressure turbine are compared with experimental results to gain insight into the interaction phenomena present between combustion chamber, stator and rotor. Experimental data obtained by means of a five-hole probe (velocity angles, static & total pressure, static & total temperature) is available on observation planes P40 (exit of the combustion chamber), P41 (exit of the stator) and P42 (exit of the rotor). The results presented herein extend on previous work published at the ETC conference [8].

First, the test rig is introduced, followed by the presentation of the numerical approach. The result section presents predictions of an integrated LES with combustion chamber and complete single-stage high-pressure turbine. The section is divided in three parts: 1. Combustion chamber, 2. High-pressure vanes, 3. Rotor.

## EXPERIMENTAL SETUP

The FACTOR test rig installed on the NG-turb test facility at DLR Göttingen is designed as a full annular non-reactive full scale closed loop wind tunnel. The non-reactive rig allows continuous operation over several hours to ensure high quality measurements. 20 identical 18° sectors, equipped with one swirler, two NGVs, three rotor blades and one strut airfoil (not simulated here) form a full annular engine representative test rig. Air heated to 513 K enters the combustion chamber through a swirler which is restrained by a duct to avoid early interaction with the effusion cooling system and neighboring swirlers. Coolant air is injected through multiperforated liners in the combustor simulator, the NGV blades and purge flows between the rotating and stationary parts. In the leading edge clocking configuration, presented in this work, the swirler is aligned with the leading edge of NGV2 (see Fig. 1). The rotor turns at a speed of 7700 rpm. The FACTOR rig allows instrumentation access at different positions in the rig as detailed in [9]. Measurements on P40, P41 and P42, shown hereafter, have been obtained by a 5-hole probe mounted on a traverse system that covers about 95 % of the channel height. Further measurements are available from pressure taps on two NGV blades at mid height of the channel.

<sup>1</sup>FACTOR (Full Aerothermal Combustor Turbine interactiOns Research) is a European research project co-funded by the European Commission within the 7th Framework Programme (2010-2017) under the Grant Agreement no265985 to investigate interactions of lean combustion chambers with the hp-turbine.

## NUMERICAL SETUP, MESH and DOMAIN

In the numerical approach one  $18^\circ$  section is simulated (see Fig. 1). Inlets are defined as mass flow inlets and the outlet boundary condition is defined as a pressure outlet. Values at the main inlet are imposed using Navier-Stokes characteristic boundary conditions [12] and the pressure imposed at the outlet allows to naturally establish a radially equilibrium pressure profile [13]. Effusion cooling systems at interior and exterior liner are modeled using a heterogeneous coolant injection model [10]. The same model is applied on the NGVs to mimic the injection of coolant fluid using a coolant distribution obtained from previous Reynolds averaged Navier Stokes (RANS) simulations of the isolated stator domain with fully featured NGV-cooling system [11]. Purge flows are included in the domain and allow for the injection of cold air at the intersection of stationary and turning parts. Walls are considered adiabatic and the near-wall behavior is modelled using wall functions based on a log law [22]. Operating conditions are summarized in Tab. 1.

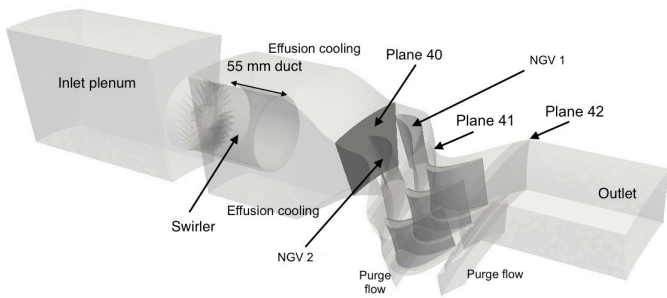


FIGURE 1: Numerical FACTOR domain from [14].

Grids for static and rotating domain are generated separately as partly overlapping fully unstructured tetrahedral grids. The overset of both grids allows by application of the MISCOG method [15] the coupling of both computational domains. The simulation of stationary and turning part is performed using two separate instances of the AVBP code coupled by OpenPALM [16]. The static domain is discretized by 70 Mio cells and has been designed in accordance with a previous mesh refinement study for the FACTOR geometry [17]. The rotor domain with fully meshed purge flows contains 35 Mio grid cells.

Simulations presented in this work are performed using AVBP by [18], a code developed at CERFACS and IFPEN to solve the filtered compressible Navier-Stokes equations for LES. The simulation is converged for 150 ms, corresponding to 15 characteristic through flow times of the combustor module, using the Lax-Wendroff scheme [19]. Data collected for comparison extends over 40 ms. Sub-grid scale (SGS) turbulent contributions are computed using the Smagorinsky model [20].

TABLE 1: Nominal operating conditions and inlets for one sector of the full annular FACTOR test rig at DLR Göttingen.

P40 (static = total)	[kPa]	143
Outlet static pressure	[kPa]	53.7
Pressure ratio (total-to-static)		2.7
Swirler mass flow	[kg/s]	0.1545
Effusion cooling interior liner	[kg/s]	0.0335
Effusion cooling exterior liner	[kg/s]	0.0475
Rotor front cavity purge flow	[kg/s]	0.0036
Rotor back cavity purge flow	[kg/s]	0.0036
NGV coolant feed mass flow	[kg/s]	0.018
Swirler air temperature	[K]	513
Coolant temperature (all nominal feeds)	[K]	300
Turbine rotor RPM	[rpm]	7700

Using the classical gradient diffusion hypothesis [21] the SGS heat flux is related to the filtered temperature gradient with a SGS thermal conductivity computed with a SGS turbulent Prandtl number of 0.6. Time marching is done, respecting CFL number [23] (convection scheme) and Fourier number [24] (diffusion scheme) to guarantee linear stability. For the purpose of statistical evaluations, the time step is fixed to  $4.E-8$  s ( $CFL \approx 0.9$ ) during the data collection period. The computational cost for convergence of the simulation is estimated at 1 Mio CPU hours.

## RESULTS

In this section, LES predictions for the fully integrated LES of combustion chamber and complete single-stage high-pressure turbine are discussed and validated against experimental data obtained at the FACTOR test rig at DLR Göttingen. First, the flow field in the combustor module, then the flow in the stator domain and at last the flow field in the rotor part, is discussed. All observation planes (P40, P41, P42) are in the stationary domain. Note that average values and profiles presented in this section are not weighted by the mass flow, but by surface area. The simulation is still converging and the operating point is not yet entirely matched (see Tab. 2).

P40	Experiment	Simulation
Total temperature [K]	447.52	441.02
Total pressure [kPa]	142.35	147.38
Mass flow [kg/s]	0.2355	0.2374
<hr/>		
P41		
Total temperature [K]	427.67	427.60
Total pressure [kPa]	139.78	141.30
Mass flow [kg/s]	0.2535	0.2552
<hr/>		
P42		
Total temperature [K]	353.15	342.10
Total pressure [kPa]	62.30	61.36
Mass flow [kg/s]	0.2607	0.2625

**TABLE 2:** Comparison of 0D-values for experiment and simulation interpolated on experimental investigation window.

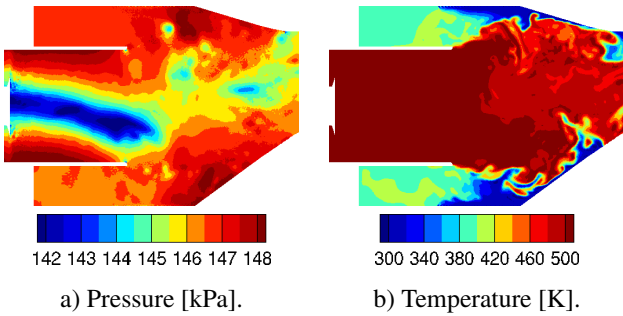


**FIGURE 2:** Central axial cross section cuts of the instantaneous flow field through the swirler from swirler to P40.

### Flow field in the combustor simulator

The main flow enters the combustor simulator through a swirler which creates a Processing Vortex Core (PVC), visible as a low pressure zone in Fig. 2a. Kelvin-Helmholtz instabilities at the duct edges are visible as low pressure zones and the injection of coolant is seen to locally increase the static pressure level near the liners. Coolant injected at the combustion chamber liners penetrates into the flow and locally mixes with hot air coming from the swirler (see Fig. 2b). Due to the presence of a confining duct and the absence of dilution holes in the FACTOR combustion chamber, the hot streak traveling through the chamber remains largely undiluted by the coolant air. Shortly after the exit of the duct, the flow field features a central re-circulation zone, evidenced by negative axial velocity (see Fig. 3a). This

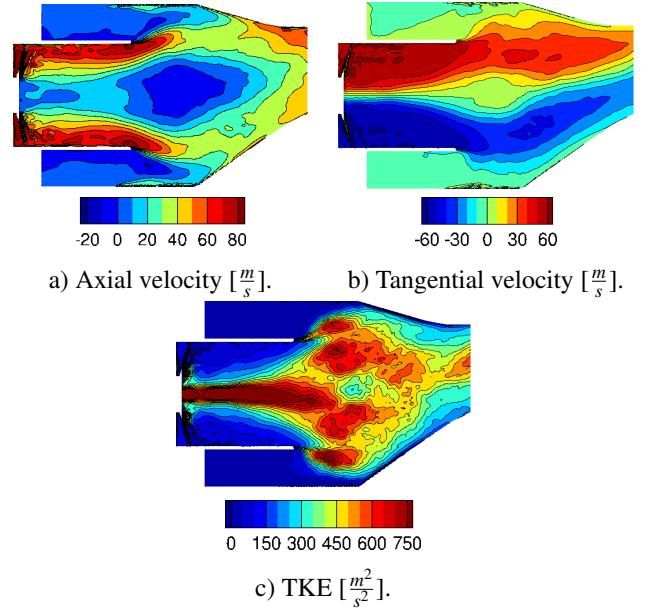


**FIGURE 3:** Central axial cross section cuts of the averaged flow field through the swirler from swirler to P40.

recirculation is caused by the break down of the fuel injection system generated PVC. High levels of tangential velocity (see Fig. 3b) induced by the swirler can be found throughout the domain and contribute to a complex flow field on P40 as well as to a redistribution of coolant flow (to be discussed later). In the center of the duct, as well as at the edges of the duct in the shear layer high levels of turbulent kinetic energy (TKE) can be observed (see Fig. 3c). In the center of the duct, high activity is created by the PVC, whereas at the edges the shear between the stagnant flow outside the duct and the high velocity flow inside the duct is responsible for the high levels of TKE. The flow field in the FACTOR combustion chamber is dominated by the PVC (see Fig. 4) and excitation at PVC frequency can be found in the entire computational domain.

On P40, experimental data and predictions from high fidelity LES show an acceptable agreement for velocity angles and temperature (see Fig. 5a,b,d). The flow angles (see Fig. 5a,b) indicate strong residual swirl at the exit of the combustion chamber which is due to the absence of dilution holes and the compact design of the non-reactive lean combustion demonstrator. Note that on all observation planes the pitch angle shows the strongest deviation from simulations which may point to a systematic error in the measurements. Non-dimensional data shows a good qualitative correspondence for total pressure (see Fig. 5c). The residual swirl core is visible as a low total pressure region on P40. In the experiment differences between minimum and maximum pressure values are more pronounced than in the simulation. This

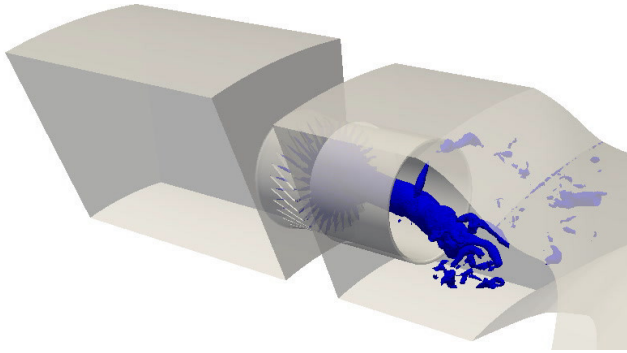


**FIGURE 4:** PVC visualized as isosurface of pressure for an instantaneous solution. The PVC is created by the swirled flow and breaks down shortly after leaving restraining duct.

finding together with elevated velocity angles in the experiment may point to a better conserved PVC in the experiment than in the simulation. Residual swirl impacts the temperature distribution by transporting coolant flow away from the liners to the center of the channel which creates a wavy pattern in the temperature distribution on P40 (see Fig. 5d). The temperature profile on P40 agrees well, except for the hub region, and shows a very pronounced hot spot at channel mid height, typical for lean combustion configurations. Downstream of P40, the marked hot streak impinges on NGV2.

Previous studies and validation of simulations extending over combustion chamber or combustion chamber and high-pressure vanes are similar to the flow field obtained from the fully integrated simulation of combustor and complete single-stage high-pressure turbine [25,26]. These studies underline the importance and impact of an unsteady chamber flow field on the flow in the high-pressure turbine domain [27,28].

### Flow field in the high-pressure vane passage

The activity in the chamber strongly impacts the flow in the high-pressure turbine [28] (see Fig. 6). Coherent flow structures, mainly created by the PVC, travel through the chamber and impact the NGVs. Horseshoe-vortices with a short lifespan are created at blade mid height and shortly afterwards transported away by new flow packages arriving from the chamber. Corner vortices created close to hub and shroud are more persistent. In the NGV passage secondary flow structures are seen to impact the temperature distribution on the NGV surface by transporting cold air away from the liners over the NGV surface and by influencing the trajectory of coolant jets.

Isentropic Mach numbers calculated using the average total pressure on P40 and pressure taps at around mid height of the channel ( $h/H \approx 0.5$ ) agree well with experimental results (see Fig. 7). Note that the pressure taps are placed on two different NGVs and the pressure for the simulation is obtained accord-

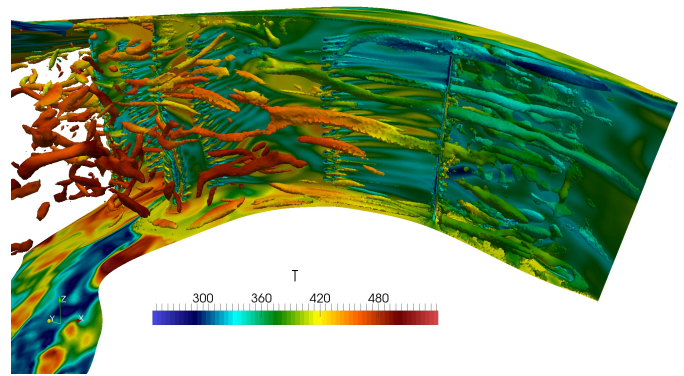


**FIGURE 6:** NGVs and q-criterion [29] of an instantaneous solution colored by static temperature.

ingly. Differences in the operating point result in higher Mach numbers in the simulation. Although  $Mach=1$  is reached, the passage is not entirely choked. Fig. 8a shows the acceleration of the flow in the nozzle and the formation of a shock at the NGV trailing edge. The spike in the isentropic Mach number plot (see Fig. 7) is due to the shock hitting the next NGVs suction side. The hot spot is clearly centered on NGV2 (see Fig. 8b) and the coolant injected on the NGV surface is seen to stay close to the NGVs.

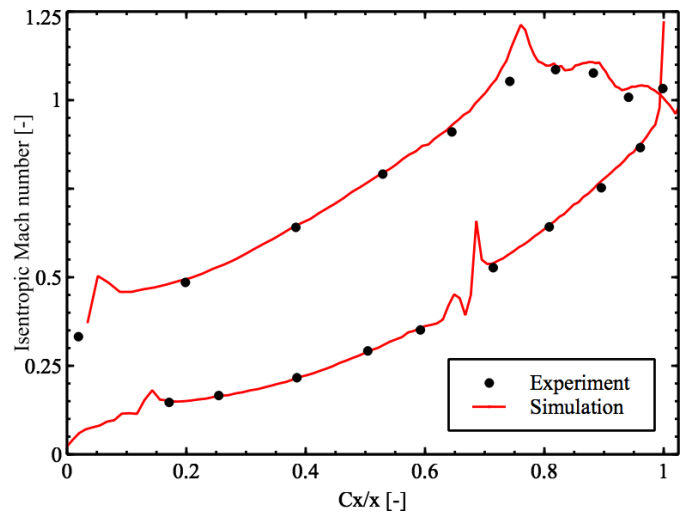


**FIGURE 7:** Isentropic mach number on NGV surface at mid height of the channel.

Velocity angles on P41 show an acceptable agreement with experimental data (see Fig. 9a,b). The pitch profile deviates most in the shroud area, whereas the swirl profile is off in the hub

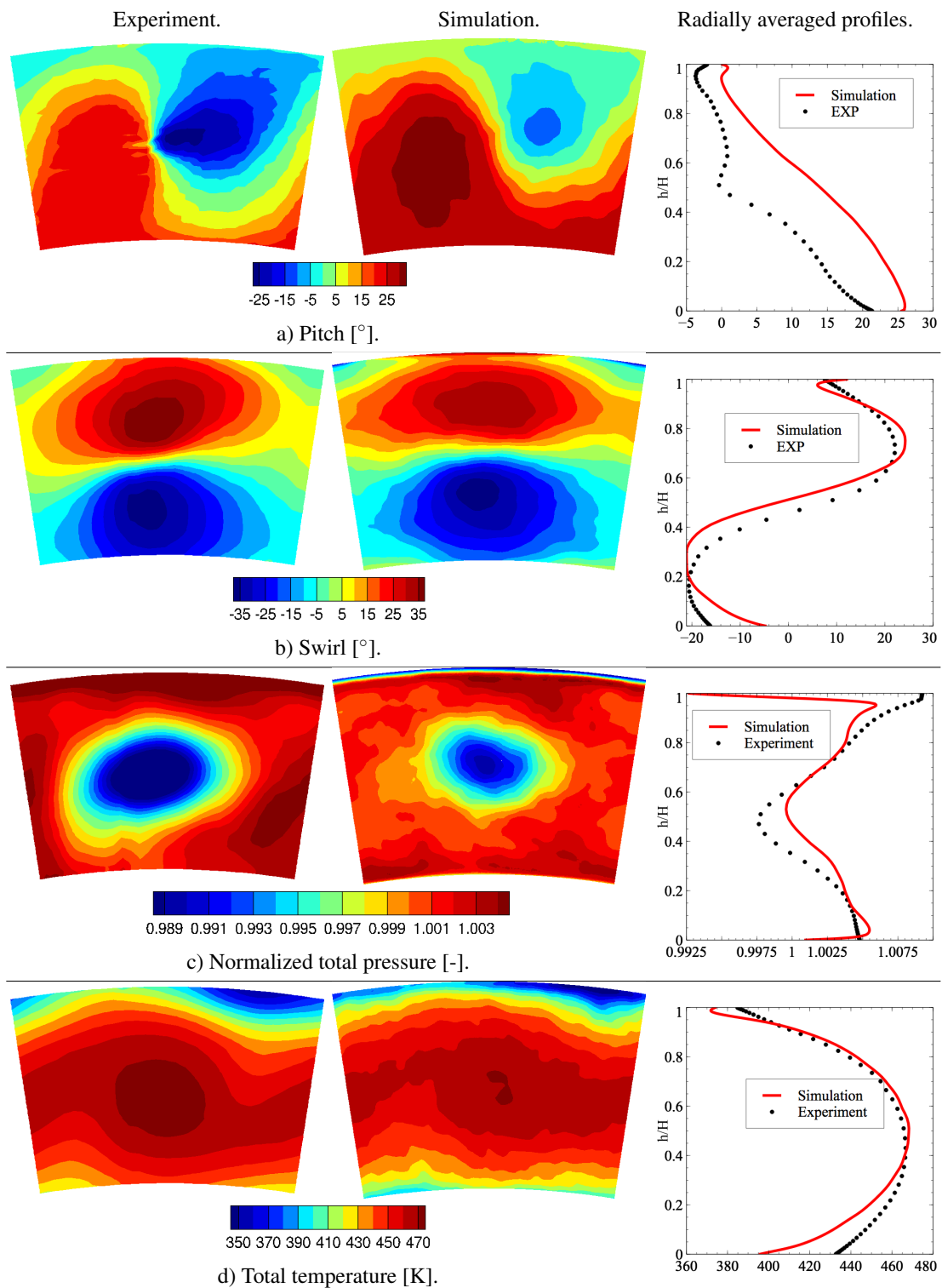


**FIGURE 5:** Flow field on P40 for simulation and experiment. View direction: downstream.

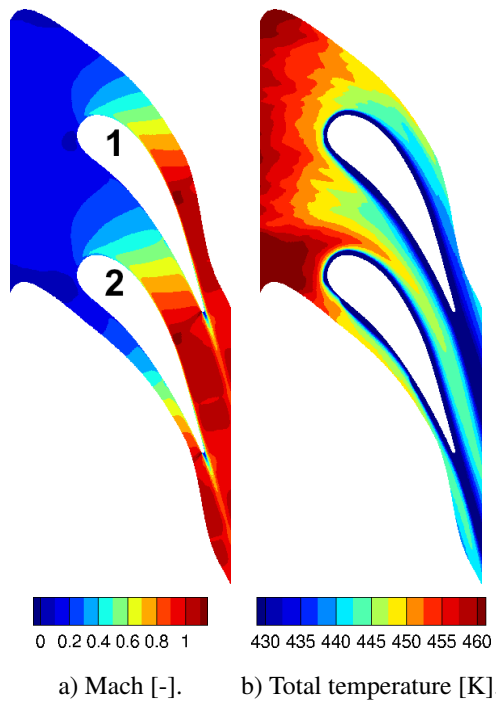


**FIGURE 8:** Average flow field at channel mid height in the high-pressure vane passage.

region. Elsewhere the velocity angles show a good correspondence to experimental data. Wakes of the NGVs are visible as low total pressure areas on P41 (see Fig. 9c). Whereas wake positions show a reasonably good agreement, the pressure difference between wake region and channel is more pronounced in the simulation. The total temperature plot shows that the hot spot migrates mostly through one passage (see Fig. 9d), whereas an important part of the coolant fluid injected by the effusion cooling system of the exterior liner migrates through the upper half of the second passage. The redistribution of coolant fluid is provoked by the residual swirl present in the entire compact design chamber and already visible on P40 (see Fig. 5d). In the simulation, the NGV coolant system consisting of 342 coolant injection holes is not resolved, but coolant is directly injected through discrete surface patches on the NGV surface. A previous study [11] shows that this may lead to underpredicted mixing between coolant flow and main flow which explains colder NGV wakes in the simulation. In the shroud area the total temperature profile of the simulation agrees well with the experiment, whereas over the rest of the channel, total temperature values are higher.

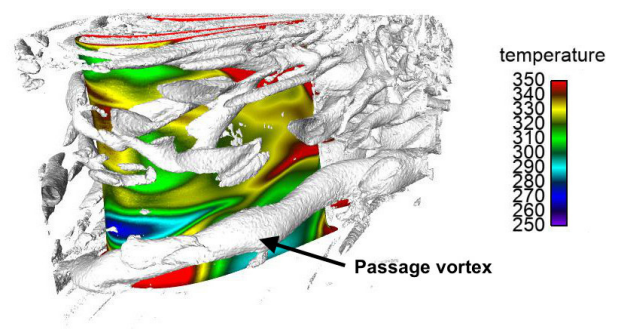


**FIGURE 10:** Vortex structures in rotor domain visualized by iso-surface of  $q$ -criterion [29] and blade surface temperature [K] for one instantaneous solution. View on suction side of rotor 1.

### Flow field in the rotor

The flow field in the rotating domain is highly unsteady (see Fig. 10). In the blade passage dominant vortex structures originating from tip and hub of the rotor blade impact the flow in the passage and have visible effects on P42 (to be discussed later). The rotor blade pressure side is generally exposed to higher temperatures than the blade's suction side. LES predictions on plane P42, situated after the exit of the rotor, show a good agreement to experimental results (see Fig. 11). The agreement is a major improvement as compared to results from RANS/URANS simulations [30] that are very limited in their capacity to correctly predict instationary behavior that strongly influences the flow field in the high-pressure turbine. Effects of the rotor are azimuthally averaged and 2D plots (see Fig. 11) show a pattern of two similar structures that is created by the two NGV blades. Flow angles in the simulation only deviate by a few degrees from the experiment (see Fig. 11a,b). In the tip region differences are more important which may be due to the small tip clearance that is expensive to resolve. Tip vortices, created in this region are sensitive to small changes in the flow field and may thereby behave different in the simulation. Passage and tip vortices induce losses that are visible in the swirl profile (see Fig. 11b) and also as lower total pressure values close to upper and lower liner (see Fig. 11c). The total pressure distribution is very close to experimental data. Whereas aerodynamics show few variance in radial direction, temperature distribution is more irregular (see Fig. 11d). This can be attributed to the redistribution of coolant flow due to high levels of swirl in the chamber, already observed on planes P40 and P41. In the hub region the total temperature profile corresponds better than in the shroud region which can again be attributed to the impact of secondary flow structures originating from the tip of the rotor blades. In the simulation, which covers a larger radial extent than the experiment, cool air injected at the seals of the rotor is seen to migrate along the inner liner.

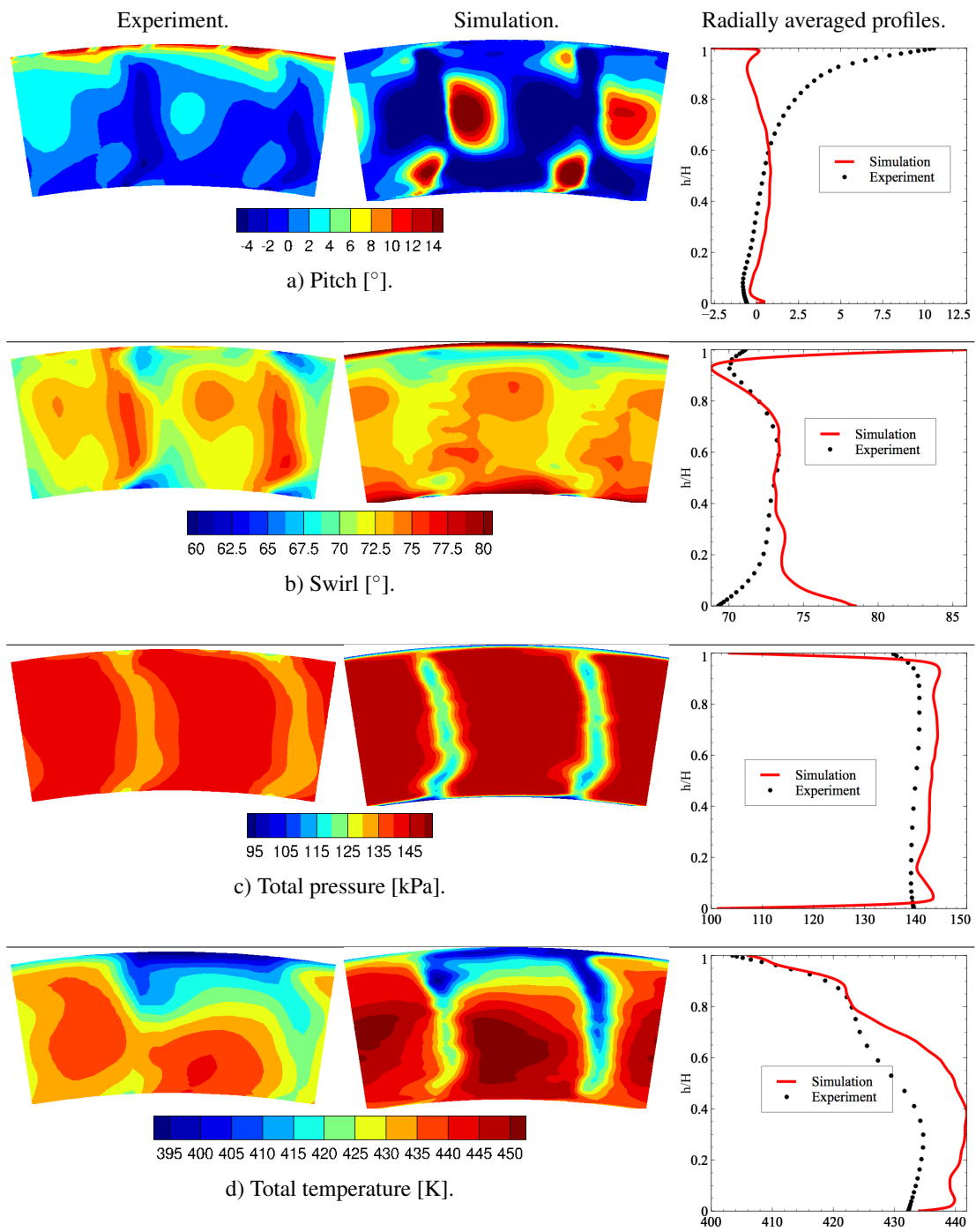


**FIGURE 9:** Flow field on P41 for simulation and experiment. View direction: downstream.

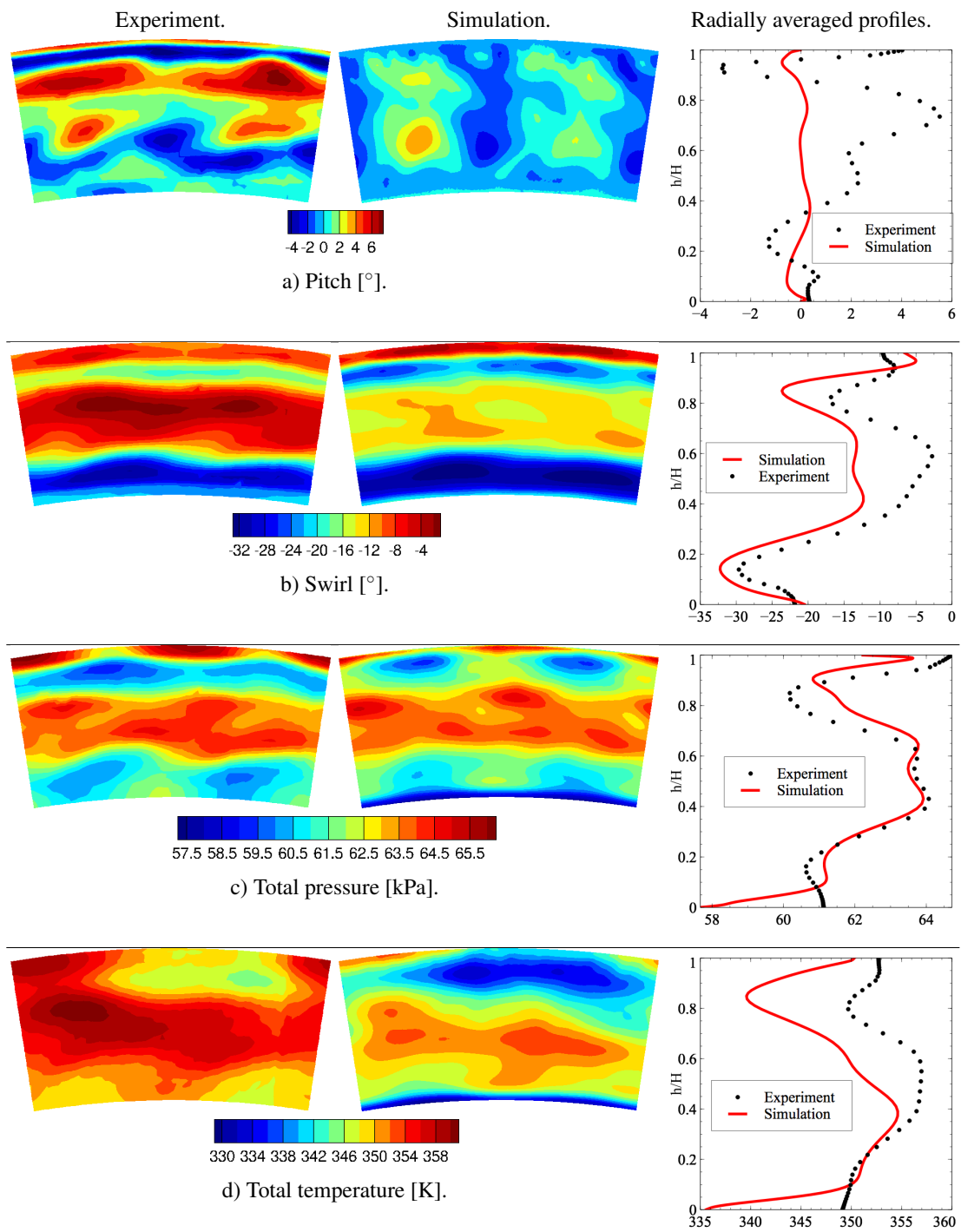


FIGURE 11: Flow field on P42 for simulation and experiment. View direction: downstream.

## CONCLUSIONS

First results from a high fidelity LES of the FACTOR combustion chamber and complete single-stage high-pressure turbine are presented and compared to experimental data on different observation planes (P40, P41, P42) as well as to pressure measurements on the NGV surface. In general there is a good agreement between simulation and experiment. Flow field predictions in the high-pressure turbine show a great improvement over RANS simulations, that only models the unsteady behavior of the flow field. Certain differences observed in the simulation on P41 may be contributed to the NGV coolant injection model, that leads to less mixing between main flow and coolant than a fully resolved coolant system. The simulation may be further improved by application of higher order numerical schemes and further convergence.

## ACKNOWLEDGEMENTS

The authors wish to gratefully acknowledge FACTOR (Full Aerothermal Combustor-Turbine interactions Research) Consortium for the kind permission of publishing the results herein. FACTOR is a Collaborative Project co-funded by the European Commission within the Seventh Framework Programme (2010 - 2017) under the Grant Agreement n° 265985. This work was granted access to the HPC resources of IDRIS under the allocation 2018 - A0032B10157 made by GENCI.

## REFERENCES

- [1] Varatharajan, B., Balan, C., and Bowman, M. J., 2010. "Systems and methods of reducing nox emissions in gas turbine systems and internal combustion engines". *US Patent 7,650,744*.
- [2] Cha, C. M., Ireland, P. T., Denman, P. A., and Savarianandam, V., 2012. "Turbulence Levels Are High At the Combustor-Turbine Interface". *Proceedings of ASME Turbo Expo 2012*, pp. 1–20.
- [3] Hermanson, K. S., and Thole, K. a., 2000. "Effect of Inlet Conditions on Endwall Secondary Flows". *Journal of Propulsion and Power*, **16**(2), pp. 286–296.
- [4] Povey, T., and Qureshi, I., 2009. "Developments in Hot-Streak Simulators for Turbine Testing". *Journal of Turbomachinery*, **131**(3), p. 31009.
- [5] Schwab, J. R., Stabe, R. G., and Whitney, W. J., 1983. "Analytical and Experimental Study of Flow Through and Axial Turbine Stage with a Nonuniform Inlet Radial Temperature Profile". *19th AIAA/SAE/ASME Joint Propulsion Conference*.
- [6] Dorney, D. J., Gundy-Burlet, K. L., and Sondak, D. L., 1999. "A Survey Of Hot Streak Experiments And Simulations". *International Journal of Turbo and Jet Engines*, **16**(1), pp. 1–16.
- [7] Battisti, C., Kost, F., Atkins, N., Playford, W., Orain, M., Cacioli, G., Tarchi, L., Mersinligil, M., and Raffel, J., 2012. "Full aerothermal combustor turbine interaction research". *Proceedings of 2nd EASN WORKSHOP on Flight Physics*.
- [8] Thomas, M., Dombard, J., Duchaine, F., Gicquel, L., and Kopper, C., 2019. "Large-eddy simulation of combustor-turbine interactions of a lean burn gas turbine engine model". *Proceedings of 13th European Conference on Turbomachinery Fluid Dynamics & Thermodynamics ETC13*.
- [9] Krumme, A., Tegler, M., and S., G., 2019. "Design, integration and operation of a rotating combustor-turbine-interaction test rig within the scope of ec fp7 project factor". *Proceedings of 13th European Conference on Turbomachinery Fluid Dynamics & Thermodynamics ETC13*, pp. 1–13.
- [10] Lahbib, D., 2015. "Modelisation aerodynamique et thermique des multiperforations en LES". *Ph.D. Thesis, Université de Montpellier*.
- [11] Harnieh, M., Thomas, M., Bizzari, R., Gicquel, L., and Duchaine, F., 2018. "Assessment of a coolant injection model on cooled high-pressure vanes in large eddy simulation". *12th International ERCOFTAC Symposium on Engineering Turbulence Modelling and Measurements*.
- [12] Poinot, T. J., and Lele, S. K., 1992. "Boundary Conditions for Direct Simulation of Compressible Viscous Flows". *Journal of Computational Physics*, **101**, pp. 104–129.
- [13] Koupper, C., Poinot, T., Gicquel, L., and Duchaine, F., 2014. "Compatibility of Characteristic Boundary Conditions with Radial Equilibrium in Turbomachinery Simulations". *AIAA Journal*, **52**(12), pp. 2829–2839.
- [14] Duchaine, F., Dombard, J., Gicquel, L., and Koupper, C., 2017. "Integrated large eddy simulation of combustor and turbine interactions: Effect of turbine stage inlet condition". *Proceedings of the ASME Turbo Expo*, **2B-2017**, pp. 1–12.
- [15] Wang, G., Duchaine, F., Papadogiannis, D., Duran, I., Moreau, S., and Gicquel, L. Y. M., 2014. "An overset grid method for large eddy simulation of turbomachinery stages". *Journal of Computational Physics*, **274**, pp. 333–355.
- [16] Piacentini, A., Morel, T., Thévenin, A., and Duchaine, F., 2011. "O-palm: An open source dynamic parallel coupler". In *Proceedings of the IV International Conference on Computational Methods for Coupled Problems in Science and Engineering—Coupled Problems*.
- [17] Koupper, C., 2015. "Unsteady multi-component simulations dedicated to the impact of the combustion chamber on the turbine of aeronautical gas turbines". *Institut National Polytechnique de Toulouse (INP Toulouse)*.
- [18] Schoenfeld, T., and Rudgyard, M., 1999. "Steady and unsteady flow simulations using the hybrid flow solver

- AVBP". *AIAA Journal*, **37**(11), pp. 1378–1385.
- [19] Lax, P., and Wendroff, B., 1960. "Systems of conservation laws". *Communications on Pure and Applied mathematics*, **13**(2), pp. 217–237.
- [20] Smagorinsky, J., 1963. "General circulation experiments with the primitive equations: I. the basic experiment". *Monthly weather review*, **91**(3), pp. 99–164.
- [21] Pope, S. B., 2001. *Turbulent Flows*. Cambridge University Press.
- [22] Jaegle, F., Cabrit, O., Mendez, S., and Poinso, T., 2010. "Implementation methods of wall functions in cell-vertex numerical solvers". *Flow, Turbulence and Combustion*, **85**(2), pp. 245–272.
- [23] Courant, R., Friedrichs, K., and Lewy, H., 1928. "Über die partiellen Differenzgleichungen der mathematischen Physik". *Mathematische annalen*, **100**(1), pp. 32–74.
- [24] Hirsch, C., 2007. *Numerical Computation of Internal and External Flows*. Butterworth-Heinemann.
- [25] Thomas, M., Gicquel, L., and Koupper, C., 2017. "Comparison of heterogeneous and homogeneous coolant injection models for Large Eddy Simulation of multiperforated liners present in a combustion simulator". *ASME Turbo Expo 2017: Turbomachinery Technical Conference and Exposition*.
- [26] Koupper, C., Bonneau, G., Gicquel, L., and Duchaine, F., 2016. "Large eddy simulations of the combustor turbine interface: Study of the potential and clocking effects". In *ASME Turbo Expo 2016: Turbomachinery Technical Conference and Exposition*.
- [27] Duchaine, F., Dombard, J., Gicquel, L. Y., and Koupper, C., 2017. "On the importance of inlet boundary conditions for aerothermal predictions of turbine stages with large eddy simulation". *Computers and Fluids*, **154**, pp. 60–73.
- [28] Thomas, M., Duchaine, F., Gicquel, L., and Koupper, C., 2018. "Impact of realistic inlet condition on the predictions of isolated high pressure vanes". In *12th International ERCOFTAC Symposium on Engineering Turbulence Modelling and Measurements*.
- [29] Jeong, J., and Hussain, F., 1995. "On the identification of a vortex". *Journal of Fluid Mechanics*, **285**(-1), p. 69.
- [30] Cottier, F., Pinchaud, P., and Dumas, G., 2019. "Aerothermal predictions of combustor / turbine interactions using advanced turbulence modeling".

GT2019-91215

## DRAFT: ANALYSIS OF SAND PARTICLE INGESTION AND EROSION IN A TURBOMACHINE USING LARGE-EDDY SIMULATION

Benjamin Martin\*, Martin Thomas, Jérôme Dombard, Florent Duchaine, Laurent Gicquel  
CFD Team CERFACS  
Toulouse, France  
bmartin@cerfacs.fr

### ABSTRACT

*Erosion of compressor and turbine blades operating in extreme environment fouled with sand particles is a serious problem for gas turbine manufacturers and users. Indeed, operation of a gas turbine engine in such hostile conditions leads to drastic degradation of the aerodynamic performance of the components, mostly through surface roughness modification, tip clearance height increase or blunting of blade leading edges. To evaluate associated risks, the computation of particle trajectories and impacts through multiple turbomachinery stages by Computational Fluid Dynamics (CFD) seems a decent path but remains a challenge. The numerical prediction of complex turbulent flows in compressors and turbines is however necessary in such a context and validations are still required. Recently, Large-Eddy Simulation (LES) has shown promising results for compressor and turbine configurations for a wide range of operating conditions at an acceptable cost. With this in mind, this article presents the assessment of a LES solver able to treat turbomachine configurations to predict erosion induced by sand particles. To do so, the governing equations of particle dynamics are introduced using the Lagrangian formalism and are solved to compute locations and conditions of impact, namely particle velocity, angle and radius. The fully unsteady and coupled strategy is applied to blade geometries for studying the main areas and conditions of impacts obtained with LES. For comparison, a one-way coupling computation based on a mean steady flow field where only the Lagrangian particles are advanced in time is performed to evaluate the gain and drawbacks of both methods.*

### NOMENCLATURE

#### Acronyms

AVBP	LES solver developed by CERFACS and IFP-En
CFD	Computational Fluid Dynamics
CFL	Courant-Friedrichs-Lewy condition
FACTOR	Full Aerothermal Combuster Turbine interactions Research
LES	Large-Eddy Simulation
NGV	Nozzle Guide Vane
PVC	Processing Vortex Core
NSCBC	Navier-Stokes Characteristic Boundary Condition
RANS	Reynolds-Averaged Navier-Stokes
SGS	Sub-Grid Scale

#### Symbols

i	Direction	T	Temperature
x	Coordinates	$\rho$	Density
t	Time	$\tau$	Relaxation time
u	Velocity	m	Mass
v	Relative velocity between particle and surrounding fluid	d	Diameter
		g	Gravity

#### Subscripts

x	Axial	p	Particle quantity
r	Radial	RMS	Root mean square
t	Tangential		

\*Address all correspondence to this author.

## INTRODUCTION

When operating in desert areas, ingestion of sand particles by aircraft and helicopter engines is inevitable. This however comes with multiple detrimental effects for the different components of the engines. In particular, rotating parts suffer from drastic degradation of performance and significant drop of lifetime after operations in such hostile environments. Indeed, the abrasive impacts of sand particle can cause substantial erosion near the blade leading edges, tips and on pressure sides of compressor blades [1]. In the past, multiple aircraft engine failures leading to serious accidents have been linked to ingestion of high concentration of sand particles or volcanic ash clouds [2–4].

To quantify the effects of erosion on performance, experiments remain very expensive as they require the setup of a complete compressor or turbine stage. Experimental investigations also only provide limited information on the phenomenon. Numerical simulation of particle trajectories within these conditions of impact throughout a turbomachine is an attractive alternative which remains rarely used today.

To simulate erosion with numerical tools, modeling is required. Multiple authors attempted to develop models to quantify the degradation caused by sand particles using theoretical analysis [5] or taking into account different mechanism of sand erosion [6, 7]. The most successful model for erosion prediction for turbomachinery was elaborated by Grant and Tabakoff [8]. In this case, the model shows the influence of velocity and angle of impact, particle size and concentration as well as the physical properties of particles and impacted surfaces. For an accurate prediction of wall erosion, these parameters have to be obtained precisely from numerical simulations. The objective of this paper is twofold. First, it aims at demonstrating the ability of a high fidelity Large-Eddy Simulation (LES) solver with a Lagrangian framework for particle tracking to provide useful quantities to predict erosion on a turbine's high pressure vane. Then, based on the reference simulation, the sensitivity of particle impacts on walls to inlet velocity conditions as well as to carrier flow is investigated. To do so, two inlet conditions are considered: a stationary inlet where velocities are constant in time during the simulation and an unsteady inlet with injected velocities obtained from an integrated LES of combustion chamber and high pressure vanes. To analyse the effect of the flow prediction on particle impacts, the two-way coupling simulations with steady and unsteady inlet are compared to one-way coupling computations. In these latter, the mean steady flow fields obtained by time-averaged simulations are used to advance in time the Lagrangian particles. These one-way coupling simulations can be seen as a RANS simulation.

The paper is organized as follows. First the high pressure vane configuration used in the study is described along with the numerical setup. Then, the LES solver is presented along with the metrics used to characterize the particle impact on walls. The reference two-way coupling simulations with unsteady and

steady inlet conditions are then presented, followed by a discussion on sensitivities of particle impact to flow conditions at inlet and in the passage.

## SIMULATED CONFIGURATION

The studied configuration is the high pressure turbine vane of the FACTOR test rig <sup>1</sup>. Dedicated to investigate interactions of lean combustion chambers with the high-pressure turbines, the FACTOR project has generated a large database around two state-of-the-art experiments: a trisector combustor studied at UNIFI [9] and a full annular combustor equipped with its turbine stage located at DLR Gottingen [10]. The configuration is CFD-friendly as it features an annular periodicity of 18 degrees with one combustor, 2 vanes and 3 rotor blades. Many simulations of the combustor simulator as well as of the turbine stage have been performed and compared to experimental data [11–16]. In this context, intensive efforts have been made to simulate with LES the combustion chamber either isolated or within integrated computations along with the turbine [17, 18]. These high fidelity results provide relevant data in the chamber, turbine stage as well as at their interface. It has been shown by these studies that the flow field features a central re-circulation zone in the combustion chamber, caused by the break down of the fuel injection system flow generating a Processing Vortex Core (PVC, Fig. 1). The vanes are specifically positioned so that the hot streak exiting the swirler impacts the leading edge of vane 1. At the exit of the combustion chamber high levels of turbulence (Turbulence intensity up to 20%), residual swirl and temperature non-uniformities are observed (Fig. 2). Certain flow features in the vane passage appear at the PVC frequency and can thereby be linked directly to the PVC in the chamber [18]. As a result, both unsteady and time-averaged flow fields at the chamber exit are available making possible the simulations of isolated vanes with realistic inlet conditions [18]. This is of particular interest to investigate the key parameters controlling the particles behavior in the passages and impacts on vane walls.

## LES SOLVER AND PARTICLE DYNAMICS

Simulations presented in this work are performed using AVBP, a massively parallel CFD code developed at CERFACS and IFPEN [19]. The code solves the 3D filtered compressible Navier-Stokes equations based on a fully explicit cell-vertex formulation. A two-step time-explicit Taylor-Galerkin scheme (TTG4A) is used for the discretization of the convective terms, which provides fourth-order accuracy in time and third-order accuracy in space [20]. This scheme guaranties low dispersion and

---

<sup>1</sup>FACTOR (Full Aerothermal Combustor Turbine interactiOns Research) is a collaborative European research project co-funded by the European Commission within the 7th Framework Programme (2010-2017) under the Grant Agreement no265985.

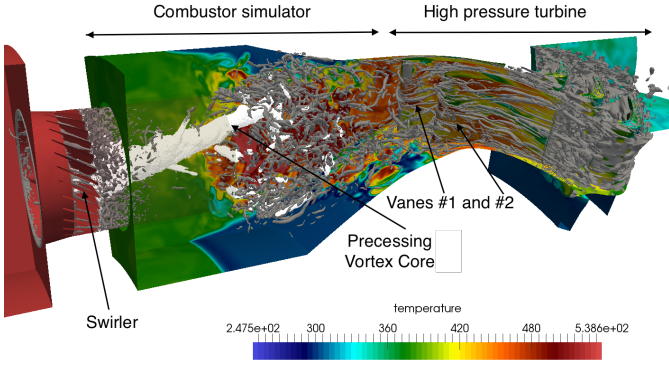


**FIGURE 1:** Periodical domain of the FACTOR combustor simulator and high pressure turbine stage.

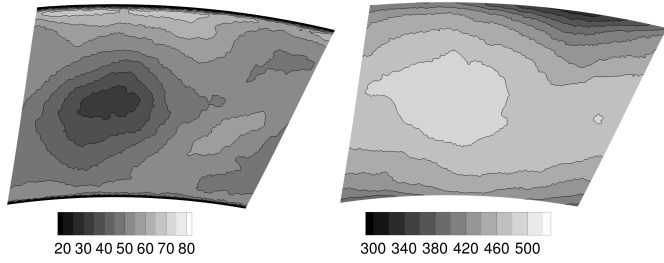


**FIGURE 2:** (Left) Time averaged axial velocity (m/s) and (right) temperature (K) at the combustor / turbine interface [18].

diffusion properties, in agreement with high fidelity LES applications [21]. Diffusive terms are discretized using a second-order Galerkin scheme [22]. The SGS viscosity  $\mu_{SGS}$  is computed using the Smagorinsky model [23]. To ensure linear stability, time marching is performed respecting both CFL condition [24] (convection scheme) and Fourier condition [25] (diffusion scheme).

### Particle dynamics

In this study, the Lagrangian framework is used to solve the particle dynamics. In this approach, point mechanics applies to each individual particle. The gas phase (or carrier phase) is solved in the Eulerian framework and a projection/interpolation procedure is needed to exchange information between the particle coordinate system and the gas phase Eulerian grid. The forces acting on the carrier phase are constructed by taking into account particles in neighboring cells of the Eulerian grid node. Likewise, forces acting on the particle are obtained thanks to interpolation of the gas properties at the particle location. In the context of sand erosion, particle mass is considered constant and gravity is neglected. There is furthermore no mass transfer between the solid and gaseous phases. Additionally, it is assumed that no heat transfer exists between the two phases. The only

coupling that may influence the flow local behavior is hence momentum transfer through drag.

In the Lagrangian formalism, particles are assumed to be rigid spheres with diameter comparable or smaller than the Kolmogorov length scale. If the particle density is much larger than the fluid density ( $\rho_p/\rho \gg 1$ ) then, the forces acting on particles reduce to drag [26, 27]. With the additional assumptions that particles are diluted in the fluid (i.e. number of particles in the domain is small compared to the simulated total volume) with a diameter smaller than the grid size, the particle equations of motion can be written for the position  $x_{p,i}$  as:

$$\frac{dx_{p,i}}{dt} = u_{p,i}, \quad (1)$$

and for the velocity  $u_{p,i}$

$$\frac{du_{p,i}}{dt} = \frac{F_{p,i}}{m_p} = \frac{1}{\tau_p} (u_i - u_{p,i}), \quad (2)$$

where  $F_{p,i}$  is the drag force,  $m_p$  is the mass of the particle and  $u_i$  is the fluid velocity at the position of the particle assuming that the flow field is locally undisturbed by the presence of this particle [27, 28]. As a first approximation, the velocity is assumed to be equal to the interpolation of the filtered velocity at the position of the particle [29–31]. The particle relaxation time noted  $\tau_p$  becomes the Stokes characteristic time

$$\tau_p = \frac{4}{3} \frac{\rho_p}{\rho} \frac{d_p}{C_D |v_r|}, \quad (3)$$

where the local instantaneous relative velocity between the particle and the surrounding fluid is  $v_{r,i} = u_{p,i} - u_i$ ,  $\rho$  and  $\rho_p$  are respectively the fluid and particle densities and  $d_p$  is the particle diameter. The local drag coefficient  $C_D$  is expressed as [32]

$$C_D = \frac{24}{Re_p} \left[ 1 + 0.15 Re_p^{0.687} \right], \quad (4)$$

where the particle Reynolds number  $Re_p$  is defined by

$$Re_p = \frac{|v_r| d_p}{\nu} \leq 800, \quad (5)$$

where  $\nu$  is the kinematic viscosity of the gas phase.

In a two-way coupling approach, the particles are influenced by the local gaseous phase as described previously and particle physical properties also affect the flow fields. A local averaging procedure of the particle properties is used to alter the local

gaseous flow behavior. The averaged drag force in a fluid control volume  $\Delta V$  corresponding to a cell of the mesh in which are located  $N$  particles is expressed as:

$$F_{d,i} = \frac{1}{\Delta V} \sum_{n=1}^N \Psi_n(x_p)(F_{p,i})_n \quad (6)$$

with  $\Psi_n(x_p)$  is a grid dependent interpolation function. The weights in the projection operation are inversely proportional to the distances between the particle and the nodes of the containing cell. This calculated force term is then used as a source term in the fluid momentum equations.

Finally, three types of boundary conditions are used in the presented computations for the particles: injection at inlet, exit at outlet and elastic rebound on walls.

### Impact metrics

A brief study of erosion mechanism shows that this phenomenon is highly dependent on the particle impact velocity, angle, particle mass (linked to the diameter) and concentration, as well as the physical properties of the particles and the impacted wall. For the purpose of erosion predictions, four physical quantities of specific interest are extracted on wall boundaries from the LES predictions:

- $\beta_I$ : the number of impacts per unit wall surface,
- $U_I$ : the averaged velocity of the impacting particles,
- $\theta_I$ : the average angle  $\theta$  between the particle velocity vectors  $\vec{u}_p$  and the wall normal  $\vec{n}$  (Fig. 3):

$$\theta = \arcsin \frac{\vec{u}_p \cdot \vec{n}}{|\vec{u}_p| \cdot |\vec{n}|}, \quad (7)$$

- $D_I$ : the averaged diameter of the impacting particles on the walls.

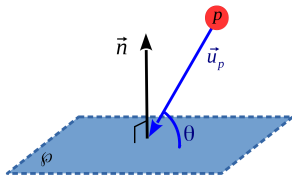


**FIGURE 3:** Definition of particle impact velocity and impact angle.

These four quantities defined for the Lagrangian particles are then projected on the wall Euler mesh nodes when particles

impact. The weights used for the projection are inversely proportional to the distance between the particle and the wall grid nodes of the cells in which particles are identified as impacting.

## NUMERICAL SETUP

### Geometry and associated mesh

The studied geometry contains the two uncooled Nozzle Guide Vanes (NGVs) of the 18 degrees periodic domain of the FACTOR configuration (Fig. 4). The vane inlet Reynolds number based on the vane axial chord (40 mm) and inlet velocity is about 106.000 while the outlet vane Reynolds number is about 424.000 for a Mach number of 0.96. The inlet of the domain located at about half an axial chord upstream of the NGVs corresponds to the interface between the combustor and the turbine. This plane has been intensively studied experimentally and numerically allowing to directly impose boundary conditions at this location. Note that the outlet is placed sufficiently distant from the NGV trailing edges to reduce the impact of boundary conditions on the flow developing around the blades (6 axial chords downstream of the vanes).

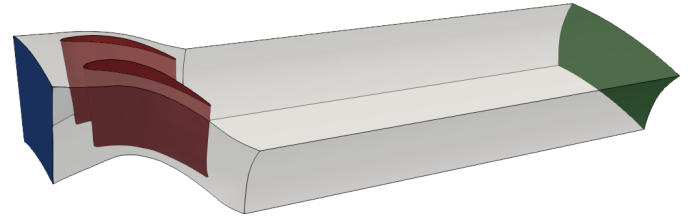


**FIGURE 4:** Two NGVs from the FACTOR configuration.

The mesh contains 32 million tetrahedral cells with a refinement around the two NGVs as shown on Fig. 5. The resulting wall resolution is around  $y^+ = 40$ .

### Boundary conditions

Two reference two-way coupling computations are performed which differ by their inlet boundary conditions. For the first reference simulation, named in the following *Ref 1*, temporal unsteady data obtained from an integrated combustion chamber/turbine simulation is imposed at the inlet of the domain. The data was stored at a frequency of 50 kHz over a period of 40 ms corresponding to more than 40 flow through times of the vane passage. Based on this database, mass flow ( $\rho u$ ,  $\rho v$  and  $\rho w$ ) and temperature are imposed at each inlet node of the mesh at the acquisition frequency of 50 kHz. The 2D-inlet solutions

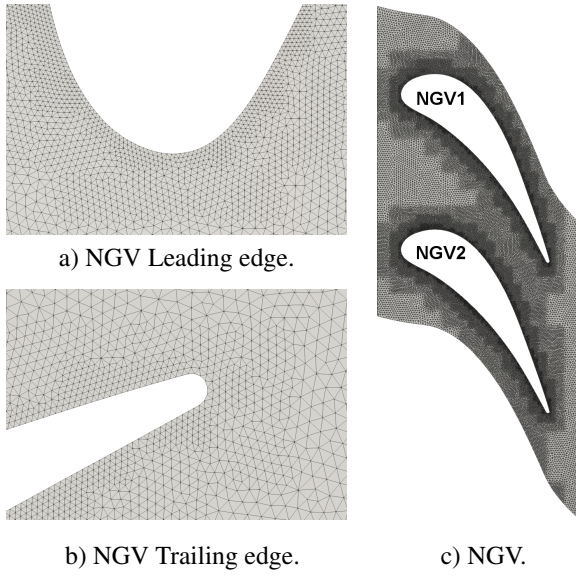


**FIGURE 5:** Visualisations of the unstructured mesh.

are imposed using Navier-Stokes characteristic boundary conditions [33] with a high relaxation parameter to guarantee the matching between boundary condition values and stored data. Concerning the second reference simulation, denoted as *Ref 2*, time-averaged data obtained by the integrated combustor / turbine simulation is imposed as a steady inlet through mass flow ( $\rho u$ ,  $\rho v$  and  $\rho w$ ) and temperature. This inlet condition corresponds to a steady swirling hotspot generated by the combustion chamber (Fig 2). In these two reference simulation a mean mass flow of about 0.235 kg/s is injected leading to a mean Mach number of 0.14. Particles are injected at the inlet plane with a velocity equal to the fluid local velocity. For both cases, the positions of injection are chosen randomly at the inlet plane and evolve in time. The consequence for simulation *Ref 1* is that the injection velocities vary in time with the same frequency used for the fluid: *i.e.* 50 kHz. Overall injected particle diameters follow a log-normal distribution with a mean diameter of 24  $\mu\text{m}$  and a variance of 16  $\mu\text{m}$  (Fig. 6). Particle concentration and density are set to 20  $\text{g}/\text{m}^3$  and  $\rho_p = 2700 \text{ kg}/\text{m}^3$ , respectively, which represents approximately 460.000 particles every convective time. The resulting Stokes numbers of the particles defined by:

$$St = \frac{\tau_p}{\tau_{conv}} \quad (8)$$

where  $\tau_{conv}$  is a convective time scale estimated by the ratio of the particle diameter  $d_p$  and the mean inlet velocity in the domain, are larger than 10 000. As a results, particles are dominated by their inertia rather than being tracers of fluid streamlines.

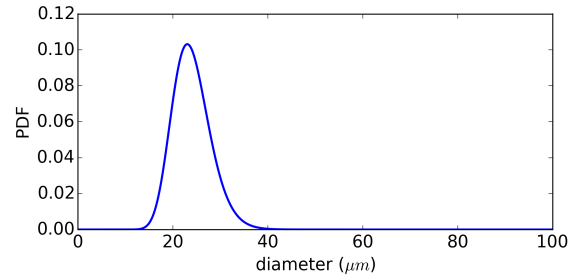


**FIGURE 6:** Probability density function of injected particle diameters.

In both simulations, constant pressure of 87.000 Pa is imposed at the outlet with Navier-Stokes characteristic boundary conditions accounting for transverse terms [34, 35]. Walls are considered adiabatic and a log-law wall model is imposed in accordance with the near wall mesh resolution [36]. Finally, axi-periodicity is applied for the two lateral sides of the domain.

## REFERENCE TWO-WAY COUPLING LARGE-EDDY SIMULATIONS

In this section, the flow topologies obtained by the two reference simulations are first described in terms of unsteady and time-averaged features. Then the effect of the inlet conditions on particle transport and impact on walls are analyzed.

### Flow field description

The differences between reference simulations are clearly illustrated when looking at coherent structures on instantaneous fields as shown in Fig. 7 and Fig. 8. *Ref 1* appears to have multiple vortex structures in the vein due to the unsteady inlet injecting a large range of eddies in the domain. On the contrary, coherent structures are only sparse for *Ref 2* and mainly due to secondary flow generated by the leading edge of the vanes as well as by end-walls and the wakes of the blades: horseshoe vortex (1)&(1'), passage vortex (2), vortex generated by the interaction of the swirl with leading edge of vane 1 (3) [37], induced vortex (4) and wake (5). Depending on the particle characteristics, these coherent eddies of different sizes and strengths can drastically impact the dynamics of the particles (depending on their Stokes number) and thus the impacts on the walls.

Figure 9a presents the mean flow features in the simulation *Ref 1* in terms of total pressure and total temperature at mid-span of the vane passages. Note all the statistics have been obtained by time-averaging the simulations over more than 10 flow through times. The total pressure remains almost constant throughout the domain (Fig 9a). A slight decrease is observed in the wake of both NGVs due to losses in this region. The hotspot injected at the inlet of the domain appears clearly when looking at the time-

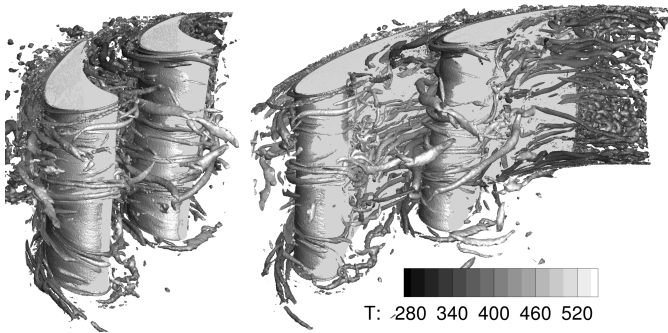


**FIGURE 7:** Q-criterion isosurface ( $4 \cdot 10^8$ ) colored by static temperature on instantaneous solution for *Ref 1*.

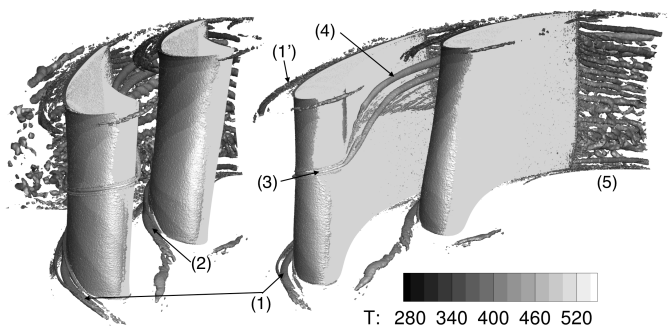
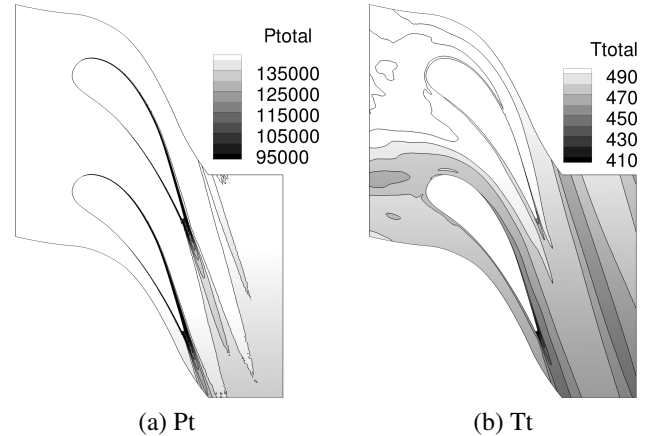


**FIGURE 8:** Q-criterion isosurface ( $4 \cdot 10^8$ ) colored by static temperature on instantaneous solution for *Ref 2*.

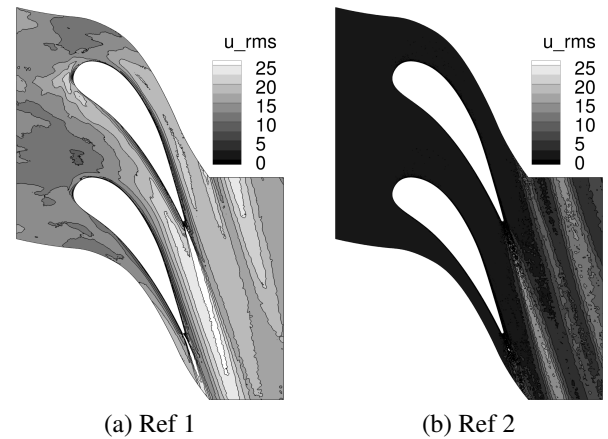
averaged total temperature (Fig. 9b). The hot spot impacts NGV 1 with a total temperature higher than 490 K. The difference between the spatially averaged values of total temperature at inlet and outlet is approximately zero as the fluid is not exchanging any work with the fixed NGVs.

Figure 10 shows a comparison of axial velocity fluctuations  $u_{x,RMS}$  at mid-span of the passage for simulations *Ref 1* and *Ref 2*. For computation *Ref 1*, the contour clearly presents a high level of velocity fluctuations generated by the unsteady boundary condition imposed at the inlet. On the contrary, the velocity fluctuations of *Ref 2* are approximately zero at the inlet. Only small fluctuations are produced because of instabilities appearing in the wake of both NGVs.

Flow expansions in the vane passages are quantitatively compared on Fig. 11 with the time-averaged pressure distribution at mid-span of NGVs 1 and 2 for simulations *Ref 1* and 2. The flow is smoothly accelerated on the first half of pressure sides, followed by a more important increase of the velocity. As expected, the suction sides experience a more pronounced acceleration of the flow until  $x = -0.044$  m followed by a recompression of the flow until the trailing edge. Due to the clocking with respect to the inlet hot spot, it is worth noting that the expansion



**FIGURE 9:** Total pressure and temperature at mid-span of the vane passage for simulation *Ref 1*.



**FIGURE 10:** Axial velocity fluctuations  $u_{x,RMS}$  at mid-span of the passages for the two reference simulations.

on the first half of the pressure sides presents some differences for the 2 NGVs, the stagnation pressure of NGV 2 being more important. Both simulations *Ref 1* and *Ref 2* provide the same expansion for the two NGVs confirming that the same operating points are simulated. Moreover, this indicates that the inlet condition does not alter much the first order moment of the mean aerodynamic field as already discussed in [17].

The wall shear stresses induced by the different flow features on the 2 NGVs for both reference simulations are presented on Fig. 12. To ease the observations, NGV skins are unwrapped. Coordinates for which  $x > 0$  correspond to the blade pressure side and  $x < 0$  to the blade suction side. The global patterns of wall friction are similar for the 2 NGVs of each reference simulation and seems to be controlled by the acceleration / deceleration zones evidenced previously by the pressure distributions

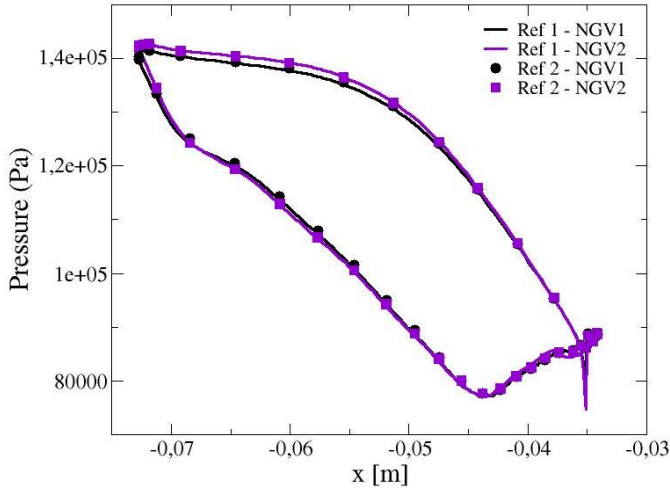


**FIGURE 11:** Pressure distribution at mid-span of NGVs 1 and 2 for simulations *Ref 1* and 2.

around the blades (Fig. 11). On the 2 vanes, computation *Ref 2* exhibits localized strong streaks on the suction sides due to secondary vortices mainly originating from hub and shroud close to leading edge. These structures migrate radially along the passage. At mid-span, the shear stress pattern also features a strong footprint of the coherent structure visible on the instantaneous visualisation depicted on Fig. 8 (item 3). These marked traces obtained with computation *Ref 2* point out that coherent structures are steady while they are disturbed by the incoming turbulent flows in simulation *Ref 1* yielding smoother patterns.

This section has illustrated the differences and similarities in terms of turbulent activity on instantaneous as well as on time-averaged fields between reference simulations with steady and unsteady inlet conditions. All these unsteady and mean flow topologies are susceptible to influence the transport of particles in the passages and thus the distribution of impacts on walls. The following section compares the results in term of particle impact on walls for these two reference cases.

### Wall impact statistics

To highlight regions where the number of particle impacts is important, the number of impact per unit of wall surface  $\beta_I$  for the first reference computation is presented in Fig. 13. The average is calculated over 11 convective times. The majority of impacts are localized on the pressure side of the blade due to preferential migration of the flow. A high accumulation of impacts is observed at the leading edge of both NGVs linked to a direct impact of incoming particles in this stagnation zone. It is worth noting that less particles impact NGV 1 at mid-span than NGV 2 due to a centrifugation of the particles by the swirl motion imposed at the inlet. On the pressure side, regions around the

casing and shroud concentrate an important number of impacts which can be related to secondary flow structures described previously. Concerning the suction side, the number of impacts is close to zero. The flow accelerates along the suction side and does not impact the NGVs. As a result, the particle trajectories are mainly parallel to the walls.

Figure 14 presents the number of particle impacts per unit of wall surface  $\beta_I$  for the two NGVs of *Ref 2*. The global topology of the impact distribution is almost the same as in *Ref 1* with a larger number of impacts close to leading edges and in given regions of the pressure side governed by secondary flow structures. Nonetheless, important differences exist concerning the amplitude and spread of the metric. Higher and more concentrated levels are obtained with simulation *Ref 2* than with *Ref 1* which exhibit more diffuse patterns. Two main phenomena linked to either the fluid or the particle parts can explain these differences: the unsteady injection of particles used in case *Ref 1* and not in *Ref 2* or the turbulent fluid inlet in *Ref 1* which creates a large range of flow structures in the domain not present in the second case. To discriminate the effect of the particle injection and the carrier flow on impact topology, the next section proposes to use mean steady fluid fields to perform one-way coupled simulations of wall particle impacts.

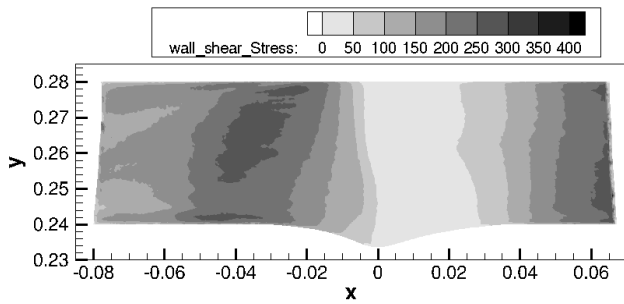
## ONE-WAY COUPLING RESULTS

### Cases details

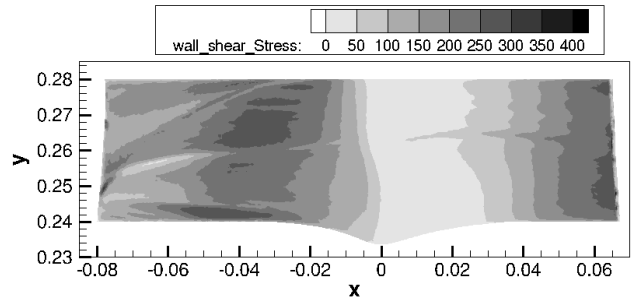
To analyze the effect of the carrier flow field as well as to assess the potential benefits of a LES compared to a time-averaged simulation, four cases are compared in this section. The first two cases correspond to the two reference simulations introduced previously. The two other cases, namely *Froz 1* and *Froz 2* are simulated in a one-way coupling approach for particles with a frozen fluid as carrier. The mean fluid field for *Froz 1* (*Froz 2* respectively) is obtained from a time-average of the LES with unsteady inlet *Ref 1* (steady inlet *Ref 2* respectively) during 30 convective times. In the one-way approach, the fluid acts on the particles but the particles have no impact on the fluid. Note that in simulation *Froz 1*, the injection of particles is kept unsteady with injection velocities performed in the same way as in case *Ref 1*.

### Results

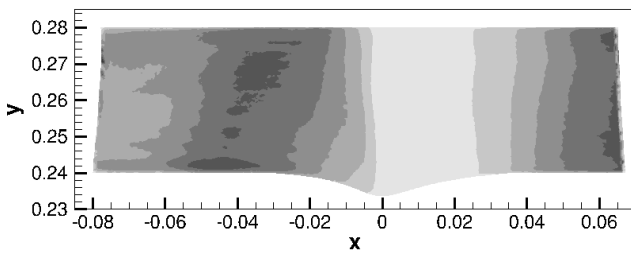
Figure 15 presents the unwrapped contours of averaged number of impacts per unit of wall surface  $\beta_I$  for NGV1 and NGV2 for the frozen computations. For both NGVs, it is clear that simulations *Froz 1* and 2 are very similar to their associated reference. The regions with high concentration of particle impacts are identical and  $\beta_I$  values are comparable between *Ref 1* and *Froz 1* (*Ref 2* and *Froz 2* respectively). Hence, LES gives



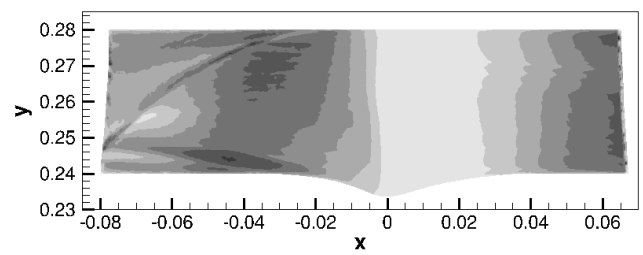
(a) *Ref 1* - NGV1



(b) *Ref 2* - NGV1

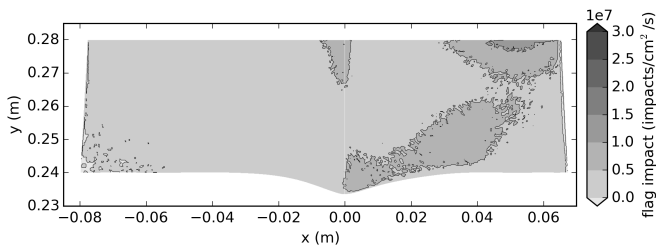


(c) *Ref 1* - NGV2

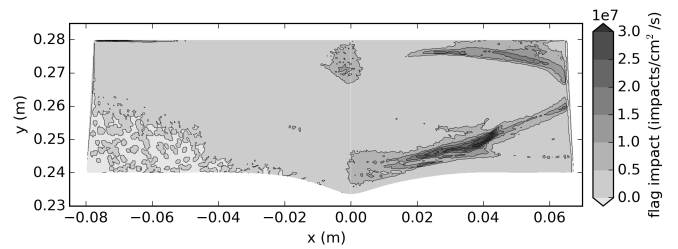


(d) *Ref 2* - NGV2

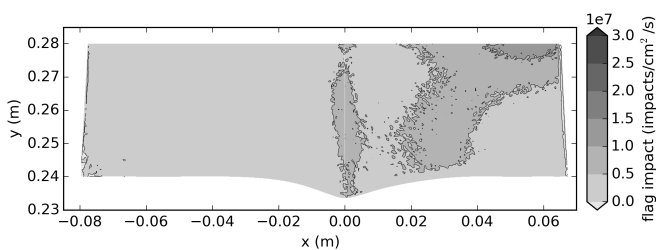
**FIGURE 12:** Wall shear stress on NGV skins for simulations *Ref 1* and *Ref 2*.



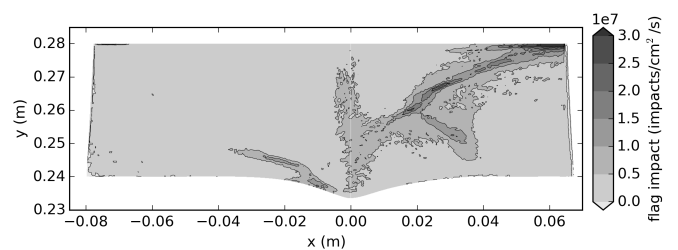
(a) NGV1



(a) NGV1



(b) NGV2



(b) NGV2

**FIGURE 13:** Time-averaged number of impacts per unit of wall surface  $\beta_I$  (impacts/cm<sup>2</sup>/s) on unwrapped NGVs of simulation *Ref 1*.

**FIGURE 14:** Time-averaged number of impacts per unit of wall surface  $\beta_I$  (impacts/cm<sup>2</sup>/s) on unwrapped NGVs of simulation *Ref 2*.

similar results compared to a frozen fluid simulation in terms of particle impact locations. However, the condition imposed at the inlet (unsteady or steady) strongly influences these locations. With a steady inlet, the impacted regions are more pronounced (*Ref 2* and *Froz 2*). On the contrary, with an unsteady inlet, particle impacts are widespread and maximum values are significantly reduced (*Ref 1* and *Froz 1*).

To precisely compare the four cases, the number of impacts per unit of wall surface  $\beta_I$  is plotted along the chord at 3 constant blade heights (10%, 50% and 90%) for NGV1 and NGV2 (Fig. 16 and Fig 17). Similarly to the unwrapped contours, coordinates with  $x > 0$  correspond to the blade pressure side and  $x < 0$  to the blade suction side. Regarding the evolution of  $\beta_I$ , the observations are in agreement with the contours presented above. Simulation *Ref 1* and *Froz 1* are found to provide results almost identical. A minor discrepancy appears close to the trailing edge on the pressure side of NGV1 for  $0.45 < x < 0.6$ . Likewise, the comparison between *Ref 2* and *Froz 2* shows a good match. The peak positions are well retrieved by the frozen fluid case and the maximum values are in line with the reference.

These results demonstrate that for this configuration and for the injected particle diameters and density, the mean field seems to be sufficient to accurately reproduce particle impact contours on the blade surfaces. This is true for both steady and unsteady inlets. On the other hand, the injection and inlet profile conditions (steady or unsteady) strongly influence the impact distributions. In the case of an unsteady inlet, the velocity fluctuations tend to spread the particle impacts. On the other hand, for a steady inlet, the impacts are far more concentrated. Note that such conclusions hold for the particular case considered: *i.e.* small loading of sand particles and small particle sizes. These conclusions would need to be further investigated in the case of larger particles and/or larger loadings for which the impact of the particle on the flow is to be expected. Such issues are however out of the scope of the present study and can now be considered on the basis of the available tool.

## CONCLUSIONS AND OUTLOOK

Large-Eddy Simulations with Lagrangian formalism have been assessed as a tool to predict relevant transport and impact of particles within a turbomachinery configuration, namely a high pressure nozzle guide vane. A particular light has been shed on the importance of a correct injection of flow characteristics at the inlet, *i.e.* relevant unsteadiness, in comparison with the common practice of steady flow *e.g.* in RANS simulations. The injection and inlet profile conditions (steady or unsteady) strongly influence the impact distributions on the vane walls. On the one hand in the case of an unsteady inlet, the velocity fluctuations tend to spread the particle impacts. On the other hand, for a steady inlet, the impacts are far more concentrated. Note that such conclusions hold for the particular case considered: *i.e.* small load-

ing of sand particles and small particle sizes. These conclusions would need to be further investigated in the cases of larger particles and/or larger loadings for which the impact of the particle on the flow is to be expected. To reduce the CPU cost, the strategy to advance in time Lagrangian particles from a previously computed time-averaged LES has also been investigated. Results show no major difference compared to a fully two-way coupling Eulerien-Lagrangian unsteady simulation. The impact distribution on the vanes are rather similar. This solution may pave the way to do sensitivity analysis of the transported phase, density and spatial distribution at the inlet, for a marginal CPU cost (in comparison with a two-way coupling LES).

## ACKNOWLEDGMENT

This work was granted access to the HPC resources of CINES under the allocation 2018-A0042A06074 made by GENCI.

## REFERENCES

- [1] Tabakoff, W., 1984. "Turbomachinery performance deterioration exposed to solid particulates environment". *Journal of Fluids Engineering*, **106**(2), pp. 125–134.
- [2] Tabakoff, W., 1987. "Compressor erosion and performance deterioration". *ASME Journal of Fluids Engineering*, **109**, pp. 297–306.
- [3] Dunn, M. G., Baran, A. J., and Miatech, J., 1996. "Operating of gas turbine engines in volcanic ash clouds". *ASME Journal of Engineering for Gas Turbines and Power*, **118**, pp. 724–731.
- [4] Hamed, A., and Tabakoff, W., 1990. "Jet engines performance deterioration". *International Congress of Fluids Mechanics 3 RD 1990 Proceeding*, **2**.
- [5] Finnie, I., 1960. "Erosion of surfaces by solid particles". *Wear*, **3**(2), pp. 87–103.
- [6] Bitter, J. G. A., 1963. "A study of erosion phenomena. Part II". *Wear*, **6**(3), pp. 169–190.
- [7] Neilson, J. H., and Gilchrist, A., 1968. "Erosion by a stream of solid particles". *Wear*, **11**(2), pp. 111–122.
- [8] Grant, G., and Tabakoff, W., 1975. "Erosion prediction in turbomachinery resulting from environmental solid particles". *AIAA Journal of Aircraft*, **12**(5), pp. 471–478.
- [9] Bacci, T., Caciolli, G., Facchini, B., Tarchi, L., Koupper, C., and Champion, J.-L., 2015. "Flowfield and temperature profiles measurements on a combustor simulator dedicated to hot streaks generation". In *ASME Turbo Expo 2015: Turbine Technical Conference and Exposition*, no. GT2015-42217.
- [10] Krumme, A., Tegeler, M., and Gattermann, S., 2019. "Design, integration and operation of a rotating combustor-turbine-interaction test rig within the scope of the ec fp7

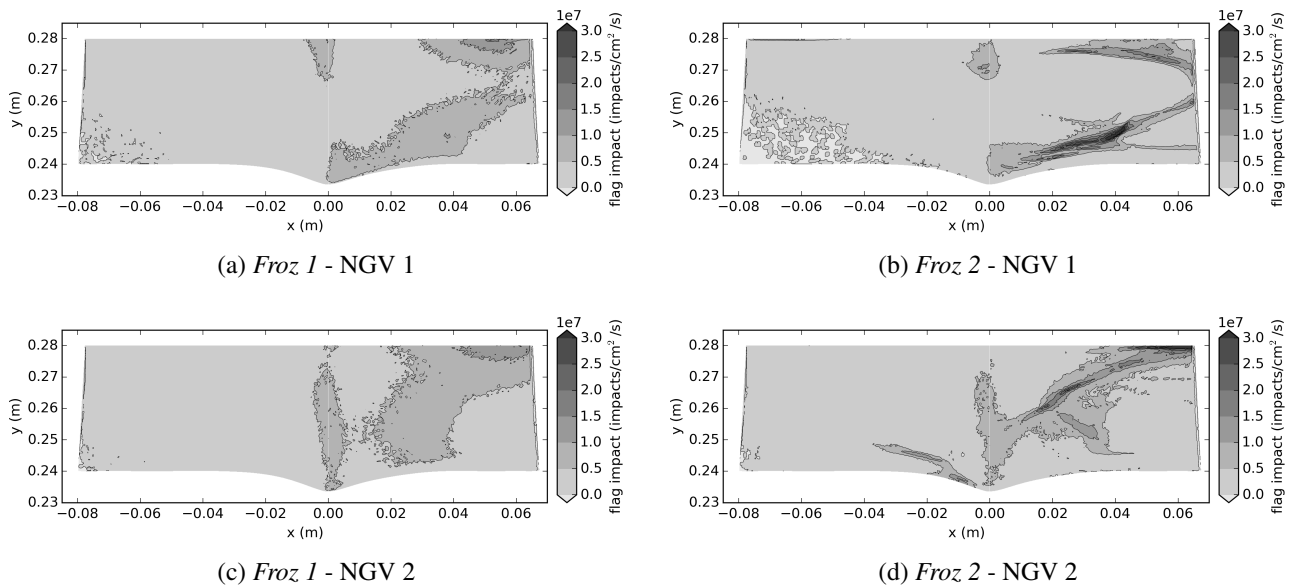


**FIGURE 15:** Time-averaged number of impacts per unit of wall surface (impacts/cm<sup>2</sup>/s) on unwrapped NGVs of simulations *Froz 1* and *Froz 2*.

- project FACTOR”. In Proceedings of 13th European Conference on Turbomachinery Fluid Dynamics & Thermodynamics ETC13.
- [11] Koupper, C., Gicquel, L., Duchaine, F., Bacci, T., Facchini, B., Picchi, A., Tarchi, L., and Bonneau, G., 2015. “Experimental and numerical calculation of turbulent timescales at the exit of an engine representative combustor simulator”. *Journal of Engineering for Gas Turbines and Power*, **138**(2), 09, pp. 021503–021503.
- [12] Andreini, A., Facchini, B., Insinna, M., Mazzei, L., and Salvadori, S., 2015. “Hybrid RANS-LES modeling of a hot streak generator oriented to the study of combustor-turbine interaction”. In ASME Turbo Expo 2015: Turbine Technical Conference and Exposition, no. GT2015-42402.
- [13] Koupper, C., Gicquel, L., Duchaine, F., and Bonneau, G., 2015. “Advanced combustor exit plane temperature diagnostics based on large eddy simulations”. *Flow, Turbulence and Combustion*, **95**(1), pp. 79–96.
- [14] Andreini, A., Bacci, T., Insinna, M., Mazzei, L., and Salvadori, S., 2016. “Hybrid RANS-LES modeling of the aerothermal field in an annular hot streak generator for the study of combustor-turbine interaction”. In SME Turbo Expo 2016: Turbine Technical Conference and Exposition, no. GT2016-56583.
- [15] Andreini, A., Bacci, T., Insinna, M., Mazzei, L., and Salvadori, S., 2018. “Modelling strategies for the prediction of hot streak generation in lean burn aeroengine combustors”. *Aerospace Science and Technology*, **79**, pp. 266 – 277.
- [16] Cubeda, S., Mazzei, L., Bacci, T., and Andreini, A., 2018. “Impact of predicted combustor outlet conditions on the aerothermal performance of film-cooled hpt vanes”. *ASME. J. Eng. Gas Turbines Power*(In press).
- [17] Duchaine, F., Dombard, J., Gicquel, L., and Koupper, C., 2017. “On the importance of inlet boundary conditions for aerothermal predictions of turbine stages with large eddy simulation”. *Computers & Fluids*, **154**, pp. 60–73.
- [18] Thomas, M., Duchaine, F., Gicquel, L., and Koupper, C., 2018. “Impact of realistic inlet condition on les predictions of isolated high pressure vanes”. In 12th International Symposium on Engineering Turbulence Modelling and Measurements (ETMM12).
- [19] Schoenfeld, T., and Rudgyard, M., 1999. “Steady and unsteady flow simulations using the hybrid flow solver avbp”. *AIAA journal*, **37**(11), pp. 1378–1385.
- [20] Colin, O., and Rudgyard, M., 2000. “Development of high-order taylor–galerkin schemes for LES”. *Journal of Computational Physics*, **162**(2), pp. 338 – 371.
- [21] Lamarque, N., 2007. “Schémas numériques et conditions limites pour la simulation aux grandes échelles de la combustion diphasique dans les foyers d’hélicoptère.”. *PhD Thesis, Université de Toulouse*.
- [22] Colin, O., Benkenida, A., and Angelberger, C., 2003. “3d modeling of mixing, ignition and combustion phenomena in highly stratified gasoline engines”. *Oil & Gas Science*

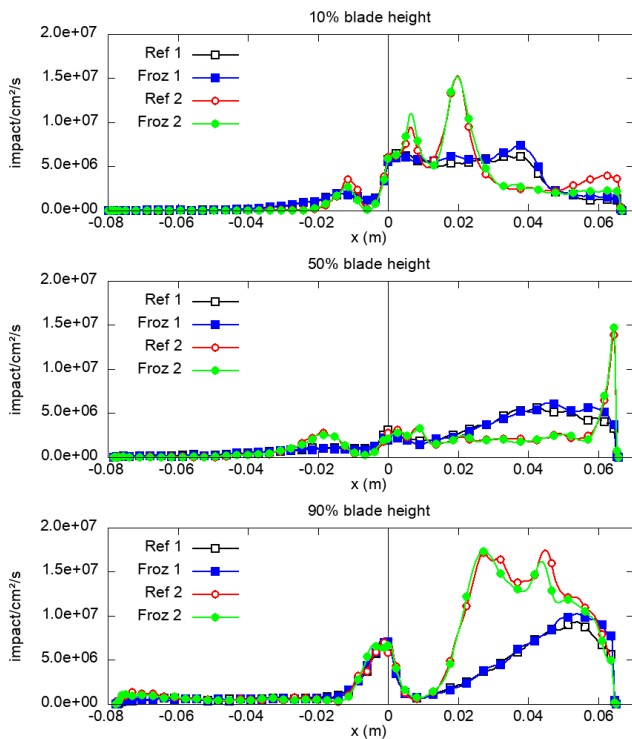


**FIGURE 16:** Time-averaged number of impacts per unit of wall surface  $\beta_I$  (impacts/cm<sup>2</sup>/s) at constant blade heights on unwrapped NGV 1.

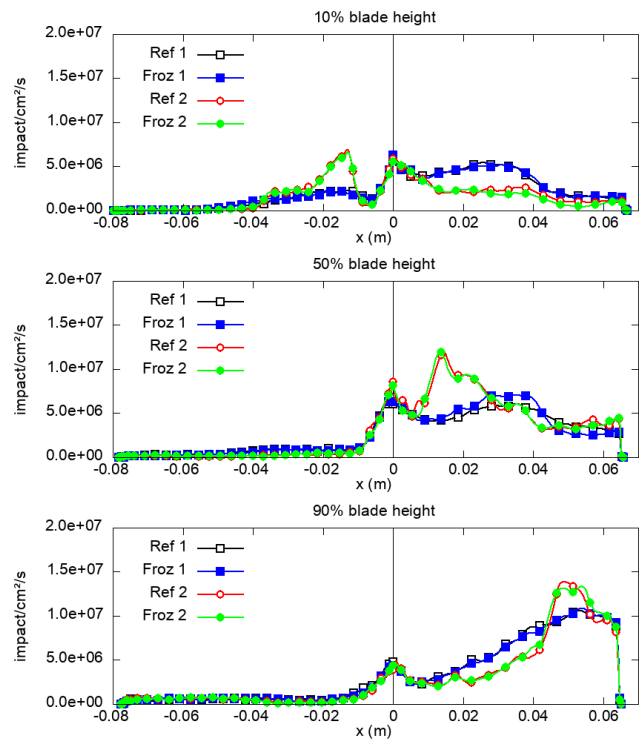


**FIGURE 17:** Time-averaged number of impacts per unit of wall surface  $\beta_I$  (impacts/cm<sup>2</sup>/s) at constant blade heights on unwrapped NGV 2.)

and Technology - Rev. IFP, **58**(1), pp. 47–62.

[23] Smagorinsky, J., 1963. “General circulation experiments with the primitive equations, I. the basic experiment”. *Monthly Weather Review*, **91**, pp. 99–164.

[24] Courant, R., Friedrichs, K., and Lewy, H., 1928. “Über die partiellen differenzgleichungen der mathematischen physik”. *Mathematische Annalen*, **100**(1), Dec, pp. 32–74.

[25] Hirsch, C., 2007. *Numerical Computation of Internal and External Flows*, second edition ed. Butterworth-Heinemann, Oxford.

[26] Maxey, M. R., 1987. “The gravitational settling of aerosol particles in homogeneous turbulence and random flow fields”. *J. Fluid Mech.*, pp. 441–465.

[27] Gatignol, R., 1983. “The faxén formulae for a rigid particle in an unsteady non-uniform stokes flow”. *J. Méc. Théor. Appl.*, pp. 143–160.

[28] Maxey, M., and Riley, J., 1983. “Equation of motion for a small rigid sphere in a nonuniform flow”. *Phys. Fluids*, **26**, 04, pp. 883–889.

[29] Yamamoto, Y., Potthoff, M., Tanaka, T., Kajishima, T., and Tsuji, Y., 2001. “Large-eddy simulation of turbulent gas-particle flow in a vertical channel: Effect of considering

inter-particle collisions”. *Journal of Fluid Mechanics*, **442**, 09, pp. 303–334.

[30] Choi, H. S., and Suzuki, K., 2005. “Large eddy simulation of turbulent flow and heat transfer in a channel with one way wall”. *International Journal of Heat and Fluid Flow*, **26**(5), pp. 681–694.

[31] Apte, S., Mahesh, K., and Lundgren, T., 2003. “An eulerian-lagrangian model to simulate two-phase/particulate flows in complex geometries”. *Center for Turbulence Research, NASA Ames/Stanford Univ.*, **72**, pp. 161–171.

[32] Schiller, L., and Nauman, A., 1935. “A drag coefficient correlation”. *VDI Zeitung* **77**, pp. 318–320.

[33] Poinot, T., and Lelef, S., 1992. “Boundary conditions for direct simulations of compressible viscous flows”. *Journal of Computational Physics*, **101**(1), pp. 104–129.

[34] Granet, V., Vermorel, O., Leonard, T., Gicquel, L., and Poinot, T., 2010. “Comparison of nonreflecting outlet boundary conditions for compressible solvers on unstructured grids”. *AIAA journal*, **48**(10), pp. 2348–2364.

[35] Koupper, C., Poinot, T., Gicquel, L., and Duchaine, F., 2014. “Compatibility of characteristic boundary conditions

with radial equilibrium in turbomachinery simulations”. *AIAA Journal*, **52**(12), pp. 2829–2839.

- [36] Jaegle, F., Cabrit, O., Mendez, S., and Poinso, T., 2010. “Implementation methods of wall functions in cell-vertex numerical solvers”. *Flow, Turbulence and Combustion*, **85**(2), Sep, pp. 245–272.
- [37] Jacobi, S., Mazzoni, C., K., B. R., and Chana, 2017. “Investigation of unsteady flow phenomena in first vane caused by combustor flow with swirl”. *Journal of Turbomachinery*, **139**(4), p. 041006.



# Bibliography

- [1] S. Airbus, “Airbus global market forecast 2018-2037,” Presentation by Eric Schulz, 2018.
- [2] A. Krein and G. Williams, “Flightpath 2050: europe,Äôs vision for aeronautics,” Innovation for Sustainable Aviation in a Global Environment: Proceedings of the Sixth European Aeronautics Days, p. 63, 2012.
- [3] C. Battisti, F. Kost, N. Atkins, W. Playford, M. Orain, G. Caciolli, L. Tarchi, M. Mersinligil, and J. Raffel, “Full aerothermal combustor turbine interaction research,” Proceedings of 2nd EASN WORKSHOP on Flight Physics, 2012.
- [4] A. H. Lefebvre and D. R. Ballal, Gas Turbine Combustion, vol. 1. CRC Press, 2015.
- [5] B. Weigand, J. Köhler, and J. von Wolfersdorf, Thermodynamik kompakt. Springer, 2010.
- [6] D. Papadogiannis, “Coupled large eddy simulations of combustion chamber - turbine interactions,” Ph.D. Thesis, Université de Toulouse, 2015.
- [7] J. Han, S. Dutta, and S. Ekkad, Gas Turbine Heat Transfer and Cooling Technology, Second Edition. Taylor & Francis, 2012.
- [8] M. Harnieh, “Prediction de la generation des pertes des ecoulements compressibles anisothermes appliquee aux distributeurs hautes pressions de turbine avec les simulations aux grandes echelles,” Institut National Polytechnique de Toulouse (INP Toulouse) - Ecole doctorale: Mécanique, Energétique, Génie Civil & Procédés, 2020.
- [9] The Jet Engine. Rolls Royce Technical Publications, 5th edition ed., 2005.
- [10] J.-C. Han and L. M. Wright, “Enhanced internal cooling of turbine blades and vanes,” The Gas Turbine Handbook, DOE, Office of Fossil Energy, National Energy Technology Laboratory, pp. 321–352, 2007.
- [11] F. Duchaine, J. Dombard, L. Y. Gicquel, and C. Koupper, “On the importance of inlet boundary conditions for aerothermal predictions of turbine stages with large eddy simulation,” Computers and Fluids, vol. 154, pp. 60–73, 2017.

- [12] K. Chana, D. Cardwell, and T. Jones, "A review of the oxford turbine research facility," in ASME Turbo Expo 2013: Turbine Technical Conference and Exposition, pp. V03CT14A026–V03CT14A026, American Society of Mechanical Engineers, 2013.
- [13] G. Caciolli, "A close investigation of the aerothermal behaviour of modern aeroengine combustors," PhD Thesis, Università degli Studi di Firenze, 2012.
- [14] T. Bacci, "Experimental investigation on a high pressure ngv cascade in the presence of a representative lean burn aero-engine combustor outflow," PhD Thesis, Università degli Studi di Firenze, 2017.
- [15] C. Koupper, G. Caciolli, L. Gicquel, F. Duchaine, G. Bonneau, L. Tarchi, and B. Facchini, "Development of an Engine Representative Combustor Simulator Dedicated to Hot Streak Generation," Journal of Turbomachinery, vol. 136, no. 11, p. 111007, 2014.
- [16] C. Koupper, "Unsteady multi-component simulations dedicated to the impact of the combustion chamber on the turbine of aeronautical gas turbines," Ph.D. Thesis, Université de Toulouse, 2015.
- [17] A. Krumme, M. Tegler, and G. S., "Design, integration and operation of a rotating combustor-turbine-interaction test rig within the scope of ec fp7 project factor," Proceedings of 13th European Conference on Turbomachinery Fluid Dynamics & Thermodynamics ETC13, pp. 1–13, 2019.
- [18] F. Cottier, P. Pinchaud, and G. Dumas, "Aerothermal predictions of combustor / turbine interactions using advanced turbulence modeling," 13th European Turbomachinery Conference, 2019.
- [19] L. Mazzei, A. Picchi, A. Andreini, B. Facchini, and I. Vitale, "Unsteady cfd investigation of effusion cooling process in a lean burn aero-engine combustor," in ASME Turbo Expo 2016: Turbomachinery Technical Conference and Exposition, pp. V05BT17A008–V05BT17A008, American Society of Mechanical Engineers, 2016.
- [20] S. Cubeda, L. Mazzei, T. Bacci, and A. Andreini, "Impact of predicted combustor outlet conditions on the aerothermal performance of film-cooled high pressure turbine vanes," Journal of Engineering for Gas Turbines and Power, vol. 141, no. 5, p. 051011, 2019.
- [21] S. Vagnoli, T. Verstraete, C. Koupper, and G. Bonneau, "Assessment of rans against les for the aero-thermal behavior of high pressure turbine stages under realistic inlet conditions," in ASME Turbo Expo 2016: Turbomachinery Technical Conference and Exposition, pp. V02CT39A023–V02CT39A023, American Society of Mechanical Engineers, 2016.

- 
- [22] C. Koupper, T. Poinso, L. Gicquel, and F. Duchaine, “Compatibility of Characteristic Boundary Conditions with Radial Equilibrium in Turbomachinery Simulations,” AIAA Journal, vol. 52, no. 12, pp. 2829–2839, 2014.
- [23] C. Koupper, L. Gicquel, F. Duchaine, T. Bacci, B. Facchini, A. Picchi, L. Tarchi, and G. Bonneau, “Experimental and Numerical Calculation of Turbulent Timescales at the Exit of an Engine Representative Combustor Simulator,” Journal of Engineering for Gas Turbines and Power, vol. 138, no. 2, p. 021503, 2015.
- [24] C. Koupper, G. Bonneau, L. Gicquel, and F. Duchaine, “Large eddy simulations of the combustor turbine interface: Study of the potential and clocking effects,” in ASME Turbo Expo 2016: Turbomachinery Technical Conference and Exposition, 2016.
- [25] S. Mendez and F. Nicoud, “Adiabatic Homogeneous Model for Flow Around a Multiperforated Plate,” AIAA Journal, vol. 46, no. 10, pp. 2623–2633, 2008.
- [26] R. Bizzari, D. Lahbib, A. Dauplain, F. Duchaine, S. Richard, and F. Nicoud, “Low order modeling method for assessing the temperature of the multiperforated plates,” International Journal of Heat and Mass Transfer, 2018.
- [27] R. Bizzari, Modélisation aérodynamique et thermique des plaques multiperforées en LES. Phd thesis, Institut National Polytechnique de Toulouse (INP Toulouse) - Ecole doctorale: Mécanique, Énergétique, Génie Civil & Procédés, 11 2018.
- [28] M. Harnieh, M. Thomas, R. Bizzari, J. Dombard, F. Duchaine, and L. Gicquel, “Assessment of a coolant injection model on cooled high-pressure vanes with large-eddy simulation,” Flow, Turbulence and Combustion, Nov 2019.
- [29] C. Koupper, L. Gicquel, F. Duchaine, and G. Bonneau, “Advanced Combustor Exit Plane Temperature Diagnostics Based on Large Eddy Simulations: Going Further than the Radial Temperature Distribution Factor,” Flow, Turbulence and Combustion, vol. 95, no. 1, pp. 79–96, 2015.
- [30] M. Thomas, J. Dombard, F. Duchaine, L. Gicquel, and C. Koupper, “Large Eddy Simulation of combustor and complete single stage high-pressure turbine of the FACTOR test rig,” ASME Turbo Expo 2019: Turbomachinery Technical Conference and Exposition, 2019.
- [31] P. Sagaut and S. Deck, “Large eddy simulation for aerodynamics: Status and perspectives,” Philosophical transactions. Series A, Mathematical, physical, and engineering sciences, vol. 367, pp. 2849–60, 08 2009.
- [32] D. Anderson, J. C. Tannehill, and R. H. Pletcher, Computational fluid mechanics and heat transfer. CRC Press, 2016.

- [33] J. C. Tyacke and P. G. Tucker, “Future use of large eddy simulation in aero,Ä engines,” Journal of Turbomachinery, vol. 137, pp. 081005–081005–16, 08 2015.
- [34] J. G. Koomey, S. Berard, M. Sanchez, and H. Wong, “Implications of historical trends in the electrical efficiency of computing,” IEEE Annals of the History of Computing, vol. 33, no. 3, pp. 46–54, 2011.
- [35] R. E. Moore, “Methods and Applications of Interval Analysis,” SIAM Studies in Applied Mathematics, 1979 edition, 1979.
- [36] A. Jameson, “Computational Fluid Dynamics: Past, Present and Future,” AMS Seminar, p. 78, 2012.
- [37] M. Roser, “Moore’s law: The number of transistors on integrated circuit chips (1971 - 2018),” <https://ourworldindata.org/uploads/2019/05/Transistor-Count-over-time-to-2018.png>, CC BY-SA 4.0, <https://commons.wikimedia.org/w/index.php?curid=79751151>, 2019.
- [38] S. B. Pope, Turbulent Flows. Cambridge Univeristy Press, 2001.
- [39] J. Blazek, Computational fluid dynamics: principles and applications. Butterworth-Heinemann, 2015.
- [40] P. Sagaut, Large eddy simulation for incompressible flows: an introduction. Springer Science & Business Media, 2006.
- [41] P. Sagaut and C. Cambon, Homogeneous turbulence dynamics, vol. 10. Springer, 2008.
- [42] S. Kawai and J. Larsson, “Wall-modeling in large eddy simulation: Length scales, grid resolution, and accuracy,” Physics of Fluids, vol. 24, no. 1, p. 015105, 2012.
- [43] P. Moin, “Advances in large eddy simulation methodology for complex flows,” International journal of heat and fluid flow, vol. 23, no. 5, pp. 710–720, 2002.
- [44] N. Gourdain, L. Gicquel, G. Staffelbach, O. Vermorel, F. Duchaine, J. Bousuge, and T. Poinso, “High performance parallel computing of flows in complex geometries: Ii. applications,” Computational Science & Discovery, vol. 2, no. 1, p. 015004, 2009.
- [45] P. Moin and K. Mahesh, “Direct numerical simulation: a tool in turbulence research,” Annual review of fluid mechanics, vol. 30, no. 1, pp. 539–578, 1998.
- [46] T. Poinso and D. Veynante, Theoretical and numerical combustion. RT Edwards, Inc., 2005.

- 
- [47] M. Gad-el Hak, “Questions in fluid mechanics: Stokes’ hypothesis for a newtonian, isotropic fluid,” Journal of Fluids Engineering, vol. 117, pp. 3–5, 03 1995.
- [48] W. Sutherland, “Lii. the viscosity of gases and molecular force,” The London, Edinburgh, and Dublin Philosophical Magazine and Journal of Science, vol. 36, no. 223, pp. 507–531, 1893.
- [49] A. N. Kolmogorov, “The local structure of turbulence in incompressible viscous fluid for very large reynolds numbers,” in Dokl. Akad. Nauk SSSR, vol. 30, pp. 301–305, JSTOR, 1941.
- [50] J. Boussinesq, Essai sur la théorie des eaux courantes. Imprimerie nationale, 1877.
- [51] J. Smagorinsky, “General circulation experiments with the primitive equations: I. the basic experiment\*,” Monthly weather review, vol. 91, no. 3, pp. 99–164, 1963.
- [52] F. Ducros, F. Nicoud, and T. Poinsot, “Wall-adapting local eddy-viscosity models for simulations in complex geometries,” Conference on Numerical Methods in Fluid Dynamics, pp. 1–7, 1998.
- [53] F. Nicoud and F. Ducros, “Subgrid-scale stress modelling based on the square of the velocity gradient tensor Subgrid-scale stress modelling based on the square of the velocity gradient tensor,” Flow, Turbulence and Combustion, vol. 62, no. 3, pp. 183–200, 1999.
- [54] J. Vanharen, G. Puigt, X. Vasseur, J.-F. Boussuge, and P. Sagaut, “Revisiting the spectral analysis for high-order spectral discontinuous methods,” Journal of Computational Physics, vol. 337, pp. 379 – 402, 2017.
- [55] K. W. Thompson, “Time dependent boundary conditions for hyperbolic systems,” Journal of computational physics, vol. 68, no. 1, pp. 1–24, 1987.
- [56] T. J. Poinsot and S. K. Lele, “Boundary Conditions for Direct Simulation of Compressible Viscous Flows,” Journal of Computational Physics, vol. 101, pp. 104–129, 1992.
- [57] CERFACS, AVBP Handbook - [http://cerfacs.fr/~avbp/AVBP\\_V5.X/HANDBOOK](http://cerfacs.fr/~avbp/AVBP_V5.X/HANDBOOK). CERFACS, 2009.
- [58] T. von Kármán, “Mechanische Ähnlichkeit und Turbulenz,” in AB Sveriges Lifografska Tryckenier, vol. 1, pp. 85–93, 1931.
- [59] E. R. Van Driest, “On Turbulent Flow Near a Wall,” Journal of the Aeronautical Sciences, vol. 23, no. 11, pp. 1007–1011, 1956.
- [60] T. Schoenfeld and M. Rudgyard, “Steady and unsteady flow simulations using the hybrid flow solver AVBP,” AIAA Journal, vol. 37, no. 11, pp. 1378–1385, 1999.

- [61] V. Moureau, G. Lartigue, Y. Sommerer, C. Angelberger, O. Colin, and T. Poinso, “Numerical methods for unsteady compressible multi-component reacting flows on fixed and moving grids,” Journal of Computational Physics, vol. 202, no. 2, pp. 710–736, 2005.
- [62] P. Schmitt, T. Poinso, B. Schuermans, and K. P. Geigle, “Large-eddy simulation and experimental study of heat transfer, nitric oxide emissions and combustion instability in a swirled turbulent high-pressure burner,” Journal of Fluid Mechanics, vol. 570, p. 17, 2007.
- [63] G. Wang, F. Duchaine, D. Papadogiannis, I. Duran, S. Moreau, and L. Y. M. Gicquel, “An overset grid method for large eddy simulation of turbomachinery stages,” Journal of Computational Physics, vol. 274, pp. 333–355, 2014.
- [64] L. Selle, G. Lartigue, T. Poinso, R. Koch, K.-U. Schildmacher, W. Krebs, B. Prade, P. Kaufmann, and D. Veynante, “Compressible large eddy simulation of turbulent combustion in complex geometry on unstructured meshes,” Combustion and Flame, vol. 137, no. 4, pp. 489 – 505, 2004.
- [65] L. Gicquel, G. Staffelbach, and T. Poinso, “Large eddy simulations of gaseous flames in gas turbine combustion chambers,” Progress in Energy and Combustion Science, vol. 38, no. 6, pp. 782 – 817, 2012.
- [66] P. Lax and B. Wendroff, “Systems of conservation laws,” Communications on Pure and Applied mathematics, vol. 13, no. 2, pp. 217–237, 1960.
- [67] O. Colin and M. Rudgyard, “Development of High-Order Taylor-Galerkin Schemes for LES,” Journal of Computational Physics, vol. 162, no. 2, pp. 338–371, 2000.
- [68] P. M. N. Lamarque, “Schémas numériques et conditions limites pour la simulation aux grandes échelles de la combustion diphasique dans les foyers d ’ hélicoptère,” PhD thesis. Université de Toulouse - MeGeP - Dynamique des Fluides, 2007.
- [69] O. Colin, A. Benkenida, and C. Angelberger, “3D Modeling of Mixing , Ignition and Combustion Phenomena in Highly Stratified Gasoline Engines,” Oil I& Gas Science and Technology, vol. 58, no. 1, pp. 47–62, 2003.
- [70] C. Hirsch, Numerical Computation of Internal and External Flows. Butterworth-Heinemann, 2007.
- [71] O. Colin, Large Eddy Simulation of evaporating sprays in complex geometries using eulerian and lagrangian methods. PhD thesis, INSA de Rouen, 2000.
- [72] H. Tennekes and J. L. Lumley, A first course in turbulence. MIT press, 1972.

- [73] A. Nix, A. Smith, T. Diller, W. Ng, and K. Thole, "High intensity, large length-scale freestream turbulence generation in a transonic turbine cascade," in ASME Turbo Expo 2002: Power for Land, Sea, and Air, pp. 961–968, American Society of Mechanical Engineers, 2002.
- [74] A. Chatterjee, "An introduction to the proper orthogonal decomposition," Current science, pp. 808–817, 2000.
- [75] K. Taira, S. L. Brunton, S. T. M. Dawson, C. W. Rowley, T. Colonius, B. J. McKeon, O. T. Schmidt, S. Gordeyev, V. Theofilis, and L. S. Ukeiley, "Modal Analysis of Fluid Flows: An Overview," AIAA Journal, vol. 1452, no. October, pp. 1–29, 2017.
- [76] P. J. Schmid, "Dynamic mode decomposition of numerical and experimental data," Journal of fluid mechanics, vol. 656, pp. 5–28, 2010.
- [77] "Machined and fabricated components for gas turbine engines." <http://palmermfgco.com/>. Accessed: 2018-11-03.
- [78] R. J. Goldstein, "Film cooling," Advances in heat transfer, vol. 7, pp. 321–379, 1971.
- [79] R. Colladay, J. Esgar, and A. Kaufman, "An analysis of the capabilities and limitations of turbine air cooling methods," NASA technical note TN D-5992, 1970.
- [80] S. Colladay, "Importance of combining convection with film cooling," N72- TECHNICAL MEMORANDUM NASA TM X- 67962, 1972.
- [81] A. R. Wadia, "Advanced combustor linear cooling technology for gas turbines," Defence Science Journal, vol. 38, no. 4, pp. 363–380, 1988.
- [82] S. Voigt, B. Noll, and M. Aigner, "Development of a Macroscopic Cfd Model for Effusion Cooling Applications," Proceedings of ASME Turbo Expo 2012, pp. 1–9, 2012.
- [83] A. Burdet, R. S. Abhari, and M. G. Rose, "Modeling of Film Cooling - Part II: Model for Use in Three-Dimensional Computational Fluid Dynamics," Journal of Turbomachinery, vol. 129, no. 2, p. 221, 2007.
- [84] D. Lahbib, "Modelisation aerodynamique et thermique des multiperforations en LES," Ph.D. Thesis, Université de Montpellier, 2015.
- [85] M. Crawford, W. Kays, and R. Moffat, "Full-coverage film cooling - part II: heat transfer data and numerical simulation," Journal of engineering for power, vol. 102, no. 4, pp. 1006–1012, 1980.
- [86] S. D. Hunter, "Source term modeling of endwall cavity flow effects on gaspath aerodynamics in an axial flow turbine," Ph.D.Thesis, U. of Cincinnati, 1998.

- [87] D. Heidmann and D. Hunter, “Coarse Flows Grid Using Modeling Volumetric of Turbine Source Film Terms Cooling,” NASA-TM/2001-210817, no. May, 2001.
- [88] R. Bizzari, D. Lahbib, A. Dauplain, F. Duchaine, L. Gicquel, and F. Nicoud, “A thickened-hole model for large eddy simulations over multiperforated liners,” Flow Turbulence and Combustion, vol. Online First Articles, pp. 1–13, 2018.
- [89] T. Bacci, B. Facchini, A. Picchi, L. Tarchi, C. Koupper, and J.-l. Champion, “Turbulence Field Measurements At the Exit of a Combustor Simulator,” ASME Turbo Expo, pp. 1–14, 2015.
- [90] S. Mendez and F. Nicoud, “Large-eddy simulation of a bi-periodic turbulent flow with effusion,” Journal of Fluid Mechanics, vol. 598, pp. 27–65, 2008.
- [91] H. Baya Toda, O. Cabrit, K. Truffin, G. Bruneaux, and F. Nicoud, “Assessment of subgrid-scale models with a large-eddy simulation-dedicated experimental database: The pulsatile impinging jet in turbulent cross-flow,” Physics of Fluids, vol. 26, p. 075108, jul 2014.
- [92] D. Lahbib, A. Dauplain, F. Duchaine, and F. Nicoud, “Large eddy simulation of conjugate heat transfer around a multi-perforated plate with deviation,” in ASME Turbo Expo 2016: Turbomachinery Technical Conference and Exposition, pp. V05AT10A002–V05AT10A002, American Society of Mechanical Engineers, 2016.
- [93] M. Israeli and S. A. Orszag, “Approximation of Radiation Boundary Conditions,” Journal of Computational Physics 41.1, vol. 20, pp. 115–135, 1981.
- [94] R. Courant, K. Friedrichs, and H. Lewy, “Über die partiellen differenzengleichungen der mathematischen physik,” Mathematische annalen, vol. 100, no. 1, pp. 32–74, 1928.
- [95] M. Harnieh, M. Thomas, R. Bizzari, L. Gicquel, and F. Duchaine, “Assessment of a coolant injection model on cooled high-pressure vanes in large eddy simulation,” 12th International ERCOFTAC Symposium on Engineering Turbulence Modelling and Measurements, 2018.
- [96] L. Andrei, L. Innocenti, A. Andreini, B. Facchini, and L. Winchler, “Film cooling modeling for gas turbine nozzles and blades: Validation and application,” Journal of Turbomachinery, vol. 139, pp. 011004–011004–9, 2016.
- [97] A. Andreini, R. Da Soghe, B. Facchini, L. Mazzei, S. Colantuoni, and F. Turri, “Local source based cfd modeling of effusion cooling holes: Validation and application to an actual combustor test case,” Journal of Engineering for Gas Turbines and Power, vol. 136, pp. 011506–011506–11, 10 2013.

- 
- [98] T. a. d. Kampe and S. Völker, “A model for cylindrical hole film cooling—part ii: Model formulation, implementation and results,” Journal of Turbomachinery, vol. 134, pp. 061011–061011–8, 09 2012.
- [99] J. Dickhoff, K. Kusterer, S. K. Bhaskar, and D. Bohn, “Cfd simulations for film cooling holes: Comparison between different isotropic and anisotropic eddy viscosity models,” in ASME Turbo Expo 2018: Turbomachinery Technical Conference and Exposition, pp. V05AT12A008–V05AT12A008, American Society of Mechanical Engineers, 2018.
- [100] T. E. Dyson, D. G. Bogard, and S. D. Bradshaw, “Evaluation of cfd simulations of film cooling performance on a turbine vane including conjugate heat transfer effects,” International Journal of Heat and Fluid Flow, vol. 50, pp. 279–286, 2014.
- [101] S. Ravelli and G. Barigozzi, “Comparison of rans and detached eddy simulation modeling against measurements of leading edge film cooling on a first-stage vane,” Journal of Turbomachinery, vol. 139, no. 5, p. 051005, 2017.
- [102] P. Sagaut, Large Eddy Simulation for incompressible flows. Scientific computation series, Springer-Verlag, 2000.
- [103] P. Tucker, “Computation of unsteady turbomachinery flows: Part 1 progress and challenges,” Prog. Aerospace Sci., vol. 47, no. 7, pp. 522 – 545, 2011.
- [104] S. Mendez and F. Nicoud, “Adiabatic homogeneous model for flow around a multiperforated plate,” AIAA J., vol. 46, no. 10, pp. 2623–2633, 2008.
- [105] R. Bizzari, M. Férand, A. Dauptain, G. Staffelbach, S. Richard, J.-D. Mueller, T. Ogier, G. Exilard, and F. Nicoud, “Mesh local refinement to enhance effusion cooling models; invited conference,” in 12th International Symposium on Engineering Turbulence Modelling and Measurements (ETMM12) (ERCOFTAC, ed.), (Montpellier (France)), 9 2018.
- [106] T. Bacci, G. Caciolli, B. Facchini, L. Tarchi, C. Koupper, and J.-L. Champion, “Flowfield and temperature profiles measurements on a combustor simulator dedicated to hot streaks generation,” in ASME Turbo Expo 2015: Turbine Technical Conference and Exposition, pp. V05CT17A001–V05CT17A001, American Society of Mechanical Engineers, 2015.
- [107] Y. Peet and S. Lele, “Near field of film cooling jet issued into a flat plate boundary layer: Les study,” Proceedings of the ASME Turbo Expo, vol. 4, 01 2008.
- [108] Z. X. Han, B. Dennis, and G. Dulikravich, “Simultaneous prediction of external flow-field and temperature in internally cooled 3-d turbine blade material,” International Journal of Turbo and Jet Engines, vol. 18, pp. 47–58., 2001.

- [109] E. Garnier, N. Adams, and P. Sagaut, Large eddy simulation for compressible flows. Springer Science & Business Media, 2009.
- [110] T. Poinso and D. Veynante, Theoretical and Numerical Combustion. Third Edition (www.cerfacs.fr/elearning), 2011.
- [111] F. Nicoud and F. Ducros, “Subgrid-scale stress modelling based on the square of the velocity gradient tensor,” Flow, turbulence and Combustion, vol. 62, no. 3, pp. 183–200, 1999.
- [112] N. Gourdain, L. Gicquel, M. Montagnac, O. Vermorel, M. Gazaix, G. Staffelbach, M. Garcia, J. Boussuge, and T. Poinso, “High performance parallel computing of flows in complex geometries: I. methods,” Comput. Sci. Disc., vol. 2, p. 015003, 2009.
- [113] P. Tucker, “Computation of unsteady turbomachinery flows: Part 2 LES and hybrids,” Prog. Aerospace Sci. , vol. 47, no. 7, pp. 546 – 569, 2011.
- [114] T. Poinso and S. Lele, “Boundary conditions for direct simulations of compressible viscous flows,” J. Comput. Phys. , vol. 101, no. 1, pp. 104–129, 1992.
- [115] N. Odier, M. Sanjose, L. Gicquel, T. Poinso, S. Moreau, and F. Duchaine, “A characteristic inlet boundary condition for compressible, turbulent, multispecies turbomachinery flows,” Computers and Fluids, vol. 178, pp. 41–55, 2018.
- [116] V. Granet, O. Vermorel, T. Leonard, L. Gicquel, , and T. Poinso, “Comparison of nonreflecting outlet boundary conditions for compressible solvers on unstructured grids,” AIAA J. , vol. 48, no. 10, pp. 2348–2364, 2010.
- [117] J. Donea and A. Huerta, Finite Element Methods for Flow Problems. New York: John Wiley & Sons Inc, 2003.
- [118] C. Dapogny, C. Dobrzynski, and P. Frey, “Three-dimensional adaptive domain remeshing, implicit domain meshing, and applications to free and moving boundary problems,” Journal of computational physics, vol. 262, pp. 358–378, 2014.
- [119] G. D. et al., “A mesh adaptation strategy to predict pressure losses in les of swirled flows,” Flow Turbulence and Combustion, vol. 99, pp. 93–118, 2017.
- [120] A. Favre, “Statistical equations of turbulent gases,” in Problems of hydrodynamics and continuum mechanics, pp. 231–266, Philadelphia: SIAM, 1969.
- [121] X. Wu, Life prediction of gas turbine materials. INTECH Open Access Publisher, 2010.

- [122] J. R. Schwab, R. G. Stabe, and W. J. Whitney, “Analytical and Experimental Study of Flow Through and Axial Turbine Stage with a Nonuniform Inlet Radial Temperature Profile,” 19th AIAA/SAE/ASME Joint Propulsion Conference, 1983.
- [123] K. S. Chana, J. R. Hurrion, and T. V. Jones, “The design, development and testing of a non-uniform inlet temperature generator for the qinetiq transient turbine research facility,” in ASME Turbo Expo 2003, collocated with the 2003 International Joint Power Generation Conference, pp. 273–280, American Society of Mechanical Engineers, 2003.
- [124] M. D. Barringer, K. A. Thole, and M. D. Polanka, “Experimental Evaluation of an Inlet Profile Generator for High-Pressure Turbine Tests,” Journal of Turbomachinery, vol. 129, no. 2, p. 382, 2007.
- [125] J. B. Nickol, R. M. Mathison, M. F. Malak, R. Rana, and J. S. Liu, “Time-resolved heat transfer and surface pressure measurements for a fully cooled transonic turbine stage,” Journal of Turbomachinery, vol. 137, no. 9, p. 091009, 2015.
- [126] C. M. Cha, S. Hong, P. T. Ireland, P. Denman, and V. Savarianandam, “Experimental and numerical investigation of combustor-turbine interaction using an isothermal, nonreacting tracer,” Journal of Engineering for Gas Turbines and Power, vol. 134, no. 8, p. 081501, 2012.
- [127] D. J. Dorney, K. L. Gundy-Burlet, and D. L. Sondak, “A Survey Of Hot Streak Experiments And Simulations,” International Journal of Turbo and Jet Engines, vol. 16, no. 1, pp. 1–16, 1999.
- [128] T. Povey and I. Qureshi, “Developments in Hot-Streak Simulators for Turbine Testing,” Journal of Turbomachinery, vol. 131, no. 3, p. 31009, 2009.
- [129] C. M. Cha, P. T. Ireland, P. A. Denman, and V. Savarianandam, “Turbulence Levels Are High At the Combustor-Turbine Interface,” Proceedings of ASME Turbo Expo 2012, pp. 1–20, 2012.
- [130] K. S. Hermanson and K. a. Thole, “Effect of Inlet Conditions on Endwall Secondary Flows,” Journal of Propulsion and Power, vol. 16, no. 2, pp. 286–296, 2000.
- [131] M. Thomas, F. Duchaine, L. Gicquel, and C. Koupper, “Advanced statistical analysis estimating the heat load issued by hot streaks and turbulence on a high-pressure vane in the context of adiabatic large eddy simulations,” in ASME Turbo Expo 2017: Turbomachinery Technical Conference and Exposition, American Society of Mechanical Engineers, 2017.
- [132] C. Koupper, G. Bonneau, L. Gicquel, and F. Duchaine, “Large eddy simulations of the combustor turbine interface: Study of the potential and clocking effects,” in ASME Turbo Expo 2016: Turbomachinery Technical Conference

## BIBLIOGRAPHY

---

- and Exposition, pp. V05BT17A003–V05BT17A003, American Society of Mechanical Engineers, 2016.
- [133] S. Jacobi, C. Mazzoni, B. Rosic, and K. Chana, “Investigation of Unsteady Flow Phenomena in First Vane Caused by Combustor Flow With Swirl,” Journal of Turbomachinery, vol. 139, 01 2017. 041006.
- [134] H. P. Wang, S. J. Olson, R. J. Goldstein, and E. R. G. Eckert, “Flow Visualization in a Linear Turbine Cascade of High Performance Turbine Blades,” Journal of Turbomachinery, vol. 119, pp. 1–8, 01 1997.
- [135] W. Liu, Q. Yang, R. Xue, and H. Wang, “Large eddy simulation study of flow dynamics in a multiswirl model combustor at elevated pressure and high temperature,” Journal of Thermal Science and Engineering Applications, vol. 11, no. 6, 2019.
- [136] J. Jeong and F. Hussain, “On the identification of a vortex,” Journal of Fluid Mechanics, vol. 285, no. -1, p. 69, 1995.
- [137] F. Jaegle, O. Cabrit, S. Mendez, and T. Poinsot, “Implementation methods of wall functions in cell-vertex numerical solvers,” Flow, Turbulence and Combustion, vol. 85, no. 2, pp. 245–272, 2010.
- [138] F. Duchaine, J. Dombard, L. Gicquel, and C. Koupper, “Integrated large eddy simulation of combustor and turbine interactions: Effect of turbine stage inlet condition,” Proceedings of the ASME Turbo Expo, vol. 2B-2017, pp. 1–12, 2017.
- [139] G. Wang, F. Duchaine, D. Papadogiannis, I. Duran, S. Moreau, and L. Y. M. Gicquel, “An overset grid method for large eddy simulation of turbomachinery stages,” Journal of Computational Physics, vol. 274, pp. 333–355, 2014.
- [140] A. Piacentini, T. Morel, A. Thévenin, and F. Duchaine, “O-palm: An open source dynamic parallel coupler,” in Proceedings of the IV International Conference on Computational Methods for Coupled Problems in Science and Engineering–Coupled Problems, 2011.
- [141] M. Thomas, L. Gicquel, and C. Koupper, “Comparison of heterogeneous and homogeneous coolant injection models for Large Eddy Simulation of multiperforated liners present in a combustion simulator,” in ASME Turbo Expo 2017: Turbomachinery Technical Conference and Exposition, 2017.
- [142] M. Thomas, F. Duchaine, L. Gicquel, and C. Koupper, “Impact of realistic inlet condition on les predictions of isolated high pressure vanes,” in 12th International ERCOFTAC Symposium on Engineering Turbulence Modelling and Measurements, 2018.
- [143] J. D. Anderson Jr, Fundamentals of aerodynamics. Tata McGraw-Hill Education, 2010.

- [144] “Philipp Grete, postdoctoral research associate in the Department of Physics & Astronomy at Michigan State University.” <https://pgrete.de/images/cascade.jpg>. Accessed: 2018-09-30.